

UC Berkeley

UC Berkeley Electronic Theses and Dissertations

Title

Liquefaction-Induced Building Performance and Near-Fault Ground Motions

Permalink

<https://escholarship.org/uc/item/89d1g8hg>

Author

Hayden, Connor Patrick

Publication Date

2014

Peer reviewed|Thesis/dissertation

Liquefaction-Induced Building Performance and Near-Fault Ground Motions

By

Connor Patrick Hayden

A dissertation submitted in partial satisfaction of the

requirements for the degree of

Doctor of Philosophy

in

Engineering - Civil and Environmental Engineering

in the

Graduate Division

of the

University of California, Berkeley

Committee in charge:

Professor Jonathan D. Bray, Chair

Professor Raymond B. Seed

Professor Douglas S. Dreger

Fall 2014

Liquefaction-Induced Building Performance and Near-Fault Ground Motions

Copyright © 2014

by

Connor Patrick Hayden

Abstract

Liquefaction-Induced Building Performance and Near-Fault Ground Motions

by

Connor Patrick Hayden

Doctor of Philosophy in Engineering – Civil and Environmental Engineering

University of California, Berkeley

Professor Jonathan D. Bray, Chair

Recent earthquakes in Chile, New Zealand, and Japan have re-emphasized the damaging consequences of liquefaction on infrastructure. Due to the complexity of the problem and limited well-documented field case histories, liquefaction-induced building settlements are often estimated using empirical correlations developed for free-field sites on level ground that account for post-liquefaction volumetric strains only. Additional effects due to the presence of a structure are not accounted for with these procedures. The earthquake performance of structures founded on liquefiable ground depends on a complex interaction between the soil properties, the ground motion characteristics, and the structural properties. This thesis presents three related research projects that address aspects of the effects of soil liquefaction including near-fault sites. This research thesis is focused on characterizing and selection of near-fault ground motions, geotechnical centrifuge testing of model buildings affected by liquefaction, and the development of field case histories in Chile following the 2010 Maule, Chile earthquake.

Earthquake ground motions are important in liquefaction-induced building performance. Ground motions in the near-fault region frequently have intense, double-sided pulses in the velocity-time series that can be very damaging to structures; forward directivity is a leading cause of these pulses. However, pulses do not always occur in the forward directivity region, and some pulses are not caused by forward directivity. The present study used a new, automated algorithm to classify a large database of records as pulse or nonpulse motions. A straightforward model was developed to estimate the proportion of pulse motions as a function of closest site-to-source distance and epsilon of the seismic hazard.

Geotechnical centrifuge tests provide valuable insight into the performance of structures affected by liquefaction. An area particularly lacking understanding is the interaction of closely spaced structures subjected to liquefaction. Two well-instrumented centrifuge tests were performed to investigate the response of three types of model structures founded on liquefiable ground in isolated and adjacent configurations. Acceleration, pore water pressure, and settlement measurements indicated that liquefaction-induced settlement of structures depends on a complex interaction of ground motion, soil, and structural characteristics. For the particular scenarios

examined in this study, adjacent structures experienced moderately lower foundation accelerations, tended to tilt away from each other, and settled less than isolated structures.

The 2010, $M_w = 8.8$, Maule, Chile earthquake caused substantial damage, including liquefaction-induced damage to infrastructure and provides an important opportunity to learn from these field case histories. This project focuses on improved characterization of the subsurface conditions using penetration testing (i.e., SPT and CPT) at a hospital and two bridges that suffered liquefaction-induced damage. The recently constructed hospital has 10 structurally isolated wings varying in height from one to six stories, which provides a unique opportunity to examine the differing response of varying wings. Liquefaction of plastic, silty soils at the hospital resulted in differential settlement, whereas liquefaction of clean, medium-dense sandy soils resulted in lateral spreading and damage to bridge piers.

TABLE OF CONTENTS

ACKNOWLEDGEMENTS.....	iii
CHAPTER 1: INTRODUCTION.....	1
1.1 OVERVIEW.....	1
1.2 ORGANIZATION OF THIS THESIS.....	2
CHAPTER 2: SELECTION OF NEAR-FAULT PULSE MOTIONS.....	3
2.1 LITERATURE REVIEW.....	3
2.1.1 Introduction.....	3
2.1.2 Near-Fault Ground Motions.....	4
2.2 DATA.....	5
2.3 PULSE MOTION CLASSIFICATION SCHEME.....	6
2.3.1 Summary.....	6
2.3.2 Record Filtering.....	8
2.3.3 PPV Pulse Identification.....	10
2.3.4 Pulse Motion Classification.....	11
2.3.5 Pulse Period.....	13
2.3.6 FD Scoring.....	14
2.4. PROPORTION OF PULSE MOTIONS.....	15
2.5. SELECTION OF PULSE MOTIONS.....	19
2.6 CONCLUSIONS.....	22
CHAPTER 3: CENTRIFUGE TESTS OF ADJACENT MAT-SUPPORTED BUILDINGS AFFECTED BY LIQUEFACTION.....	26
3.1 INTRODUCTION.....	26
3.2 LITERATURE REVIEW.....	27
3.3 EXPERIMENTAL DESIGN.....	28
3.4 EXPERIMENTAL RESULTS AND DISCUSSION.....	32
3.4.1 Free-Field Soil Response.....	32
3.4.2 Response of Soil under Structures and Structural Settlement.....	34
3.4.3 Structural Tilt and Separation.....	39
3.4.4 Structural Response.....	42
3.5 CONCLUSIONS.....	44
CHAPTER 4: LIQUEFACTION-INDUCED BUILDING PERFORMANCE DURING THE 2010 CHILE EARTHQUAKE.....	46

4.1 LITERATURE REVIEW	46
4.1.1 Liquefaction and Soil-Foundation-Structure Interaction	46
4.1.2 Summary of 2010 Maule, Chile Earthquake.....	48
4.2. TESTING PROCEDURES	51
4.2.1. Cone Penetration Testing.....	51
4.2.2. Standard Penetration Testing and Index Tests.....	54
4.2.3. Overview of Analysis Methods	57
4.3 CASE HISTORIES OF STRUCTURE PERFORMANCE AT LIQUEFACTION SITES	59
4.3.1 Hospital Provincial, Curanilahue.....	59
4.3.1 Juan Pablo II Bridge, Concepción	77
4.3.3 Llacolén Bridge, Concepción.....	85
4.4 CONCLUSIONS.....	89
CHAPTER 5: CONCLUSIONS	90
5.1. SUMMARY.....	90
5.2. FINDINGS.....	90
5.3 RECOMMENDATIONS FOR FUTURE RESEARCH.....	92
REFERENCES	94
APPENDICIES	101

ACKNOWLEDGEMENTS

It has been a great opportunity to learn from and work with many exceptional professors and fellow students throughout the course of my PhD. The research projects presented in this thesis were highly collaborative and would not have been possible the contributions of numerous individuals.

Prof. Jonathan Bray, my thesis advisor, has been especially influential in my development and growth as an engineer and researcher. I am grateful to have had the opportunity to work with him on three diverse and challenging projects. His guidance, collaboration, and support have been essential for the work presented in this thesis.

Professors Raymond Seed and Douglas Dreger served as members of my dissertation committee, and their contribution is appreciated. I am fortunate to have received an NSF Graduate Research Fellowship, which funded me during much of my PhD and allowed increased flexibility to work on a variety of interesting projects. I would also like to thank my undergraduate thesis advisor, Mandar Dewoolkar, because his example, as a teacher and researcher, was a major factor in my decision to attend graduate school in geotechnical engineering.

Prof. Norman Abrahamson was critical in developing the pulse motion research presented in this thesis. Working with him on this research and taking his course has greatly developed my interest in seismic hazard. Ana Luz Acevedo-Cabrera also contributed to the early stages of this research. The use of the NGA-West2 ground motion database through the Pacific Earthquake Engineering Research Center (PEER) is appreciated. Financial support was provided by the ATC-82 project through an Applied Technology Council (ATC)–Consortium of Universities for Research in Earthquake Engineering (CUREE) joint venture sponsored by NIST/National Earthquake Hazards Reduction Program (NEHRP). Any opinions, findings, and conclusions or recommendations expressed in this material are those of the authors and do not necessarily reflect the views of NIST or National Science Foundation.

The centrifuge work presented in this thesis was immensely collaborative. Prof. Bruce Kutter's extensive experience and in-person assistance at the centrifuge was extremely helpful. Jackee Allmond was an invaluable team member throughout the entire process, and without her past centrifuge experience, the test would have been significantly more difficult. The test carried out as part of this thesis built on the results of the test led by Josh Zupan, and he made valuable suggestions and assisted in interpreting and combining the results of the two tests. Isabelle Rawlings was a great help at the centrifuge. The assistance and suggestions of the staff at the Center for Geotechnical Modeling at UC Davis is also appreciated. Tara Hutchinson, Nicholas Trombetta, Gregg Fiegel, Ben Mason, Chandu Bolisetti, A. Whittaker, and R. Reitherman also assisted in various ways, particularly during the planning stages. This research was supported by the National Science Foundation (NSF) under Grant No. CMMI-0830331. Opinions, findings, and conclusions or recommendations expressed in this material are those of the authors and do not necessarily reflect the views of the NSF.

In Chile, Nick Trombetta and Carla B. Serrano W. were valuable teammates. Prof. Christian Ledezma was essential in preparing, planning, and assisting in site access. Prof. Tara Hutchinson also assisted in planning. Numerous people generously cooperated by allowing site access, sharing information, and assisting in other ways. In particular, Paulo Oróstegui generously helped in surveying, and Emerson Figueroa was very patient and flexible while performing SPT energy measurements in the face of SPT rig issues. The Pacific Earthquake Engineering Research Center (PEER) funded this research, and any findings presented in this thesis do not necessarily reflect their views.

Finally, I would like to thank my parents for their unwavering support and encouragement throughout this and many other endeavors.

CHAPTER 1: INTRODUCTION

1.1 OVERVIEW

Recent earthquakes in Chile (Bray et al. 2012), New Zealand (Cubrinovski et al. 2011), and Japan (Tokimatsu et al. 2012) have re-emphasized the damaging consequences of liquefaction on infrastructure. The earthquake performance of structures founded on liquefiable ground depends on the complex interaction between the ground motion, the soil profile, and the structural properties. However, liquefaction-induced building settlements are often estimated using empirical correlations developed for free-field sites on level ground that account for post-liquefaction volumetric strains only; additional effects due to the presence of a structure are not accounted for with these methods (Dashti et al. 2010a). A lack of well-documented liquefaction case histories has made the development of procedures to account for soil-foundation-structure interaction (SFSI) difficult. This thesis includes three research projects that relate to near-fault pulse motions and liquefaction-induced damage to infrastructure.

The February 27, 2010 Chile Earthquake ($M_w = 8.8$) off the coast of central Chile caused damage to a wide area and triggered a damaging tsunami. Although adherence to the strict Chilean building code reduced the overall damage, there were notable failures of key infrastructure. Liquefaction damaged many buildings (Bray et al. 2012) and several bridges (Ledezma et al. 2012). As part of the present study, standard penetration tests (SPT) and cone penetration tests (CPT) were performed at a hospital and two bridges identified by the Geotechnical Extreme Events Reconnaissance (GEER) Association (Ashford et al. 2011) as suffering liquefaction damage. Liquefaction of silty soils underlying the recently constructed hospital in the city of Curanilahue resulted in settlement and internal distortion. The 10 structurally isolated hospital wings, which vary in height from one to six stories, provide an important opportunity to examine the effects of differing structural properties and the interaction of adjacent wings. Liquefaction of medium dense sandy soils at the Juan Pablo II and Llacolén bridges in Concepción led to lateral spreading and pier settlement, which forced the bridges to close until repaired.

Although field case histories provide an important opportunity to learn from past events, geotechnical centrifuge tests have a number of advantages as well. The input ground motion, soil profile, and structural properties are controlled and the response measured with accelerometers, pore pressure transducers, and displacement transducers. Recent centrifuge tests (e.g., Dashti et al. 2010a,b; Allmond and Kutter 2012; da Silva Marques et al. 2014) focused on the response of isolated structures on liquefiable ground in soil-foundation-structure interaction (SFSI). However, in urban environments, structures are frequently quite close to neighboring structures and interact through the soil in structure-soil-structure interaction (SSSI). Mason et al. (2013) and Trombetta et al. (2013) examined SSSI in unsaturated models. The present study used a saturated soil profile with a variety of structural models, in both isolated and adjacent configurations, to examine SSSI as well as key liquefaction mechanisms.

The ground motion at a site also plays an important role in liquefaction-induced settlement of structures. Kramer and Mitchell (2006) suggest that traditional ground-motion intensity measures, such as peak ground acceleration (a_{\max}), are relatively poor indicators of the likelihood of liquefaction triggering. In the near-fault region, pulse motions may occur due to forward directivity or other phenomena. These intense velocity pulse motions can greatly affect the seismic performance of structures (e.g., Alavi and Krawinkler 2000; Anderson and Bertero 1987; Hall et al. 1995). The differing structure and soil response during pulse and nonpulse motions in the centrifuge experiments of this thesis also illustrated the importance of ground motion characteristics. The near fault project in this thesis focuses on providing guidance on an appropriate proportion of pulse motions to include in a suite for time history analysis. However, it also has implications for pulse motions in liquefaction susceptibility assessments.

1.2 ORGANIZATION OF THIS THESIS

The three research projects that comprise this thesis are organized as follows:

- Chapter 2 describes the near-fault ground motion research. This includes a discussion of the causes and consequences of near-fault pulses, the automated classification algorithm, and the model of pulse occurrence based on distance and epsilon. Additional results and guidance on the selection of near-fault pulses in a suite of design ground motions are included.
- Chapter 3 summarizes the final two experiments (i.e., Test-5 and Test-6) in the NEESR Seismic Performance Assessment in Dense Urban Environments project. These experiments examine the interaction between adjacent structures on liquefiable ground. Test-6 was performed as part of this thesis and builds upon the results of Test-5 (Zupan 2014), so it is natural to include a discussion of both tests and summarize the results. A summary of the model layout and test parameters is provided, and key results are presented and discussed.
- Chapter 4 summarizes case histories of liquefaction-induced damage at two bridges and a hospital during the 2010 Chile Earthquake. The subsurface investigation results, primarily from SPT and CPT, are presented and interpreted. The application of simplified liquefaction triggering and settlement correlations illustrate that free-field methods are often not appropriate if a structure is present. Silty, plastic soils at the hospital liquefied causing extensive damage whereas the liquefiable soils at the bridges were clean sands.
- Chapter 5 concludes with an overall summary, key findings, and recommendations for future research.

CHAPTER 2: SELECTION OF NEAR-FAULT PULSE MOTIONS

Chapter 2 is primarily from the following journal article:

Hayden, C., Bray, J., and Abrahamson, N. (2014). "Selection of Near-Fault Pulse Motions." *Journal of Geotechnical and Geoenvironmental Engineering*, ASCE, Vol. 140(7), 04014030.

2.1 LITERATURE REVIEW

2.1.1 Introduction

Earthquake ground motions recorded at small site-to-source distances often have substantially different characteristics than those recorded at larger distances. Sites in the near-fault region may be affected by forward directivity (FD; rupture toward the site) or backward directivity (rupture away from the site). FD frequently results in intense, double-sided pulses that arrive early in the velocity-time series. These intense velocity pulse motions can greatly affect the seismic performance of structures (Alavi and Krawinkler 2000; Anderson and Bertero 1987; Hall et al. 1995). In addition to higher than normal peak ground velocity (PGV) values, the period of the velocity pulse (T_v) in relation to the fundamental period of the structure (T) is important to seismic performance (Anderson and Bertero 1987). Importantly, these intense velocity pulses do not always occur when seismological models indicate that the conditions for generating FD-pulses are optimal. Moreover, pulses can be caused by other near-fault phenomena, including fling step and fault rupture asperities.

When selecting a suite of design ground motions for dynamic analysis, it is the current state of practice (Structural Engineering Institute 2006) that the magnitude, distance, and potentially other key parameters of the selected records are similar to those that control the hazard (e.g., obtained by a probabilistic seismic hazard analysis (PSHA) disaggregation by distance and magnitude). The unique nonstationary characteristics of pulse-like motions can greatly influence structural performance (Anderson and Bertero 1987; Hall et al. 1995). Unfortunately, there is a relative lack of guidance regarding how to best incorporate pulse-like motions into a suite of design ground motions. Often too many or too few pulse-type motions are used in the suite of design ground motions, which can adversely affect the reliability of the evaluation of seismic performance. This study aims at providing guidance regarding deciding how many of the design ground motions should be pulse-like motions and how individual records might be selected. With that in mind, near-fault ground motions from the recently enhanced next-generation attenuation (NGA) West2 ground motion database are classified as either pulse or nonpulse motions using a new classification scheme. Pulse motions are further divided into those that are well explained by FD and those that are not. A straightforward model is developed to estimate the appropriate proportion of pulse motions in the near-fault region. The

resulting equation can be used with the results of a standard PSHA to provide guidance on the appropriate number of pulse-type motions to include in a suite of design ground motions for use in time-history analysis. The identified pulse motions are sorted by pulse period and provided to assist in the selection of appropriate pulse motions. Guidance is provided for selecting pulse records.

2.1.2 Near-Fault Ground Motions

As a fault ruptures toward a site, a rupture velocity that is slightly slower than the shear wave velocity results in the accumulation of the seismic energy released during rupture (Benioff 1955; Ben-Menahem 1961; Somerville et al. 1997). This typically results in an intense double-sided pulse arriving early in the velocity-time series at the recording site. In the backward directivity region, an opposite effect is observed, and recordings generally have long durations but low amplitudes. The radiation pattern of horizontally polarized shear waves (SH waves) has maxima aligned along the strike of the fault, and it is the superposition of SH waves that results in the observed pulse (Archuleta and Hartzell 1981; Somerville et al. 1997). These SH waves are oriented normal to the fault, and as a result, the pulse is also oriented in the fault normal direction. FD can occur on both strike-slip and dip-slip faults. In the case of strike-slip faults, sites located in the direction of fault rupture and near the end of the fault are typically most affected by FD. For dip-slip faults, sites located updip of the rupture plane are most affected by FD.

Somerville et al. (1997) identified relatively simple parameters based on source-site geometry that can be used to estimate the effects of directivity on the response spectra, ratio of fault normal to fault parallel spectra, and duration. A follow-up model by Abrahamson (2000) recommends decreasing the maximum amount of long period spectral amplification estimated from FD for strike-slip earthquakes. Spudich and Chiou (2008) developed a more complex model to estimate the spatial variations of ground motions caused by the effects of directivity. The Spudich and Chiou model (2008) offers several advantages over the older Somerville et al. (1997) model and estimates around half the amplification or deamplification caused by directivity compared with the Somerville et al. (1997) model.

A second near-fault phenomenon that can influence recordings and result in a pulse in the velocity-time series is fling-step. Fling-step is a permanent static displacement caused by tectonic offset. In contrast to the dynamic phenomenon of directivity, which produces a double-sided velocity pulse, fling-step results in a single-sided velocity pulse (integration results in a permanent offset in the displacement-time series). For strike-slip faults, the displacement caused by the fling-step is primarily oriented parallel to the fault, but in dip-slip faults, the displacement is primarily oriented normal to the fault.

Because of directivity, fling-step, and potentially other near-fault phenomena (e.g., fault rupture asperities), the characteristics of near-fault motions often differ significantly from those from more distant recordings. These differences are typically most apparent in the velocity-time series. Near-fault motions are not just scaled up versions of more distant recordings. Bray and

Rodriguez-Marek (2004) identified key parameters in the characterization of FD-pulse motions including its amplitude (PGV), pulse period (T_v), and number of significant cycles. The amplitude of a pulse is often much larger than the median PGV estimated using the NGA ground motion prediction equations (see Abrahamson et al. (2008) for a summary of the NGA models). The period of the pulse is also important to the seismic performance of structures. If the period of the pulse and fundamental period of a structure align, resonance can greatly increase the demands on the structure (Anderson and Bertero 1987). The number of significant cycles (as defined in Bray and Rodriguez-Marek 2004) is also important to structural performance, because a larger number of significant cycles can be more demanding to an inelastic structure. Fortunately, FD typically only produces one or two significant cycles (Bray and Rodriguez-Marek 2004).

Several researchers have identified pulse-like motions using a variety of manual or automatic classification schemes (Bray and Rodriguez-Marek 2004; Shahi and Baker 2011; Zhai et al. 2013). Bray and Rodriguez-Marek (2004) use a largely qualitative classification scheme, to develop a database of motions likely affected by FD. An updated version of this database is contained in Bray et al. (2009). Recent work by Shahi and Baker (2011) also examined the occurrence of near-fault pulses. A wavelet transform procedure (Baker 2007) is used to extract pulse-like signals from velocity-time series, and each recording is then classified as pulse-like or non-pulse-like. Their algorithm is explicit and reproducible, but it contains subjective thresholds, which are unavoidable when classifying ground motions into binary categories of either pulse or nonpulse motions. Using their database of 179 pulse-like motions, Shahi and Baker (2011) developed a model that estimates the probability of observing a pulse-like motion based on several parameters. Modifications are made to a PSHA calculation to include adjustments to account for the characteristics of near-fault ground motions. Zhai et al. (2013) provided a quantitative classification technique based on relative energy of a pulse.

Bradley (2013) stated that the conventional approach wherein one performs a ground motion intensity measure hazard assessment and then separately performs dynamic analysis to calculate engineering demand parameters can underestimate the seismic demand hazard. Thus, he argued for the use of a seismic demand hazard framework in the evaluation of seismic performance rather than the use of a ground motion intensity-based PSHA. Dabaghi et al. (2013) also argued that seismic hazard should be assessed in terms of the response of an inelastic structural model because this better reflects the contribution of pulse-like motions than when defined as a ground motion intensity parameter. However, engineering practice largely defines seismic hazard in terms of ground motion parameters, so this approach is used in this study.

2.2 DATA

All ground motion records and supporting data were from the recently enhanced NGA-West2 database for shallow crustal earthquakes along active plate margins (Ancheta et al. 2012). The database of 21,539 records was sorted to form a subset of records from sites with closest site-to-source distances (R) less than 30 km and moment magnitudes (M_w) greater than 6.0. The

maximum distance was selected to extend slightly beyond the range of distances where near fault pulse motions are of primary importance, as shown subsequently in the paper. Only records with moment magnitudes greater than 6.0 are used to focus on the range of magnitudes that will generally control the hazard in high seismicity regions along active plate margins. Additionally, earthquakes with smaller moment magnitudes are less likely to produce substantial FD and pulses (e.g., in the current study only 9% of records with moment magnitudes between 5 and 6 were classified as pulses compared with 21% for magnitudes greater than 6.0). Lastly, there is precedent in the use of magnitude thresholds of around 6.0 from previous studies (Somerville et al. 1997).

Records missing acceleration-time series for a horizontal component, records with unknown component orientations, or those not used by Abrahamson and Silva (2008a) were excluded from the near-fault ground motion database used in this study. Abrahamson and Silva (2008a) removed motions from unrepresentative earthquakes, records from inside certain building types, duplicated stations, and those missing key metadata (see Abrahamson and Silva (2008b) for a more in depth discussion of excluded motions). The Kobe 1995 Port Island (0 m) record (NGA#1114) was removed because it was influenced by liquefaction. The Landers 1992 Lucerne (NGA#879) record had two slightly nonorthogonal horizontal components (85°), but for this study they were treated as orthogonal. In total, 84 motions were excluded for the reasons mentioned. The resulting ground motion database contained 673 records from 52 earthquakes (see Appendix A-1 for a list of these records).

2.3 PULSE MOTION CLASSIFICATION SCHEME

2.3.1 Summary

The proposed classification scheme identifies pulse motions as records that are dominated by one or two intense cycles of motion in the velocity-time series through the use of an automated algorithm. The philosophy adopted initially was that a fully automated algorithm would always miss important nuances of pulse or nonpulse motions, so that human intervention through the use of expert judgment was not only necessary but desirable. However, with refinement of the automated algorithm, the number of records that were judged to be misclassifications became small, and the key trends in the data and resulting model were unaffected by whether a fully automated classification scheme was used. Hence, a fully automated pulse motion classification scheme was developed. A large number of records can be automatically classified efficiently using the software *MATLAB 2011b* and the proposed algorithm, which is available at <https://sites.google.com/site/connorphayden/>. The algorithm is also contained in Appendix A-2.

Examination of pulse records led to the development of an improved ground motion parameterization of near-fault ground motions. Peak-to-peak velocity (PPV) is the difference between the two peaks in one cycle of motion, as shown in Fig. 2.1(a). PPV is used as the measure of the amplitude of the ground motion in this study instead of PGV, because FD theoretically produces two-sided velocity pulses, and two-sided pulses can be more damaging

than one-sided pulses (Kalkan and Kunnath 2006). The two as-recorded horizontal components of the Imperial Valley 1979 Brawley Airport record, which are shown in Fig. 2.2, illustrate the benefits of using PPV instead of PGV. In this case (and in several other cases), the PGV of Component 225 shown in Fig. 2.2(a) is smaller than the PGV of the orthogonal component shown in Fig. 2.2(b) (i.e., 37 versus 41 cm/s). However, Component 225 is more damaging to structures with its two-sided velocity pulse as opposed to the one-sided pulse of Component 315. The PGV in Component 225, which is nearly in the fault-normal direction, is only slightly less than the PGV of the Component 315, which is nearly in the fault-parallel direction. However, Component 225 displays the characteristic two-sided pulse of a FD motion. Its larger PPV is significantly larger than that of Component 315 (i.e., 64 versus 51 cm/s). PPV better captures one of the key attributes of velocity-pulse motions, and it better reflects the potential of the ground shaking to cause damage. Thus, PPV is used to describe near-fault pulse motions.

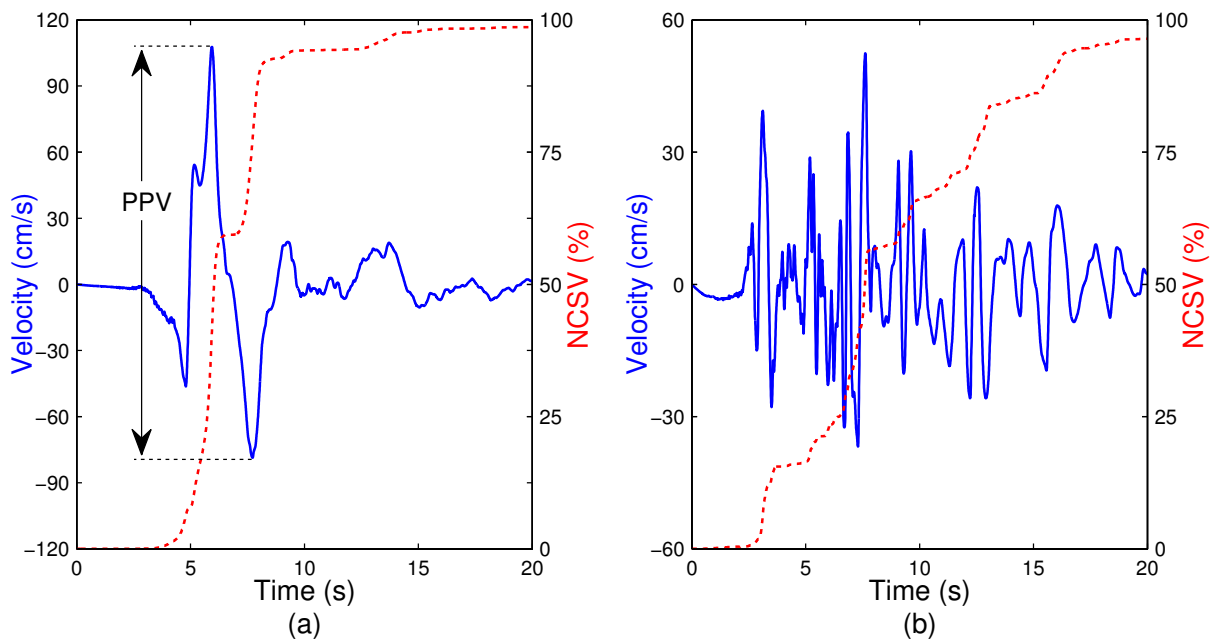


Fig. 2.1. (a) Pulse-like recording of Imperial Valley 1979 El Centro Array 7 (NGA#182); (b) non-pulse-like recording of Imperial Valley 1979 Bonds Corner (NGA#160)

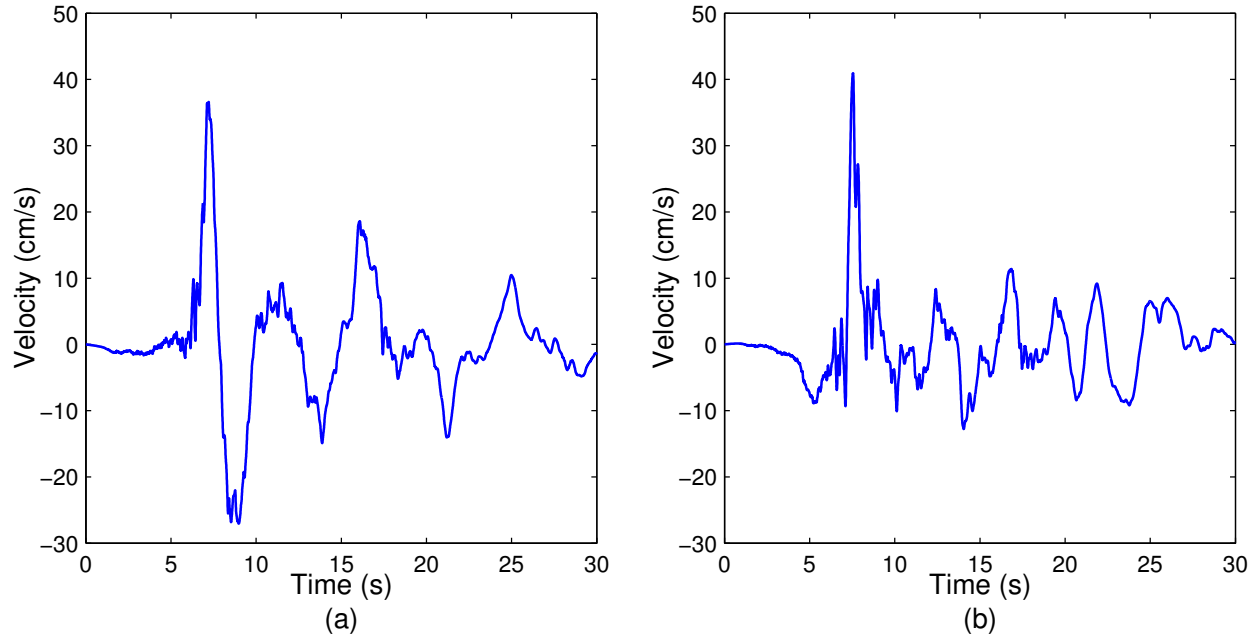


Fig. 2.2. Imperial Valley 1979 Brawley Airport record (NGA#161), as-recorded components with azimuths of (a) 225 and (b) 315

The normalized cumulative squared velocity (NCSV) at a given time in a record is the sum of the squared velocities at each preceding time increment normalized by the sum of the squared velocities of the entire record. The NCSV of a record increases from 0 to 100% and rapidly increases during intervals of high velocity relative to the rest of the record. For example, the NCSV parameter increases rapidly during the pulse shown in Fig. 2.1(a), whereas NCSV increases gradually for the nonpulse motion shown in Fig. 2.1(b). NCSV is thus a useful parameter to include in a pulse classification scheme along with PPV. Zhai et al. (2013) use a similar parameter in their pulse classification scheme.

2.3.2 Record Filtering

Each time series was filtered using a low-pass, three-pole, causal Butterworth filter (NIST 2011). Filtering allowed the focus to be placed on the velocity-dominated range of the record, which contains the primary velocity pulse. Additionally, removing erratic high-frequency content improved the classification results. The pulse periods in this study varied from less than a second to more than 10 s, so using a constant cutoff frequency for all records would be inappropriate. An individual cutoff frequency for each motion was automatically calculated using the following steps:

1. The orientation that maximized the ratio of the PGV of one component to the PGV of the other orthogonal component was calculated.

2. The pseudospectral velocity (5% damping) of the record rotated to the orientation from Step 1 was calculated at 0.05-s period increments for a range of natural periods from 0.5 to 10.0 s (or if less than 10.0 s, the maximum usable period from the NGA flatfile was the upper limit).
3. The median spectral velocities were estimated using the equally weighted NGA ground motion prediction equations of Abrahamson and Silva (2008a), Boore and Atkinson (2008), Campbell and Bozorgnia (2008), and Chiou and Youngs (2008). Linear interpolation was used to estimate the median prediction at 0.05-s increments.
4. The pulse period was estimated as the period that maximized the ratio of the velocity spectrum of the record (Step 2) to the median NGA velocity spectrum (Step 3).
5. The acceleration-time series was filtered using a corner period of one-third the estimated pulse period from Step 4. The corner period of 40 of the 673 records was adjusted slightly to produce acceptable results for these records.

An example of the estimated pulse period is shown in Fig. 2.3 for the Imperial Valley 1979 Brawley Airport record. The solid line shows the ratio of the two spectra and reaches its maximum at a period of 4.7 s. A corner period of $4.7/3 = 1.57$ s (a frequency of 0.64 Hz) was then used to filter the record.

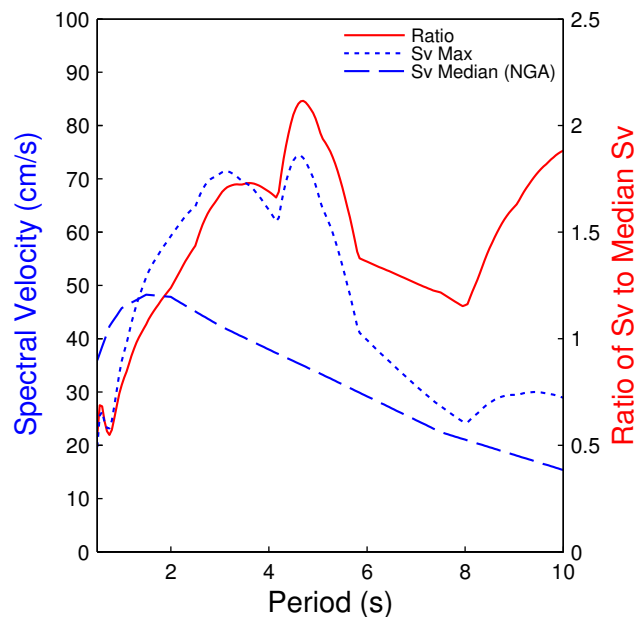


Fig. 2.3. Example of the period estimate used in filtering the Imperial Valley 1979 Brawley Airport record (NGA#161)

2.3.3 PPV Pulse Identification

After filtering the acceleration-time series, the orthogonal components were integrated to velocity-time series and then rotated through all possible orientations at 1° increments. At each orientation, the largest PPV pulse was identified along with other relevant parameters. The algorithm is outlined in the following steps, and an illustration is provided in Fig. 2.4.

1. Identify the zero crossings and the peak velocity of each half-cycle between each pair of zero crossings.
2. Identify the significant half-cycles with a peak velocity that exceeds a threshold of 25% of the difference between the maximum and minimum (i.e., largest negative) velocities of the entire record. There are three significant half-cycles indicated by 1a, 1b, and 1c in Fig. 2.4.
3. Adjacent significant half-cycles are considered associated if the time difference separating them is less than a threshold of the average half-period (from zero crossings) of the two adjacent significant half-cycles. Half-cycle 1c is not associated with 1b in Fig. 2.4, because the average of 2a and 2b is less than 2c.
4. The PPV is calculated for each pair of adjacent, associated half-cycles.
5. The two adjacent, associated half-cycles that have the largest PPV form the primary velocity pulse. The primary velocity pulse is indicated by 3a in Fig. 2.4 and has a PPV of 58 cm/s.
6. The additional half-cycles associated with the PPV pulse are those adjoining the PPV pulse as outlined in Step 3. There are no additional half-cycles associated with the PPV pulse, so the number of associated cycles is 1.0. However, if the additional half-cycle labeled 1c was closer to the PPV pulse, then it would be associated and the number of associated cycles would have been 1.5.
7. The values of the NCSV at the last zero crossing of the primary velocity pulse and the first zero crossing are calculated. The difference between these two values is the NCSV-difference. In Fig. 2.4, the value of NCSV at the last (labeled 4b) and first (labeled 4a) zero crossing of the primary velocity pulse is 0.628 and 0.004, respectively, and the NCSV-difference is 0.624.

The NCSV-difference is an indication of the pulse-like nature of a record. When the NCSV increases significantly during the largest pulse of a record, it suggests that this pulse is substantially larger than the other cycles of motion in the record. The number of additional half-

cycles associated with the primary velocity pulse also indicates the pulse-like nature of a record. If several half-cycles are associated with the primary velocity pulse, the motion is less pulse-like and more similar to an ordinary nonpulse motion.

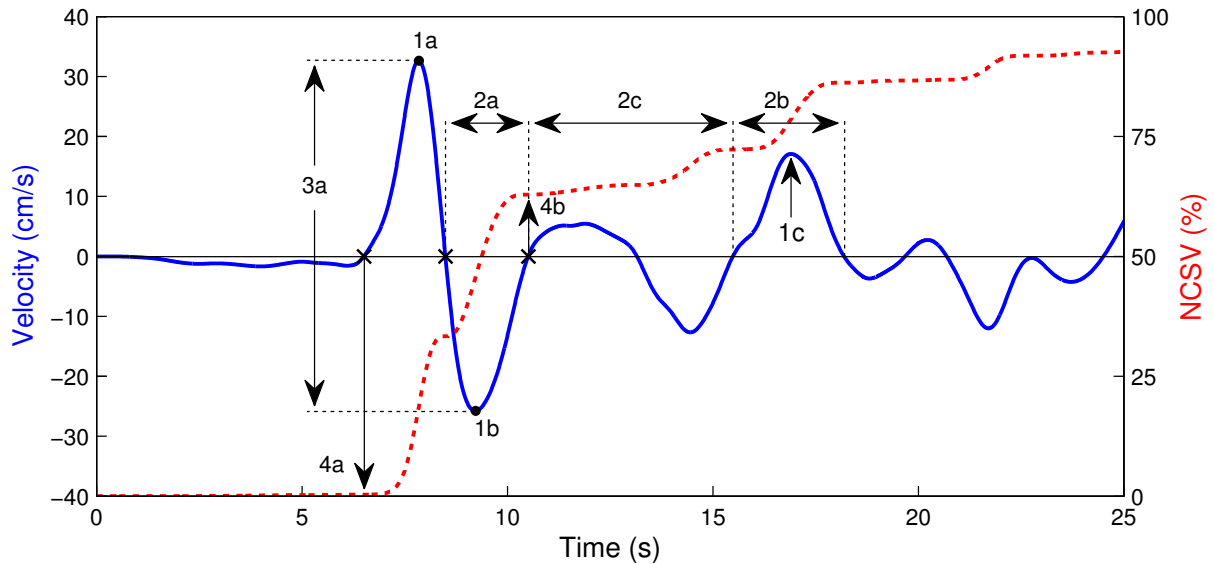


Fig. 2.4. Example of the steps in the PPV algorithm for the Imperial Valley 1979 Brawley Airport record

2.3.4 Pulse Motion Classification

Several classification schemes were initially considered before converging on the proposed scheme. It became apparent that a composite score of several relevant criteria results in a more robust classification than using any single criterion alone or a series of discriminating thresholds. For example, requiring all pulse motions to have a NCSV-difference greater than a set value and simultaneously have a number of significant cycles less than a second threshold will result in some motions being classified as nonpulse because they just slightly did not meet the subjective threshold for one factor even though they far surpassed the threshold for the second factor. By scoring each record on two criteria and then combining the scores, a record that would have been just barely below one threshold but far above the second will actually score higher than a less pulse-like motion that only slightly exceeds the thresholds for both separate criteria. Additionally, a screening criterion that required the PPV of a record to be greater than 25 cm/s to be considered a pulse was established to remove records with low amplitude velocity-time series where a long period signal is picked up by the filtering algorithm and results in an unreasonable classification. The PPV threshold of 25 cm/s is set low enough that it does not interfere with the classification of legitimate pulses.

Scores in an individual category range from 0 to 100%. In the case of NCSV-difference, motions with a NCSV-difference greater than 0.7 scored 100% and motions with a NCSV-

difference below 0.5 scored 0%. Motions between 0.5 and 0.7 received a score that transitioned linearly from 0 to 100%. For example, the Brawley Airport record had a NCSV-difference of 0.624, so the NCSV score is 62%. A similar taper was used to score the number of associated significant cycles. Records with 1.5 cycles or less scored 100%, those with two cycles scored 50% and those with 2.5 or more cycles scored 0%. The Brawley Airport record had only one significant associated cycle, so it scored 100%. The scores from the two factors with equal weighting (50% each) results in an overall pulse score of 81%.

The results of the proposed pulse classification scheme were compared with the existing pulse databases of Shahi and Baker (2011) and Bray and Rodriguez-Marek (2004). Fig. 2.5(a) shows the proportion of motions (of the 380 records that overlap with this study) classified as pulses by Shahi and Baker (2011) or FD by Bray and Rodriguez-Marek (2004) as a function of NCSV-difference. The data shown were binned by NCSV-difference, and the proportion of motions that were classified as pulses was calculated for each bin. As the NCSV difference increased, it was more likely that a given record had been classified as a pulse. Logistic regression, which is appropriate for binary data, resulted in a similar trend also shown in Fig. 2.5(a). Fig. 2.5(b) is a similar plot based on the number of significant cycles associated with the primary velocity pulse. As the number of significant cycles increased for a given record, it was less likely to have been classified as a pulse in the two existing classification databases. Several alternate parameters that could also be used to classify pulses were considered, but this relatively simple combination of NCSV-difference and number of significant cycles worked best.

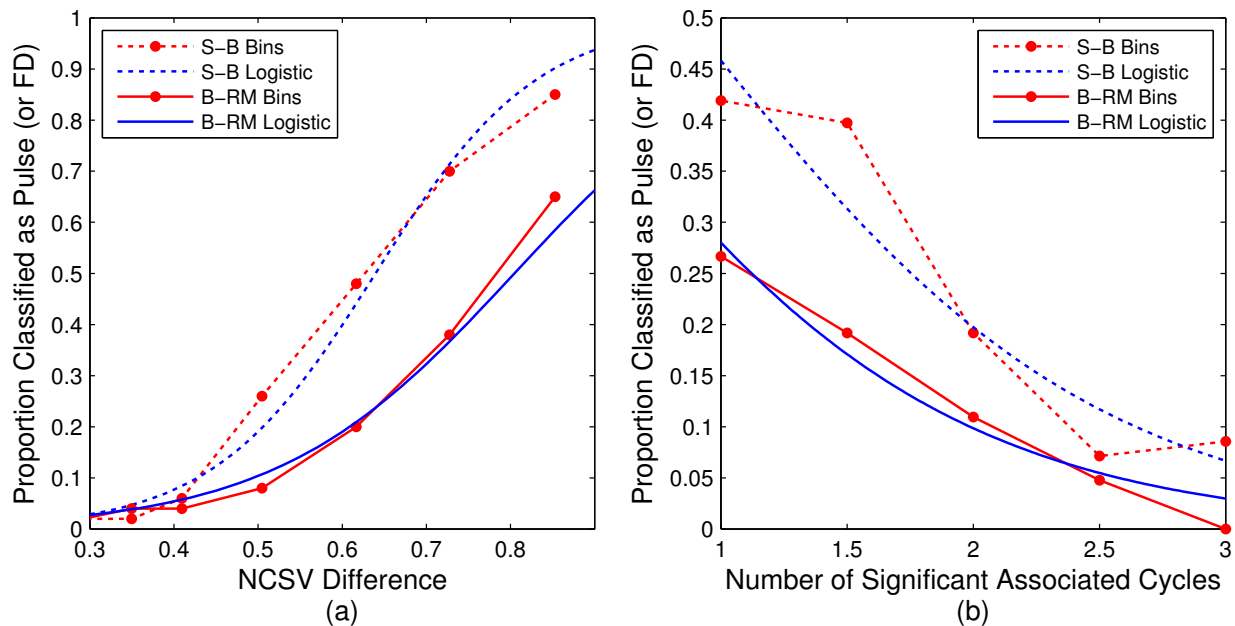


Fig. 2.5. Proportion classified as pulses by Shahi and Baker (2011) (S-B) or forward directivity by Bray and Rodriguez-Marek (2004) (B-RM) as a function of (a) NCSV-difference and (b) number of significant associated cycles

The 673 motions in the near-fault database were sorted by their pulse classification score, and a threshold of 60% in the score was selected to best mark the transition from pulse to nonpulse motions. Above a score of 60%, most of the motions appeared visually pulse-like, and most records appeared to be non-pulse-like below 60%. A subjective threshold is unavoidable in any classification scheme that categorizes something as complex as a velocity-time series into binary categories. However, by using a threshold in the composite score, the effectiveness of the classification scheme was greatly improved compared with using thresholds on individual parameters. Through the proposed classification scheme, 141 records had scores greater than the 60% and were classified as pulse motions.

Table 2.1 presents the final set of near-fault pulse motions. As noted previously, manual intervention was not used so that the scheme could be used by others and produce reproducible results. Four of the 673 records were believed to be misclassified, but reclassifying this small set of records did not influence the results of this study. However, the use of an individual motion within a suite of just seven records, for example, can be important. For this reason, it is noted that four records were classified as pulse-like, but in the authors' opinion, they are best not used in practice as near-fault pulse motions. Some of these motions include late arriving pulses that are likely caused by other non-near-fault phenomena, such as site effects, which should be considered separately from this study. Additionally, three near-fault motions that were not classified as pulse motions, but possess the key traits of a pulse motion, were added to Table 2.1 to provide a larger number of motions from which to select. These motions are also noted in Table 2.1. The total number of near-fault pulse motions is 144. As a comparison, Shahi and Baker (2011) identified 179 pulse motions using their algorithm with the NGA-West1 database. Several of these motions were recorded at distances greater than 30 km from the source, so their pulse characteristics were caused by other factors such as site and basin effects. Hence, these particular motions should not be used in a suite of design motions to represent near-fault pulse effects.

2.3.5 Pulse Period

The pulse period of each pulse motion was estimated with an approach similar to that used to estimate the period of the pulse in the filtering process. The only modification is that the motion is rotated to the maximum PPV orientation (instead of the maximum PGV ratio) prior to calculating the spectral velocities. The pulse period is the period that maximized the ratio of the spectral velocity of the PPV pulse to the median spectral velocity from the NGA models. Several other methods of identifying the pulse period were also investigated. These methods included using the period associated with the maximum spectral velocity, the ratio of the spectral velocity of the two orthogonal components, or the zero crossings of the pulse in the velocity-time series. However, these alternate methods did not prove to be as effective. The pulse motions are grouped by the period of the primary pulse in the velocity-time series in Table 2.1. Engineers

should select pulse records from the motions listed in Table 2.1 that cover the period range of interest for the structure being analyzed.

2.3.6 FD Scoring

Another scoring system was developed to quantify the number of pulse motions that could be explained potentially by FD. The isochrone directivity predictor (IDP) proposed by Spudich and Chiou (2008) was used as one factor in the FD score. The IDP takes into account the rupture and site geometry and is used to estimate the directivity amplification (or deamplification) of the spectral acceleration obtained from the NGA ground motion prediction equations as a function of period, closest distance, and magnitude. Higher IDP values indicate higher expected amplification caused by directivity. Although it depends on the period, magnitude, distance, and the particular NGA model used, IDP values of around 1.5 mark the transition from backward directivity deamplification to FD amplification. A second parameter used in the FD score was the PGV ratio. Researchers such as Somerville et al. (1997) have noted that FD records tend to have high ratios of PGV in the fault-normal to fault-parallel directions because of the superposition of SH waves that cause FD. The final parameter used in the FD score was the orientation of the maximum PPV pulse. Because of the physical processes that lead to FD, the pulse is expected to be oriented near fault-normal. The approach was similar to that used in calculating the pulse score and again used a linear transition between the two values subsequently listed for each parameter:

1. Value of IDP (100% > 2, 0% < 1.5). Weighted as 60% of the FD score.
2. Value of the maximum PGV ratio (100% > 2.2, 0% < 1.7). Weighted as 25% of the FD score.
3. Deviation of the orientation of the PPV pulse from fault-normal (100% < 30°, 0% > 50°). Weighted as 15% of the FD score.

Of the 141 records classified as pulses, 74 received FD scores greater than 60% and were considered likely to have been caused by FD. These motions will be referred to as FD-pulses. The remaining 67 motions that had been classified as pulses had FD scores lower than 60% and in this study were considered unlikely to be caused by FD. Therefore, of the 141 near-fault pulse motions, only a little over half were likely caused by FD. The current model presented in this study does not distinguish between these two categories of pulses, but this distinction could become important in the future. For example, ground motion prediction equations may incorporate directivity models in the future and thus reduce the epsilon of the FD-pulse motions, but this should have little effect on non-FD-pulse epsilon, which necessitates this distinction.

2.4. PROPORTION OF PULSE MOTIONS

Pulse motions differ significantly from ordinary motions. Hence, a common question is what is the appropriate number of pulse motions that should be included within a suite of design ground motions to represent the proper contribution of pulse motions to the seismic hazard? In estimating the number of pulse motions, engineers have commonly considered factors such as source-to-site distance, earthquake magnitude, and the geometric relation of the site to the source. The proportion of FD-pulse motions should increase as the source-to-site distance decreases, as magnitude increases, or as the IDP parameter increases. Additionally, it was hypothesized that intense pulse motions are more likely to occur when the design ground motions parameter at the selected seismic hazard level is caused by a high epsilon value. Ground motion intensity measures (e.g., PGA, PGV, and spectral acceleration) are generally assumed to follow a log-normal distribution, and the output of a ground motion prediction equation consists of the mean and standard deviation (SD) of the natural log of a given intensity measure. The epsilon is a standard normal variable (i.e., a mean of 0 and variance of 1) that represents the number of SDs above or below the mean value from a ground motion prediction equation. For example, a pulse motion with a $\ln(\text{PGV})$ that falls 1.2 SDs above the mean $\ln(\text{PGV})$ from a ground motion prediction equation would have an epsilon of 1.2. In PSHA, deaggregation of the hazard curve at a specified ground motion level is commonly performed to evaluate the contribution of different earthquake scenarios, commonly as a function of distance, magnitude, and epsilon. Representative epsilon values from this deaggregation can be used in the proposed model.

The influence of each of these parameters was investigated. Source-to-site distance and epsilon of the design ground motion parameter emerged as the most influential parameters. Earthquake magnitude was not as influential. The trends in the data regarding the likelihood of a pulse motion occurring are depicted in Fig. 2.6, which shows the occurrence of pulse and nonpulse motions as functions of closest distance and the intra-event epsilon of the record's PGV based on the Abrahamson and Silva (2008a) NGA model. The data clearly indicate that the likelihood of a pulse motion occurring is highest at short distances and high epsilon values. The contour lines of proportion pulse shown in Fig. 2.6 were developed by calculating the proportion of pulses in overlapping bins (see Appendix A-3). The exact position of the contour lines depends on how the data are binned; however, the overall trend is consistent regardless of the exact procedure used. It is expected that contours of probability should monotonically decrease with increasing distance, and this trend is generally observed. However, for high epsilon values (e.g., 1–2), there is an area at a distance of around 15–20 km where the probability contours decrease and then increase again with increasing distance. This is likely because of the limited amount of data available.

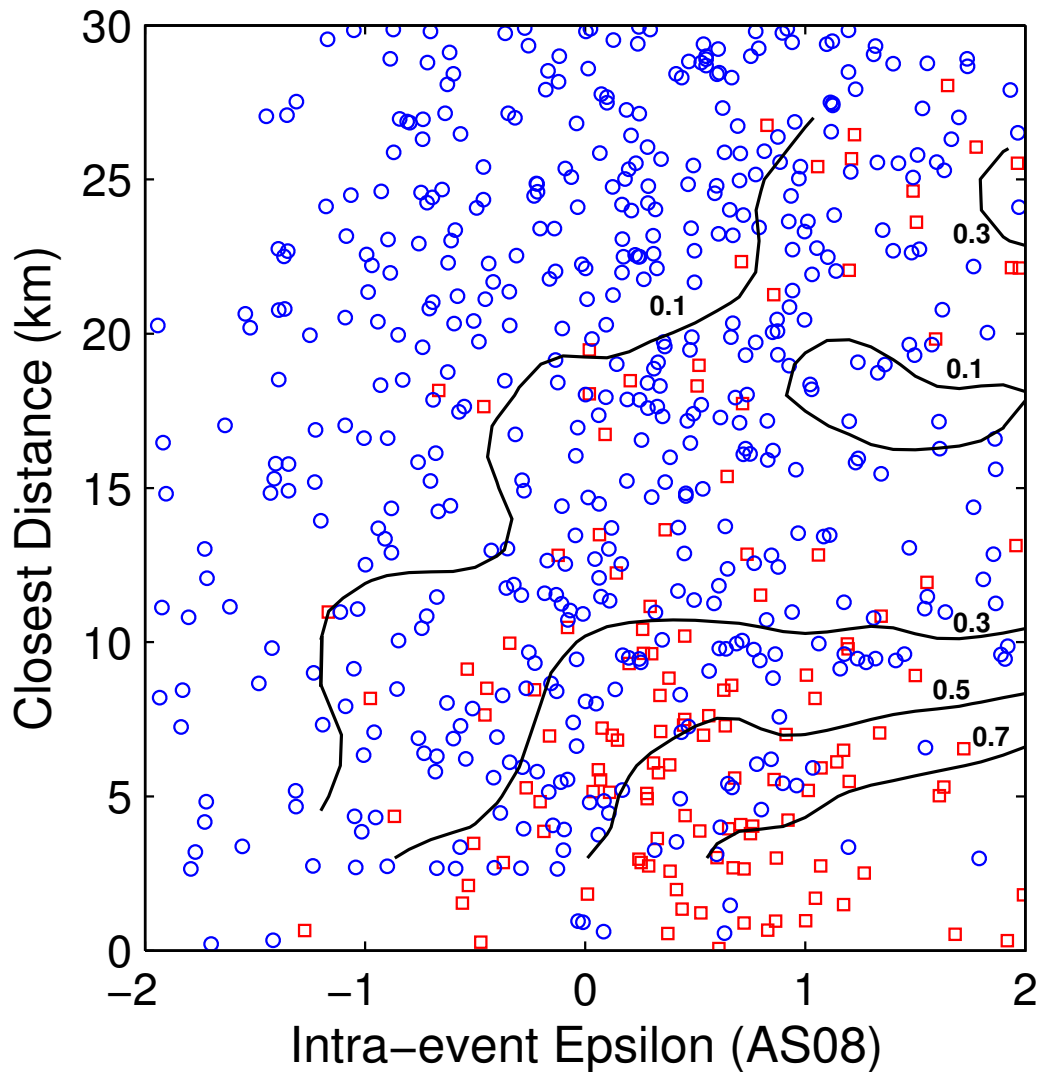


Fig. 2.6. Contour lines of probability of observing a pulse along with a scatter plot of the 673 records with squares indicating motions classified as pulses and circles indicating nonpulse motions

In developing the initial model, the PGV intra-event epsilon of each record was obtained from the Abrahamson and Silva (2008a) model using a new constant term of 5.878 from regression on the NGA-West2 dataset. The final model was adjusted to use total epsilon by normalizing the intra-event residual by the total SD instead of the intra-event SD to obtain an estimate of the mean total epsilon for future earthquakes with random event terms. This total epsilon is consistent with the total epsilon used by the engineer in practice. Therefore, the proposed model can be used directly with total epsilon. The epsilon of PGV should be used if available. However, the epsilon of PGV is not currently available at the USGS seismic hazards

website. In those cases, the epsilon of the 5% damped spectral acceleration (Sa) at a period of 1 s can be used as a proxy to the epsilon of PGV for $M_w \leq 7$ and Sa at 2 s for $M_w > 7$ (Bradley 2012).

Logistic regression was used to develop a model that captured the dependence of the proportion of pulse motions in the near-fault region on epsilon and distance. The proportion of pulse motions is estimated using

$$\textit{Proportion of Pulse Motions} = \frac{1}{1 + \exp(-3.87 + 1.04 \times R^{0.5} + 15.99 \times (\epsilon + 3)^{-2})}$$

Where R = closest distance from the site to the source (in kilometers); and ϵ = epsilon of the design ground motion parameter, which at this time is typically the spectral acceleration at 1 s at the design seismic hazard level, but it is preferably PGV. The trends in the proposed model are illustrated in Fig. 2.7 for select distances. This relationship may be used by the engineer to estimate the number of ground motions within a suite of records that should be selected from Table 2.1 to represent the proper contribution of pulse motions to the seismic hazard. For example, if R = 10 km for an $M_w = 7$ governing event and $\epsilon = 1.0$ for the 5% damped spectral acceleration at a period of 1s, the proportion of ground motions that should be pulse motions is 0.40. For a suite of seven motions, three of the motions should be pulse motions in this example [i.e., $(0.40)(7) = 2.8 \approx 3$]. This model can be used with the results of a probabilistic seismic hazard analysis by performing a disaggregation by distance and epsilon and using the values of these two parameters that control the hazard.

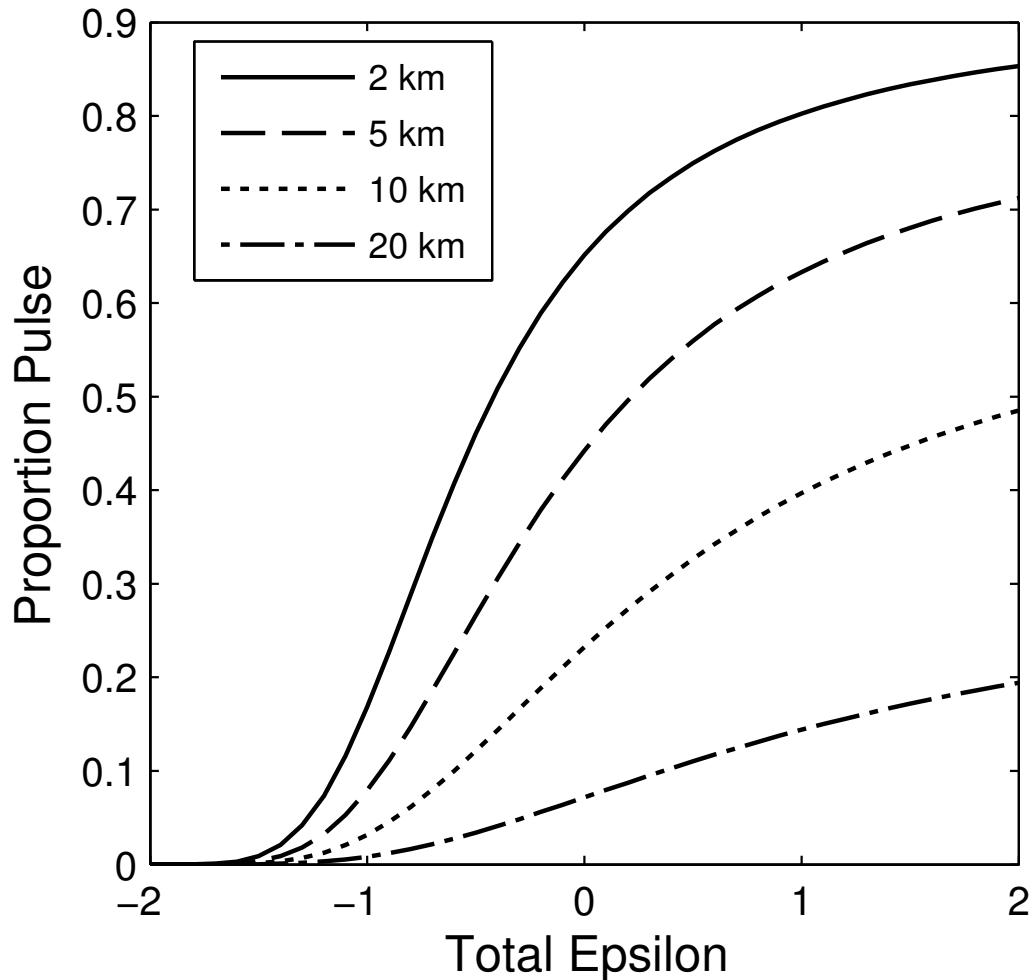


Fig. 2.7. Proposed model for estimating the proportion of pulse motions as a function of epsilon and distance

As mentioned previously, several other model parameters were considered in addition to epsilon and distance. The improvement in model fit with additional parameters was evaluated using the deviance, which is twice the difference between the maximum possible log-likelihood (i.e., a model where the data are fit exactly) and the model under consideration. Thus, deviance provides a relative index of fit with lower deviances preferred. A model with only ϵ as the independent parameter had a deviance of 656, and by adding a distance parameter, this was greatly reduced to 506. A model using ϵ and magnitude instead of distance had a much higher deviance of 651, and thus it is clear that magnitude is not as important as distance for the ranges of magnitudes and distances used in this study. Adding a magnitude parameter in addition to distance and ϵ only slightly further reduced the deviance from 520 to 509, whereas using IDP instead of magnitude decreased the deviance from 520 to 491. However, including additional parameters (particularly complicated ones such as IDP) makes the application of the model more

difficult. The goal of this study is to provide a straightforward method that can be applied to the results of a traditional PSHA without excessive additional calculations.

In previous work, the probability contours from logistic regression fit the raw data quite well (NIST 2011; Hayden et al. 2012). However, with the addition of new records from the NGA-West2 database, the logistic regression on transformed values of R and ϵ better fit the data. Hence, R was raised by an exponent and ϵ plus a constant was raised by another exponent. The constant term added to ϵ before being raised by an exponent was required to make the base positive so that a real number resulted for negative, non-integer exponents. The exponents of R and ϵ were optimized to minimize the deviance, decreasing it from 520 to 506. In addition to the decrease in deviance, it was confirmed by visual inspection that the probability contours better conformed to the data.

2.5. SELECTION OF PULSE MOTIONS

With a reliable estimate of the appropriate number of near-fault pulse motions to include in the suite of design ground motions, individual records are selected for use in dynamic analyses. Pulse motions should be chosen so that they possess pulse periods near the fundamental period of the structure when a relatively small number of ground motions are used. Pulse motions are provided in period bins of 0.7–2.2 and 2.2–10.0 s in Table 2.1, and Figures are contained in Appendix A-4. The bins include ground motions just outside their nominal period ranges to increase the number of potential records to choose from given the limited number of pulse-type records currently available. The engineer should select from the bin of pulse-type motions that best reflects the period range of interest of the structure being considered. With a limited number of design ground motions in the suite of motions (e.g., a suite of seven motions is often used in practice, and only a portion of these will be pulses), it is important to focus on the period range of interest of the structure. If many ground motions were used instead (e.g., more than 30 or so), then a more comprehensive suite of motions that captures all key earthquake scenarios including a wide range of pulse periods based on the potential near-fault earthquake scenarios could be used. Conventional good practices, such as selecting design motions that best represent the governing earthquake magnitude and distance, should still be followed. The key attributes of pulse motions [i.e., amplitude (PGV) and frequency content (T_v)] should be checked against estimates of these parameters for the governing earthquake scenario using empirical relationships such as Bray et al. (2009). Intense pulse motions should have significant durations well less than those of ordinary motions, as their relatively high intensity results from their compactness. The overall energy level of the motions can be checked using Arias intensity with empirical relationships, such as Travarasou et al. (2003), because Arias intensity is not significantly affected by FD.

The time domain characteristics of a pulse motion (e.g., PPV and pulse period) are important. Amplitude scaling preserves these characteristics. If spectral (frequency) matching is used, ideally, the motion should be spectrally matched using the concept of a conditional

spectrum (Baker 2011), because pulse motions contain high spectral ordinates within a narrow period range. Thus, spectral ordinates at other periods are likely to be below spectral acceleration values derived from a uniform hazard spectrum. However, more often a uniform hazard spectrum is used in earthquake engineering design practice, and for this case, it will be necessary to match the target spectrum over the specified period range (e.g., $0.2T-1.5T$, where T is the fundamental period of vibration of the structure). The spectral matching process should not eliminate the key time domain characteristics of the pulse, nor should it produce an unrealistic time series through the addition of excessive energy away from the pulse period. One way to achieve this is to use loose spectral matching for pulse-type motions wherein the spectral ordinate at the period of the pulse is not more than about 15–30% larger than the target spectral ordinate at this period, and spectral ordinates at periods away from the period of the pulse are not smaller than about 10–20% less than the target spectral values at these periods. Additional work is warranted to understand the implications of spectrally matching pulse motions to a uniform hazard spectrum. Most importantly, the velocity-time series of the matched motion and the seed motion must be inspected to ensure that the nonstationary aspects of the seed motion are preserved in the matching process.

FD motions have a tendency for the maximum PPV component to be oriented in the fault-normal direction. As the orientation of the maximum PPV component was used as a minor factor in the FD score, using these records would lead to a somewhat circular argument when examining preferred orientation. Instead, the IDP parameter is used with the pulse motion data in Fig. 2.8 to examine this issue. There is significant scatter in the orientation of pulses with IDP values greater than 2.0 (i.e., motions that are more likely caused by FD), but most of these motions (i.e., 49 of 63) fall within 30° of the fault-normal direction (indicated by the dashed lines). There is no clear dependence of the orientation of the component with the maximum PPV with distance. As expected, there is not a clear pattern to the orientation of those pulses not well explained by FD (i.e., motions with $IDP < 2.0$). Thus, there is a tendency for FD-pulses to be orientated in the fault-normal direction on average, but there is uncertainty in the orientation of any single motion.

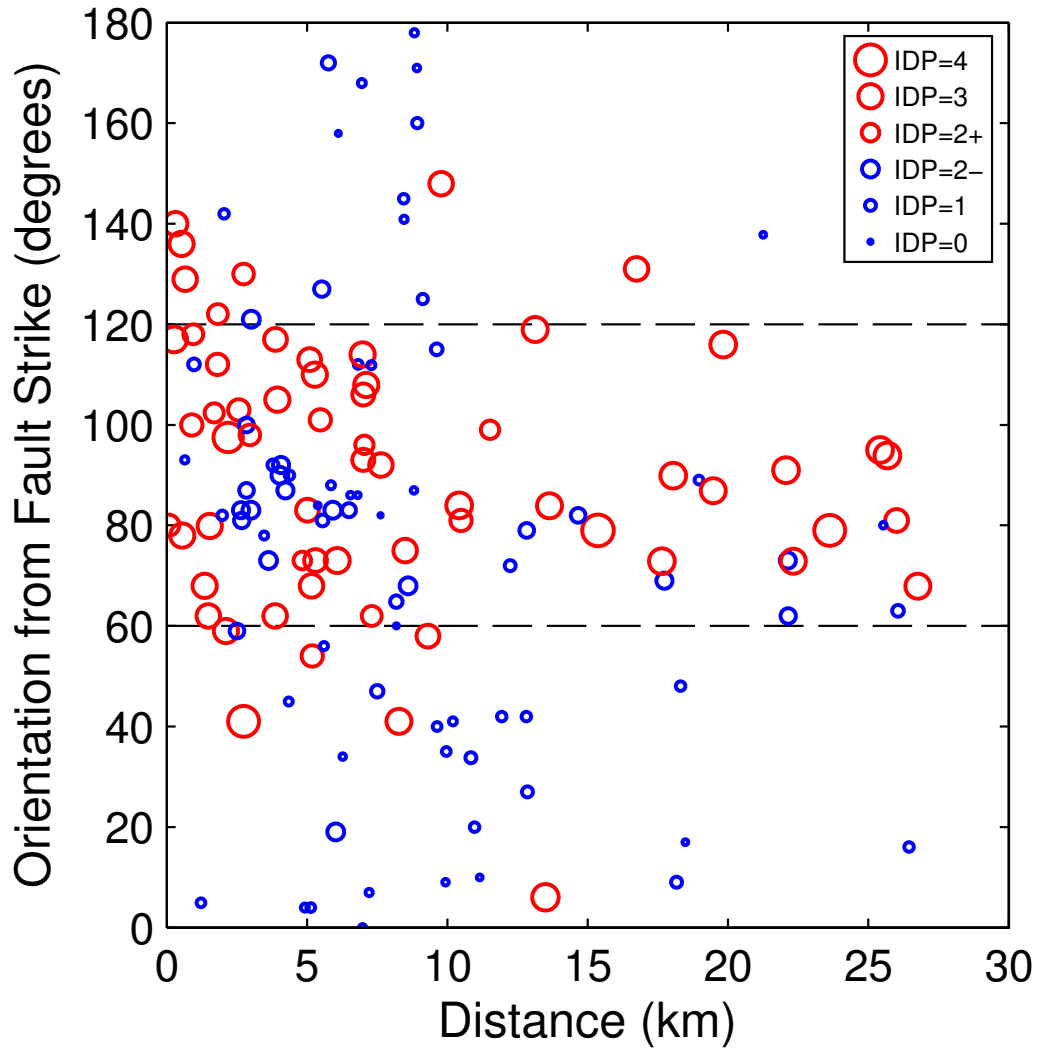


Fig. 2.8. Orientation of pulses categorized by IDP values

The model was developed using pulses of all periods because of the limited data available. This may overestimate the likelihood of pulse occurrence if one is only interested in pulses with a specific period. For example, a pulse with a period of 6 s may not have a pulse-like effect on a building with a structural period of 1 s. One difficulty in addressing this issue is the lack of a clear transition when a pulse of a given period no longer has a pulse-like effect on buildings with varying fundamental periods. For example, a pulse with a period of 3 s will have a pulse-like effect on structures with periods of around 3 s, but it is not clear if it will have a pulse-like effect on a structure with a fundamental period 1.5 s. Another issue is that the database is dominated by a few well-recorded earthquakes. For example, Chi-Chi and its aftershocks have more than 130 records in this database of 673 records, and the current model gives equal weight to each recording. These issues warrant future investigations when additional near-fault data becomes available.

2.6 CONCLUSIONS

Near-fault ground motion records are classified as either pulse motions or nonpulse motions using a newly developed quantitative classification scheme. The scheme involves first filtering the record, calculating several parameters at all orientations, and then scoring motions based on two key ground motion parameters (normalized cumulative squared velocity and number of significant cycles). The scheme was used to automatically classify 673 records from shallow crustal earthquakes along active plate margins with moment magnitudes greater than 6.0 and closest distances less than 30 km. Of these records, 141 records were classified as pulse motions. Of the 141 pulse motions, 74 were explained well by forward directivity. Although forward directivity may be the leading phenomenon contributing to the occurrence of pulses in near-fault motions, it does not explain all of the pulse motions in this study. FD-pulse motions had a tendency for the largest PPV pulse to be oriented within 30° of fault-normal, but significant scatter exists. Pulse motions that were not explained by forward directivity showed no clear preferred orientation.

An empirical model was developed using logistic regression that can be used to estimate the likelihood of occurrence of pulse motions in the near-fault region. The proposed equation can be used to estimate the proportion of pulse motions as a function of source-to-site closest distance and the epsilon of the design ground motion parameter at the design seismic hazard level. Thus, the commonly performed disaggregation of the PSHA can be used to estimate the appropriate values of distance and epsilon for use in the provided equation.

Pulse motions are sorted by period in Table 2.1 and Appendix A-4 to facilitate the selection of pulse motions to include in a suite of design earthquake ground motions for time-history analysis. Recognizing that no simple classification scheme can capture all the nuances of a record and that the particular motions included in a suite of motions can have a significant effect on the subsequent analysis, the motions in Table 2.1 were reviewed subjectively by the authors. Four of the motions classified as pulses are not recommended for use in practice to represent near-fault pulse motions, and three motions not classified as pulses by the automatic pulse classification scheme were added manually, because they possess key attributes of FD-pulse motions. In the interests of repeatability, these manual subjective adjustments were made after performing the regression and therefore do not affect the proposed model. An alternative model using these manual adjustments in the regression did not produce different results.

Table 2.1. Near-Fault FD-Pulse and Pulse Ground Motions

NGA # ^a	Earthquake	Station	M _w	Closest Distance km	Max PGV cm/s	Orth. PGV cm/s	PPV ^b cm/s	PPV Azimuth deg.	Pulse Period ^c s
4101	Parkfield-02, CA	Parkfield - Cholame 3E	6	5.6	35	19	56	42	0.5 A
4126	Parkfield-02, CA	PARKFIELD - STONE CORRAL 1E	6	3.8	45	31	81	53	0.5 A
4482	L'Aquila, Italy	L'Aquila - V. Aterno -F. Aterno	6.3	6.6	33	20	49	45	0.5 A
461 ^d	Morgan Hill	Halls Valley	6.2	3.5	40	12	67	46	0.6 A
496	Nahanni, Canada	Site 2	6.8	4.9	34	25	52	164	0.6 A
3966	Tottori, Japan	TTR009	6.6	8.8	46	24	69	152	0.6 A
4103	Parkfield-02, CA	Parkfield - Cholame 4W	6	4.2	39	24	70	48	0.6 A
4104	Parkfield-02, CA	Parkfield - Cholame 4AW	6	5.5	27	17	38	88	0.6 A
828	Cape Mendocino	Petrolia	7	8.2	98	42	140	110	0.7 A
4102	Parkfield-02, CA	Parkfield - Cholame 3W	6	3.6	45	15	75	34	0.7 A
4352	Umbria Marche, Italy	NOCERA UMBRA	6	8.9	34	26	55	155	0.7 A
4480	L'Aquila, Italy	L'Aquila - V. Aterno - Centro Valle	6.3	6.3	47	42	66	105	0.7 A
6877	Joshua Tree, CA	Indio - Jackson Road	6.1	25.5	53	13	85	80	0.7 A
451	Morgan Hill	Coyote Lake Dam (SW Abut)	6.2	0.5	79	55	129	104	0.8 A
1004	Northridge-01	LA - Sepulveda VA Hospital	6.7	8.4	78	76	149	87	0.8 A
1051	Northridge-01	Pacoima Dam (upper left)	6.7	7	107	50	169	35	0.8 A
3968	Tottori, Japan	TTRH02	6.6	1	145	47	203	38	0.8 A
4100	Parkfield-02, CA	Parkfield - Cholame 2WA	6	3	64	45	109	82	0.8 A
4116	Parkfield-02, CA	Parkfield - Stone Corral 4E	6	8.8	85	35	99	48	0.8 A
1602 ^e	Duzce, Turkey	Bolu	7.1	12	67	51	126	88	0.9 A
1752	Northwest China-03	Jiashi	6.1	17.7	37	22	58	90	0.9 A
2627	Chi-Chi, Taiwan-03	TCU076	6.2	14.7	62	21	91	98	0.9 A
3475	Chi-Chi, Taiwan-06	TCU080	6.3	10.2	41	20	72	46	0.9 A
4065	Parkfield-02, CA	PARKFIELD - EADES	6	2.9	36	13	61	48	0.9 A
4099	Parkfield-02, CA	Parkfield - Cholame 2E	6	4.1	25	18	40	53	0.9 A
4481	L'Aquila, Italy	L'Aquila - V. Aterno -Colle Grilli	6.3	6.8	39	33	59	45	0.9 A
4084	Parkfield-02, CA	PARKFIELD - 1-STORY S.	6	2.7	58	17	101	42	1 A
4107	Parkfield-02, CA	Parkfield - Fault Zone 1	6	2.5	82	67	129	20	1 A
4115	Parkfield-02, CA	Parkfield - Fault Zone 12	6	2.7	58	20	103	44	1 A
4130	Parkfield-02, CA	Parkfield - Vineyard Cany 1E	6	3	35	21	49	59	1 A
529	N. Palm Springs	North Palm Springs Post Office	6.1	4	71	29	109	17	1.1 A
1063	Northridge-01	Rinaldi Receiving Sta	6.7	6.5	151	57	259	25	1.1 A
3548	Loma Prieta	Los Gatos - Lexington Dam	6.9	5	121	31	160	45	1.1 A
4098	Parkfield-02, CA	Parkfield - Cholame 1E	6	3	53	20	80	44	1.1 A
4113	Parkfield-02, CA	Parkfield - Fault Zone 9	6	2.9	27	10	48	61	1.1 A
4879	Chuetsu-oki	Yan Sakuramachi City	6.8	19	39	27	72	123	1.2 A
285	Irpinia, Italy-01	Bagnoli Irpinio	6.9	8.2	39	19	57	68	1.3 A
763	Loma Prieta	Gilroy - Gavilan Coll.	6.9	10	34	27	44	93	1.4 A
765	Loma Prieta	Gilroy Array #1	6.9	9.6	42	29	49	88	1.4 A
1119	Kobe, Japan	Takarazuka	6.9	0.3	96	61	148	113	1.4 A
2618	Chi-Chi, Taiwan-03	TCU065	6.2	26.1	36	22	58	117	1.4 A
3943	Tottori, Japan	SMN015	6.6	9.1	21	14	37	25	1.4 A
764	Loma Prieta	Gilroy - Historic Bldg	6.9	11	44	24	70	148	1.5 A
766 ^e	Loma Prieta	Gilroy Array #2	6.9	11.1	49	25	81	67	1.5 A
4040	Bam, Iran	Bam	6.6	1.7	124	61	169	97	1.6 A-B
4228	Niigata, Japan	NIGH11	6.6	8.9	68	38	75	52	1.6 A-B
4451	Montenegro, Yugo.	Bar-Skupstina Opstine	7.1	7	63	28	102	120	1.6 A-B
4458	Montenegro, Yugo.	Ulcinj - Hotel Olympic	7.1	5.8	63	31	93	128	1.6 A-B
3746	Cape Mendocino	Centerville Beach, Naval Fac	7	18.3	58	30	102	38	1.7 A-B
517	N. Palm Springs	Desert Hot Springs	6.1	6.8	30	20	43	175	1.8 A-B
159	Imperial Valley-06	Agrarias	6.5	0.7	54	20	74	50	1.9 A-B
723	Superstition Hills-02	Parachute Test Site	6.5	1	144	38	194	65	1.9 A-B
4483	L'Aquila, Italy	L'Aquila - Parking	6.3	5.4	46	18	58	43	1.9 A-B

NGA # ^a	Earthquake	Station	M _w	Closest Distance km	Max PGV cm/s	Orth. PGV cm/s	PPV ^b cm/s	PPV Azimuth deg.	Pulse Period ^c s
4847	Chuetsu-oki	Joetsu Kakizakiku Kakizaki	6.8	11.9	95	46	135	76	1.9 A-B
767	Loma Prieta	Gilroy Array #3	6.9	12.8	50	38	73	86	2 A-B
722	Superstition Hills-02	Kornbloom Road (temp)	6.5	18.5	34	10	53	144	2.1 A-B
1013	Northridge-01	LA Dam	6.7	5.9	86	53	108	25	2.3 A-B
2114	Denali, Alaska	TAPS Pump Station #10	7.9	2.7	125	58	182	75	2.3 A-B
1077 ^d	Northridge-01	Santa Monica City Hall	6.7	26.5	42	25	68	106	2.4 A-B
6906	Darfield, NZ	GDLC	7	1.2	148	101	228	90	2.4 A-B
821	Erzican, Turkey	Erzincan	6.7	4.4	118	56	160	32	2.5 A-B
1086	Northridge-01	Sylmar - Olive View Med FF	6.7	5.3	132	72	160	15	2.5 A-B
1529	Chi-Chi, Taiwan	TCU102	7.6	1.5	113	70	165	67	2.6 A-B
725	Superstition Hills-02	Poe Road (temp)	6.5	11.2	45	25	60	137	2.7 A-B
1084 ^e	Northridge-01	Sylmar - Converter Sta	6.7	5.4	125	83	209	40	2.8 A-B
1045	Northridge-01	Newhall - W Pico Canyon Rd.	6.7	5.5	119	65	169	43	2.9 A-B
8130	Christchurch, NZ	SHLC	6.2	5.6	75	75	119	115	2.9 A-B
171	Imperial Valley-06	El Centro - Meloland Geot. Array	6.5	0.1	117	29	152	63	3 A-B
1085	Northridge-01	Sylmar - Converter Sta East	6.7	5.2	121	62	120	176	3 A-B
3947	Tottori, Japan	SMNH01	6.6	5.9	43	32	44	62	3 A-B
292	Irpinia, Italy-01	Sturno (STN)	6.9	10.8	74	39	107	99	3.1 B
5658	Iwate	IWTH26	6.9	6	59	47	69	10	3.1 B
1050	Northridge-01	Pacoima Dam (downstr)	6.7	7	50	24	34	48	3.2 B
779	Loma Prieta	LGPC	6.9	3.9	106	47	144	11	3.3 B
8123	Christchurch, NZ	REHS	6.2	5.1	98	48	146	63	3.3 B
8158	Christchurch, NZ	LPCC	6.2	6.1	49	41	51	37	3.4 B
2650	Chi-Chi, Taiwan-03	TCU116	6.2	22.1	33	19	51	107	3.5 B
181	Imperial Valley-06	El Centro Array #6	6.5	1.4	122	62	208	75	3.6 B
182	Imperial Valley-06	El Centro Array #7	6.5	0.6	113	56	159	65	3.6 B
1158	Kocaeli, Turkey	Duzce	7.5	15.4	63	53	103	13	3.9 B
4071	Parkfield-02, CA	PARKFIELD - MIDDLE MTN	6	2.6	33	20	37	64	3.9 B
1165	Kocaeli, Turkey	Izmit	7.5	7.2	40	22	52	99	4 B
2628	Chi-Chi, Taiwan-03	TCU078	6.2	7.6	57	17	54	98	4 B
180	Imperial Valley-06	El Centro Array #5	6.5	4	98	55	150	38	4.2 B
1193	Chi-Chi, Taiwan	CHY024	7.6	9.6	64	39	100	120	4.2 B
825	Cape Mendocino	Cape Mendocino	7	7	128	39	59	2	4.4 B
879	Landers	Lucerne	7.3	2.2	134	29	170	74	4.4 B
1176	Kocaeli, Turkey	Yarimca	7.5	4.8	93	64	155	19	4.4 B
1511	Chi-Chi, Taiwan	TCU076	7.6	2.7	73	29	93	135	4.5 B
179	Imperial Valley-06	El Centro Array #4	6.5	7.1	89	62	140	47	4.6 B
286 ^d	Irpinia, Italy-01	Bisaccia	6.9	21.3	23	14	45	175	4.6 B
1476	Chi-Chi, Taiwan	TCU029	7.6	28	64	40	110	157	4.6 B
8119	Christchurch, NZ	PRPC	6.2	2	124	38	147	141	4.6 B
1244	Chi-Chi, Taiwan	CHY101	7.6	9.9	109	65	162	14	4.7 B
1510	Chi-Chi, Taiwan	TCU075	7.6	0.9	110	35	145	105	4.7 B
161	Imperial Valley-06	Brawley Airport	6.5	10.4	47	35	58	59	4.8 B
3473	Chi-Chi, Taiwan-06	TCU078	6.3	11.5	40	35	32	104	4.8 B
1548	Chi-Chi, Taiwan	TCU128	7.6	13.1	79	57	128	124	4.9 B
3744	Cape Mendocino	Bunker Hill FAA	7	12.2	82	28	65	62	4.9 B
143	Tabas, Iran	Tabas	7.4	2.1	136	73	207	8	5.3 B
1480	Chi-Chi, Taiwan	TCU036	7.6	19.8	65	45	111	121	5.4 B
3852	Chi-Chi (aftershock 3)	CHY006	6.2	24.6	25	9	41	164	5.4 B
1483	Chi-Chi, Taiwan	TCU040	7.6	22.1	57	46	92	96	5.7 B
2658	Chi-Chi, Taiwan-03	TCU129	6.2	12.8	37	18	33	101	5.7 B
77	San Fernando	Pacoima Dam (upper left abut)	6.6	1.8	122	45	125	175	5.9 B
1481	Chi-Chi, Taiwan	TCU038	7.6	25.4	57	38	82	100	5.9 B
183	Imperial Valley-06	El Centro Array #8	6.5	3.9	71	44	89	81	6.1 B

NGA # ^a	Earthquake	Station	M _w	Closest Distance km	Max PGV cm/s	Orth. PGV cm/s	PPV ^b cm/s	PPV Azimuth deg.	Pulse Period ^c s
802	Loma Prieta	Saratoga - Aloha Ave	6.9	8.5	58	44	62	53	6.2 B
1549	Chi-Chi, Taiwan	TCU129	7.6	1.8	73	45	80	127	6.2 B
6962	Darfield, NZ	ROLC	7	1.5	97	62	146	165	6.2 B
803	Loma Prieta	Saratoga - W Valley Coll.	6.9	9.3	77	57	83	70	6.3 B
6927	Darfield, NZ	LINC	7	7.1	117	49	141	13	6.3 B
1501	Chi-Chi, Taiwan	TCU063	7.6	9.8	87	40	139	153	6.4 B
173	Imperial Valley-06	El Centro Array #10	6.5	8.6	58	46	73	75	6.7 B
6897	Darfield, NZ	DSLCL	7	8.5	67	38	107	46	6.7 B
1486	Chi-Chi, Taiwan	TCU046	7.6	16.7	34	22	60	136	6.8 B
1148	Kocaeli, Turkey	Arcelik	7.5	13.5	40	11	60	86	6.9 B
6911	Darfield, NZ	HORC	7	7.3	106	72	127	17	7.1 B
8090	Christchurch, NZ	HPSC	6.2	4.4	50	30	88	104	7.1 B
1530	Chi-Chi, Taiwan	TCU103	7.6	6.1	70	25	105	78	7.4 B
184	Imperial Valley-06	El Centro Differential Array	6.5	5.1	76	42	85	76	7.5 B
185	Imperial Valley-06	Holtville Post Office	6.5	7.5	74	26	96	96	7.5 B
2661	Chi-Chi, Taiwan-03	TCU138	6.2	22.1	26	13	47	118	7.5 B
6887	Darfield, NZ	CBGS	7	18.1	61	21	80	175	7.7 B
6960	Darfield, NZ	RHSC	7	13.6	64	23	104	169	7.7 B
6959	Darfield, NZ	REHS	7	19.5	65	25	93	172	7.8 B
6928	Darfield, NZ	LPCC	7	25.7	30	17	36	179	8 B
900	Landers	Yermo Fire Station	7.3	23.6	56	17	66	55	8.1 B
1496	Chi-Chi, Taiwan	TCU056	7.6	10.5	46	35	69	86	8.2 B
6890	Darfield, NZ	CMHS	7	17.6	50	21	72	158	8.4 B
1550	Chi-Chi, Taiwan	TCU136	7.6	8.3	63	34	96	46	8.5 B
1528	Chi-Chi, Taiwan	TCU101	7.6	2.1	78	47	97	64	8.6 B
6966	Darfield, NZ	SHLC	7	22.3	66	28	93	158	8.6 B
178	Imperial Valley-06	El Centro Array #3	6.5	12.9	58	31	73	116	8.7 B
6942	Darfield, NZ	NNBS	7	26.8	57	24	71	153	8.9 B
1519	Chi-Chi, Taiwan	TCU087	7.6	7	52	41	72	119	9 B
1485	Chi-Chi, Taiwan	TCU045	7.6	26	53	41	52	86	9.8 B
170	Imperial Valley-06	EC County Center FF	6.5	7.3	73	38	97	81	10 ^f B
1491	Chi-Chi, Taiwan	TCU051	7.6	7.6	54	41	78	97	10 ^f B
1492	Chi-Chi, Taiwan	TCU052	7.6	0.7	209	88	304	134	10 ^f B
1494	Chi-Chi, Taiwan	TCU054	7.6	5.3	53	42	83	115	10 ^f B
1505	Chi-Chi, Taiwan	TCU068	7.6	0.3	343	108	442	145	10 ^f B
1515	Chi-Chi, Taiwan	TCU082	7.6	5.2	63	48	92	73	10 ^f B
1520 ^d	Chi-Chi, Taiwan	TCU088	7.6	18.2	36	15	44	14	10 ^f B

- Notes: a) Bold NGA record numbers indicate motion was classified as a FD-pulse.
b) The PPV is the peak to peak velocity from the filtered record.
c) The letter A or B indicates the period bin, and A-B indicates overlap between bins.
d) Motion not recommended for use in practice as a near-fault pulse motion.
e) Motion added manually (not initially a pulse from automatic classification scheme).
f) Pulse period 10 seconds or greater.

CHAPTER 3: CENTRIFUGE TESTS OF ADJACENT MAT-SUPPORTED BUILDINGS AFFECTED BY LIQUEFACTION

3.1 INTRODUCTION

Liquefaction-induced settlements have caused significant damage to structures during recent earthquakes. Geotechnical centrifuge experiments can provide insight into the mechanisms governing liquefaction-induced building settlements, and several recent studies have focused on the effects of liquefaction on isolated buildings (e.g., Dashti et al. 2010a,b; Allmond and Kutter 2012; da Silva Marques et al. 2014). However, structures in urban environments are often close to adjacent structures. During earthquakes, adjacent structures can interact through the soil in a phenomenon known as structure-soil-structure interaction (SSSI), which can affect structural performance (Mason et al. 2013; Trombetta et al. 2013). A dramatic case of liquefaction-induced building damage is shown in Figure 3.1, where two adjacent buildings tilted away from each other (Bray et al. 2000). Despite recent progress, there is still much to be learned from well-documented model case histories of soil-structure interaction (SSI) and SSSI on liquefied soils.



Fig. 3.1. Two adjacent buildings that tilted away from each other due to liquefaction in foundation soils (Bray et al. 2000)

This study examines the influence of SSSI effects during episodes of liquefaction or cyclic softening in two centrifuge experiments performed at the NEES Center for Geotechnical Modeling at UC Davis. Several key design parameters in the present study were adopted from past studies (i.e., Dashti et al. 2010a,b; Allmond and Kutter 2012, 2013) to facilitate comparisons between experiments. The physical models in this study contained layered, saturated soil profiles with a layer of loose to medium-dense Nevada Sand designed to liquefy during strong shaking. Shallow-founded model structures were isolated or next to an adjacent structure. The response of structures subjected to soil liquefaction or cyclic softening depended on the complex interaction of the ground motion, soil, and structural characteristics including those of adjacent structures.

3.2 LITERATURE REVIEW

A brief overview of recent pertinent findings is presented in this paper. The interested reader can refer to the papers by Dashti et al. (2010a,b) for recent, in-depth reviews on liquefaction effects on isolated buildings and to papers by Mason et al. (2013) and Trombetta et al. (2013) for in-depth discussions of SSI and SSSI effects.

Recent earthquakes in Chile (Bray et al. 2012), New Zealand (Cubrinovski et al. 2011), and Japan (Tokimatsu et al. 2012) have re-emphasized the damaging consequences of liquefaction on infrastructure. Due to the complexity of the problem and limited well-documented field case histories, liquefaction-induced building settlements are often estimated using empirical correlations developed for free-field sites on level ground that account for post-liquefaction volumetric strains only. These procedures do not account for additional effects due to the presence of a structure. Geotechnical centrifuge experiments provide a means to examine key aspects of liquefaction-induced building movements. For example, Dashti et al. (2010a,b) performed a series of four centrifuge experiments and identified key liquefaction-induced building settlement mechanisms. These mechanisms included: a) volumetric mechanisms: rapid localized drainage, sedimentation, and consolidation; and b) shear mechanisms: partial bearing capacity loss and SSI-induced building ratcheting (i.e., the rocking foundation works its way into the soil). Settlement caused by ground loss beneath the foundation due to eroded sediment ejecta is an additional mechanism highlighted by several case histories in Christchurch during the 2010–2011 Canterbury earthquakes (Cubrinovski et al. 2011; Bray et al. 2014). Consistent with previous studies (e.g., Liu and Dobry 1997), Dashti et al. (2010a,b) observed that most building settlement occurred during strong shaking in their experiments, and this indicated that post-liquefaction volumetric strains were less important than the other liquefaction-induced building settlement mechanisms described previously. Additionally, they showed that the practice of normalizing foundation settlements by the liquefiable layer thickness should be avoided. Other recent centrifuge tests that investigated SSI effects in liquefied ground include the examination of rocking foundations (Allmond and Kutter 2012) and the effects of bearing pressure and settlement mitigation techniques (da Silva Marques et al. 2014).

Andrianopoulos et al. (2010) developed numerical procedures that accounted for SSI effects during liquefaction, and their results compared favorably with those of geotechnical centrifuge tests. Using these numerical procedures, Karamitros et al. (2013a,b) examined the beneficial effects of a non-liquefiable surface layer using numerical simulations and developed a methodology to estimate liquefaction-induced building settlement under these conditions. Unutmaz and Cetin (2012) developed another methodology for estimating liquefaction-induced building settlement based on data from the 1999 Kocaeli and Duzce, Turkey earthquakes. Lastly, using numerical simulations in FLAC-2D with the UBCSAND model, Dashti and Bray (2013) produced results that were generally consistent with the Dashti et al. (2010a,b) centrifuge test results, which highlighted the importance of mechanisms such as SSI-induced building ratcheting.

A review of the early development of SSI is provided by Kausel (2010), and a recent literature review of SSSI can be found in Menglin et al. (2011). Although a few numerical studies of SSSI exist, well-documented case histories to calibrate and evaluate these analyses are lacking. However, recent centrifuge tests have examined SSSI effects with various model structures on dry, dense sand including a one-level inelastic frame structure with individual spread footings, a two-level elastic shear wall structure on a mat foundation, and a three-level inelastic frame structure with a basement (Mason et al. 2013; Trombetta et al. 2013a; Trombetta et al. 2013b). Trombetta et al. (2013b) concluded that elastic wave-propagation-based SSSI had limited effects on the scenarios tested in which the soil responded nonlinearly to intense ground shaking. However, SSSI due to physical restraints induced by adjacent structures was important. For example, Mason et al. (2013) noted that spread footings settled less when adjacent to a deep basement. There is limited information on the effects of SSSI during liquefaction, which is the focus of this study.

3.3 EXPERIMENTAL DESIGN

The centrifuge experiments described in this study are the final two tests (i.e., Test-5 and Test-6) in the NEESR Seismic Performance Assessment in Dense Urban Environments project. These two experiments are subsequently referred to as T4.5-50 and T4.6-40, which is consistent with the terminology used by Dashti et al. (2010a,b). The first number indicates the thickness of the liquefiable layer in meters (prototype scale), and the second number indicates the estimated initial relative density of the liquefiable layer. For example, the liquefiable layer in T4.5-50 (Test-5) was 4.5 meters thick, and its initial nominal relative density was 50%.

All measurements presented in this paper are in prototype scale, unless otherwise noted. The large centrifuge at the NEES Center for Geotechnical Modeling at UC Davis was used in these tests, and details of its capabilities can be found at <http://nees.ucdavis.edu>. Both experiments were performed at a centrifugal acceleration of 55 g. Garnier et al. (2007) present relevant scaling laws. The key components of the experimental design are summarized in this section, and the centrifuge data reports (i.e., Zupan et al. 2013; Hayden et al. 2014) contain

further information. All data, including complete instrument recordings, are provided on NEEShub at <https://nees.org>, under the project: *Seismic Performance Assessment in Dense Urban Environments*.

These experiments include three types of single-degree-of-freedom structural models, constructed of steel and aluminum, with the properties listed in Table 3.1. Several of these structures are identical to those used in previous studies to facilitate comparisons. Structure A was used by Dashti et al. (2010a,b) and roughly corresponds to a heavy, three-story building. Structure J is substantially taller, with a longer fixed-base period, and almost three times the bearing pressure of Structure A (Allmond and Kutter (2012, 2013). Structure K, a new model, has a bearing pressure similar to Structure J but maintains other key characteristics of Structure A.

Table 3.1. Key structural properties in prototype units

Structure	Mat Width (m)	Mat Length (m)	Height (m)	Weight (kN)	Bearing Pressure (kPa)	Fixed-Base Period ¹ (s)	Center of Mass ² (m)
A	6.0	9.0	4.4	3510	65	0.33	3.9
K	6.0	9.0	5.3	9700	180	0.38	3.9
J	7.5	7.5	13.5	10470	186	0.85	15.0

Notes: 1) Measured in lab; and 2) The deck center of mass measured from the bottom of the foundation

The model layouts for experiments T4.5-50 and T4.6-40 are presented in Figure 3.2. The four quadrants of the flexible shear beam model container (FSB2) in each test contain either an isolated model structure or pair of model structures. The isolated A structure used in T4.5-50 and T4.6-40 provides a common link between the two experiments. For example, because the input motions matched closely, the response of this identical isolated structure indicates the effect of the different relative densities used in the liquefiable layer of each test. The subscript of each structure letter designation (i.e., A, J, or K) indicates the adjacent structure type and pertinent details. For example, Structure A_J, shown in the northeast quadrant of T4.6-40, is an A-type structure located adjacent to a J-type structure. Structure J_{A-P} is located adjacent to an A-type structure, and the subscript P designates the J-type structure has a pile foundation. Structure A_{A-N} is the northern structure in the A-A pair from T4.5-50, and A_{A-S} is the southern structure. The initial spacing between the foundations of adjacent structures was increased from 0.2–0.3 m in T4.5-50 to 1.5–1.7 m in T4.6-40 to investigate foundation spacing effects.

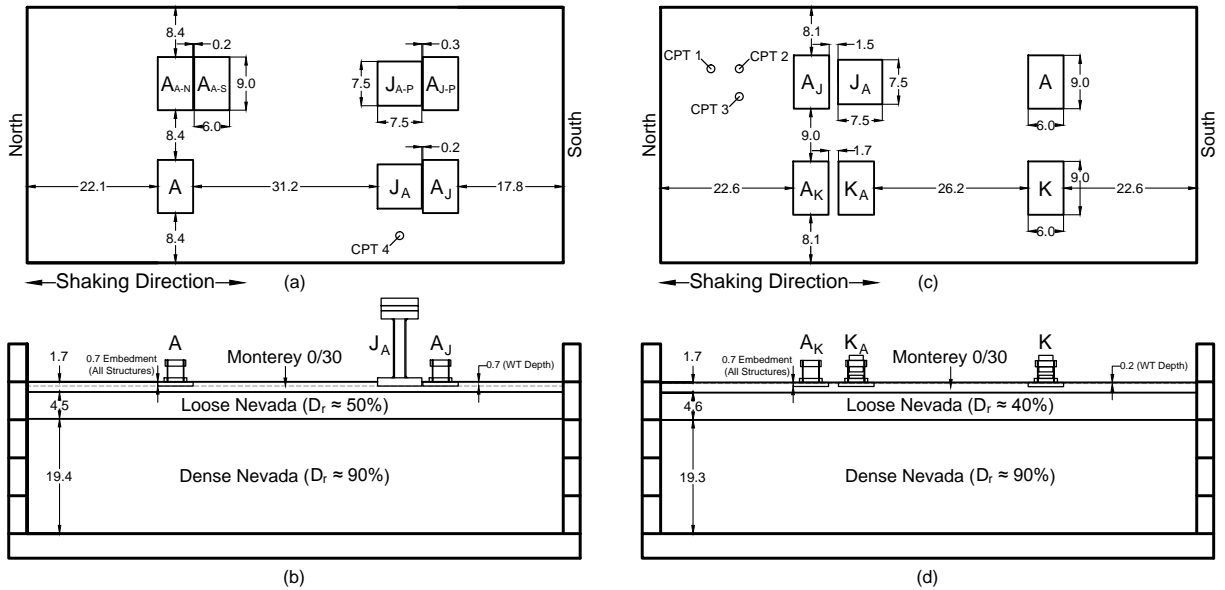


Fig. 3.2. Centrifuge test layout with prototype dimensions in meters: (a) T4.5-50 plan view; (b) T4.5-50 profile view; (c) T4.6-40 plan view; (d) T4.6-40 profile view

As shown in the soil profiles in Figure 3.2, the structure foundations are embedded 0.7 m in a 1.6 m (T4.6-40) or 1.7 m (T4.5-50) -thick layer of dense Monterey 0/30 Sand ($D_{50} \approx 0.40$ mm, $e_{\min} \approx 0.54$, $e_{\max} \approx 0.84$). An approximately 4.5 m (T4.5-50) or 4.6 m (T4.6-40) thick layer of loose to medium-dense Nevada Sand ($D_{50} \approx 0.14$ mm, $e_{\min} \approx 0.52$, $e_{\max} \approx 0.78$) underlies the Monterey Sand. A thick, dense layer of Nevada Sand extends to the bottom of the model container. The surface of the model was curved slightly and the structures were tilted in the east-west direction so they were aligned perpendicular to the radial g -field at 55 g . A methylcellulose-water solution with a viscosity approximately 21 (± 2) times that of water was used as the pore fluid (Stewart et al. 1998). Although there were some minor fluctuations over the course of the experiments, the water table was approximately 0.7 m below the ground surface in T4.5-50 and at a depth of 0.2 m in T4.6-40.

Cone tip resistances from cone penetration tests (CPTs) performed at 55 g are shown in Figure 3.3 (see Figure 3.2 for test locations). CPT-1 (T4.6-40) and CPT-4 (T4.5-50) provide the initial conditions prior to any shaking event. CPT-2 and CPT-3 were performed just before and after the final T4.6-40 shaking event. The boundaries between the layers shown in Figure 3.3 are based on measurements taken during model construction. The cone tip senses the dense Nevada Sand layer well before it reaches the interface, and this effect is significant due to the large cone diameter (330 mm prototype scale). The nominal relative densities of the liquefiable Nevada Sand layer in each experiment (i.e., $50 \pm 5\%$ for T4.5-50 and $40 \pm 5\%$ for T4.6-40) are estimated primarily from several CPT based correlations (see Hayden et al. 2014 for details). Pluviator calibrations performed prior to model construction as well as mass and volume measurements taken during construction were also considered in the relative density estimates. The relative

density of the dense Nevada Sand layer is estimated to be $90\pm 5\%$ for both tests. The Monterey Sand surface layer has an estimated relative density of $85\pm 5\%$ in both tests.

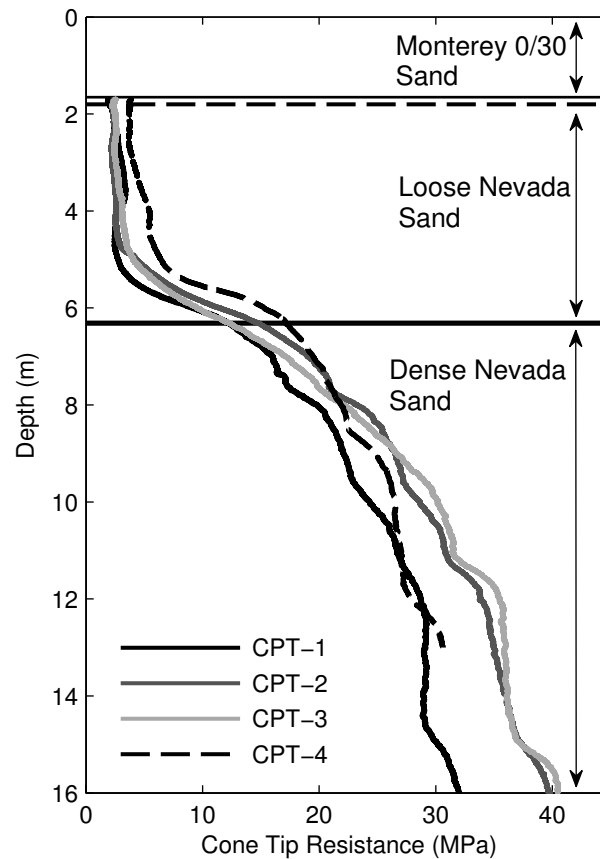


Fig. 3.3. Cone tip resistance profiles using a 330 mm-diameter cone (prototype scale) at 2 cm/s. Solid lines are from (T4.6-40) and dashed lines are from test (T4.5-50)

Four primary shaking events (i.e., “small” Port Island, “moderate” Port Island, “moderate” TCU, and “large” Port Island) were applied to the base of the model following the sequence used in Test T3-50 (Dashti et al. 2010b) to facilitate comparisons with previous tests. The Port Island events are modified and scaled versions of the ground motion recorded in the Port Island down-hole array at a depth of 83 m during the 1995 M_w 6.9 Kobe, Japan earthquake (Dashti et al. 2010b). The moderate TCU event is a modified and scaled version of the TCU078 record from the 1999 M_w 7.6 Chi-Chi, Taiwan earthquake (Dashti et al. 2010b). It has a longer significant duration and slower energy buildup relative to the Port Island record. For example, Dashti et al. (2010b) reported significant durations, D_{5-95} , of approximately 28 s for the TCU motion versus 8 s for the Port Island motion.

Approximately 140 sensors, including accelerometers, pressure transducers, and displacement transducers, captured the response of the physical model during each test. There was sufficient instrumentation to track the movement of each structure, the soil accelerations,

and distribution of pore water pressures beneath the various structures as well as accelerations and pore water pressures in free-field vertical arrays. The details, locations, and data of each sensor are provided in the experiment data reports (i.e., Zupan et al. 2013; Hayden et al. 2014).

3.4 EXPERIMENTAL RESULTS AND DISCUSSION

3.4.1 Free-Field Soil Response

Vertical arrays of horizontal accelerometers in the free-field captured the soil response at key locations away from the model structures and container walls. Figure 3.4 shows the response during the moderate and large Port Island events. The individual subplots share a common axis in this figure (and most subsequent figures) to facilitate direct comparisons. The input acceleration-time histories in T4.5-50 and T4.6-40 were nearly identical; however, the time-histories nearer to the surface were less similar. This is expected when noting the different relative densities of the liquefiable layer. The brief, high acceleration spikes near the surface, particularly for the large event, are likely due to soil dilation and re-stiffening (e.g., Fiegel and Kutter 1994; Dashti et al. 2010a). The moderate TCU acceleration-time series also diverged near the surface and showed small dilatancy spikes. As will be shown later, there was significant amplification of the long period component of the ground motions as well as amplification at short periods due to the soil dilation spikes in the free-field site response due to liquefaction of the loose to medium-dense Nevada Sand.

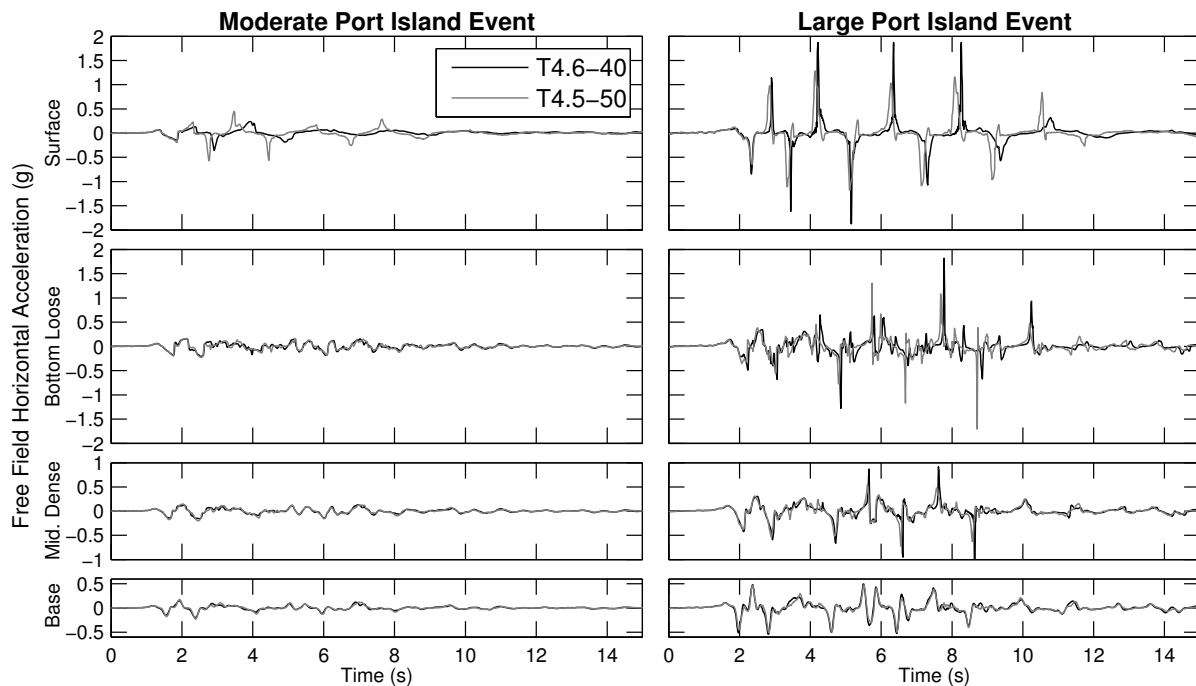


Fig. 3.4. Free-field horizontal acceleration during the moderate and large Port Island events

The long-term settlement and pore water pressure time histories in the free-field are shown in Figure 3.5 for the moderate Port Island event; the input base acceleration is also shown as a frame of reference. The calculated excess pore pressure ratio (i.e., $r_u = \Delta u / \sigma'_{vo}$, where Δu = excess pore water pressure and σ'_{vo} = the vertical effective stress immediately prior to the shaking event) quickly reached and then slightly exceeded a value of one during strong shaking. Estimates of the initial vertical effective stress require knowledge of the soil profile geometry, water level, soil density, and sensor position. These parameters change slightly during shaking and are subject to measurement error, which explains why the calculated r_u values can exceed 1.0. The lower relative density of the T4.6-40 liquefiable layer as well as minor differences in the pore fluid viscosity and pore water pressure generation in the dense layer (and the resulting upward flow) may explain the longer duration of high excess pore water pressure in Test 4.6-40 compared to T4.5-50. Similarly, r_u also reached 1.0 at the midpoint of the liquefiable layer during the moderate TCU and large Port Island events, and slower dissipation of excess pore water pressures also occurred in T4.6-40 (see Appendix B-2).

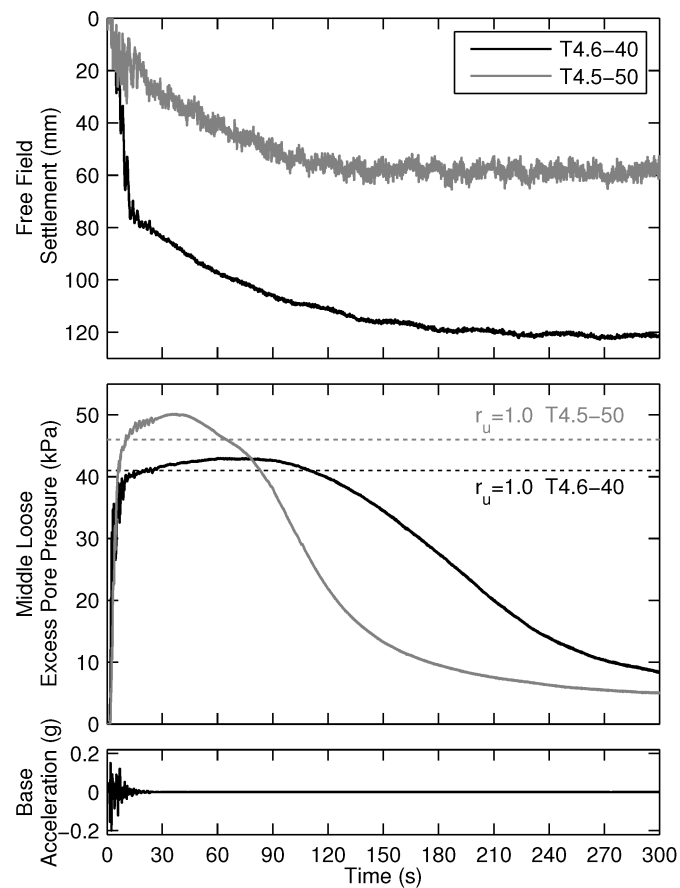


Fig. 3.5. Free-field response during the moderate Port Island event

About 60% of the free-field settlement occurred before the end of strong shaking in T4.6-40 indicating that a significant degree of partial drainage occurred during shaking. This is consistent with observations made by Dashti et al. (2010a). The free-field settled substantially less in T4.5-50 than in T4.6-40, as expected, due to the higher relative density of the liquefiable layer. It is worth noting that volumetric strains in the thick, dense Nevada Sand layer also contribute a small amount to the total settlement. The amount of free-field settlement during strong shaking as a proportion of total settlement was also less in T4.5-50 compared to T4.6-40. However, free-field settlements will vary from location to location, and T4.5-50 used only one free-field displacement transducer compared to three in T4.6-40, so the T4.5-50 results are not corroborated with additional measurements. The moderate TCU and large Port Island events exhibited trends similar to those shown in Figure 3.5; the T4.6-40 free-field settled around twice as much as T4.5-50, and a larger proportion of total settlement occurred during strong shaking in T4.6-40 compared to T4.5-50.

3.4.2 Response of Soil under Structures and Structural Settlement

Figure 3.6 summarizes the T4.6-40 free-field and building settlements, excess pore water pressure at the midpoint of the liquefiable layer beneath the center of each structure, and input acceleration-time histories. The moderate Port Island, moderate TCU, and large Port Island events are shown in separate columns. Each of these three columns is subdivided into two additional columns with different time scales to clearly show the initiation of pore water pressure generation and settlement as well as the response after strong shaking. For example, the first moderate Port Island column shows the response from 0 to 10 seconds to focus on the initiation of strong shaking; the second column shows from 10 to 50 seconds, which includes the long-term response after the end of strong shaking. All six structures from T4.6-40 are shown in addition to the free-field ground settlement (labeled FF). The isolated Structure A settlement from T4.6-40 as well as T4.5-50 is included to provide a reference point between plots. The first row of pore water pressure plots displays records under the A-type structures and in the free-field, and the second row contains the soil response under the J and K type structures. The initial vertical effective stresses, estimated using Boussinesq's equations to account for the structure load, are labeled in parentheses in Figure 3.6. Structure J_A tilted excessively during the final event (large Port Island) in T4.6-40 and came in contact with a displacement transducer holder. Although this occurred near the end of strong shaking, after much of the settlement occurred, this pair of structures (i.e., A_J and J_A) is excluded in the analysis of the large Port Island event for T4.6-40.

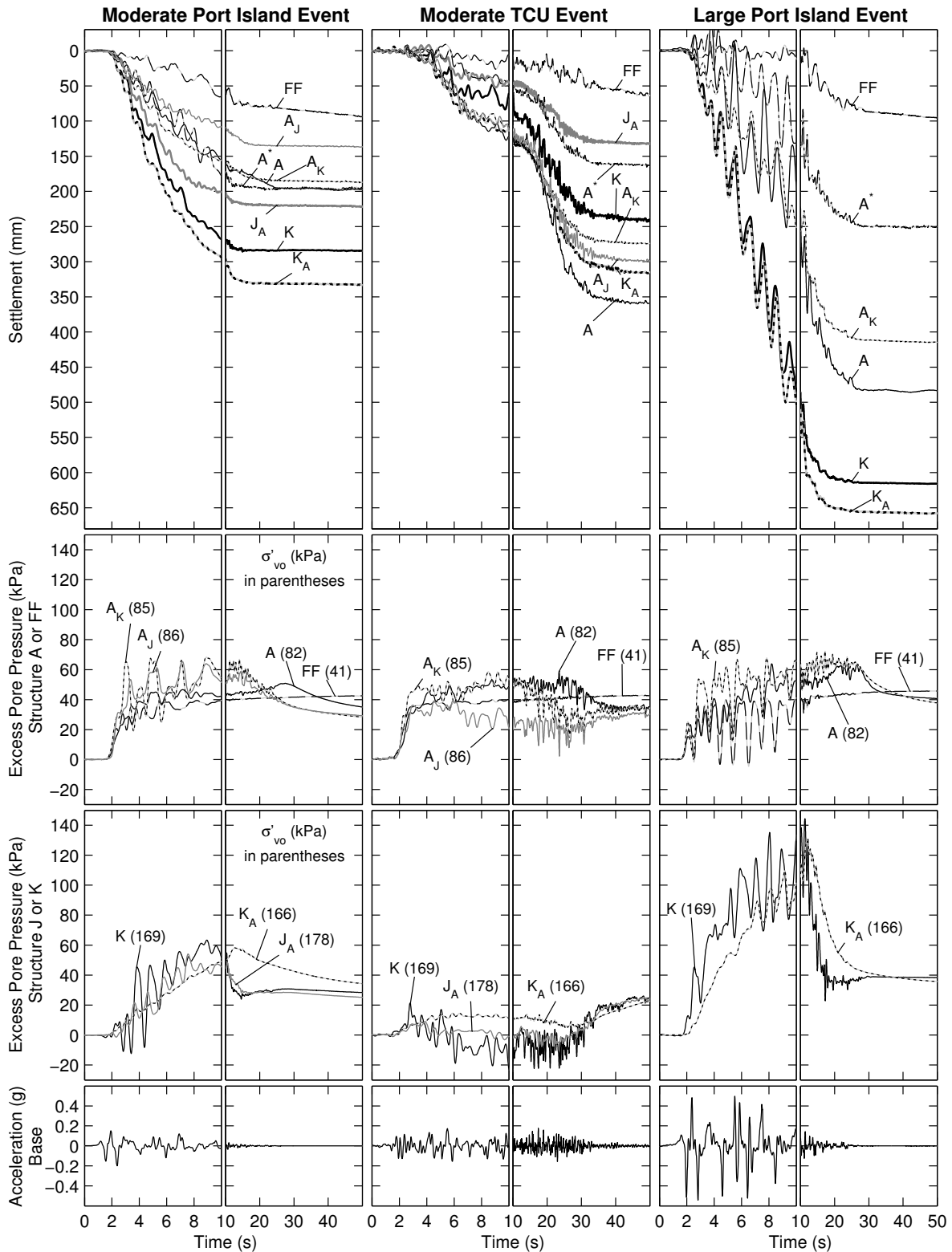


Fig. 3.6. Summary plot of T4.6-40 including structure settlement, excess pore water pressure at the middle of the liquefiable layer beneath the foundation center, and base acceleration. The isolated A structure from T4.5-50 is indicated by A*. Initial calculated vertical effective stress shown in parentheses.

Excess pore water pressure observations beneath the A-type structures include:

- Excess pore water pressures were generally higher than in the free-field during all three events, though excess pore pressure ratios were generally lower due to the higher initial vertical effective stress under the structures.
- Values of r_u reached 0.6 to 0.8 during the moderate and large Port Island events.
- Values of r_u were smaller (0.4 to 0.6) during the moderate TCU event.

Excess pore water pressure observations beneath the heavier J and K type structures include:

- Excess pore water pressures were similar to those of the A-type structures during the moderate Port Island event, but the increased bearing pressure resulted in lower r_u values of 0.3 to 0.4.
- During the moderate TCU event, almost no excess pore water pressures developed, and in the case of structures K and J_A , the excess pore water pressures were slightly negative at times. Immediately after strong shaking, however, the pore pressures increased.
- Substantially higher pore water pressures developed during the large Port Island event, with r_u values reaching as high as 0.8.

Observations involving structure settlement include:

- Most of the settlement occurred during strong shaking, confirming the importance of settlement mechanisms other than post-liquefaction reconsolidation volumetric strains.
- During the moderate and large Port Island events, the heavier J- and K-type structures settled substantially more than the lighter A-type structures.
- In contrast, the heavier structures often settled less than the lighter A-type structures during the moderate TCU event, consistent with the minimal excess pore water pressures observed.

Figure 3.7 summarizes T4.5-50 in a format similar to Figure 3.6 but includes fewer excess pore water pressure time histories, because several pressure transducers malfunctioned. The excess pore water pressures under the A-type structures are in a similar range as those observed in T4.6-40. The general settlement patterns in T4.5-50 are similar to those from T4.6-40. Nearly all settlement occurred during strong shaking with only minor post-shaking settlement. During the moderate Port Island event, Structure J_A settled within the range of the lighter A structures in contrast to observations of larger settlement during T4.6-40. However, Structure J_A did settle less than the A structures during the TCU event similar to T4.6-40. Structure J_A also settled more than most of the A structures during the large Port Island event, again following the T4.6-40 trends. As expected, the pile-supported structure (J_{A-P}) settled the least. However, there were settlements, likely caused by two mechanisms: 1) cyclic softening of the dense Nevada Sand layer due to excess pore water pressure generation; and 2) load transfer from side friction to end bearing caused by excess pore water pressure generation in the liquefiable Nevada Sand. Importantly, the adjacent A structure (A_{J-P}) consistently settled more

than Structure A_J (i.e., the A structure adjacent to the shallow-founded J structure). In fact, Structure A_J settled the least of the A structures.

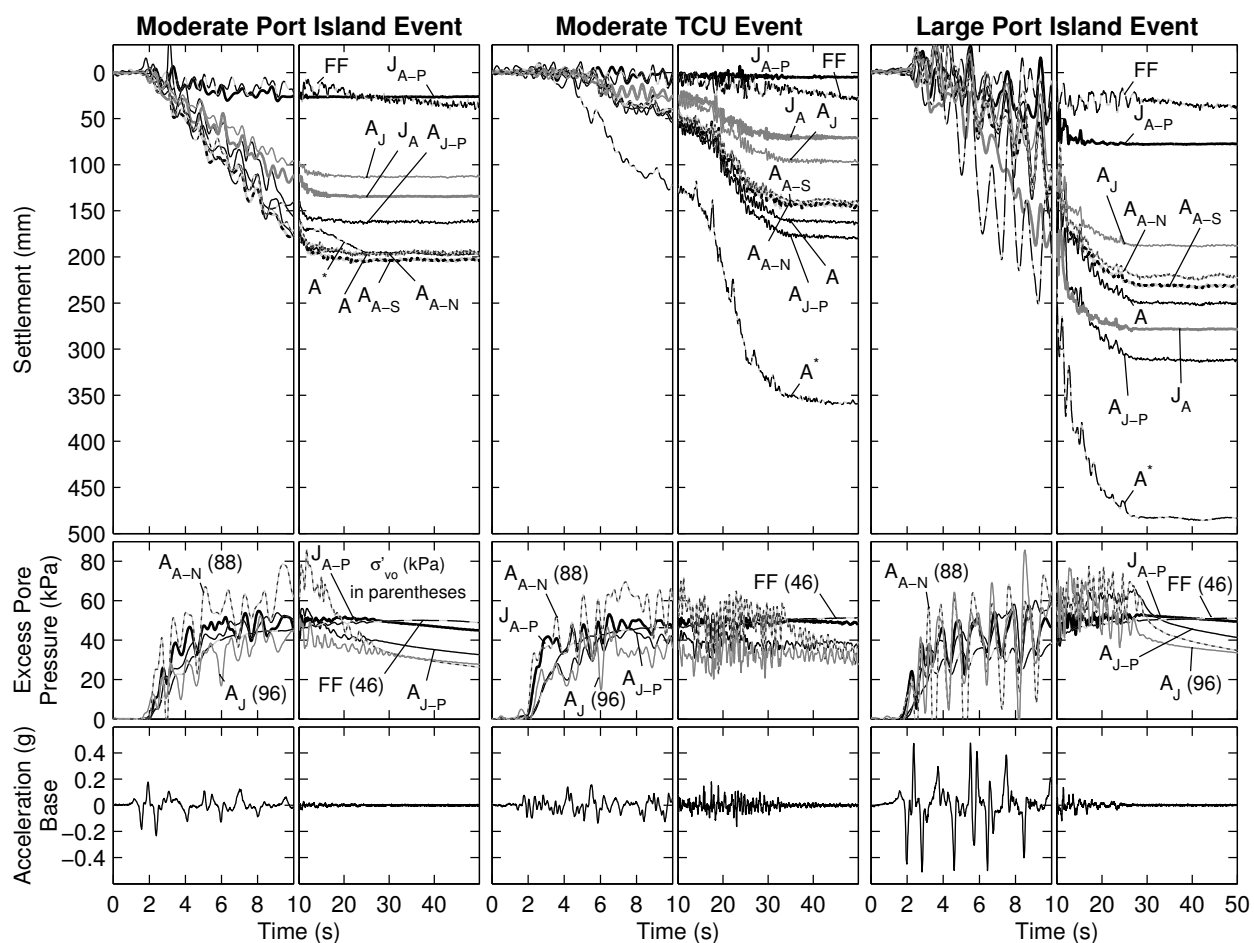


Fig. 3.7. Summary plot of T4.5-50 including structure settlement, excess pore water pressure at the middle of the liquefiable layer beneath the foundation center, and base acceleration. The isolated A structure from T4.6-40 is indicated by A^* . Initial calculated vertical effective stress shown in parentheses.

Comparison between T4.6-40 and T4.5-50 indicate that structures in the 40% relative density test settled approximately twice as much as comparable structures in the 50% relative density test. For example, the isolated A structure in T4.6-40 settled roughly twice as much as in T4.5-50. The single exception is the roughly equal settlement of the isolated A structures in T4.6-40 and T4.5-50 during the moderate Port Island event. This may be explained by the slightly higher input acceleration achieved in T4.5-50 compared to T4.6-40 as well as potential differences in model construction that may have been reduced after the first substantial shake (i.e., moderate Port Island). The A-type structure settlements from the present study were also compared to those from Dashti et al. (2010a; 2010b). Although there are several differences

between test configurations, the settlements generally follow the expected trend with varying relative density. Structure J_A also settled roughly twice as much in T4.6-40 than in T4.5-50 during all three events. Appendix B-2 compares the J-type structure settlements to the experiments of Allmond and Kutter (2012, 2013) and shows that a reasonable trend of increasing settlement with decreasing relative density generally exists, while also considering differences between the test profiles, the applied motions, and the sequence of applied motions.

Figure 3.8 shows the spatial variation of excess pore water pressures around structures A and K to provide insight into the low excess pore water pressures observed under heavy structures during the T4.6-40 moderate TCU event. The isolated A and K structures illustrate the effect of bearing pressure with otherwise similar models and without the additional complexity from adjacent structures. However, similar overall trends exist for all A-type structures relative to J-type or K-type structures. The legend indicates the location of each pressure transducer relative to the structure foundation. The initial vertical effective stress, including structure-induced stress estimated using Boussinesq's equations, is labeled in parentheses next to each sensor.

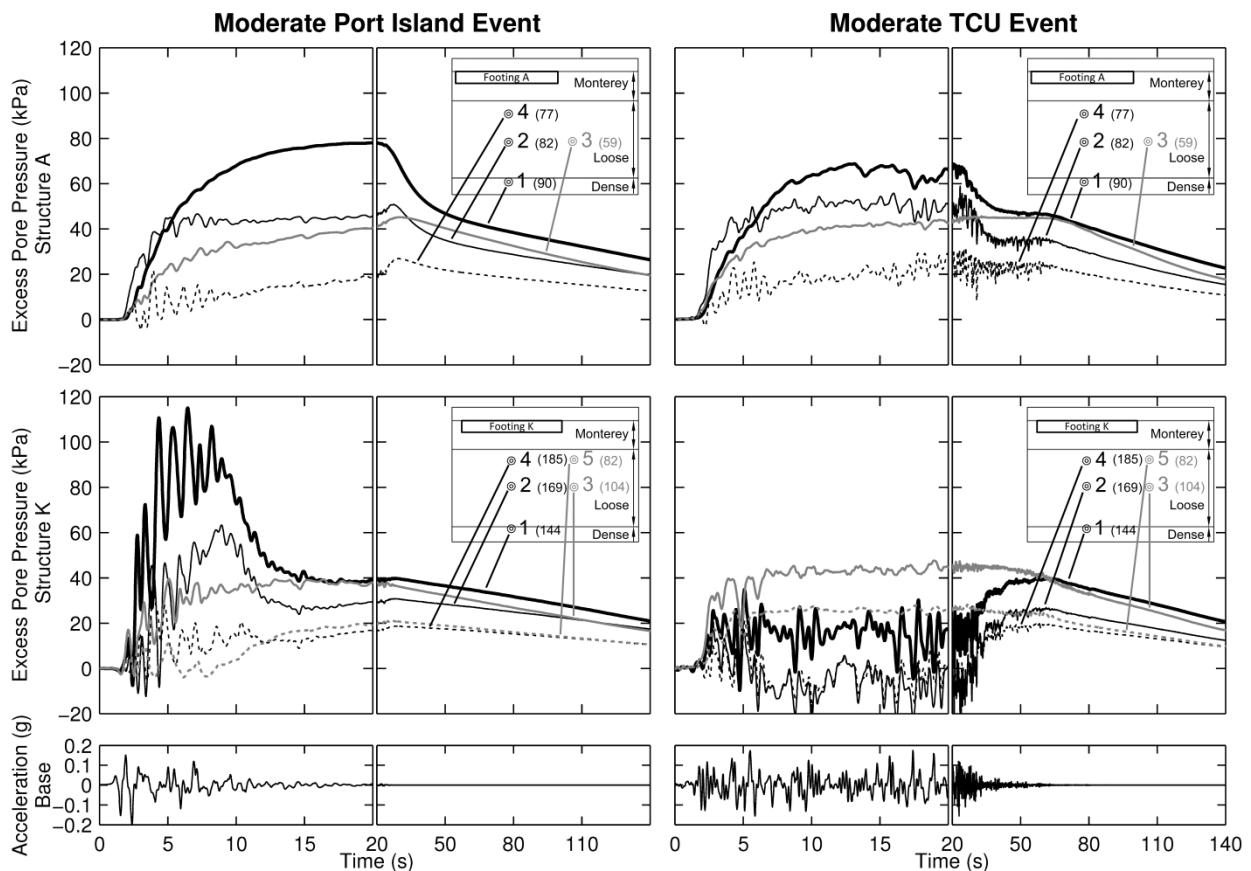


Fig. 3.8. Excess pore water pressures around the isolated A and K structures in T4.6-40. Initial calculated vertical effective stress shown in parentheses.

Substantial excess pore water pressures developed under both A and K during the moderate Port Island event. Sensor 1, at the base of the liquefiable layer directly under the structure, detected the largest excess pore water pressure followed by Sensor 2 at the midpoint of the liquefiable layer. Sensor 3, located at the midpoint of the liquefiable layer but near the edge of each foundation, detected slightly lower excess pore water pressures than Sensor 2, located at the same elevation. Finally, the sensors near the top of the liquefiable layer exhibited the lowest excess pore water pressures. After the end of strong shaking, the excess pore water pressures of sensors at the same elevation (i.e., sensors 2 and 3 for both A and K, sensors 4 and 5 for A only) tended to converge during long-term drainage.

Although similar during the moderate Port Island event, the pore water pressures beneath Structure A and Structure K were drastically different during the moderate TCU event. Structure A exhibited general trends comparable to those during the moderate Port Island event. However, the excess pore water pressure under Structure K was small or even negative during the moderate TCU event. The excess water pore pressures beneath the edge of the foundation were still small but higher than those at the center. This indicates water flowed laterally from the edges of the foundation toward the center. The excess pore water pressures of the sensors under the center of the foundation actually increased at the end of strong shaking and converged with sensors at the same elevation but near the edge of the foundation (i.e., sensors 2 and 3 or sensors 4 and 5). For the less intense TCU event, the relatively higher stresses in the foundation soils beneath the heavier structures were beneficial, and this resulted in smaller excess pore water pressures and settlements compared to the lighter structures.

The lower settlement of structures J and K during the moderate TCU event is due to the small excess pore water pressures that developed under these structures. The shear strain induced in the soils under these structures was likely lower for this moderate event. Moreover, some dilation of the soil is apparent due to the development of negative excess pore water pressures. Conversely, higher excess pore water pressures developed during the moderate Port Island event even though its peak base acceleration of 0.20 g was only slightly more than that of the moderate TCU event (0.17 g). Liquefaction during the moderate Port Island event likely resulted in some densification of the liquefiable sand layer. However, this densification is unlikely the primary cause of the reduced pore water pressures observed during the subsequent event (moderate TCU). It is more likely that the response of the structure and soil depends on shaking characteristics besides the peak base acceleration. In this case, the TCU motion had a slower energy buildup and longer duration compared to the moderate Port Island event. This suggests the need for further study and recognition that response observed in one ground motion may not be applicable to other ground motions.

3.4.3 Structural Tilt and Separation

In addition to total settlement, structure tilt is also of practical interest. Figure 3.9 shows

the cumulative tilt of adjacent structures in the shaking direction. Rotation to the south is positive, and rotation to the north is negative. A dashed line indicates the northern structure in each pair, and a solid line represents the southern structure. For example, Structure K_A is the southern structure, and it tilted to the south (positive); Structure A_K is the northern structure, and it tilted to the north (negative). Therefore, the structures in this pair tended to tilt away from each other similar to other pairs of adjacent structures. The A_J and J_A pair of structures in T4.5-50 is an exception. Following the large Port Island event, Structure A_J had tilted 1.5 degrees away from Structure J_A ; however, Structure J_A had tilted a slight 0.3 degrees toward Structure A_J . This observation is not surprising given that the substantially heavier structure will likely influence the lighter structure more than the lighter structure influences the heavier structure.

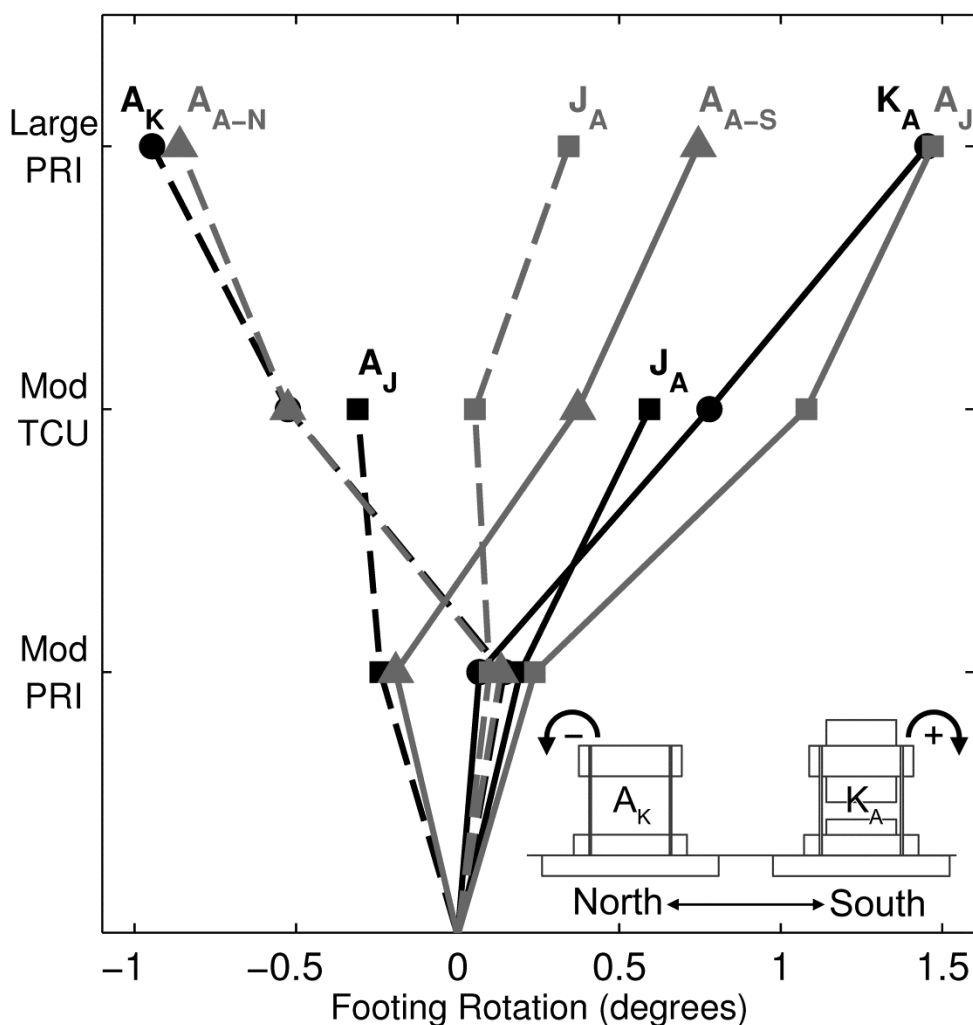


Fig. 3.9. Cumulative foundation rotations in the shaking direction of adjacent structures after each event listed. Solid lines indicate the southern structure in each pair, while dashed lines indicate the northern structure; T4.6-40 structures are shown in black, T4.5-50 in grey.

The photographs in Figure 3.10 further illustrate the tendency of adjacent structures to tilt away from each other. A vertical cut in the soil profile made during the excavation of the T4.6-40 model shows the tilt of the A_J and J_A pair of structures. Colored sand columns, which were placed vertically during model construction, indicate the lateral movement of soil beneath the structures. The sand columns neighboring the isolated Structure A foundation bulged outward in the liquefiable layer on both sides of the structure. In contrast, the middle sand column between the A_J and J_A structures remained nearly vertical, indicating limited lateral movement of this soil. The two sand columns at the exterior of this pair bulged outward similar to those around the isolated A structure. The sand columns adjacent to the isolated K structure displaced in the same way as those around the isolated A structure; the sand column between the A_K and K_A structures also remained almost vertical, and the exterior columns displaced outward. The adjacent structure provides restraint against the lateral movement of soil from underneath it, which accounts for the tendency of adjacent structures to tilt away from each other.

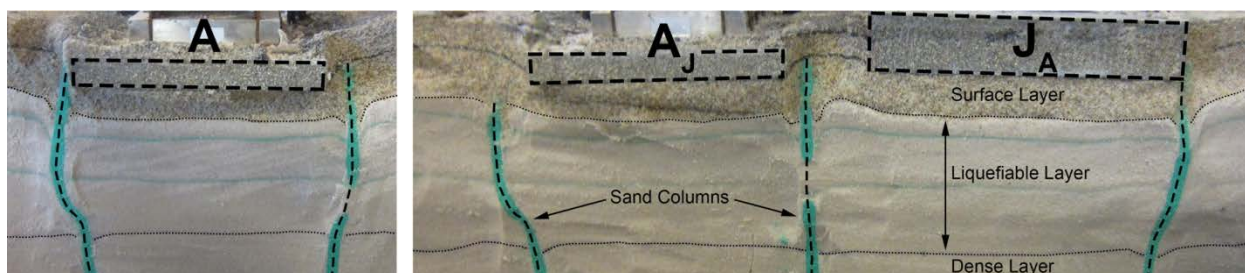


Fig. 3.10. Post-T4.6-40 test photographs of excavated soil beneath structures A, A_J and J_A .

In addition to the observation that adjacent structures generally tilted away from each other, A-type structures adjacent to other structures tended to settle less than isolated A-type structures. These two related observations are likely due to several mechanisms. The area of increased effective stress between each pair of structures is likely more resistant to liquefaction than the exterior edges of each pair, though the shear stresses transferred from the buildings to the soil are also important. Pore water pressures in this area were observed to be moderately higher than at the same relative location near the isolated A structure. However, the r_u values were actually lower, indicating decreased susceptibility to liquefaction due to the increased initial effective stress from the overlapping contributions of the adjacent structures.

There are other potential effects contributing to the observed tilt and decreased settlement of adjacent structures. Strength loss of the underlying soil can lead to a partial bearing capacity failure, sometimes in the form of foundation punching. In this case, an adjacent structure limits the ability of soil to displace laterally in that direction, which is consistent with the observed differential settlement and tilt direction. Additionally, as liquefaction generally occurs first in the free-field, the sudden loss of lateral support can cause non-liquefied soil beneath the structure foundation and adjacent to the free-field to deform under the structure induced static stresses. For pairs of adjacent structures, this effect will be more pronounced at the exterior foundation edge,

which is consistent with the observed tilt.

Lastly, the horizontal separation distance between all structure pairs increased during all events in both tests; after the three primary shaking events, the distance had increased by an average of 30 cm in T4.5-50 and 55 cm in T4.6-40. This pattern of lateral movement is consistent with the same mechanisms that influenced the settlement and tilt. These include the physical restraint of adjacent structures, increased liquefaction susceptibility under the exterior foundation edges, and a loss of lateral support as the free-field liquefies.

3.4.4 Structural Response

Individual structure accelerations are also of interest. Figure 3.11 shows the foundation and free-field spectral accelerations at 5% damping for the moderate TCU and large Port Island events. The input motions for T4.6-40 and T4.5-50 are similar and have similar spectra. However, the free-field surface spectral accelerations were notably larger in T4.5-50 for a large range of periods. The exception is the short period range during the large Port Island event due to the higher amplitude dilation spikes in T4.6-40 (as shown in Figure 3.4). The J-type structures had substantially different acceleration spectra compared to the K-type structures, particularly at longer periods. Figure 3.12 compares the acceleration-time histories of structures K_A and J_A during the T4.6-40 large Port Island event. Structure K_A has slightly higher acceleration spectral values in the 1.0 to 2.5 second period range.

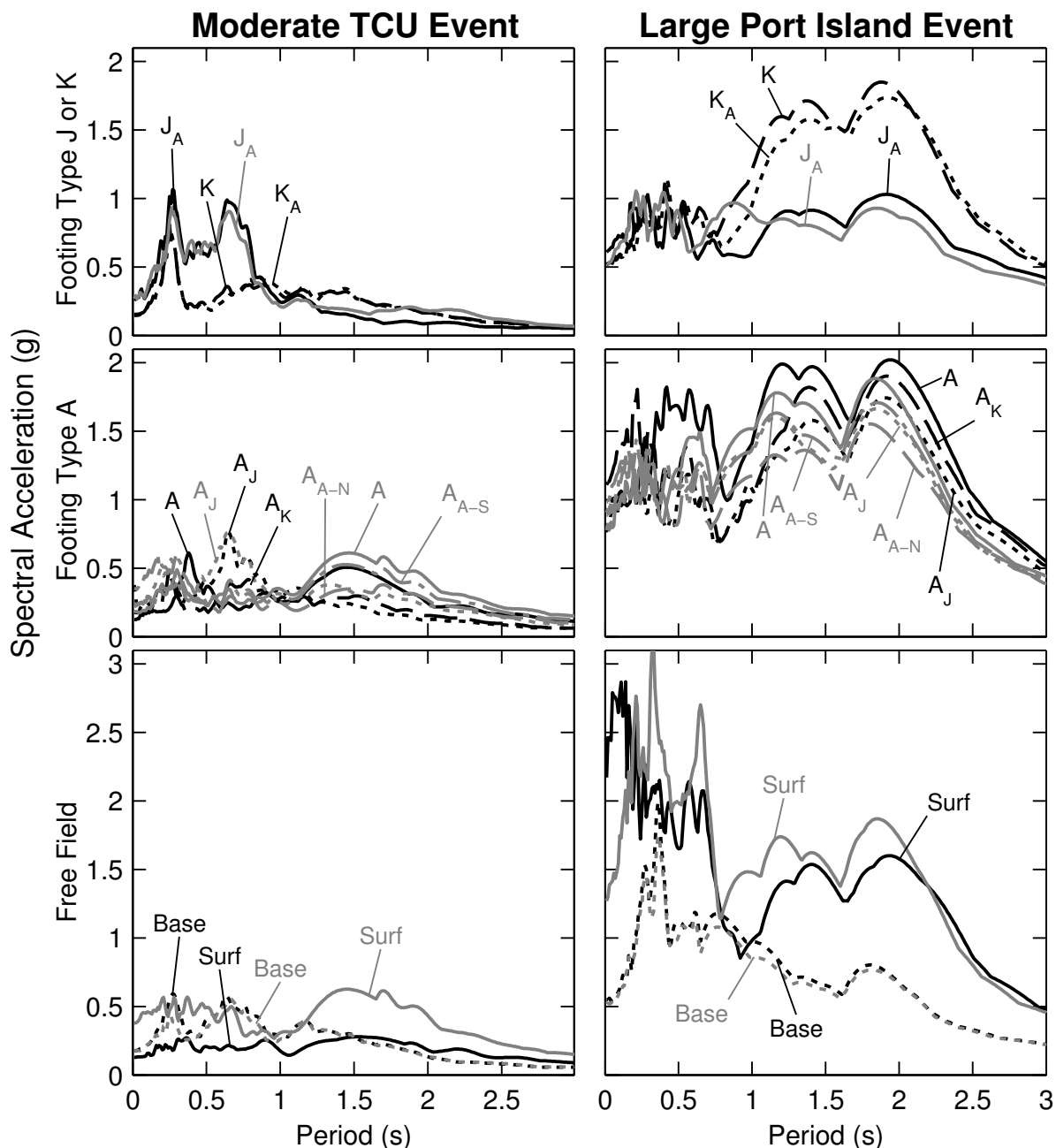


Fig. 3.11. Spectral acceleration (5% damping) with grey lines indicating T4.5-50 results and black lines indicating T4.6-40

There appears to be an adjacency effect that reduces the foundation acceleration spectral values for most period ranges during these experiments. This is most clear for the A structures. The isolated A structure generally had higher acceleration spectral values than the other A-type structures; this trend is present in both experiments. The only exception was at low periods during the TCU event, where the opposite trend occurred in the 0.5 to 1.0 second period range.

Figure 3.12 shows the acceleration-time histories for all three A-type structures in T4.6-40. The isolated A structure often has slightly higher accelerations at the peak of each cycle compared to structures A_J or A_K .

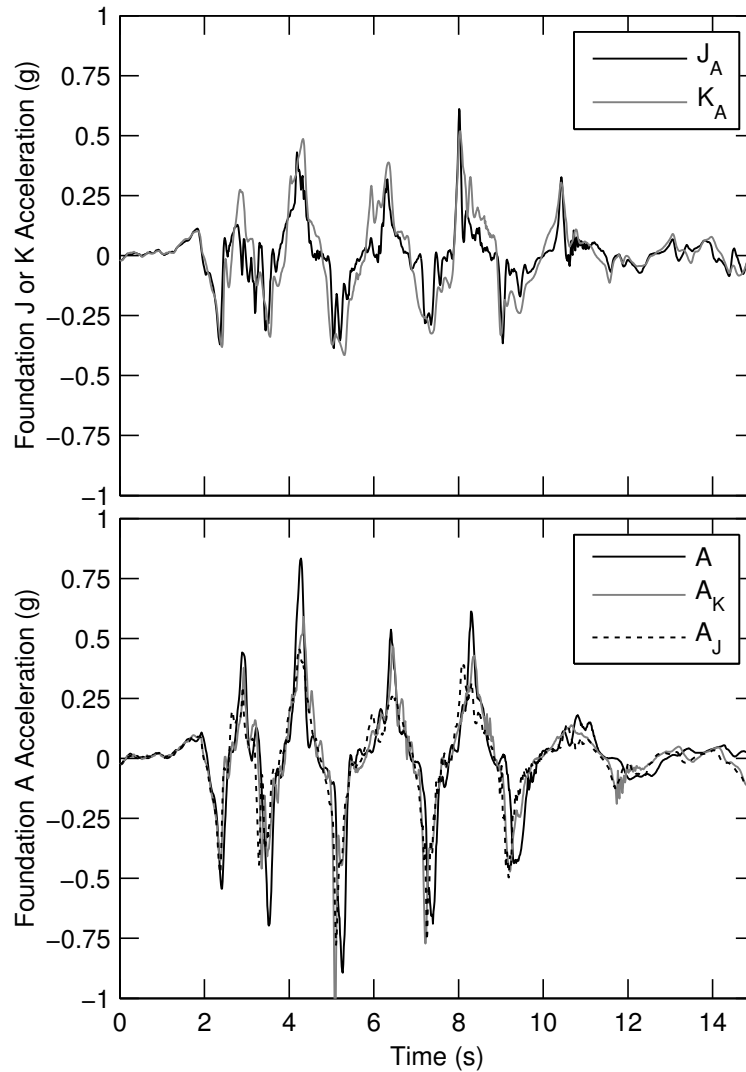


Fig. 3.12. Foundation horizontal acceleration-time histories during large Port Island event in T4.6-40

3.5 CONCLUSIONS

The geotechnical centrifuge experiments in this study provide important insights regarding the seismic performance of isolated and adjacent mat-founded model structures subjected to liquefaction or cyclic softening. Building settlements occurred primarily during strong shaking, and if supported on shallow foundations, the settlements were larger than

free-field settlements, often by a factor of two or more. This is generally consistent with the findings of other researchers and supports the importance of shear-induced deformations, such as SSI induced ratcheting and partial loss of bearing capacity, in addition to volumetric deformation mechanisms such as partial drainage.

The performance of the model structures in these experiments depended on a complex interaction between the soil properties, the ground motion characteristics, and the structural properties. Each factor is essential to consider when evaluating the potential for liquefaction effects on buildings. For example, the structural settlements measured during the moderate TCU event illustrate that it is not always correct to assume that a heavier mat-founded structure will settle more than a lighter mat-founded structure. A centrifuge test program that only used Port Island events would have missed this key response. This complex phenomenon is dependent on several factors. Thus, it is important to recognize that the trends presented in this and other studies may not be universally applicable beyond the particular scenarios tested.

For the particular combination of structures, soil conditions, and ground motions used in these centrifuge tests, it was observed that:

- A higher relative density leads to less settlement with all else equal, consistent with other studies (e.g., Dashti et al. 2010a).
- A-type structures that were adjacent to other shallow-founded structures often settled less than isolated A-type structures.
- Adjacent pairs of structures tended to tilt and move laterally away from each other.
- Structures adjacent to other shallow-founded structures tended to have lower foundation spectral acceleration values compared to isolated structures.

The post-test excavation photographs of the models confirmed that adjacent structures restrained the lateral movement of soils from underneath closely spaced foundations, which in turn reduced the measured building settlement. In these experiments, the physical restraint imposed by the adjacent foundation on the liquefied soil beneath the structure led to reduced settlements. The results of centrifuge tests can be valuable in developing, evaluating, and calibrating numerical models for use in more extensive parametric studies. Although these tests provide important insights, caution should be exercised with respect to generalizing the findings from this study as they are based on a limited number of cases. Additional work is warranted to extend the insights developed through this testing program and to continue to advance the profession's knowledge of the seismic performance of buildings subjected to soil liquefaction or cyclic softening.

CHAPTER 4: LIQUEFACTION-INDUCED BUILDING PERFORMANCE DURING THE 2010 CHILE EARTHQUAKE

4.1 LITERATURE REVIEW

4.1.1 Liquefaction and Soil-Foundation-Structure Interaction

Liquefaction case histories are essential in the development of liquefaction triggering and settlement correlations; they also facilitate calibration of numerical models and comparisons to geotechnical centrifuge tests. Recent earthquakes in Chile (Bray et al. 2012), New Zealand (Cubrinovski et al. 2011), and Japan (Tokimatsu et al. 2012) caused extensive liquefaction-induced damage to infrastructure and provide important opportunities to develop comprehensive, insightful case histories and to learn from the performance of structures affected by liquefaction. Current SPT and CPT-based correlations for free-field liquefaction triggering (e.g., Youd et al. 2001; Cetin et al. 2004; Moss et al. 2006; Boulanger and Idriss 2014) do not account for the influence of cyclic shear mechanisms due to the presence of a structure. Volumetric settlement correlations (e.g., Tokimatsu and Seed 1987; Ishihara and Yoshimine 1992; Zhang et al. 2002; Cetin et al. 2009) also do not account for the structure-induced shear mechanisms outlined by Dashti et al. (2010a). The following field investigation summaries provide recent examples of the importance and value in developing case histories of liquefaction involving SFSI.

The 1999, M_w 7.4, Kocaeli, Turkey earthquake caused settlement and lateral movement to many structures in Adapazari, Turkey (Sancio 2003). Extensive field investigations, including SPT and CPT, identified a shallow layer of low plasticity silt that liquefied resulting in widespread damage (Sancio et al. 2002). Based on an extensive laboratory testing program of silty soils collected during this investigation, Bray and Sancio (2006) suggest that plasticity index (PI) is a better indicator of liquefaction susceptibility than the Chinese Criteria presented by Seed and Idriss (1982). Soils with PI less than or equal to 12 were liquefiable, soils with PI between 12 and 18 were moderately susceptible to liquefaction when intensely shaken, and those with PI greater than 18 were not susceptible to liquefaction. SPT energy measurements helped ensure accurate $(N_1)_{60}$ values and were later used to show the limited impact of short rods on the transmitted energy (Sancio and Bray 2005).

Widespread liquefaction in Christchurch, New Zealand during the 2010–2011 Canterbury sequence caused extensive damage. Although smaller in magnitude than the earlier M_w 7.1 Darfield earthquake, the M_w 6.2 Christchurch earthquake damaged far more structures in the Christchurch Central Business District, which was built over a highly variable floodplain consisting of fluvial gravels, sands, and fine grained soils (Cubrinovski et al. 2011). Bray et al. (2014) examined the effects of liquefaction on several shallow-founded multi-story structures; these cases emphasize that empirical correlations of liquefaction triggering and settlement developed for free-field sites do not adequately account for the effects of structures. Additionally, the large volume of liquefaction ejecta observed after this event (e.g., Cubrinovski

et al. 2011; Bray et al. 2014) serves as a reminder that ground loss through ejecta can also contribute substantially to total settlements. Zupan (2014) presents a detailed investigation of numerous structures affected by liquefaction and observed that the volumetric strain-based method of Zhang et al. (2002) underestimated settlements.

The 2011, M_w 9.0, Tohoku earthquake caused extensive damage and triggered a large tsunami. Although the tsunami was the largest source of damage, liquefaction affected structures in many areas as noted by Tokimatsu et al. (2012). Ashford et al. (2011) observed that although residential buildings in the Kanto Plain Region suffered liquefaction-induced settlement, the use of mat foundations limited structural damage in many cases. Of the roughly 27,000 residential structures damaged by liquefaction, around half were located in the Tokyo Bay Area, commonly on land reclaimed by dredging (Yasuda et al. 2012). One of these reclaimed areas, Urayasu City, suffered extensive damage (Tokimatsu and Katsumata 2012), and the performance of closely spaced buildings provide potential examples of SSSI.

Geotechnical centrifuge tests complement field studies by permitting careful control of the soil, ground motion, and structure properties and enable the response to be measured with hundreds of sensors. Dashti (2009) provides an in-depth, recent review of liquefaction and SFSI as well as valuable findings from a series of four geotechnical centrifuge tests summarized in Dashti et al. (2010a,b). They identified key liquefaction-induced building settlement mechanisms including: a) volumetric mechanisms—rapid drainage, sedimentation, and consolidation; and b) shear mechanisms—partial bearing capacity loss and soil-structure interaction (SSI)-induced building ratcheting. A number of recent centrifuge tests (e.g., Dashti et al. 2010; Allmond and Kutter 2012; da Silva Marques et al. 2014), along with the centrifuge tests presented in Chapter 3 of this work, illustrate the importance of SFSI and found that structures generally settle substantially more than the free-field ground.

Lastly, numerical modeling can improve understanding and help develop methods that account for SFSI involving liquefaction. Numerical models, after properly calibrated, allow a systematic variation of parameters (i.e., ground motion, soil profile, and structural properties) to a level that would not be feasible with centrifuge testing. Dashti and Bray (2013) produced results in FLAC-2D with the UBCSAND model that were generally consistent with the Dashti et al. (2010a,b) centrifuge test results, which illustrates the potential of numerical models to capture complex phenomena. Andrianopoulos et al. (2010) developed numerical procedures accounting for SFSI effects during liquefaction with results that compared favorably to those of geotechnical centrifuge tests. Karamitros et al. (2013a,b) applied these procedures to examine the beneficial effects of a non-liquefiable surface layer and developed a methodology for estimating liquefaction-induced building settlement under these conditions. Unutmaz and Cetin (2012) provide a simplified method to estimate liquefaction-induced building settlement based on the earlier numerical work of Cetin et al. (2012) combined with data from the 1999 Kocaeli and Duzce, Turkey earthquakes.

4.1.2 Summary of 2010 Maule, Chile Earthquake

The M_w 8.8 February 27, 2010 Maule, Chile earthquake caused damage over a wide area and triggered a damaging tsunami. As one of the largest earthquakes recorded, this provides an important opportunity to learn about the performance of infrastructure subjected to such a large and long duration event. Adherence to the strict Chilean building code likely reduced the total damage. However, there were still 521 deaths, damage to over 300,000 structures, and an estimated \$30 billion in damages (Elnashai et al. 2010). Most critical infrastructure performed acceptably on the whole, but there were notable cases of liquefaction-induced damage to bridges (Ledezma et al. 2012) and a hospital (Bray et al. 2012), which are essential after a large earthquake. Learning from the liquefaction-induced damage to these key structures is important in advancing the understanding of SFSI and liquefaction.

The subduction of the Nazca plate beneath the South American plate occurs at roughly 7 cm/year (Schellart et al. 2007), and this plate boundary makes up much of the western coast of Chile. This subduction zone has a history of producing very large events, including the largest ever recorded: the 1960 Valdivia event (M_w 9.5). The 2010 Chile earthquake averaged 5 m of slip over an 81,500 km² rupture area (Lay et al. 2010). The epicenter was located at 35.95°S, 73.15°W with an 18° strike and dip of 18°. The fault rupture occurred in the seismic gap between the 1960 Valdivia and 1985 Valparaiso events (Delouis et al. 2010). Co-seismic energy release resulted in 1.8 m of uplift at the Arauco peninsula and 30 cm to 70 cm of subsidence in the central valley (Vigny et al. 2011). High intensity ground motions were felt over a large area as indicated in the USGS ShakeMap in Fig. 4.1. Boroschek et al. (2012) summarize the 31 available strong ground motion recordings, ranging in rupture distance from 30 km to 700 km.

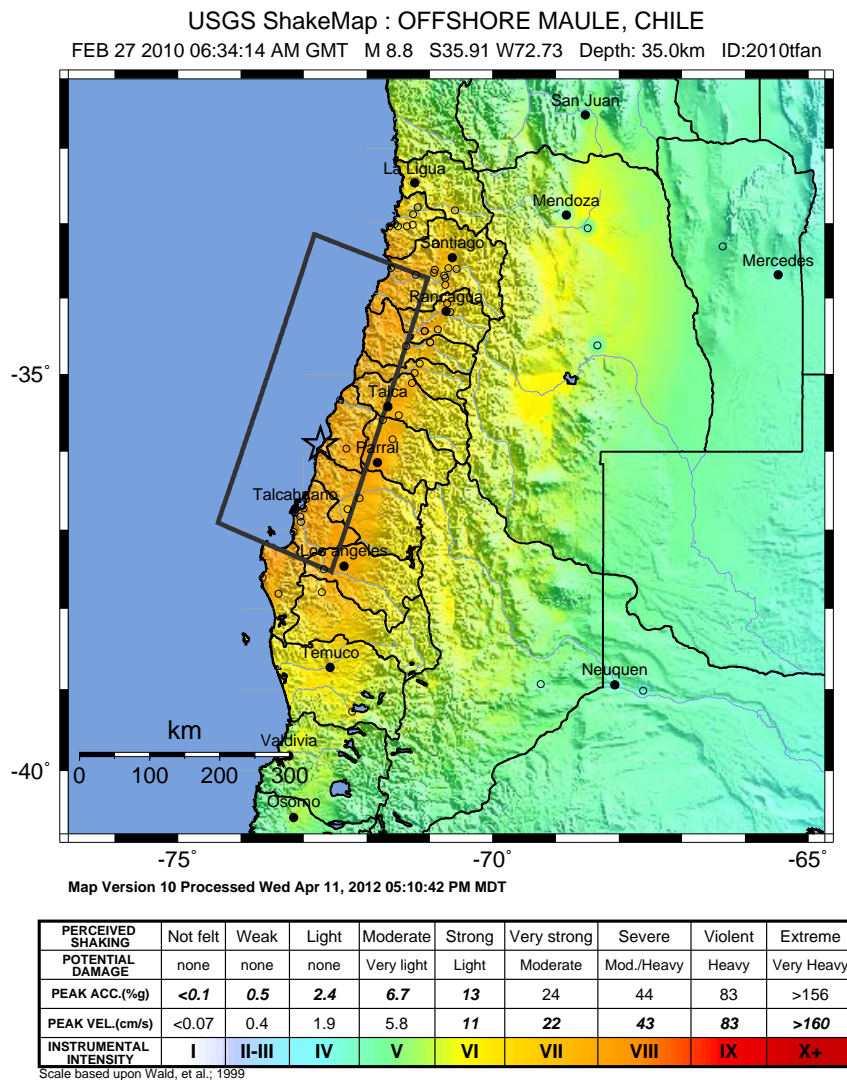


Fig. 4.1. 2010 Chile earthquake USGS ShakeMap

The Geotechnical Extreme Events Reconnaissance (GEER) post-event reconnaissance and report (Bray and Frost 2010) has been invaluable to this study. They summarize damage to the Hospital Provincial in Curanilahue, Juan Pablo II Bridge, and Llacolén Bridge, which are the focus of this study. Improved characterization of the subsurface conditions at these sites is essential to develop detailed case histories of SFSI. The details of the hospital and bridges are summarized in the relevant sections; however, valuable findings from other sites involving liquefaction and SFSI are briefly summarized below.

The widespread occurrence of liquefaction is not surprising given the large number of rivers flowing from the Andes to the Pacific and the resulting fluvial deposits. Major roads run north-south, including in the Pan American Highway, creating a large number of river crossings. Although widespread, damage to roads tended to be related to settlement of underlying fills and

was quickly repaired with temporary gravel patches to reopen the roads (Ledezma et al. 2012). However, several cases of embankment failures also affected roads.

Most bridges performed reasonably well, only 439 of 7730 bridges suffered damage, with settlement of approach fills representing the most common failure mechanism (Ledezma et al. 2012). GEER observed liquefaction and lateral spreading damage at a number of important bridges (Bray and Frost 2010). For example, four large bridges cross the Bío-Bío River near Concepción. Two of these, the Llacolén and Juan Pablo II Bridges, handle vehicular traffic and suffered liquefaction-induced lateral spreading and settlement of embankments and piers (Ledezma et al. 2012); these two bridges will be discussed in detail in later sections. The Puente Viejo (Puente Bío-Bío) Bridge, constructed in the 1930s, closed in 2002 due to its poor structural integrity and was used as a pedestrian bridge only (Bray and Frost 2010). This bridge suffered extensive damage including the collapse of numerous slab sections and bents. The final bridge crossing the Bío-Bío River in this area is a railroad bridge built in 1889. Although retrofitted in 2005, it suffered moderate damage including some likely caused by lateral spreading of the river banks (Bray and Frost 2010). Several other damaged bridges are also documented by Bray and Frost (2010) and Ledezma et al. (2012).

Four, nearly identical, eight-story condominiums in a complex in Concepción suffered varying degrees of damage, ranging from negligible to severe liquefaction-induced damage (Bray et al. 2012). The shallow foundations sit on a sandy fill placed to increase the elevation of the previously marshy ground. Two of the buildings experienced large settlements, substantial tilt, and damage to the superstructure, rendering them uninhabitable; they were eventually demolished. However, of the remaining two structures, one was only slightly damaged, and the other was essentially undamaged. This provides a significant opportunity to evaluate how differing soils conditions affected the performance of these identical structures, and further research is currently underway to better characterize the subsurface conditions.

Given Chile's unique geography, ports are another critical infrastructure component. Liquefaction-induced damage was severe at ports in Coronel and Concepción, which are among the most important in the country. The port at Coronel has two main piers for loading cargo and a flat cargo storage area restrained by a 9 m sheet pile wall located at the beach. Although the piers performed well, widespread liquefaction in the cargo storage area resulted in substantial damage including maximum lateral displacements of around 1 m at the wall (Bray et al. 2012). Similarly, at the Concepción Port area (S36.727°, W73.132°) notable lateral spreading resulted in an estimated horizontal displacement of 50 cm and deep cracks in the wharf (Bray et al. 2012).

The detailed documentation of damage contained in the GEER Report (Bray and Frost 2010) and summarized in subsequent articles (e.g., Bray et al. 2012; Ledezma et al. 2012; Verdugo et al. 2012) has been vital for this study. This type documentation must take place shortly following an earthquake so that the damage can be documented and learned from before repaired. GEER also used rapid, portable methods to roughly investigate subsurface conditions, including dynamic cone penetration testing (DCPT) and shear wave velocity estimates using spectral analysis of surface waves (SASW). However, in many cases a more rigorous subsurface

site investigation should be performed to develop comprehensive field case histories. The present study involves site investigations, including SPT and CPT, performed at sites of critical interest identified from the GEER reconnaissance. These improved case histories can then be used in calibrating numerical models, comparing to geotechnical centrifuge tests, and improving empirical methods for SFSI and liquefaction.

4.2. TESTING PROCEDURES

4.2.1. Cone Penetration Testing

Cone penetration testing has increased in recent years because it is generally fast, reliable, and cost effective. Data acquisition systems automatically log tip resistance, sleeve friction, and pore water pressure at small increments, resulting in an essentially continuous profile. Disadvantages include poor performance in gravel and the inability to collect samples with a typical CPT apparatus. The use of CPT is uncommon in Chile; however, given its advantages, it was included as a tool in the site investigations of this study.

A Chilean company associated with the University of Chile, IDIEM, performed all CPT soundings. The CPT rig was not truck based as is common in the US and elsewhere, but instead, consisted of a hydraulic press mounted to two, 6 m long I-beams. A truck-mounted crane lowered the CPT apparatus into position. Four, two-ton concrete blocks were then placed on the I-beams to act as a counterweight. Fig. 4.2 shows a concrete counterweight being lowered onto the I-beams, and Fig. 4.3 illustrates the final configuration. Although this unusual equipment allowed access to small spaces inaccessible to a truck, it had substantial disadvantages. Positioning, preparing, and removing the CPT equipment for each test was time intensive, so it was only possible to do one CPT sounding per day. Thick gravel layers or buried concrete blocks were particularly problematic because the equipment could not be moved quickly to a new location. To help mitigate this issue, excavations up to 1 m deep were dug by hand to bypass surface fills and any shallow obstructions before positioning the CPT equipment.



Fig. 4.2. CPT frame in position with a concrete counterweight being placed



Fig. 4.3. CPT in use at Hospital Provincial in Curanilahue

The CPT cone, manufactured by GeoMil Equipment, had a cross-sectional area of 10 cm^2 and an apex angle of 60° . The friction sleeve had an approximate surface area of 150 cm^2 , and the pore pressure filter was located just behind the cone base (i.e., the “u2” position). The data acquisition system recorded the cone tip resistance, sleeve friction, pore pressure, inclination, and time at 1 cm increments. The friction sleeve readings were shifted to align with the cone tip readings at equal depth. Cone tip resistance was converted to corrected cone tip resistance (q_t) using a net area ratio of 0.81.

Damage to the clamp component of the hydraulic press often led to an insufficient grip of the CPT push rods. While lowering the hydraulic press, the push rods would occasionally slip through the faulty clamp and the cone would not advance. The clamp condition worsened as time passed. Fig. 4.4 shows a push rod scraped by the clamp as the rod slipped through it. Shaking the push rods while slowly lowering the hydraulic press generally forced the clamp to properly grip the rods. Fig. 4.5 shows this process in action with the clamp contained in the silver box. The downward displacement of the hydraulic press triggered data recordings at 1 cm increments and resulted in erroneous recordings during intervals when the cone was not actually advancing. However, these extra data points were generally identifiable as the cone and sleeve readings were near zero. Removing these extra data points resulted in reasonable cone tip resistance and sleeve friction profiles. A second, smaller issue involved the penetration rate, which was frequently less than the 2 cm/s standard because the operators were concerned with encountering gravel or other debris.



Fig. 4.4. Scraped CPT push rod due to insufficient clamp grip



Fig. 4.5. IDIEM operators manually shaking the push rods while slowly lowering the hydraulic press to force the clamp grip the push rod

4.2.2. Standard Penetration Testing and Index Tests

One SPT boring performed at each site supplemented the CPT soundings and provided soil samples. IDIEM carried out all SPT testing using a self-contained drill rig, similar to the CPT equipment; Fig. 4.6 shows this rig lowered into place with a crane. Again, this required considerable time to prepare and dismantle, but was able to fit into tight areas. The drilling method used coring with a diamond bit and a 3.5 inch outer diameter.



Fig. 4.6. Lowering SPT equipment into position

SPT procedures followed ASTM D1586 and D6066 using a safety hammer manually operated with a rope and cathead system. Fig. 4.7 shows an SPT in progress using a standard split spoon sampler (i.e., 2 in. outer diameter and 1 3/8 in. inner diameter) with a flexible plastic core catcher. The rods were 1.5 m long AW type. Samples were visually identified, photographed, and stored in plastic bags for later index testing.



Fig. 4.7. SPT performed with energy measurements

SPT blow counts are highly sensitive to the operator and equipment used. Accordingly, Emerson Figueroa, using an SPT Analyzer from Pile Dynamics Inc., carried out SPT energy measurements following ASTM D4633. The rod instrumented with force transducers and accelerometers is visible in Fig. 4.7. Timing constraints limited the energy measurements to two sites: the Juan Pablo II Bridge, and the Llacolén Bridge. Table 4.1 shows the energy transfer ratio (ETR) for each SPT in these two borings. The original drill rig (JOY 21) suffered

mechanical problems after Z3-B1, so the final boring (Z4-B1) used a replacement rig sent from Santiago (JOY 22). However, both drill rigs used the same SPT hammer.

Table 4.1. Summary of measured energy values

Boring	SPT Test	Final Depth of Test (m)	ETR (%)		
			Mean	SD	Max
Z3-B1 (JOY 21)	1	0.45	53.8	6.5	65.5
	2	5.45	56.1	4.6	71.1
	3	6.2	47.1	3.8	53.2
Z4-B1 (JOY 22)	4	3.7	50.5	3.7	54.1
	5	4.45	64.1	5.3	71.8
	6	5.2	65.9	2.9	73.2
	7	5.95	60.7	2.5	65.2
	8	6.7	70.3	2.4	73.4
	9	7.45	64.5	2.4	69.0

Index tests on SPT samples (and a few other sources), were performed either in Chile by IDIEM or in the UC Berkeley soils lab. IDIEM performed sieve analysis to estimate grain size and estimated liquid and plastic limits following ASTM D4318. At the UC Berkeley lab, soil tests included grain size characteristics following ASTM D422 on all samples, and Atterberg limits following ASTM D4318 for potentially plastic soils. Liquid limits were estimated using the multipoint method with a minimum of three points but typically more. The results of these tests are discussed in the relevant sections, and detailed information including gradation curves and sample photographs can be found in Appendix C-2.

4.2.3. Overview of Analysis Methods

Empirical correlations of liquefaction triggering and settlement developed for free-field sites are often used in practice even when a structure is present at the site. These methods do not account for the effects of structures; unfortunately, well-developed alternative methods accounting for structure effects are lacking. Several recent SPT and CPT-based methods applied to the present study illustrate potential shortcomings of this process. This section summarizes the overall approach taken, and subsequent sections discuss issues and assumptions specific to individual sites.

Three recent correlations were applied to the SPT borings and CPT soundings of this study. For SPT these methods include Youd et al. (2001), Cetin et al. (2004), and Boulanger and Idriss (2014); for CPT the three methods are Youd et al. (2001), Moss et al. (2006), and Boulanger and Idriss (2014). Youd et al. (2001) represents a consensus from several workshops held in the late 1990s aimed at providing practical guidance on liquefaction triggering

correlations. The SPT based correlation in Youd et al. (2001) is largely based on Seed et al. (1985), and the CPT correlation is primarily from Robertson and Wride (1998). Cetin et al. (2004) provide deterministic and probabilistic SPT-based correlations base on rigorous statistical analysis of an updated dataset of liquefaction case histories. Moss et al. (2006) present a parallel method using CPT data. Boulanger and Idriss (2014) is an updated version of Idriss and Boulanger (2008). Although a detailed review of each method is beyond the scope of this study, the paragraphs below describe important assumptions and deviations from these methods.

Each method requires an estimate of total and effective stress profiles. For CPT data, the correlation of Robertson and Cabal (2010) provides soil unit weight estimates. The resulting unit weights also served as an estimate for SPT-based correlations. Water table estimates were based on direct measurements taken from borings or from pore water pressure measurements taken during CPT soundings. The water table at all three sites likely fluctuates with the season and recent weather conditions. Accordingly, liquefaction-triggering plots show results for the entire profile, even above the water table. For example, the factor of safety against liquefaction is calculated and shown above the water table to give a rough sense of the liquefaction susceptibility of that material if the water table was marginally higher during the earthquake. Of course, changes in the water table will change the stress profiles and thus affect the analysis to a relatively minor degree for moderate water table fluctuations.

Cone tip resistance (q_c) was converted to the corrected cone tip resistance (q_t) to account for pore pressure acting on the cone geometry (net area ratio of 0.81) for all three analysis methods. The measured energy transfer ratio (ETR) was used to convert from N to N_{60} , and in cases with no ETR measurements, the average ETR for that particular SPT rig was used. The overburden correction factor (C_N) was capped at 1.7 for Youd et al. (2001), 1.6 for Cetin et al. (2004), and 1.7 for Boulanger and Idriss (2014).

One input parameter in Cetin et al. (2004) is the shear wave velocity in the top 12 m ($V_{s,12m}^*$). Shear wave velocity profiles measured by Robert Kayen in the Bray and Frost (2010) effort using spectral analysis of surface waves (SASW) suggest $V_{s,12m}^*$ values of 200 m/s at Hospital Provincial and Llacolén Bridge and 150 m/s at the Juan Pablo II Bridge. The Boulanger and Idriss (2014) method requires fines content, and for their CPT methodology, they provide a fines estimate based on the soil behavior type index (I_c) and a fitting parameter C_{FC} . They suggest estimating C_{FC} by regressing fines content (from index tests) against I_c . However, as there was considerable heterogeneity in the soil profiles and a lack of CPTs in close proximity to SPTs, C_{FC} was assumed to be zero. A sensitivity analysis performed with $C_{FC} = 0.29$ and -0.29 (i.e., approximately plus or minus one standard deviation) had a negligible effect on the analysis and estimated factors of safety.

The SPT-based liquefaction triggering summary plots (e.g., Fig. 4.18) contain subplots of $(N_1)_{60}$, plasticity index (PI) and fines content, cyclic stress ratio (CSR), cyclic resistance ratio (CRR), and factor of safety against liquefaction. Soils with $(N_1)_{60cs} > 30$ are generally considered non-liquefiable (Youd et al. 2001). Therefore, the CRR and FS of soils exceeding this amount are plotted as an arbitrarily large number. However, given the large earthquake, soils with

$(N_1)_{60cs}$ slightly less than 30 (e.g., 29) were likely to liquefy, so the cutoff at a $(N_1)_{60cs}$ value of 30 results in sharp discontinuities. Dashed CRR and factor of safety lines indicate soils that are unlikely to liquefy based on the PI (i.e., $PI > 18$). They are shown, however, as the heterogeneity of this deeper deposit and the limited number of Atterberg limit tests performed by IDIEM lead to substantial uncertainty. The deterministic method (i.e., 15 percent probability of liquefaction) of Cetin et al. (2004) is plotted when compared to the other methods.

The CPT-based liquefaction triggering summary plots (e.g., Fig. 4.19) show the corrected cone tip resistance (q_t), the soil behavior type index (I_c), CSR, CRR, and factor of safety against liquefaction triggering. Youd et al. (2001) suggest that a soil behavior type index (I_c) of 2.6 marks the transition from liquefiable to non-liquefiable soil. For values of I_c exceeding 2.6, the factor of safety is not plotted, and there is a gap instead.

The final subplot in the CPT analysis plots present volumetric settlements based on Zhang et al. (2002). This method estimates the volumetric strains at free-field, level-ground sites based on the factor of safety against liquefaction and the equivalent clean sand normalized CPT tip resistance ($(q_{c1N})_{cs}$). The Zhang et al. (2002) method is based on the results of the Robertson and Wride (1998) triggering assessment, so in the present study, the volumetric strains are calculated from the results of Youd et al. (2001), which is largely based on Robertson and Wride (1998). Interpolation was used to estimate the volumetric strains at safety factors between the discrete values provided by Zhang et al. (2002). Again, the cumulative settlement profile is calculated above the water table given the uncertainty its location at the time of the earthquake. Therefore, the liquefaction-induced settlement should be read off the plot at water level.

4.3 CASE HISTORIES OF STRUCTURE PERFORMANCE AT LIQUEFACTION SITES

4.3.1 Hospital Provincial, Curanilahue

4.3.1.1 Background

Liquefaction-induced damage strongly affected the recently constructed Hospital Provincial ($S37.473084^\circ$, $W73.348712^\circ$) in the city of Curanilahue, Chile. Fig. 4.8 shows the location of the city of Curanilahue in Arauco Province, Bío-Bío Region. GEER (Bray and Frost 2010) identified this site as an important opportunity to examine SFSI as well as SSSI effects, given the hospital consists of a number of structurally isolated wings.



Fig. 4.8. Location of the Hospital Provincial site and recording stations

Hospital Provincial opened in 2008 and replaced several one story structures at the site (Bray et al. 2012). The hospital consists of 10 structurally isolated wings varying in height from one to six stories. Fig. 4.9 shows the 10 individual wings. Wing 1C and part of 1A are six stories,

Wings 1A and 1B are five stories, 1D is three stories, 1F, 2G, 2H, 2I, and 2J are 2 stories, and 1E is one story. Most other structures in the city of Curanilahue are one to two stories and did not suffer notable liquefaction damage (Bray and Frost 2010).



Fig. 4.9. Plan view of hospital foundations (foundation measurements in cm)

The foundation of the hospital consists of a combination of shallow spread and strip footings with interconnected grade-beams. Fig. 4.9 shows the footings, grade-beams, and first story structural walls. Fig. 4.9 also shows typical foundation cross sections including elevations. In general, wings 1A through 1F had similar footing elevations, which were lower than the footings of Wings 2G through 2J. Concrete shear walls coupled with deep spandrel beams provide lateral load resistance in the superstructure. Gravity loads are carried by interior concrete columns in a conventional cast-in-place, slab-girder style diaphragm (Bray et al. 2012).

The nearest available ground motion records are from Angol (ANGO), located 67 km from Curanilahue, and in Concepción (CSP and CONC), located 73 km and 76 km from Curanilahue, respectively; Fig. 4.8 shows the location of these recording stations. Figs. 4.10 through 4.12 show the individual ground motion records obtained from the University of Chile (<http://terremotos.ing.uchile.cl/registros/164>) for these three stations. Boroschek et al. (2012) include a summary of the available ground motion records. The 0.93 g PGA from the Angol

record is the largest PGA recorded during the event, which is surprising given the recording station is relatively distant from areas of maximum fault slip. It appears that it is a result of one high frequency spike and that a horizontal PGA of 0.7 *g*, which was measured in the other direction, is more reasonable. The horizontal PGAs from the stations in Concepción are on the order of 0.4 *g* to 0.6 *g*, which is more in line with typical recordings during this event at these distances. Unfortunately, the large distances to the closest recording stations lead to considerable uncertainty in the ground motion at the site. Bray et al. (2012) estimated the horizontal PGA at the site to be on the order of 0.3 *g*, with a significant duration of around 80 s. This estimate seems reasonable based on the USGS ShakeMap in Fig. 4.1, the nearest ground motion records, and other considerations. Given the considerable uncertainty, however, the sensitivity to variations in the PGA is explored in this study.

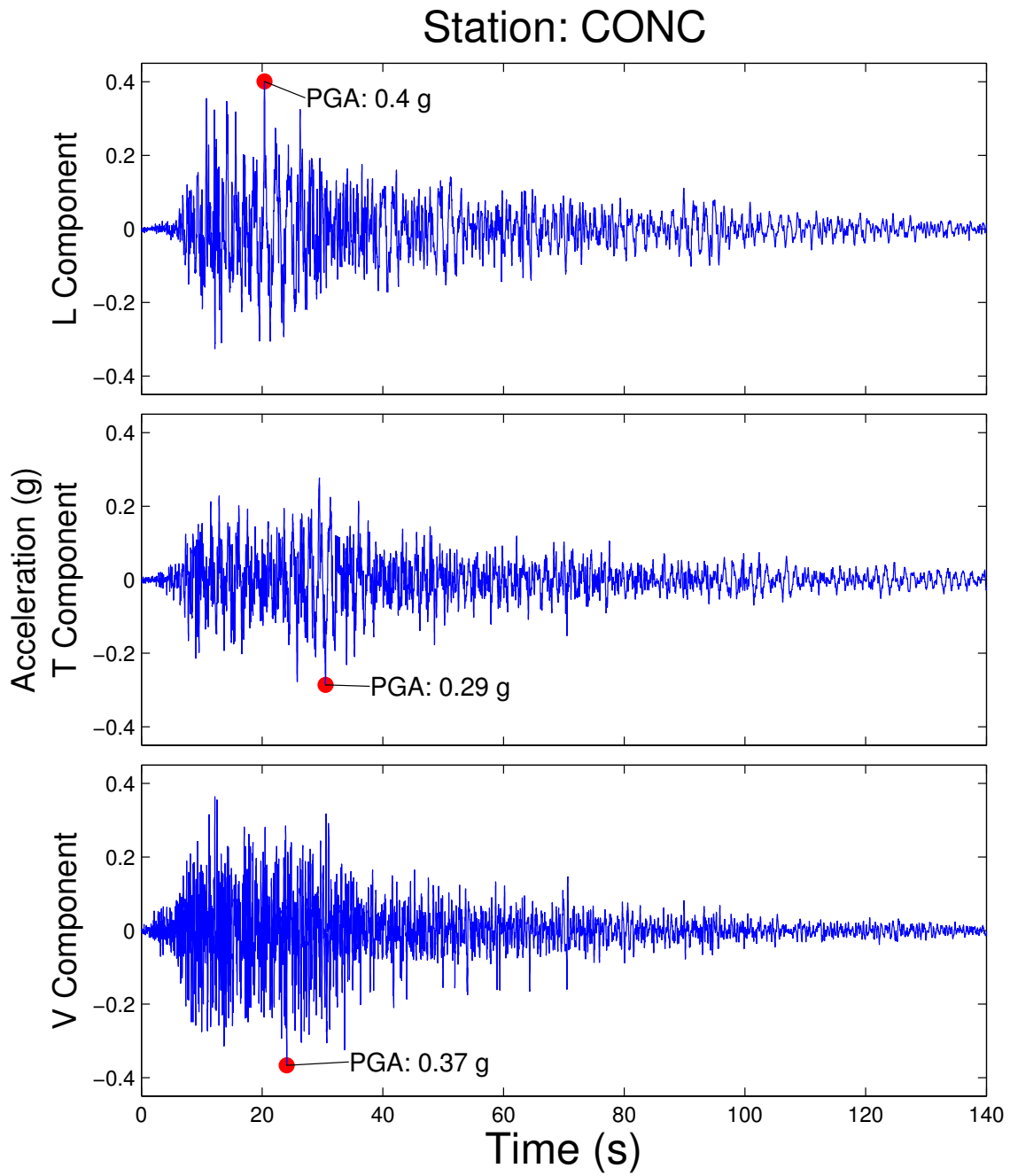


Fig. 4.10. Acceleration-time histories at recording station CONC

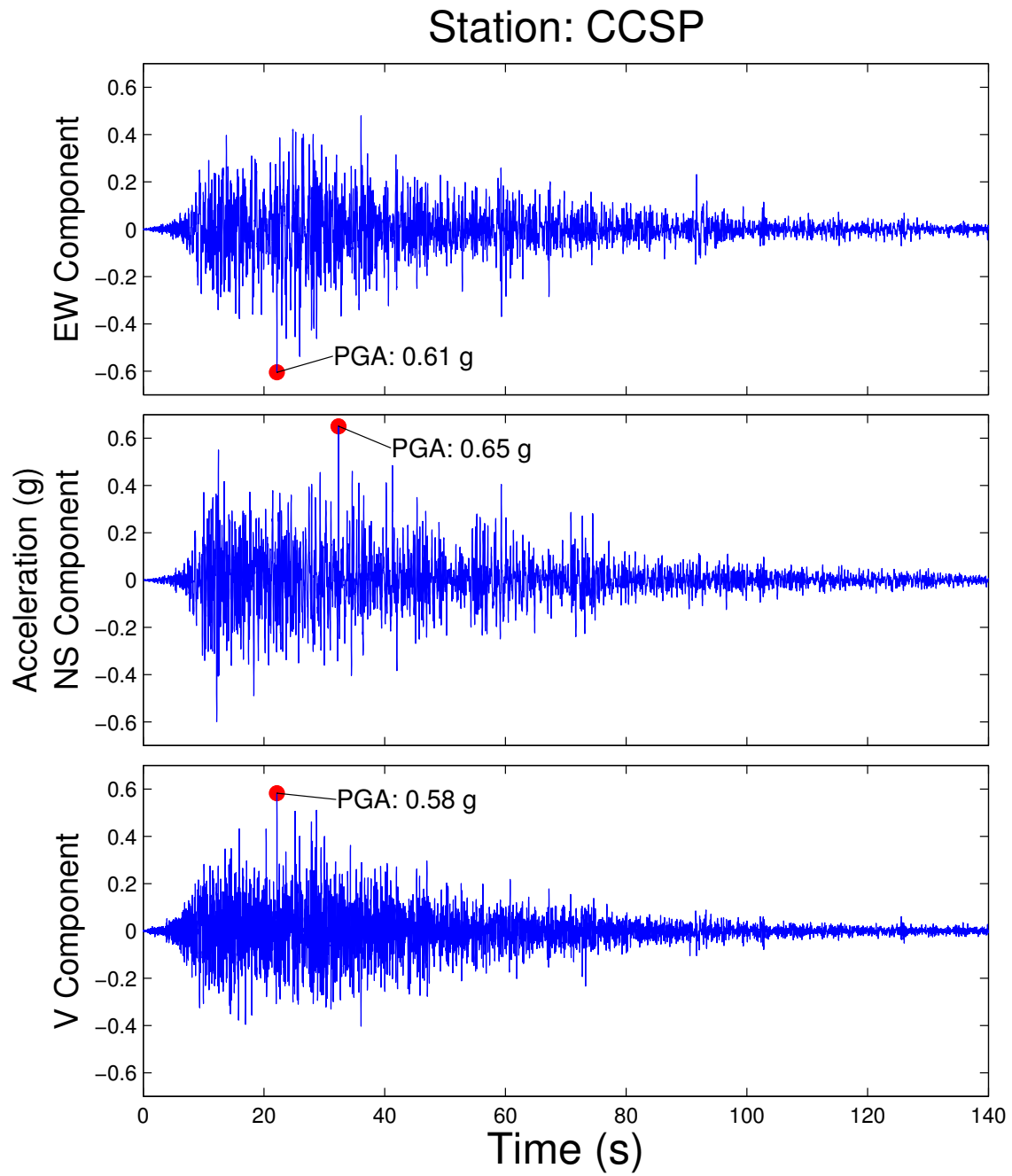


Fig. 4.11. Acceleration-time histories at recording station CCSP

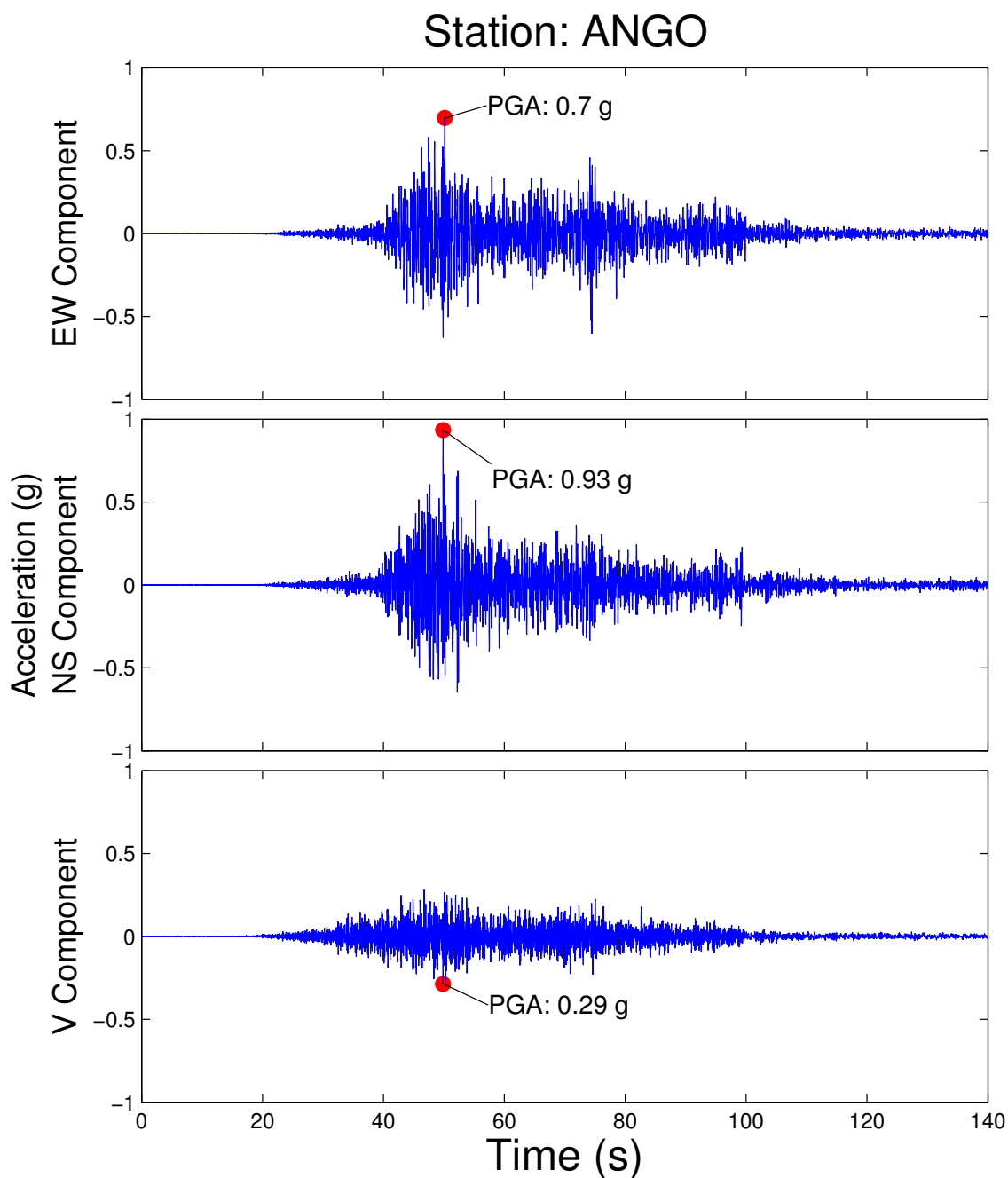


Fig. 4.12. Acceleration-time histories at recording station ANGO

4.3.1.2 Subsurface Characterization

VST Ingenieros (2003) performed a geotechnical site investigation prior to construction of the hospital. This investigation included four SPTs to a maximum depth of 6.5 m and several test pits. A river runs just south of the hospital grounds, and the report notes an old channel ran roughly underneath the area now occupied by Wings 1A and 1F. Based on SPTs and test pits,

they concluded the subsurface to be complex and heterogeneous. The simplified profile reported consists of a 0.7 m thick layer of fill, followed by a 1.6 m layer of sandy silt, clayey silt, and silty clay, which were generally colored brown. Soils samples in this layer ranged from non-plastic to a plasticity index of 23. The next layer consisted of 1.1 m of highly compact, silty sand with a scattering of gravel. Next, a 0.8 m layer of sandy gravel included cobbles reaching a 9 in. maximum diameter. Finally, a layer of gray, silty clay was noted to extend at least an additional 3 m. Importantly, the thickness of these layers varied substantially at different borings and test pits, and in several cases, particular soil layers were absent. The water table, based on borings and test pits, varied in depth from 0.6 m to 1.7 m.

The SPT equipment used in that study appears to be a donut hammer raised with a simple tripod. The N-values reported by VST Ingenieros (2003) are higher than expected based on their observations and other subsequent investigations. Unfortunately, SPT and test pit locations are unclear, so they cannot be used to supplement later investigations beyond a qualitative assessment. Based on their investigations, VST Ingenieros (2003) concluded that the site was a Class III site in the Chilean seismic code (NCh 433-96), which is similar to Soil Class D in IBC 2006. Curanilahue is located in a Seismic Zone 3 according to the Chilean code, with a corresponding PGA of 0.4 g. Compacted fill added to north side of hospital during construction raised the ground elevation to the level of the second floor.

GEER (Bray and Frost 2010) performed a detailed reconnaissance of the damage to Hospital Provincial in March 2010, which will be summarized in a later section. However, they also performed a limited soil investigation that is relevant to this section. A dynamic cone penetration test (DCPT) combined with a hand augur performed to the southwest of the hospital indicated a medium dense sandy silt layer near the water table followed by a gravel layer. Hand augurs in other locations were unable to penetrate the surface fill. SASW performed west of Wing 1D indicated shear wave velocities from 140 m/s to 180 m/s in the top 6 m. This is consistent with the medium dense soils encountered with the DCPT (Bray et al. 2012). Fig. 4.13 includes the location of these tests. Index tests indicated the brown silty ejecta varied from non-plastic to a PI of 5.

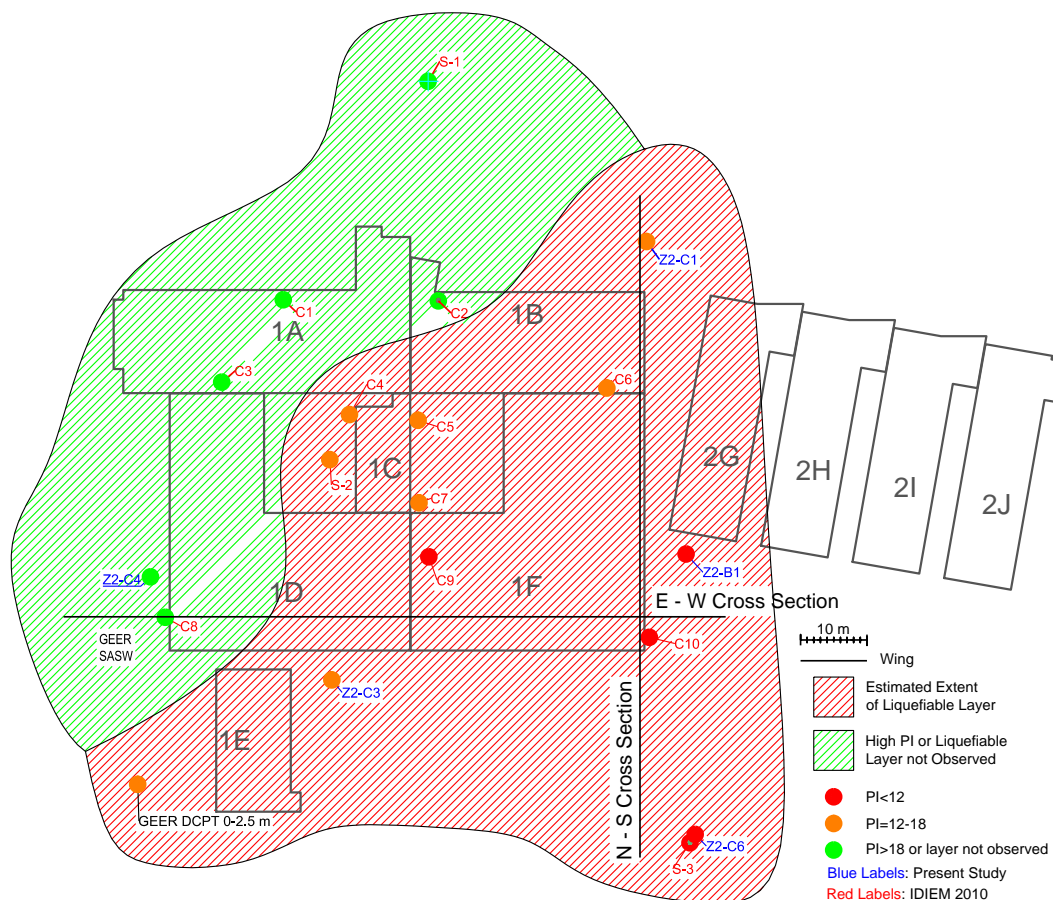


Fig. 4.13. Plan view of subsurface investigations at Hospital Provincial

In September and October 2010, IDIEM (2011) performed an investigation at the hospital, unrelated to the work performed in the present study, to provide an improved subsurface characterization following the earthquake. This investigation included three SPTs to depths up to 15 m as well as 10 test pits around 2.5 m deep. Fig. 4.13 shows the locations of these SPTs (labeled S-1, S-2, and S-3) and the test pits (C-1, C-2, etc.). Many of these test pits, performed inside the hospital wings, are particularly valuable in estimating the extents of the shallow, silty layer immediately below the surface fill. The markers for these test pits, and other borings and soundings, are color-coded in Fig. 4.13 indicating the characteristics of this silty layer based on field logging and index tests. A red icon indicates the layer had a low plasticity index (i.e., $PI < 12$) and was likely liquefiable by the criteria of Bray and Sancio (2006). Orange icons indicate the plasticity index fell into an intermediate range (12 to 18) and soils were likely resistant to liquefaction but still potentially liquefiable. Ideally, these intermediate soils would be tested for liquefaction susceptibility. Finally, green icons indicate that the silty layer was either absent (at least to a depth of 2.5 m) or it had a sufficiently high plasticity index so that it was not susceptible to liquefaction (i.e., $PI > 18$).

IDIEM (2011) performed SPTs using a drill rig similar to those used in the present study. In this instance, the self-contained nature of the drill rig allowed assembly in the interior courtyard, which would have been inaccessible with a truck-mounted rig. They did not perform energy measurements; however, given that energy measurements from the present study were slightly above and slightly below 60 percent for the two rigs used, an ETR of 60 percent has been assumed for analysis. These SPTs supplement the investigation in the present study, and their $(N_1)_{60}$ profiles are included in Appendix C-1.

The present study involved an SPT and CPTs performed at the hospital in early April 2012. Fig. 4.13 indicates the location of the four CPTs (Z2-C1, Z2-C2, etc.) and the SPT (Z2-B1). Appendix C-1 contains cone tip resistances and $(N_1)_{60}$ profiles. As mentioned, the long CPT preparation times were problematic due to shallow gravel layers at the site. As a result, several of the CPTs stopped after encountering gravel at shallow depths. CPT Z2-C1 starts at a depth of 4.3 m because the drill rig was used to pre-drill through the gravelly fill at the surface.

Fig. 4.14 presents a north-south cross section based mainly on the present study and the IDIEM (2011) investigation. The layer thickness varied across the site with considerable heterogeneity in the subsurface. In general, a gravelly surface fill was followed by a layer of loose brown silty soil with varying plasticity. Another gravel layer followed, beneath which a heterogeneous mix of primarily high plasticity, fine-grained soils extended to a depth of up to 15 m. The layering described is qualitatively similar to that outlined by VST Ingenieros (2003). Fig. 4.15 contains a similar cross section running east-west. These cross sections only include borings, soundings, or test pits within 10 m of the locations indicated in Fig. 4.13. Dashed lines indicate moderate uncertainty in the interface between layers, and question-mark lines indicate substantial uncertainty. The $(N_1)_{60}$ and q_t values are plotted to scale next to the SPT borings and CPT soundings.

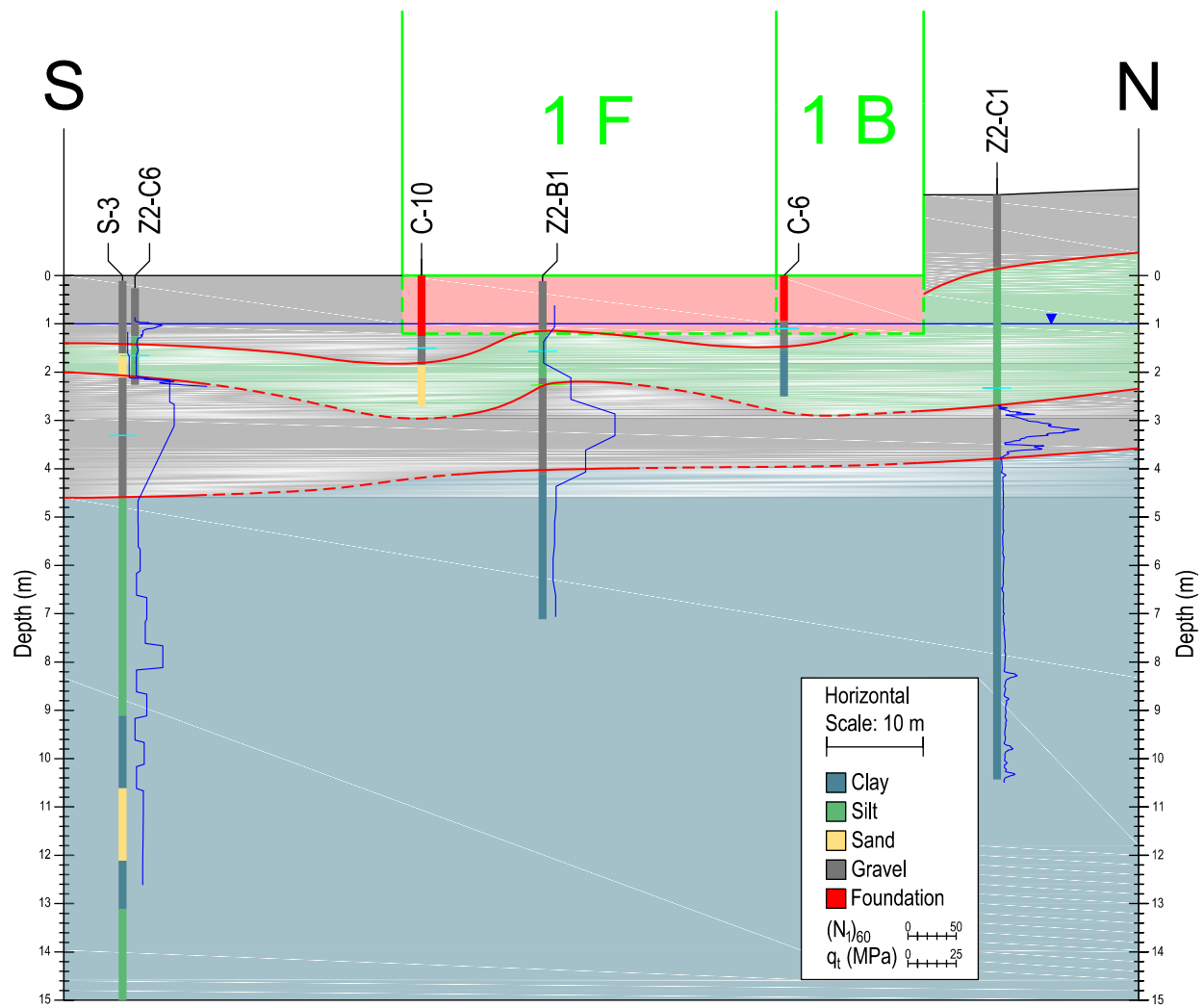


Fig. 4.14. North-south cross section at Hospital Provincial

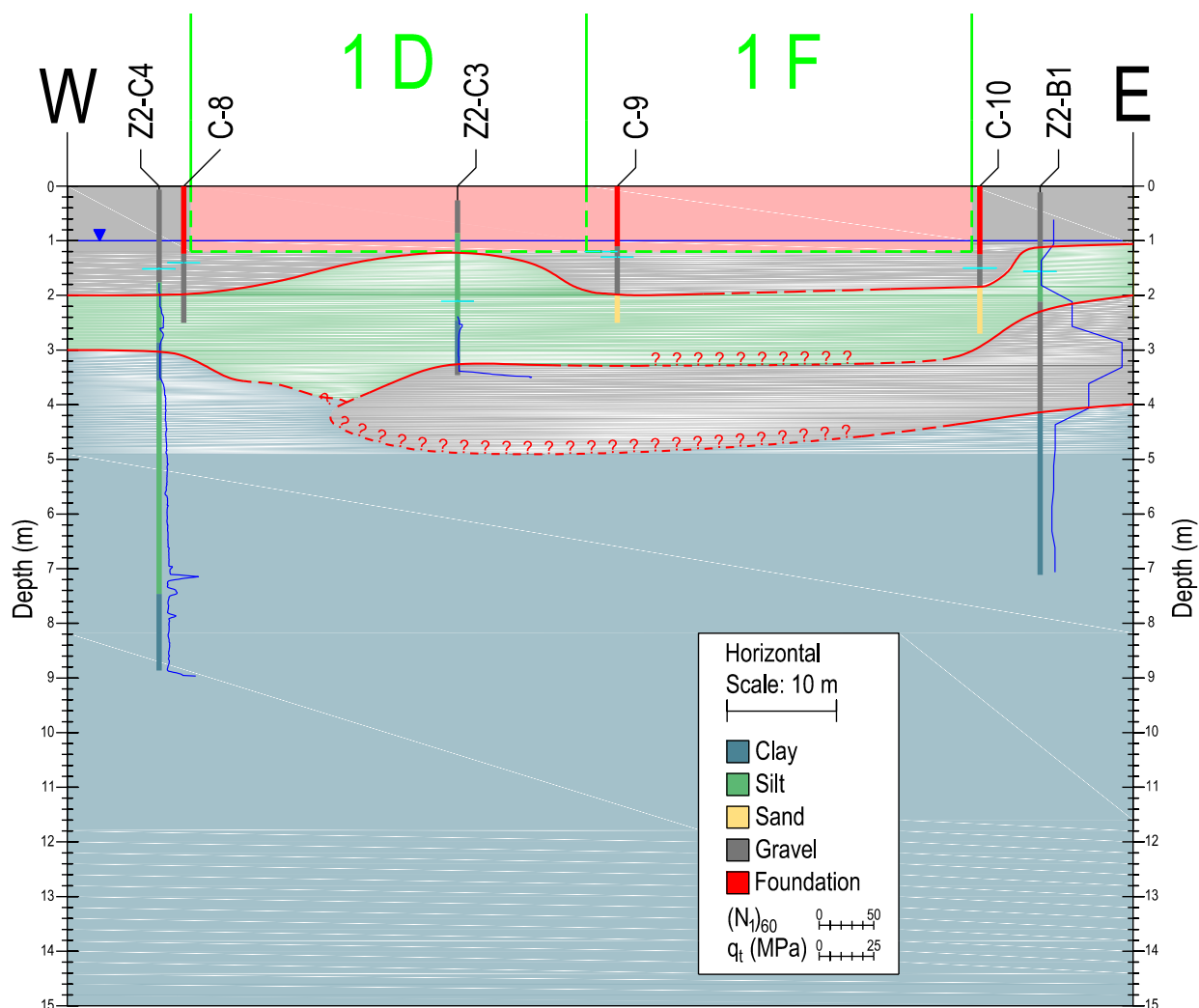


Fig. 4.15. East-west cross section at Hospital Provincial

The plasticity characteristics of these soils are of great importance because liquefaction susceptibility generally decreases with increasing plasticity. Fig. 4.16 contains a plasticity chart with samples grouped by depth; red indicates samples from the shallow silty layer of primary interest. These samples ranged from non-plastic to plasticity indices of over 20 and straddle the A-line (i.e., classified as ML or CL). The dotted lines mark the transitions in plasticity index for soils that are susceptible to liquefaction ($PI < 12$), soils that are more resistant but still potentially susceptible to liquefaction ($12 < PI < 18$), and soils that are not likely susceptible to liquefaction ($PI > 18$) based on the recommendations of Bray and Sancio (2006). Most of the samples in this layer have plasticity indices that fall into the susceptible to liquefiable or intermediate ranges (i.e., $PI < 18$). The index tests by VST Ingenieros (2003) on samples from this shallow silty layer are also plotted as black circles, and they fall in a plasticity range similar to the more recent data. Given the uncertainty in the test locations and procedures used, these data are less reliable. At greater depths, the plasticity indices tend to be much higher, although several samples did fall in

the intermediate 12 to 18 range. In all but one case, the PI of the fine-grained soils investigated at this site had $PI \geq 7$. Yet, there was clear evidence of soil liquefaction at this site in the form of sediment ejecta. If one assumes that sediment ejecta provide evidence of “sand-like” behavior, these data are at odds with the liquefaction susceptibility criteria of Idriss and Boulanger (2008), wherein only soils with $PI < 7$ are considered to exhibit “sand-like” behavior.

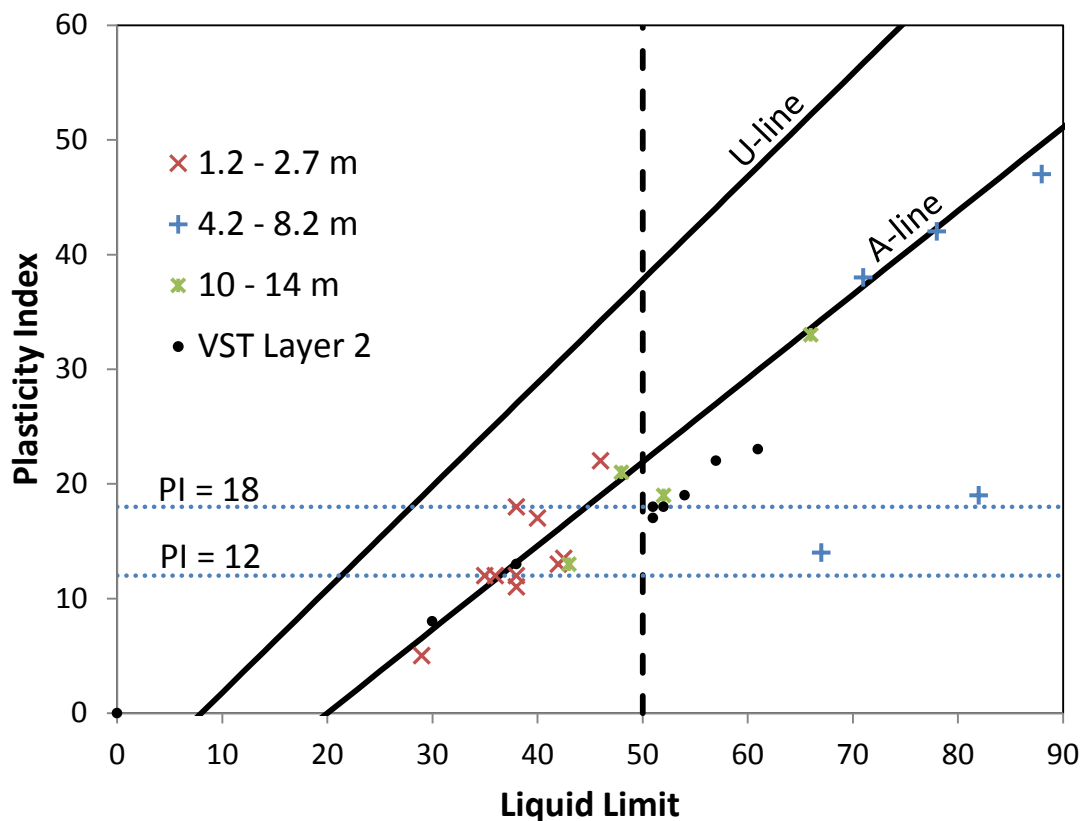


Fig. 4.16. Plasticity chart of samples collected at Hospital Provincial

4.3.1.3 Field Observations of Ground and Structural Performance

GEER (Bray and Frost 2010) provide detailed documentation of hospital damage based on their reconnaissance. Widespread liquefaction was observed adjacent to many hospital wings; ejecta was observed between Wings 1B/1F and 2G, the two interior courtyards, the west and south sides of the hospital, and elsewhere (Bray et al. 2012). The ejecta consisted primarily of brown silty material with low plasticity.

Fig. 4.17, taken from Bray and Frost (2010), shows measured settlements, lateral displacements, and tilts. Wings 2G through 2J did not experience notable movement, and they can serve as a valuable frame of reference. Relative to 2G, Wing 1B settled between 4.5 cm and 14 cm and tilted 1.5° to the south. Wing 1F settled less but translated 5 cm to the south. Wing

1C, the tallest wing containing the primary elevator shaft, settled around 10 cm relative to Wings 1A and 1B. Wings 1A, 1F, and 1D (with the exception of its northeast corner) did not tilt substantially. Wing 1D did not appear to settle noticeably but did translate around 8 cm to the south.

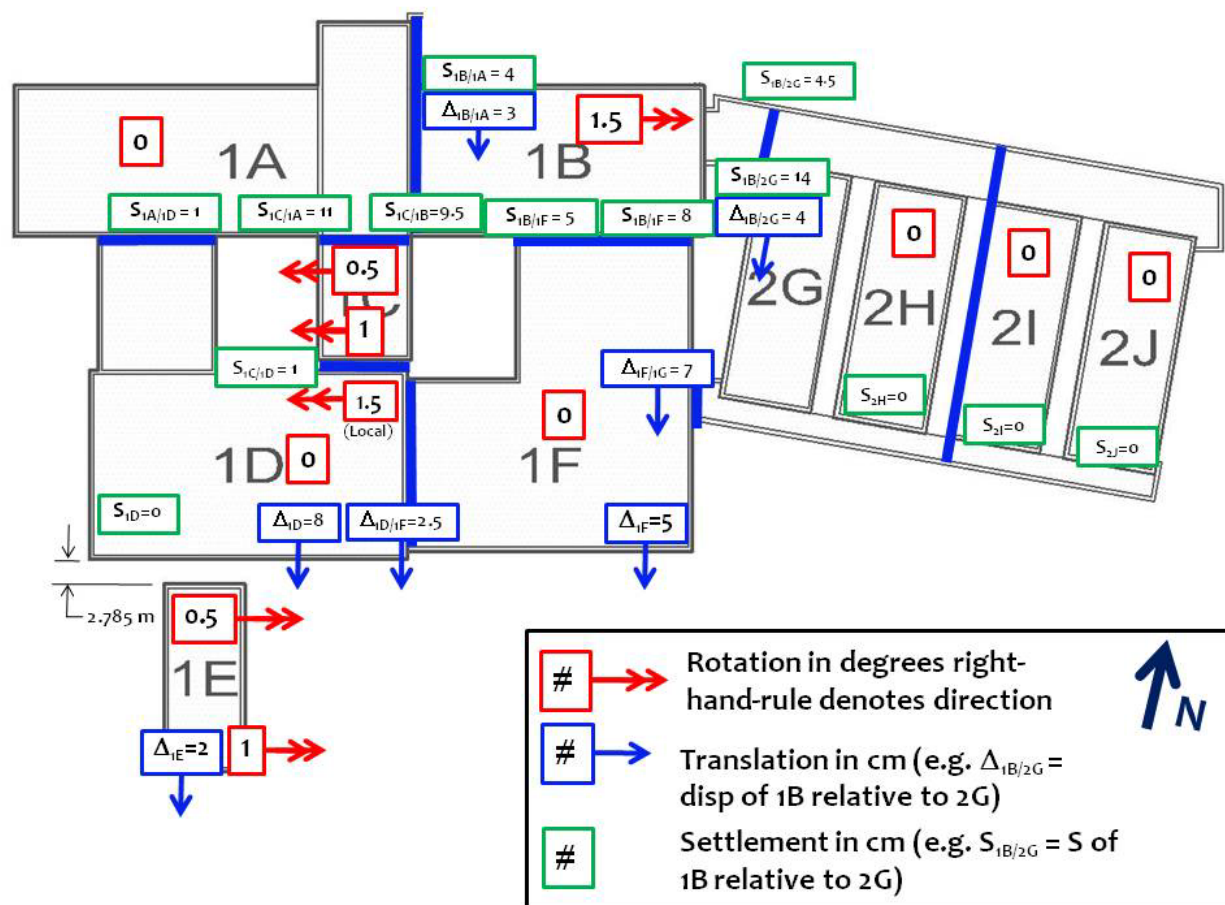


Fig. 4.17. Measurements of relative building movements; figure taken from Bray and Frost (2010)

Although throughout the hospital wings, the isolation gaps between wings likely reduced the overall damage (Bray et al. 2012). Wing 1C, however, did experience significant pounding damage after colliding with 1A and 1B. Wing 1C also suffered numerous shear cracks and a bulging ground slab from liquefaction-induced settlement. Wings 2G through 2J suffered the least amount of damage to the superstructure with only hairline cracks in nonstructural walls. Mechanical, electrical, and plumbing systems, designed flexibly to accommodate movement between wings, fared well. Much of the superstructure damage had been repaired as of the April 2012 visit to the hospital. Most wings were functional and in use; however, Wing 1C remained abandoned and was likely to be demolished.

4.3.1.4 Simplified Liquefaction Evaluation

Using the methods previously described, Fig. 4.18 shows liquefaction triggering analysis results for SPT Z2-B1, based on an assumed PGA of 0.3 g. There was a very low blow count SPT between 1.25 m and 1.70 m, which corresponds to the silty layer shown in the cross sections. This sample had a PI of 13, which is within the intermediate range (i.e., $12 < PI < 18$) from Bray and Sancio (2006). In contrast, the deeper layer generally had higher PIs that fell within the non-liquefiable range. The cyclic resistance ratio (CRR) is shown as a dashed line for this deeper layer to acknowledge it was likely non-liquefiable due to its high PI. However, some samples from this layer, including samples from the IDIEM (2011) SPTs, did have PIs that were less than 18. The safety factors were below one for most of the profile with the exception of the gravel layer between depths of 2 m to 4 m. Given the generally high PIs of the lower layer, it appears that the shallow silty layer was primarily responsible for liquefaction settlements. Additionally, GEER (Bray and Frost 2010) observed that the ejecta was generally brown colored. This matches the color of the shallow silt layer, but not grey color of the deep, higher PI layer.

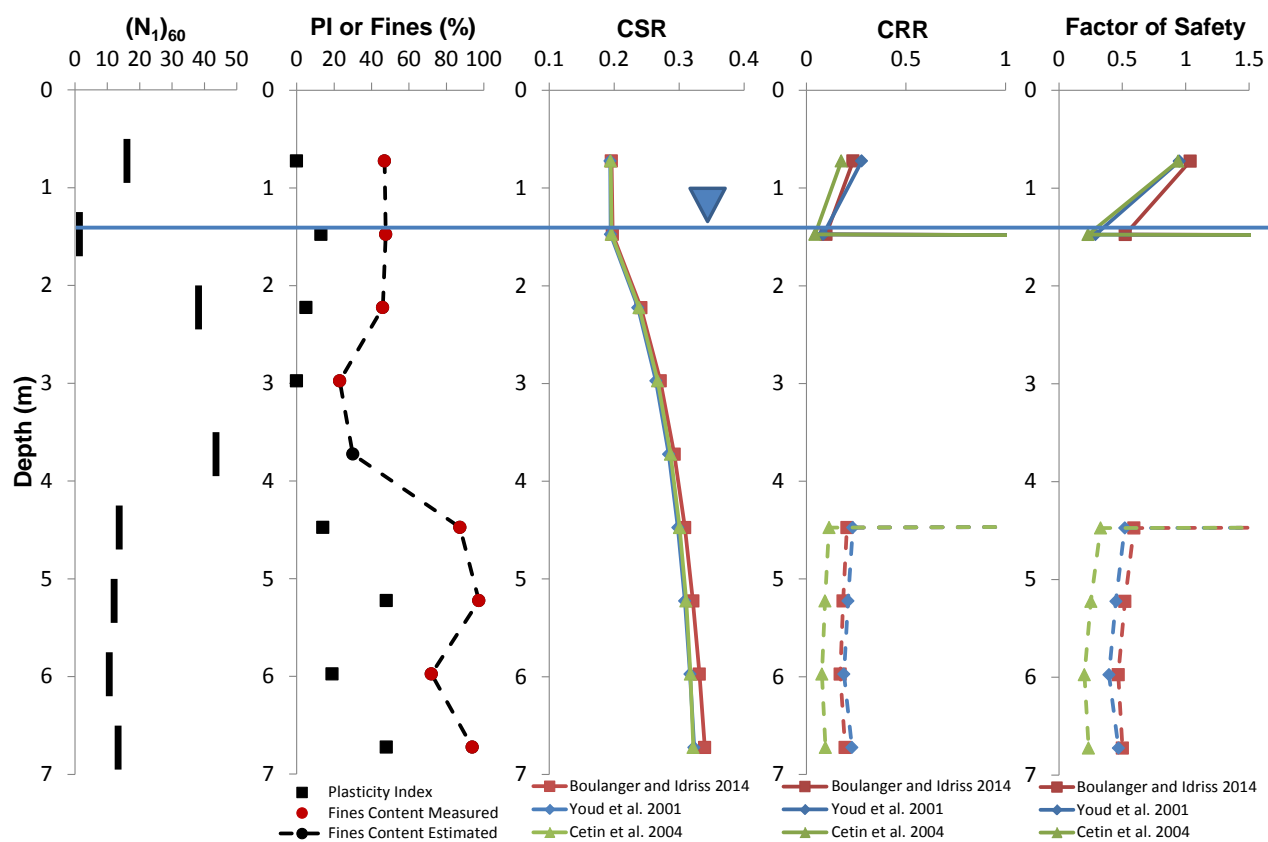


Fig. 4.18. Liquefaction triggering assessment of Z2-B1

A comparison between the three SPT based liquefaction-triggering correlations indicates the CSR values were similar regardless of the method. However, Cetin et al. (2004) has lower values of CRR, resulting in lower factors of safety against liquefaction. Regardless of the method used, the safety factors for liquefaction triggering in the shallow silty soil layer are far less than one. Youd et al. (2001) suggest that layers with $(N_1)_{60cs}$ values exceeding 30 are non-liquefiable. Accordingly, their CRR and safety factors have been set to an arbitrarily large number so they are not plotted. Given the large event, however, soils with $(N_1)_{60cs}$ values only slightly less than 30 (e.g., 28 or 29) are susceptible to liquefaction and have factors of safety less than one. This results in a number of sharp discontinuities as $(N_1)_{60cs}$ values fluctuate slightly around 30. This is not the case for Fig. 4.18, but these discontinuities are present in other borings contained in Appendix C-1 (e.g., SPT S-2).

Fig. 4.19 shows the results of the CPT-based liquefaction triggering assessments of Youd et al. (2001), Moss et al. (2006), and Boulanger and Idriss (2014). CPT Z2-C1 starts at a depth of 4.3 because pre-drilling was used in an attempt to bypass gravel layers, unfortunately this also resulted in pre-drilling through the liquefiable silt layer. The cores were saved, however, and index tests indicated an area of soil with a PI of 11 consistent with the liquefiable shallow silt layer observed elsewhere. The soil behavior type index (I_c) of the deeper, generally high PI layer, straddles a value of 2.6, which Youd et al. (2001) suggest marks the transition from liquefiable to non-liquefiable material. Increments exceeding this value are excluded from the safety factor calculations and are shown as gaps in the profile. It is important to note that slightly increasing this cutoff value would result in essentially all of this thick layer being classified as liquefiable. Shifting it slightly downward would cause nearly the entire layer to be classified as non-liquefiable thus showing the high sensitivity to this value. The Moss et al. (2006) correlation safety factors fall below the other two methods, similar to the Cetin et al. (2004) SPT-based method with which it is closely related. Regardless of the method used, nearly the entire deep layer has a safety factor less than one, indicating this layer could also liquefy if the plasticity of this soil was sufficiently low.

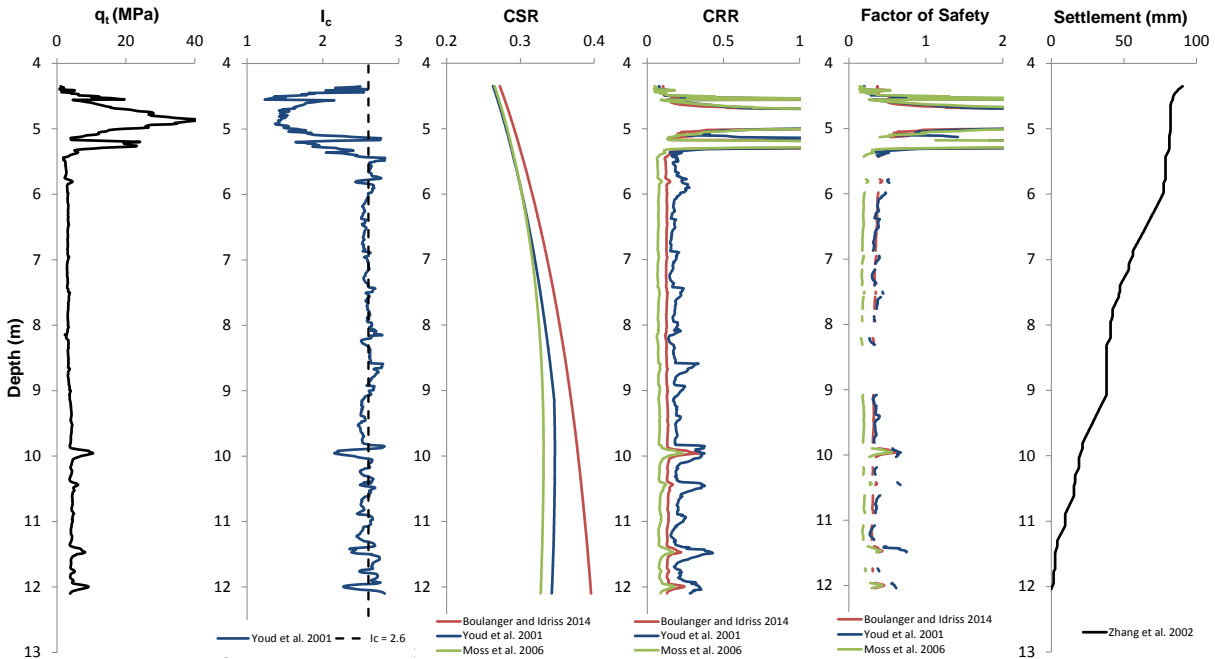


Fig. 4.19. Liquefaction triggering and volumetric settlement assessment of Z2-C1

The volumetric settlement shown in the final column of Fig. 4.19 is based on the method of Zhang et al. (2002) using the safety factors and $(q_{cIN})_{cs}$ values from the Youd et al. (2001) method. Volumetric strains are assumed to be zero for intervals with I_c values exceeding 2.6; hence, the settlement calculations are highly sensitive to this cutoff as the majority of the profile straddles this value. Over the depths tested by CPT, the total calculated volumetric settlement is approximately 9 cm. This does not include volumetric settlement in the approximately 1 m thick shallow silty layer (e.g. 5 cm assuming 5 percent strain) or any additional volumetric strains below the CPT end depth.

As mentioned previously, the nearest ground motion recordings are over 60 km away, resulting in considerable uncertainty in the ground motion at the hospital site. Fig. 4.20 explores the sensitivity of the Youd et al. (2001) correlations applied to SPT Z2-B1 and CPT Z2-C1. The factor of safety is shown for PGA values of 0.2 g , 0.3 g , and 0.4 g . The best estimate of PGA at the site was 0.3 g , but even at lower values, the safety factors for much of the deep layer are below one, indicating this layer could liquefy depending on the plasticity of the soil.

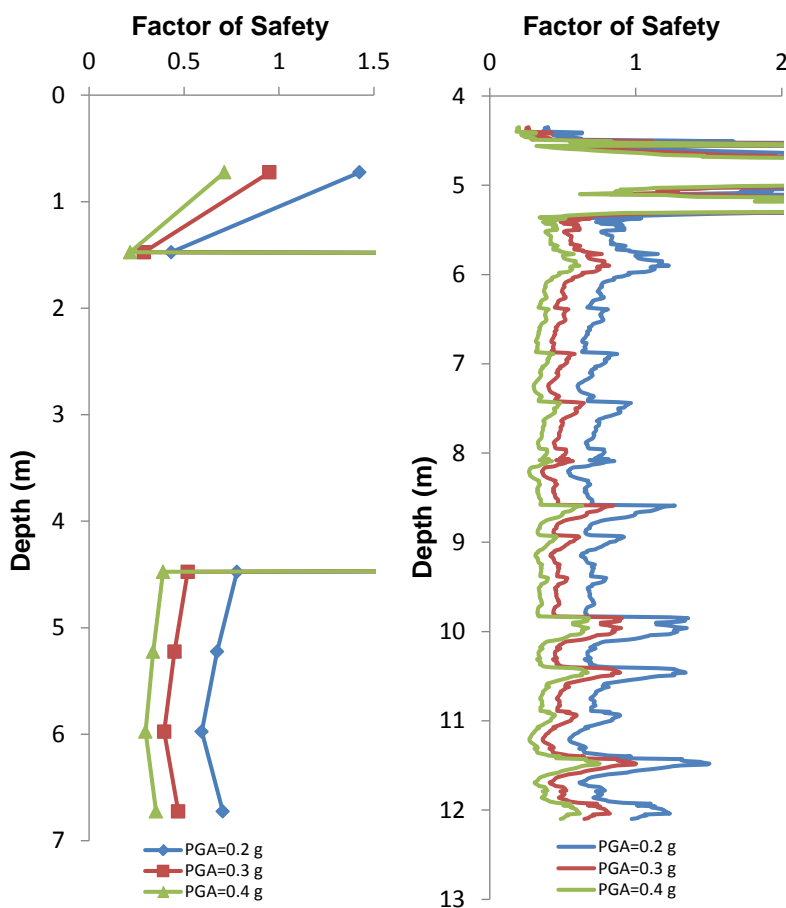


Fig. 4.20. Sensitivity of liquefaction safety factor from Youd et al. (2001) to variations in PGA

4.3.1.5 Key Findings

The recently constructed Hospital Provincial in Curanilahue suffered extensive liquefaction-induced damage. Reconnaissance by GEER documented the post-event movements of the 10 structurally isolated hospital wings. Structural damage was primarily limited to Wing 1C which suffered pounding damage after colliding with Wings 1A and 1B, as well as large liquefaction-induced settlements. The present study involved improved site characterization using CPT and SPT, supplemented with soil information from three additional sources.

Although the hospital site subsurface is complex and heterogeneous, in general there are four major layers identified: a fill layer at the surface, a shallow silty layer, a gravel layer, and a thick heterogeneous layer with generally high plasticity. Given its low values of $(q_{c1N})_{cs}$ or $(N_1)_{60cs}$ and its PI values that are below 12 or within the intermediate range (i.e., 12 to 18) of Bray and Sancio (2006), this shallow silty layer likely liquefied and is responsible for much of the settlement and damage to the hospital. Additionally, the color of liquefaction ejecta (Bray and Frost 2010), matches the brown color of the silty layer, but not the grey color of the deeper layer. Liquefaction triggering analyses indicate that the deeper layer would also have liquefied if

its plasticity was sufficiently low. Based on SPT and CPT data, this deeper layer generally has higher plasticity but also has some areas of borderline plasticity, which may have liquefied or softened cyclically as well.

The approximate extents of the shallow liquefiable silt layer included in Fig. 4.13 were based primarily on data from the present study and IDIEM (2011). These extents generally match areas of liquefaction noted by GEER, including the interior courtyards, south of 1D and 1F, and the walkway between 1F and 2G. GEER observed ejecta along the west edge of Wing 1D, but based on a CPT and test pit, the shallow silty layer was absent in this area. Given the heterogeneity of the site, it is possible that it was missed. Alternatively, the deeper layer could have liquefied, particularly because this CPT sounding (Z2-C3) did have marginally lower I_c values than those shown previously (Fig. 4.19). The extents of the silty layer also generally match expectations based on structural movement; Wings 1B and 1C experienced the most settlement and tilt, 1D and 1F sustained lateral displacements, and 1A appeared to move settle and tilt negligible amounts.

4.3.1 Juan Pablo II Bridge, Concepción

4.3.1.1 Background

The Juan Pablo II Bridge, the longest in Chile, serves as an important link across the Bío-Bío River and was completed in 1974. Its 2310 m length consists 70 spans each made up of seven reinforced concrete girders with a concrete deck (Ledezma et al. 2012). GEER (Bray and Frost 2010) documented the severe liquefaction-induced damage, including lateral spreading and settlement at the northeast approach ($36^{\circ}48'57.44''S$, $73^{\circ}5'3.04''W$). The bridge suffered column shear failure, rotations of 1° to 3° , and up to 1 m of vertical displacements to the bridge deck. Piers also settled substantially in several locations along the length of the bridge, and in one area more than a meter. The damage forced this essential lifeline to close until temporary repaired. The present study focuses on documenting the subsurface conditions at the northeast approach.

The two recording stations near the Juan Pablo II Bridge are shown in Fig. 4.21. Figs. 4.10 and 4.11 contain the acceleration-time histories. Station CONC, located in Concepción, had smaller PGA values compared to CCSP, located across the river in San Pedro de la Paz. Based on these two records, the ground motion at the Juan Pablo II Bridge was likely around 0.5 g, consistent with the estimate of Bray et al. (2012).



Fig. 4.21. Bridge sites and recording stations near Concepción

4.3.1.2 Subsurface Characterization

Following the earthquake, SPTs were performed along the length of the bridge with details provided by Verdugo and Peters (2010) and summarized as part of Ledezma et al. (2012). Figure 4.22 shows boring locations in addition to settlement measurements along the bridge span (Verdugo and Peters 2010). Energy measurements were not performed on these SPTs, and Verdugo and Peters (2010) assumed an energy transfer ratio of 60%. Figure 4.23 contains the SPT profiles as well as the liquefaction assessment results of Verdugo and Peters (2010). In general, these borings show several layers of liquefiable sands, particularly in areas that underwent substantial settlements. Dense non-liquefiable sand layers and silt layers were interbedded throughout the subsurface. Liquefiable layers are more prevalent near the northeast approach, which is consistent with the settlement and damage observations in this area. GEER (Bray and Frost 2010) also performed DCPT and SASW at the northeast approach. Shear wave velocities ranged from 150 m/s to 180 m/s at depths from 2 m to 14 m.

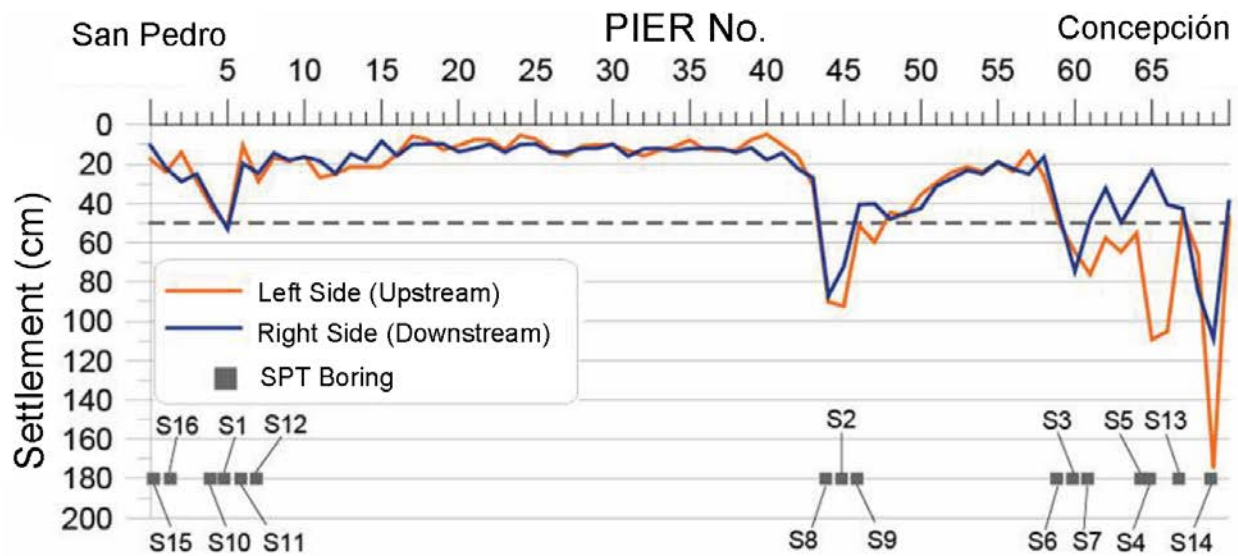


Fig. 4.22. Settlements and SPT locations along Juan Pablo II Bridge (Verdugo and Peters 2010)

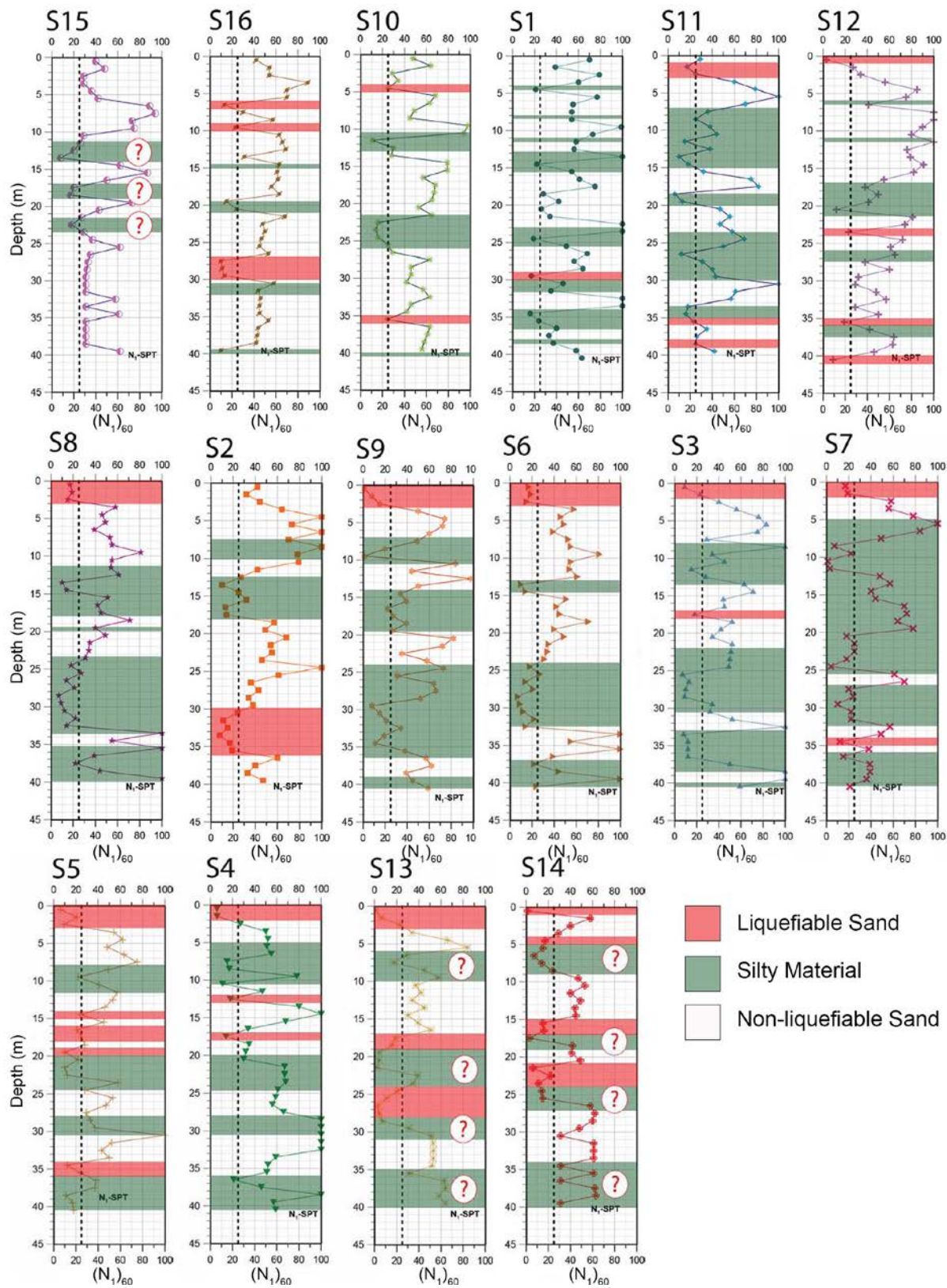


Fig. 4.23. SPT profiles at the Juan Pablo II Bridge (Verdugo and Peters 2010)

The present study focuses on the northeast approach of the bridge. Unfortunately, the thick fill at the site proved problematic in performing CPT soundings. Fig. 4.24 shows the northeast approach and the location of the SPT boring and CPT soundings. The 7.5 m SPT boring (Z3-B1) encountered a thick fill to a depth of around 4.5 m, followed by clean sand. The fill at this site was particularly difficult to penetrate, because it contained concrete debris 0.5 m or more in length. Because of this fill, CPT Z3-C4 was performed down the hole left by the SPT boring. CPT Z3-C5 involved hand digging several excavations up to a meter deep or more before finding a suitable location that did not have shallow concrete debris. Fig. 4.25 shows this CPT in progress and part of the highway that suffered liquefaction-induced settlement is visible in the top left.

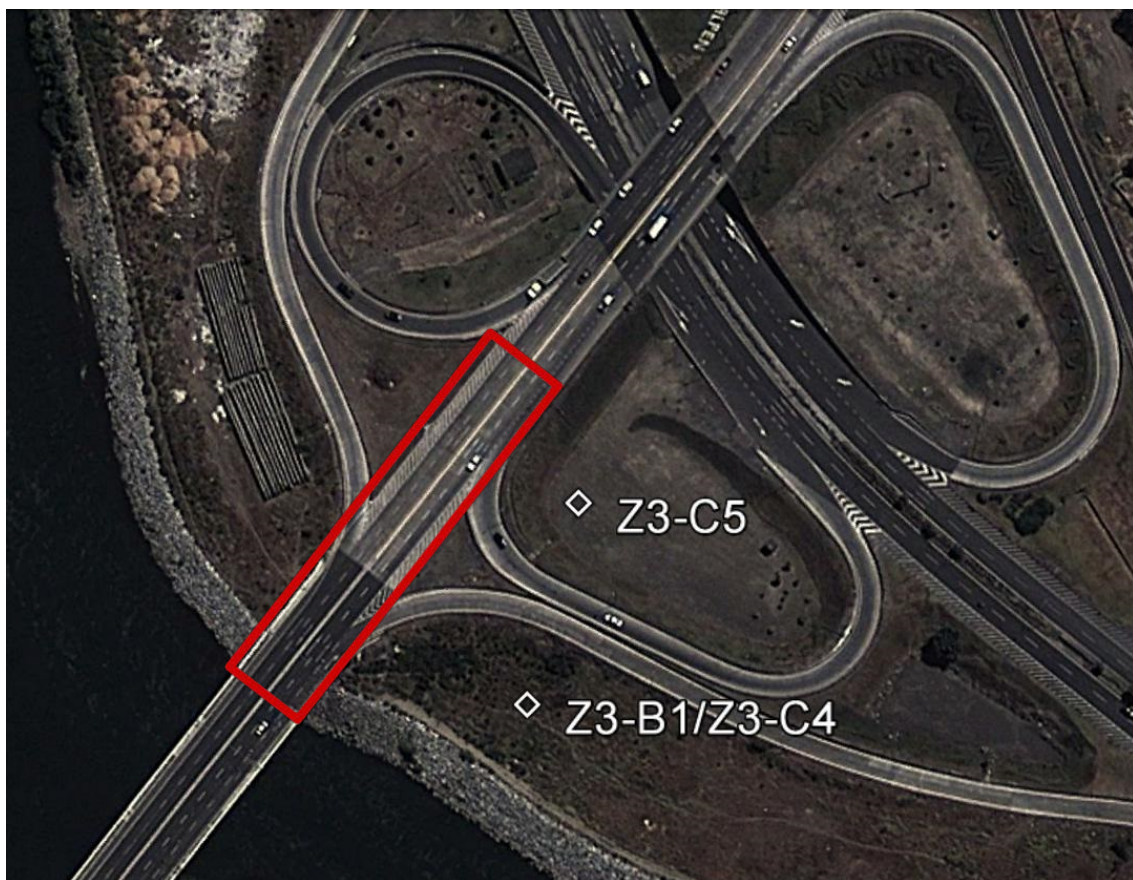


Fig. 4.24. Boring/sounding locations at northeast approach of Juan Pablo II Bridge with area of deck settlement indicated in red (GEER, Bray and Frost 2010)



Fig. 4.25. CPT Z3-C5 in progress with an area of the highway that suffered liquefaction-induced settlement visible in top left corner

The cross section shown in Fig. 4.26 is based on the SPT and CPTs shown in Fig. 4.24. The geometry of the surface between the two tests is approximate. Based on the limited CPT testing, the profile is almost entirely sand beneath the fill, with the exception of a small silt layer. Index tests performed on SPT samples from below the fill indicated sands with 3 to 7 percent fines. The water table shown is based on pore pressure measurements taken during testing; however, the water table likely fluctuates depending on season and recent rainfall.

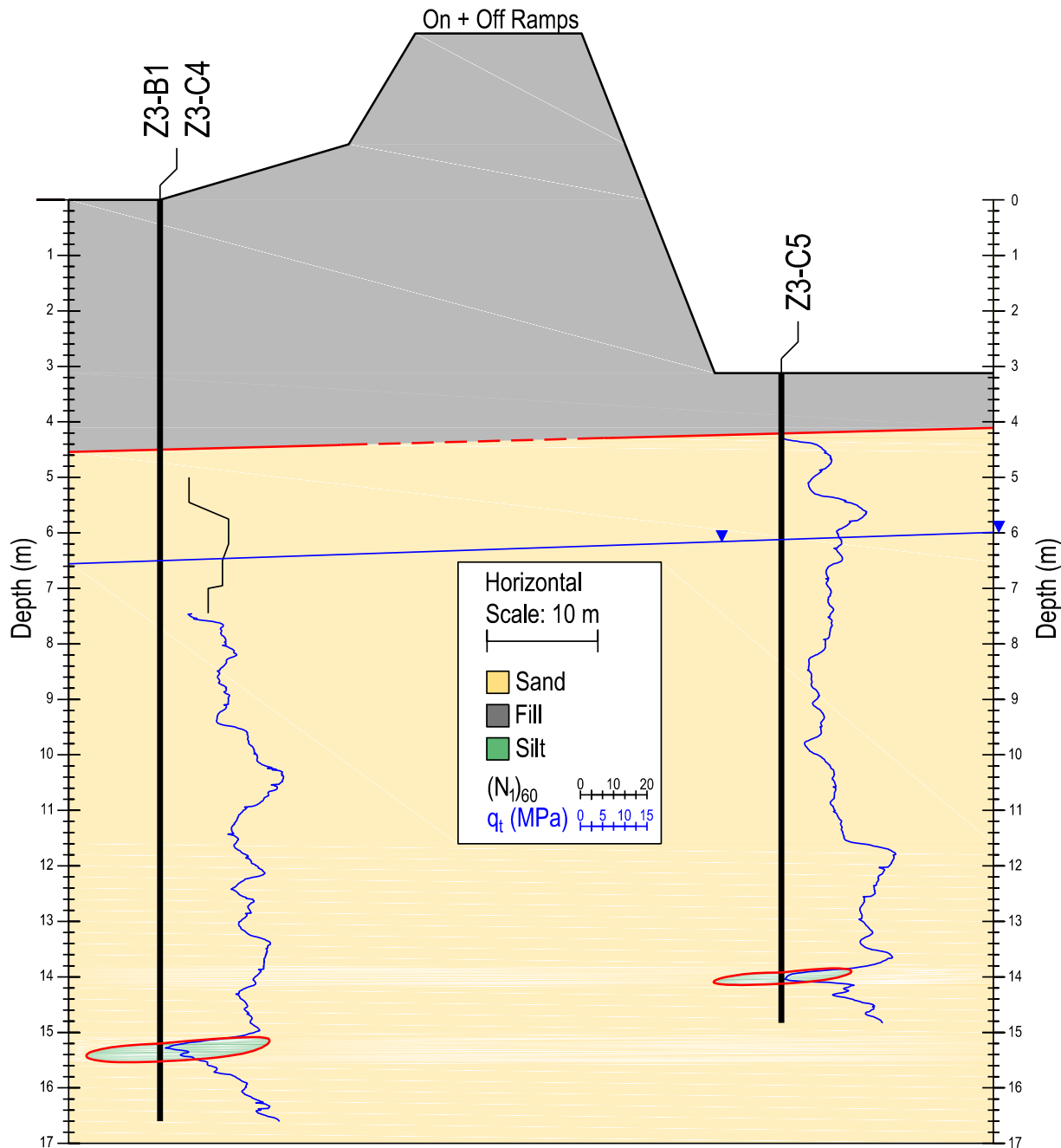


Fig. 4.26. CPT and SPT locations at northeast approach of Juan Pablo II Bridge

4.3.2.3 Simplified Liquefaction Evaluation

Liquefaction triggering analysis is shown in Fig. 4.27 for CPT Z3-C5 using a PGA of 0.5 g. The soil behavior type index (I_c) indicates that the material is sand throughout the entire profile with the exception of the thin silt seams between the depths of 14 m to 15.5 m. The area between 3.5 m and 8.2 m has factors of safety against liquefaction well below one using all three

methods. The other CPT, Z3-C4, is more erratic and has several zones of liquefiable sands mixed between areas of dense, non-liquefiable sands (see appendix C-1).

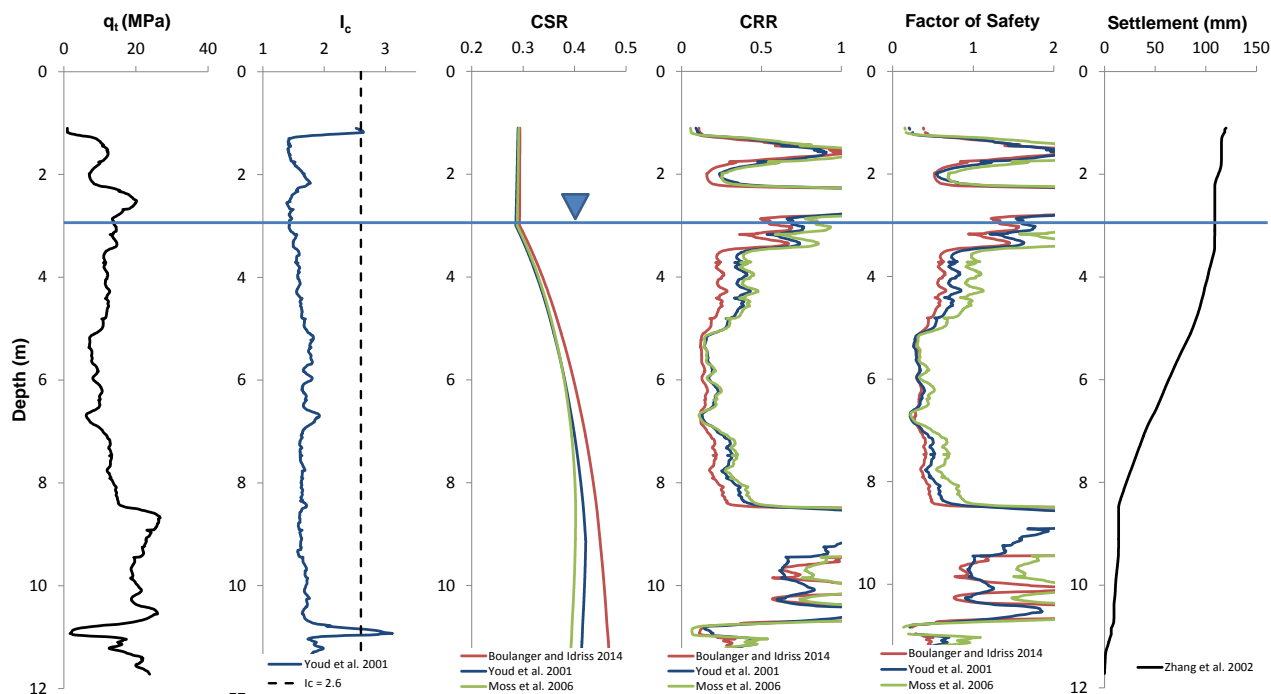


Fig. 4.27. CPT Z3-C5 liquefaction analysis

Volumetric settlement estimates based on Zhang et al. (2002) shown in Fig. 4.27 indicate 11 cm of liquefaction-induced volumetric settlement (read at the water table). Volumetric strains occurring in the liquefiable material between 3.5 m and 8.2 m contribute to most of the settlement. The soil below the depth reached by CPT also may have been liquefiable, which would add to the settlement. This simplified method indicates much less settlement than observed at the approach. Of course, the damaged highway in this area was partially supported by an embankment that suffered lateral spreading and by a short approach structure that failed. For example, a report by the Federal Highway Administration (2011) documents damage to the approach structure (i.e., the northeast portion of the red outline in Fig. 4.24). They noted that a pier supporting this structure settled 1 m. Obviously, a simplified volumetric method such as Zhang et al. (2002) cannot capture these failure mechanisms. Unfortunately, no settlement measurements exist in close proximity to the CPTs, so a comparison is not possible.

4.3.2.4 Key Findings

The Juan Pablo II Bridge is an important crossing of the Bío-Bío River and sustained liquefaction-induced damage that forced its closure following the earthquake. Damage included liquefaction-induced settlements and lateral spreading at the northeast approach as well as pier

settlement along the length of the bridge. Based on CPTs performed as part of this study, the soils underlying the northeast embankment consist primarily of medium-dense to dense sands. Liquefaction triggering analysis showed that areas of these sands had factors of safety against liquefaction far less than one, which is consistent with sand boils, lateral spreading and liquefaction-induced settlement observed in this area by GEER (Bray and Frost 2010).

4.3.3 Llacolén Bridge, Concepción

4.3.3.1 Background and Damage

The four-lane Llacolén Bridge is a second major crossing of the Bío-Bío River in the Concepción area. GEER (Bray and Frost 2010) reconnaissance documents the damage due to liquefaction-induced settlement and lateral spreading at the northeast approach (36°49'48.21"S, 73° 4'6.28"W). Fig. 4.28 shows the site layout and approximate extent of the lateral spreading noted by GEER.



Fig. 4.28. Test location with red indicating the extents of lateral spreading observed by GEER

Lateral spreading unseated the traffic support deck and flexural cracks were observed at the base of columns supporting the deck (Bray and Frost 2010). This failure forced closing the bridge until a temporary deck replaced the collapsed one. Liquefaction-induced settlements of

around 30 cm were also observed at the exit ramp bents (Ledezma et al. 2012). As noted for the Juan Pablo II Bridge, there are two recording stations in the vicinity (Fig. 4.21 with records in Figs. 4.10 and 4.11), and a PGA estimate of around 0.5 g is reasonable.

4.3.3.2 Subsurface Characterization

Verdugo and Peters (2010) provide details of SPTs performed along the bridge at the locations shown in Figure 4.29. Ledezma et al. (2012) also summarize this data. Figure 4.30 shows the SPT profiles based on Verdugo and Peters (2010) assumed ETR of 60%. The present study focuses on the northeast approach, and Boring S-6 indicates likely liquefiable sands (i.e., $(N_1)_{60}$ values less than 30) between the surface and a depth of 9 m as well as at greater depths. GEER (Bray and Frost 2010) performed DCPT and SASW at the site; shear wave velocities increased from 80 m/s to 200 m/s in the top 4 m and up to 280 m/s at a 14 m depth. DCPTs and hand augurs near the river edge (i.e., not on the embankment) encountered black sands, which became dense and impenetrable at depths of 2 m to 3 m.



Fig. 4.29. Locations of SPT borings along the Llacolén Bridge (Verdugo and Peters 2010)

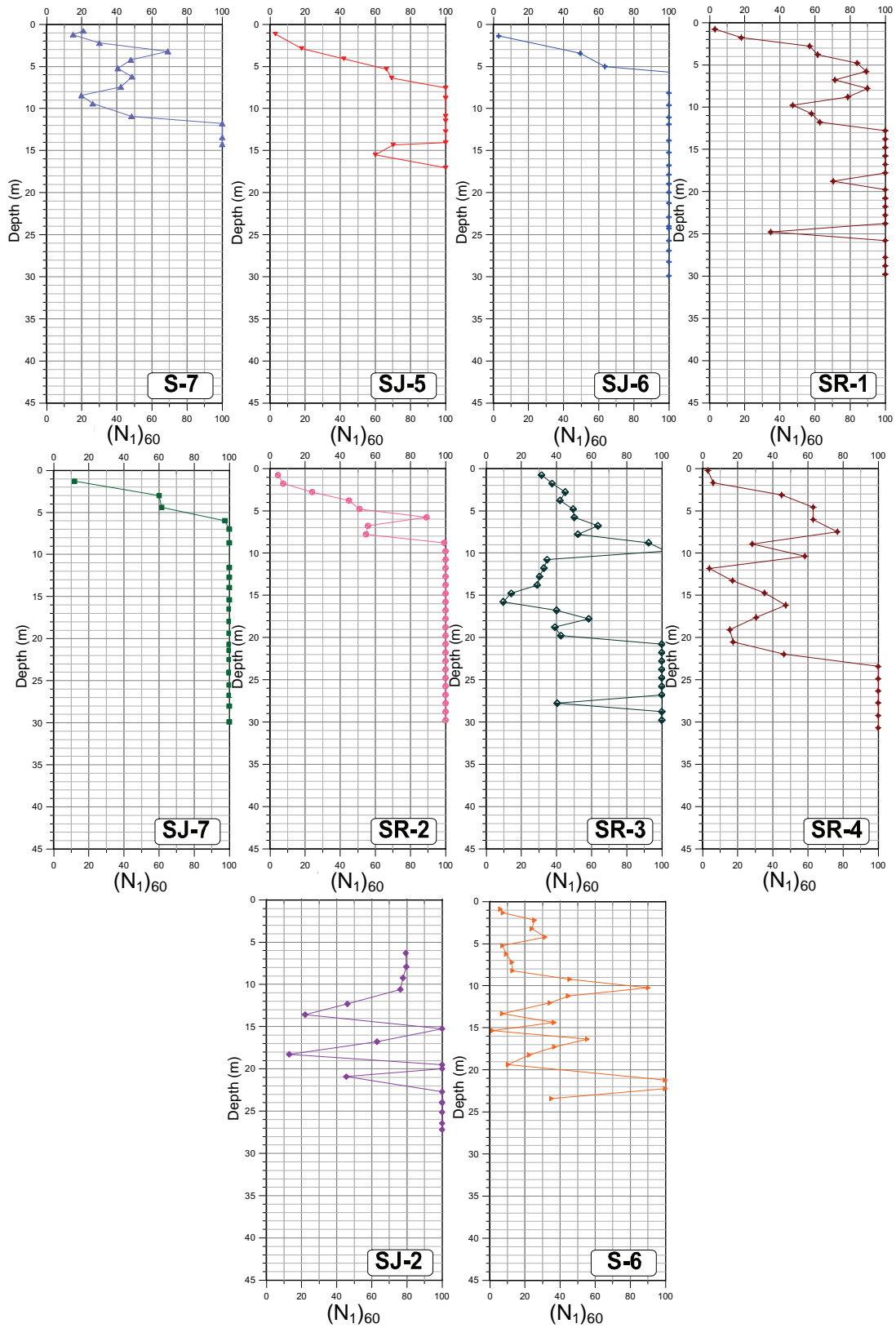


Fig. 4.30. SPT blow counts at the Llacolén Bridge (Verdugo and Peters 2010)

The location of the SPT and CPT performed as part of this study are shown in Fig. 4.28. Unfortunately, due to equipment failure and time constraints there was only enough time to attempt one SPT and CPT at this site. Fig. 4.31 shows the 7.5 m SPT boring, which encountered primarily clean to silty sands. The CPT performed 1.5 m from the SPT to develop a site specific calibration between the two tests encountered a hard material at 3.7 m depth and was unable to proceed. The water table was below the 3.7 m depth reached by the CPT, and the SPT boring was filled in before the water table could be determined. Based on the elevation of the river and the elevation at the top of the embankment, it is unlikely that much, if any, of the SPT extended below the water table. Therefore, liquefaction triggering analysis is not presented. However, if soils below the water table had $(N_1)_{60}$ values similar to the relatively low values in Fig. 4.31, liquefaction would be very likely.

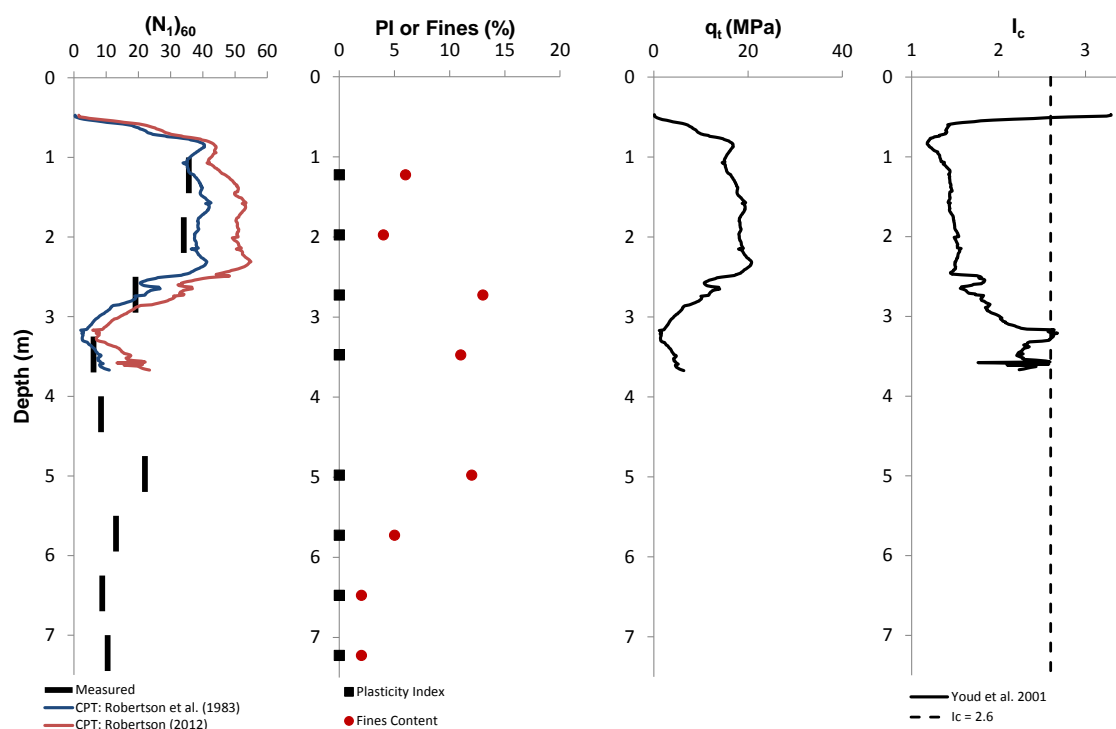


Fig. 4.31. SPT boring and CPT sounding at Llacolén Bridge

Although the CPT stopped after only 3.7 m, Fig. 4.31 presents a comparison between the measured $(N_1)_{60}$ values and $(N_1)_{60}$ values estimated from CPT-based correlations. Index tests performed on SPT samples between depths of 1.0 m and 3.7 m, indicated the median particle size, D_{50} , ranged from 0.55 mm to 0.59 mm. Robertson et al. (1983) examine the relationship between N_{60} and q_c/p_a , and for a D_{50} of 0.57 mm they suggest the ratio of q_c/p_a to N_{60} of 6.7. Using this value, q_c values were converted to N_{60} values and then the $(N_1)_{60}$ values plotted on Fig. 4.31. A second relationship from Robertson and Cabal (2012) defines the q_c/p_a to N_{60} ratio as

a function of the behavior soil type index (I_c). As shown in Fig. 4.31, the Robertson and Cabal (2012) correlation overestimates the measured $(N_1)_{60}$ values whereas the Robertson et al. (1983) correlation matches the data quite well. This is somewhat unsurprising because the method of Robertson et al. (1983) requires information on the grain size, which is obtained from the adjacent SPT. However, the method of Robertson and Cabal (2012) depends only on the CPT and does not use information from the adjacent SPT in this case. The close match between estimates from Robertson et al. (1983) and the measured $(N_1)_{60}$ values increase confidence in the quality of these two measurements.

4.4 CONCLUSIONS

The M_w 8.8 February 27, 2010, Maule, Chile earthquake affected a large area, causing extensive damage, including many cases of liquefaction-induced settlement and lateral spreading. The development of case histories has been essential in improving the state of liquefaction and SFSI knowledge. Well-developed case histories are invaluable in calibrating numerical models, comparing to centrifuge tests, and developing empirical methods. This chapter presents liquefaction case histories at three sites identified by GEER (Bray and Frost 2010) as suffering liquefaction-induced damage. SPT borings with energy measurements and CPT soundings performed at a hospital and two bridges supplement the damage documented by GEER and other sources. Simplified liquefaction and settlement correlations developed for the free-field are commonly used in practice and were performed to illustrate potential shortcomings with these methods.

The recently constructed Hospital Provincial in Curanilahue consists of 10 structurally isolated wings, and this provides an important opportunity to learn from liquefaction-induced damage involving SFSI and SSSI. CPTs and an SPT performed at the site, supplemented with past investigations, indicate a complex heterogeneous subsurface. A shallow silt layer with plasticity indices generally below 18 but above 7 appears to have liquefied and caused the settlement, tilt, and lateral movement of several hospital wings. The borderline plasticity characteristics of the soils at this site point to the importance of screening tools such as Bray and Sancio (2006) in estimating the liquefaction potential of plastic silts.

The Juan Pablo II Bridge, an important crossing of the Bío-Bío River, closed after suffering significant damage following the earthquake. Liquefaction-induced settlement and lateral spreading at the northeast approach was the focus of this investigation. SPT and CPTs indicated medium dense sands liquefied leading to settlement, lateral spreading, and failure of the approach. The Llacolén Bridge suffered liquefaction-induced lateral spreading and settlement leading to the collapse of a deck at the northeast approach. Although the SPT and CPT tests performed at this site were of insufficient depth to perform liquefaction triggering analysis, the profiles are provided as well as comparison between SPT and CPT measurements.

CHAPTER 5: CONCLUSIONS

5.1. SUMMARY

Recent earthquakes in Chile, New Zealand, and Japan emphasize the damaging potential of liquefaction and the importance of SFSI effects. This thesis combines several related research projects examining the complex interaction between ground motion, soil profile, and structural properties that controls liquefaction-induced building damage. Ground motion characteristics, including pulse-like qualities of a motion, have an important effect on liquefaction triggering and performance. The model of pulse occurrence developed in this research could be valuable in both liquefaction analyses and in selecting a representative suite of motions for non-linear structural analysis. The geotechnical centrifuge experiment provides a case history in a carefully controlled and well-documented environment, allowing a systematic examination of the effects of SFSI and SSSI on mat-founded buildings on a liquefiable subsurface. Lastly, field case histories, such as the case of the hospital in Curanilahue, Chile, are important in advancing the understanding of liquefaction, SFSI, and SSSI.

5.2. FINDINGS

Ground motion characteristics greatly affect liquefaction triggering and settlement. Pulse motions in the near-fault region can be due to forward directivity or other phenomena, and they are sometimes absent when expected (e.g., at sites in the forward directivity region). In this study, the application of a newly developed automated pulse classification method to a set of 673 records from the NGA-West2 database resulted in 141 records classified as pulses. Based on the classification results, a straightforward model was developed that can be used by practicing engineers to estimate the likelihood of pulse motions occurring at a site and an appropriate proportion of pulse motions to include in a suite for time-history analysis. A second classification method identified pulses that were likely due to forward directivity. The key results of this study include the following:

- The number of significant pulses and NCSV worked well as parameters to identify pulses in an automated classification algorithm.
- A model of pulse probability was developed based on closest distance and epsilon, two of most important factors in pulse occurrences.
- A second classification indicated that 74 out of 141 pulse motions were well explained by forward directivity, suggesting there are other important sources of pulse motions as well.
- Pulses well explained by forward directivity tended to be oriented within 30° of fault normal, but other pulses had more uniformly distributed orientations.
- A table and figures of 141 pulse motions are provided to aid other researchers or practicing engineers in selecting individual time histories.

Geotechnical centrifuge tests provide valuable insight into many geotechnical problems, including liquefaction. This study expanded on observations from the previous test in the series by Zupan (2014) and involved a saturated model with a liquefiable layer of Nevada Sand subjected to three major shaking events. Three types of single degree of freedom structures, in isolated and adjacent configurations, demonstrate the effects of SFSI and SSSI involving liquefaction. The key findings based on the combined results of these two tests are:

- The performance of structures on liquefiable soil depends on complex interactions between the ground motion, soil conditions, and soil profile. For example, heavier structures settled more than lighter structured during the Moderate Port Island Event, but during the Moderate TCU event, lighter structures settled more than heavier ones. These two motions had similar peak accelerations, but Port Island was more pulse-like and TCU was a longer duration non-pulse record.
- The majority of free-field settlement occurred during shaking indicating partial drainage.
- Most structure settlement occurred during strong shaking and structures settled substantially more than the free-field, demonstrating the importance of shear-induced settlement mechanisms.
- A higher relative density leads to less settlement with all else equal, consistent with other studies (e.g., Dashti et al. 2010a).
- Structures that were adjacent to other shallow-founded structures often settled less than isolated structures. Sand columns indicated that adjacent structures tended to restrain the lateral movement of soil beneath neighboring structures.
- Adjacent pairs of structures tended to tilt and move laterally away from each other. Again, this is likely due to the neighboring structure restraining movement of soil in their direction, and as a result, the unrestrained edge settles more.
- Structures adjacent to other shallow-founded structures tended to have lower foundation spectral acceleration values compared to isolated structures.
- It is important to note that the above observations are from a limited combination of soil, ground motion, and structural properties and may not be true of all configurations.

Widespread liquefaction during the 2010 Chile earthquake damaged buildings, bridges, and other infrastructure. Liquefaction case histories are important to develop because they advance the understanding of liquefaction-induced damage, can be used to calibrate numerical models, serve as comparisons to geotechnical centrifuge tests, and aid in development of empirical correlations. This study involves SPT and CPT investigations to improve subsurface characterizations at three key sites identified by GEER (Bray and Frost 2010) reconnaissance. The key findings from this study at these sites are:

- The 10 structurally isolated wings of Hospital Provincial in Curanilahue present an important opportunity to examine SFSI and SSSI. Liquefaction of a shallow silty layer with plasticity indices frequently in the intermediate susceptibility range of Bray and Sancio (2006) points to the importance of understanding the liquefaction behavior of plastic soils. Simplified liquefaction triggering analyses indicate the factor of safety against liquefaction was well below one for most of the soil profile if the soil is classified as susceptible to liquefaction as defined by Bray and Sancio (2006). However, this soil deposit would not be expected to exhibit “sand-like” behavior according to Idriss and Boulanger (2008), because its PI was generally well above 7.
- Simplified free-field volumetric settlement correlations such as Zhang et al. (2002) do not account for the effects of a structure and are potentially misleading even if only used as an index of damage because they treat volumetric strains equally regardless of depth. At the hospital site, the shallow liquefiable silt layer likely had a much larger impact on the structural performance than potentially liquefiable areas in deeper deposits. The observation of settlements, lateral movements, and tilts coincided with the approximate extents of this silty layer, which points to the higher impact of shallow liquefiable layers on building performance.
- Liquefaction of medium dense sands at the Juan Pablo II Bridge in Concepción caused settlement and lateral spreading at the northeast approach, forcing this important lifeline closed.
- The tests performed at the Llacolén Bridge in Concepción did not extend deep enough for liquefaction triggering analyses. However, the measured CPT tip resistances were comparable to the $(N_1)_{60}$ values of the adjacent SPT boring based on the correlation of Robertson et al. (1983); this increases confidence in the reliability of measurements at the other sites.

5.3 RECOMMENDATIONS FOR FUTURE RESEARCH

The seismic performance of structures on liquefiable ground depends on the ground motion, soil profile, and structural properties. Commonly used free-field correlations for liquefaction triggering (e.g., Youd et al. 2001; Cetin et al. 2004; Moss et al. 2006; Boulanger and Idriss 2014) and volumetric settlements (e.g., Zhang et al. 2002) cannot account for the additional effects from the presence of a structure. Unfortunately, simple analysis methods that do account for structure-induced shear effects are lacking. There have been some recent efforts on this front (e.g., Cetin et al. 2012; Unutmaz and Cetin 2012), but more work is needed. Case histories, such as those developed in Chile and from geotechnical centrifuge tests, will aid in these efforts.

Numerical modeling of liquefaction is essential for both advanced analysis at critical sites in engineering practice as well as improving understanding and development of simplified procedures for more routine projects. The limited number of well-documented field cases

histories as well as the time and expense required to perform centrifuge tests means that well-calibrated numerical models aid development of simplified methods by allowing sensitivity analyses to explore a full range of ground motion, soil profile, and structural property combinations. A natural starting place would be numerical modeling of the centrifuge tests in this thesis to ensure the applicability of liquefaction models (e.g., UBCSAND and PM4Sand). Next, systematically varying key parameters (e.g., soil density, thickness, structure bearing pressure, ground motion characteristics, spacing between adjacent structures, etc.) would indicate the importance of each parameter. Interestingly, Dashti and Bray (2013) found that UBCSAND in FLAC-2D worked well for the Port Island Events, but it overestimated the excess pore pressures and settlement during TCU, illustrating a potential shortcoming of the model. The same TCU motion in the centrifuge studies of this thesis also caused extremely low or even negative excess pore pressures under the heavier structures, an observation not fully explained.

Heavier structures responded very differently to the Port Island Moderate and TCU Moderate events during geotechnical centrifuge testing, illustrating the importance of ground motion characteristics beyond simple parameters such as PGA (both motions had similar peak accelerations). The significance of various ground motion characteristics is an important opportunity for additional research. In the particular case of the pulse motion research in this thesis, there are several opportunities for improvement. This study identified 74 of 141 pulse motions were likely due to forward directivity. This leaves a large proportion from other sources, potentially including fling-step, site effects, basin effects, or asperities during fault rupture. An improved understanding of the significance of these effects would be valuable. The current method is based on residuals from Abrahamson and Silva (2008), and it would be useful to examine the difference when using the NGA West2 correlations. Finally, in this study, pulses of all periods were included together, which is conservative considering that pulse periods significantly different from the fundamental period of the structure will likely have limited impact. This simplification should be examined to determine if it is overly conservative.

REFERENCES

- Abrahamson, N., et al. (2008). "Comparisons of the NGA ground-motion relations." *Earthquake Spectra*, 24(1), 45–66.
- Abrahamson, N., and Silva, W. (2008a). "Summary of the Abrahamson & Silva NGA ground-motion relations." *Earthquake Spectra*, 24(1), 67–97.
- Abrahamson, N. A. (2000). "Effects of rupture directivity on probabilistic seismic hazard analysis." *Proc., 6th Int. Conf. on Seismic Zonation*, Earthquake Engineering Research Institute, Oakland, CA.
- Abrahamson, N. A., and Silva, W. J. (2008b). "Abrahamson and Silva NGA ground motion relations for the geometric mean horizontal component of peak and spectral ground motion parameters." *Final Rep. Prepared for the Pacific Earthquake Engineering Research Center*, Pacific Earthquake Engineering Research Center, Berkeley, CA.
- Alavi, B., and Krawinkler, H. (2000). "Consideration of near-fault ground motion effects in seismic design." *Proc., 12th World Conf. on Earthquake Engineering*, Int. Association for Earthquake Engineering, Tokyo.
- Allmond, J., and Kutter, B. (2012). "Centrifuge Testing of Rocking Foundations on Saturated Sand and Unconnected Piles: The Fluid Response." *GeoCongress 2012*, ASCE, 1760–1769.
- Allmond, J. D., and Kutter, B. L. (2013). "Centrifuge Testing of Rocking Foundations on Saturated and Submerged Sand: Centrifuge Data Report for JDA02." Center for Geotechnical Modeling Data Report UCD/CGMDR – 13/01.
- Ancheta, T. D., et al. (2012). "PEER NGA-West2 database: A database of ground motions recorded in shallow crustal earthquakes in active tectonic regions." *Proc., 15th World Conf. on Earthquake Engineering*, Int. Association for Earthquake Engineering, Tokyo.
- Anderson, J., and Bertero, V. (1987). "Uncertainties in establishing design earthquakes." *J. Struct. Eng.*, 113(8), 1709-1724.
- Andrianopoulos, K. I., Papadimitriou, A. G., and Bouckovalas, G. D. (2010). "Bounding surface plasticity model for the seismic liquefaction analysis of geostructures." *Soil Dyn. Earthquake Eng.*, 30(10), 895–911.
- Archuleta, R. J., and Hartzell, S. H. (1981). "Effects of fault finiteness on near-source ground motion." *Bull. Seismol. Soc. Am.*, 71(4), 939–957.
- Ashford, S. A., Boulanger, R., Donahue, J. L., and Stewart, J. P. (2011). "Geotechnical Quick Report on the Kanto Plain Region during the March 11, 2011, Off Pacific Coast of Tohoku Earthquake, Japan." *GEER Association Report No. GEER-025a*.
- Baker, J. (2011). "Conditional mean spectrum: Tool for ground-motion selection." *J. Struct. Eng.*, 137(3), 322-331.
- Baker, J. W. (2007). "Quantitative classification of near-fault ground motions using wavelet analysis." *Bull. Seismol. Soc. Am.*, 97(5), 1486–1501.
- Benioff, H. (1955). "Mechanism and strain characteristics of the White Wolf fault as indicated by the aftershock sequence." *California Div. Mines Bull.*, 171, 199–202.

- Ben-Menahem, A. (1961). "Radiation of seismic surface-waves from finite moving sources." *Bull. Seismol. Soc. Am.*, 51(3), 401–435.
- Boore, D. M., and Atkinson, G. M. (2008). "Ground-motion prediction equations for the average horizontal component of PGA, PGV, and 5%-damped PSA at spectral periods between 0.01 s and 10.0 s." *Earthquake Spectra*, 24(1), 99–138.
- Boroschek, R. L., Contreras, V., Kwak, D. Y., and Stewart, J. P. (2012). "Strong Ground Motion Attributes of the 2010 M_w 8.8 Maule, Chile, Earthquake." *Earthquake Spectra*, 28(S1), S19–S38.
- Boulanger, R., and Idriss, I. (2014). *CPT and SPT based liquefaction triggering procedures*. Center for Geotechnical Modeling, University of California, Davis, CA.
- Bradley, B. A. (2012). "Empirical correlations between peak ground velocity and spectrum-based intensity measures." *Earthquake Spectra*, 28(1), 17–35.
- Bradley, B. A. (2013). "Practice-oriented estimation of the seismic demand hazard using ground motions at few intensity levels." *Earthquake Eng. Struct. Dyn.*, 42(14), 2167–2185.
- Bray, J., Cubrinovski, M., Zupan, J., and Taylor, M. (2014). "Liquefaction Effects on Buildings in the Central Business District of Christchurch." *Earthquake Spectra*, 30(1), 85–109.
- Bray, J. D., and Rodriguez-Marek, A. (2004). "Characterization of forward directivity ground motions in the near-fault region." *Soil Dyn. Earthquake Eng.*, 24(11), 815–828.
- Bray, J. D., Rodriguez-Marek, A., and Gillie, J. L. (2009). "Design ground motions near active faults." *Bull. N. Z. Soc. Earthquake Eng.*, 42(1), 1–8.
- Bray, J., and Sancio, R. (2006). "Assessment of the Liquefaction Susceptibility of Fine-Grained Soils." *J. of Geotech. Geoenviron. Eng.*, 132(9), 1165–1177.
- Bray, J. D., Stewart, J. P., Baturay, M. B., Durgunoglu, T., Onalp, A., Sancio, R. B., Stewart, J. P., Ural, D., Ansal, A., Bardet, J. B., Barka, A., Boulanger, R., Cetin, O., and Erten, D. (2000). "Damage Patterns and Foundation Performance in Adapazari." *Earthquake Spectra*, 16(S1), 163–189.
- Bray, J. D., and Frost, J. D., Eds., 2010. *Geo-engineering Reconnaissance of the 2010 Maule, Chile, Earthquake, a Report of the NSF- Sponsored GEER Association Team*, primary authors: Arduino et al., <http://www.geerassociation.org/>.
- Bray, J., Rollins, K., Hutchinson, T., Verdugo, R., Ledezma, C., Mylonakis, G., Assimaki, D., Montalva, G., Arduino, P., Olson, S. M., Kayen, R., Hashash, Y. M. A., and Candia, G. (2012). "Effects of Ground Failure on Buildings, Ports, and Industrial Facilities." *Earthquake Spectra*, 28(S1), S97–S118.
- Bray, J., Cubrinovski, M., Zupan, J., and Taylor, M. (2014). "Liquefaction Effects on Buildings in the Central Business District of Christchurch." *Earthquake Spectra*, 30(S1), In-Press.
- Campbell, K. W., and Bozorgnia, Y. (2008). "NGA ground motion model for the geometric mean horizontal component of PGA, PGV, PGD and 5% damped linear elastic response spectra for periods ranging from 0.01 to 10 s." *Earthquake Spectra*, 24(1), 139–171.
- Cetin, K., Bilge, H., Wu, J., Kammerer, A., and Seed, R. (2009). "Probabilistic Model for the Assessment of Cyclically Induced Reconsolidation (Volumetric) Settlements." *J. of Geotech. Geoenviron. Eng.*, 135(3), 387–398.

- Cetin, K. O., Unutmaz, B., and Jeremic, B. (2012). "Assessment of seismic soil liquefaction triggering beneath building foundation systems." *Soil Dyn. Earthquake Eng.*, 43, 160–173.
- Cetin, K., Seed, R., Der Kiureghian, A., Tokimatsu, K., Harder, L., Kayen, R., and Moss, R. (2004). "Standard Penetration Test-Based Probabilistic and Deterministic Assessment of Seismic Soil Liquefaction Potential." *J. of Geotech. Geoenviron. Eng.*, 130(12), 1314–1340.
- Chiou, B. S. J., and Youngs, R. R. (2008). "An NGA model for the average horizontal component of peak ground motion and response spectra." *Earthquake Spectra*, 24(1), 173–215.
- Cubrinovski, M., Bray, J. D., Taylor, M., Giorgini, S., Bradley, B., Wotherspoon, L., and Zupan, J. (2011). "Soil liquefaction effects in the central business district during the February 2011 Christchurch earthquake." *Seismol. Res. Lett.*, 82(6), 893–904.
- Dabaghi, M., Der Kiureghian, A., Rezaeian, S., and Luco, N. (2013). "Seismic hazard analysis using simulated ground motions." *Proc., 11th Int. Conf. on Structural Safety & Reliability*, Int. Association for Structural Safety and Reliability, New York.
- Dashti, S. (2009). *Toward developing an engineering procedure for evaluating building performance on softened ground*. Ph.D. Dissertation, University of California, Berkeley, CA.
- Dashti, S., and Bray, J. (2013). "Numerical Simulation of Building Response on Liquefiable Sand." *J. of Geotech. Geoenviron. Eng.*, 139(8), 1235–1249.
- Dashti, S., Bray, J., Pestana, J., Riemer, M., and Wilson, D. (2010a). "Mechanisms of Seismically Induced Settlement of Buildings with Shallow Foundations on Liquefiable Soil." *J. of Geotech. Geoenviron. Eng.*, 136(1), 151–164.
- Dashti, S., Bray, J., Pestana, J., Riemer, M., and Wilson, D. (2010b). "Centrifuge Testing to Evaluate and Mitigate Liquefaction-Induced Building Settlement Mechanisms." *J. of Geotech. Geoenviron. Eng.*, 136(7), 918–929.
- Delouis, B., Nocquet, J.-M., and Vallée, M. (2010). "Slip distribution of the February 27, 2010 Mw = 8.8 Maule Earthquake, central Chile, from static and high-rate GPS, InSAR, and broadband teleseismic data." *Geophysical Research Letters*, 37(17), L17305.
- Elnashai, A. S., Gencturk, B., Kwon, O.-S., Al-Qadi, I. L., Hashash, Y., Roesler, J. R., Kim, S. J., Jeong, S.-H., Dukes, J., and Valdivia, A. (2010). "The Maule (Chile) Earthquake of February 27, 2010: consequence assessment and case studies."
- Federal Highway Administration (FHWA). (2011). *Post-Earthquake reconnaissance report on transportation infrastructure: Impact of the 27 February 2010, Offshore Maule Earthquake in Chile*.
- Garnier, J., Gaudin, C., Springman, S. M., Culligan, P. J., Goodings, D. J., Konig, D., Kutter, B. L., Phillips, R., Randolph, M. F., and Thorel, L. (2007). "Catalogue of scaling laws and similitude questions in geotechnical centrifuge modelling." *International Journal of Physical Modelling in Geotechnics*, 7(3), 1–23.
- Hall, J. F., Heaton, T. H., Halling, M. W., and Wald, D. J. (1995). "Near-source ground motion and its effects on flexible buildings." *Earthquake Spectra*, 11(4), 569–605.
- Hayden, C. P., Allmond, J. D., Rawlings, I. A., Zupan, J. D., Bray, J. D., Kutter, B. L.,

- Hutchinson, T. C., Fiegel, G. L., and Whittaker, A. S. (2014). "Seismic Performance Assessment in Dense Urban Environments: Centrifuge Data Report for Test-6." University of California at Davis Center for Geotechnical Modeling Report No. UCD/CGMDR-XX/XX, Davis, CA.
- Hayden, C. P., Bray, J. D., Abrahamson, N. A., and Acevedo-Cabrera, A. L. (2012). "Selection of near-fault pulse motions for use in design." *Proc., 15th World Conf. on Earthquake Engineering*, Int. Association for Earthquake Engineering, Tokyo.
- IDIEM. (2011). *Recimentacion Hospital de Curanilahue*. IDIEM, Sección Ingeniería y Prospecciones Geotecnicas (in Spanish).
- Idriss, I. M., and Boulanger, R. W. (2008). *Soil liquefaction during earthquakes*. Earthquake engineering research institute, Oakland, CA.
- Ishihara, K., and Yoshimine, M. (1992). "Evaluation of settlements in sand deposits following liquefaction during earthquakes." *Soils and Foundations*, 32(1), 173–188.
- Kalkan, E., and Kunnath, S. K. (2006). "Effects of fling step and forward directivity on seismic response of buildings." *Earthquake Spectra*, 22(2), 367–390.
- Karamitros, D., Bouckovalas, G., and Chaloulos, Y. (2013a). "Insight into the Seismic Liquefaction Performance of Shallow Foundations." *J. of Geotech. Geoenviron. Eng.*, 139(4), 599–607.
- Karamitros, D. K., Bouckovalas, G. D., and Chaloulos, Y. K. (2013b). "Seismic settlements of shallow foundations on liquefiable soil with a clay crust." *Soil Dyn. Earthquake Eng.*, 46, 64–76.
- Kausel, E. (2010). "Early history of soil–structure interaction." *Soil Dyn. Earthquake Eng.*, 30(9), 822–832.
- Lay, T., Ammon, C. J., Kanamori, H., Koper, K. D., Sufri, O., and Hutko, A. R. (2010). "Teleseismic inversion for rupture process of the 27 February 2010 Chile (Mw 8.8) earthquake." *Geophysical Research Letters*, 37(13), L13301.
- Ledezma, C., Hutchinson, T., Ashford, S. A., Moss, R., Arduino, P., Bray, J. D., Olson, S., Hashash, Y. M. A., Verdugo, R., Frost, D., Kayen, R., and Rollins, K. (2012). "Effects of Ground Failure on Bridges, Roads, and Railroads." *Earthquake Spectra*, 28(S1), S119–S143.
- Liu, L., and Dobry, R. (1997). "Seismic Response of Shallow Foundation on Liquefiable Sand." *J. of Geotech. Geoenviron. Eng.*, 123(6), 557–567.
- Mason, H. B., Trombetta, N. W., Chen, Z., Bray, J. D., Hutchinson, T. C., and Kutter, B. L. (2013). "Seismic soil–foundation–structure interaction observed in geotechnical centrifuge experiments." *Soil Dyn. Earthquake Eng.*, 48, 162–174.
- MATLAB 2011b* [Computer software]. Natick, MA, MathWorks.
- Menglin, L., Huaifeng, W., Xi, C., and Yongmei, Z. (2011). "Structure–soil–structure interaction: Literature review." *Soil Dyn. Earthquake Eng.*, 31(12), 1724–1731.
- Moss, R., Seed, R., Kayen, R., Stewart, J., Der Kiureghian, A., and Cetin, K. (2006). "CPT-Based Probabilistic and Deterministic Assessment of In Situ Seismic Soil Liquefaction Potential." *J. of Geotech. Geoenviron. Eng.*, 132(8), 1032–1051.

- Da Silva Marques, A. S. P., de Figueiredo Coelho, P. A. L., Haigh, S., and Madabhushi, G. (2014). "Centrifuge Modeling of Liquefaction Effects on Shallow Foundations." *Seismic Evaluation and Rehabilitation of Structures*, Springer, 425–440.
- NIST. (2011). *Selecting and scaling earthquake ground motions for performing response-history analyses*, NEHRP Consultants Joint Venture for NIST, Gaithersburg, MD.
- Robertson, P., Campanella, R., and Wightman, A. (1983). "SPT-CPT Correlations." *J. of Geotech. Eng.*, 109(11), 1449–1459.
- Robertson, P. K., and Cabal, K. L. (2012). *Guide to cone penetration testing for geotechnical engineering*. Gregg drilling, November, 2012.
- Robertson, P. K., and Wride, C. E. (1998). "Evaluating cyclic liquefaction potential using the cone penetration test." *Canadian Geotech. J.*, 35(3), 442–459.
- Sancio, R. B. (2003). *Ground failure and building performance in Adapazari, Turkey*. Ph.D. Dissertation, University of California, Berkeley, CA.
- Sancio, R. B., and Bray, J. D. (2005). "An assessment of the effect of rod length on SPT energy calculations based on measured field data." *Geotech. Test. J.*, 28(1), 22–30.
- Sancio, R. B., Bray, J. D., Stewart, J. P., Youd, T. L., Durgunoğlu, H. T., Önalp, A., Seed, R. B., Christensen, C., Baturay, M. B., and Karadayılar, T. (2002). "Correlation between ground failure and soil conditions in Adapazari, Turkey." *Soil Dyn. Earthquake Eng.*, 22(9–12), 1093–1102.
- Schellart, W. P., Freeman, J., Stegman, D. R., Moresi, L., and May, D. (2007). "Evolution and diversity of subduction zones controlled by slab width." *Nature*, 446(7133), 308–311.
- Seed, H. B., and Idriss, I. M. (1982). *Ground motions and soil liquefaction during earthquakes*. Earthquake Engineering Research Institute Berkeley.
- Seed, H., Tokimatsu, K., Harder, L., and Chung, R. (1985). "Influence of SPT Procedures in Soil Liquefaction Resistance Evaluations." *J. Geotech. Eng.*, 111(12), 1425–1445.
- Shahi, S. K., and Baker, J. W. (2011). "An empirically calibrated framework for including the effects of near-fault directivity in probabilistic seismic hazard analysis." *Bull. Seismol. Soc. Am.*, 101(2), 742–755.
- Somerville, P. G., Smith, N. F., Graves, R. W., and Abrahamson, N. A. (1997). "Modification of empirical strong ground motion attenuation relations to include the amplitude and duration effects of rupture directivity." *Seismol. Res. Lett.*, 68(1), 199–222.
- Spudich, P., and Chiou, B. S. J. (2008). "Directivity in NGA earthquake ground motions: Analysis using isochrone theory." *Earthquake Spectra*, 24(1), 279–298.
- Stewart, D. P., Chen, Y.-R., and Kutter, B. L. (1998). "Experience with the Use of Methylcellulose as a Viscous Pore Fluid in Centrifuge Models." *Geotech. Test. J.*, 21(4), 365–369.
- Structural Engineering Institute (SEI). (2006). *Minimum design loads for buildings and other structures*, ASCE/Structural Engineering Institute, Reston, VA.
- Tokimatsu, K., Tamura, S., Suzuki, H., and Katsumata, K. (2012). "Building damage associated with geotechnical problems in the 2011 Tohoku Pacific Earthquake." *Soils Found.*, 52(5), 956–974.

- Tokimatsu, K., and Katsumata, K. (2012). “Liquefaction-induced damage to buildings in Urayasu City during the 2011 Tohoku Pacific Earthquake.” *Proceedings of the International Symposium on Engineering Lessons Learned from the 2011 Great East Japan Earthquake*, 665–674.
- Tokimatsu, K., and Seed, H. (1987). “Evaluation of Settlements in Sands Due to Earthquake Shaking.” *J. Geotech. Eng.*, 113(8), 861–878.
- Travasarou, T., Bray, J. D., and Abrahamson, N. A. (2003). “Empirical attenuation relationship for Arias Intensity.” *Earthquake Eng. Struct. Dyn.*, 32(7), 1133–1155.
- Trombetta, N., Mason, H., Hutchinson, T., Zupan, J., Bray, J., and Kutter, B. (2013). “Nonlinear Soil–Foundation–Structure and Structure–Soil–Structure Interaction: Centrifuge Test Observations.” *J. of Geotech. Geoenviron. Eng.*, 0(0), Advance online publication. DOI: 10.1061/(ASCE)GT.1943–5606.0001074.
- Trombetta, N. W., Mason, H. B., Chen, Z., Hutchinson, T. C., Bray, J. D., and Kutter, B. L. (2013). “Nonlinear dynamic foundation and frame structure response observed in geotechnical centrifuge experiments.” *Soil Dyn. Earthquake Eng.*, 50, 117–133.
- Unutmaz, B., and Cetin, K. O. (2012). “Post-cyclic settlement and tilting potential of mat foundations.” *Soil Dyn. Earthquake Eng.*, 43, 271–286.
- Verdugo, R., and Peters, G. (2010). *Informe Geotécnico Fase Anteproyecto Infraestructura Puente Mecano Eje Chacabuco, Rev7* (in Spanish).
- Verdugo, R., Sitar, N., Frost, J. D., Bray, J. D., Candia, G., Eldridge, T., Hashash, Y., Olson, S. M., and Urzua, A. (2012). “Seismic Performance of Earth Structures during the February 2010 Maule, Chile, Earthquake: Dams, Levees, Tailings Dams, and Retaining Walls.” *Earthquake Spectra*, 28(S1), S75–S96.
- Vigny, C., Socquet, A., Peyrat, S., Ruegg, J.-C., Métois, M., Madariaga, R., Morvan, S., Lancieri, M., Lacassin, R., Campos, J., Carrizo, D., Bejar-Pizarro, M., Barrientos, S., Armijo, R., Aranda, C., Valderas-Bermejo, M.-C., Ortega, I., Bondoux, F., Baize, S., Lyon-Caen, H., Pavez, A., Vilotte, J. P., Bevis, M., Brooks, B., Smalley, R., Parra, H., Baez, J.-C., Blanco, M., Cimbaro, S., and Kendrick, E. (2011). “The 2010 Mw 8.8 Maule Megathrust Earthquake of Central Chile, Monitored by GPS.” *Science*, 332(6036), 1417–1421.
- VST Ingenieros. (2003). *Geotechnical Report for Curanilahue Regional Hospital*. VST Ingenieros, Ltda., Santiago, Chile (in Spanish).
- Yasuda, S., Harada, K., Ishikawa, K., and Kanemaru, Y. (2012). “Characteristics of liquefaction in Tokyo Bay area by the 2011 Great East Japan Earthquake.” *Soils and Foundations*, Special Issue on Geotechnical Aspects of the 2011 off the Pacific Coast of Tohoku Earthquake, 52(5), 793–810.
- Youd, T., Idriss, I., Andrus, R., Arango, I., Castro, G., Christian, J., Dobry, R., Finn, W., Harder, L., Hynes, M., Ishihara, K., Koester, J., Liao, S., Marcuson, W., Martin, G., Mitchell, J., Moriwaki, Y., Power, M., Robertson, P., Seed, R., and Stokoe, K. (2001). “Liquefaction Resistance of Soils: Summary Report from the 1996 NCEER and 1998 NCEER/NSF Workshops on Evaluation of Liquefaction Resistance of Soils.” *J. of Geotech. Geoenviron.*

Eng., 127(10), 817–833.

- Zhai, C., Chang, Z., Li, S., Chen, Z., and Xie, L. (2013). “Quantitative identification of near-fault pulse-like ground motions based on energy.” *Bull. Seismol. Soc. Am.*, 103(5), 2591–2603.
- Zhang, G., Robertson, P. K., and Brachman, R. W. . (2002). “Estimating liquefaction-induced ground settlements from CPT for level ground.” *Canadian Geotech. J.*, 39(5), 1168–1180.
- Zupan, J. D., Trombetta, N. W., Puangnak, H., Paez, D., Bray, J. D., Kutter, B. L., Hutchinson, T. C., Fiegel, G. L., Bolisetti, C., and Whittaker, A. S. (2013). “Seismic Performance Assessment in Dense Urban Environments: Centrifuge Data Report for Test-5.” University of California at Davis Center for Geotechnical Modeling Report No. UCD/CGMDR-XX/XX, Davis, CA.

APPENDICIES

CHAPTER 2: Selection of Near-Fault Pulse Motions

A-1: Near-Fault Database: List of 673 Records Used in this Study	102
A-2: MATLAB Algorithm.....	109
A-3: Contour Generation	119
A-4: Pulse Motion Figures.....	121

CHAPTER 3: Centrifuge Tests of Adjacent Mat-Supported Buildings Affected by Liquefaction

B-1: Test-6 (T4.6-40) Centrifuge Data Report	138
B-2: Supplemental Plots	324

CHAPTER 4: Liquefaction-Induced SFSI Damage in the 2010 Chile Earthquake

C-1: SPT and CPT Liquefaction Analysis	337
C-2: Index Tests	350

APPENDIX A-1: List of NGA records used.

NGA #	Earthquake Name	Station Name	NGA #	Earthquake Name	Station Name
28	Parkfield	Cholame - Shandon Array #12	265	Victoria, Mexico	Cerro Prieto
30	Parkfield	Cholame - Shandon Array #5	266	Victoria, Mexico	Chihuahua
31	Parkfield	Cholame - Shandon Array #8	269	Victoria, Mexico	Victoria Hospital Sotano
33	Parkfield	Temblo pre-1969	284	Irpinia, Italy-01	Auletta
57	San Fernando	Castaic - Old Ridge Route	285	Irpinia, Italy-01	Bagnoli Irpinio
68	San Fernando	LA - Hollywood Stor FF	286	Irpinia, Italy-01	Bisaccia
70	San Fernando	Lake Hughes #1	288	Irpinia, Italy-01	Brienza
71	San Fernando	Lake Hughes #12	289	Irpinia, Italy-01	Calltri
72	San Fernando	Lake Hughes #4	290	Irpinia, Italy-01	Mercato San Severino
73	San Fernando	Lake Hughes #9	292	Irpinia, Italy-01	Sturno (STN)
77	San Fernando	Pacoima Dam (upper left abut)	295	Irpinia, Italy-02	Auletta
78	San Fernando	Palmdale Fire Station	296	Irpinia, Italy-02	Bagnoli Irpinio
88	San Fernando	Santa Felita Dam (Outlet)	297	Irpinia, Italy-02	Bisaccia
95	Managua, Nicaragua-01	Managua, ESSO	300	Irpinia, Italy-02	Calltri
125	Friuli, Italy-01	Tolmezzo	302	Irpinia, Italy-02	Rionero In Vulture
126	Gazli, USSR	Karakyr	303	Irpinia, Italy-02	Sturno (STN)
138	Tabas, Iran	Boshrooyeh	322	Coalinga-01	Cantua Creek School
139	Tabas, Iran	Dayhook	336	Coalinga-01	Parkfield - Fault Zone 11
143	Tabas, Iran	Tabas	337	Coalinga-01	Parkfield - Fault Zone 12
158	Imperial Valley-06	Aeropuerto Mexicali	338	Coalinga-01	Parkfield - Fault Zone 14
159	Imperial Valley-06	Agrarias	339	Coalinga-01	Parkfield - Fault Zone 15
160	Imperial Valley-06	Bonds Corner	340	Coalinga-01	Parkfield - Fault Zone 16
161	Imperial Valley-06	Brawley Airport	346	Coalinga-01	Parkfield - Fault Zone 8
162	Imperial Valley-06	Calexico Fire Station	359	Coalinga-01	Parkfield - Vineyard Cany 1E
163	Imperial Valley-06	Calipatria Fire Station	360	Coalinga-01	Parkfield - Vineyard Cany 1W
164	Imperial Valley-06	Cerro Prieto	368	Coalinga-01	Pleasant Valley P.P. - yard
165	Imperial Valley-06	Chihuahua	369	Coalinga-01	Slack Canyon
167	Imperial Valley-06	Compuertas	447	Morgan Hill	Agnews State Hospital
169	Imperial Valley-06	Delta	448	Morgan Hill	Anderson Dam (Downstream)
170	Imperial Valley-06	EC County Center FF	450	Morgan Hill	Corralitos
171	Imperial Valley-06	El Centro - Meloland Geot. Array	451	Morgan Hill	Coyote Lake Dam (SW Abut)
172	Imperial Valley-06	El Centro Array #1	454	Morgan Hill	Gilroy - Gavilan Coll.
173	Imperial Valley-06	El Centro Array #10	455	Morgan Hill	Gilroy Array #1
174	Imperial Valley-06	El Centro Array #11	456	Morgan Hill	Gilroy Array #2
175	Imperial Valley-06	El Centro Array #12	457	Morgan Hill	Gilroy Array #3
176	Imperial Valley-06	El Centro Array #13	458	Morgan Hill	Gilroy Array #4
178	Imperial Valley-06	El Centro Array #3	459	Morgan Hill	Gilroy Array #6
179	Imperial Valley-06	El Centro Array #4	460	Morgan Hill	Gilroy Array #7
180	Imperial Valley-06	El Centro Array #5	461	Morgan Hill	Halls Valley
181	Imperial Valley-06	El Centro Array #6	463	Morgan Hill	Hollister Diff Array #1
182	Imperial Valley-06	El Centro Array #7	470	Morgan Hill	San Juan Bautista, 24 Polk St
183	Imperial Valley-06	El Centro Array #8	495	Nahanni, Canada	Site 1
184	Imperial Valley-06	El Centro Differential Array	496	Nahanni, Canada	Site 2
185	Imperial Valley-06	Holtville Post Office	497	Nahanni, Canada	Site 3
187	Imperial Valley-06	Parachute Test Site	514	N. Palm Springs	Cabazon
190	Imperial Valley-06	Superstition Mtn Camera	516	N. Palm Springs	Cranston Forest Station
192	Imperial Valley-06	Westmorland Fire Sta	517	N. Palm Springs	Desert Hot Springs
230	Mammoth Lakes-01	Convict Creek	518	N. Palm Springs	Fun Valley
231	Mammoth Lakes-01	Long Valley Dam (Upr L Abut)	521	N. Palm Springs	Hurkey Creek Park
232	Mammoth Lakes-01	Mammoth Lakes H. S.	524	N. Palm Springs	Joshua Tree

APPENDIX A-1: List of NGA records used (continued).

NGA #	Earthquake Name	Station Name	NGA #	Earthquake Name	Station Name
527	N. Palm Springs	Morongo Valley Fire Station	810	Loma Prieta	UCSC Lick Observatory
529	N. Palm Springs	North Palm Springs Post Office	811	Loma Prieta	WAHO
530	N. Palm Springs	Palm Springs Airport	821	Erzican, Turkey	Erzincan
534	N. Palm Springs	San Jacinto - Soboba	825	Cape Mendocino	Cape Mendocino
537	N. Palm Springs	Silent Valley - Poppet Flat	827	Cape Mendocino	Fortuna - Fortuna Blvd
540	N. Palm Springs	Whitewater Trout Farm	828	Cape Mendocino	Petrolia
548	Chalfant Valley-02	Benton	850	Landers	Desert Hot Springs
549	Chalfant Valley-02	Bishop - LADWP South St	864	Landers	Joshua Tree
550	Chalfant Valley-02	Bishop - Paradise Lodge	879	Landers	Lucerne
552	Chalfant Valley-02	Lake Crowley - Shehorn Res.	880	Landers	Mission Creek Fault
553	Chalfant Valley-02	Long Valley Dam (Downst)	881	Landers	Morongo Valley Fire Station
554	Chalfant Valley-02	Long Valley Dam (L Abut)	882	Landers	North Palm Springs Post Office
558	Chalfant Valley-02	Zack Brothers Ranch	900	Landers	Yermo Fire Station
587	New Zealand-02	Matahina Dam	901	Big Bear-01	Big Bear Lake - Civic Center
718	Superstition Hills-01	Wildlife Liquef. Array	949	Northridge-01	Arleta - Nordhoff Fire Sta
719	Superstition Hills-02	Brawley Airport	952	Northridge-01	Beverly Hills - 12520 Mulhol
720	Superstition Hills-02	Calipatria Fire Station	953	Northridge-01	Beverly Hills - 14145 Mulhol
721	Superstition Hills-02	El Centro Imp. Co. Cent	954	Northridge-01	Big Tujunga, Angeles Nat F
722	Superstition Hills-02	Kornbloom Road (temp)	957	Northridge-01	Burbank - Howard Rd.
723	Superstition Hills-02	Parachute Test Site	959	Northridge-01	Canoga Park - Topanga Can
724	Superstition Hills-02	Plaster City	960	Northridge-01	Canyon Country - W Lost Cany
725	Superstition Hills-02	Poe Road (temp)	963	Northridge-01	Castaic - Old Ridge Route
726	Superstition Hills-02	Salton Sea Wildlife Refuge	974	Northridge-01	Glendale - Las Palmas
727	Superstition Hills-02	Superstition Mtn Camera	978	Northridge-01	Hollywood - Willoughby Ave
728	Superstition Hills-02	Westmorland Fire Sta	983	Northridge-01	Jensen Filter Plant Generator
729	Superstition Hills-02	Wildlife Liquef. Array	985	Northridge-01	LA - Baldwin Hills
730	Spitak, Armenia	Gukasian	986	Northridge-01	LA - Brentwood VA Hospital
737	Loma Prieta	Agnews State Hospital	987	Northridge-01	LA - Centinela St
739	Loma Prieta	Anderson Dam (Downstream)	988	Northridge-01	LA - Century City CC North
740	Loma Prieta	Anderson Dam (L Abut)	989	Northridge-01	LA - Chalon Rd
741	Loma Prieta	BRAN	993	Northridge-01	LA - Fletcher Dr
752	Loma Prieta	Capitola	995	Northridge-01	LA - Hollywood Stor FF
753	Loma Prieta	Corralitos	996	Northridge-01	LA - N Faring Rd
754	Loma Prieta	Coyote Lake Dam (Downst)	998	Northridge-01	LA - N Westmoreland
755	Loma Prieta	Coyote Lake Dam (SW Abut)	1003	Northridge-01	LA - Saturn St
763	Loma Prieta	Gilroy - Gavilan Coll.	1004	Northridge-01	LA - Sepulveda VA Hospital
764	Loma Prieta	Gilroy - Historic Bldg.	1006	Northridge-01	LA - UCLA Grounds
765	Loma Prieta	Gilroy Array #1	1008	Northridge-01	LA - W 15th St
766	Loma Prieta	Gilroy Array #2	1011	Northridge-01	LA - Wonderland Ave
767	Loma Prieta	Gilroy Array #3	1012	Northridge-01	LA 00
768	Loma Prieta	Gilroy Array #4	1013	Northridge-01	LA Dam
769	Loma Prieta	Gilroy Array #6	1016	Northridge-01	La Crescenta - New York
770	Loma Prieta	Gilroy Array #7	1020	Northridge-01	Lake Hughes #12A
776	Loma Prieta	Hollister - South & Pine	1023	Northridge-01	Lake Hughes #9
779	Loma Prieta	LGPC	1039	Northridge-01	Moorpark - Fire Sta
801	Loma Prieta	San Jose - Santa Teresa Hills	1042	Northridge-01	N Hollywood - Coldwater Can
802	Loma Prieta	Saratoga - Aloha Ave	1044	Northridge-01	Newhall - Fire Sta
803	Loma Prieta	Saratoga - W Valley Coll.	1045	Northridge-01	Newhall - W Pico Canyon Rd.
806	Loma Prieta	Sunnyvale - Colton Ave.	1048	Northridge-01	Northridge - 17645 Satcoy St
809	Loma Prieta	UCSC	1049	Northridge-01	Pacific Palisades - Sunset

APPENDIX A-1: List of NGA records used (continued).

NGA #	Earthquake Name	Station Name	NGA #	Earthquake Name	Station Name
1050	Northridge-01	Pacoima Dam (downstr)	1231	Chi-Chi, Taiwan	CHY080
1051	Northridge-01	Pacoima Dam (upper left)	1234	Chi-Chi, Taiwan	CHY086
1052	Northridge-01	Pacoima Kagel Canyon	1235	Chi-Chi, Taiwan	CHY087
1063	Northridge-01	Rinaldi Receiving Sta	1238	Chi-Chi, Taiwan	CHY092
1077	Northridge-01	Santa Monica City Hall	1244	Chi-Chi, Taiwan	CHY101
1078	Northridge-01	Santa Susana Ground	1246	Chi-Chi, Taiwan	CHY104
1080	Northridge-01	Simi Valley - Katherine Rd	1476	Chi-Chi, Taiwan	TCU029
1082	Northridge-01	Sun Valley - Roscoe Blvd	1480	Chi-Chi, Taiwan	TCU036
1083	Northridge-01	Sunland - Mt Gleason Ave	1481	Chi-Chi, Taiwan	TCU038
1084	Northridge-01	Sylmar - Converter Sta	1482	Chi-Chi, Taiwan	TCU039
1085	Northridge-01	Sylmar - Converter Sta East	1483	Chi-Chi, Taiwan	TCU040
1086	Northridge-01	Sylmar - Olive View Med FF	1484	Chi-Chi, Taiwan	TCU042
1087	Northridge-01	Tarzana - Cedar Hill A	1485	Chi-Chi, Taiwan	TCU045
1089	Northridge-01	Topanga - Fire Sta	1486	Chi-Chi, Taiwan	TCU046
1091	Northridge-01	Vasquez Rocks Park	1488	Chi-Chi, Taiwan	TCU048
1100	Kobe, Japan	Abeno	1489	Chi-Chi, Taiwan	TCU049
1101	Kobe, Japan	Amagasaki	1490	Chi-Chi, Taiwan	TCU050
1104	Kobe, Japan	Fukushima	1491	Chi-Chi, Taiwan	TCU051
1106	Kobe, Japan	KJMA	1492	Chi-Chi, Taiwan	TCU052
1107	Kobe, Japan	Kakogawa	1493	Chi-Chi, Taiwan	TCU053
1108	Kobe, Japan	Kobe University	1494	Chi-Chi, Taiwan	TCU054
1110	Kobe, Japan	Morigawachi	1495	Chi-Chi, Taiwan	TCU055
1111	Kobe, Japan	Nishi-Akashi	1496	Chi-Chi, Taiwan	TCU056
1113	Kobe, Japan	OSAJ	1497	Chi-Chi, Taiwan	TCU057
1115	Kobe, Japan	Sakai	1498	Chi-Chi, Taiwan	TCU059
1116	Kobe, Japan	Shin-Osaka	1499	Chi-Chi, Taiwan	TCU060
1119	Kobe, Japan	Takarazuka	1500	Chi-Chi, Taiwan	TCU061
1120	Kobe, Japan	Takatori	1501	Chi-Chi, Taiwan	TCU063
1121	Kobe, Japan	Yae	1502	Chi-Chi, Taiwan	TCU064
1141	Dinar, Turkey	Dinar	1503	Chi-Chi, Taiwan	TCU065
1148	Kocaeli, Turkey	Arcelik	1504	Chi-Chi, Taiwan	TCU067
1158	Kocaeli, Turkey	Duzce	1505	Chi-Chi, Taiwan	TCU068
1165	Kocaeli, Turkey	Izmit	1506	Chi-Chi, Taiwan	TCU070
1176	Kocaeli, Turkey	Yarimca	1507	Chi-Chi, Taiwan	TCU071
1180	Chi-Chi, Taiwan	CHY002	1508	Chi-Chi, Taiwan	TCU072
1182	Chi-Chi, Taiwan	CHY006	1509	Chi-Chi, Taiwan	TCU074
1184	Chi-Chi, Taiwan	CHY010	1510	Chi-Chi, Taiwan	TCU075
1193	Chi-Chi, Taiwan	CHY024	1511	Chi-Chi, Taiwan	TCU076
1194	Chi-Chi, Taiwan	CHY025	1512	Chi-Chi, Taiwan	TCU078
1195	Chi-Chi, Taiwan	CHY026	1513	Chi-Chi, Taiwan	TCU079
1197	Chi-Chi, Taiwan	CHY028	1515	Chi-Chi, Taiwan	TCU082
1198	Chi-Chi, Taiwan	CHY029	1517	Chi-Chi, Taiwan	TCU084
1201	Chi-Chi, Taiwan	CHY034	1519	Chi-Chi, Taiwan	TCU087
1202	Chi-Chi, Taiwan	CHY035	1520	Chi-Chi, Taiwan	TCU088
1203	Chi-Chi, Taiwan	CHY036	1521	Chi-Chi, Taiwan	TCU089
1205	Chi-Chi, Taiwan	CHY041	1527	Chi-Chi, Taiwan	TCU100
1206	Chi-Chi, Taiwan	CHY042	1528	Chi-Chi, Taiwan	TCU101
1208	Chi-Chi, Taiwan	CHY046	1529	Chi-Chi, Taiwan	TCU102
1209	Chi-Chi, Taiwan	CHY047	1530	Chi-Chi, Taiwan	TCU103
1227	Chi-Chi, Taiwan	CHY074	1531	Chi-Chi, Taiwan	TCU104

APPENDIX A-1: List of NGA records used (continued).

NGA #	Earthquake Name	Station Name	NGA #	Earthquake Name	Station Name
1532	Chi-Chi, Taiwan	TCU105	2650	Chi-Chi, Taiwan-03	TCU116
1533	Chi-Chi, Taiwan	TCU106	2654	Chi-Chi, Taiwan-03	TCU120
1534	Chi-Chi, Taiwan	TCU107	2655	Chi-Chi, Taiwan-03	TCU122
1535	Chi-Chi, Taiwan	TCU109	2658	Chi-Chi, Taiwan-03	TCU129
1536	Chi-Chi, Taiwan	TCU110	2661	Chi-Chi, Taiwan-03	TCU138
1537	Chi-Chi, Taiwan	TCU111	2699	Chi-Chi, Taiwan-04	CHY024
1538	Chi-Chi, Taiwan	TCU112	2700	Chi-Chi, Taiwan-04	CHY025
1540	Chi-Chi, Taiwan	TCU115	2703	Chi-Chi, Taiwan-04	CHY028
1541	Chi-Chi, Taiwan	TCU116	2704	Chi-Chi, Taiwan-04	CHY029
1542	Chi-Chi, Taiwan	TCU117	2708	Chi-Chi, Taiwan-04	CHY034
1543	Chi-Chi, Taiwan	TCU118	2709	Chi-Chi, Taiwan-04	CHY035
1545	Chi-Chi, Taiwan	TCU120	2734	Chi-Chi, Taiwan-04	CHY074
1546	Chi-Chi, Taiwan	TCU122	2739	Chi-Chi, Taiwan-04	CHY080
1547	Chi-Chi, Taiwan	TCU123	2752	Chi-Chi, Taiwan-04	CHY101
1548	Chi-Chi, Taiwan	TCU128	2871	Chi-Chi, Taiwan-04	TCU084
1549	Chi-Chi, Taiwan	TCU129	2873	Chi-Chi, Taiwan-04	TCU089
1550	Chi-Chi, Taiwan	TCU136	2888	Chi-Chi, Taiwan-04	TCU116
1551	Chi-Chi, Taiwan	TCU138	2893	Chi-Chi, Taiwan-04	TCU122
1553	Chi-Chi, Taiwan	TCU141	3300	Chi-Chi, Taiwan-06	CHY074
1602	Duzce, Turkey	Bolu	3467	Chi-Chi, Taiwan-06	TCU065
1605	Duzce, Turkey	Duzce	3468	Chi-Chi, Taiwan-06	TCU067
1611	Duzce, Turkey	Lamont 1058	3470	Chi-Chi, Taiwan-06	TCU072
1612	Duzce, Turkey	Lamont 1059	3471	Chi-Chi, Taiwan-06	TCU075
1613	Duzce, Turkey	Lamont 1060	3472	Chi-Chi, Taiwan-06	TCU076
1614	Duzce, Turkey	Lamont 1061	3473	Chi-Chi, Taiwan-06	TCU078
1615	Duzce, Turkey	Lamont 1062	3474	Chi-Chi, Taiwan-06	TCU079
1616	Duzce, Turkey	Lamont 362	3475	Chi-Chi, Taiwan-06	TCU080
1617	Duzce, Turkey	Lamont 375	3505	Chi-Chi, Taiwan-06	TCU125
1618	Duzce, Turkey	Lamont 531	3507	Chi-Chi, Taiwan-06	TCU129
1752	Northwest China-03	Jiashi	3548	Loma Prieta	Los Gatos - Lexington Dam
1787	Hector Mine	Hector	3744	Cape Mendocino	Bunker Hill FAA
2114	Denali, Alaska	TAPS Pump Station #10	3746	Cape Mendocino	Centerville Beach, Naval Fac
2457	Chi-Chi, Taiwan-03	CHY024	3748	Cape Mendocino	Ferndale Fire Station
2458	Chi-Chi, Taiwan-03	CHY025	3749	Cape Mendocino	Fortuna Fire Station
2461	Chi-Chi, Taiwan-03	CHY028	3750	Cape Mendocino	Loleta Fire Station
2490	Chi-Chi, Taiwan-03	CHY074	3753	Landers	Fun Valley
2495	Chi-Chi, Taiwan-03	CHY080	3757	Landers	North Palm Springs Fire Sta #36
2507	Chi-Chi, Taiwan-03	CHY101	3759	Landers	Whitewater Trout Farm
2618	Chi-Chi, Taiwan-03	TCU065	3852	Chi-Chi (aftershock 3), Taiwan	CHY006
2619	Chi-Chi, Taiwan-03	TCU067	3907	Tottori, Japan	OKY004
2622	Chi-Chi, Taiwan-03	TCU071	3908	Tottori, Japan	OKY005
2623	Chi-Chi, Taiwan-03	TCU072	3925	Tottori, Japan	OKYH07
2624	Chi-Chi, Taiwan-03	TCU073	3926	Tottori, Japan	OKYH08
2625	Chi-Chi, Taiwan-03	TCU074	3927	Tottori, Japan	OKYH09
2626	Chi-Chi, Taiwan-03	TCU075	3932	Tottori, Japan	OKYH14
2627	Chi-Chi, Taiwan-03	TCU076	3933	Tottori, Japan	SMN001
2628	Chi-Chi, Taiwan-03	TCU078	3934	Tottori, Japan	SMN002
2629	Chi-Chi, Taiwan-03	TCU079	3935	Tottori, Japan	SMN003
2632	Chi-Chi, Taiwan-03	TCU084	3943	Tottori, Japan	SMN015
2635	Chi-Chi, Taiwan-03	TCU089	3947	Tottori, Japan	SMNH01

APPENDIX A-1: List of NGA records used (continued).

NGA #	Earthquake Name	Station Name	NGA #	Earthquake Name	Station Name
3948	Tottori, Japan	SMNH02	4121	Parkfield-02, CA	Parkfield - Gold Hill 3E
3954	Tottori, Japan	SMNH10	4122	Parkfield-02, CA	Parkfield - Gold Hill 3W
3964	Tottori, Japan	TTR007	4123	Parkfield-02, CA	Parkfield - Gold Hill 4W
3965	Tottori, Japan	TTR008	4124	Parkfield-02, CA	Parkfield - Gold Hill 5W
3966	Tottori, Japan	TTR009	4125	Parkfield-02, CA	Parkfield - Gold Hill 6W
3968	Tottori, Japan	TTRH02	4126	Parkfield-02, CA	PARKFIELD - STONE CORRAL 1E
3979	San Simeon, CA	Cambria - Hwy 1 Caltrans Bridge	4127	Parkfield-02, CA	Parkfield - Stone Corral 2E
4013	San Simeon, CA	San Antonio Dam - Toe	4128	Parkfield-02, CA	Parkfield - Stone Corral 3E
4031	San Simeon, CA	Templeton - 1-story Hospital	4129	Parkfield-02, CA	PARKFIELD - TEBLOR
4040	Bam, Iran	Bam	4130	Parkfield-02, CA	Parkfield - Vineyard Cany 1E
4064	Parkfield-02, CA	PARKFIELD - DONNA LEE	4131	Parkfield-02, CA	Parkfield - Vineyard Cany 1W
4065	Parkfield-02, CA	PARKFIELD - EADES	4132	Parkfield-02, CA	Parkfield - Vineyard Cany 2E
4066	Parkfield-02, CA	PARKFIELD - FROELICH	4133	Parkfield-02, CA	Parkfield - Vineyard Cany 2W
4067	Parkfield-02, CA	PARKFIELD - GOLD HILL	4134	Parkfield-02, CA	Parkfield - Vineyard Cany 3W
4068	Parkfield-02, CA	PARKFIELD - HOG CANYON	4135	Parkfield-02, CA	Parkfield - Vineyard Cany 4W
4069	Parkfield-02, CA	PARKFIELD - JACK CANYON	4136	Parkfield-02, CA	Parkfield - Vineyard Cany 5W
4070	Parkfield-02, CA	PARKFIELD - JOAQUIN CANYON	4137	Parkfield-02, CA	Parkfield - Vineyard Cany 6W
4071	Parkfield-02, CA	PARKFIELD - MIDDLE MOUNTAIN	4138	Parkfield-02, CA	PARKFIELD - UPSAR 01
4072	Parkfield-02, CA	PARKFIELD - RED HILLS	4139	Parkfield-02, CA	PARKFIELD - UPSAR 02
4073	Parkfield-02, CA	PARKFIELD - STOCKDALE MTN	4140	Parkfield-02, CA	PARKFIELD - UPSAR 03
4074	Parkfield-02, CA	PARKFIELD - VINEYARD CANYON	4141	Parkfield-02, CA	PARKFIELD - UPSAR 05
4078	Parkfield-02, CA	Coalinga- Fire Station 39	4142	Parkfield-02, CA	PARKFIELD - UPSAR 06
4081	Parkfield-02, CA	Parkfield - Cholame 5W	4143	Parkfield-02, CA	PARKFIELD - UPSAR 07
4083	Parkfield-02, CA	PARKFIELD - TURKEY FLAT #1 (0M)	4144	Parkfield-02, CA	PARKFIELD - UPSAR 08
4084	Parkfield-02, CA	PARKFIELD - 1-STORY SCHOOL BLDG	4145	Parkfield-02, CA	PARKFIELD - UPSAR 09
4085	Parkfield-02, CA	Shandon-1-story High School Bldg	4146	Parkfield-02, CA	PARKFIELD - UPSAR 10
4096	Parkfield-02, CA	BEAR VALLEY RANCH	4147	Parkfield-02, CA	PARKFIELD - UPSAR 11
4097	Parkfield-02, CA	Slack Canyon	4148	Parkfield-02, CA	PARKFIELD - UPSAR 12
4098	Parkfield-02, CA	Parkfield - Cholame 1E	4149	Parkfield-02, CA	PARKFIELD - UPSAR 13
4099	Parkfield-02, CA	Parkfield - Cholame 2E	4150	Parkfield-02, CA	COALINGA - PRIEST VALLEY
4100	Parkfield-02, CA	Parkfield - Cholame 2WA	4204	Niiigata, Japan	NIG014
4101	Parkfield-02, CA	Parkfield - Cholame 3E	4207	Niiigata, Japan	NIG017
4102	Parkfield-02, CA	Parkfield - Cholame 3W	4208	Niiigata, Japan	NIG018
4103	Parkfield-02, CA	Parkfield - Cholame 4W	4209	Niiigata, Japan	NIG019
4104	Parkfield-02, CA	Parkfield - Cholame 4AW	4210	Niiigata, Japan	NIG020
4105	Parkfield-02, CA	Parkfield - Cholame 6W	4211	Niiigata, Japan	NIG021
4106	Parkfield-02, CA	Parkfield - Cholame 12W	4212	Niiigata, Japan	NIG022
4107	Parkfield-02, CA	Parkfield - Fault Zone 1	4213	Niiigata, Japan	NIG023
4108	Parkfield-02, CA	Parkfield - Fault Zone 3	4218	Niiigata, Japan	NIG028
4109	Parkfield-02, CA	Parkfield - Fault Zone 4	4219	Niiigata, Japan	NIGH01
4110	Parkfield-02, CA	Parkfield - Fault Zone 6	4226	Niiigata, Japan	NIGH09
4111	Parkfield-02, CA	Parkfield - Fault Zone 7	4228	Niiigata, Japan	NIGH11
4112	Parkfield-02, CA	Parkfield - Fault Zone 8	4229	Niiigata, Japan	NIGH12
4113	Parkfield-02, CA	Parkfield - Fault Zone 9	4231	Niiigata, Japan	NIGH15
4114	Parkfield-02, CA	Parkfield - Fault Zone 11	4284	Basso Tirreno, Italy	NASO
4115	Parkfield-02, CA	Parkfield - Fault Zone 12	4285	Basso Tirreno, Italy	PATTI - CABINA PRIMARIA
4116	Parkfield-02, CA	Parkfield - Stone Corral 4E	4345	Umbria Marche, Italy	Assisi-Stallone
4117	Parkfield-02, CA	Parkfield - Fault Zone 15	4346	Umbria Marche, Italy	BEVAGNA
4118	Parkfield-02, CA	Parkfield - Gold Hill 1W	4347	Umbria Marche, Italy	BORGO CERRETO - TORRE
4120	Parkfield-02, CA	Parkfield - Gold Hill 2W	4348	Umbria Marche, Italy	CASTELNUOVO (ASSISI)

APPENDIX A-1: List of NGA records used (continued).

NGA #	Earthquake Name	Station Name	NGA #	Earthquake Name	Station Name
4349	Umbria Marche, Italy	COLFIORITO	4880	Chuetsu-oki	Hinodecho Yoshida Tsubame City
4351	Umbria Marche, Italy	MATELICA	4881	Chuetsu-oki	Nagaoka Kouiti Town
4352	Umbria Marche, Italy	NOCERA UMBRA	4882	Chuetsu-oki	Ojiya City
4451	Montenegro, Yugo.	Bar-Skupstina Opstine	4883	Chuetsu-oki	Niigata Nishi Kaba District
4455	Montenegro, Yugo.	Herceg Novi - O.S.D. Paviviv	4886	Chuetsu-oki	Tamati Yone Izumozaki
4456	Montenegro, Yugo.	Petrovac - Hotel Olivia	4894	Chuetsu-oki	UNIT 1: GROUND SURFACE
4457	Montenegro, Yugo.	Ulcinj - Hotel Albatros	4895	Chuetsu-oki	UNIT 5: GROUND SURFACE
4458	Montenegro, Yugo.	Ulcinj - Hotel Olimpic	4896	Chuetsu-oki	SERVICE HALL: 2.4 M DEPTH
4460	L'Aquila, Italy	Antrodoco	5259	Chuetsu-oki	NIG013
4462	L'Aquila, Italy	Avezzano	5260	Chuetsu-oki	NIG014
4472	L'Aquila, Italy	Celano	5262	Chuetsu-oki	NIG016
4475	L'Aquila, Italy	Fiamignano	5263	Chuetsu-oki	NIG017
4477	L'Aquila, Italy	GRAN SASSO (Assergi)	5264	Chuetsu-oki	NIG018
4478	L'Aquila, Italy	GRAN SASSO (Lab. INFN galleria)	5265	Chuetsu-oki	NIG019
4480	L'Aquila, Italy	L'Aquila - V. Aterno - Centro Valle	5267	Chuetsu-oki	NIG021
4481	L'Aquila, Italy	L'Aquila - V. Aterno -Colle Grilli	5270	Chuetsu-oki	NIG024
4482	L'Aquila, Italy	L'Aquila - V. Aterno -F. Aterno	5271	Chuetsu-oki	NIG025
4483	L'Aquila, Italy	L'Aquila - Parking	5274	Chuetsu-oki	NIG028
4489	L'Aquila, Italy	Montereale	5275	Chuetsu-oki	NIGH01
4840	Chuetsu-oki	Joetsu Kita	5284	Chuetsu-oki	NIGH11
4841	Chuetsu-oki	Joetsu Yasuzukaku Yasuzuka	5474	Iwate	AKT019
4842	Chuetsu-oki	Joetsu Uragawaraku Kamabucchi	5478	Iwate	AKT023
4843	Chuetsu-oki	Matsushiro Tokamachi	5482	Iwate	AKTH04
4844	Chuetsu-oki	Tokamachi Matsunoyama	5484	Iwate	AKTH06
4845	Chuetsu-oki	Joetsu Oshimaku Oka	5618	Iwate	IWT010
4847	Chuetsu-oki	Joetsu Kakizakiku Kakizaki	5619	Iwate	IWT011
4848	Chuetsu-oki	Joetsu Ogataku	5620	Iwate	IWT012
4849	Chuetsu-oki	Kubikiku Hyakken Joetsu City	5623	Iwate	IWT015
4850	Chuetsu-oki	Yoshikawaku Joetsu City	5636	Iwate	IWTH04
4853	Chuetsu-oki	Joetsu City	5652	Iwate	IWTH20
4855	Chuetsu-oki	Sanjo	5654	Iwate	IWTH22
4856	Chuetsu-oki	Kashiwazaki City Center	5656	Iwate	IWTH24
4859	Chuetsu-oki	Mitsuke Kazuiti Arita Town	5657	Iwate	IWTH25
4860	Chuetsu-oki	Sanjo Shinbori	5658	Iwate	IWTH26
4861	Chuetsu-oki	Nakanoshima Nagaoka	5663	Iwate	MYG004
4862	Chuetsu-oki	Shiura Nagaoka	5664	Iwate	MYG005
4863	Chuetsu-oki	Nagaoka	5678	Iwate	MYGH02
4864	Chuetsu-oki	Yoitamachi Yoita Nagaoka	5774	Iwate	Nakashinden Town
4865	Chuetsu-oki	Tani Kozima Nagaoka	5775	Iwate	Tamati Ono
4866	Chuetsu-oki	Kawanishi Izumozaki	5776	Iwate	Kami, Miyagi Miyazaki City
4867	Chuetsu-oki	Teradomari Uedamachi Nagaoka	5780	Iwate	Iwadeyama
4868	Chuetsu-oki	Yamakoshi Takezawa Nagaoka	5783	Iwate	Semine Kurihara City
4869	Chuetsu-oki	Kawaguchi	5800	Iwate	Yokote Masuda Tamati Masu
4872	Chuetsu-oki	Sawa Mizuguti Tokamachi	5804	Iwate	Yamauchi Tsuchibuchi Yokote
4873	Chuetsu-oki	Kashiwazaki City Takayanagicho	5806	Iwate	Yuzawa Town
4874	Chuetsu-oki	Oguni Nagaoka	5807	Iwate	Yuzama Yokobori
4875	Chuetsu-oki	Kariwa	5809	Iwate	Minasa Yuzawa
4876	Chuetsu-oki	Kashiwazaki Nishiyamacho Ikeura	5810	Iwate	Machimukai Town
4878	Chuetsu-oki	Yahiko Village Yahagi	5812	Iwate	Kitakami Yanagiharach
4879	Chuetsu-oki	Yan Sakuramachi City watershed	5813	Iwate	Mizusawaku Interior O ganecho

APPENDIX A-1: List of NGA records used (continued).

NGA #	Earthquake Name	Station Name	NGA #	Earthquake Name	Station Name
5815	Iwate	Yuzawa	6928	Darfield, New Zealand	LPCC
5818	Iwate	Kurihara City	6930	Darfield, New Zealand	LRSC
5819	Iwate	Ichinoseki Maikawa	6942	Darfield, New Zealand	NNBS
5823	El Mayor-Cucapah	CHIHUAHUA	6952	Darfield, New Zealand	PPHS
5825	El Mayor-Cucapah	CERRO PRIETO GEOTHERMAL	6953	Darfield, New Zealand	PRPC
5827	El Mayor-Cucapah	MICHOACAN DE OCAMPO	6959	Darfield, New Zealand	REHS
5829	El Mayor-Cucapah	RIITO	6960	Darfield, New Zealand	RHSC
5831	El Mayor-Cucapah	EJIDO SALTILLO	6961	Darfield, New Zealand	RKAC
5832	El Mayor-Cucapah	TAMAULIPAS	6962	Darfield, New Zealand	ROLC
5836	El Mayor-Cucapah	El Centro - Meloland Geot. Array	6965	Darfield, New Zealand	SBRC
5837	El Mayor-Cucapah	El Centro - Imperial & Ross	6966	Darfield, New Zealand	SHLC
5838	El Mayor-Cucapah	El Centro - Meloland Geotechnic	6969	Darfield, New Zealand	SMTC
5975	El Mayor-Cucapah	Calexico Fire Station	6971	Darfield, New Zealand	SPFS
5985	El Mayor-Cucapah	El Centro Differential Array	6975	Darfield, New Zealand	TPLC
5990	El Mayor-Cucapah	El Centro Array #7	6988	Darfield, New Zealand	WSFC
5991	El Mayor-Cucapah	El Centro Array #10	8062	Christchurch, New Zealand	CACS
5992	El Mayor-Cucapah	El Centro Array #11	8063	Christchurch, New Zealand	CBGS
6013	El Mayor-Cucapah	El Centro - Meadows Union School	8064	Christchurch, New Zealand	CCCC
6057	Big Bear-01	Highland Fire Station	8066	Christchurch, New Zealand	CHHC
6059	Big Bear-01	Morongo Valley	8067	Christchurch, New Zealand	CMHS
6874	Joshua Tree, CA	Thousand Palms Post Office	8090	Christchurch, New Zealand	HPSC
6875	Joshua Tree, CA	Morongo Valley Fire Station	8099	Christchurch, New Zealand	KPOC
6876	Joshua Tree, CA	Whitewater Trout Farm	8102	Christchurch, New Zealand	LINC
6877	Joshua Tree, CA	Indio - Jackson Road	8110	Christchurch, New Zealand	MQZ
6878	Joshua Tree, CA	North Palm Springs Fire Sta #36	8118	Christchurch, New Zealand	PPHS
6886	Darfield, New Zealand	CACS	8119	Christchurch, New Zealand	PRPC
6887	Darfield, New Zealand	CBGS	8123	Christchurch, New Zealand	REHS
6888	Darfield, New Zealand	CCCC	8124	Christchurch, New Zealand	RHSC
6889	Darfield, New Zealand	CHHC	8126	Christchurch, New Zealand	ROLC
6890	Darfield, New Zealand	CMHS	8130	Christchurch, New Zealand	SHLC
6893	Darfield, New Zealand	DFHS	8134	Christchurch, New Zealand	SMTC
6897	Darfield, New Zealand	DSLCL	8136	Christchurch, New Zealand	SWNC
6906	Darfield, New Zealand	GDLC	8142	Christchurch, New Zealand	TPLC
6911	Darfield, New Zealand	HORC	8157	Christchurch, New Zealand	HVSC
6912	Darfield, New Zealand	HPSC	8158	Christchurch, New Zealand	LPCC
6915	Darfield, New Zealand	HVSC	8161	El Mayor-Cucapah	El Centro Array #12
6927	Darfield, New Zealand	LINC			

APPENDIX A-2
MATLAB ALGORITHM

```

%% Pulse_classification_simple
%A simplified version of the MATLAB script used in Hayden et al. 2014
%containing only the essential components to obtain pulse score and period
%for a single ground motion. See accompanying document for
%directions and an example.

%% USER Input
Time_history_path_h1='H-BRA225.AT2';%Filename or path for horizontal acceleration time
series component 1
Time_history_path_h2='H-BRA315.AT2';%Filename or path for horizontal acceleration time
series component 2

H1_azimuth=225;%Azimuth of horizontal acceleration time series component 1
H2_azimuth=315;%Azimuth of horizontal acceleration time series component 2
Lowest_usable_frequency=0.088;%DY Lowest usable frequency from NGA Flatfile
Filter_override=-999;%Set to a negative number to do nothing, set to a positive number to
override the automated filtering system and instead filter at a corner period of 1/3 the
value inputted
Sa_median=[ 0.2486%This are the median spectral accelerations from the equally
0.2504%weighted (25%) NGA relationships of AS08, BA08, CB08, CY08
0.2603%(cells E14:E34 in provided Excel file) and correspond to
0.2851%the natural periods Tn_NGA in the below Parameter section.
0.3375
0.3975
0.4870
0.5245
0.5335
0.5266
0.4989
0.4608
0.3608
0.2913
0.2032
0.1508
0.0889
0.0596
0.0424
0.0187
0.0099];

Figs_flag=1;%1 to make simple example figures
%% Parameters
tic
dTn=0.05;% increment to calculate Sv at.
Tn=dTn:dTn:10;% for column headers in excel
Angle_shift_array=0:1:179;%Modify if you wish to change the rotation increment
Zeta=0.05;% damping for use in response spectra
Zeta_primary=1;% Index of zeta from array above to be recorded in output spreadsheet
Period_fraction=1/3;%Multiply period identified as pulse by this to find cutoff period
Tn_NGA=[0.010 0.020 0.030 0.050 0.075 0.10 0.15 0.20 0.25 0.30 0.40 0.50...
0.75 1.0 1.5 2.0 3.0 4.0 5.0 7.5 10.0];%natural periods from NGA spreadsheet

```

```

%% Loop through multiple ground motions by modifying the following line and User inputs
to be (zz x 1) vectors or (: x zz) matrix for Sa_median
for zz=1:length(H1_azimuth)
%% Read in two orthogonal acceleration time series, this assumes NGA WEST-2
%%Format...Modify as needed or delete and just read in Acc1, Acc2 and dt for your data
format.
[Fid message]=fopen(Time_history_path_h1,'r');
for mm=1:4%clumsy way of getting dt
    L=fgets(Fid);
end
dt=str2num(L(21:26));%Extracts time increment from header (why format must be consistent)
Fs=1/dt;
Acc1=textscan(Fid,'%f'); Acc1=Acc1{1};%Reads first acceleration component
Fid=fclose(Fid);
Fid=fopen(Time_history_path_h2,'r');
Acc2=textscan(Fid,'%f','headerlines',4); Acc2=Acc2{1};%reads second acceleration
component
Fid=fclose(Fid);
Acc1=Acc1(1:min([size(Acc1,1) size(Acc2,1)]));%To make records the same length in some
cases....
Acc2=Acc2(1:min([size(Acc1,1) size(Acc2,1)]));
Accuf=[Acc1 Acc2];

%% Find PGV of each horizontal component rotated through 180 degrees%%%%%%%%
Vel1=cumsum(Acc1)*981*dt;%Integrate to velocity.
Vel2=cumsum(Acc2)*981*dt;%Integrate to velocity.
Veluf=[Vel1 Vel2];%Velocities from unfiltered accelerations
IA=[H1_azimuth(zz) H2_azimuth(zz)];
PGV_array=zeros(length(Angle_shift_array),2);%Initialize
Azimuth_array=zeros(length(Angle_shift_array),2);%Initialize
for ii=1:length(Angle_shift_array)
    OA=IA+Angle_shift_array(ii)*[1 1];%Azimuth to rotate to
    Phi = pi*IA/180;
    Theta = pi*OA/180;
    Veluf_rot_max = Veluf*[cos(Phi(1)-Theta(1)) cos(Phi(2)-Theta(1)); cos(Phi(1)-Theta
(2)) cos(Phi(2)-Theta(2))];%Rotated velocity time series
    PGV_array(ii,:)=max(abs(Veluf_rot_max(:,1))) max(abs(Veluf_rot_max(:,2)))];%PGV of
each comp. in each orientation
    Azimuth_array(ii,:)=OA;%Azimuth array corresponding to Rot_max array
end

%% Two components in H1 H2 order rotated such that H1_PGV/H2_PGV is maximized and
clockwise rotation from H1 azimuth
Ratio_array=PGV_array(:,1)./PGV_array(:,2);%ratio of 1st component PGV over 2nd component
PGV
[~, Index_ratio_max]=max(Ratio_array);
PGV_ratio_max=PGV_array(Index_ratio_max,:);%Maximum ratio
Rot_ratio=Angle_shift_array(Index_ratio_max);%Rotation to Maximum ratio
Azimuth_ratio=Azimuth_array(Index_ratio_max,:);%Azimuth of 1st comp. maximum ratio

```

```

%% calculate maximum ratio of Sa component rotated to max PGV ratio vs. NGA median
Max_usable_period=dTn*round(1/Lowest_usable_frequency(zz)/dTn);%Find the maximum usable
period rounded to the nearest dTn (0.05)
if Max_usable_period>10%Only consider periods of up to 10 sec in this study.
    Max_usable_period=10;
end
Tn=[0.5:dTn:Max_usable_period];%makes vector of usable periods
OA=IA+Rot_ratio*[1 1];
Phi = pi*IA/180;
Theta = pi*OA/180;
Accuf_rot_max = Accuf*[cos(Phi(1)-Theta(1)) cos(Phi(2)-Theta(1)); cos(Phi(1)-Theta(2))
cos(Phi(2)-Theta(2))];%unfiltered acceleration time series rotated to maximum PGV ratio
Sv1=respspec_simple(Accuf_rot_max(:,1), dt, Tn,Zeta);%Calculates response spectrum
Sv_median=981*Sa_median(:,zz)'.*Tn_NGA/(2*pi);%Converts NGA Sa to Sv (cm/s)
Sv2=interp1(Tn_NGA,Sv_median,Tn);%uses interpolated NGA median
Sv12=Sv1./Sv2;%find ratio
[Sv12_max Sv12_max_index] =max(Sv12);
Tn_max=Tn(Sv12_max_index);%period associated with max ratio
Cutoff_frequency=1/Tn_max/Period_fraction;%assign cutoff frequency
if Filter_override(zz)>0%override the automated cutoff frequency calculations
    Cutoff_frequency=1/Filter_override(zz)/Period_fraction;
end

%% Filter and integrate acceleration time histories
[b,a]=butter(3,Cutoff_frequency/(Fs/2));
Acc1f=filter(b,a,Acc1);
Acc2f=filter(b,a,Acc2);
Accf=[Acc1f Acc2f];%Filtered accelerations for response spectrum
Vel1f=cumsum(Acc1f)*981*dt;%Integrate to velocity.
Vel2f=cumsum(Acc2f)*981*dt;%Integrate to velocity.
Velf=[Vel1f Vel2f];%Velocities from filtered accelerations

%% Rotate filtered velocity through 180 degrees and find PPV at each
PPV_array=zeros(size(Angle_shift_array));%Initialize
NCSV_array=zeros(size(Angle_shift_array));%Initialize
Numcyc_array=zeros(size(Angle_shift_array));%Initialize
Azimuth_array=zeros(length(Angle_shift_array),2);%Initialize
for ii=1:length(Angle_shift_array)
    OA=IA+Angle_shift_array(ii)*[1 1];
    phi = pi*IA/180;
    theta = pi*OA/180;
    Rot_velf= Velf*[cos(phi(1)-theta(1)) cos(phi(2)-theta(1)); cos(phi(1)-theta(2)) cos
(phi(2)-theta(2))];%Rotated filtered velocity time series
    [PPV,Numcyc,NCSV]=zerocross_simple(Rot_velf(:,1), dt);%Calculates PPV, number of
significant cycles and NCSV difference
    PPV_array(ii)=PPV;
    NCSV_array(ii)=NCSV;
    Numcyc_array(ii)=Numcyc;
    Azimuth_array(ii,:)=OA;
end

```

```

%% Calculate Pulse Score at all orientations
Pulse_score_all=Score_simple(NCSV_array, Numcyc_array);%Pulse score for all orientations
[dummy Index_ppv_max]=max(PPV_array);
Max_azimuth=Azimuth_array(Index_ppv_max);
Pulse_score=Pulse_score_all(Index_ppv_max);%This is the pulse score at the orientation
that maximizes the PPV

Max_rot_angle=Angle_shift_array(Index_ppv_max);%find angle of rotation that resulted in
maximum PPV using CH
OA=IA+Max_rot_angle*[1 1];
phi = pi*IA/180;
theta = pi*OA/180;
Rot_velf_max= Velf*[cos(phi(1)-theta(1)) cos(phi(2)-theta(1)); cos(phi(1)-theta(2)) cos
(phi(2)-theta(2))];%Just for plotting purposes if wanted
Rot_accf_max= Accf*[cos(phi(1)-theta(1)) cos(phi(2)-theta(1)); cos(phi(1)-theta(2)) cos
(phi(2)-theta(2))];%Filtered acceleration time series rotated to max PPV for use in
response spectrum

%% Pulse Period
Sv=respspec_simple(Rot_accf_max(:,1), dt, Tn,Zeta);%Response spectrum of filtered rotated
time series
Ratio_filtered=Sv./Sv2;%Ratio of actual Sv for this motion over the median NGA predicted
[Sv_ratio_max_p Tn_idx_p]=max(Ratio_filtered);
Pulse_period=Tn(Tn_idx_p);%This is the pulse period

%% Simple output
count = ['Done GM ', num2str(zz), ' of ', num2str(length(H1_azimuth))];
disp(count)
toc
disp(['Pulse Score: ' num2str(Pulse_score*100,3) ' %'])
disp(['Pulse Period: ' num2str(Pulse_period,3) ' sec'])
disp(['Number of Significant Cycles ' num2str(Numcyc_array(Index_ppv_max))])
disp(['NCSV Difference ' num2str(NCSV_array(Index_ppv_max)*100,3) ' %'])
disp(['PPV: ' num2str(PPV_array(Index_ppv_max),3) ' cm/s'])
disp(['Azimuth of Max PPV: ' num2str(Max_azimuth) ' deg.'])

%% Simple Example Figures
if Figs_flag==1
    HH=figure('Units','normalized','Position',[0 0 1 1]);
    axes('FontSize',24);
    JJ=plot(Tn,Ratio_filtered,'r','LineWidth',2);
    xlabel('Tn (s)','FontSize',30)
    ylabel('Ratio of Sv to Median Sv','FontSize',30);
    grid on

    RR=figure('Units','normalized','Position',[0 0 1 1]);
    axes('FontSize',24);
    JJ=plot((0:dt:(length(Rot_velf_max)-1)*dt),Rot_velf_max(:,1),'r','LineWidth',2);
    xlabel('Time (s)','FontSize',30)
    ylabel('Velocity (cm/s)','FontSize',30);

```

```
    grid on  
end  
end
```

```

function [Sv]=respspec_simple(Acc, dt, Tn,Zeta)
%respspec Calculates pseudo velocity spectrum
% Acc is acceleration time series
% dt is time step
%Tn is vector of natural periods to use
%Zeta is percent damping

Acccms=Acc*981;%convert from g to cm/s^2
beta=.25;%parameters for Newmark's method
gamma=.5;

%% Preallocate
THL=length(Acc)-1;
du=zeros(THL,1);
u=zeros(THL,1);
dudot=zeros(THL,1);
udot=zeros(THL,1);
duddot=zeros(THL,1);
uddot=zeros(THL,1);
umax=zeros(length(Tn),1)';
udotmax=zeros(length(Tn),1)';
uddotmax=zeros(length(Tn),1)';
%% Loop through all periods
for jj=1:length(Tn)
    wn=2*pi/Tn(jj);
    m=1;%then c,k are interms of damping and natural period
    k=wn^2;
    c=2*wn*Zeta;
    khat=k+gamma/beta/dt*c+m/beta/dt^2;
    a=m/beta/dt+gamma*c/beta;
    b=1/2/beta*m+dt*(gamma/2/beta-1)*c;
    u(1)=0; %oscillator starting from rest
    udot(1)=0;
    uddot(1)=0;
%% Perform Newark's method
    for ii=1:THL
        du(ii)=(Acccms(ii+1)-Acccms(ii)+a*udot(ii)+b*uddot(ii))/khat;
        u(ii+1)=u(ii)+du(ii);
        dudot(ii)=gamma*du(ii)/beta/dt-gamma*udot(ii)/beta+dt*(1-gamma/2/beta)*uddot(ii);
        udot(ii+1)=udot(ii)+dudot(ii);
        duddot(ii)=du(ii)/beta/dt^2-udot(ii)/beta/dt-uddot(ii)/2/beta;
        uddot(ii+1)=uddot(ii)+duddot(ii);
    end
    umax(jj)=max(abs(u));
    udotmax(jj)=max(abs(udot));
    uddotmax(jj)=max(abs(uddot));
end
%% Calculate pseudo velocity
Sv=2*pi*umax./Tn;

```

```

function [Pulse_score]=Score_simple(NCSV, Numcyc)
%Pulse_score Calculates the pulse score
%NCSV is the NCSV_difference
%Numcyc is the number of significant cycles

%% Score Weights and Cutoffs
NCSV_weight=.5;
NCSV_zero=.5; %0.5 or less
NCSV_one=.7; %0.7 or more
Numcyc_weight=.5;
Numcyc_zero= 2.499; % 2.5 or more
Numcyc_one=1.501; % 1.5 or less

%% Calculate Score
NCSV_sub=1+((NCSV-NCSV_one)/(NCSV_one-NCSV_zero));
NCSV_sub(NCSV_sub<0)=0;
NCSV_sub(NCSV_sub>1)=1;

Numcyc_sub=1+((Numcyc-Numcyc_one)/(Numcyc_one-Numcyc_zero));
Numcyc_sub(Numcyc_sub<0)=0;
Numcyc_sub(Numcyc_sub>1)=1;

Pulse_score=NCSV_weight*NCSV_sub+Numcyc_weight*Numcyc_sub;
end

```

```

function [PPV Num_cycles NCSV_diff ]=zerocross_simple(Vel_max,dt)
%zerocross_simple: Simplified version used to calculates PPV, Number of significant
cycles and NCSV difference
%Vel_all: (n x 1) array of horizontal velocity time series
%dt: time step

Period_scale=1;%number of half periods to search for next pulse zero crossing in.
Max_min=max(Vel_max)-min(Vel_max);%First approx at PPV
T=(0:dt:(length(Vel_max)-1)*dt)';%Time

%% Cumulative squared velocity
Vel_squared=Vel_max.^2;
Vel_squared_cumsum=cumsum(Vel_squared)*dt;
Total_vel_squared=Vel_squared_cumsum(end);
Normalized_vel_squared=Vel_squared_cumsum/Total_vel_squared;
Normalized_vel_squared=[0; (diff(Normalized_vel_squared) == 0)]*10E-12.
*T+Normalized_vel_squared;%To get rid of non-unique values breaking interp

%% Find Zero Crossings
n=length(Vel_max);
x1=Vel_max(1:n-1);
x2=Vel_max(2:n);
xx=x1.*x2;
Zero_loc_index=find(xx<0);%locations of zero crossings uses 2nd of the two points
corresponding to a sign change
if Zero_loc_index(1) > 2
Zero_loc_index=[1;Zero_loc_index];%Added 1/2/2013 to fix 1 motion...
end

%% Find Extreme point between each pair of zero crossings
Extreme_value=zeros(1,length(Zero_loc_index)-1);%Preallocate
Loc_extreme_value=zeros(1,length(Zero_loc_index)-1,1);%Preallocate
Table=zeros(length(Zero_loc_index)-1,4);
for ii=1:length(Zero_loc_index)-1
    Range=Vel_max(Zero_loc_index(ii):Zero_loc_index(ii+1));
    [Extreme_value_abs Extreme_value_index]=max(abs(Range));
    Loc_extreme_value(ii)=Extreme_value_index+Zero_loc_index(ii)-1;
    Extreme_value(ii)=Extreme_value_abs*sign(Vel_max(Loc_extreme_value(ii)));
    Table(ii,:)=[Extreme_value(ii) Loc_extreme_value(ii) Zero_loc_index(ii) Zero_loc_index
(ii+1)];
end

%% Calculate PPV and number of significant cycles
SM=1;
jj=.25;
Gap_threshold=0;
while sum(Gap_threshold)==0%Need loop when there are no pulses "connected"
    while sum(SM)==1%Need loop for very rare occasion where there is only one sided pulse
so that only one point falls above Max_min...
        SM=abs(Table(:,1))>Max_min*(jj);%index of "large" peaks. The value MaxMin is just
so that

```

```

    %small peaks are ignored in calculating the PPV. Once PPV is determined use
    %that to classify # of pulses and period
    jj=jj-.01;
end
Table_threshold=Table;
Table_threshold(SM==0,:)=[];
Table_threshold=[Table_threshold (1:size(Table_threshold,1))'];
Hp=Table_threshold(:,4)-Table_threshold(:,3);%half period

ll=length(Table_threshold(:,1));
Gap=Table_threshold(2:ll,3)-Table_threshold(1:ll-1,4);%Gap between cycles
Hp1=Hp(1:ll-1);% Half period of 1st cycle
Hp2=Hp(2:ll);%Half period of second cycle
Ahp=Period_scale*(Hp1+Hp2)/2;%Maximum allowed gap

Diff_table=[abs(Table_threshold(1:ll-1,1)-Table_threshold(2:ll,1)) Ahp Gap];
Diff_table=[(1:size(Diff_table,1))' Diff_table];
Gap_threshold=Diff_table(:,3)>Diff_table(:,4);
Diff_table_threshold=Diff_table(Gap_threshold,:);
[PPV Max_PPV_index]=max(Diff_table_threshold(:,2));
Max_PPV_index=Diff_table_threshold(Max_PPV_index,1);
Gap_threshold=[0;Gap_threshold; 0];
First_cycle=find(Gap_threshold(1:Max_PPV_index+1)==0,1,'last');
Last_cycle=find(Gap_threshold(Max_PPV_index+2:end)==0,1,'first')+Max_PPV_index;
Table_cycles=Table_threshold(First_cycle:Last_cycle,:);
Num_cycles=size(Table_cycles,1)/2;
SM=abs(Table(:,1))>Max_min*(jj);
jj=jj-0.01;
end

%% Calcualte NCSV at zero crossings
PPV_zero_first=Normalized_vel_squared(Table_threshold(Max_PPV_index,3));%use Assoc_zero
because that is what PPV index is in reference to...
PPV_zero_end=Normalized_vel_squared(Table_threshold(Max_PPV_index+1,4));
NCSV_diff=PPV_zero_end-PPV_zero_first;
end

```

APPENDIX A-3: Binning process for generation of contours

The probability contours presented in Fig. 2.6 are based on a binning process. The pulse proportion in each bin (sized 7.5 km by 1 epsilon) is assigned to a pair of distance and epsilon coordinates representing the mean values of the records in each bin. This is repeated with overlapping bins at increments of 1 km and 0.1 epsilon. The MATLAB function “TriScatteredInterp” served to interpolate the scattered data onto a regular grid appropriate for use with the MATLAB “contour” function. Figure A.3.1 illustrates the result of this binning process, and it is similar to Fig 2.6 but with additional contours.

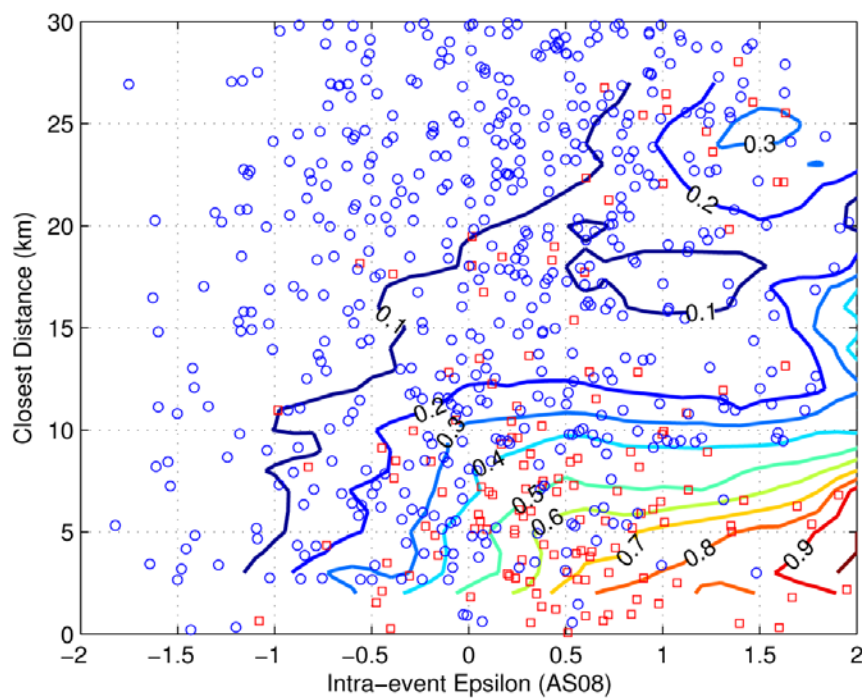


Figure A.3.1. Contour plot using the procedure described

The exact binning process described is arbitrary; the selected bin size allows there to be sufficient data in each bin to obtain a reasonable proportion estimate while also limiting the bin size to reduce overly averaged results. Figure A.3.2 provides an example with the bin sizes decreased by 50% (i.e., 3.75 km by 0.5 epsilon), which results in erratic contours due to the limited data within certain bins. An example of increasing the bin size by 50% (i.e., 1.5 epsilon and 11.25 km) is shown in Figure A.3.3. Regardless of bin size, all three cases exhibit the same overall trend: increasing pulse proportion with decreasing distance and increasing epsilon. These contours are primarily for visualization and serve as a comparison with the functional form used in the logistic regression. Therefore, the exact process does not directly affect the primary result of the study (i.e., the equation for pulse proportion).

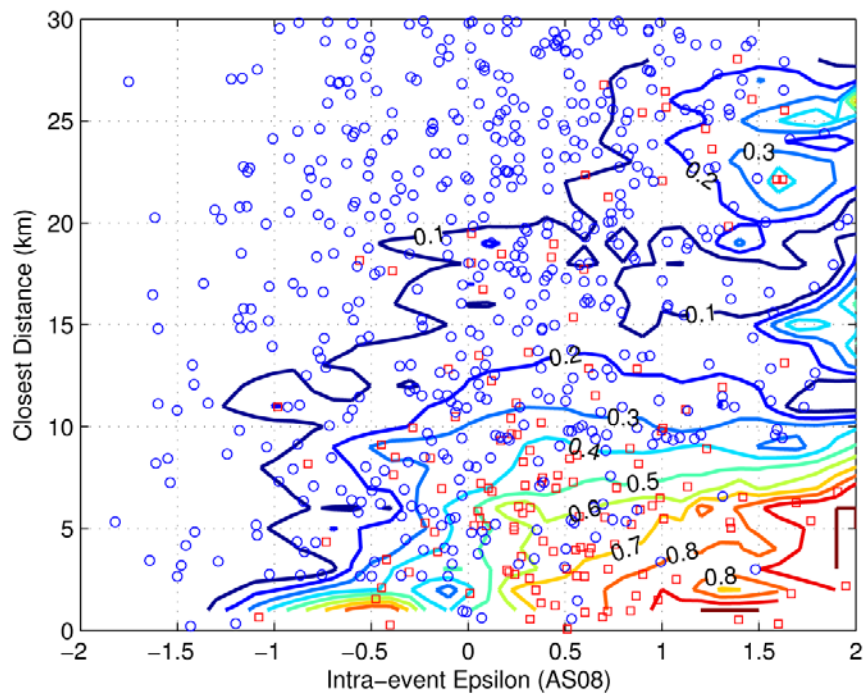


Figure A.3.2. Example of bin size decreased by 50% (0.5 epsilon and 3.75 km)

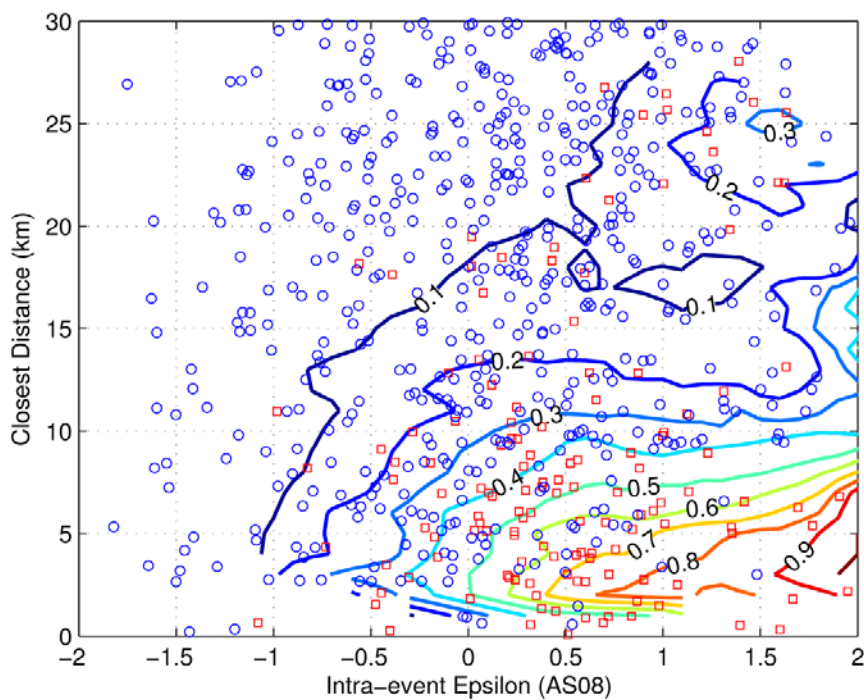
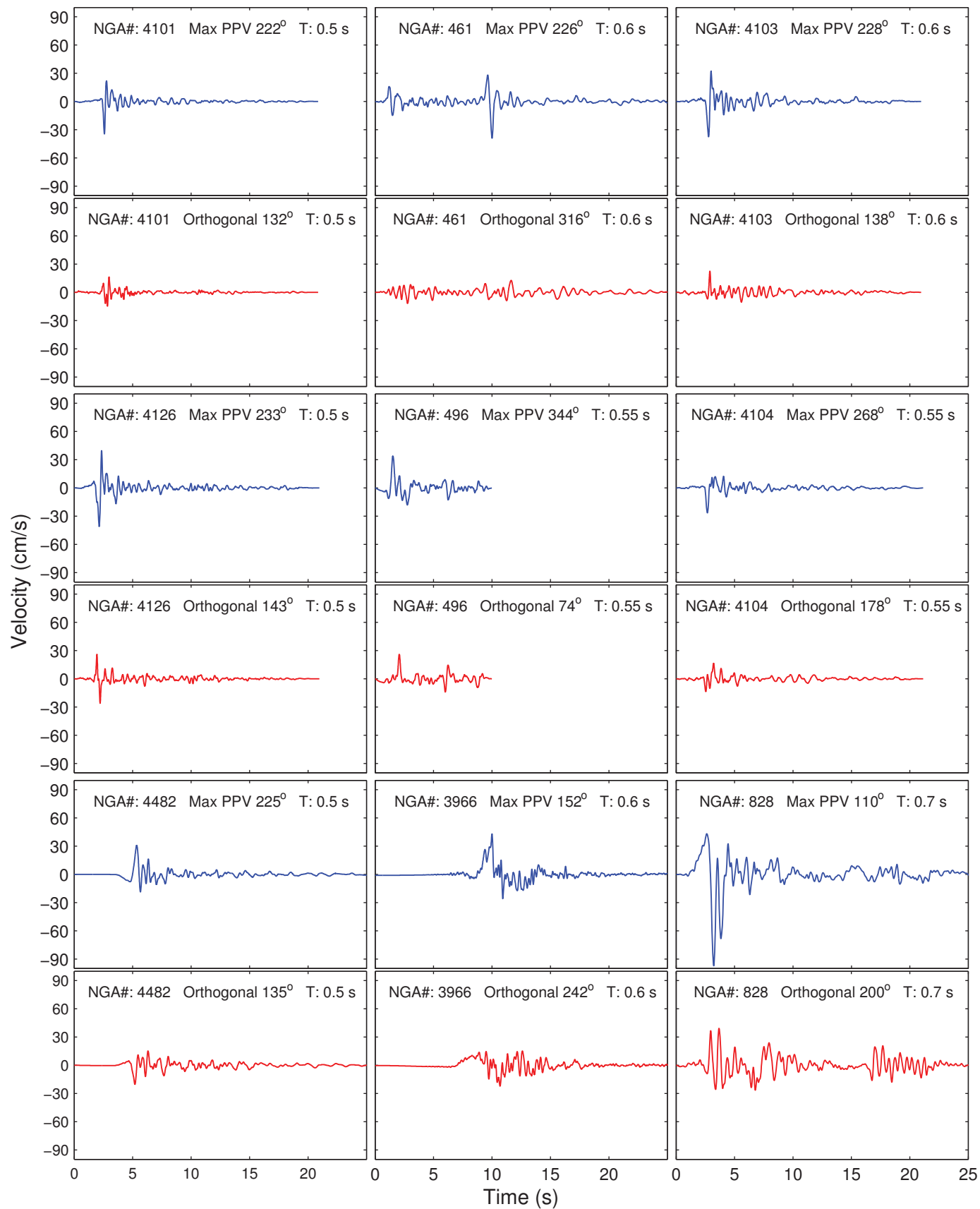
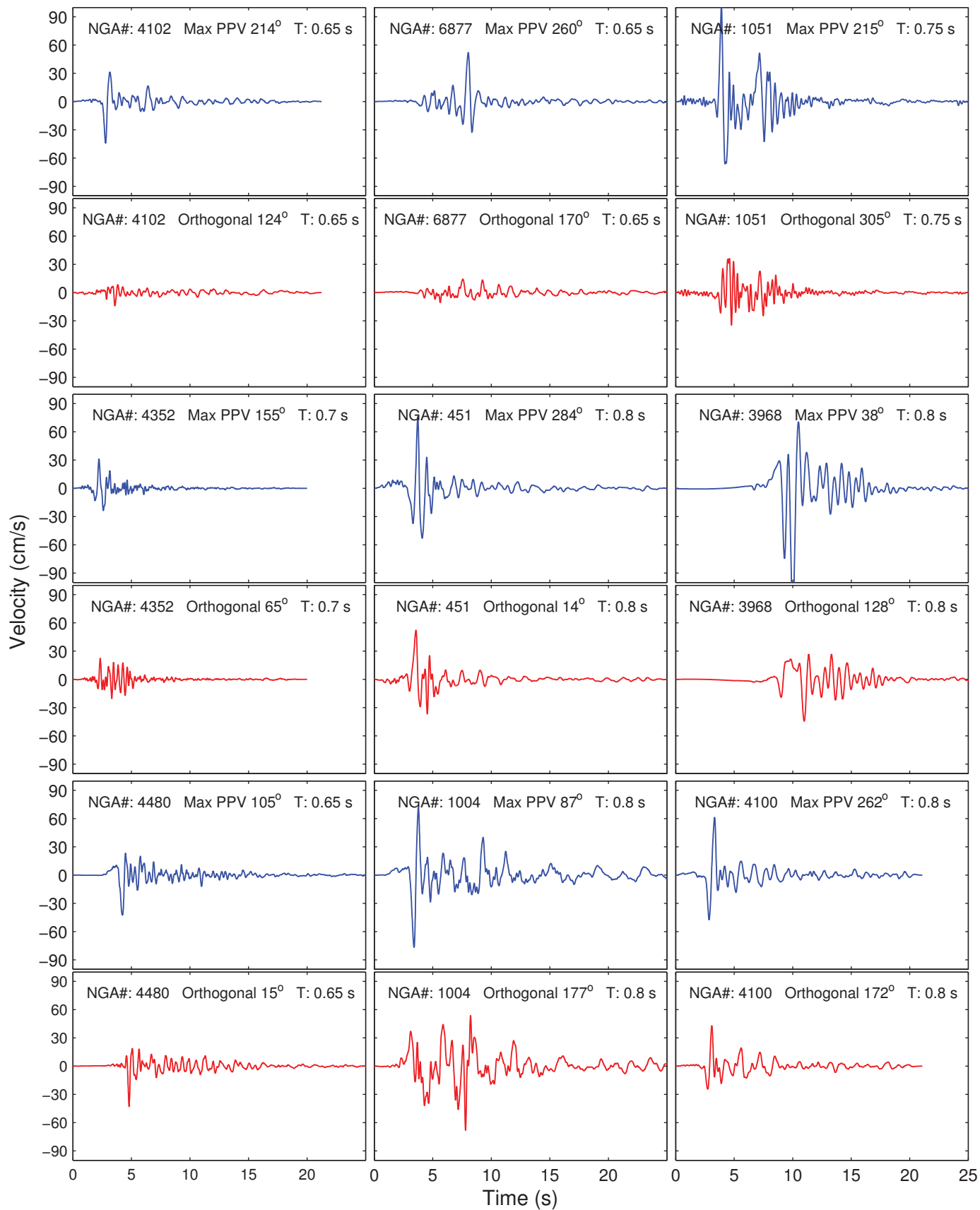
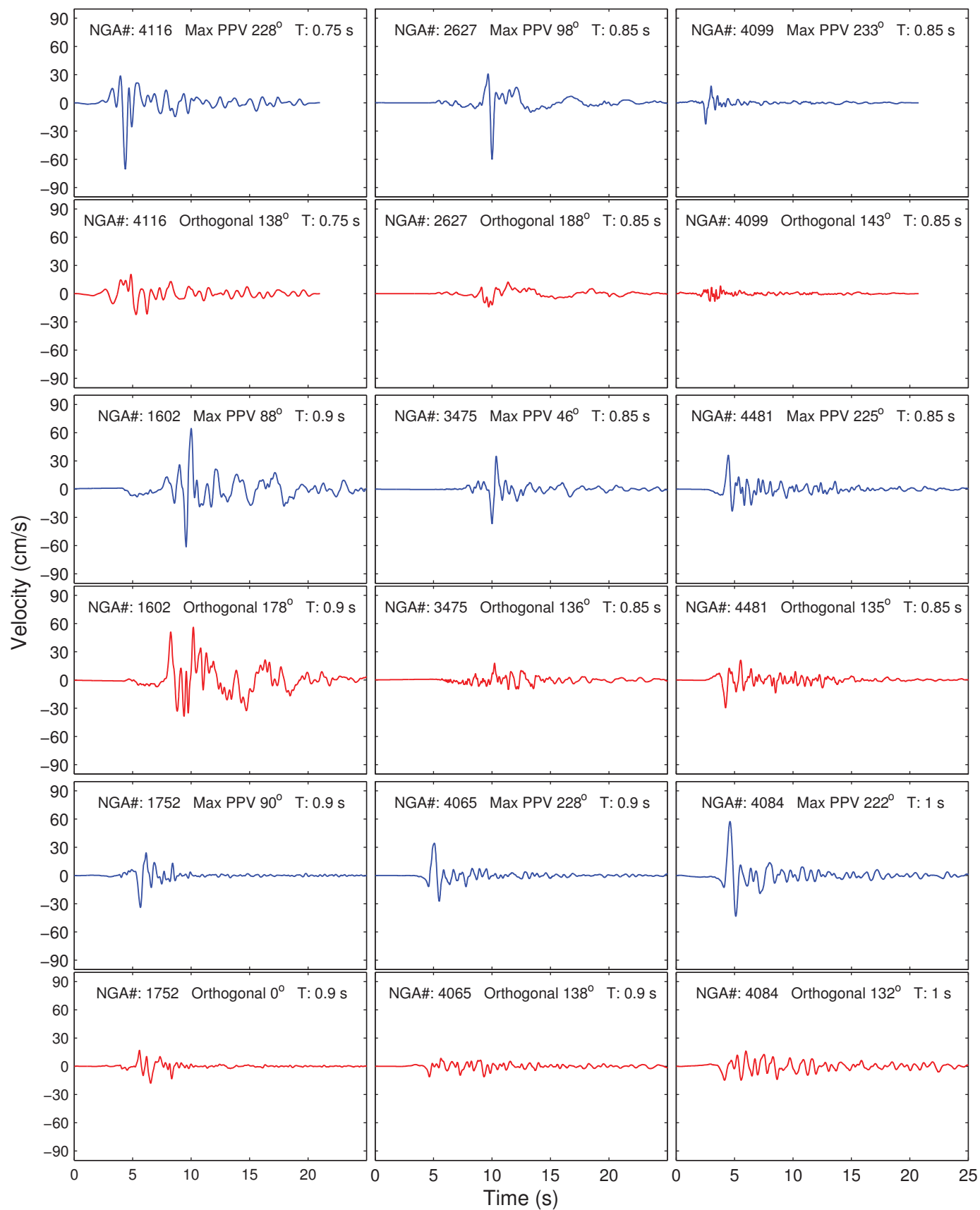


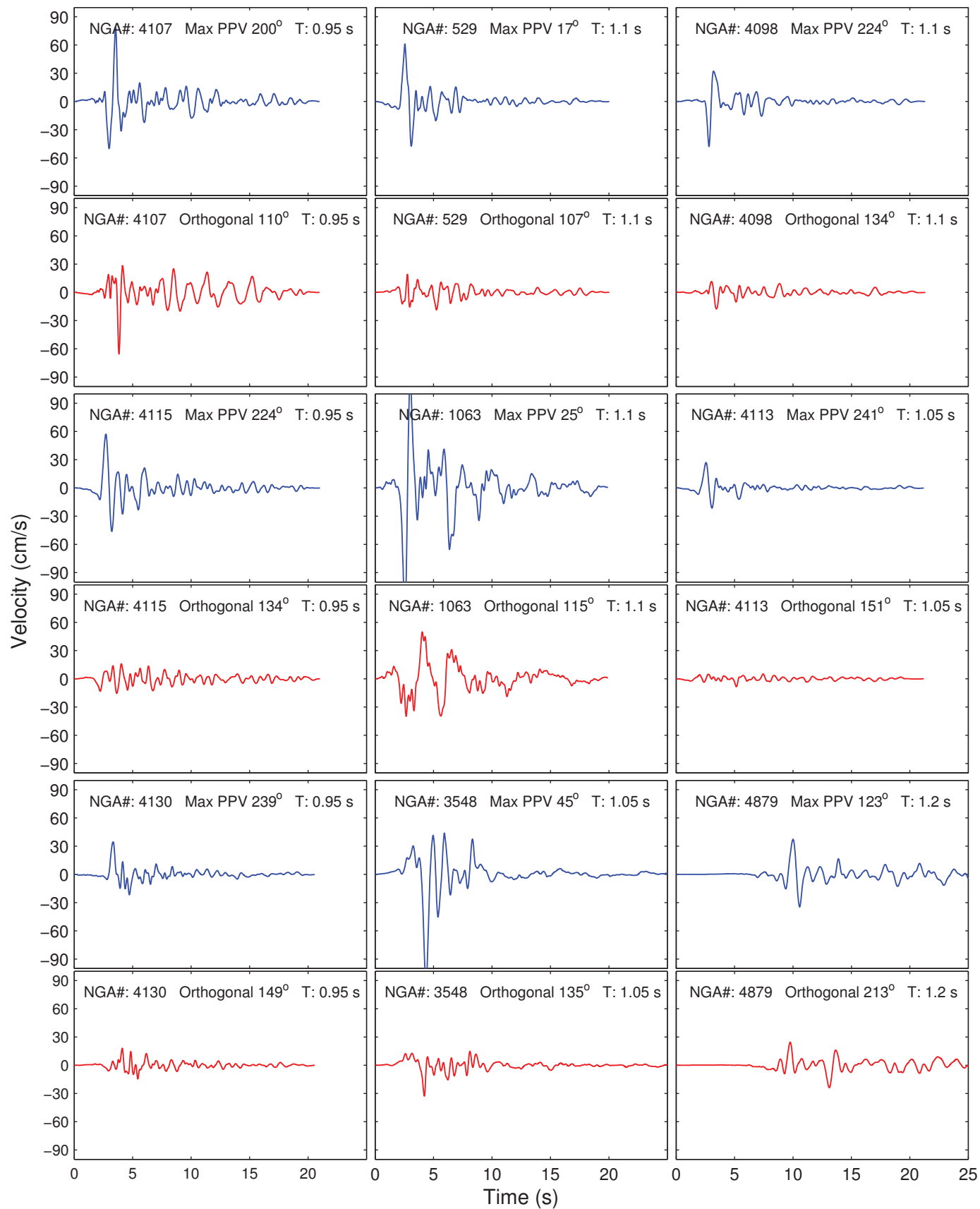
Figure A.3.3. Example of bin size increased by 50% (1.5 epsilon and 11.25 km)

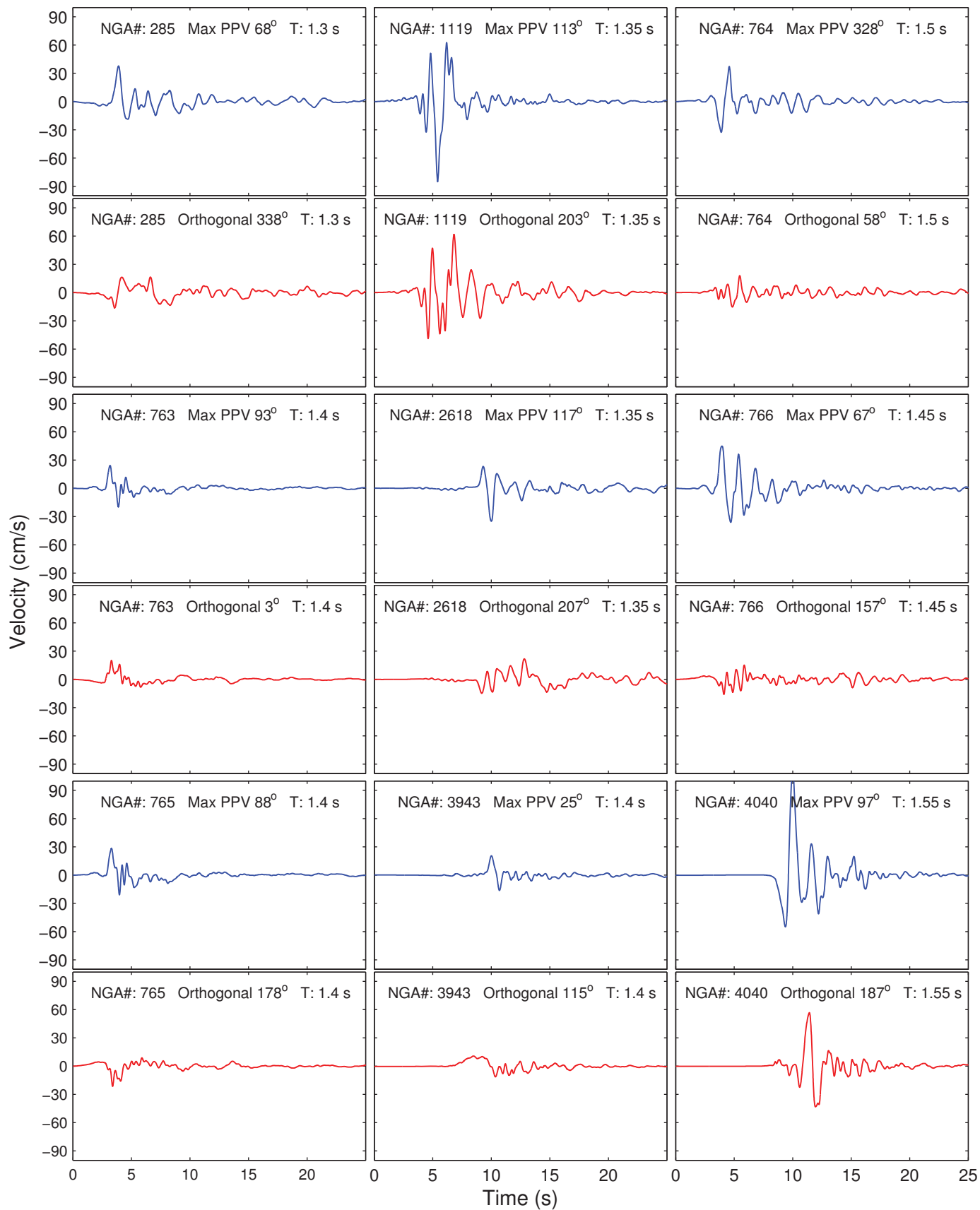
APPENDIX A-4
PULSE MOTION FIGURES

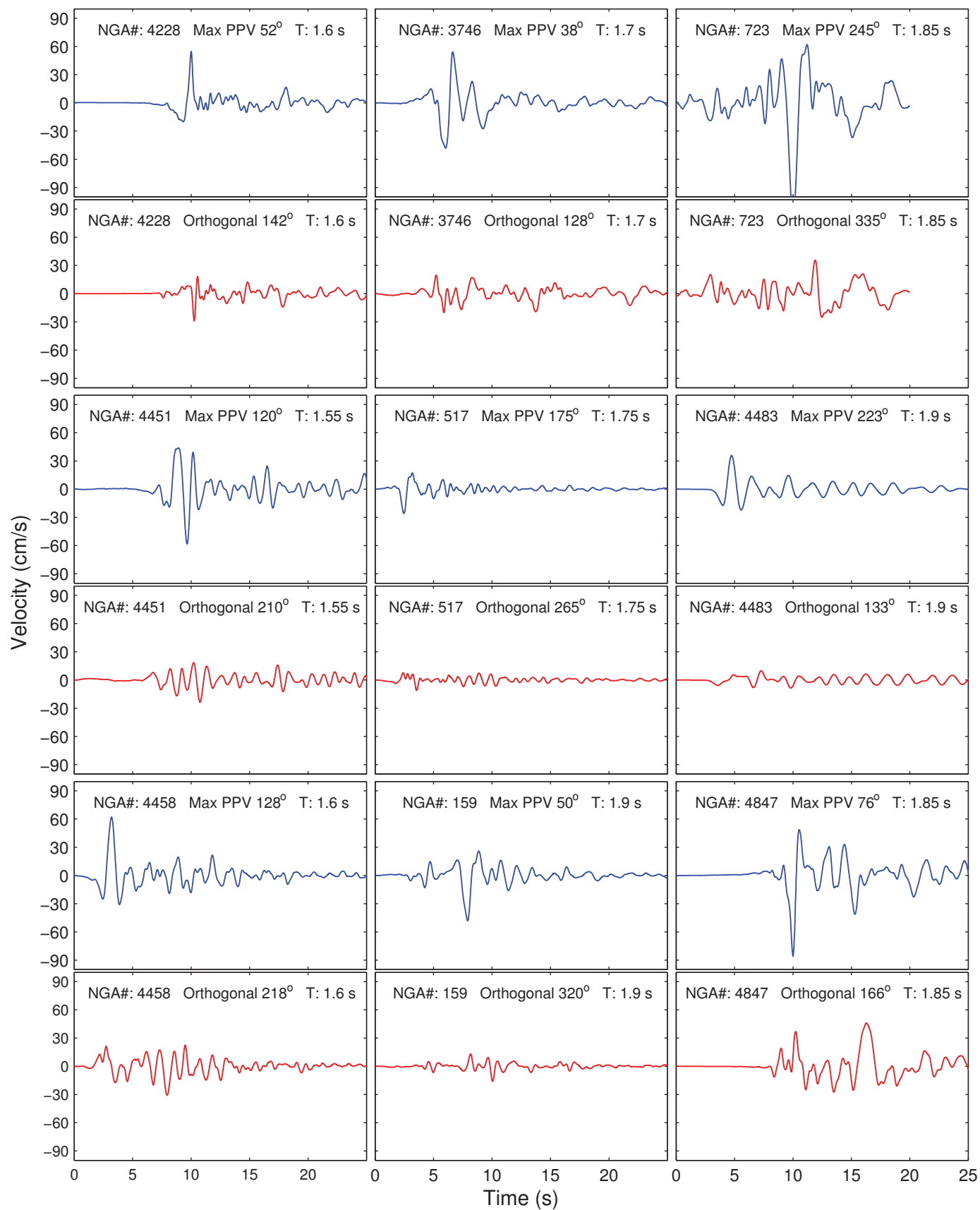


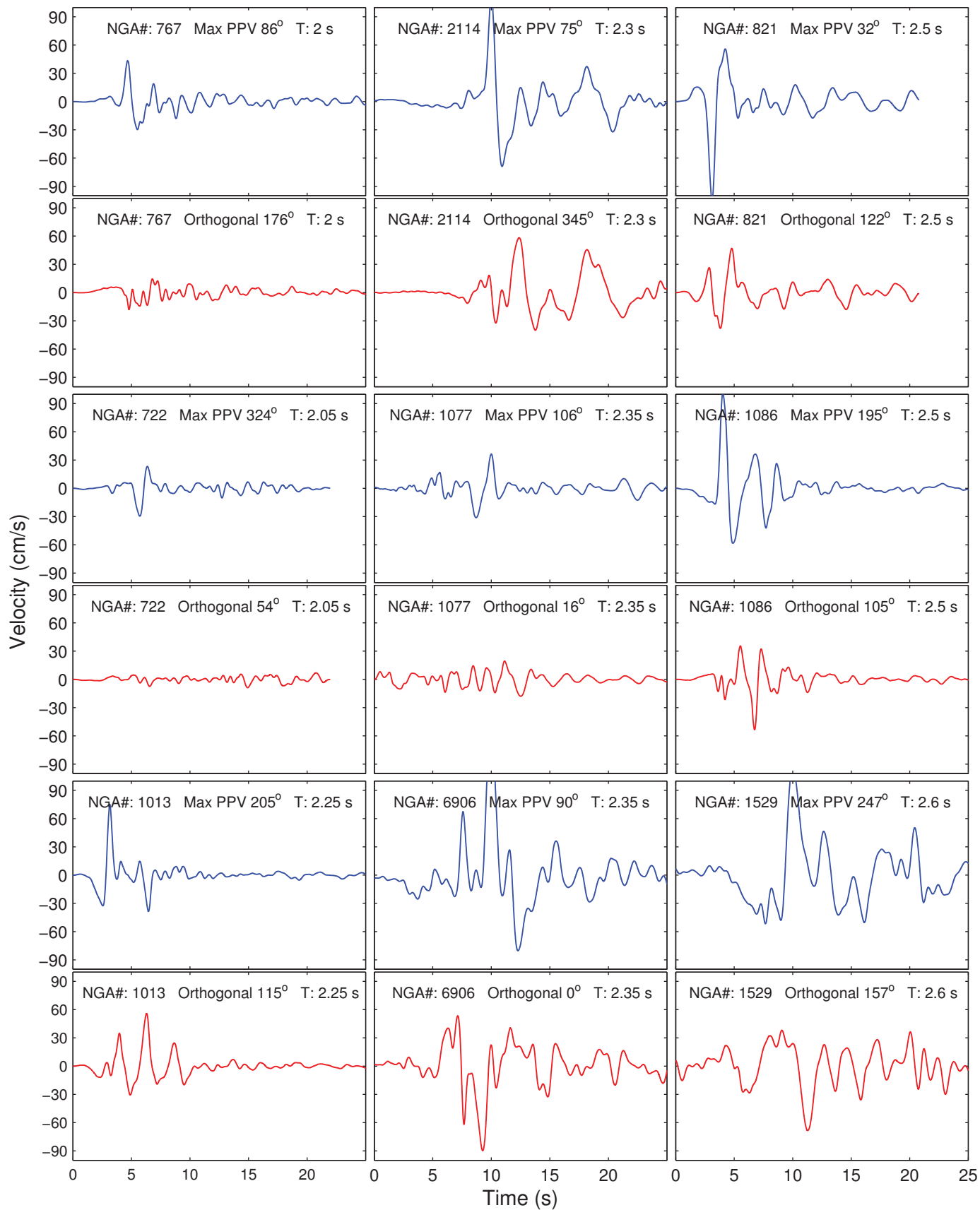


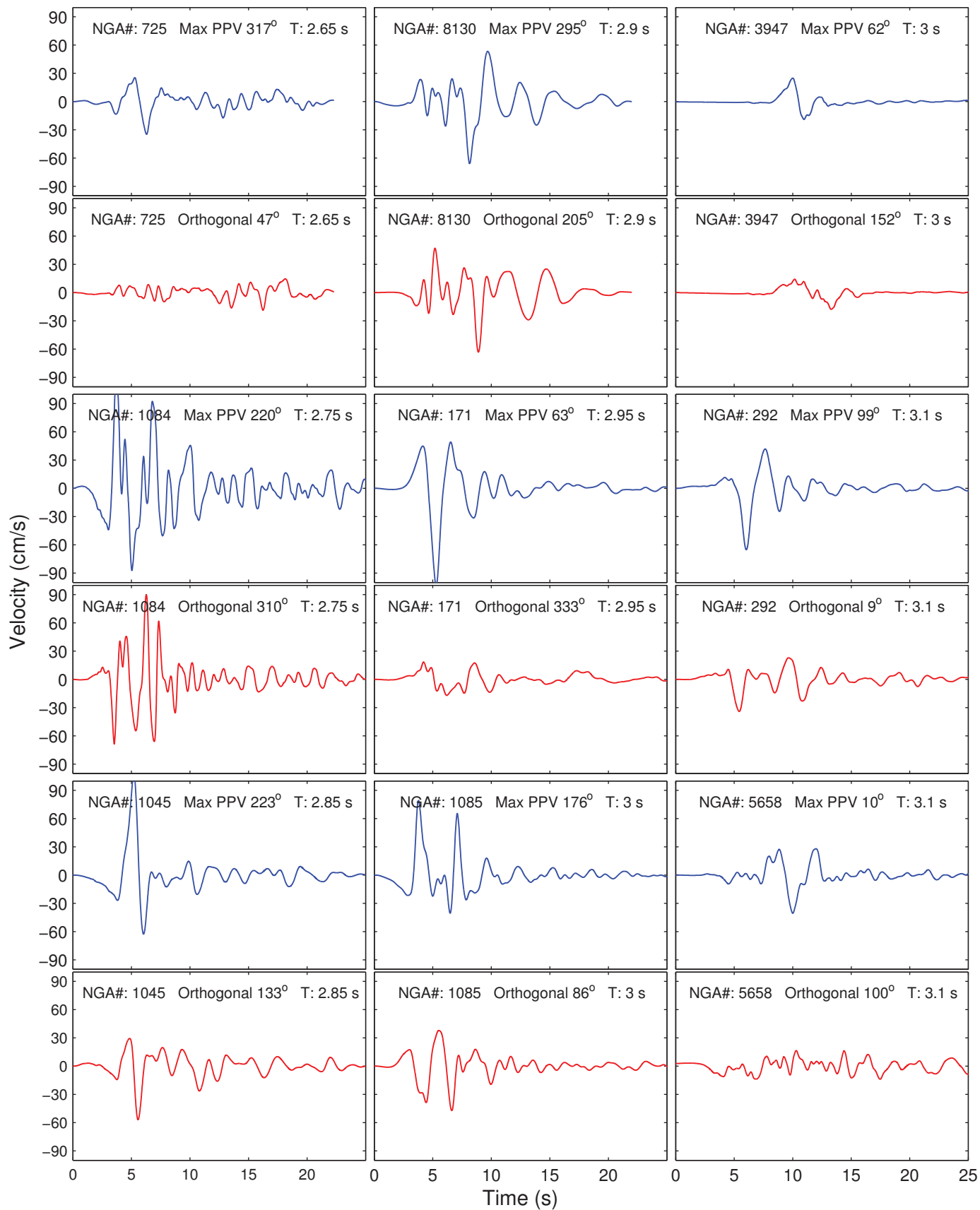


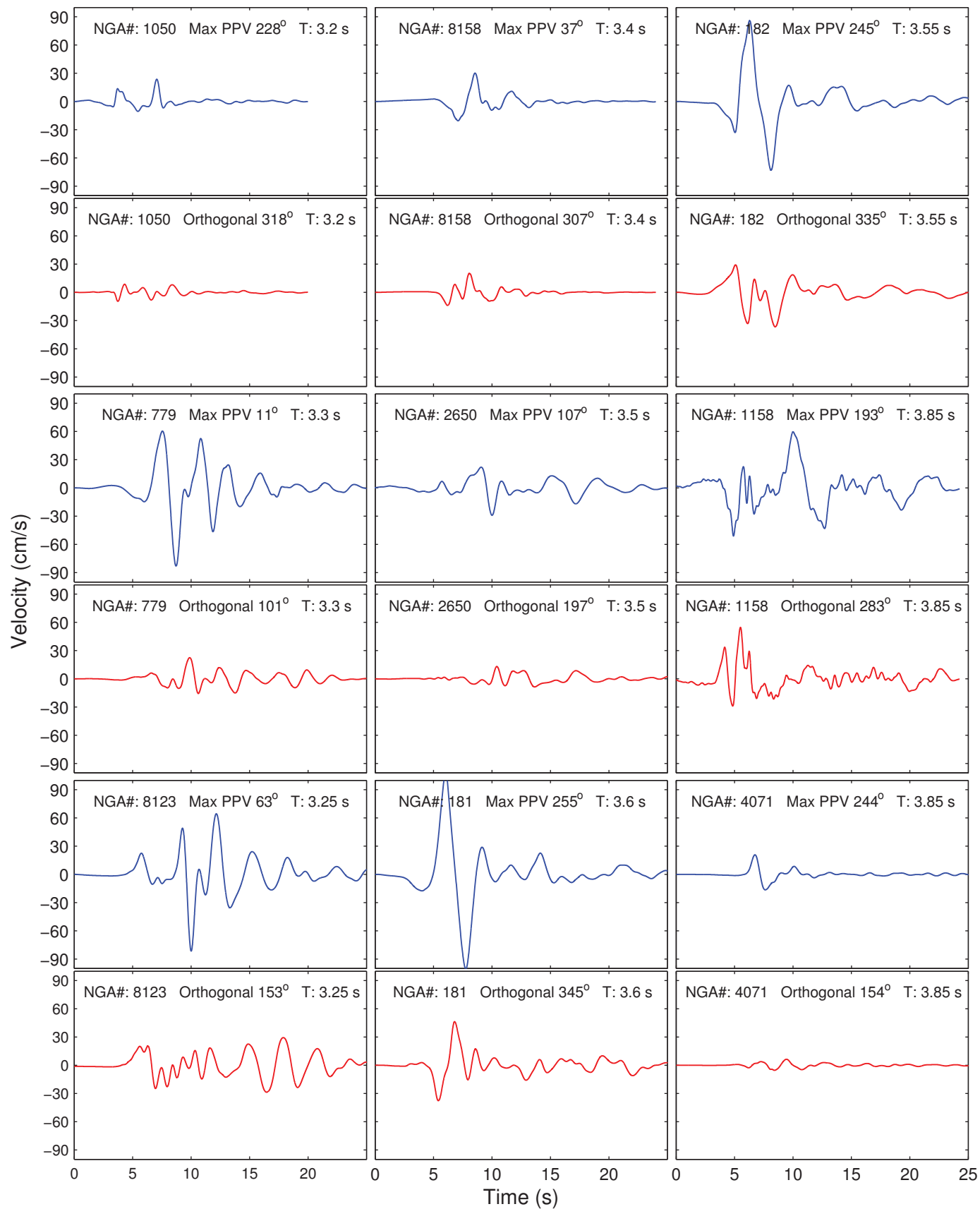


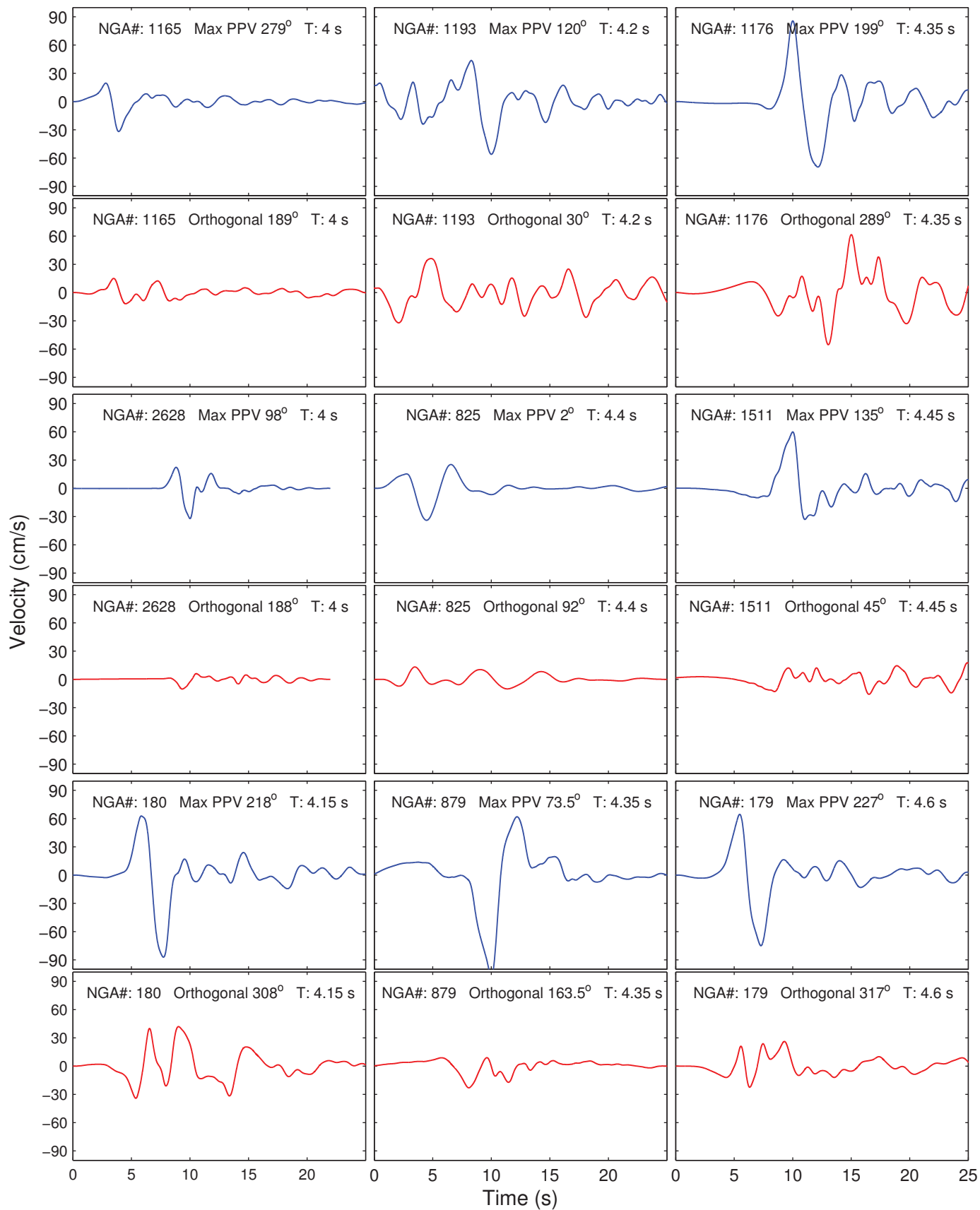


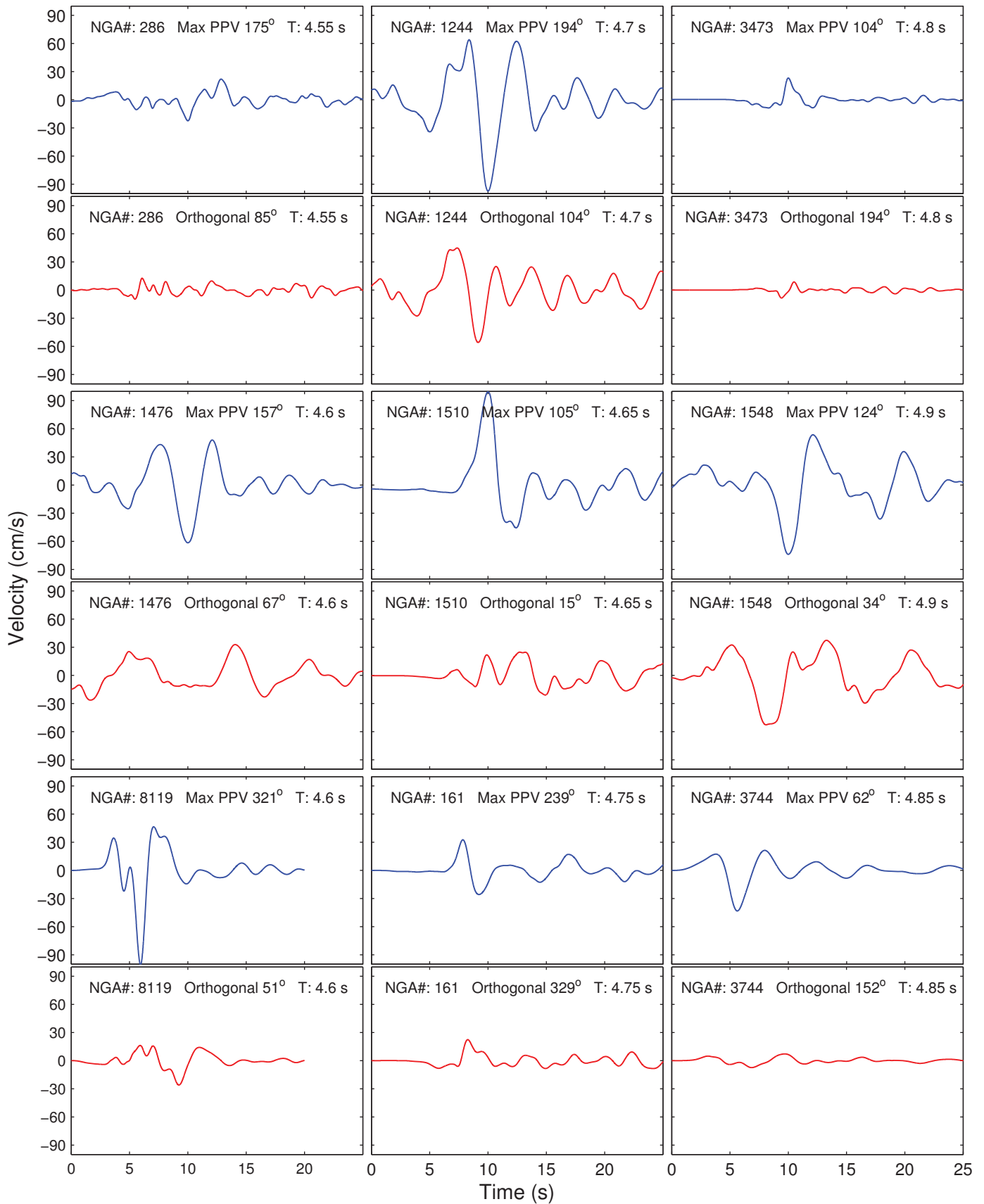


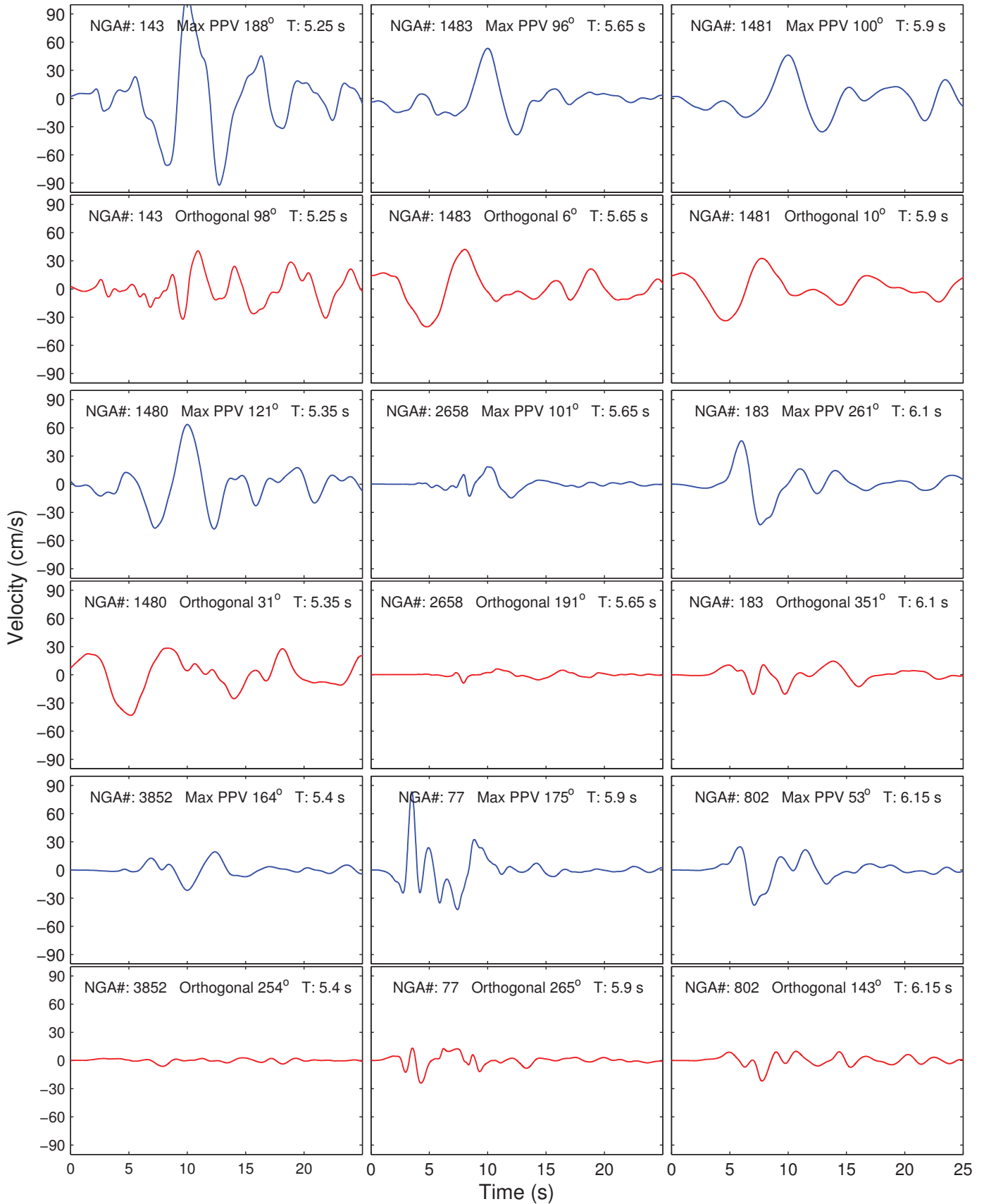


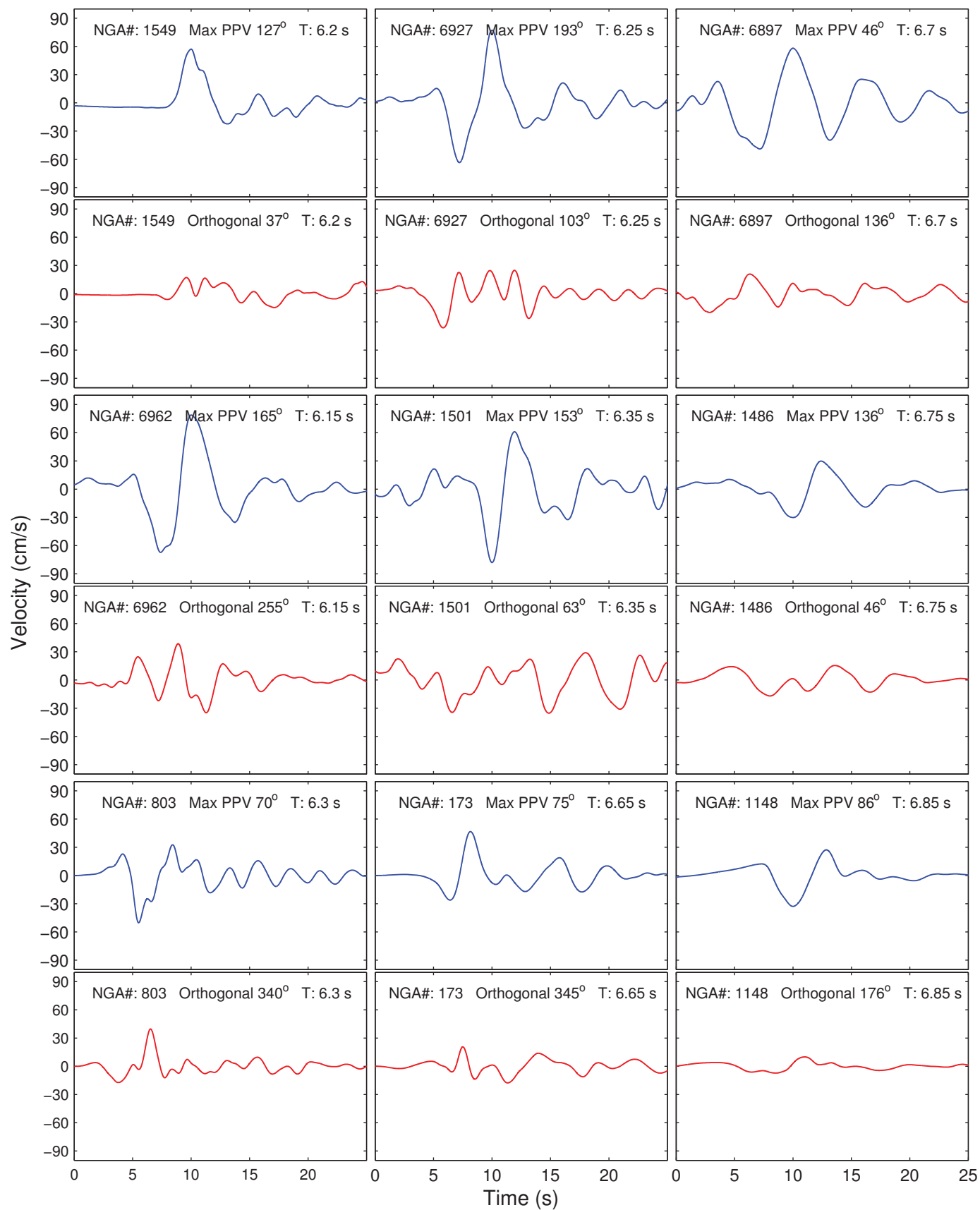


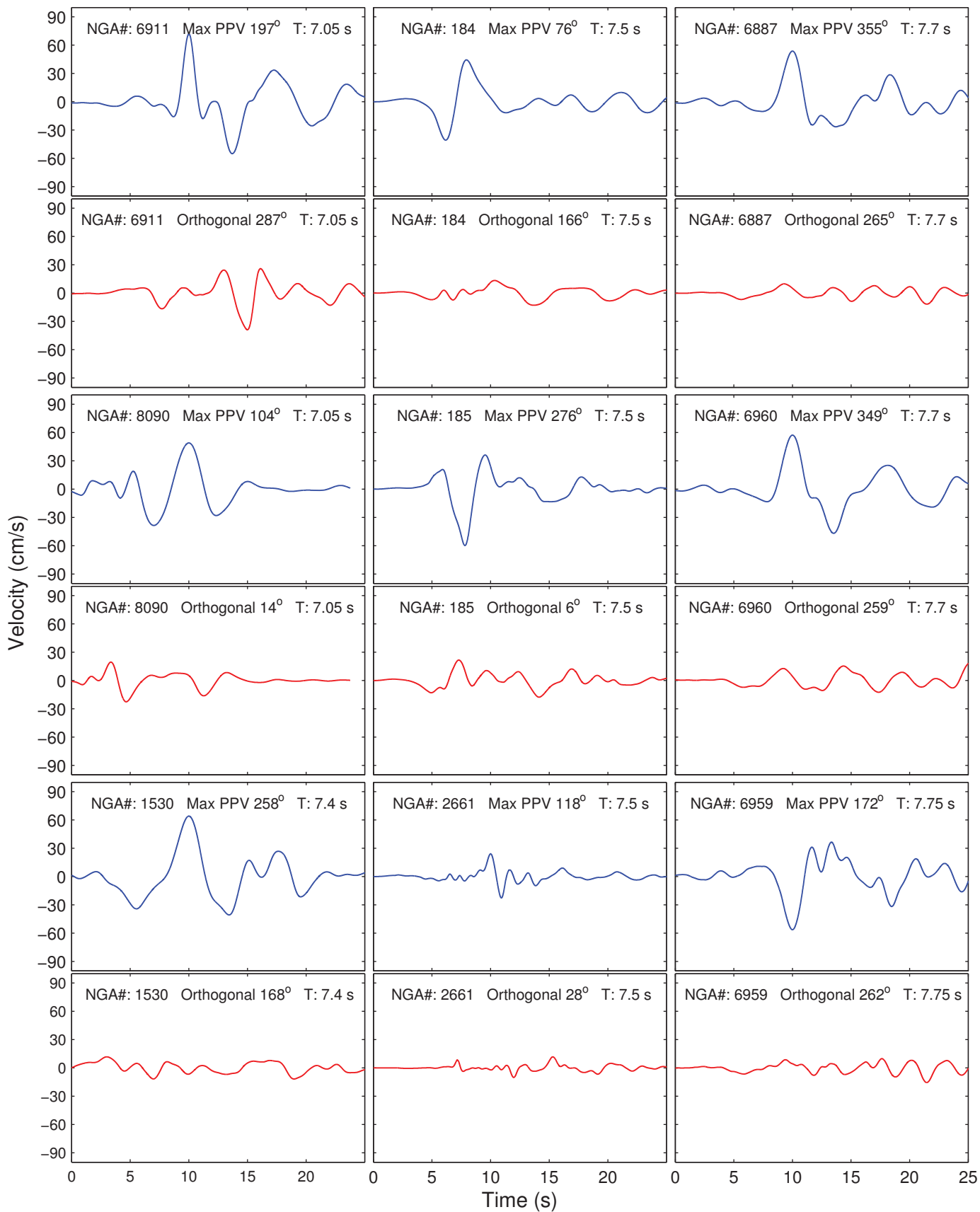


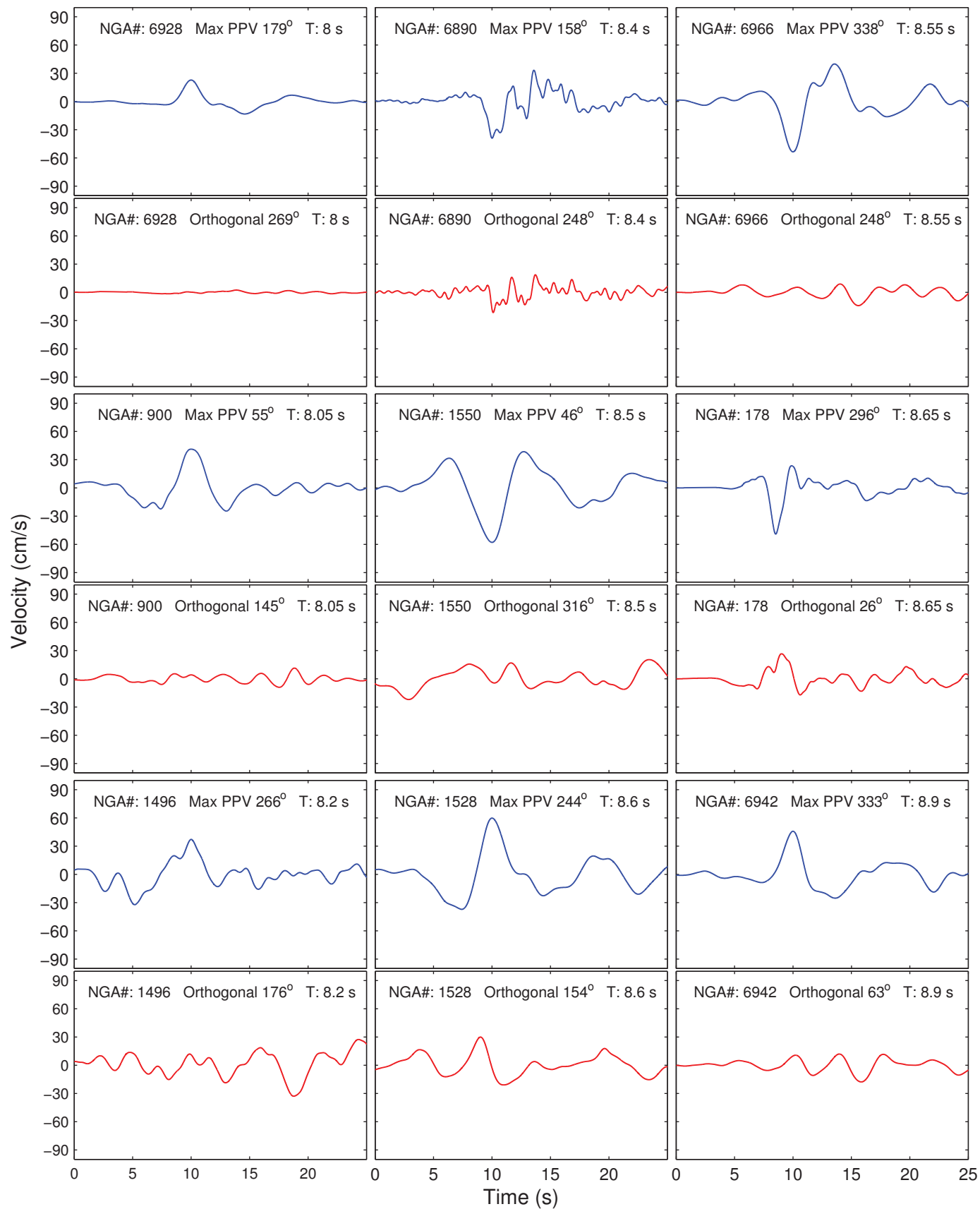


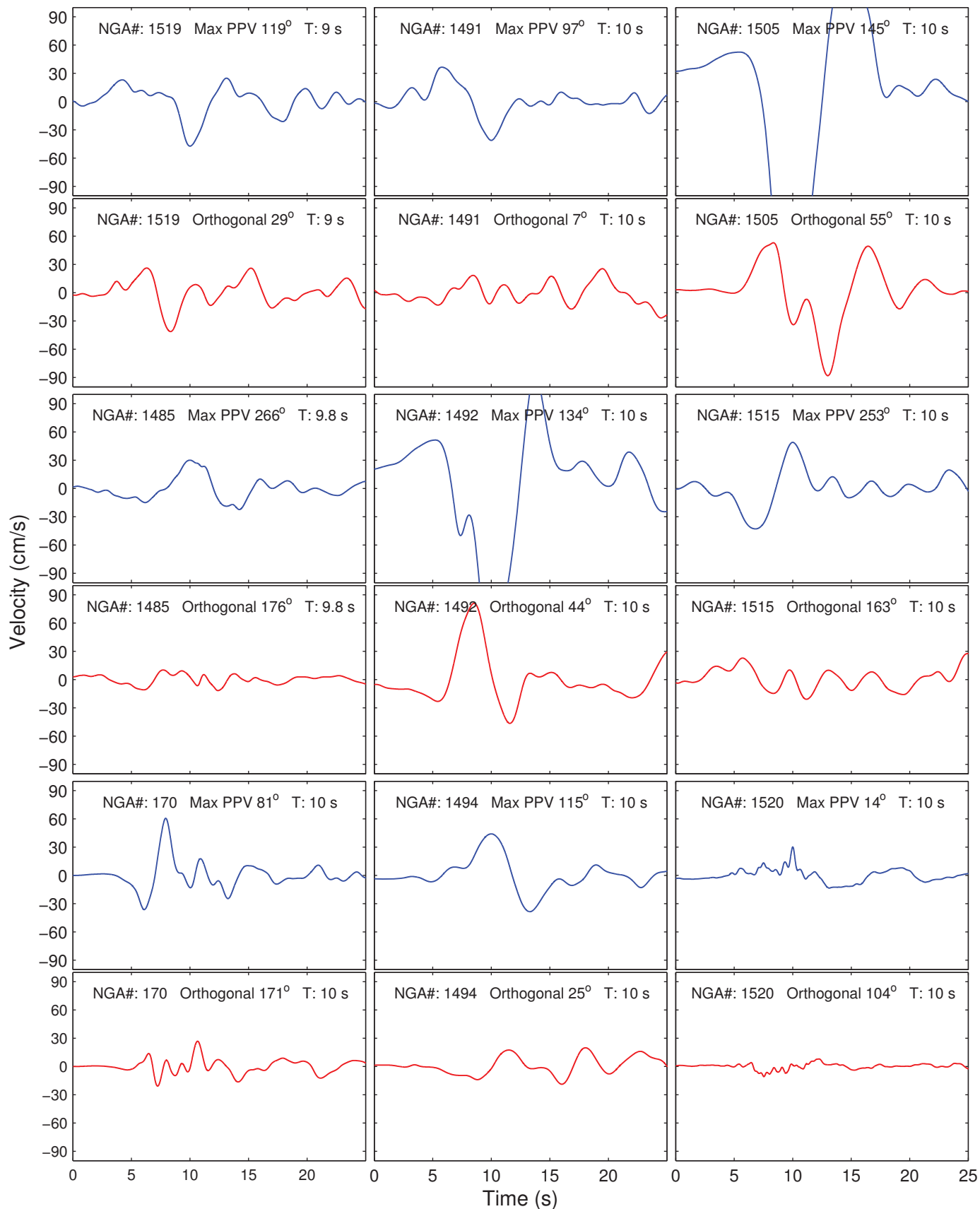












APPENDIX B-1

Test-6 (T4.6-40) Data Report

REPORT NO.
UCD/CGMDR-XX/XX

CENTER FOR GEOTECHNICAL MODELING

**SEISMIC PERFORMANCE ASSESSMENT IN
DENSE URBAN ENVIRONMENTS:
CENTRIFUGE DATA REPORT FOR TEST-6**

BY
C. P. HAYDEN
J. D. ALLMOND
I. A. RAWLINGS
B. L. KUTTER
J. D. BRAY
T. C. HUTCHINSON
G. L. FIEGEL
J. D. ZUPAN
A. S. WHITTAKER



**DEPARTMENT OF CIVIL & ENVIRONMENTAL ENGINEERING
COLLEGE OF ENGINEERING
UNIVERSITY OF CALIFORNIA AT DAVIS**

April 2014

Centrifuge Data Report

Test-6

C.P. Hayden, J.D. Allmond, I.A. Rawlings, B.L. Kutter, J.D. Bray, T.C. Hutchinson, G.L. Fiegel, J.D. Zupan, A.S. Whittaker

April 2014

Soil-Structure Interaction on the Scale of a City Block

Seismic Performance Assessment in Dense Urban Environments



This material is based upon work supported by the National Science Foundation (NSF) under Grant No. CMMI-0830331 through the George E. Brown, Jr. Network for Earthquake Engineering Simulation (NEES). The “Seismic Performance Assessment in Dense Urban Environments: Soil-Structure Interaction on the Scale of a City Block” project is a collaborative effort that includes the University of California, Berkeley (lead institution), University of Buffalo-SUNY, University of California, Davis, University of California, San Diego, California Polytechnic State University, San Luis Obispo, and the Consortium of Universities for Research in Earthquake Engineering. This project utilizes the NEES equipment site at the University of California, Davis. Any opinions, findings, and conclusions or recommendations expressed in this material are those of the authors and do not necessarily reflect the views of the NSF.



NEESR-SG Project: “Seismic Performance Assessment in Dense Urban Environments”

Centrifuge Data Report for Test-6

Connor Hayden, Jacquelyn Allmond, Isabelle Rawlings, Bruce Kutter, Jonathan Bray, Tara Hutchinson, Gregg Fiegel, Josh Zupan, Andrew Whittaker

Date:	April, 2014
Total Experiment Duration:	April 8 – July 11, 2013
Dates of Testing:	June 25 and June 26, 2013
Project:	Seismic Performance Assessment in Dense Urban Environments
NSF Contract Number:	CMMI-0830331
Sponsor(s):	NSF

Acknowledgments

This material is based upon work supported by the National Science Foundation (NSF) under Grant No. CMMI-0830331 through the George E. Brown, Jr. Network for Earthquake Engineering Simulation (NEES). Any opinions, findings, and conclusions or recommendations expressed in this material are those of the authors and do not necessarily reflect the views of the NSF. The authors would like to acknowledge the suggestions and assistance of Dan Wilson, Chad Justice, Anatoliy Ganchenko, Lars Pederson, Peter Rojas, Tom Kohnke, and the other staff at the Center for Geotechnical Modeling at UC Davis. Nicholas Trombetta, Ben Mason, and Chandu Bolisetti assisted in planning the test. Mark Stringer also provided valuable assistance and advice during the experiment.

This experiment was performed using the large geotechnical centrifuge at UC Davis. The NSF, NASA, and the University of California supported the development of this centrifuge. Additional support was obtained from Tyndall Air Force Base, the Naval Civil Engineering Laboratory and Los Alamos National Laboratories. The large shaker was funded by the California Department of Transportation, the Obayashi Corporation, NSF and the University of California. Recent upgrades have been funded by NSF award #CMS-086566 through the George E. Brown, Jr. Network for Earthquake Engineering Simulation (NEES).

Conditions and Limitations

Permission is granted for the use of these data for publication in the open literature, provided that the authors and sponsors are properly acknowledged. It is essential that the authors be consulted prior to publication to discuss the errors or limitations in the data not known at the time of the release of this report. In particular, there may be later releases of this report. Questions about this report may be directed by e-mail to: cgm@ucdavis.edu.

Table of Contents

Previous Tests in this Series	5
Configuration of Test-6	6
Soil and Pore Fluid Properties	9
Scale Factors	10
Model Construction.....	11
As-Built Model	19
Instrumentation and Measurements	23
Centrifuge Test Chronology.....	30
Data Processing.....	30
Known Limitations.....	31
Organization of Appendices	33
References	34

PREVIOUS TESTS IN THIS SERIES

This data report describes the sixth and final centrifuge test in the NEES Seismic Performance Assessment in Dense Urban Environments project. Test-6 examines structure-soil-structure interaction (SSSI) during liquefaction. Details of the initial four tests, conducted on dry sand, can be found in the relevant data reports (i.e., Mason et al. 2010a; Mason et al. 2010b; Mason et al. 2010c; Trombetta et al. 2011), which are available on NEEShub (www.nees.org/warehouse/project/639). The Test-5 data report (Zupan et al. 2013) also provides a brief overview of the initial four tests. Test-5 used a saturated model with a liquefiable layer to investigate the effects of SSSI for structures subjected to liquefaction. Test-6 builds on the findings of Test-5; therefore, the following provides a brief overview of Test-5 with further details available in Zupan et al. (2013).

Test-5 used two structure types from recent centrifuge tests to facilitate comparisons between tests. Structure A is from the Dashti et al. (2010a; 2010b) centrifuge test sequence and represents a small, two-story structure. Structure J is from Allmond and Kutter (2012; 2013) and is substantially taller than Structure A and has nearly three times the contact pressure. Table 1 summarizes key structural parameters. All measurements in this data report are in model scale unless otherwise noted.

TABLE 1. KEY STRUCTURAL PROPERTIES IN MODEL SCALE

Structure	Footing Width (mm)	Footing Length (mm)	Height (mm)	Weight (N)	Contact Pressure (kPa)	Fixed-Base Period ¹ (s)	Center of Mass ² (mm)
A	109	164	80	1160	65	0.006	71
K	109	164	96	3210	180	0.007	71
J	136	136	271	3460	186	0.015	245

¹Measured in lab

²Deck center of mass measured from the footing base

The Test-5 layout contains four quadrants and seven structures as shown in Figure 1a. The subscript in each structure label indicates the adjacent structure type and any additional information. For example, Structure J_A, in the southwest quadrant, is a J type structure that is adjacent to an A type structure. The J_{A-P} structure in the southeast quadrant is fixed to four piles. The soil profile in Figure 1b indicates the thickness of each layer. Structures are embedded 13 mm in a 31 mm thick crust of dense Monterey 0/30 sand. Beneath the Monterey sand is an 83 mm thick Nevada sand layer with a relative density of approximately 50±5% (revised from the 40±5% in the Test-5 data report). Finally, a dense layer of Nevada sand extends 353 mm to the base of the model container. The centrifuge spun at 55g with an effective radius at the center of the liquefiable layer. The Test-5 ground motion sequence followed Dashti et al. (2010b) to permit further comparisons.

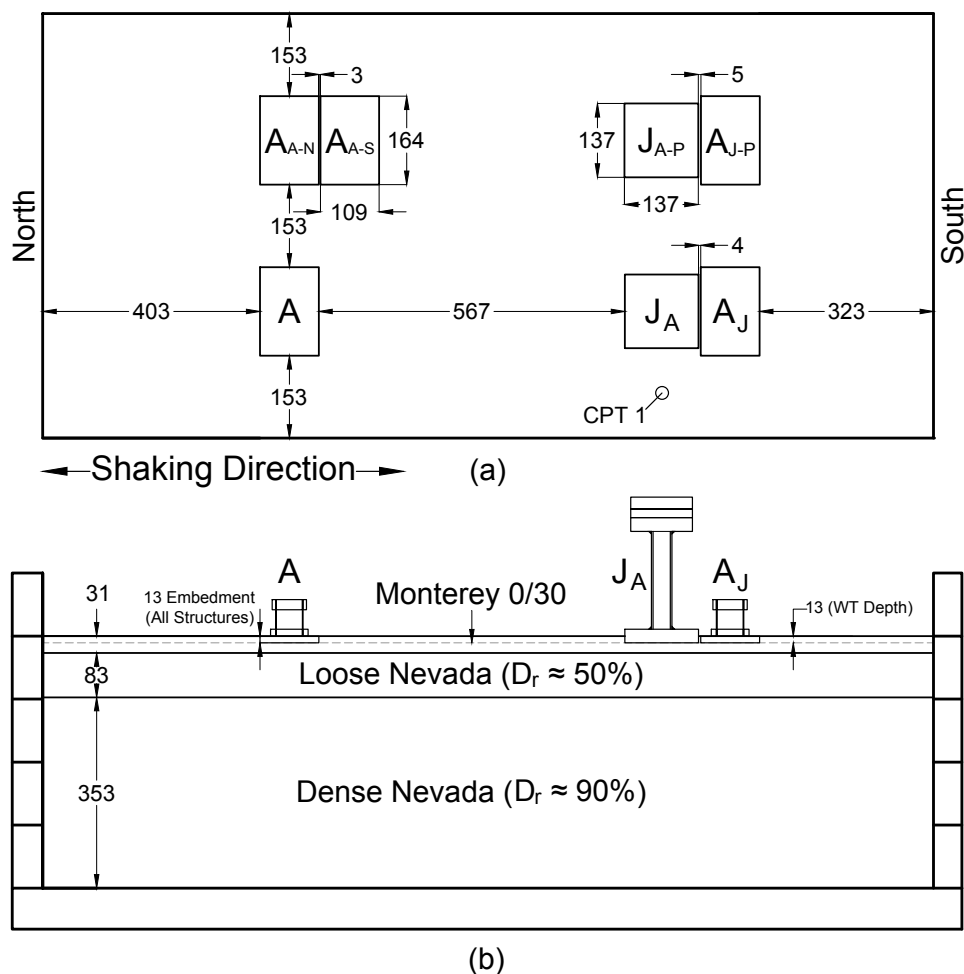


FIGURE 1. (A) PLAN VIEW OF TEST-5 WITH DIMENSIONS IN MILLIMETERS.
(B) PROFILE VIEW OF TEST-5 WITH DIMENSIONS IN MILLIMETERS.

CONFIGURATION OF TEST-6

Test-6 expands on Test-5 by using a similar test plan with some key variations. The changes include a new structure type, lower relative density in the liquefiable layer, and increased spacing between adjacent structures. Maintaining the other key test parameters permits comparisons with Test-5 as well as other recent centrifuge tests (e.g., Dashti et al. 2010a, b; Allmond and Kutter 2012, 2013).

Table 1 contains key parameters of the A and J structures described previously. The Test-5 data report (Zupan et al. 2013) already includes a detailed review of these structures, which will not be repeated here. Note that the Structure A weights listed in the Test-5 data report did not include the LP flags, which is why they are slightly lower than in Table 1. The Dashti et al. (2010a, b) tests used a

continuous wall instead of individual LP flags, which accounts for the higher weights reported in those tests.

Test-6 includes a new K structure, based on a modified version of Structure A. The increased contact pressure of K is similar to Structure J, whereas other properties remain similar to the original A structure. Table 1 lists key parameters for Structure K. The photographs in Figure 2 show Structure K with increased bearing pressure achieved by replacing the aluminum footing with steel and adding several lead weights. The symmetric placement of these weights above and below the existing deck maintained the same center of gravity as structure A. The use of thicker columns (1/16 inch) kept the period similar to structure A after accounting for the additional deck mass. The placement of the lead weights ensured sufficient clearance around the structure columns. Appendix B contains drawings of the modified steel footing and columns in addition to calculations of key parameters.



(a)



(b)

FIGURE 2. (A) PROFILE VIEW OF STRUCTURE K
(B) PLAN VIEW OF STRUCTURE K

Test-6 followed a layout similar to Test-5, with four quadrants as shown in Figure 3. The isolated A structure in the southeast quadrant acts as a control for the other two adjacent A type structures (A_J and A_K) to examine the effects of SSSI. The isolated A structure also provides a common link with Test-5 and Dashti et al. (2010a; 2010b). For example, the response of the isolated A structure can be compared between tests to investigate the effect of changing relative density. The isolated K structure in the southwest quadrant acts as a control for K_A . This isolated K structure also can be compared to the isolated A structure to examine the effect of increased contact pressure with otherwise similar conditions. The northeast quadrant contains an A-J pair similar to the A-J pair used in Test-5. However, in the present test the spacing between structures is increased. Finally, the northwest quadrant contains an A-K pair.

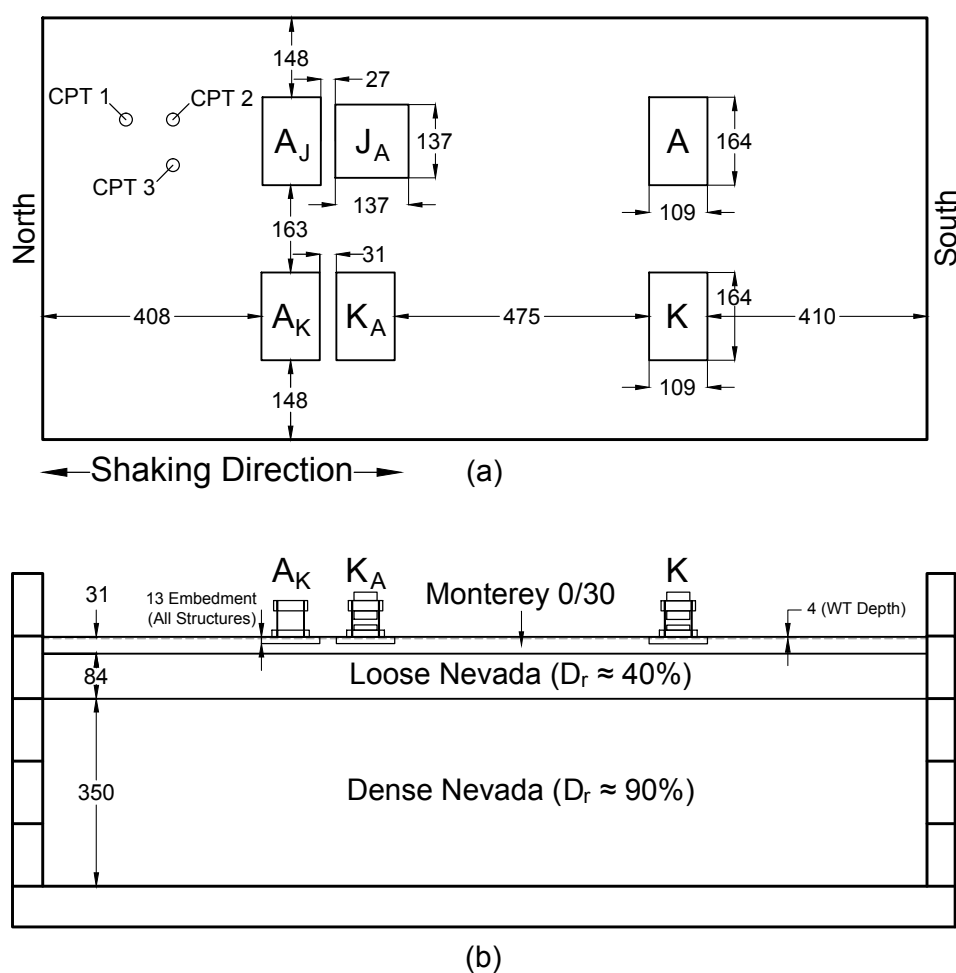


FIGURE 3. (A) PLAN VIEW OF TEST-6 WITH DIMENSIONS IN MILLIMETERS
(B) PROFILE VIEW OF TEST-6 WITH DIMENSIONS IN MILLIMETERS

SOIL AND PORE FLUID PROPERTIES

The soil profile in Test-6 has a lower relative density loose layer than Test-5, but the profiles are otherwise quite similar. Figure 3b shows the structures embedded 13 mm in a dense Monterey 0/30 surface layer 31 mm (1.7 m prototype) thick. The 84 mm (4.6 m prototype) thick loose Nevada layer has an estimated relative density of $40\pm 5\%$. Finally, a dense Nevada layer with a relative density of $90\pm 5\%$ extends 350 mm (19.3 m prototype) to the base of the model container.

A hydroxypropyl methylcellulose (HPMC) solution with a nominal viscosity of 21 cSt was used to saturate the model. Viscosity measurements taken with an Ubbelohde type viscometer before (25 cSt at 23°C) and after spinning (17 cSt at 32°C) used in equation 6 ($v_t = v_0 10^{-bt}$) from Stewart et al. (1998) result in estimates of b and v_0 . Using 27°C as the estimated temperature during shaking results in a viscosity estimate of 21 cSt. The fluid level typically had a depth of 4 mm based on static pore pressures at the base of the model container.

Nevada sand is a mined, non-processed, material. Therefore, the engineering properties of Nevada sand will change with each batch delivered to the CGM. In 2010, Cooper Testing Labs evaluated the batch of Nevada sand used during Test-6 as well as Test-5. The laboratory tests included particle size distribution, minimum and maximum index unit weight (ASTM D4254 and ASTM D4253), and specific gravity (ASTM D854). Table 2 summarizes the key findings from these tests.

As described by Wu (2002), Monterey 0/30 sand is a commercially available washed and sieved beach sand. It is a uniform, medium-grained, sub-rounded, clean sand composed primarily of white to tan quartz grains with a smaller amount of darker feldspar and mica grains (Wu 2002; Kammerer et al. 2002). The average grain size, D_{50} , is approximately 0.35 mm to 0.45 mm, and the coefficient of uniformity (C_u) is between 1.2 and 1.3 (Kammerer et al. 2002). Dashti (2009) provides a summary, reproduced here as Table 3, of the specific gravities, minimum and maximum void ratios, and minimum and maximum unit weights reported by previous researchers. The Test-6 target parameters reported in Table 3 are the same as used by Dashti (2009).

TABLE 2. IMPORTANT SOIL PROPERTIES OF NEVADA SAND

Quantity	Value
Supplier	Pyro Minerals, 2510 Wood Street Oakland, CA 94607
Classification	SP-SM
Gradation	Poor
Passing #200	6.7%
Specific Gravity ¹	2.66
D ₃₀	0.11 mm
D ₆₀	0.16 mm
Coefficient of Uniformity	2.07
$\gamma_{d,max}$ (kN/m ³) ¹	17.2
$\gamma_{d,min}$ (kN/m ³) ¹	14.7

¹ Provided by Cooper Labs (2010) and available on CGM wiki

TABLE 3. IMPORTANT SOIL PROPERTIES FOR MONTEREY 0/30 SAND (REPRODUCED FROM DASHTI, 2009)

Source	Method	G _s	e _{min}	e _{max}	$\gamma_{d,min}$ (kN/m ³)	$\gamma_{d,max}$ (kN/m ³)
Wu (1999)	Dry Tipping	2.64	0.541	0.855	13.96	16.81
Nova-Roessing (1998)	Modified Japanese	-	0.53	0.83	14.15	16.93
Our Target	-	2.64	0.536	0.843	14.06	16.86

SCALE FACTORS

Test-6 used a target centrifugal acceleration of 55g at the center of the loose layer, which corresponds to a rotational velocity of 75.9 RPM. Table 4 lists the relevant scale factors to convert data between prototype and model scale. For additional information regarding scale factors, and other seismic centrifuge testing topics, see Kutter (1995).

TABLE 4. IMPORTANT SCALE FACTORS FOR CENTRIFUGE TESTING; N= CENTRIFUGAL ACCELERATION = 55

Quantity	Model Dimension/ Prototype Dimension
Density	1
Dynamic Time	1/N
Force	1/N ²
Frequency	N
Length	1/N
Mass	1/N ³
Period	1/N
Strain	1
Stress	1

MODEL CONSTRUCTION

The following steps outline the model construction process:

1. All sensors were tested to ensure they functioned properly. Sensitivities of the linear potentiometers and pore pressure transducers were estimated following the calibration procedures recommended by the CGM staff.
2. The structures used previously in Test-5 were cleaned and prepped for testing. Two of the A structures were modified into K structures by replacing the footing, columns and adding additional lead weights. The new steel footings were coated with epoxy and Monterey 0/30 sand, similar to existing structures. Vertical and horizontal LP flags were attached to the structures as needed.
3. Plastic mounting blocks for the ICP accelerometers were glued at the desired locations. MEMS accelerometers were attached to the deck masses with screws or glue. The fixed base period of each structure was estimated using the Fourier amplitude spectrum after clamping down the structure footing and striking the deck mass.
4. Container FSB 2.1 (internal dimensions: 1651x787 mm) is shown in Figure 4. Six porous stones were placed at each end of the container base. A large tube connected each stone to a saturation trough to allow the model to saturate from the base up. A second, smaller tube attached to the other end of each porous stone allowed any trapped air to escape during saturation.

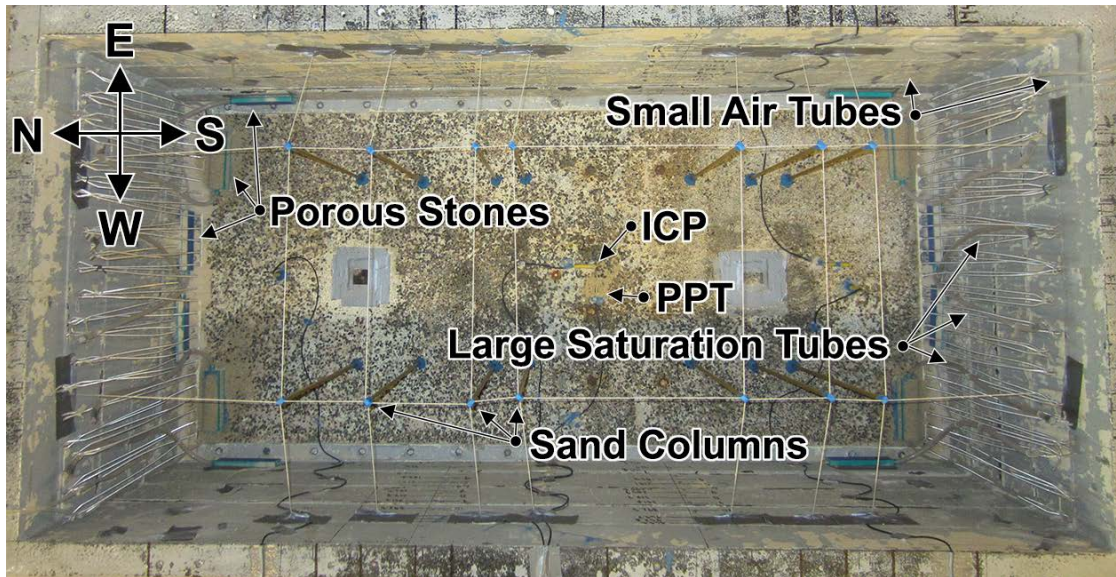


FIGURE 4. PLAN VIEW OF MODEL CONTAINER PRIOR TO PLUVIATION

5. ICP accelerometers and pore pressure transducers were positioned at the base of the container. Modeling clay held the sensors in place at the container base, whereas duct tape fixed the routed cables to the container walls
6. Thin metal tubes used in creating colored sand columns were held in place with modeling clay and string. A sand coating ensured that the modeling clay would not stick to the metal tubes during removal. Throughout construction, the metal tubes were periodically checked and adjusted to remain vertical. Following the pluviation of lift 3, there was sufficient sand in the container to hold them in place, so the string was removed.
7. The container was weighed.
8. The pluviators were calibrated by varying the drop height and sand flow rate into a cylinder of known volume shown in Figure 5a.
9. The blue, rotating-drum pluviator shown in Figure 5b was used for the dense Nevada layer. The lift heights were chosen to coincide with desired instrumentation elevations.
10. Following each lift, a vacuum was used to groom the surface to a consistent elevation as shown in Figure 5c.
11. Each dense Nevada lift was compacted using the vibratory plate shown in Figure 5d to achieve a higher density. The vibratory plate was used in a consistent manner to help achieve a uniform density in all lifts.



(a)



(b)



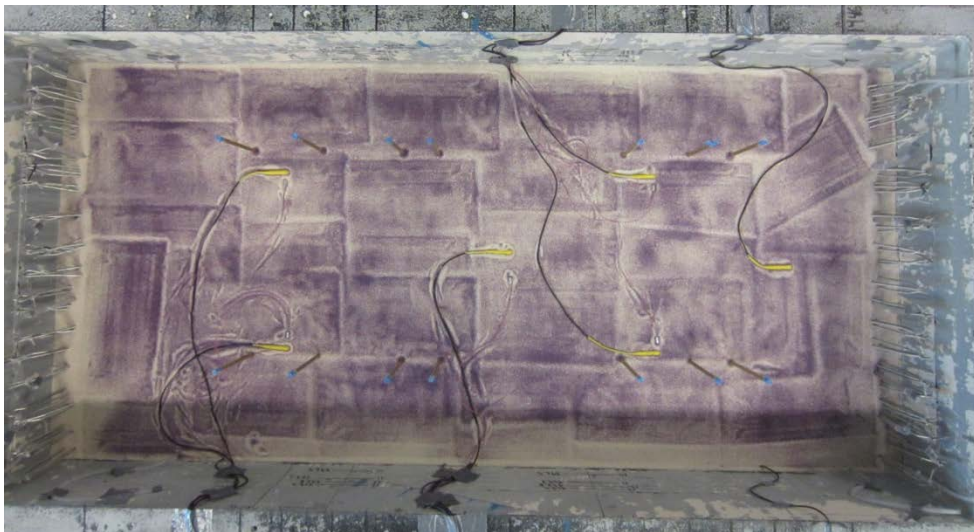
(c)



(d)

FIGURE 5. (A) CALIBRATION OF THE LARGE PLUVIATOR (B) PLUVIATION OF THE DENSE NEVADA LAYER (C) VACUUMING EXCESS SAND AFTER PLUVIATING A LIFT (D) SAND AFTER VIBRATORY DENSIFICATION

12. The final elevation of each lift was measured at a number of locations (typically 15) throughout the model container to obtain a reasonable average. The container was also weighed following each lift. Relative density calculations using the weight and thickness of each lift acted as a rough check that target densities were achieved.
13. Instruments were carefully positioned at the required elevations, and the cables were routed in a manner that limited their presence beneath structures. The as-built elevation of each sensor was also measured.
14. A thin layer of colored sand was added between the dense and loose Nevada sand layers to make the interface visible during excavation.
15. The loose Nevada layer was also pluviated using the large, blue pluviator; however, a substantially increased flow rate and lower drop height was used as shown in Figure 6b.
16. Thin layers of colored sand added near the midpoint of the loose layer and the top of the loose layer shown in Figure 6c made these elevations visible during excavation. A small plastic tube added to the northwest corner served as a fluid observation well during testing.



(a)



(b)



(c)

FIGURE 6. (A) COLORED SAND AND INSTRUMENTATION AT TOP OF DENSE LAYER.
 (B) PLUVIATION OF THE LOOSE NEVADA LAYER.
 (C) COLORED SAND AND INSTRUMENTATION AT TOP OF LOOSE LAYER.

17. The Monterey 0/30 layer was pluviated using the small pluviator shown in Figure 7a.
18. The sand column tubes were filled with colored sand and carefully removed.
19. The structures require a slight tilt in the east-west direction to account for the radial gravitational field. A slight slope was excavated using razor blades as shown in Figure 7b. This careful excavation minimized disturbance to the Monterey sand as well as the underlying loose Nevada sand. Final adjustments to tilt and position were made after placing each structure in its sloped

excavation. Only the footing component of J_A was placed at this time because of space constraints during saturation.

20. The cardboard covers shown in Figure 7c served to keep structures clean and reduce variation in the relative density around each structure due to sand bouncing during pluviation.
21. After the final Monterey lift was pluviated, the surface was curved using a series of “steps” (Figure 7d) to account for the radial gravitational field at 55g. This resulted in the edges being around 9 mm higher than the center. Any excess sand in the structures was carefully vacuumed out.

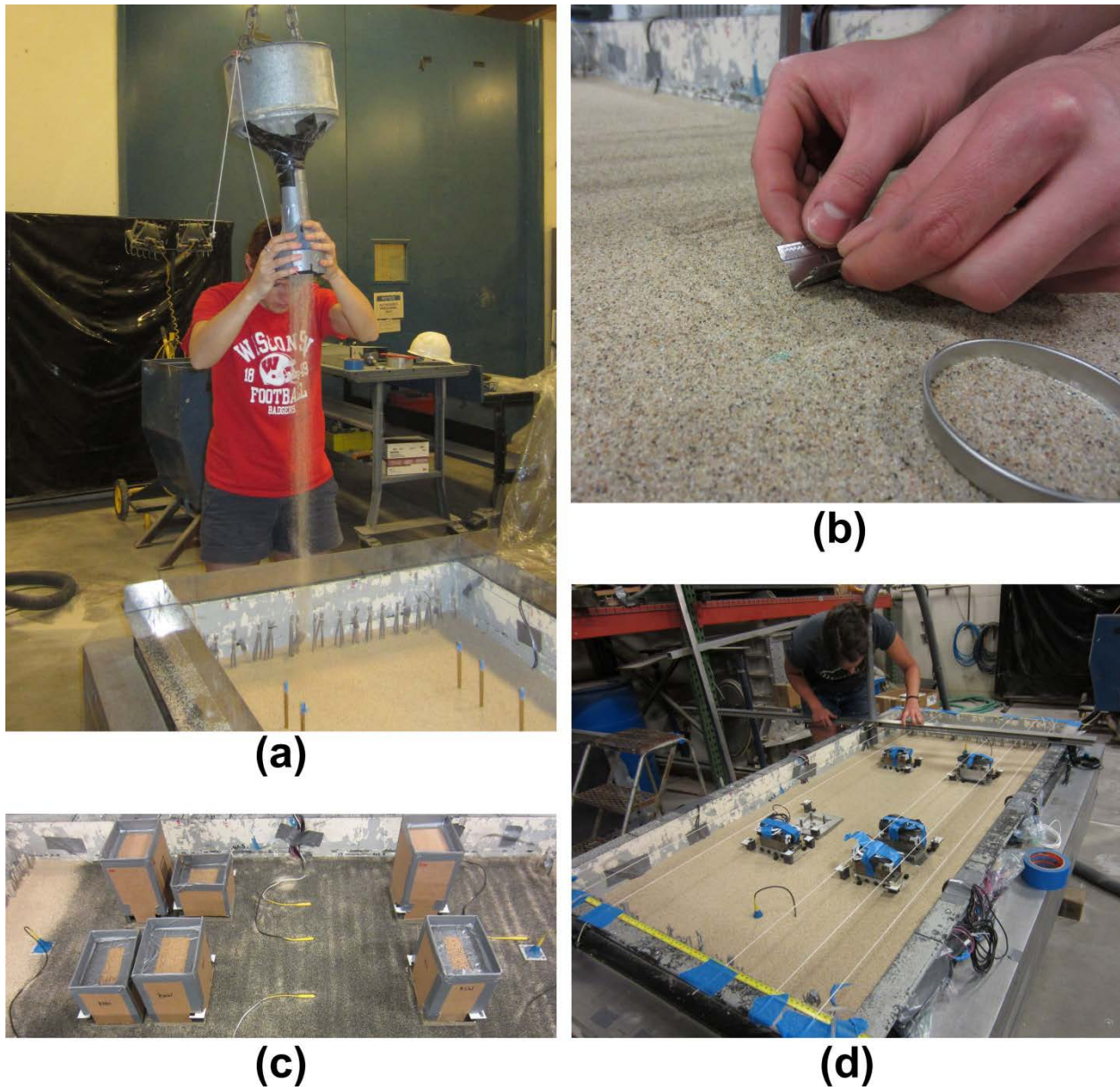


FIGURE 7. (A) SMALL PLUVIATOR USED FOR MONTEREY 0/30
 (B) EXCAVATING SMALL SLOPE FOR TILTED STRUCTURES
 (C) STRUCTURES COVERED AND THIN COLORED SAND LAYER PLACE
 (D) CREATION OF AN APPROXIMATELY CURVED SURFACE

22. The displacement rack shown in Figure 8 held the linear potentiometers in the desired locations. The rack was sufficiently stiff to limit deflections from self-weight and dynamic shaking. LP holders were aligned with the LP flags previously attached to the structures. Plastic plates on the model surface served as contact points for the free-field LPs.

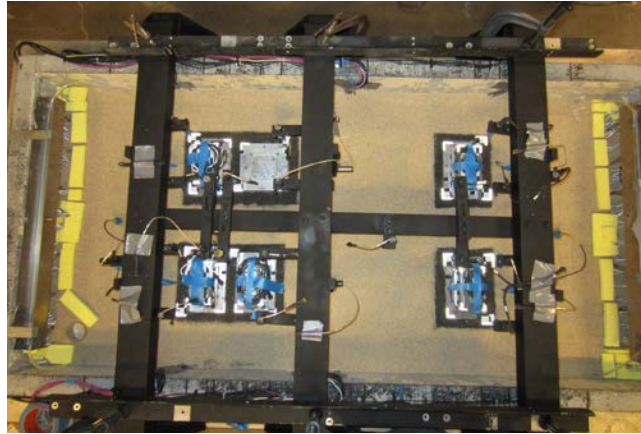


FIGURE 8. DISPLACEMENT RACK

23. The saturation troughs shown in Figure 8 were added to the north and south ends of the container and connected to the large saturation tubes. Sponges acted to catch any trough overflow and limit erosion.
24. After removing the displacement rack, the model was transported to the centrifuge arm.
25. The model was covered with the airtight saturation lid shown in Figure 9, brought under a vacuum and flushed twice with CO_2 . While under vacuum, de-aired methylcellulose solution flowed into the saturation troughs, through tubes connected to the porous stones and into the base of the container. Careful adjustment of the fluid flow rate into the troughs ensured that they remained partially filled but did not overflow. After 48 hours, the required flow rate had dramatically decreased as the bottom portion of the model became saturated. At this point, the troughs were permitted to overflow in a slow, controlled manner, while saturation continued for an additional 16 hours. The vacuum was then released and the saturation lid removed.



FIGURE 9. MODEL DURING SATURATION

26. The displacement rack was positioned and bolted to the model container.
27. The J superstructure was carefully bolted to the footing to minimize soil disturbance.
28. ICP accelerometers were attached to the structures. All instrumentation was routed toward the north end of the model, and sensor cables were positioned with sufficient slack ensuring they did not interfere with structure response or become detached during shaking. Rubber bands connecting horizontal LPs to their LP flags served to help maintain continuous contact during shaking.
29. Instrumentation cables were plugged into the appropriate channels and tested. Any problematic sensors were replaced if possible (i.e., not in the soil).

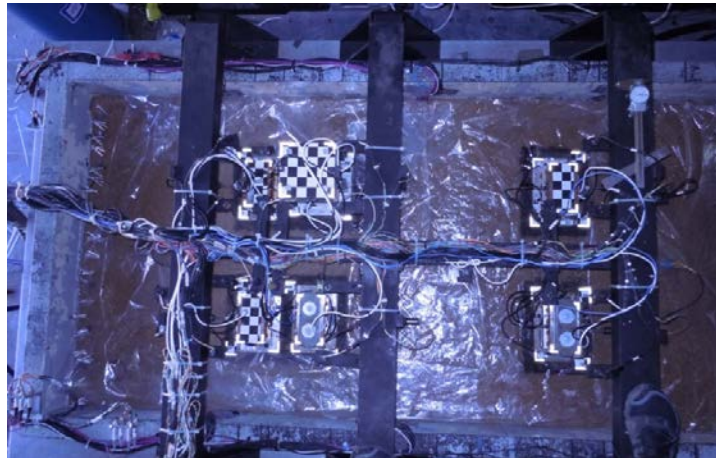


FIGURE 10. MODEL AFTER SATURATION

30. The CPT and cameras were positioned and tested.
31. Following a final inspection, the model was ready to spin up.

AS-BUILT MODEL

The model layout previously shown in Figure 3 reflects the as-built model geometry based on measurements taken during the construction process, which should be accurate to within 1 to 2 mm. Some additional measurements were taken after saturation, which were generally quite similar. Table 5 contains the thickness and weight (up to lift 12) of each lift. The initial and end elevations of each lift were based on numerous (typically 15) measurements taken across the sand surface. Relative density calculations for individual lifts are extremely sensitive to small (e.g., 1 mm) height variations. However, combining all

lifts in a layer and then calculating the relative density is more reliable due to the increased thickness; Table 5 includes these calculated values. The calculations do not include the first lift because the base of the model container is uneven, which makes the volume uncertain. The calculated relative densities, particularly for the loose layer, are still sensitive to small changes in the measured layer thickness. For example, the calculated loose layer relative density changes from 60% to 43% with only a 2 mm increase in measured thickness. Considering the thickness requires two measurements, at the bottom and top of each lift, as well as the difficulty in measuring the sand surface, a 2 mm error provides a reasonable example. The scale used to measure the weight of the model container, although less significant, is a second potential source of error.

TABLE 5. SOIL PROFILE MEASUREMENTS DURING PLUVIATION

Lift Number	Layer Type	Layer Base Elevation (mm)	Layer Top Elevation (mm)	Mass (kg)	Calculated Relative Density (%) ¹	Best Estimate Relative Density (%) ²
1		0	46	100		
2		46	89	94		
3		89	136	106		
4	Dense Nevada	136	185	107		
5		185	212	63	92	90
6		212	251	93		
7		251	283	71		
8		283	318	78		
9	318	351	72			
10	Loose Nevada	351	393	88		
11		393	423	66	60	40
12		423	435			
13	Monterey 0/30	435	456			85
14		456	466 ³			

¹Based on measured mass and layer volumes

²Based on CPT data, measured mass and volume, and pluviator calibrations

³Elevation at the midpoint of each structure in the east-west (curved) direction

Three cone penetration tests were performed during Test-6 at the locations shown in Figure 3. CPT 1 was performed prior to any shaking event, whereas CPT 2 was performed after the moderate TCU event, and CPT 3 was performed at the end of testing. Figure 11 shows the cone tip resistance as a function of depth in prototype scale; horizontal lines indicate the interface between layers. The Test-5 CPT, performed prior to shaking, is included as a comparison. Figure 11 clearly illustrates that Test-6 had lower tip resistances in the liquefiable layer compared to Test-5, which indicates lower relative densities. The cone tip senses the dense Nevada sand and begins to increase well before the interface. The 330 mm (prototype scale) cone diameter exaggerates this effect.

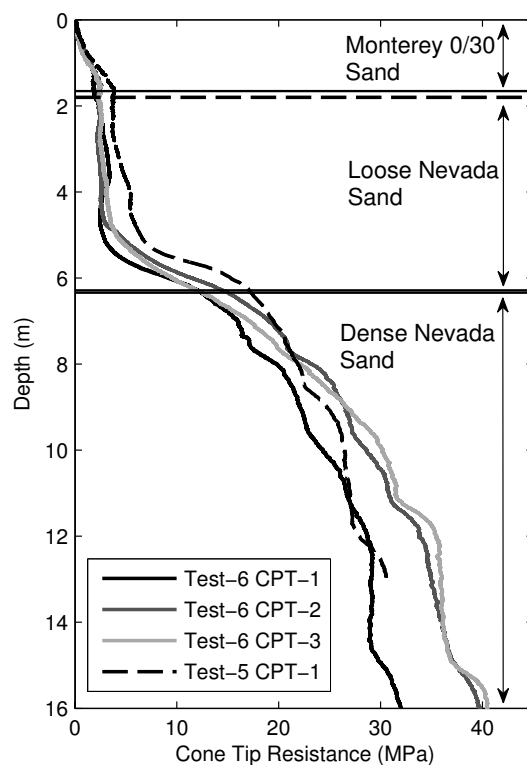


FIGURE 11. CONE TIP RESISTANCE AS A FUNCTION OF DEPTH (PROTOTYPE SCALE)

Several correlations relate measured cone tip resistance to relative density estimates. Figure 12 shows three of these correlations applied to the CPTs performed during Test-5 and Test-6. The Salgado and Prezzi (2007) correlation requires the horizontal effective stress, which was calculated assuming $K_0=0.5$. The Test-5 loose layer clearly had a higher relative density than Test-6, regardless of the correlation used. Figure 12d provides a direct comparison among the correlations using the Test-6 CPT-1 data. The 40% relative density best estimate in Table 5 takes into account the CPT data, construction measurements and pluviator calibration.

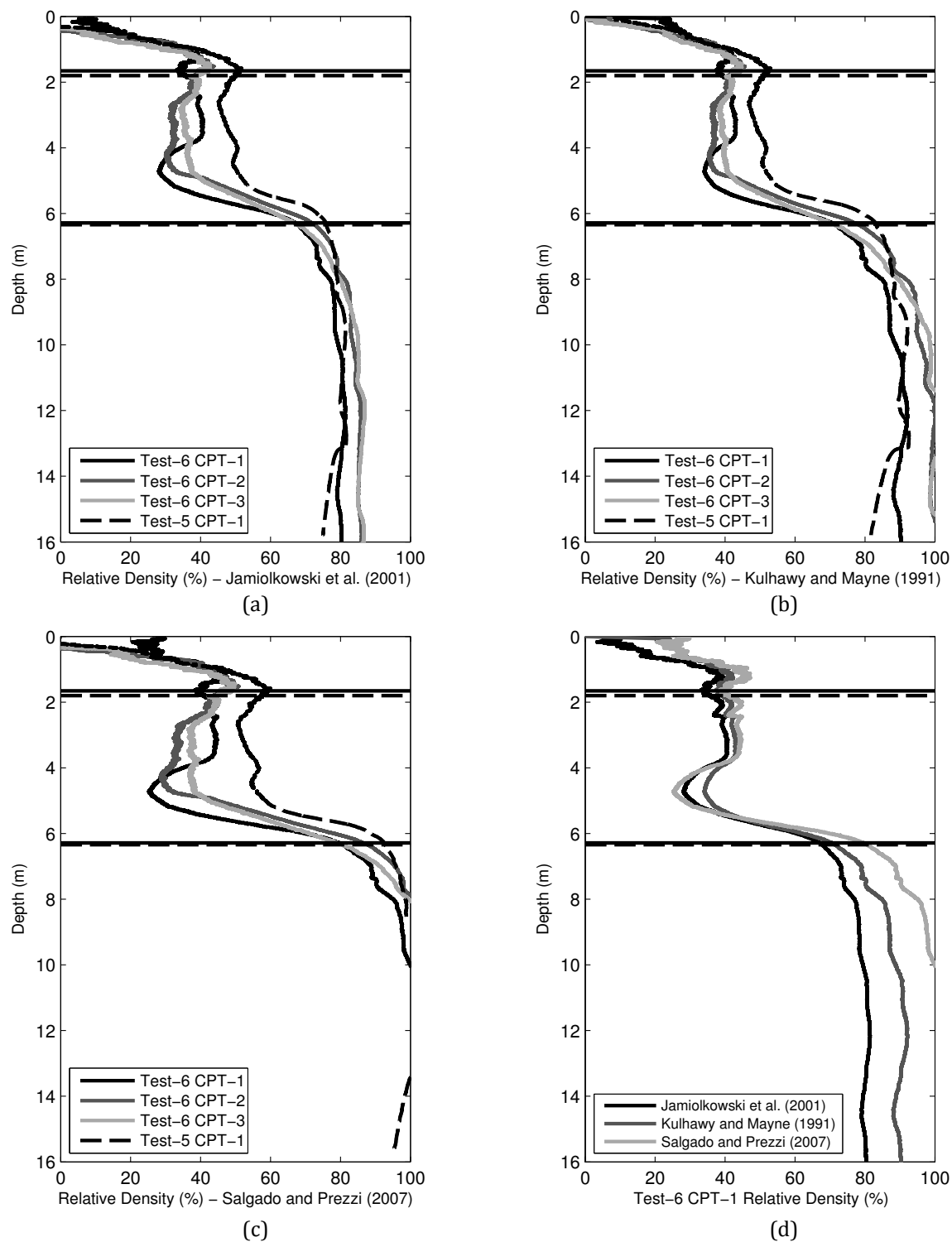


FIGURE 12. CPT BASED RELATIVE DENSITY WITH DEPTH: (A) JAMIOLKOWSKI ET AL. 2001 (B) KULHAWY AND MAYNE 1991 (C) SALGADO AND PREZZI 2007 (D) TEST-6 CPT-1 COMPARISON BETWEEN CORRELATIONS

INSTRUMENTATION AND MEASUREMENTS

This test used 64 integrated circuit piezoelectric (ICP) accelerometers, 21 micro-electro-mechanical system (MEMS) accelerometers, 27 linear potentiometers (LPs) and 29 pore pressure transducers (PPTs). In addition, the CPT used a tip load cell, a rod load cell, and an LP. The PPTs had a range of 100 psi (689 kPa). The ICP accelerometers had ranges of either ± 50 g or ± 100 g, whereas all MEMS were ± 100 g. The LPs used had strokes of 1 in (25 mm), 2 in (51 mm), and 3 in (76 mm). Appendix A contains details of each instrument including location, orientation, and sensitivity factor. Table 6 lists the initial coordinates of each structure relative to the global datum at the north-west bottom interior corner.

TABLE 6. INITIAL STRUCTURE LOCATIONS: BOTTOM CENTER OF EACH FOOTING

Structure	X Coordinate (mm)	Y Coordinate (mm)	Z Coordinate (mm)
A	1188.8	558.2	452.8
K	1193.8	230.9	452.6
A _K	473.8	230.2	452.5
K _A	611.8	230.2	453.0
A _J	472.9	551.9	452.5
J _A	619.7	553.3	452.2

In the following figures, the DAQ index is listed next to each sensor for simplicity because the instrumentation summary and data files are also organized by DAQ index. In cases where multiple sensors align out of the plane of view, there are multiple DAQ indices listed. Figure 13 and Figure 14 show the locations of the structure accelerometers. The deck accelerometers are shaded in grey to help distinguish them from the footing accelerometers shown in black. Figure 15 shows the soil accelerometers locations. There are five accelerometers not shown that were on model container exterior. These included the two house accelerometers (DAQ channels 0 and 1) on the shaker, and two MEMS accelerometers (138 and 139) on the exterior second and fourth rings (from the bottom). Finally, a vertical MEMS accelerometer on the southeast K_A LP holder provided typical movements of the rack and LP holder during shaking. Figure 16 shows the PPT locations. The measurements provided are to the top of the end of each soil accelerometer and PPT; the measurements for structure accelerometers are to the center of the instrument in contact with the structure (or mounting block). For reference, the PPTs were about 6 mm wide, and the accelerometers were 8.4 mm wide. Figure 17 shows the LP locations.

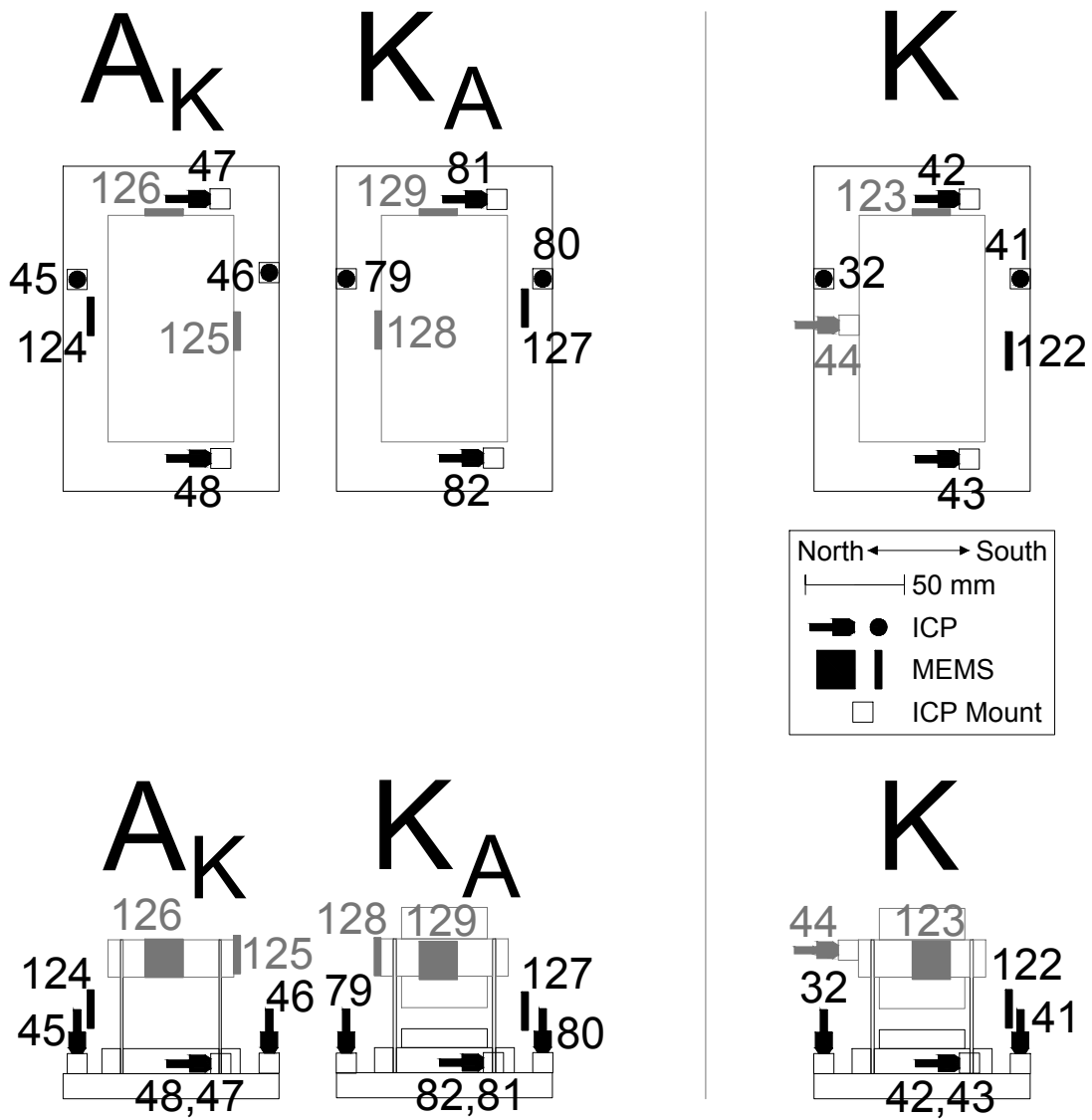


FIGURE 13. PLAN AND PROFILE VIEWS OF A_K , K_A , AND K AS-BUILT ACCELEROMETER LOCATIONS

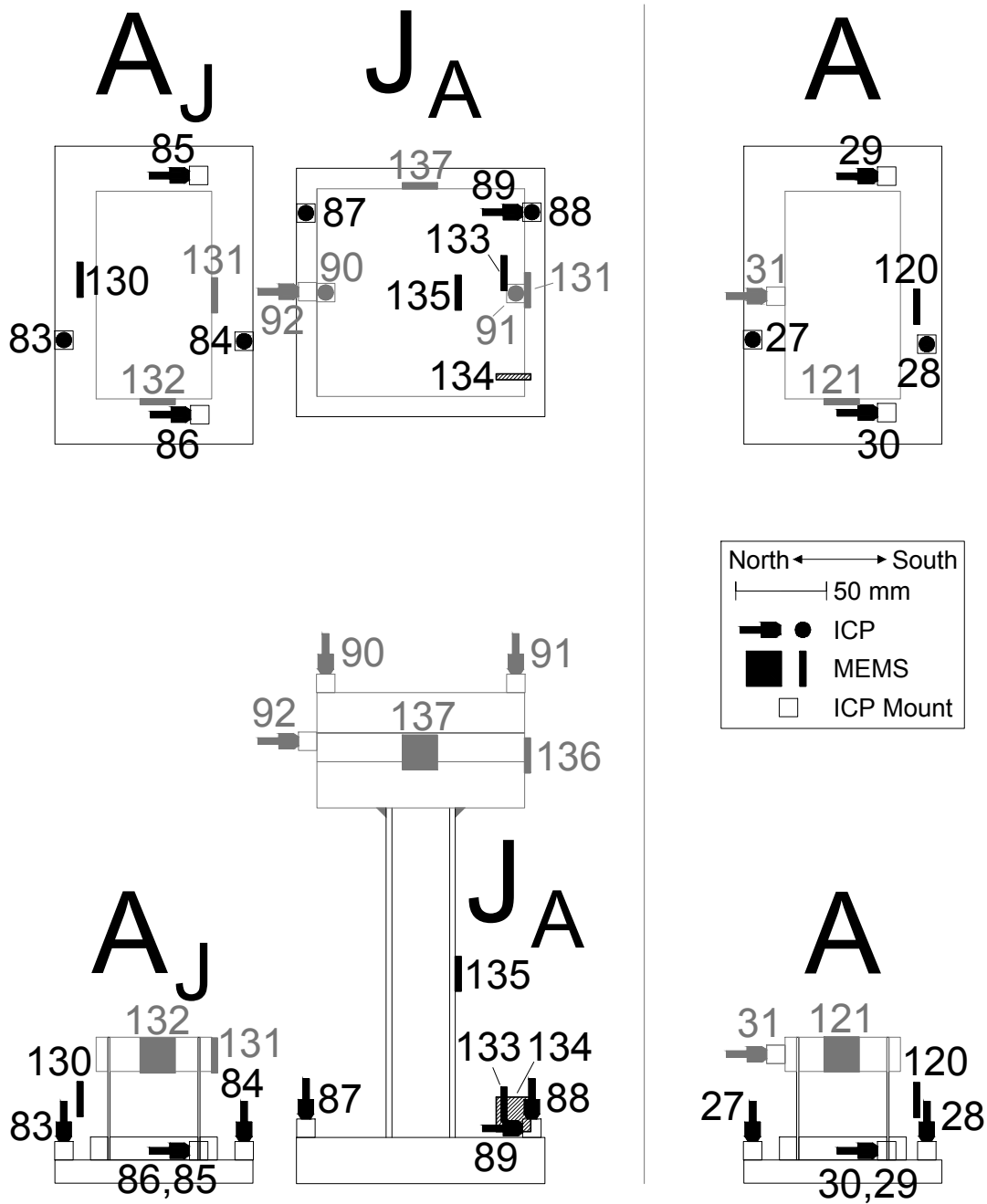


FIGURE 14. PLAN AND PROFILE VIEWS OF AJ, JA, AND A AS-BUILT ACCELEROMETER LOCATIONS

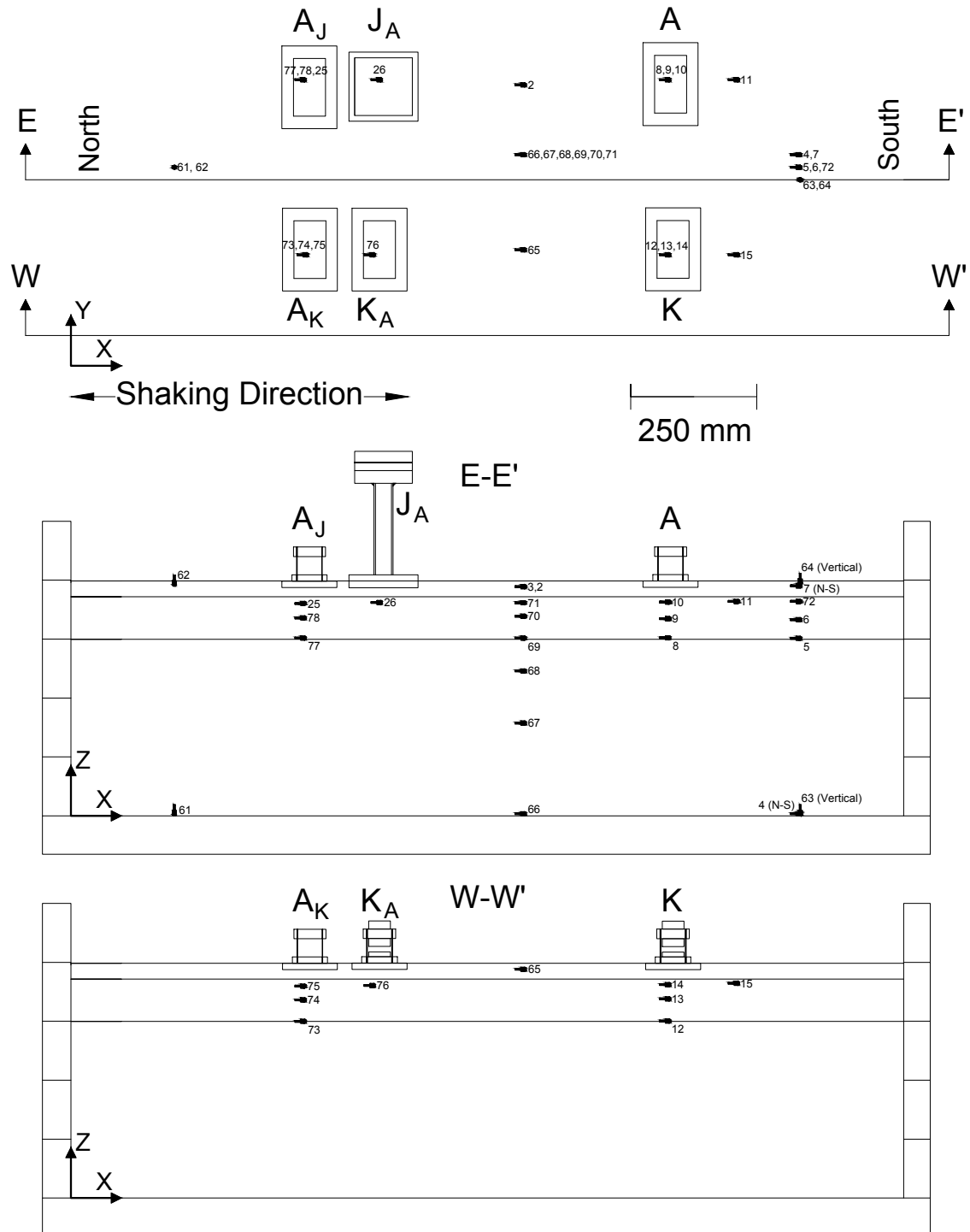


FIGURE 15. SOIL ACCELEROMETER LOCATIONS

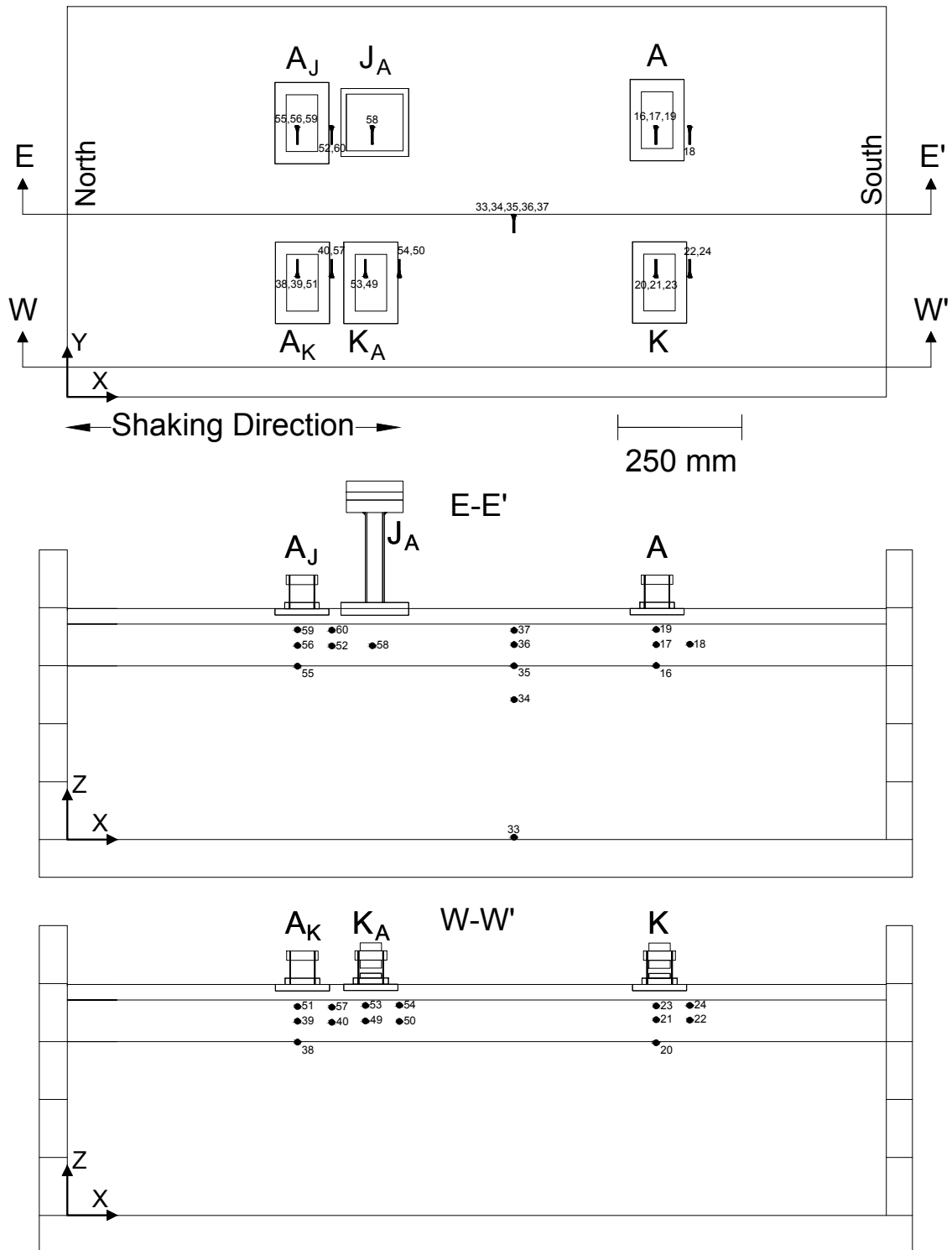


FIGURE 16. PORE PRESSURE TRANSDUCER LOCATIONS

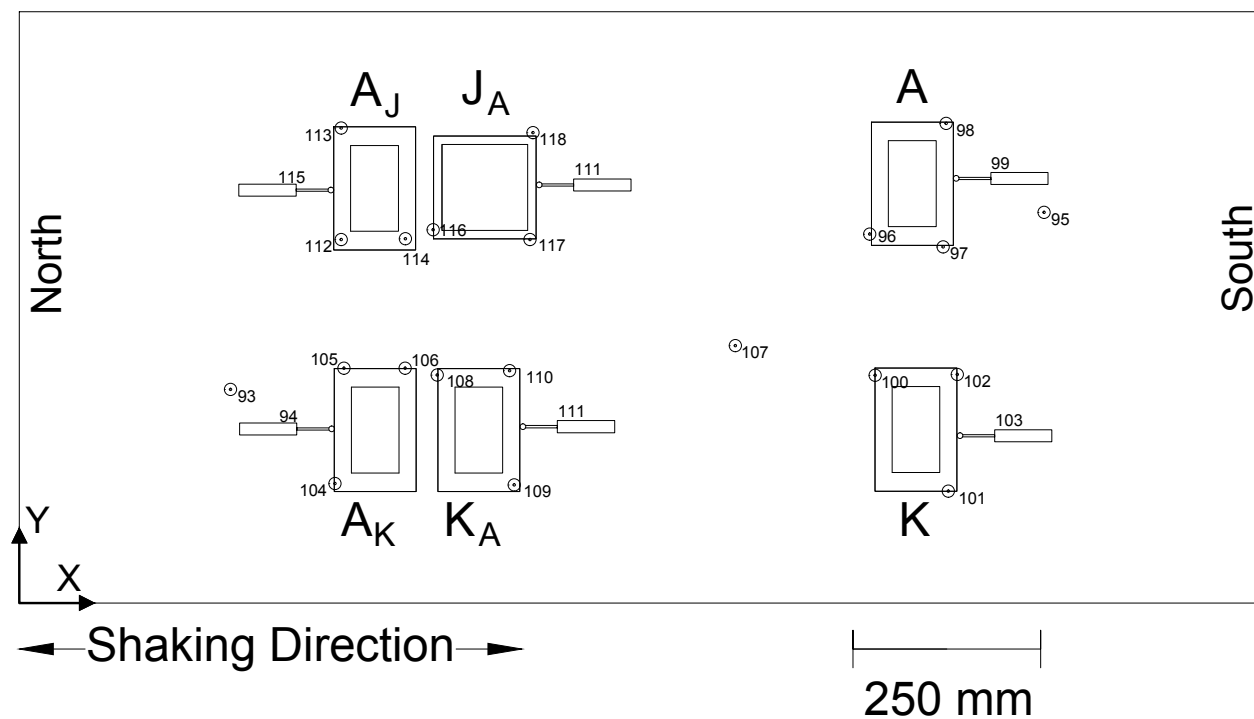


FIGURE 17. LINEAR POTENTIOMETER LOCATIONS

Nine cameras recorded the model during shaking, including two high-speed (240 frames/s) GoPro cameras, which had views of the entire model. Table 7 summarizes the camera views and NEEShub file names. Figure 18 provides an example view of each camera prior to the moderate Port Island event. Unfortunately, the second GoPro did not function during the large Port Island event. Prototype scale (1/N of the capture rate) high-speed camera footage is also available on NEEShub.

TABLE 7. CAMERA SUMMARY

Number	View	File Name
1	Entire container from west	GOPR0003
2	Entire container from east	GOPR0092
3	Bucket from end of arm	End Of Arm 212ptz-170
4	K_A with parts of J_A and A_J from southwest	AXIS P1214-E-171
5	Fluid observation well	AXIS P1204-172
6	Down container centerline from south	AXIS P1204-173
7	Down container centerline from north	AXIS P1214-174
8	CPT rod from CPT frame	AXIS P1214-E-175
9	Isolated A and K structures from northeast	AXIS P1204-176



FIGURE 18. CAMERA VIEWS PRIOR TO THE MODERATE PORT ISLAND EVENT

During the post-shaking model excavation, sensor serial numbers and positions were checked. Figure 19 shows photos of the cross-section beneath each structure. The green sand columns displaced laterally and the footings have clearly tilted as well.

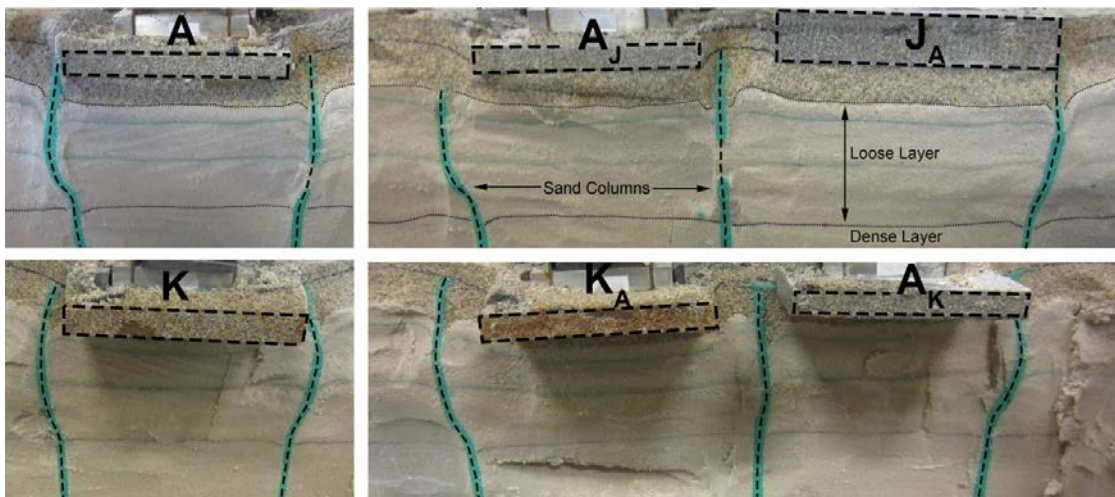


FIGURE 19. CROSS-SECTION PHOTOS TAKEN DURING EXCAVATION

CENTRIFUGE TEST CHRONOLOGY

Table 8 summarizes the testing schedule and data file organization on NEEShub. The centrifuge was spun once on 6/25/2013 and twice on 6/26/2013. The instrumentation did not change during testing, so there is a single instrumentation file for all spins. The desired centrifugal acceleration (N) during all spins was 55g at the center of the loose Nevada layer, corresponding to a nominal effective radius of 8.53 m. The step waves served to test instrumentation and warm-up the centrifuge shaking table.

TABLE 8. TEST-6 TESTING SEQUENCE

Spin ID and Date	NEES hub Trial	ID	Input File	Freq- uency	Amp. Factor	Data File
I 6/25/2013	1	CPT 1	N/A	N/A	N/A	06252013@131202@135909@75.9rpm
	3	SW1	Step.txt	4000	0.9	06252013@131202@140925@76.2rpm
	4	SW2	Step.txt	4000	0.9	06252013@153052@154424@76.5rpm
	5	PRI_small	Kobe0807.txt	2750	0.5	06252013@155037@155906@76.1rpm
II 6/26/2013	6	SW3	Step.txt	4000	0.9	06262013@124047@132612@76.0rpm
	7	PRI_mod	Kobe0807.txt	2750	1.5	06262013@124047@133843@76.0rpm
	8	TCU_mod	TCU078E_it3.txt	11000	0.28	06262013@124047@142019@75.9rpm
	9	CPT 2	N/A	N/A	N/A	06262013@124047@142300@76.1rpm
III 6/26/2013	11	SW4	Step.txt	4000	0.9	06262013@124047@165048@76.0rpm
	12	PRI_Large	Kobe0807.txt	2750	5.1	06262013@124047@170243@76.3rpm
	13	CPT 3	N/A	N/A	N/A	06262013@124047@171158@76.3rpm

DATA PROCESSING

The recently upgraded data acquisition (DAQ) system at UC Davis automatically outputs sensor data in engineering units. This requires a configuration file with a range and sensitivity input for each sensor. Each PPT and LP was calibrated prior to testing to estimate the required sensitivities. The manufacturer specified the sensitivities for the ICP and MEMS accelerometers. The unprocessed data uploaded to NEEShub is in engineering units exactly as produced by the new DAQ system.

The coordinate system used in this test has an origin at the interior northwest corner at the base of the model container. South (x), east (y) and up (z) are the positive directions in this coordinate system. Each sensor has a direction vector (+1 or -1) indicating an orientation in the positive or negative direction. The data is processed by multiplying the unprocessed data with the direction vector and then zeroing the sensors. The processed accelerometers and LPs have the mean of the first 410 data points subtracted from their time histories to zero the sensors. The static pore pressures at each PPT are of interest; therefore, PPTs are zeroed in a different manner. The PPT readings are recorded at 1g, just

before spinning, which together with the static pore pressures during testing can be used solve for the zero reading. Finally, the conversion to prototype scale using the scale factors in Table 4 produces the processed data. The processed data uploaded to NEEShub and shown in Appendix A is not filtered. The time axis of each time history in Appendix A is shifted to move the initiation of shaking to just after $t=0$ by subtracting the following from each time vector: PRI small 276.2 s, PRI moderate 275.6 s, TCU moderate 266 s, PRI large 242.1 s.

KNOWN LIMITATIONS

Structure J_A tilted substantially to the west during the large Port Island event and came to rest on a LP holder. This influenced the settlement of the structure after contact, so it should not be included in analysis for this event. Alternatively, only data after the initial contact could be ignored.

Several instruments did not function properly or at all during testing. Table 8 summarizes these issues with black boxes indicating the events during which a particular sensor did not function. Table 8 may not be exhaustive, and Appendix A and NEEShub contain all data, regardless of quality. The horizontal LPs were not always able to maintain continuous contact with their flags during shaking; however, the residual post shaking displacements should be correct. The footing MEMS mounted to the back of the horizontal LP flags (indicated in grey in Table 8) picked up excessive high frequency vibrations from the flag. However, these MEMS were largely redundant and can be ignored or used to check residual rotation. The filtering of these sensors requires special attention if they will be used in any analysis.

All raw LP data are displacement measurements of the soil or structure relative to the rack. Movements or deflections in the rack from shaking and increased gravitational acceleration are present in the data. The rack was constructed to limit deflections, but still they are often significant. Caution should be used when analyzing raw LP data, especially for time intervals at high frequency or during shaking; LP data is most reliable for low frequency and permanent displacements. High frequency components of displacement are best obtained by integration of accelerometer data.

TABLE 9. NON-FUNCTIONING AND PROBLEMATIC SENSORS DURING TEST-6

DAQ Index	Serial Number	Sensor Type	Sm. PRI	M. PRI	M. TCU	Lg. PRI	Notes
12	99513	ICP					
53	5678	PPT					
54	5883	PPT					
57	5670	PPT					
61	107064	ICP					
73	108953	ICP					
96	111	LP					Excessive drifting and incorrect readings
97	115	LP					Adjusted incorrectly, started out of range
100	119	LP					Out of range
114	216	LP					Fell out of holder during shaking
120	822	MEMS					Flag vibration issue
122	828	MEMS					Flag vibration issue
124	824	MEMS					Flag vibration issue
127	827	MEMS					Flag vibration issue
130	826	MEMS					Flag vibration issue
131	MA022	MEMS					Incorrect readings, scaled version of 130
133	825	MEMS					Flag vibration issue

ORGANIZATION OF APPENDICES

Appendix A contains the instrumentation list and the sensor time histories in prototype engineering units for the four ground motions used. The instrumentation list provides important information on each sensor as described in Table 10.

TABLE 10. COLUMN DEFINITIONS OF THE INSTRUMENTATION LIST PROVIDED IN APPENDIX A

Column	Description
DAQ Channel Number	Index number (rows) for both the unprocessed and processed data sets
Sensor Label	Nomenclature convention used in the test to differentiate between sensors
Sensor Type	ICP = Integrated Circuit Piezoelectric accelerometers PPT = Pore Pressure Transducer LP = Linear Potentiometer MEMS = Micro-Electric-Mechanical Systems LC = Load Cell
Position (mm)	X Global position of the sensor in the X-direction
	Y Global position of the sensor in the Y-direction
	Z Global position of the sensor in the Z-direction
Orientation	I Sensor measurement orientation in the X direction (1= positive, -1= negative)
	J Sensor measurement orientation in the Y direction (1= positive, -1= negative)
	K Sensor measurement orientation in the Z direction (1= positive, -1= negative)
Serial Number	Specific serial number for the sensor either by the manufacturer or by the CGM
Sensor Units	Engineering data units
Channel Name	Channel used for the specific sensor on the arm DAQ system
Calibration Constant (Unit/v)	Constant used internally by the DAQ system to convert raw data to the engineering data provided in the unprocessed data set

Appendix B contains shop drawings for Structure K and a summary of the properties. All data is on NEEShub (www.nees.org) in both unprocessed model scale, as output from the DAQ, and in processed, prototype-scale as described in the data processing section.

REFERENCES

- Allmond, J., and Kutter, B. (2012). “Centrifuge Testing of Rocking Foundations on Saturated Sand and Unconnected Piles: The Fluid Response.” *GeoCongress 2012*, ASCE, 1760–1769.
- Allmond, J. D., and Kutter, B. L. (2013). “Centrifuge Testing of Rocking Foundations on Saturated and Submerged Sand: Centrifuge Data Report for JDA02.” Center for Geotechnical Modeling Data Report UCD/CGMDR – 13/01.
- Dashti, S. (2009). *Toward developing an engineering procedure for evaluating building performance on softened ground*. University of California, Berkeley.
- Dashti, S., Bray, J., Pestana, J., Riemer, M., and Wilson, D. (2010a). “Mechanisms of Seismically Induced Settlement of Buildings with Shallow Foundations on Liquefiable Soil.” *J. of Geotech. Geoenviron. Eng.*, 136(1), 151–164.
- Dashti, S., Bray, J., Pestana, J., Riemer, M., and Wilson, D. (2010b). “Centrifuge Testing to Evaluate and Mitigate Liquefaction-Induced Building Settlement Mechanisms.” *J. of Geotech. Geoenviron. Eng.*, 136(7), 918–929.
- Jamiolkowski, M., LoPresti, D. C. F., and Manassero, M. (2001). “Evaluation of Relative Density and Shear Strength of Sands from Cone Penetration Test and Flat Dilatometer Test.” *Soil Behavior and Soft Ground Construction (GSP119)*, ASCE, Reston, VA., 201–238.
- Kammerer, A., Wu, J., Pestana, J., Riemer, M., and Seed, R. (2002). “Undrained response of Monterey 0/30 sand under multidirectional cyclic simple shear loading conditions: electronic data files.” *University of California, Berkeley, Calif. Report No. UCB/GT/02-02*.
- Kulhawy, F. H., and Mayne, P. W. (1991). “Relative density, SPT, and CPT interrelationships.” *Calibration Chamber Testing*, 197–211.
- Kutter, B. L. (1995). “Recent advances in centrifuge modeling of seismic shaking.” *Proc., 3rd Int. Conf. on Recent Advances in Geotechnical Earthquake Engineering and Soil Dynamics*, 927–942.
- Mason, H. B., Trombetta, N. W., Gille, S. M., Lund, J. N., Zupan, J. D., Jones, K. C., Puangnak, H., Bolisetti, C., Bray, J. D., Hutchinson, T. C., Fiegel, G. L., Kutter, B. L., and Whittaker, A. S. (2010). “Seismic Performance Assessment in Dense Urban Environments: Centrifuge Data Report for HBM04.” University of California at Davis Center for Geotechnical Modeling Report No. UCD/CGMDR-XX/XX, Davis, CA.
- Mason, H. B., Trombetta, N. W., Gille, S. M., Lund, J. N., Zupan, J. D., Puangnak, H., Choy, B. Y., Chen, Z., Bolisetti, C., Bray, J. D., Hutchinson, T. C., Fiegel, G. L., Kutter, B. L., and Whittaker, A. S. (2010). “Seismic Performance Assessment in Dense Urban Environments: Centrifuge Data Report for HBM02.” University of California at Davis Center for Geotechnical Modeling Report No. UCD/CGMDR-XX/XX, Davis, CA.

- Mason, H., Bolisetti, C., Chen, Z., Choy, B., Montgomery, J., Trombetta, N., Patel, J., Bray, J., Fiegel, G., Hutchinson, T., Kutter, B. L., Puangnak, H., Reitherman, R., and Whittaker, A. (2010). "Seismic Performance Assessment in Dense Urban Environments: Centrifuge Data Report for HBM03." University of California at Davis Center for Geotechnical Modeling Report No. UCD/CGMDR-XX/XX, Davis, CA.
- Salgado, R., and Prezzi, M. (2007). "Computation of Cavity Expansion Pressure and Penetration Resistance in Sands." *International Journal of Geomechanics*, 7(4), 251–265.
- Stewart, D. P., Chen, Y.-R., and Kutter, B. L. (1998). "Experience with the Use of Methylcellulose as a Viscous Pore Fluid in Centrifuge Models." *Geotech. Test. J.*, 21(4), 365–369.
- Trombetta, N. W., Zupan, J. D., Bolisetti, C., Puangnak, H., Jones, K. C., Tran, J. K., Bassal, P., Bray, J. D., Hutchinson, T. C., Fiegel, G. L., Kutter, B. L., and Whittaker, A. S. (2011). "Seismic Performance Assessment in Dense Urban Environments: Centrifuge Data Report for NWT01." University of California at Davis Center for Geotechnical Modeling Report No. UCD/CGMDR-XX/XX, Davis, CA.
- Wu, J. (2002). "Liquefaction Triggering and Post-Liquefaction Deformation of Monterey 0/30 Sand Under Uni-Directional Cyclic Simple Shear Loading." University of California, Berkeley.
- Zupan, J. D., Trombetta, N. W., Puangnak, H., Paez, D., Bray, J. D., Kutter, B. L., Hutchinson, T. C., Fiegel, G. L., Bolisetti, C., and Whittaker, A. S. (2013). "Seismic Performance Assessment in Dense Urban Environments: Centrifuge Data Report for Test-5." University of California at Davis Center for Geotechnical Modeling Report No. UCD/CGMDR-XX/XX, Davis, CA.

Appendix B1-A

Test-6 Sensor Time Histories in Prototype Scale

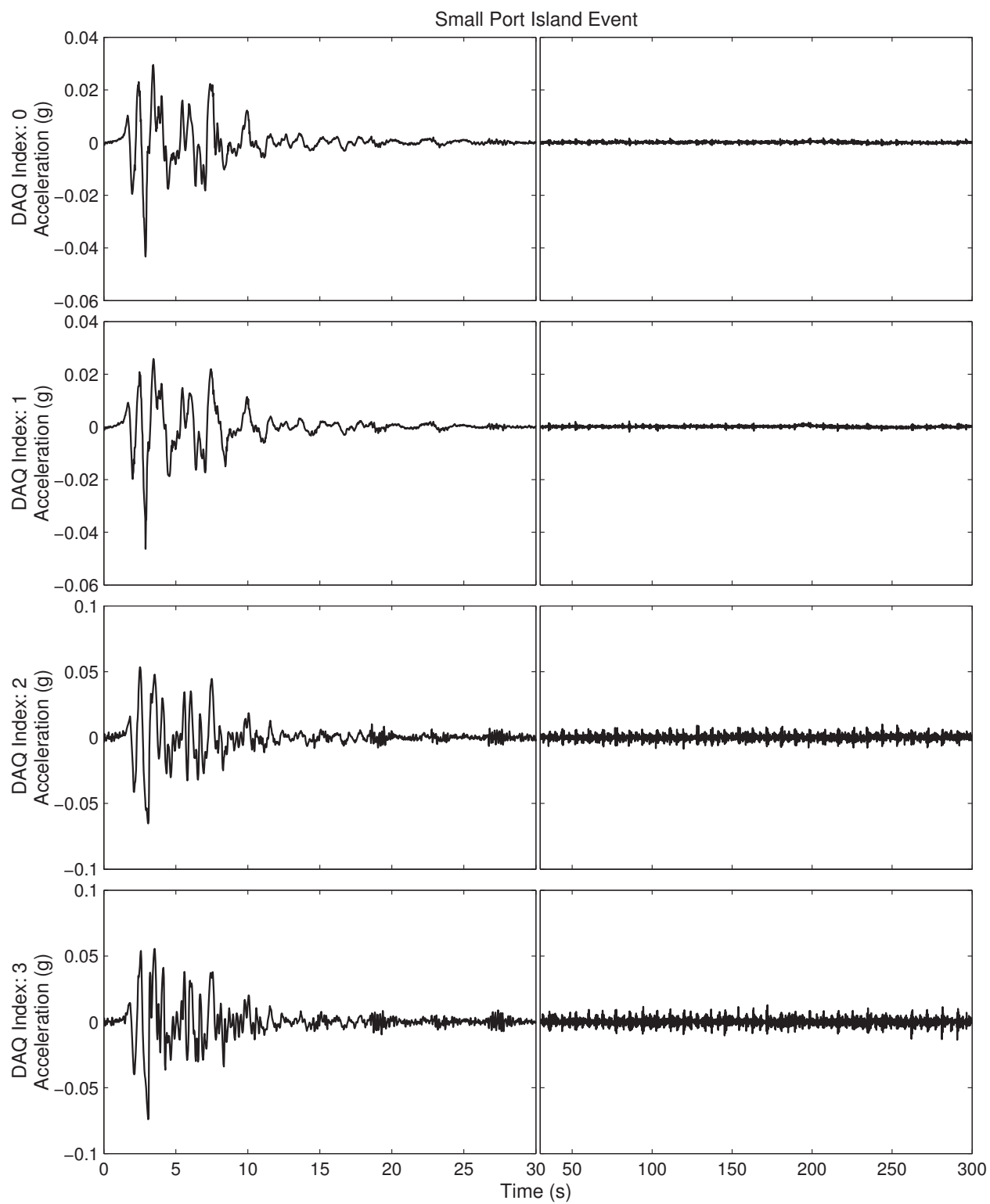
Section	Page Numbers
Instrumentation List	176-179
Small Port Island Event	180-214
Moderate Port Island Event	215-249
Moderate TCU Event	250-284
Large Port Island Event	285-319

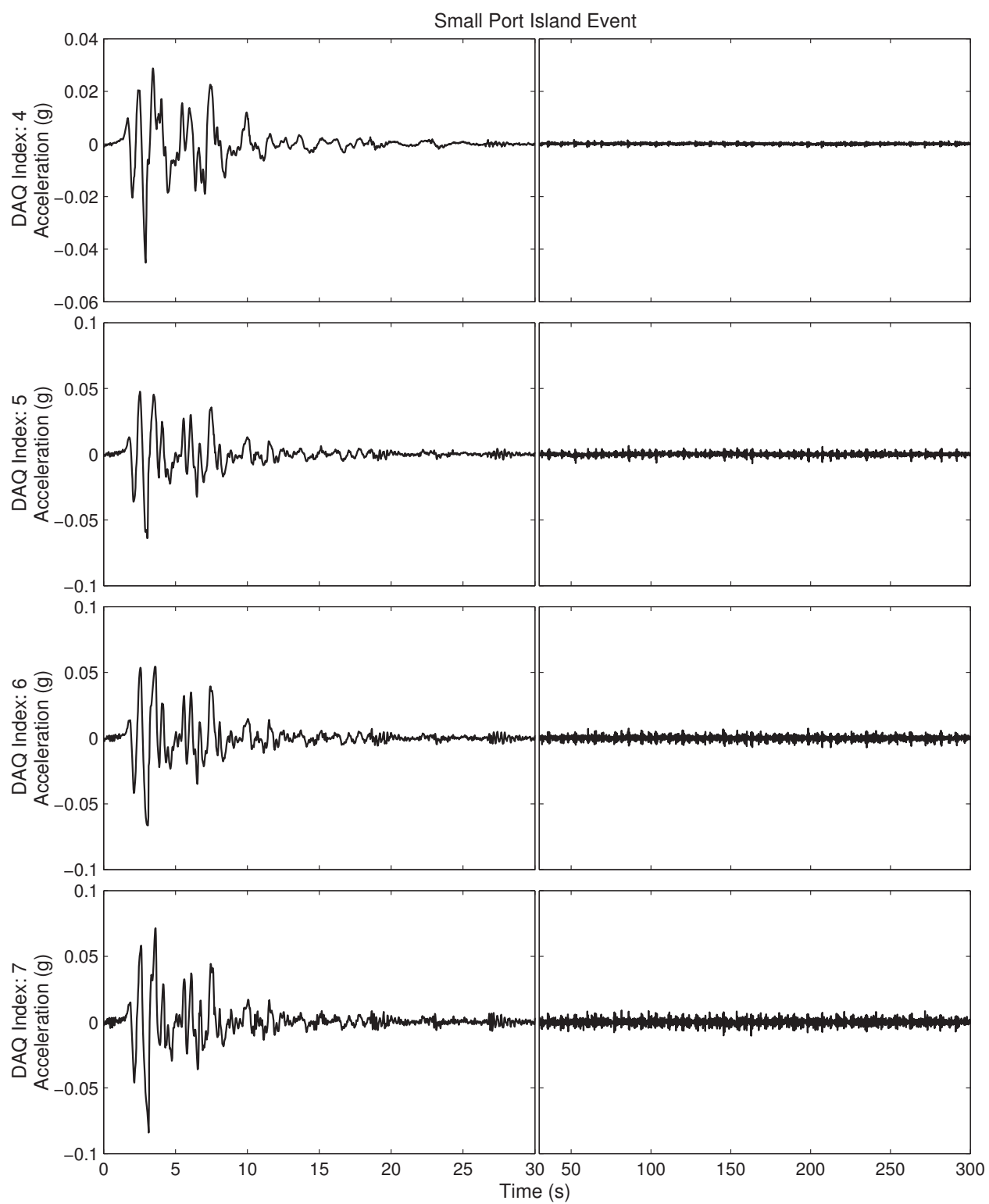
DAQ Channel Number	Sensor Label	Sensor Type	Position (mm)			Orientation			Serial Number	Sensor Units	Channel Name	Calibration Constant (Unit/V)
			X	Y	Z	I	J	K				
0	BHAE	ICP	0.0	787.0	0.0	1	0	0	6025	g	ICP1_0	19.08
1	BHAW	ICP	0.0	0.0	0.0	1	0	0	6021	g	ICP1_1	18.66
2	GHAE	ICP	900.0	557.0	458.5	1	0	0	107646	g	ICP1_2	20.41
3	GHAC7	ICP	900.0	418.5	459.5	1	0	0	127801	g	ICP1_3	20.12
4	GHAS1	ICP	1446.0	418.5	8.4	1	0	0	107273	g	ICP1_4	20.33
5	GHAS2	ICP	1446.0	393.5	356.0	1	0	0	73960	g	ICP1_5	19.27
6	GHAS3	ICP	1446.0	393.0	393.8	1	0	0	107065	g	ICP1_6	20.04
7	GHAS5	ICP	1446.0	418.5	460.0	1	0	0	127803	g	ICP1_7	19.88
8	AIGHA1	ICP	1186.5	567.0	357.0	1	0	0	127923	g	ICP2_0	20.08
9	AIGHA2	ICP	1186.5	567.0	395.0	1	0	0	21048	g	ICP2_1	19.49
10	AIGHA3	ICP	1186.5	567.0	427.9	1	0	0	127918	g	ICP2_2	20.45
11	AIGHA4	ICP	1322.8	567.0	429.2	1	0	0	21067	g	ICP2_3	18.48
12	KIGHA1	ICP	1186.5	220.0	712.0	1	0	0	99513	g	ICP2_4	19.80
13	KIGHA2	ICP	1186.5	220.0	756.0	1	0	0	127921	g	ICP2_5	20.62
14	KIGHA3	ICP	1186.5	220.0	784.3	1	0	0	99518	g	ICP2_6	20.16
15	KIGHA4	ICP	1322.8	220.0	787.0	1	0	0	99509	g	ICP2_7	20.28
16	AIGP1	PPT	1186.5	547.0	354.5	0	1	0	5879	kPa	Bridge3_0	21298
17	AIGP2	PPT	1186.5	547.0	397.0	0	1	0	5885	kPa	Bridge3_1	21696
18	AIGP3	PPT	1254.7	547.0	397.7	0	1	0	5880	kPa	Bridge3_2	19311
19	AIGP4	PPT	1186.5	547.0	427.1	0	1	0	5877	kPa	Bridge3_3	20507
20	KIGP1	PPT	1186.5	240.0	352.0	0	1	0	5713	kPa	Bridge3_4	11725
21	KIGP2	PPT	1186.5	240.0	398.2	0	1	0	NONO	kPa	Bridge3_5	13391
22	KIGP3	PPT	1254.7	240.0	397.3	0	1	0	5878	kPa	Bridge3_6	17628
23	KIGP4	PPT	1186.5	240.0	426.0	0	1	0	5440	kPa	Bridge3_7	12022
24	KIGP5	PPT	1254.7	240.0	427.2	0	1	0	5669	kPa	Bridge4_4	19035
25	AJGHA3	ICP	463.6	567.0	425.1	1	0	0	21051	g	ICP3_0	19.19
26	AJGHA4	ICP	614.7	567.0	427.1	1	0	0	21059	g	ICP3_1	18.32
27	AIFVA1	ICP	1139.2	533.7	475.4	0	0	-1	3948	g	ICP3_2	9.45
28	AIFVA2	ICP	1235.0	531.2	475.4	0	0	-1	3203	g	ICP3_3	9.72
29	AIFHA3	ICP	1208.2	623.6	470.3	1	0	0	107648	g	ICP3_4	20.24
30	AIFHA4	ICP	1207.9	493.5	470.3	1	0	0	108848	g	ICP3_5	20.00
31	AIDHA1	ICP	1147.1	557.6	523.7	1	0	0	127805	g	ICP3_6	20.33
32	KIFVA1	ICP	1144.2	256.9	475.2	0	0	-1	3950	g	ICP3_7	9.55
33	GPS1	PPT	900.0	368.5	6.0	0	1	0	7984	kPa	Bridge6_0	18850
34	GPS2	PPT	900.0	368.5	285.8	0	1	0	5672	kPa	Bridge6_1	19751
35	GPS3	PPT	900.0	368.5	354.0	0	1	0	5882	kPa	Bridge6_2	18981
36	GPS4	PPT	900.0	368.5	396.7	0	1	0	5857	kPa	Bridge6_3	20208
37	GPS5	PPT	900.0	368.5	425.4	0	1	0	5752	kPa	Bridge6_4	37007
38	AKGP1	PPT	463.6	240.0	353.0	0	1	0	5884	kPa	Bridge6_5	16276
39	AKGP2	PPT	463.6	240.0	395.4	0	1	0	5482	kPa	Bridge6_6	14586
40	AKGP3	PPT	532.7	240.0	393.2	0	1	0	5876	kPa	Bridge6_7	20598
41	KIFVA2	ICP	1243.4	256.1	475.2	0	0	-1	5274	g	ICP4_0	9.50
42	KIFHA3	ICP	1212.7	296.3	470.1	1	0	0	107647	g	ICP4_1	20.49
43	KIFHA4	ICP	1212.5	165.1	470.1	1	0	0	128309	g	ICP4_2	20.62
44	KIDHA1	ICP	1151.8	232.7	527.6	1	0	0	21056	g	ICP4_3	18.25
45	AKFVA1	ICP	426.5	255.0	475.1	0	0	-1	3160	g	ICP4_4	9.26
46	AKFVA2	ICP	523.4	258.5	475.1	0	0	-1	96939	g	ICP4_5	10.14

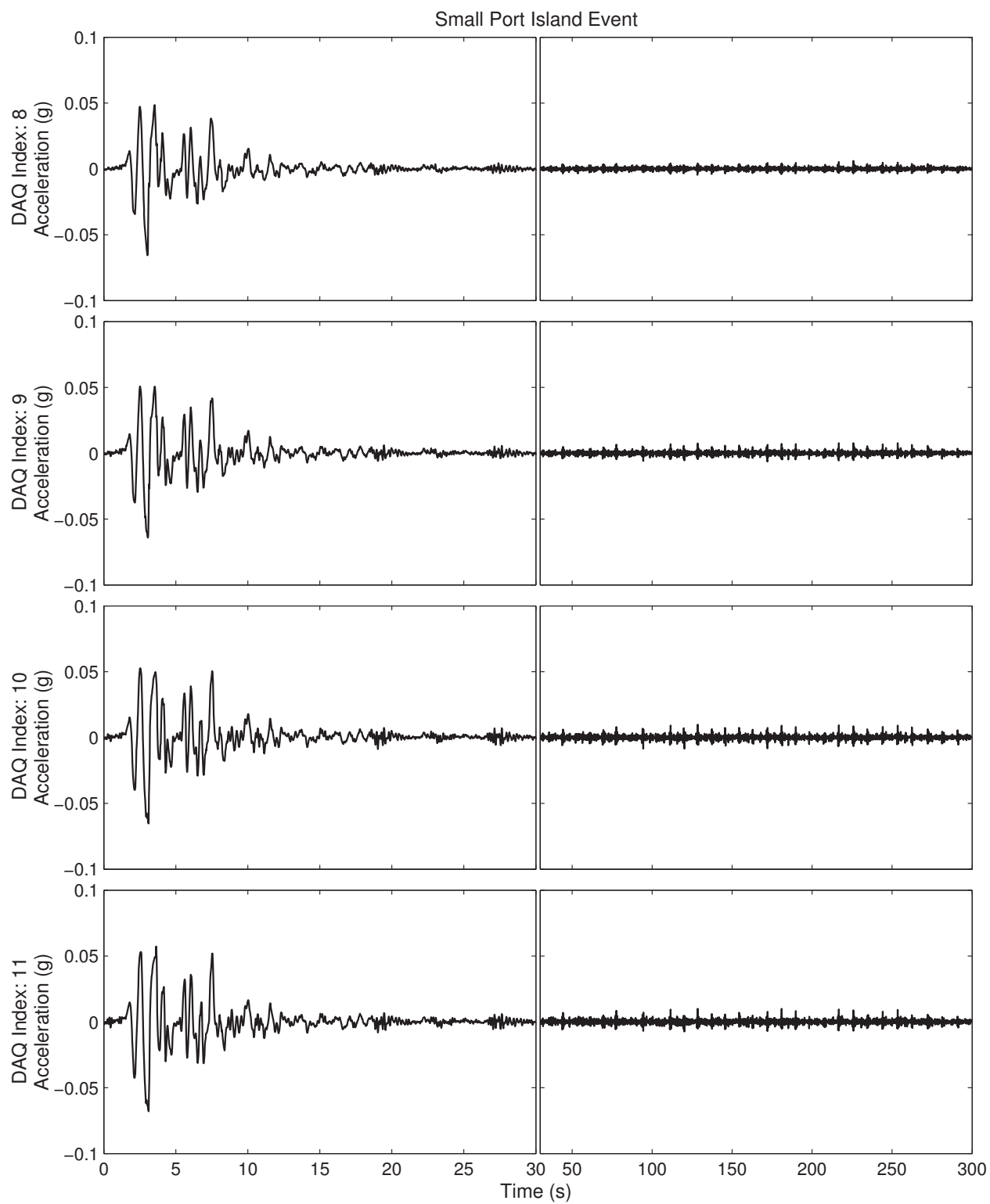
DAQ Channel Number	Sensor Label	Sensor Type	Position (mm)			Orientation			Serial Number	Sensor Units	Channel Name	Calibration Constant (Unit/V)
			X	Y	Z	I	J	K				
47	AKFHA3	ICP	493.5	295.7	470.0	1	0	0	128304	g	ICP4_6	20.41
48	AKFHA4	ICP	493.9	164.7	470.0	1	0	0	21321	g	ICP4_7	19.65
49	AKGP4	PPT	600.8	240.0	395.5	0	1	0	5856	kPa	Bridge7_0	19810
50	AKGP5	PPT	669.0	240.0	395.0	0	1	0	5671	kPa	Bridge7_1	17189
51	AKGP6	PPT	463.6	240.0	425.0	0	1	0	5751	kPa	Bridge7_2	20112
52	AJGP3	PPT	532.7	547.0	394.2	0	1	0	5675	kPa	Bridge7_3	17744
53	AKGP8	PPT	600.8	240.0	427.0	0	1	0	5678	kPa	Bridge7_4	24308
54	AKGP9	PPT	669.0	240.0	427.5	0	1	0	5883	kPa	Bridge7_5	21425
55	AJGP1	PPT	463.6	547.0	353.5	0	1	0	5881	kPa	Bridge7_6	20486
56	AJGP2	PPT	463.6	547.0	394.9	0	1	0	5442	kPa	Bridge7_7	16489
57	AKGP7	PPT	532.7	240.0	423.4	0	1	0	5670	kPa	Bridge8_0	21222
58	AJGP4	PPT	614.7	547.0	394.7	0	1	0	5950	kPa	Bridge8_5	23846
59	AJGP5	PPT	463.6	547.0	426.8	0	1	0	5750	kPa	Bridge8_6	47168
60	AJGP6	PPT	532.7	547.0	426.1	0	1	0	5863	kPa	Bridge8_7	20171
61	GVAN1	ICP	205.0	393.5	0.0	0	0	-1	107064	g	ICP5_0	20.41
62	GVAN2	ICP	205.0	393.5	455.1	0	0	-1	127804	g	ICP5_1	19.80
63	GVAS1	ICP	1446.0	368.5	0.0	0	0	-1	107323	g	ICP5_2	20.66
64	GVAS2	ICP	1446.0	368.5	458.7	0	0	-1	99512	g	ICP5_3	19.96
65	GHAW	ICP	900.0	230.0	457.7	1	0	0	107645	g	ICP5_4	20.28
66	GHAC1	ICP	900.0	418.5	8.4	1	0	0	21046	g	ICP5_5	18.73
67	GHAC2	ICP	900.0	418.5	188.1	1	0	0	127925	g	ICP5_6	19.76
68	GHAC3	ICP	900.0	418.5	291.4	1	0	0	99511	g	ICP5_7	19.84
69	GHAC4	ICP	900.0	418.5	356.5	1	0	0	99514	g	ICP6_0	19.53
70	GHAC5	ICP	900.0	418.5	399.7	1	0	0	107272	g	ICP6_1	20.28
71	GHAC6	ICP	900.0	418.5	426.5	1	0	0	73967	g	ICP6_2	18.66
72	GHAS4	ICP	1446.0	393.5	429.2	1	0	0	21044	g	ICP6_3	18.83
73	AKGHA1	ICP	463.6	220.0	354.5	1	0	0	108953	g	ICP6_4	19.80
74	AKGHA2	ICP	463.6	220.0	396.9	1	0	0	127917	g	ICP6_5	19.76
75	AKGHA3	ICP	463.6	220.0	424.2	1	0	0	127920	g	ICP6_6	19.72
76	AKGHA4	ICP	600.8	220.0	425.5	1	0	0	73964	g	ICP6_7	18.80
77	AJGHA1	ICP	463.6	567.0	356.5	1	0	0	107039	g	ICP7_0	20.20
78	AJGHA2	ICP	463.6	567.0	396.5	1	0	0	21069	g	ICP7_1	18.80
79	KAFVA1	ICP	562.2	255.4	475.6	0	0	-1	5267	g	ICP7_2	9.63
80	KAFVA2	ICP	661.4	255.4	475.6	0	0	-1	96938	g	ICP7_3	9.91
81	KAFHA3	ICP	633.2	295.5	470.5	1	0	0	132245	g	ICP7_4	20.70
82	KAFHA4	ICP	631.5	164.9	470.5	1	0	0	21323	g	ICP7_5	21.28
83	AJFVA1	ICP	423.3	527.2	475.1	0	0	-1	96937	g	ICP7_6	9.83
84	AJFVA2	ICP	522.5	526.5	475.1	0	0	-1	3162	g	ICP7_7	9.25
85	AJFHA3	ICP	492.4	617.7	470.0	1	0	0	127802	g	ICP8_0	20.04
86	AJFHA4	ICP	493.1	486.1	470.0	1	0	0	131509	g	ICP8_1	20.79
87	JAFVA1	ICP	682.9	597.0	487.5	0	0	-1	128306	g	ICP8_2	20.45
88	JAFVA2	ICP	680.9	597.5	487.5	0	0	-1	21061	g	ICP8_3	20.20
89	JAFHA3	ICP	675.8	597.5	482.4	1	0	0	97112	g	ICP8_4	10.06
90	JADVA1	ICP	567.4	553.3	732.1	0	0	-1	21319	g	ICP8_5	19.16
91	JADVA2	ICP	672.0	552.8	732.1	0	0	-1	131508	g	ICP8_6	20.08
92	JADHA3	ICP	552.9	553.7	695.7	1	0	0	3164	g	ICP8_7	9.38
93	GVLN	LP	281.0	284.0	471.1	0	0	-1	306	mm	HOC_1_0	15.11

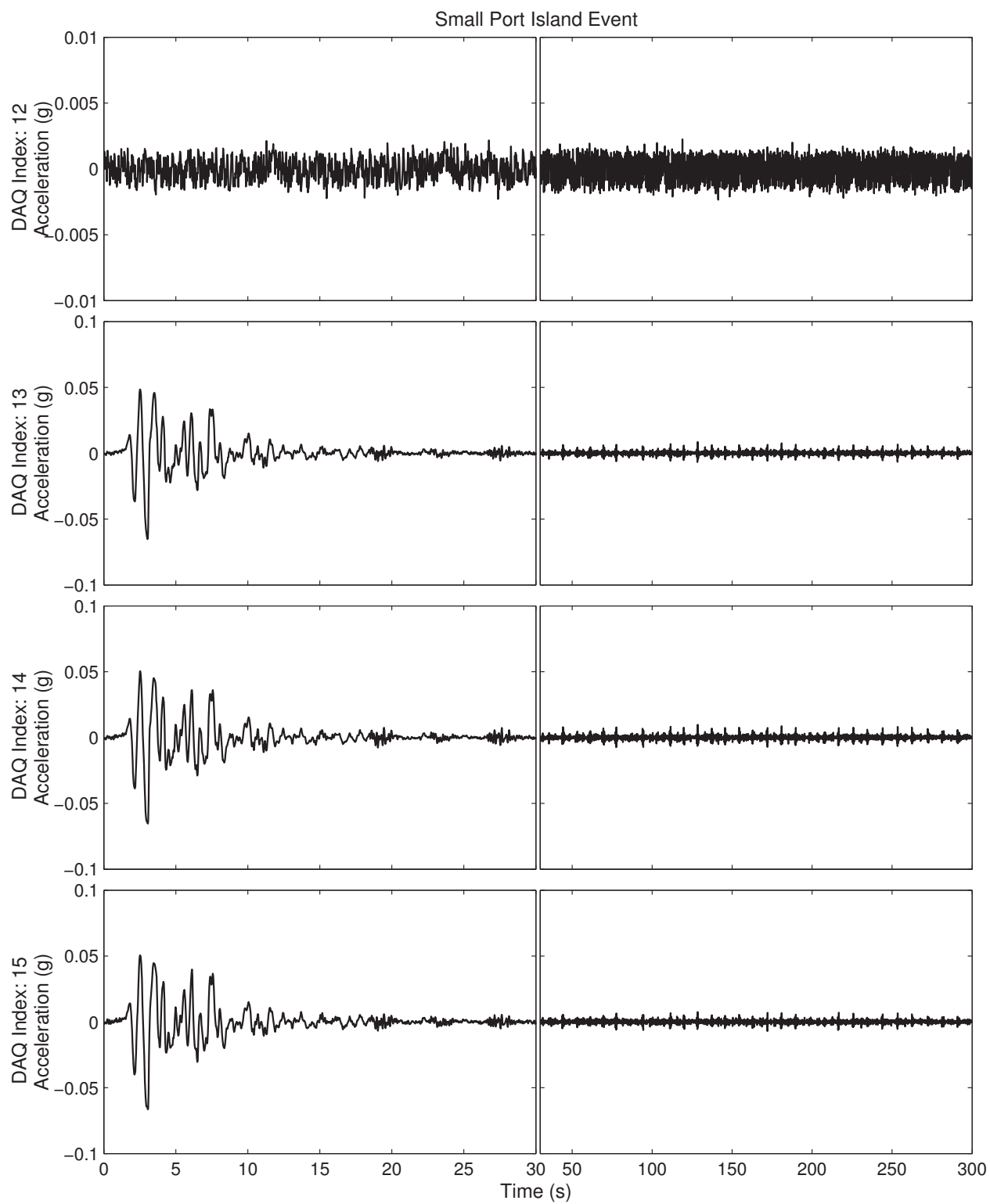
DAQ Channel Number	Sensor Label	Sensor Type	Position (mm)			Orientation			Serial Number	Sensor Units	Channel Name	Calibration Constant (Unit/V)
			X	Y	Z	I	J	K				
94	AKFHL4	LP	419.3	231.6	502.0	1	0	0	217	mm	HOC 1_1	10.22
95	GVLS	LP	1364.0	520.0	474.7	0	0	-1	224	mm	HOC 1_2	10.26
96	AIFVL1	LP	1132.1	491.1	492.5	0	0	-1	111	mm	HOC 1_3	4.96
97	AIFVL2	LP	1229.6	474.1	492.6	0	0	-1	115	mm	HOC 1_4	5.45
98	AIFVL3	LP	1233.6	638.4	494.6	0	0	-1	117	mm	HOC 1_5	5.16
99	AIFHL4	LP	1243.3	565.2	504.8	-1	0	0	228	mm	HOC 1_6	10.23
100	KIFVL1	LP	1139.1	303.1	492.1	0	0	-1	119	mm	HOC 1_7	5.54
101	KIFVL2	LP	1236.6	148.8	497.3	0	0	-1	121	mm	HOC 2_0	4.96
102	KIFVL3	LP	1248.6	304.1	494.5	0	0	-1	102	mm	HOC 2_1	5.10
103	KIFHL4	LP	1248.3	222.7	499.4	-1	0	0	230	mm	HOC 2_2	10.25
104	AKFVL1	LP	420.1	159.1	497.2	0	0	-1	222	mm	HOC 2_3	10.24
105	AKFVL2	LP	432.1	312.4	493.2	0	0	-1	215	mm	HOC 2_4	10.26
106	AKFVL3	LP	513.6	312.4	491.0	0	0	-1	229	mm	HOC 2_5	10.22
107	GVLC	LP	953.0	342.0	471.2	0	0	-1	305	mm	HOC 2_6	15.08
108	KAFVL1	LP	556.1	303.4	494.1	0	0	-1	205	mm	HOC 2_7	10.12
109	KAFVL2	LP	658.6	157.1	497.4	0	0	-1	214	mm	HOC 3_0	9.76
110	KAFVL3	LP	661.6	309.4	492.7	0	0	-1	203	mm	HOC 3_1	10.19
111	KAFHL4	LP	666.3	234.7	498.6	-1	0	0	226	mm	HOC 3_2	10.23
112	AJFVL1	LP	428.2	483.8	493.6	0	0	-1	220	mm	HOC 3_3	10.28
113	AJFVL2	LP	428.2	632.1	496.5	0	0	-1	207	mm	HOC 3_4	10.17
114	AJFVL3	LP	513.7	484.8	494.3	0	0	-1	216	mm	HOC 3_5	10.13
115	AJFHL4	LP	418.4	549.7	498.1	1	0	0	223	mm	HOC 3_6	10.24
116	JAFVL1	LP	550.7	496.8	504.2	0	0	-1	219	mm	HOC 3_7	10.27
117	JAFVL2	LP	679.8	483.8	503.7	0	0	-1	227	mm	HOC 4_0	10.26
118	JAFVL3	LP	683.8	625.8	506.3	0	0	-1	218	mm	HOC 4_1	10.46
119	JAFHL4	LP	688.0	556.5	510.9	-1	0	0	232	mm	HOC 4_2	10.43
120	AIFHM1	MEMS	1231.1	551.8	498.5	-1	0	0	822	g	HOC 4_3	25.00
121	AIDHM1	MEMS	1188.2	501.1	523.7	0	1	0	MA016	g	HOC 4_4	25.00
122	KIFHM1	MEMS	1236.0	219.6	498.0	-1	0	0	828	g	HOC 4_5	25.00
123	KIDHM1	MEMS	1198.4	288.1	522.6	0	-1	0	MA019	g	HOC 4_6	25.00
124	AKFHM1	MEMS	431.7	236.4	497.8	-1	0	0	824	g	HOC 4_7	25.00
125	AKDHM1	MEMS	505.6	229.0	525.3	-1	0	0	MA001	g	HOC 5_0	25.00
126	AKDHM2	MEMS	470.3	287.4	523.5	0	-1	0	819	g	HOC 5_1	25.00
127	KAFHM1	MEMS	654.0	240.6	496.8	-1	0	0	827	g	HOC 5_2	25.00
128	KADHM1	MEMS	580.1	229.5	524.3	1	0	0	MA018	g	HOC 5_3	25.00
129	KADHM2	MEMS	608.7	287.4	522.4	0	-1	0	MA033	g	HOC 5_4	25.00
130	AJFHM1	MEMS	430.6	560.3	498.7	-1	0	0	826	g	HOC 5_5	25.00
131	AJDHM1	MEMS	504.7	551.8	522.7	-1	0	0	MA022	g	HOC 5_6	25.00
132	AJDHM2	MEMS	474.9	494.8	522.7	0	1	0	820	g	HOC 5_7	25.00
133	JAFHM1	MEMS	667.1	564.0	495.8	-1	0	0	825	g	HOC 6_0	25.00
134	JAFHM2	MEMS	670.7	505.4	490.3	0	-1	0	821	g	HOC 6_1	25.00
135	JACHM1	MEMS	638.8	553.3	568.3	-1	0	0	829	g	HOC 6_2	25.00
136	JADHM1	MEMS	676.9	554.7	687.8	-1	0	0	830	g	HOC 6_3	25.00
137	JADHM2	MEMS	619.2	610.5	689.5	0	-1	0	823	g	HOC 6_4	25.00
138	BHMN1	MEMS	0.0	393.5	16.3	1	0	0	MA011	g	HOC 6_5	25.00
139	BHMN2	MEMS	0.0	393.6	39.5	1	0	0	MA035	g	HOC 6_6	25.00
140	BHMN3	MEMS	646.6	309.4	620.4	0	0	-1	MA009	g	HOC 6_7	25.00

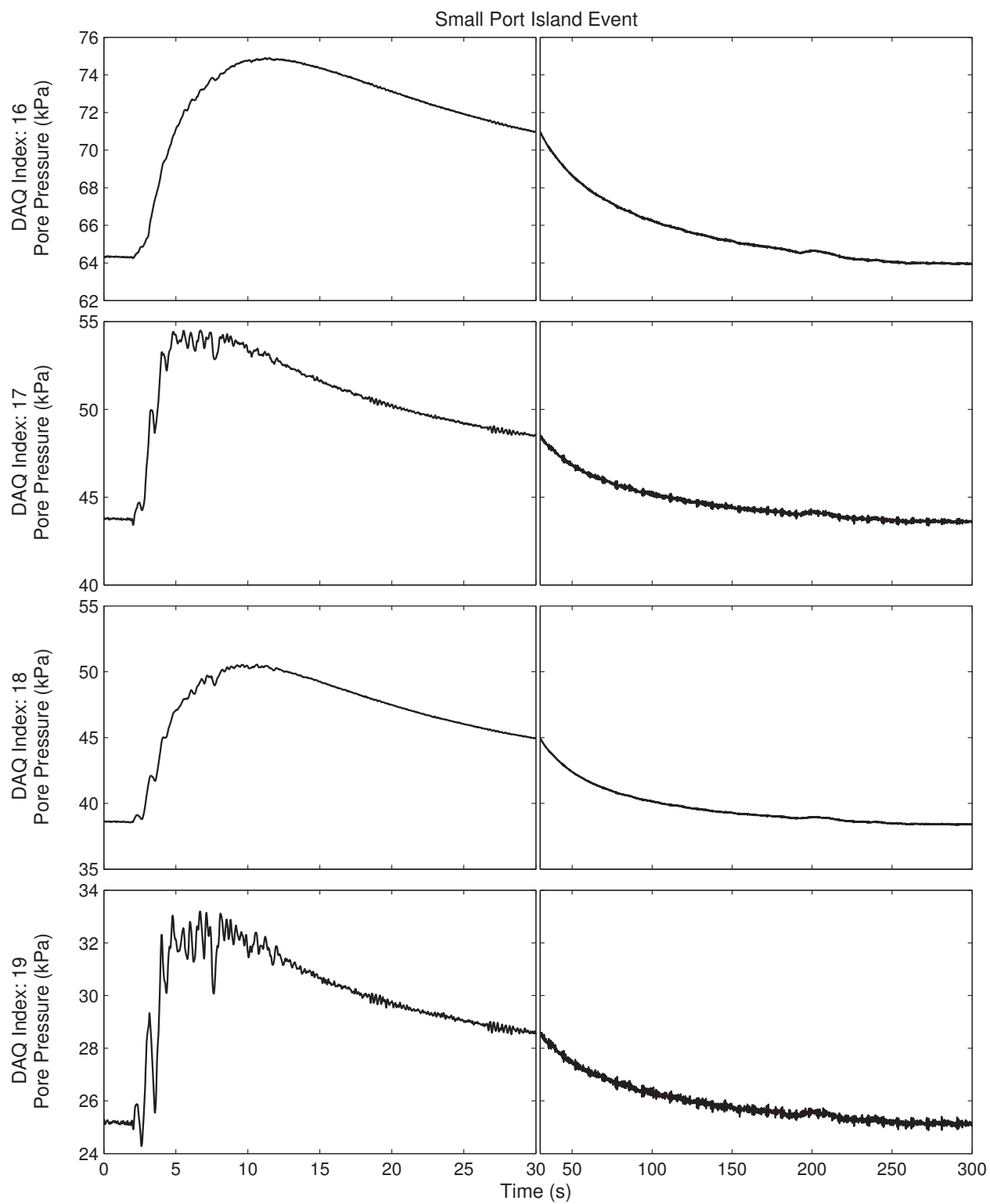
DAQ Channel Number	Sensor Label	Sensor Type	Position (mm)			Orientation			Serial Number	Sensor Units	Channel Name	Calibration Constant (Unit/V)
			X	Y	Z	I	J	K				
141	CPTtip	LC	0.0	0.0	0.0	-	-	-	25437-02	lb	LC1	64725
142	CPTload	LC	0.0	0.0	0.0	-	-	-	181325	lb	LC2	50150
143	CPTdisp	LP	0.0	0.0	0.0	-	-	-	CPT3	mm	ACT1_FB	32.99

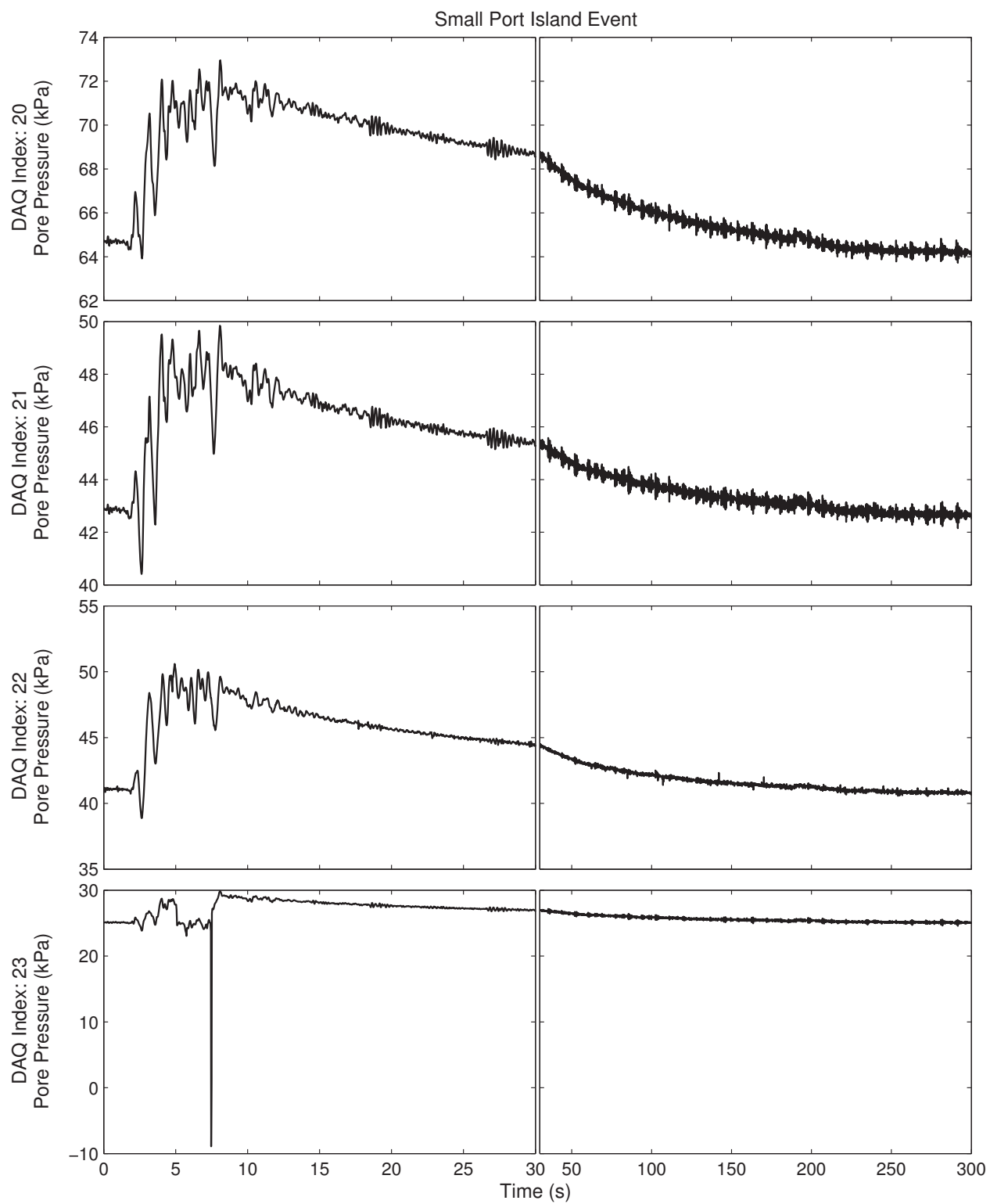


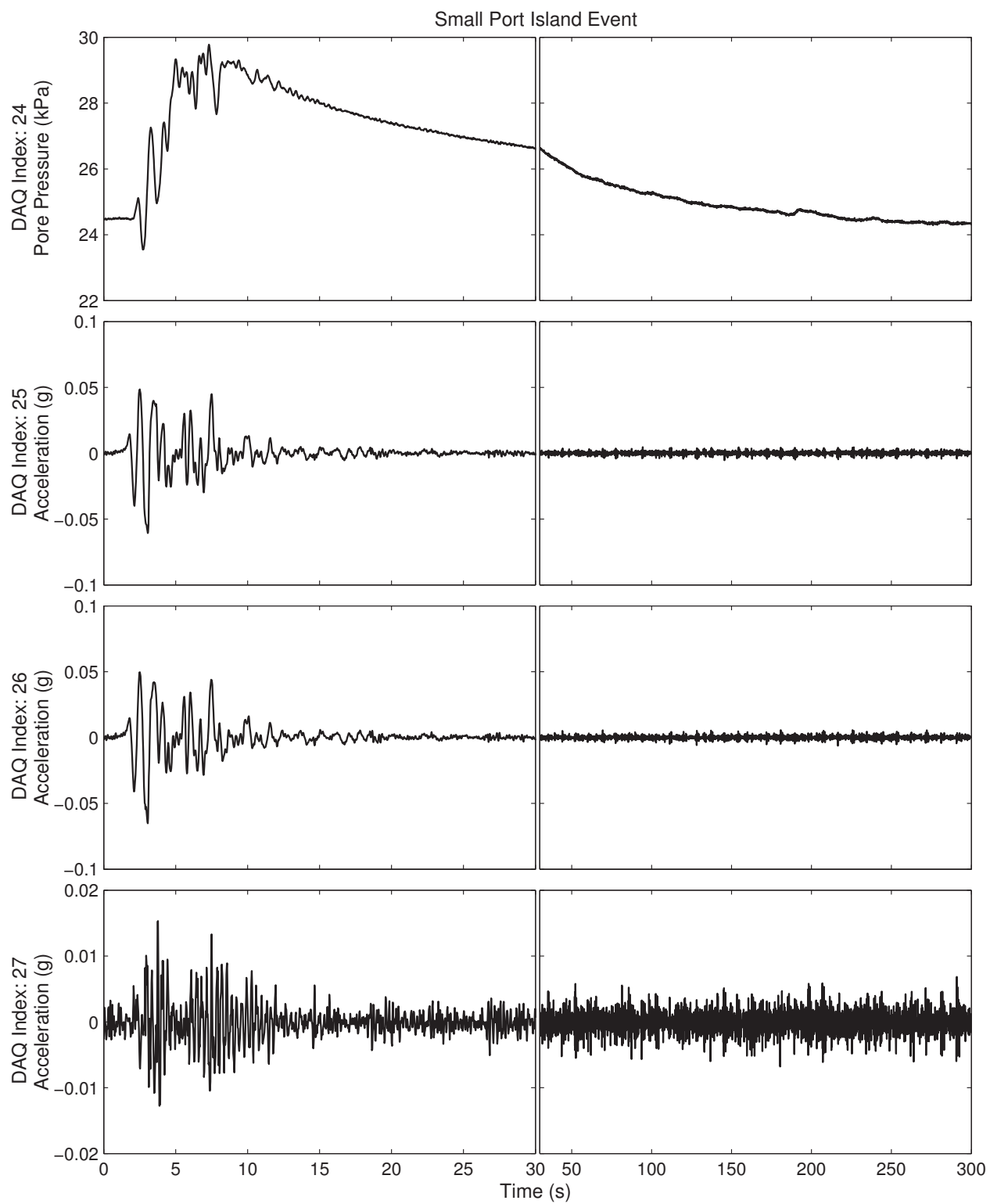


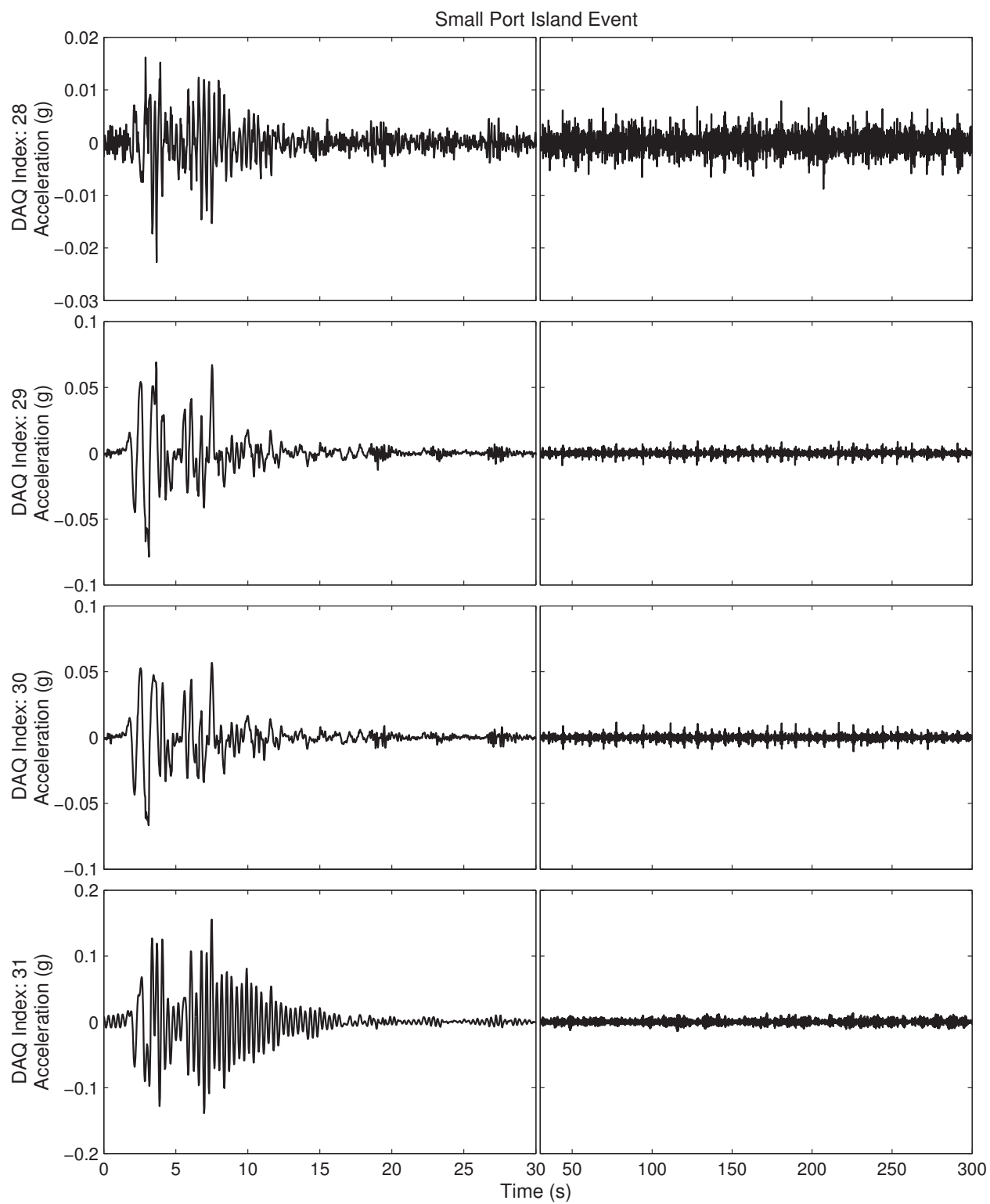


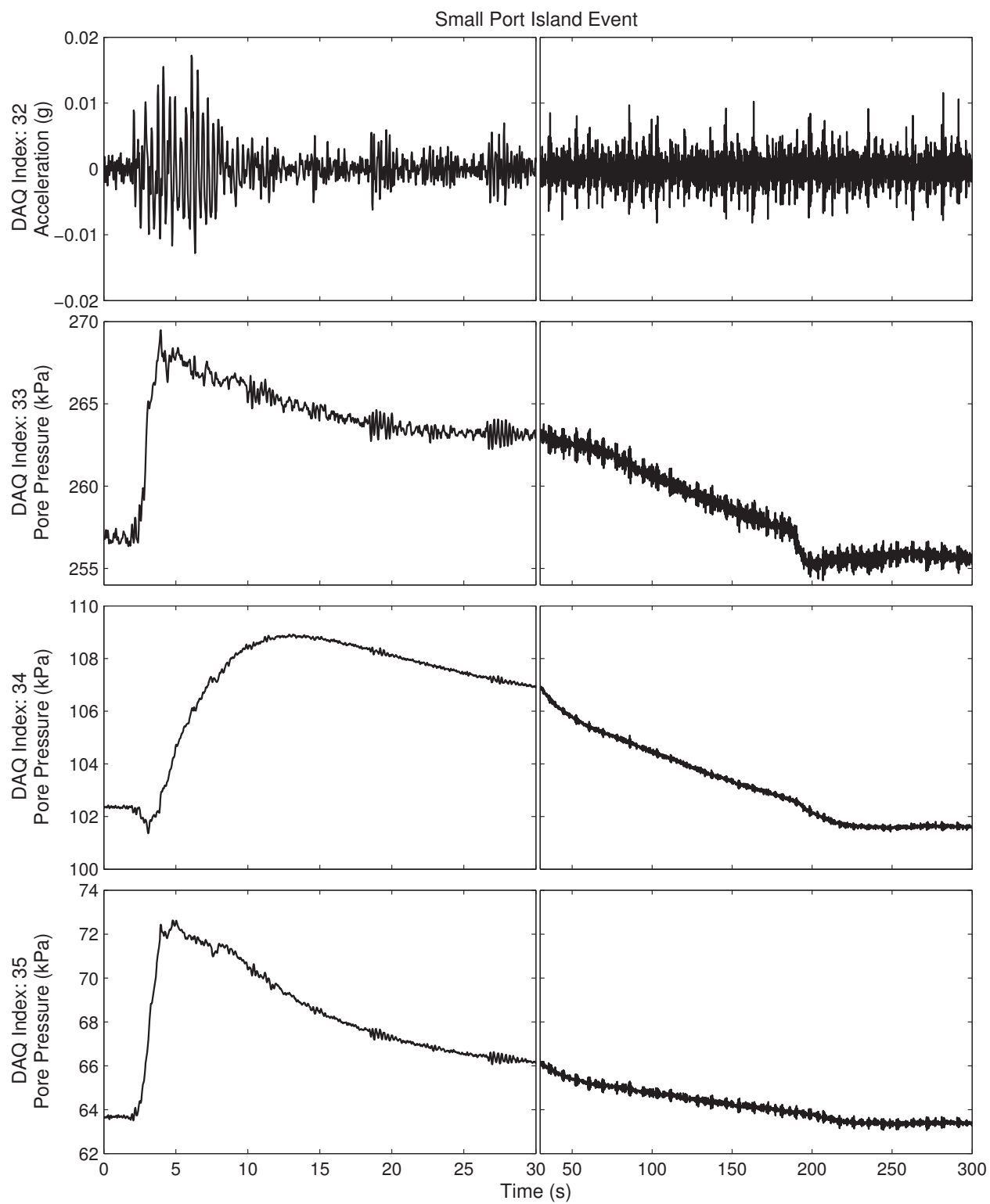


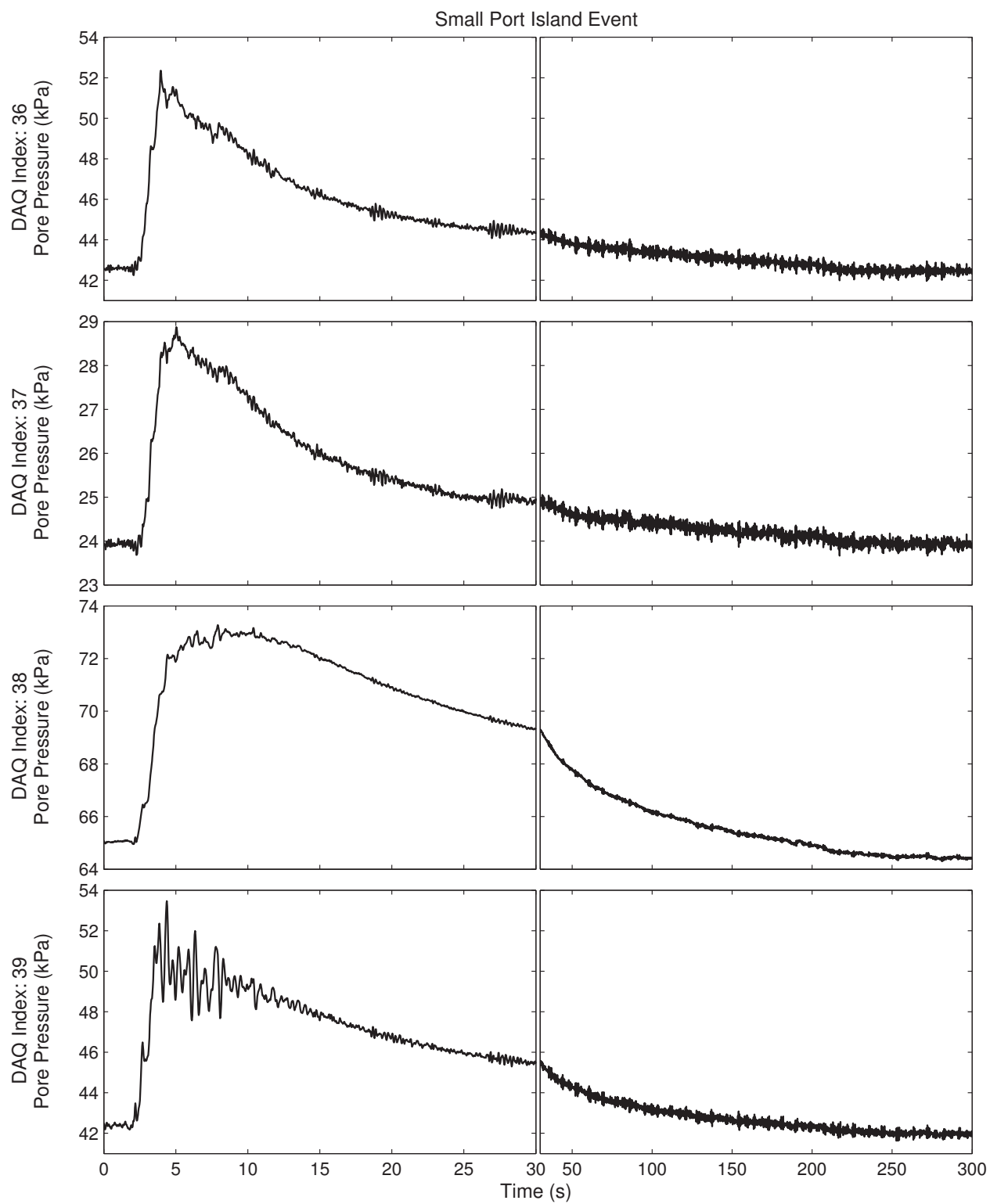


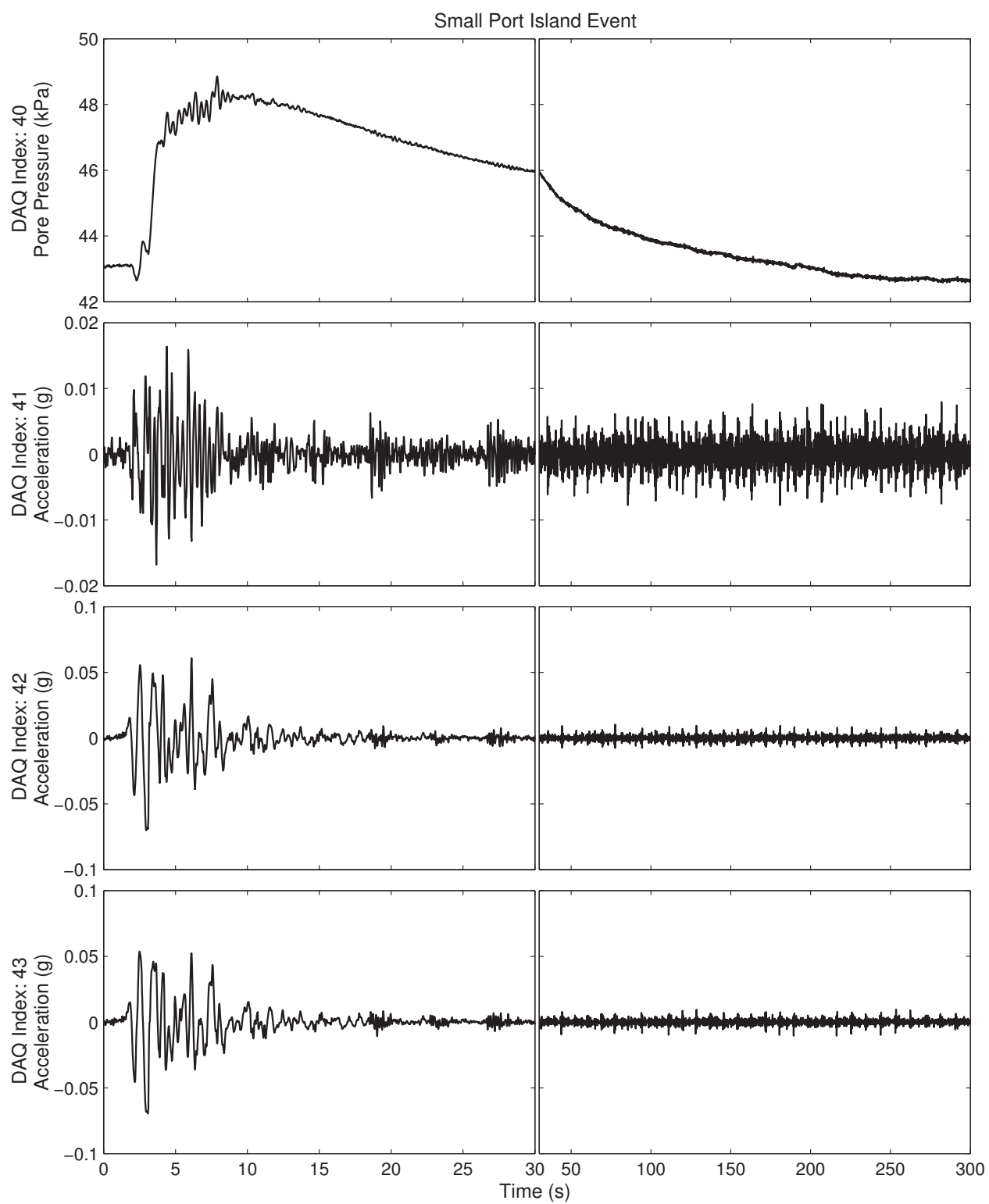


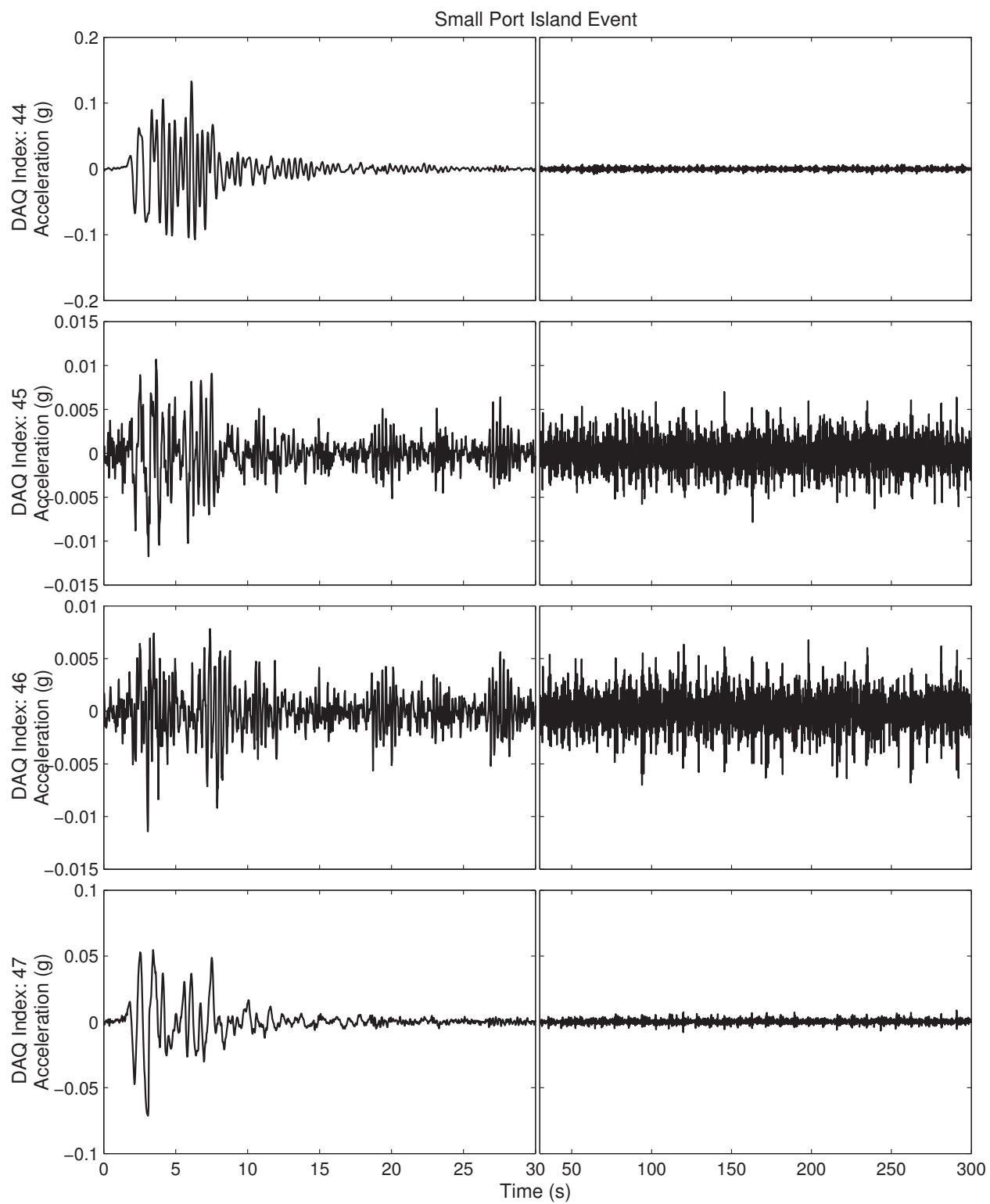


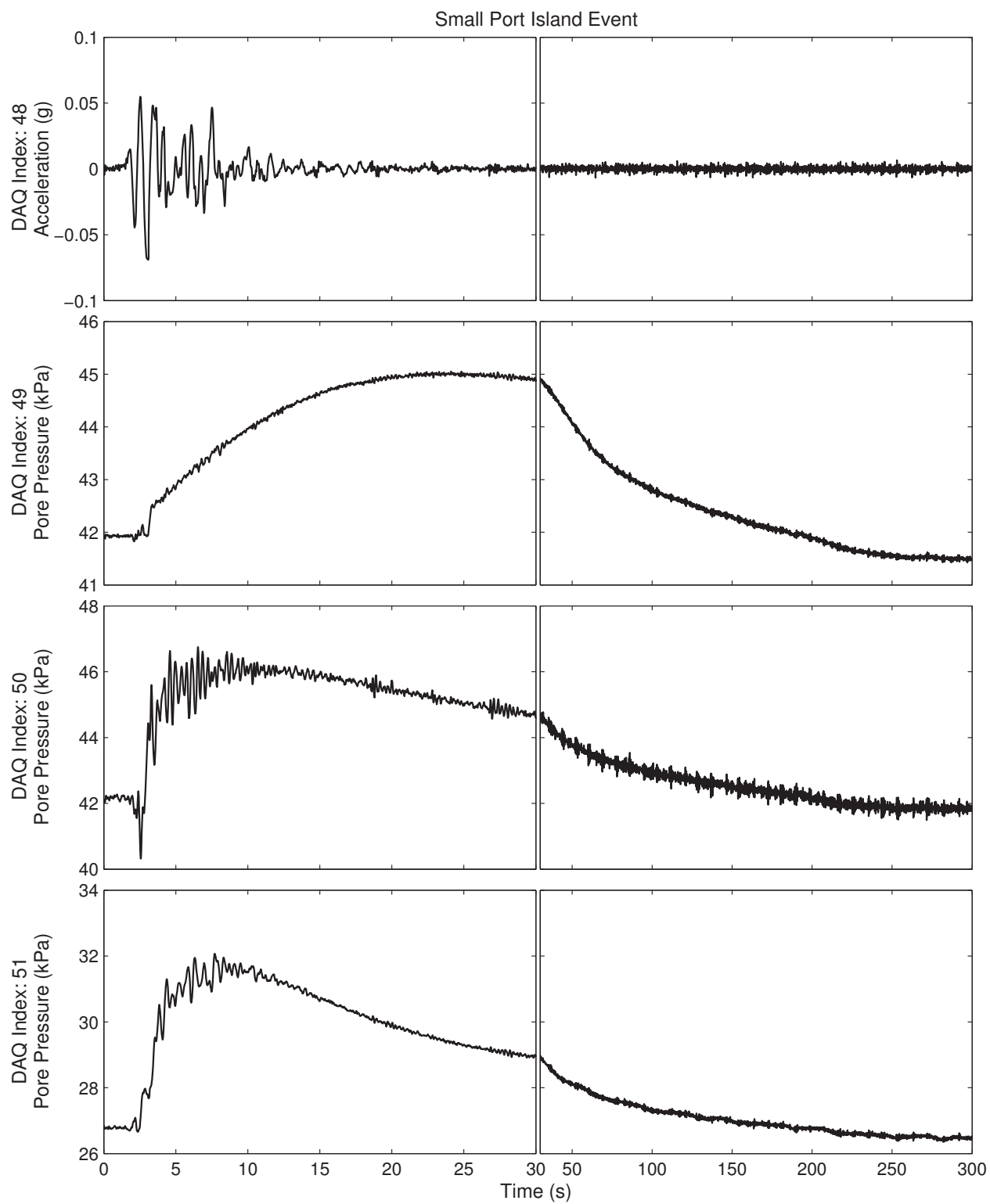


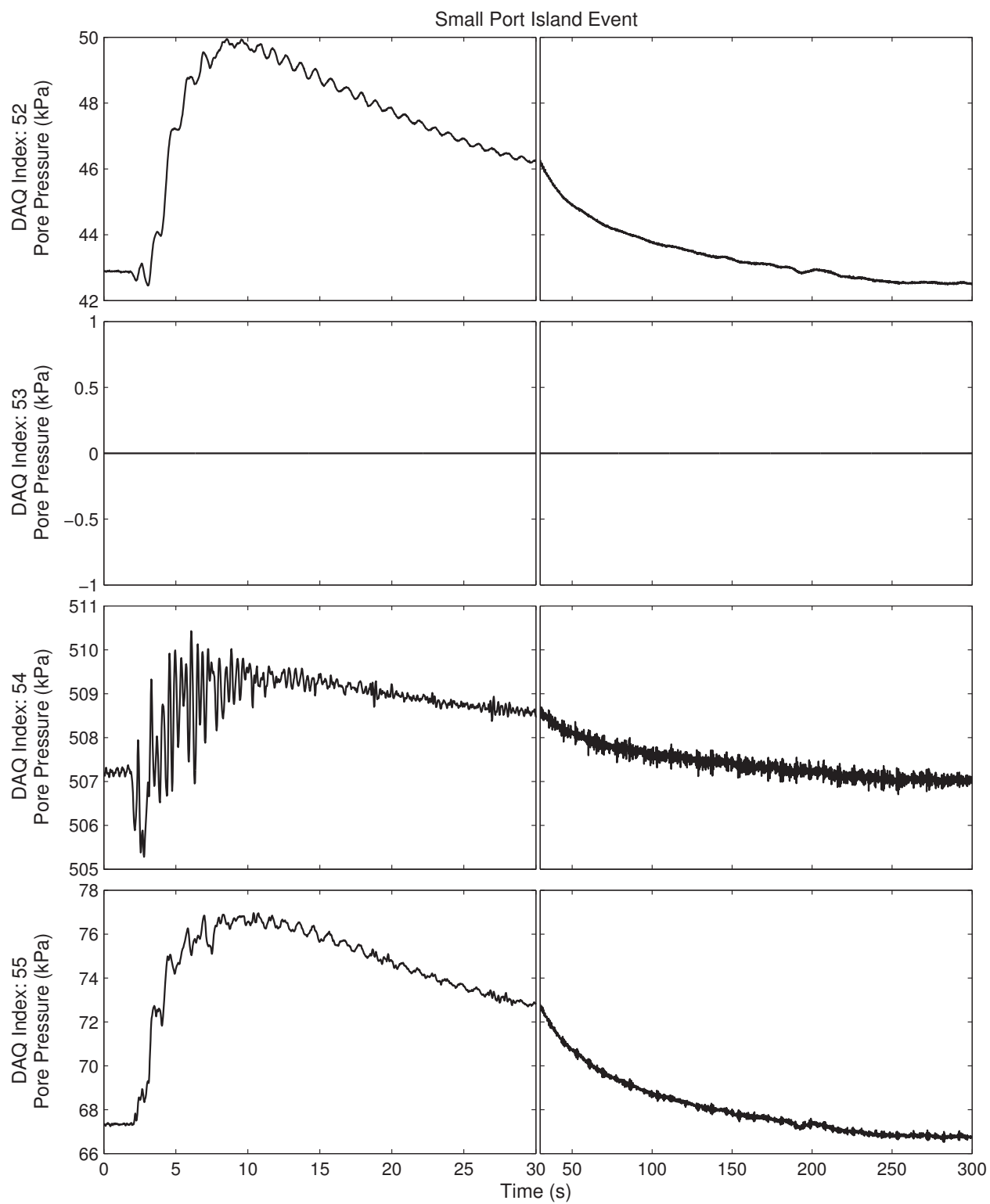


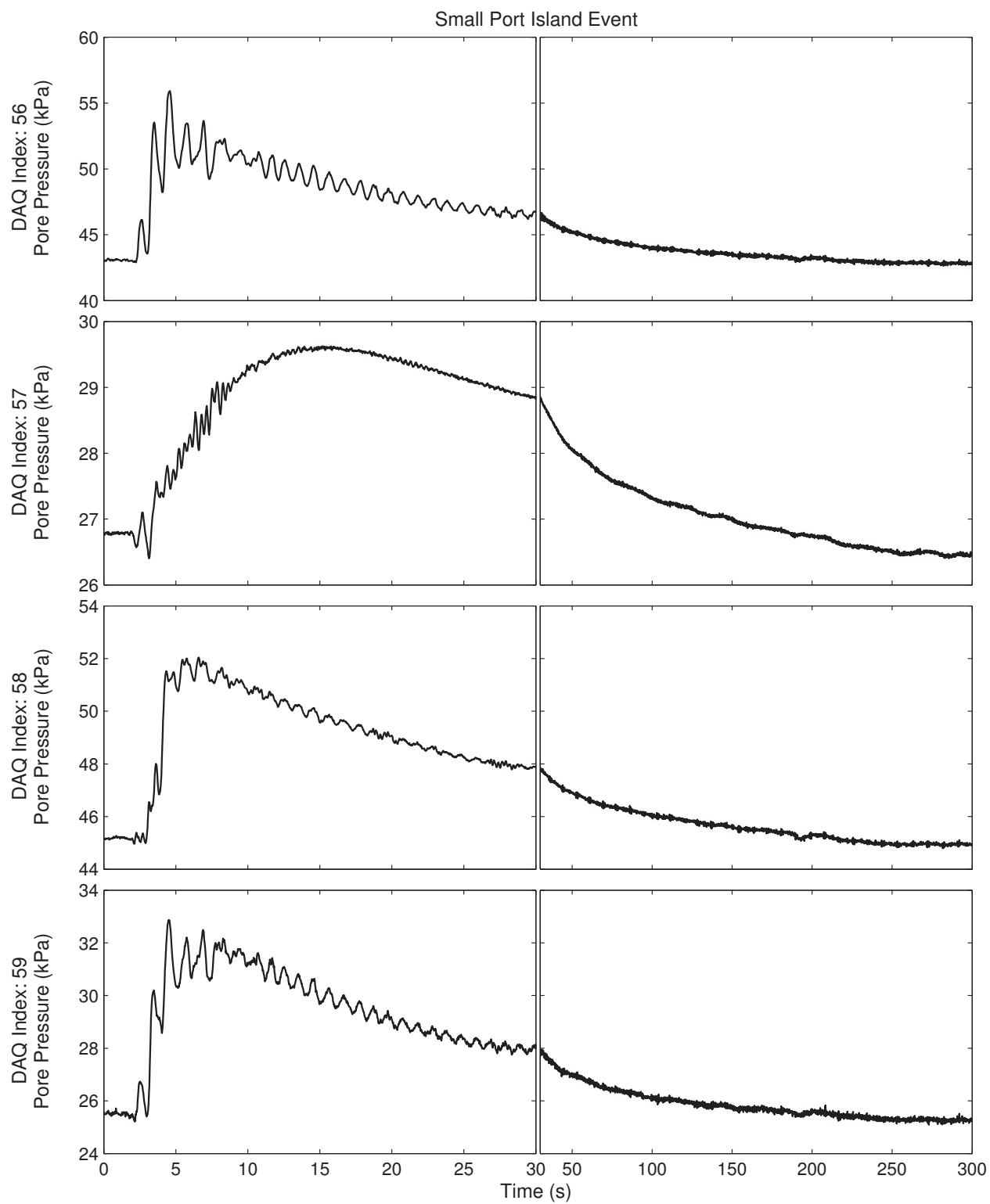


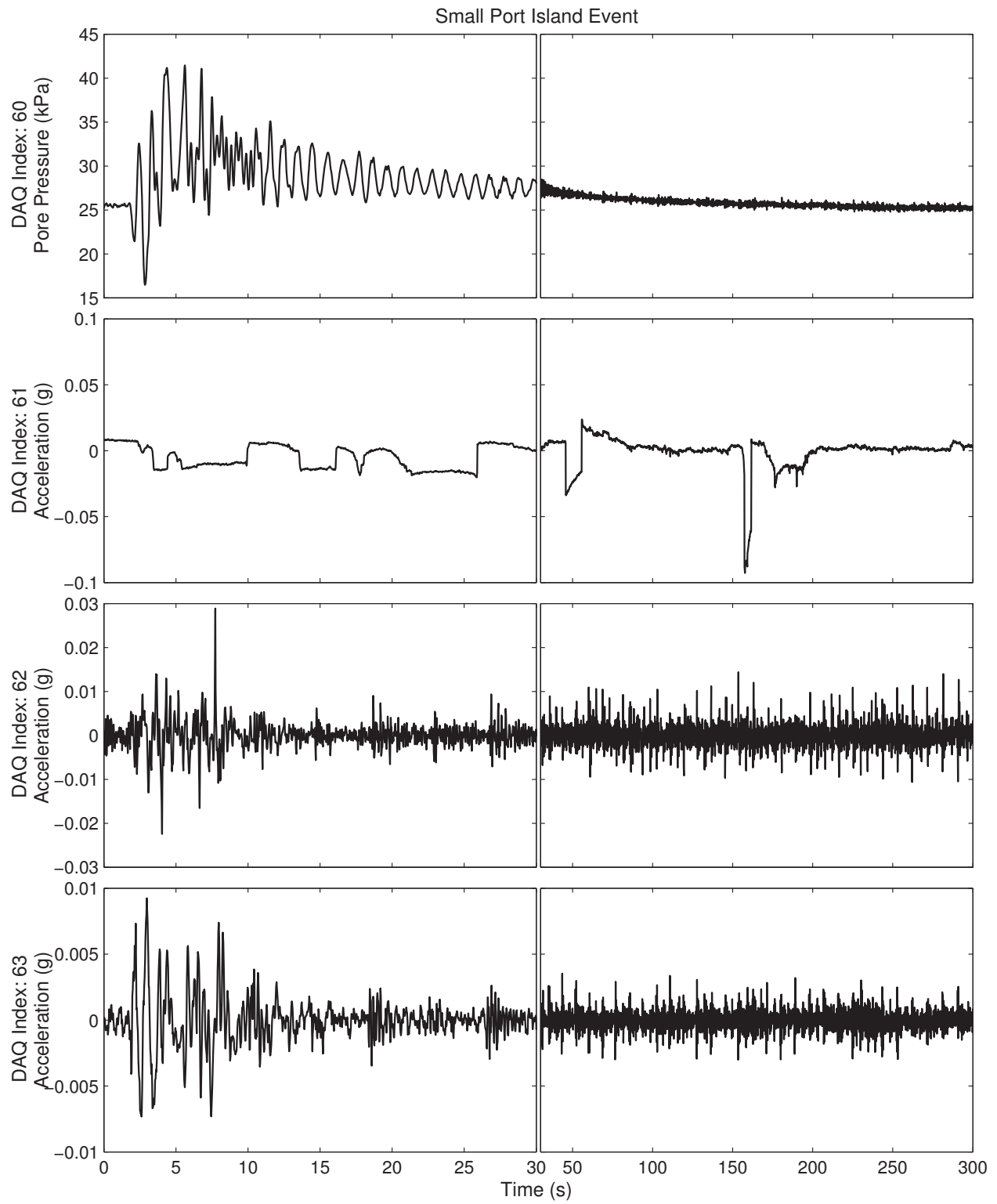


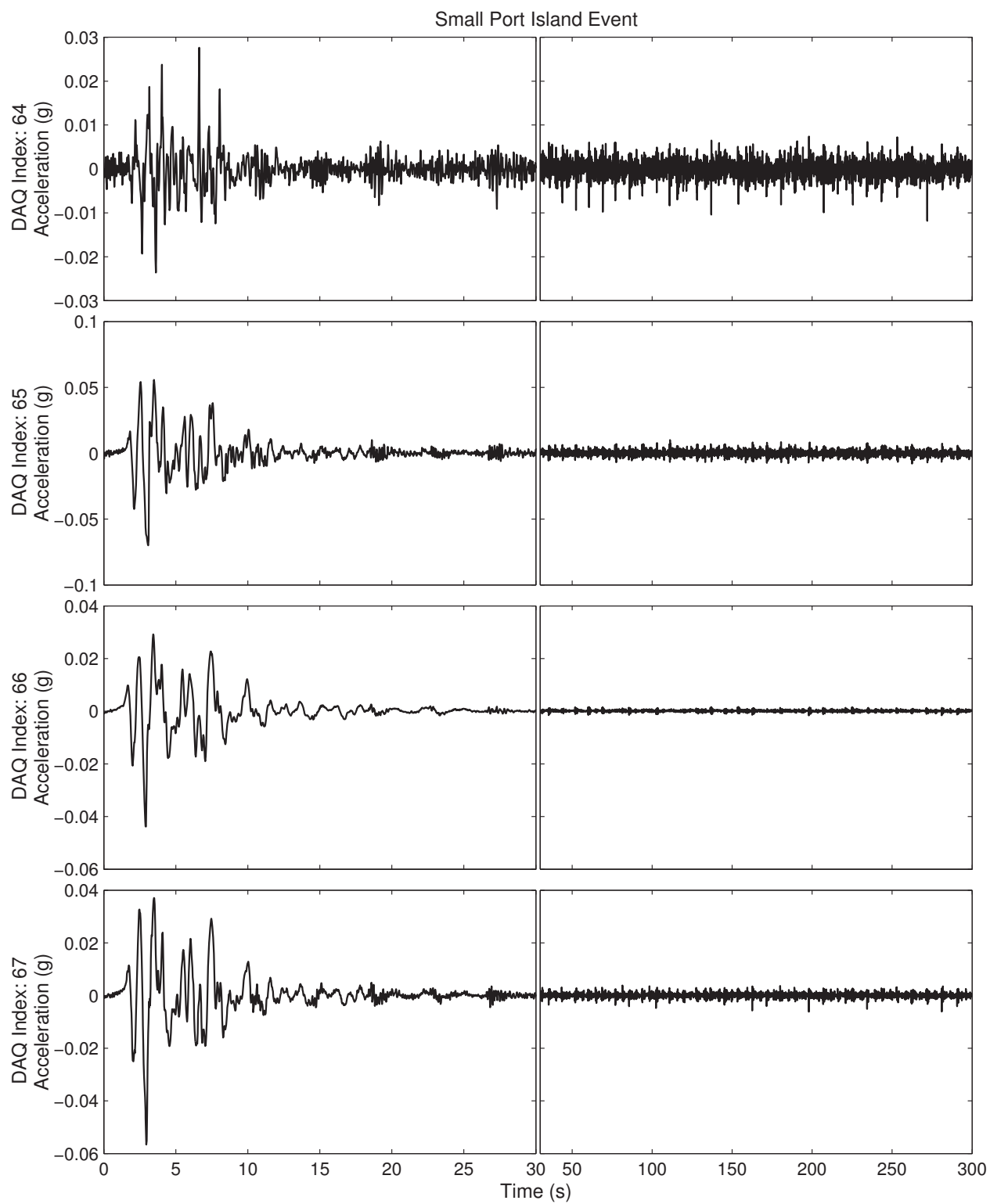


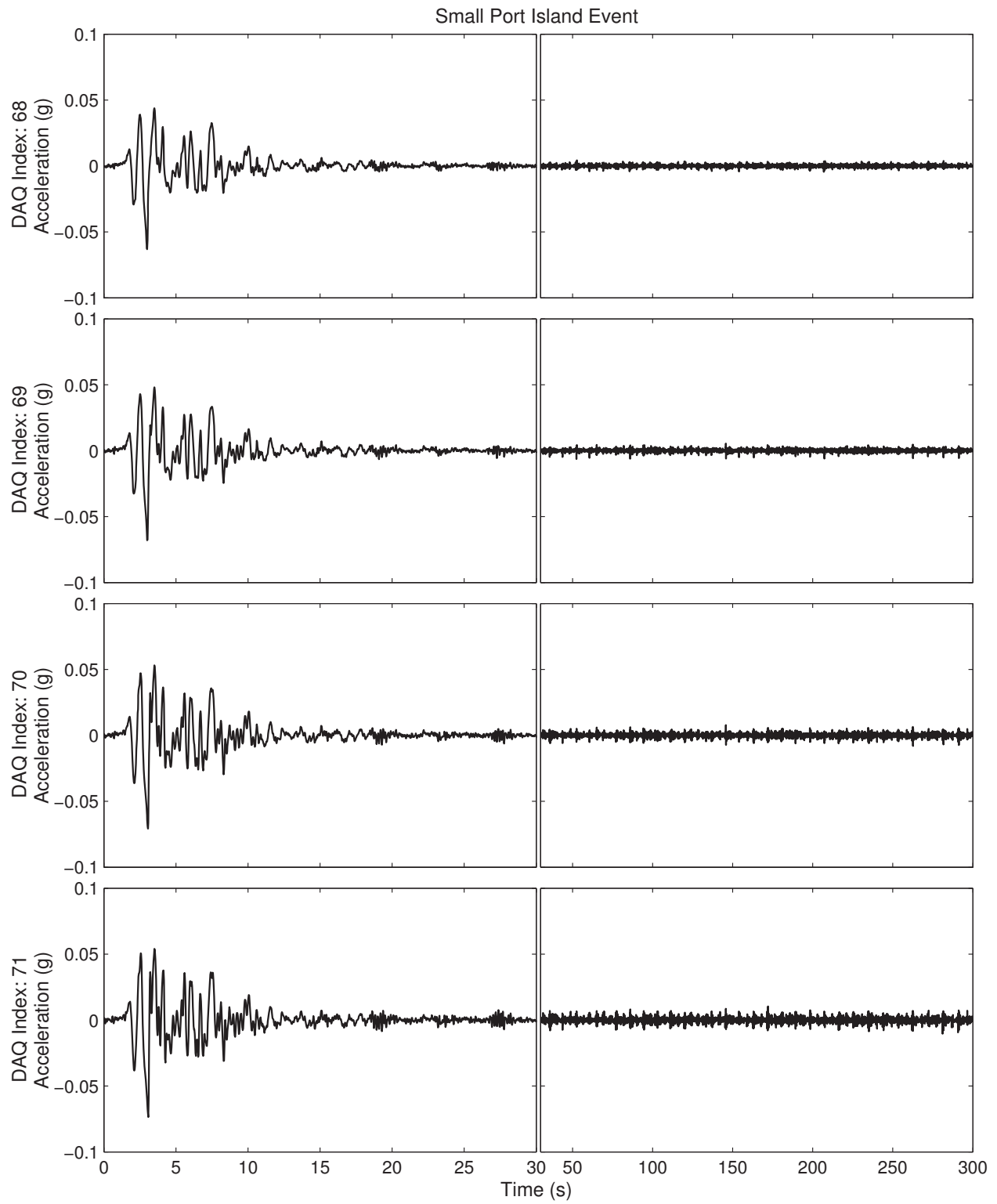


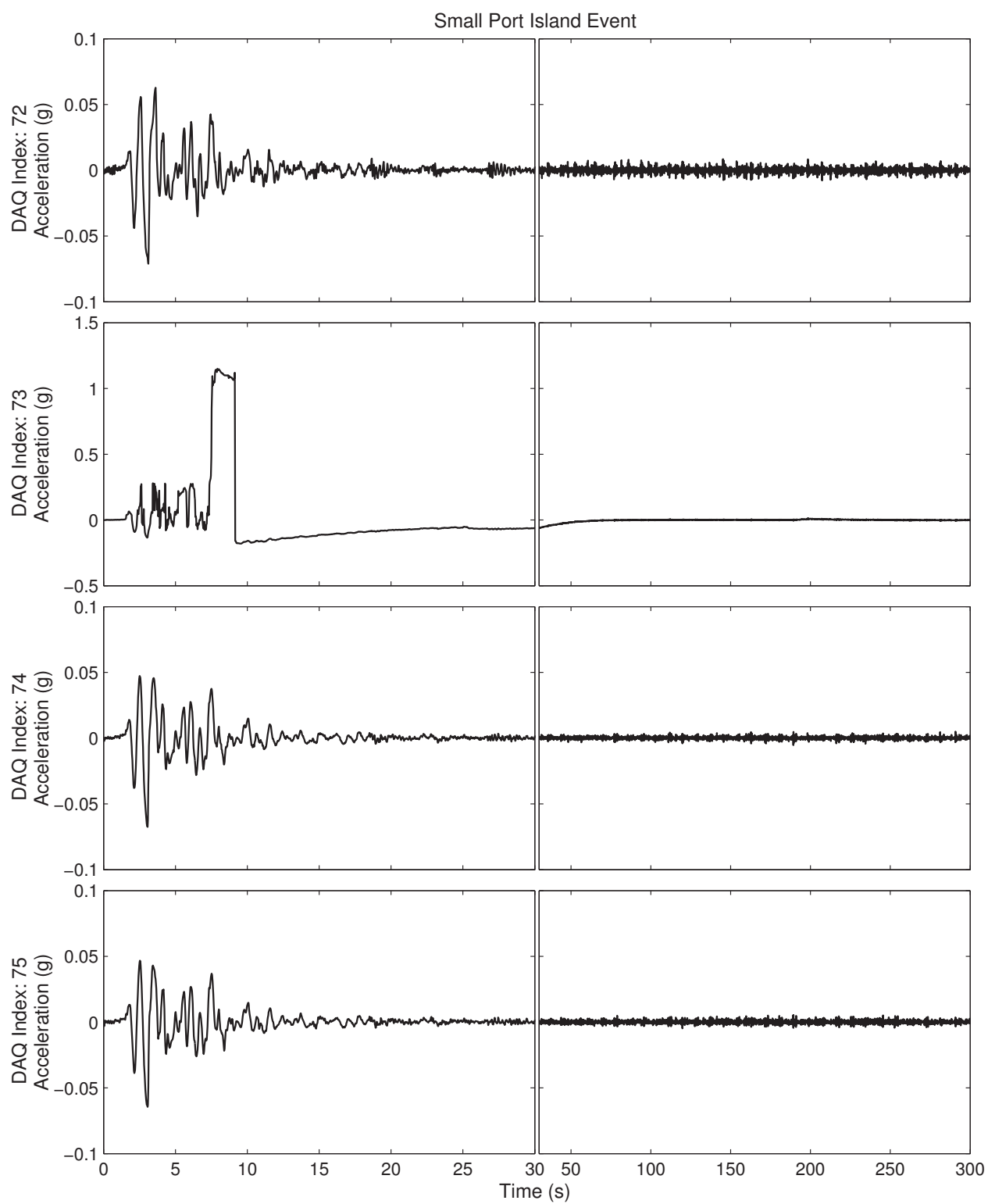


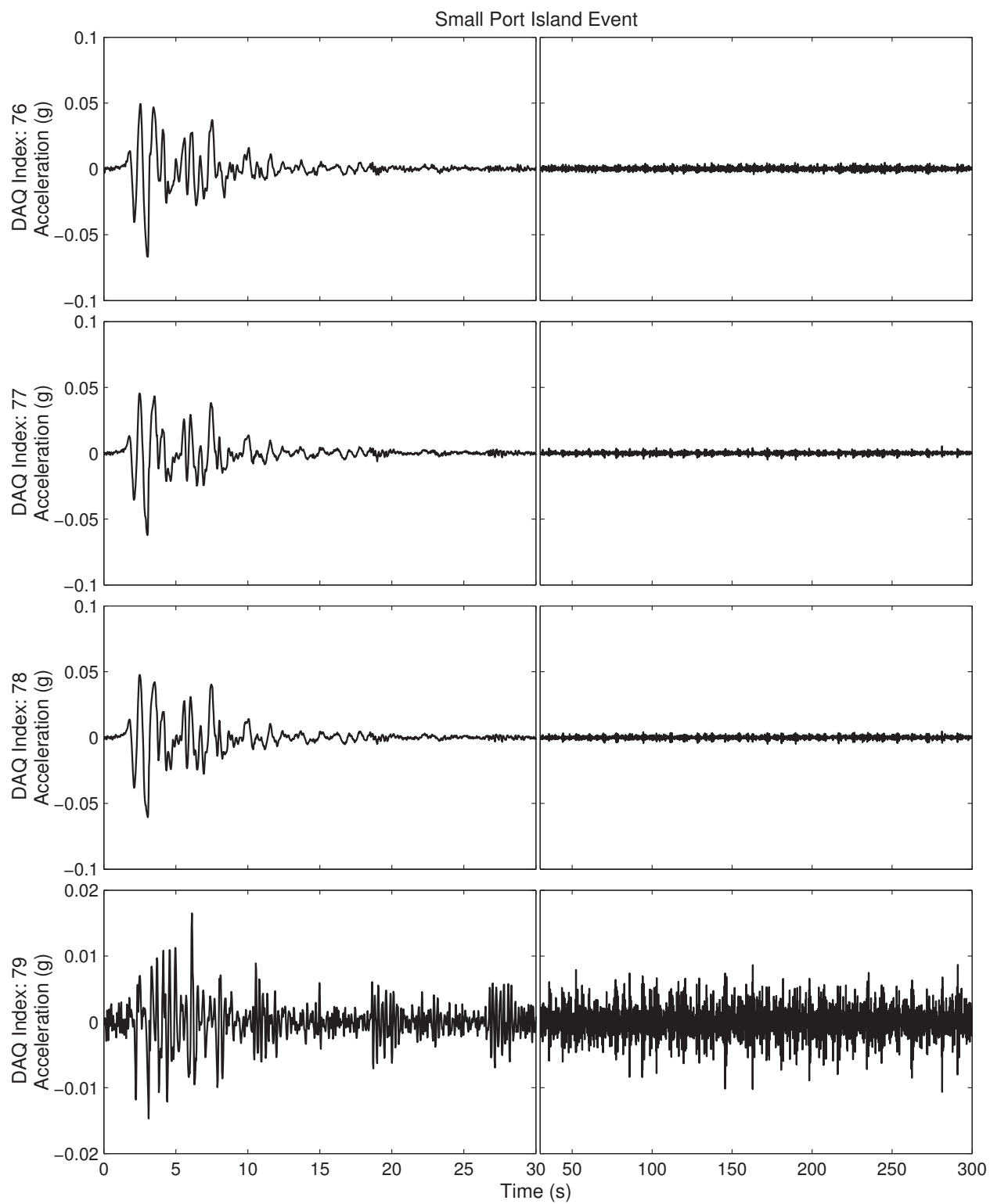


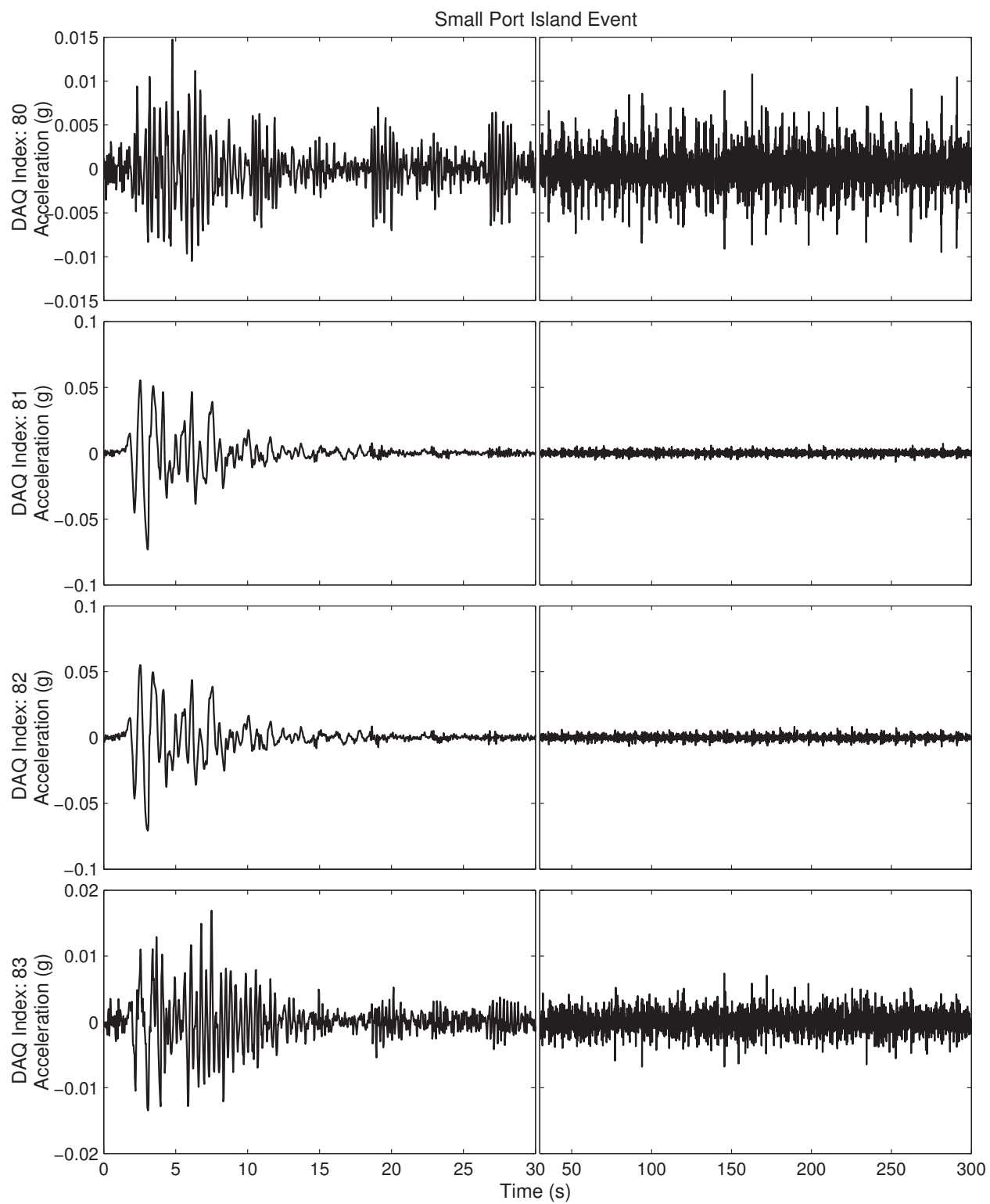


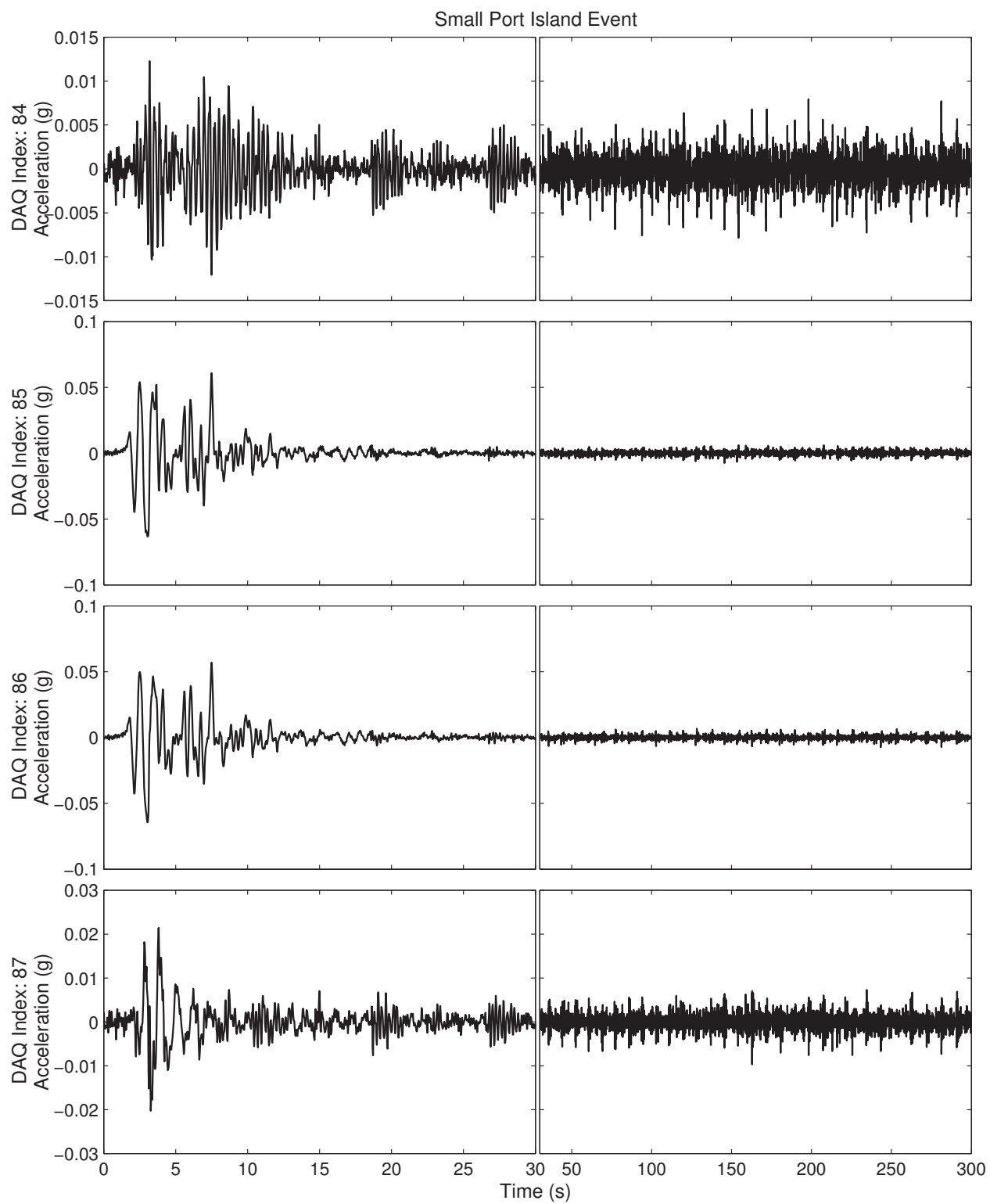


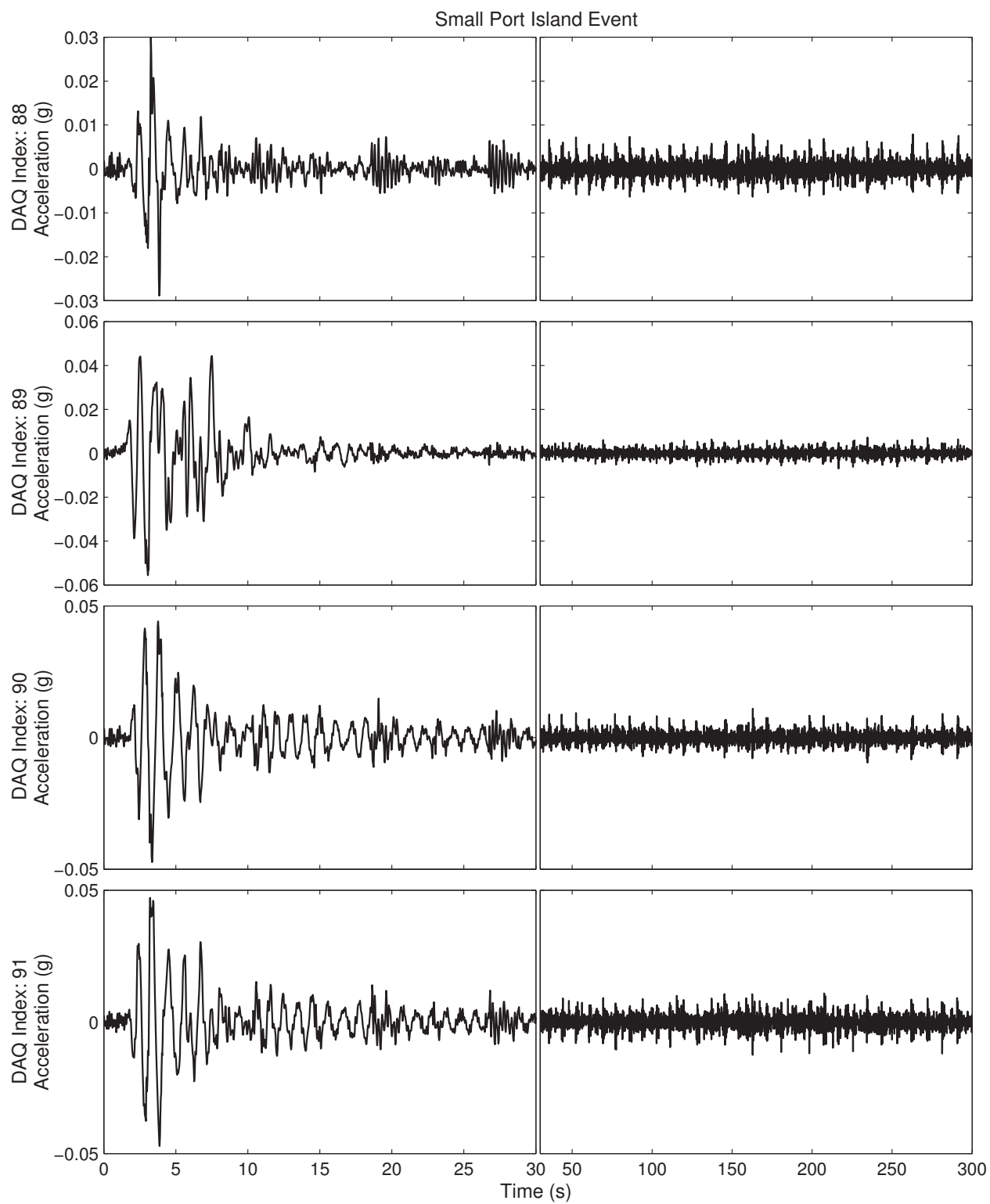


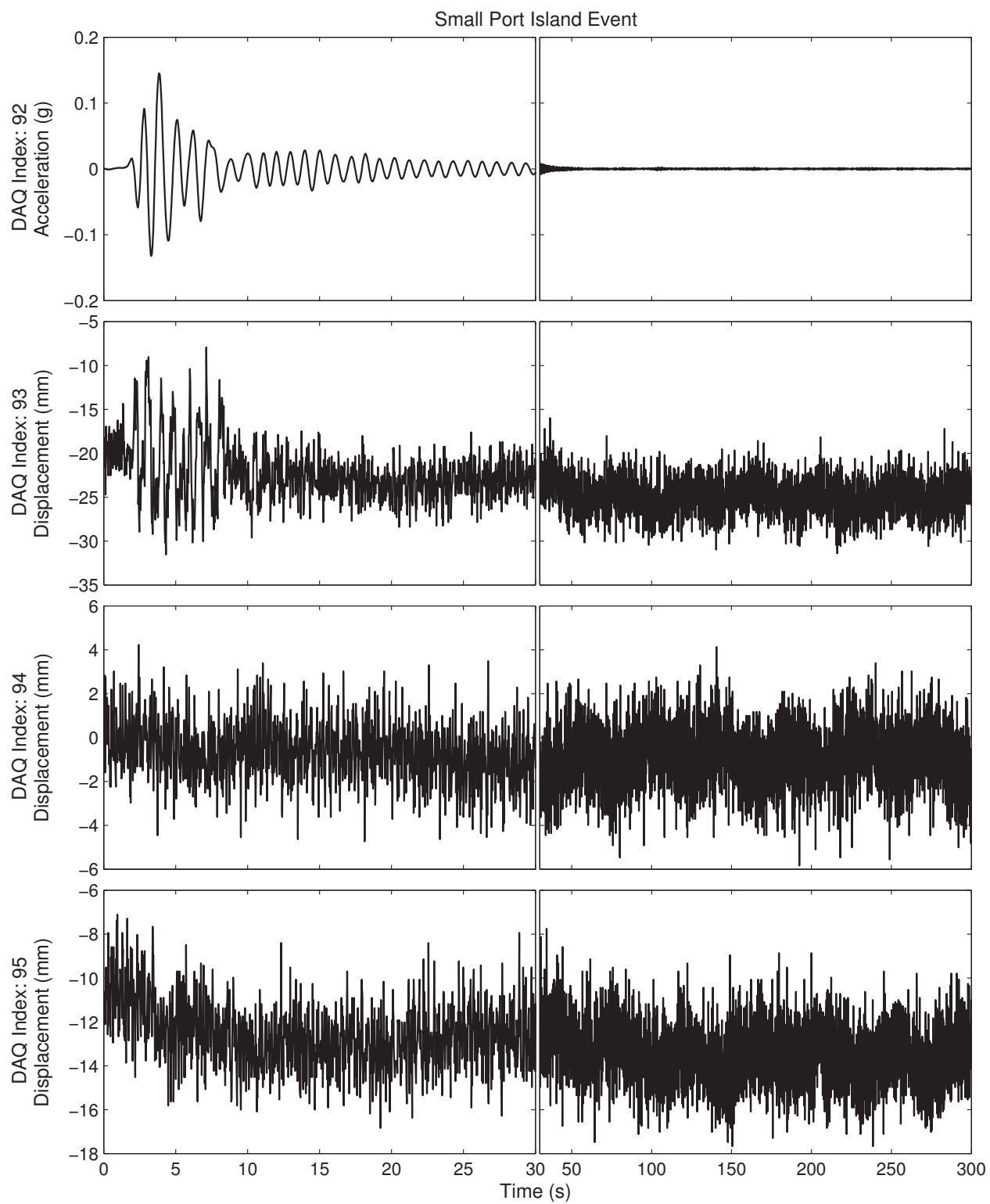


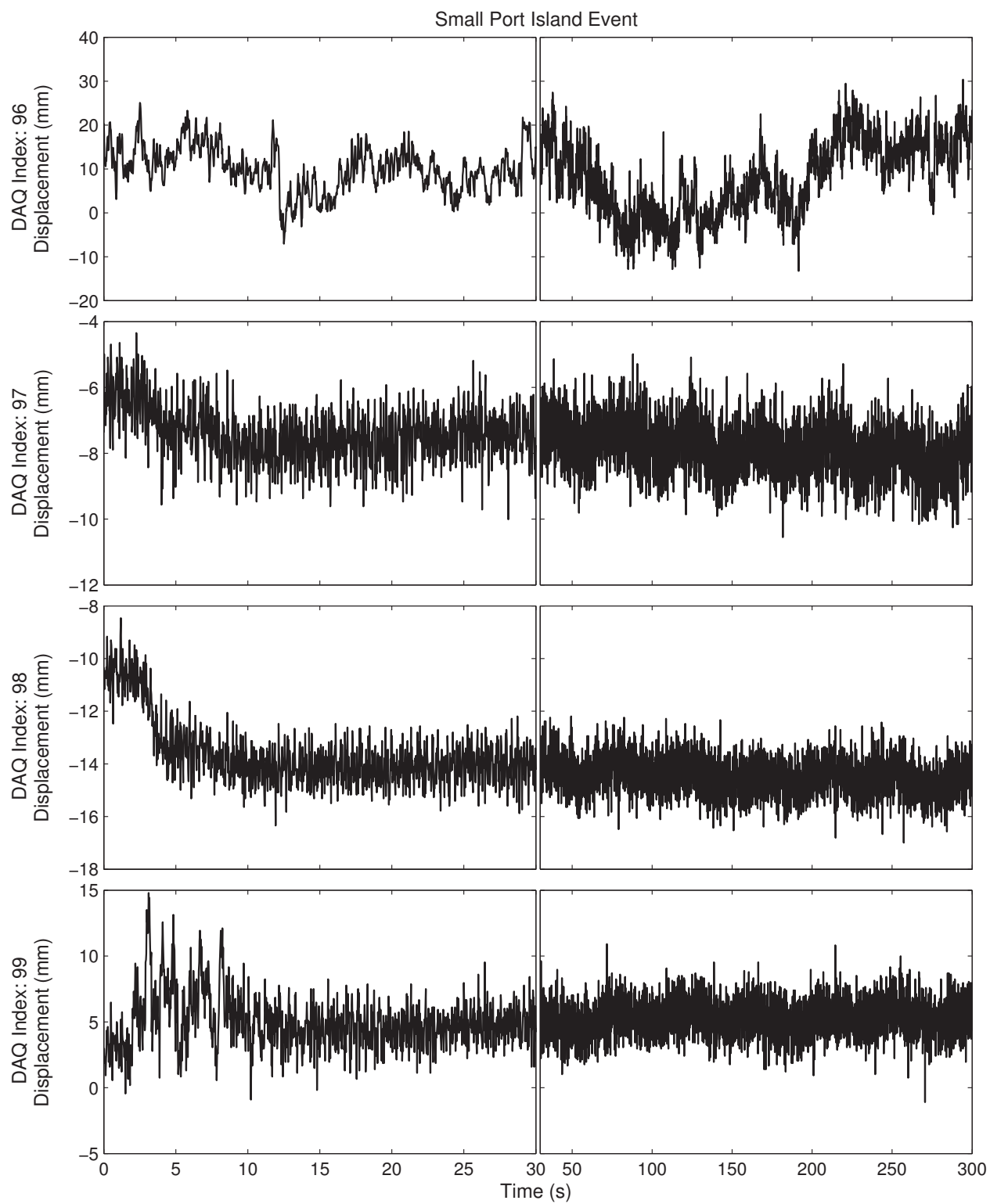


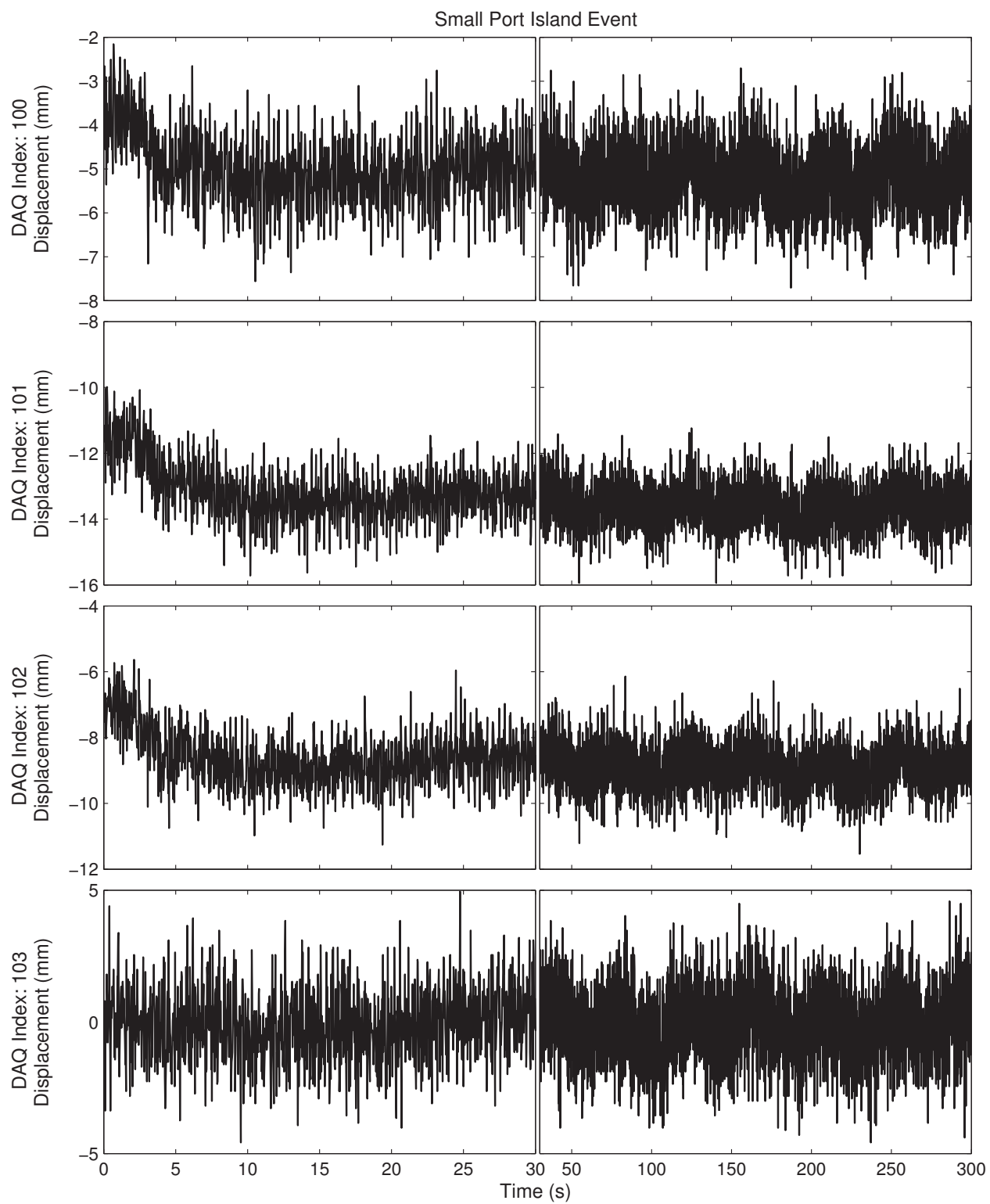


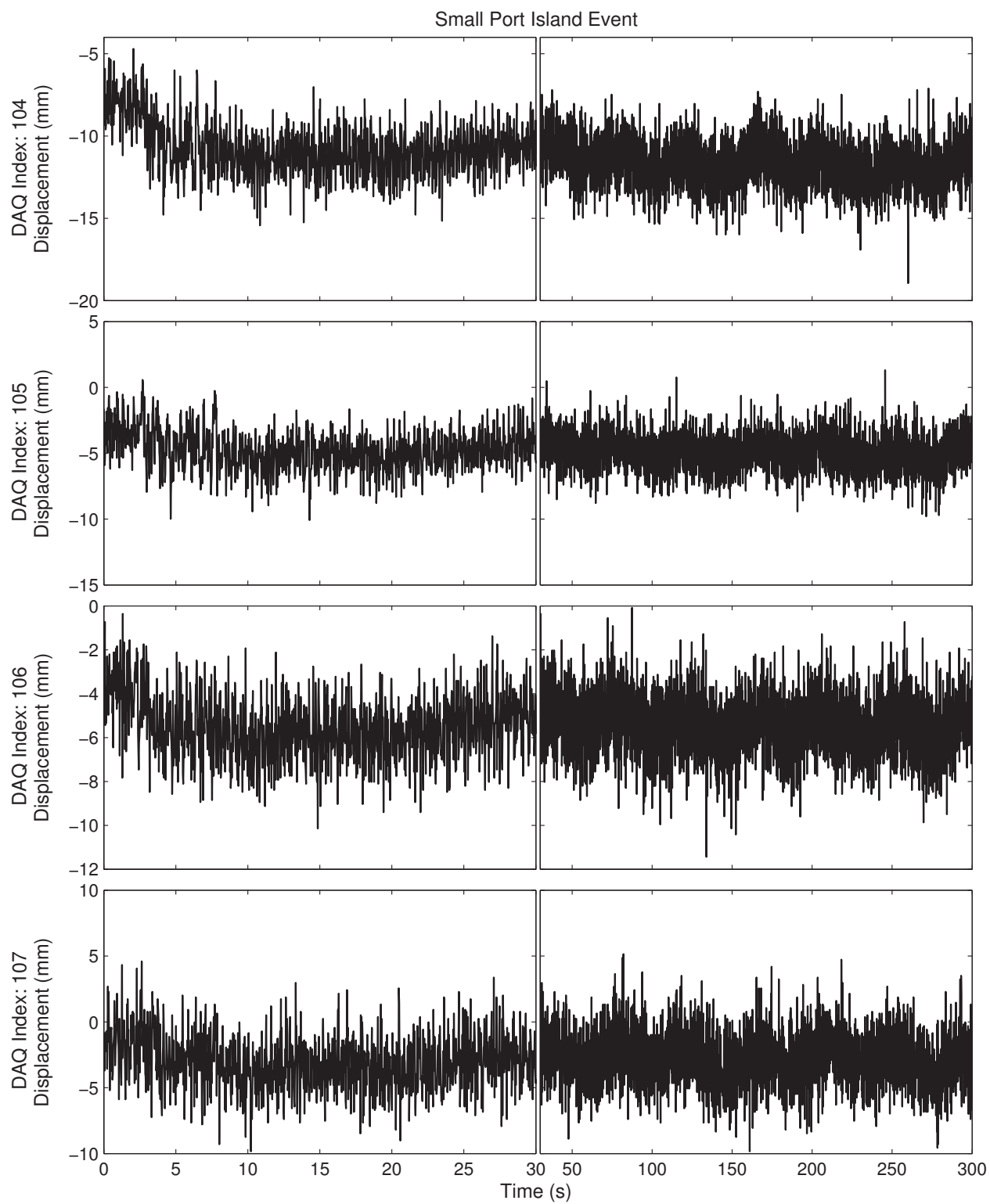


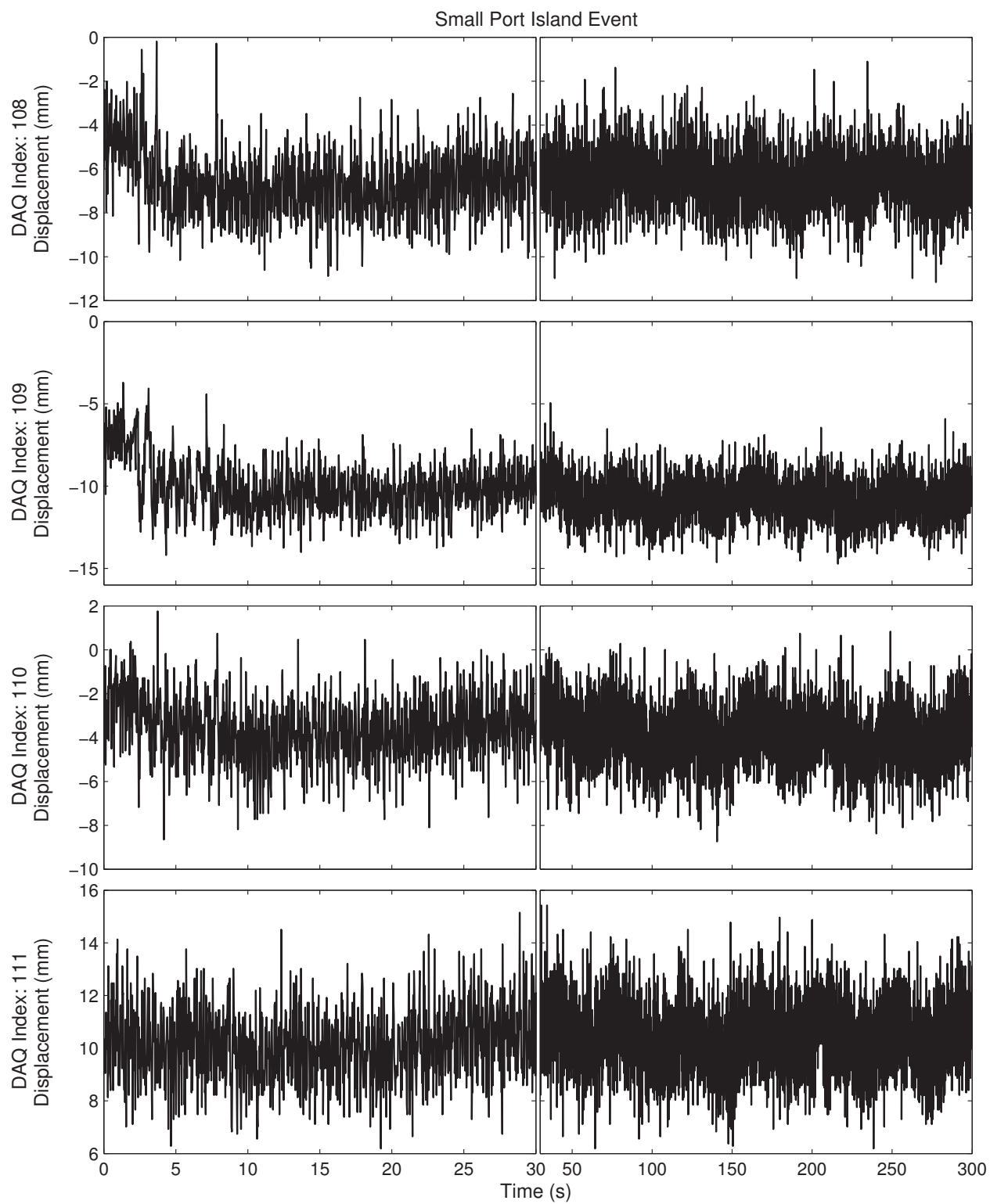


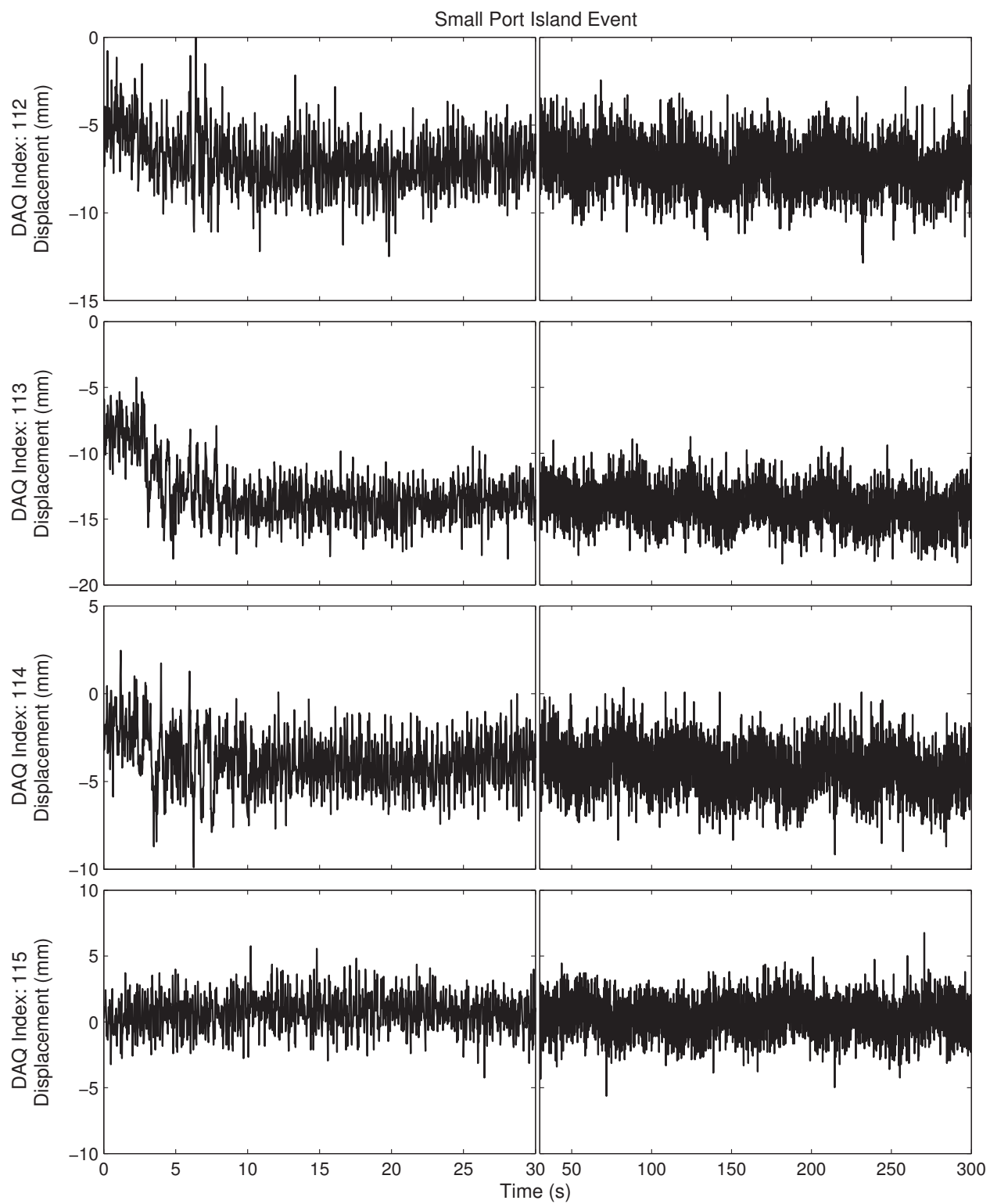


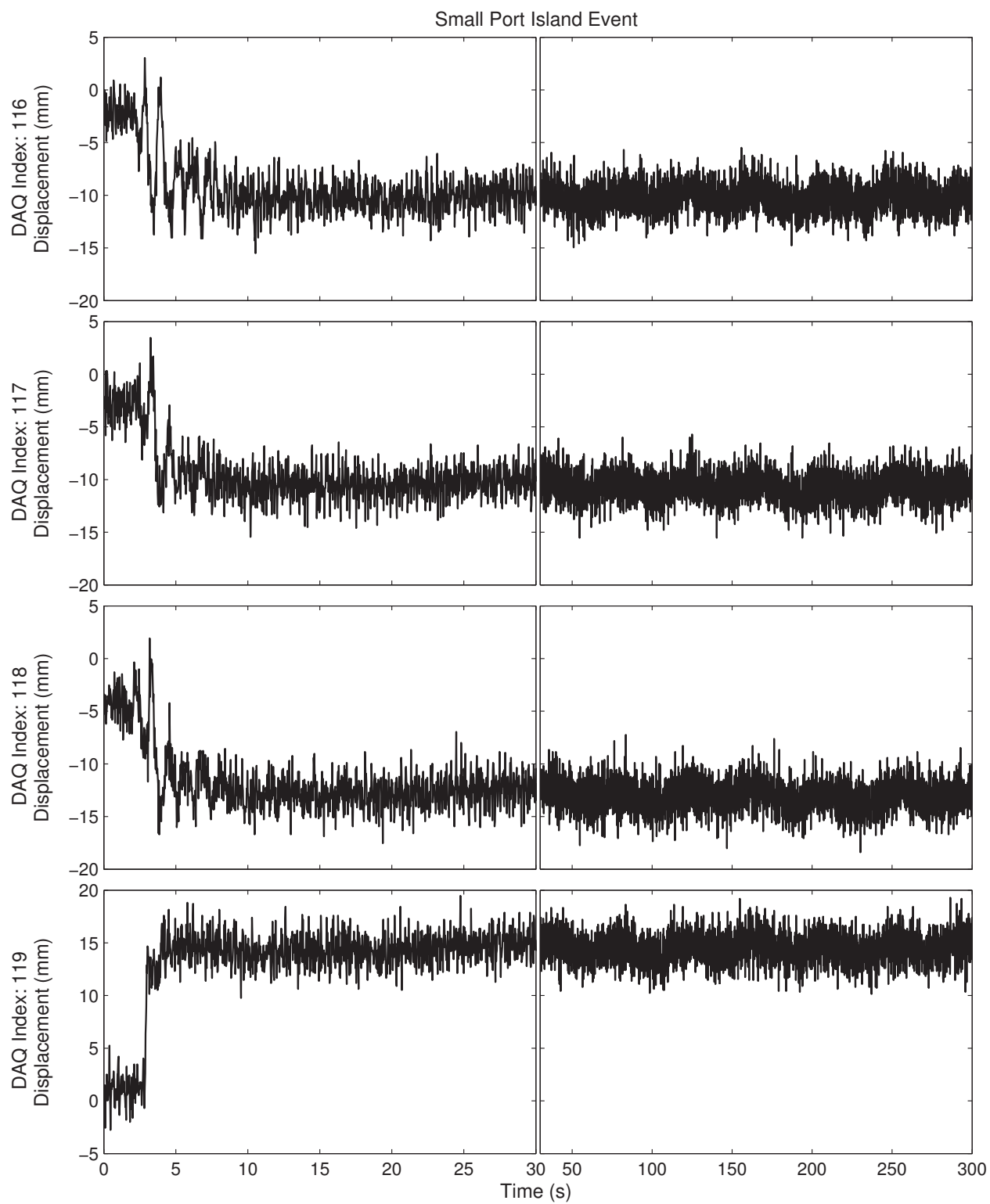


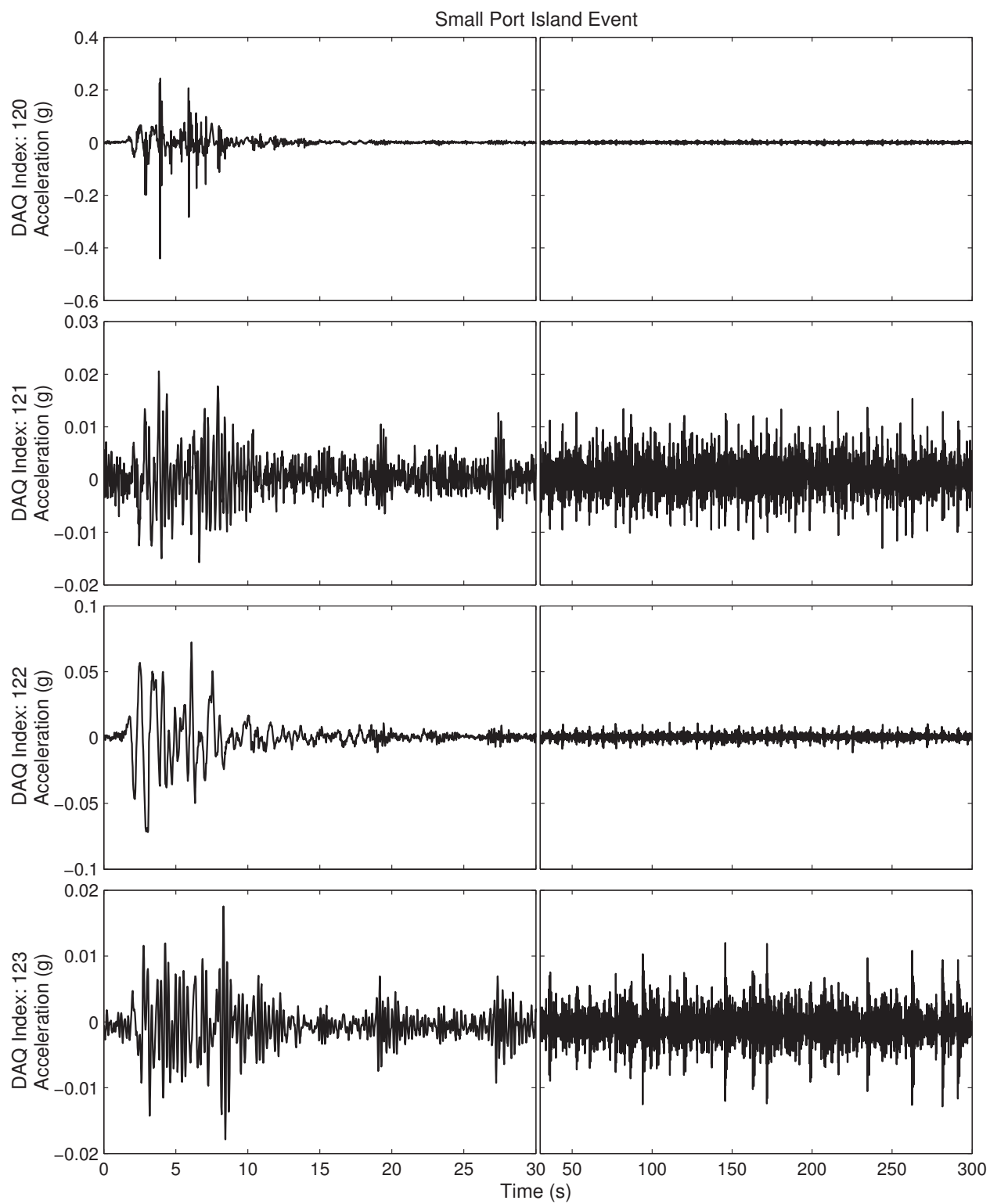


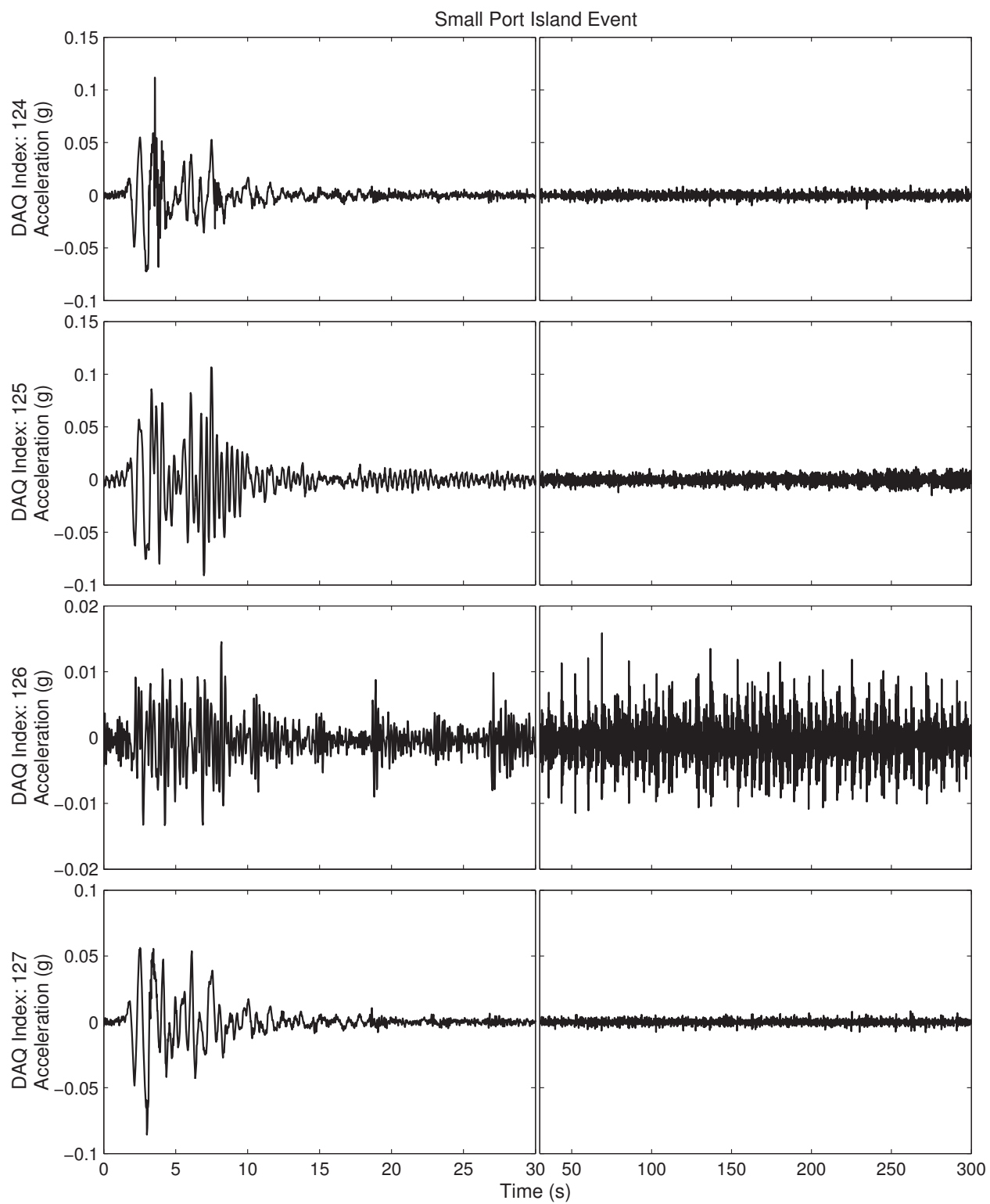


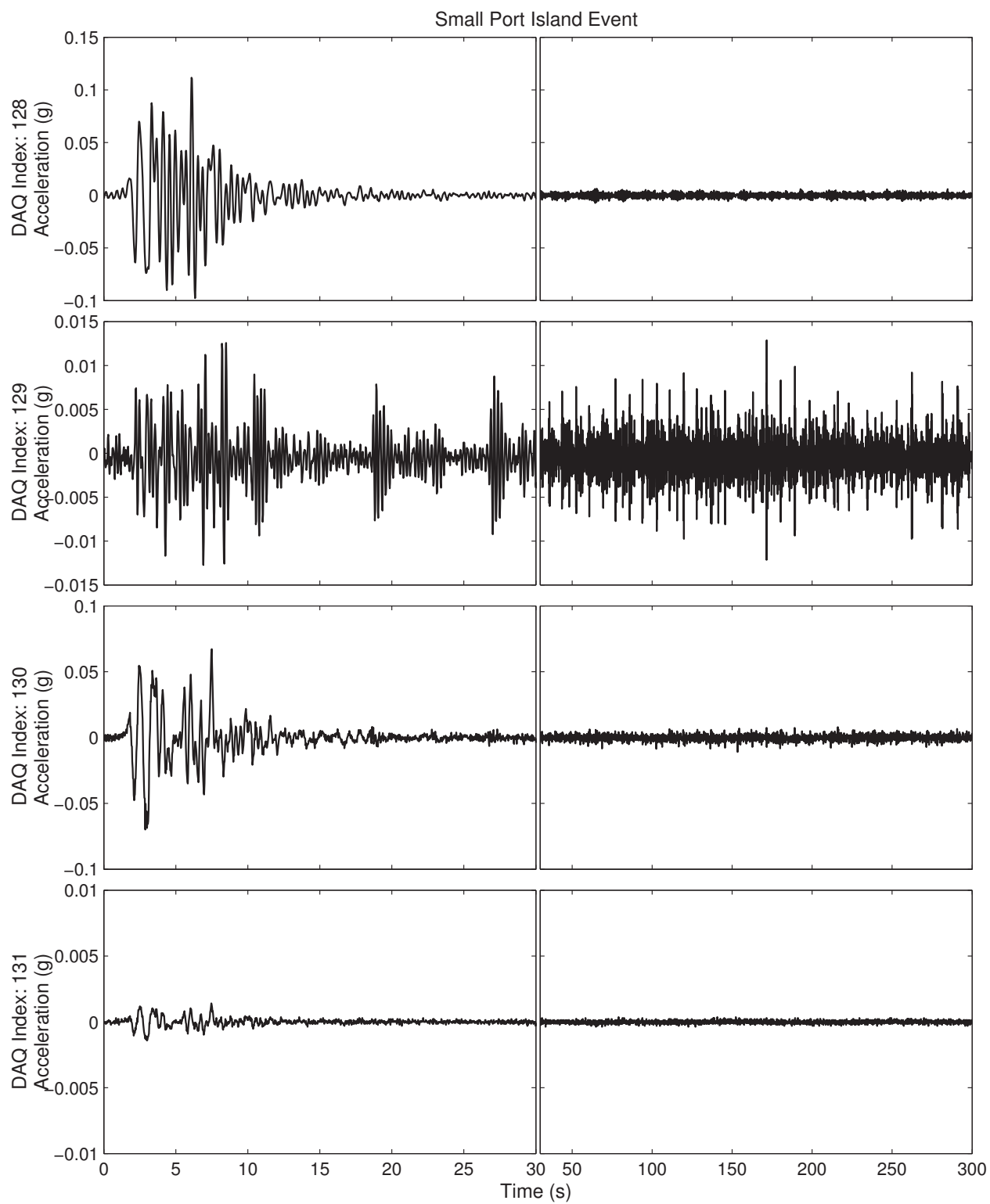


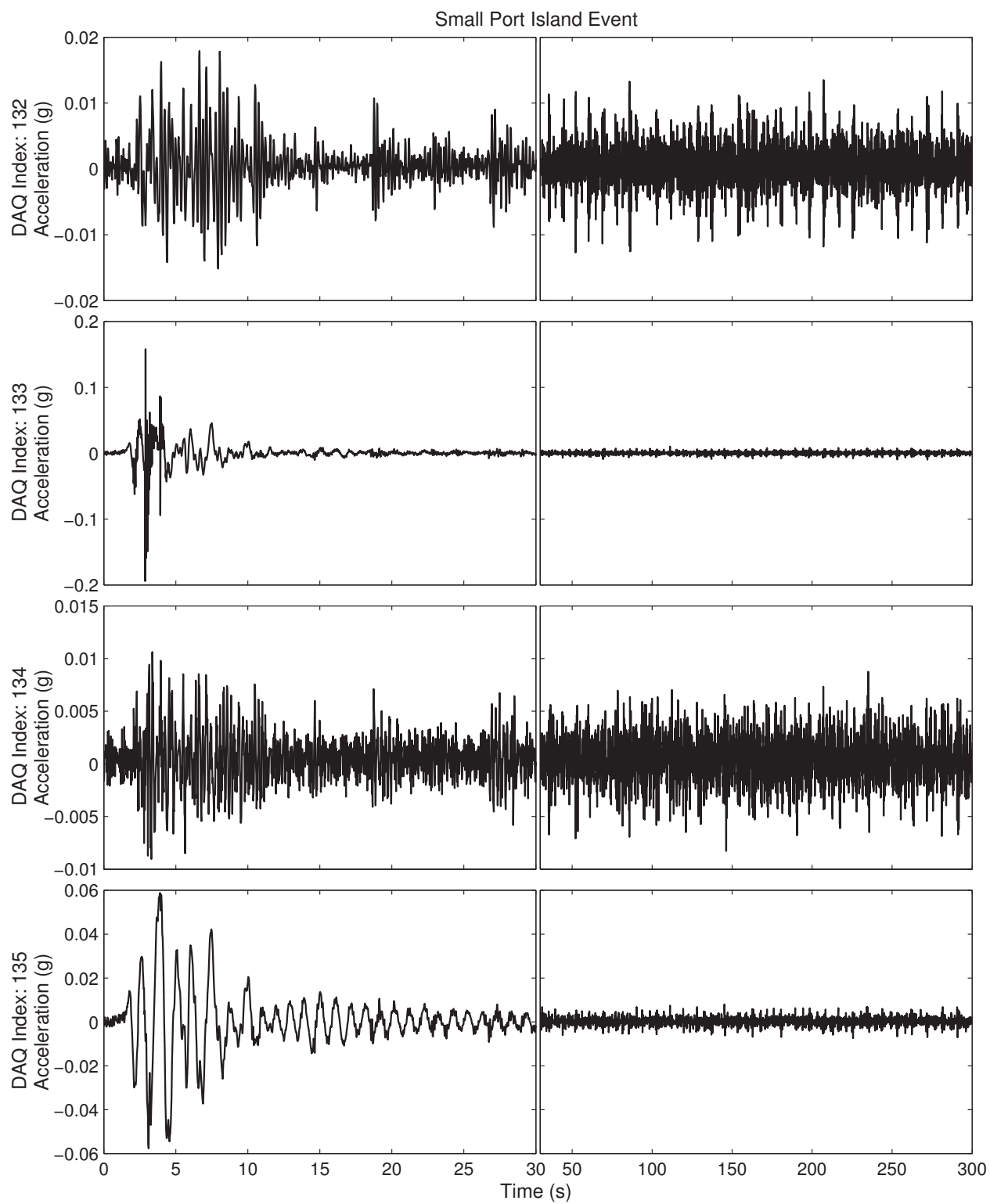


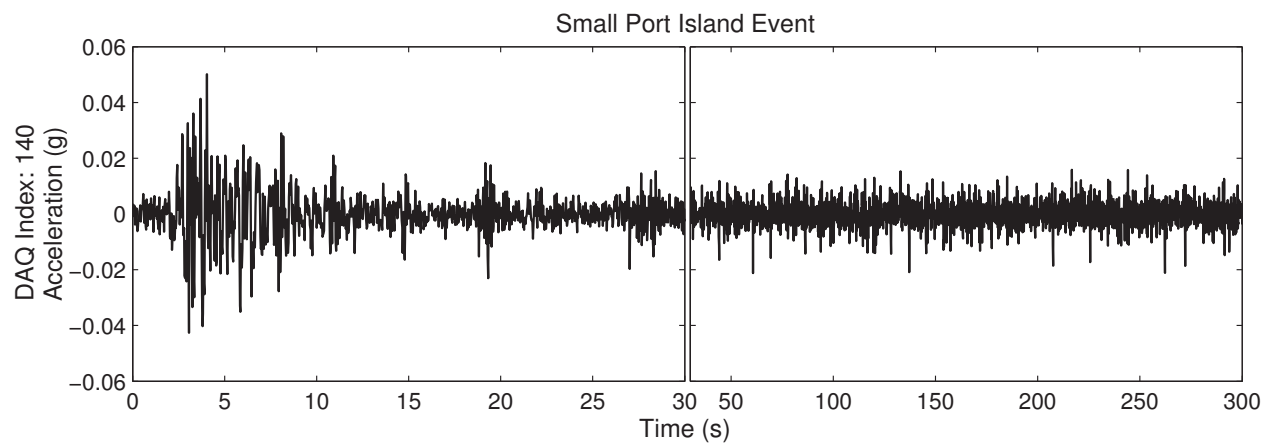


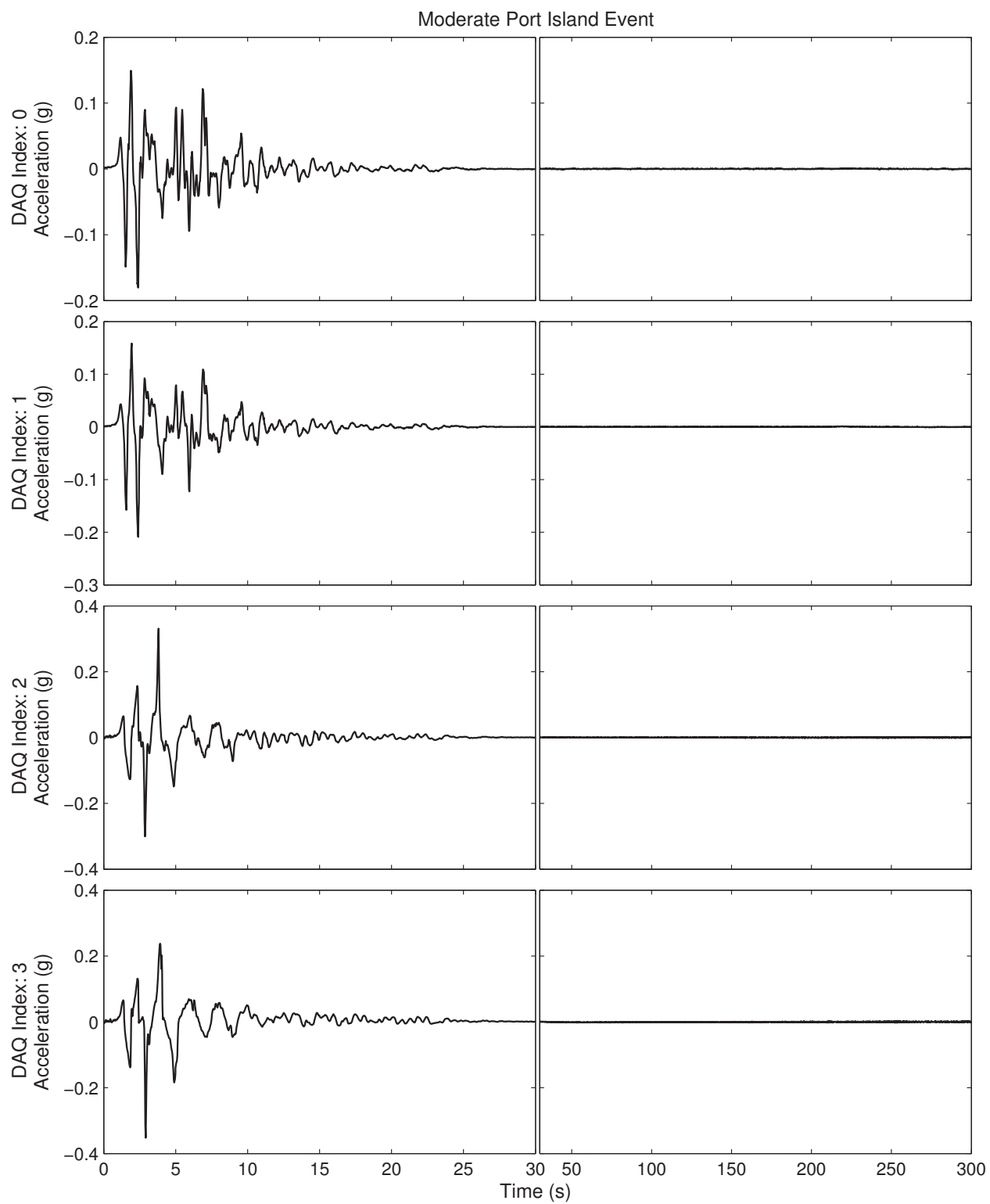


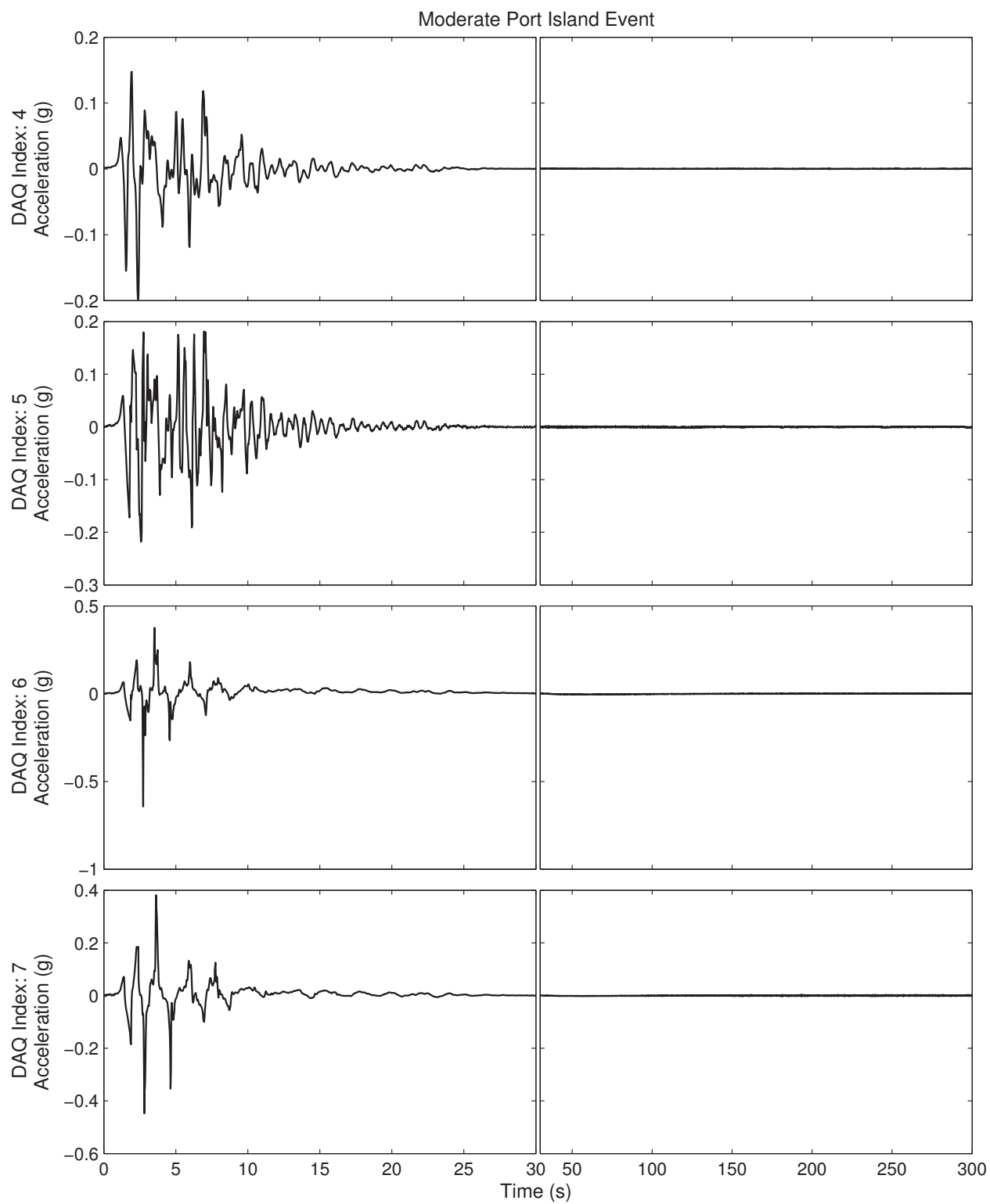


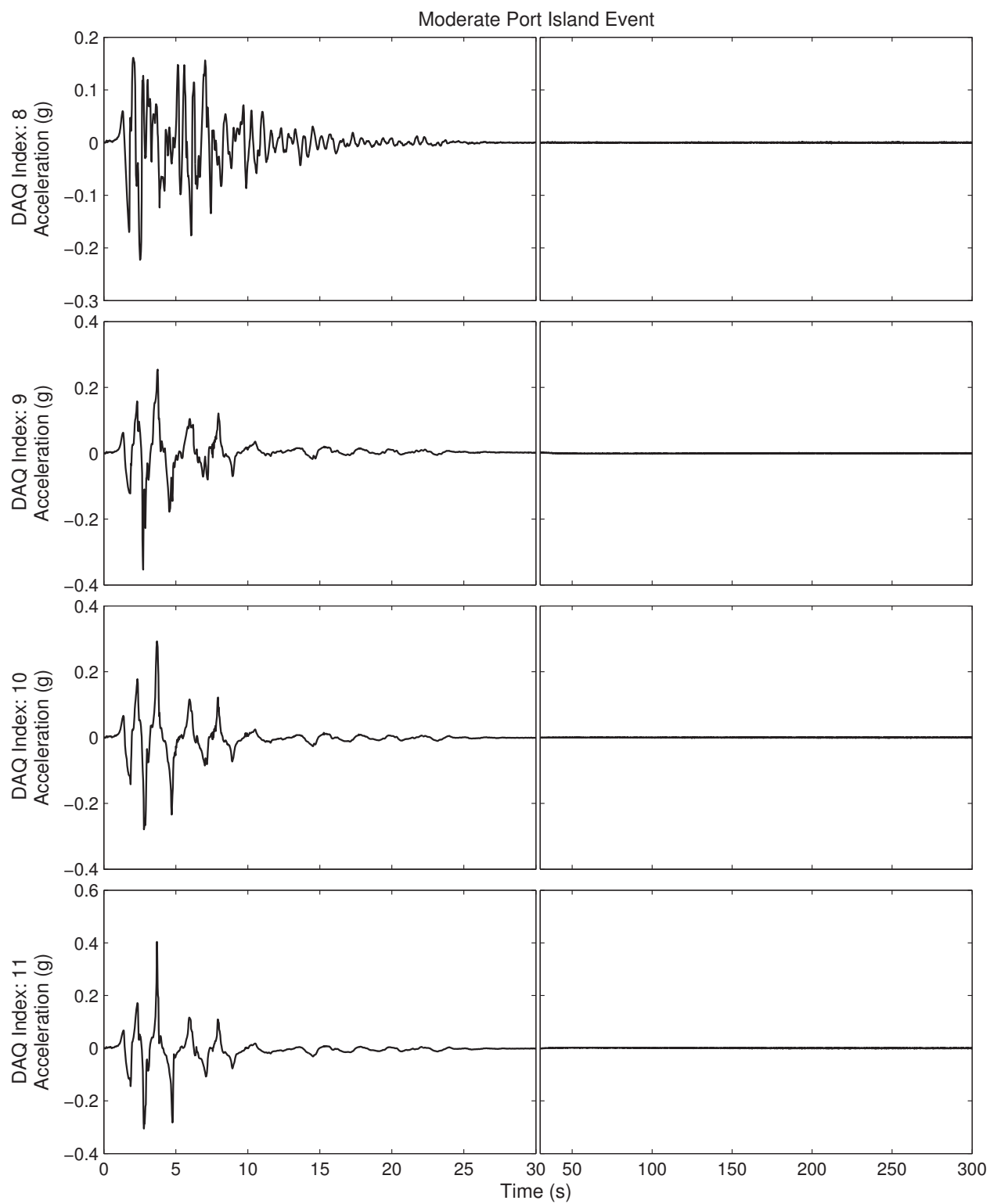


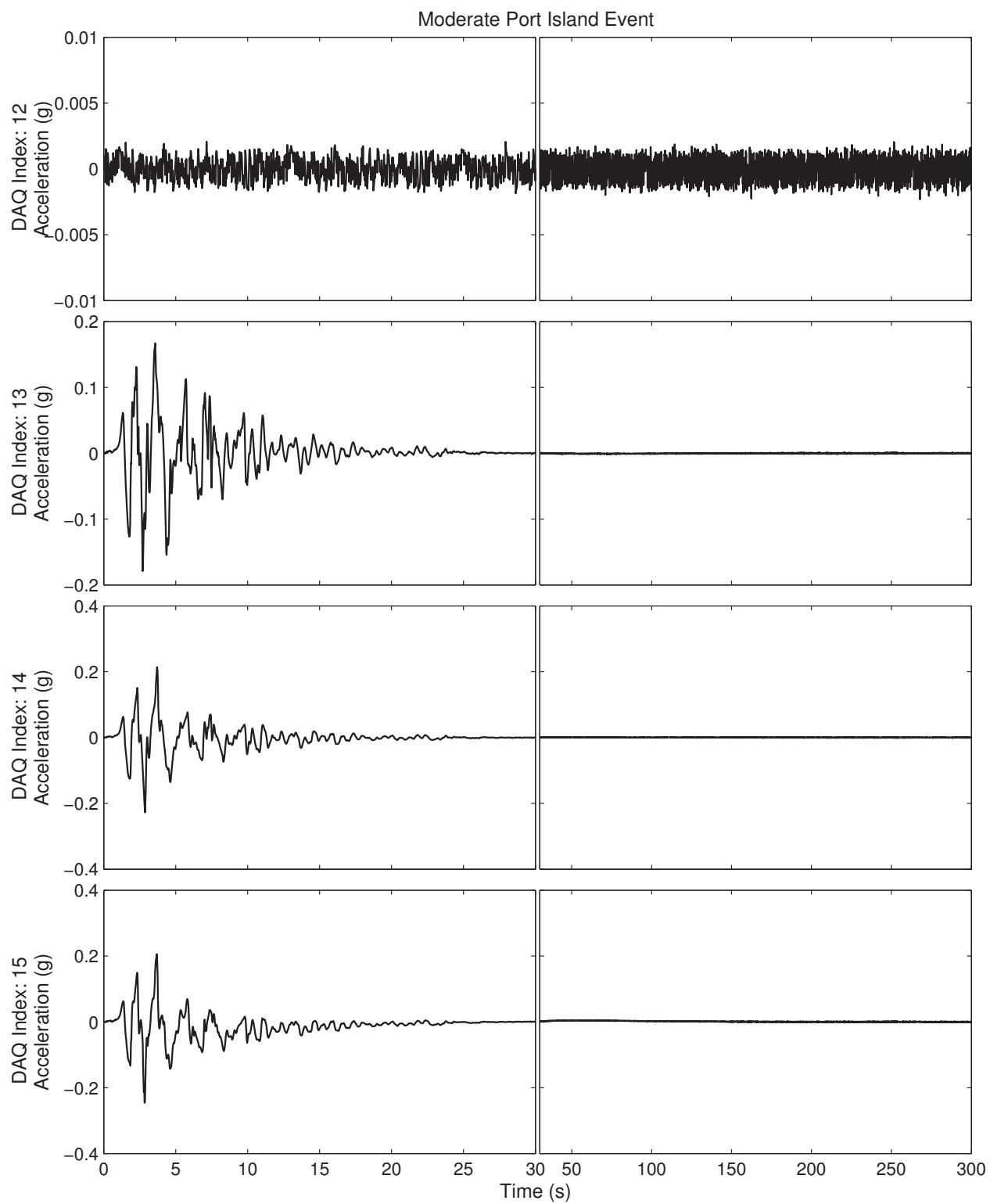


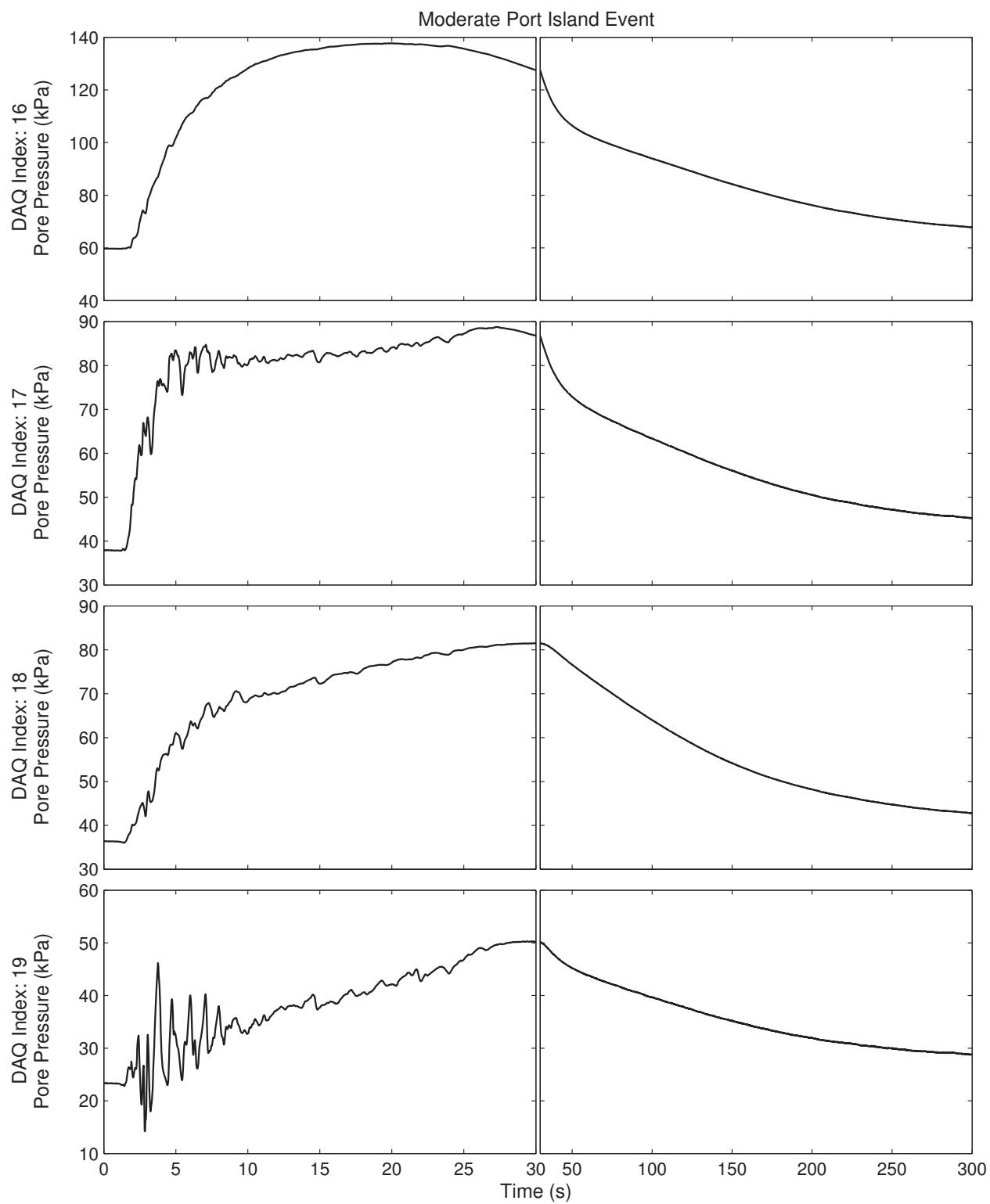


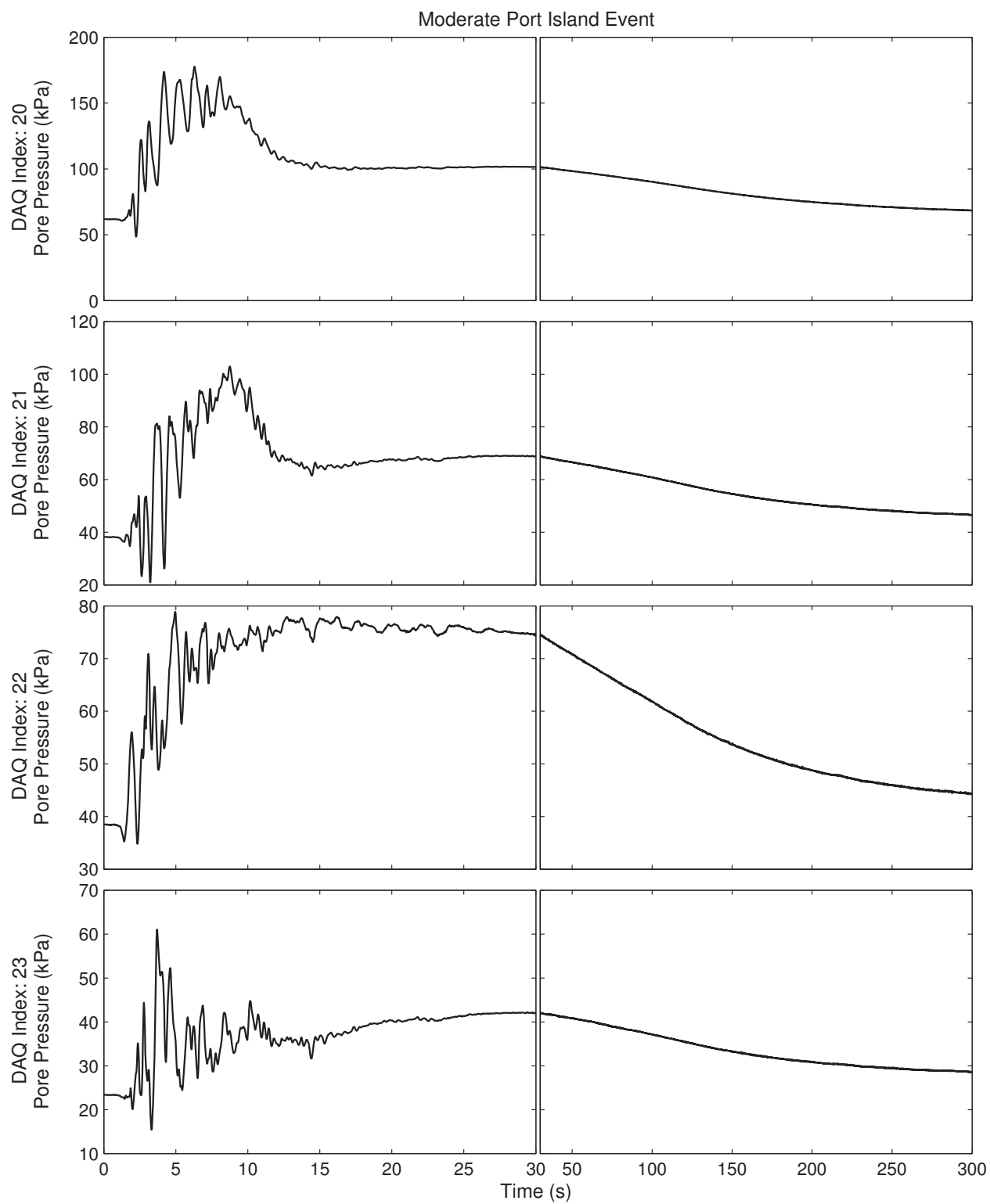


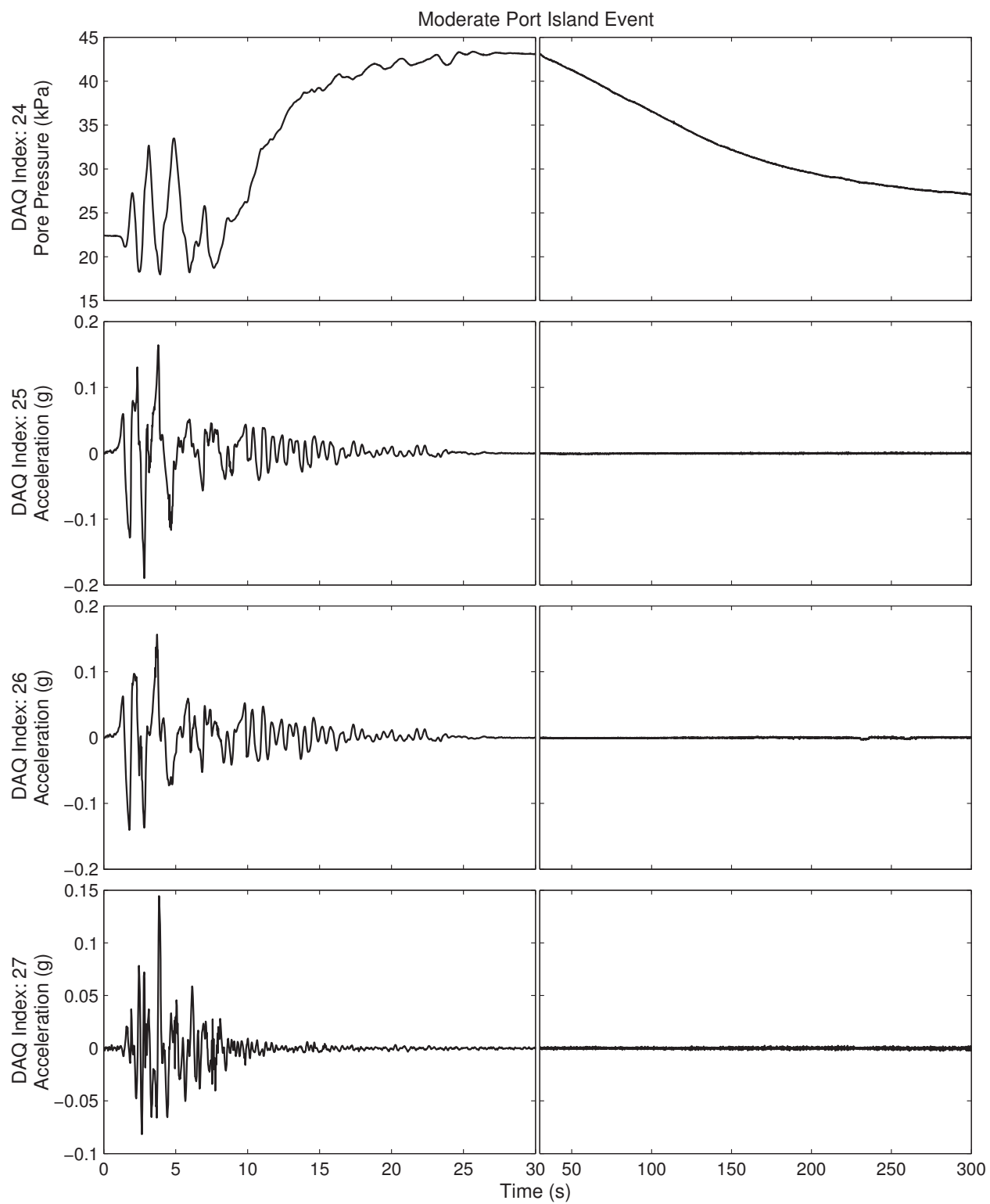


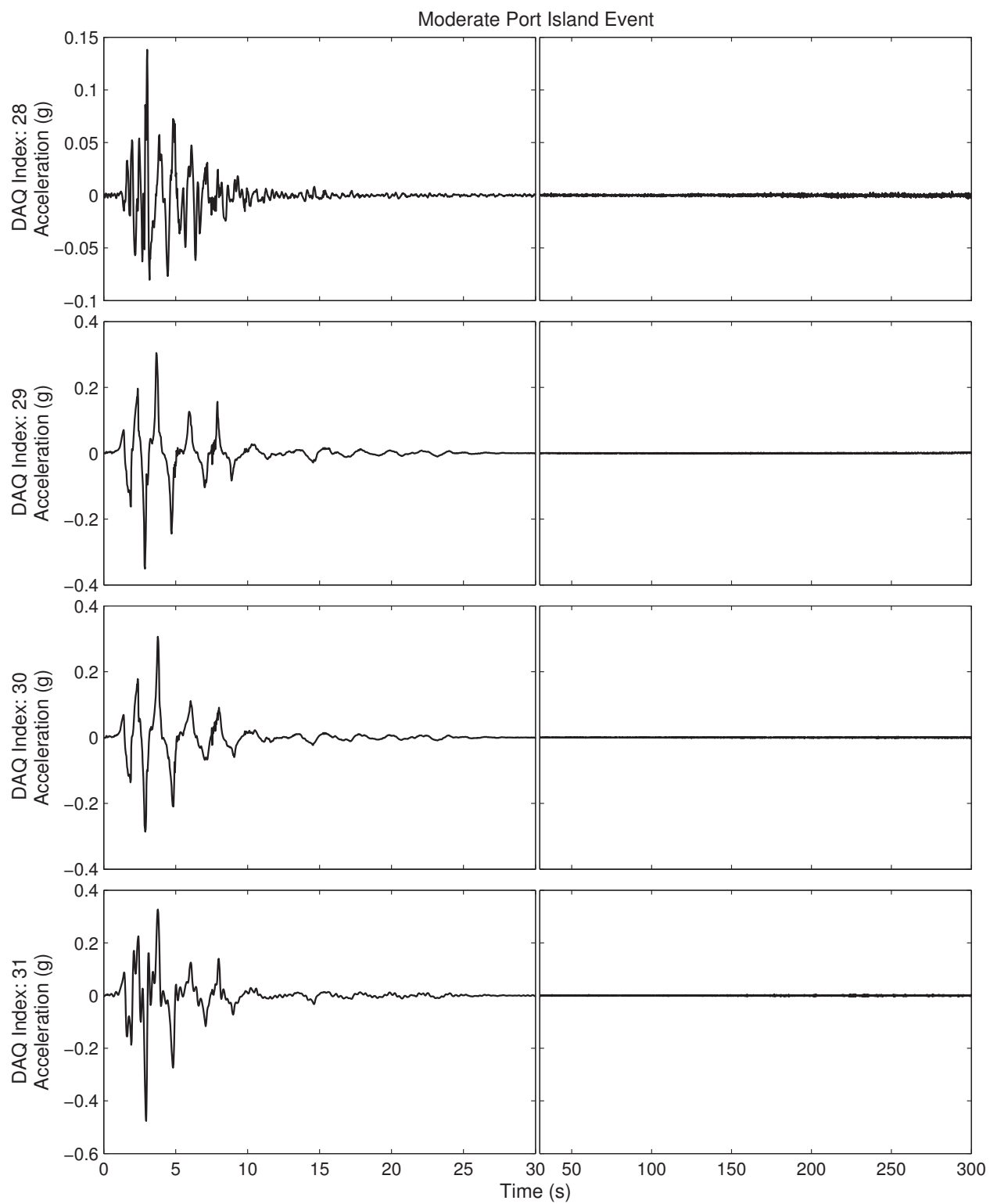


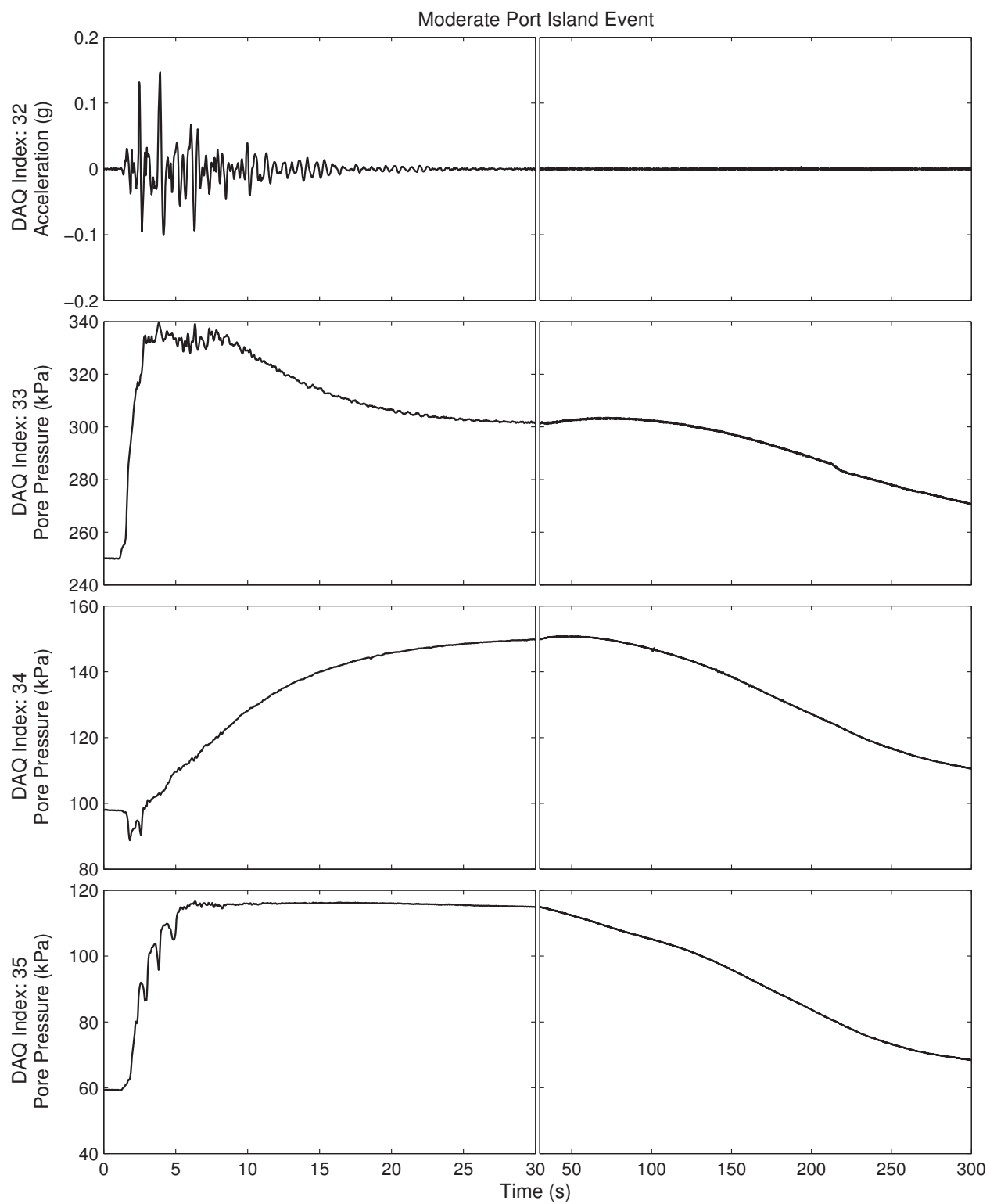


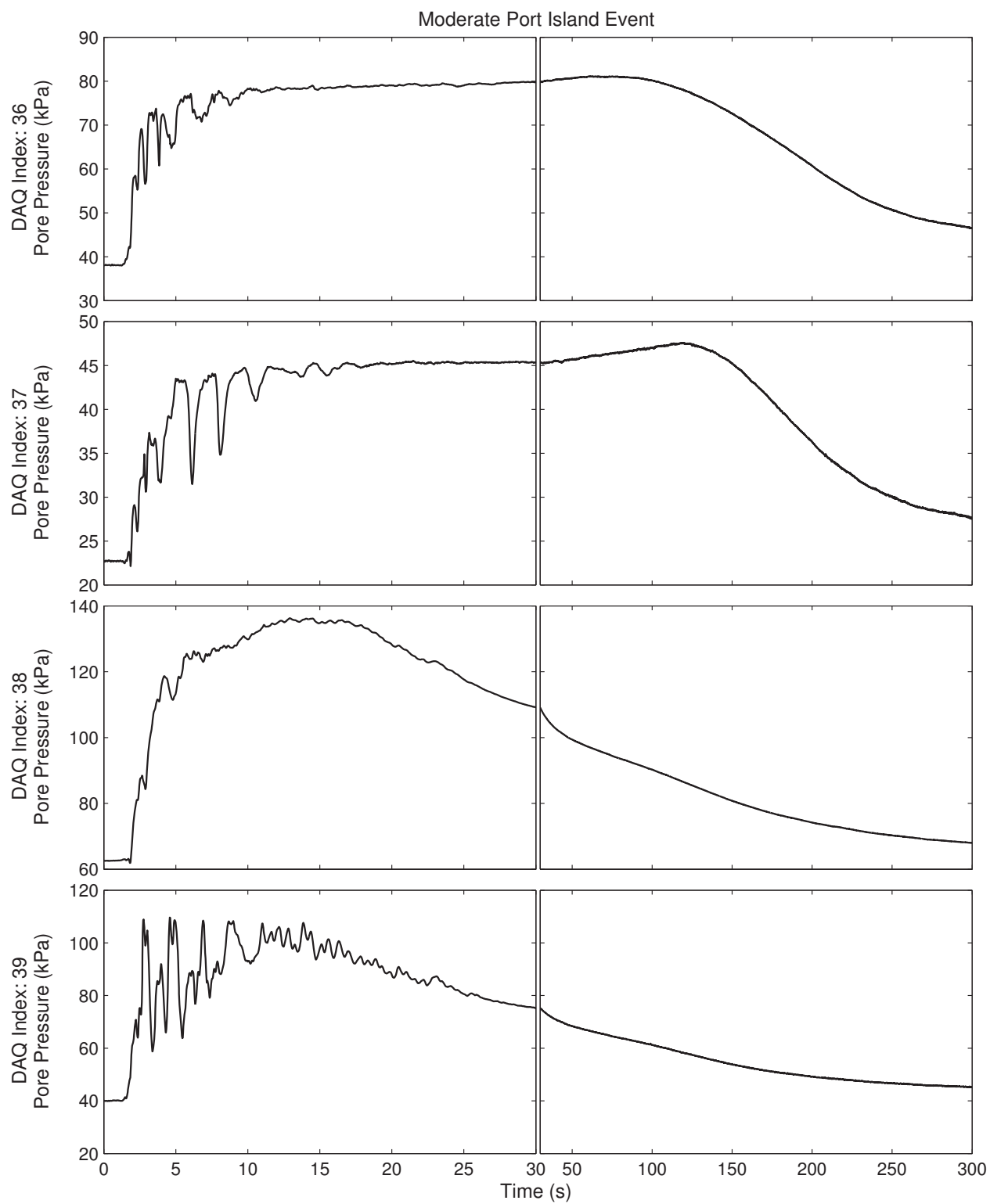


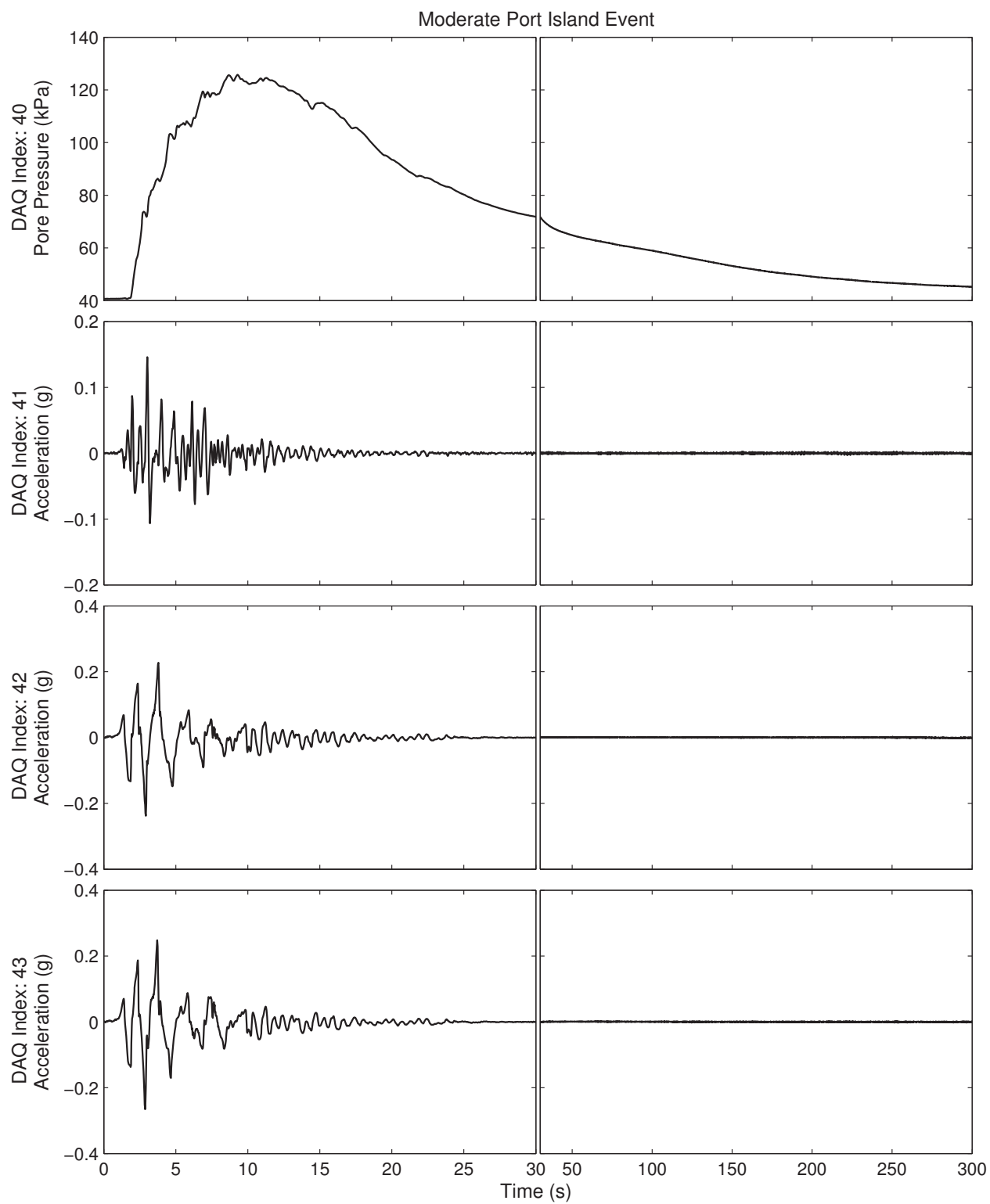


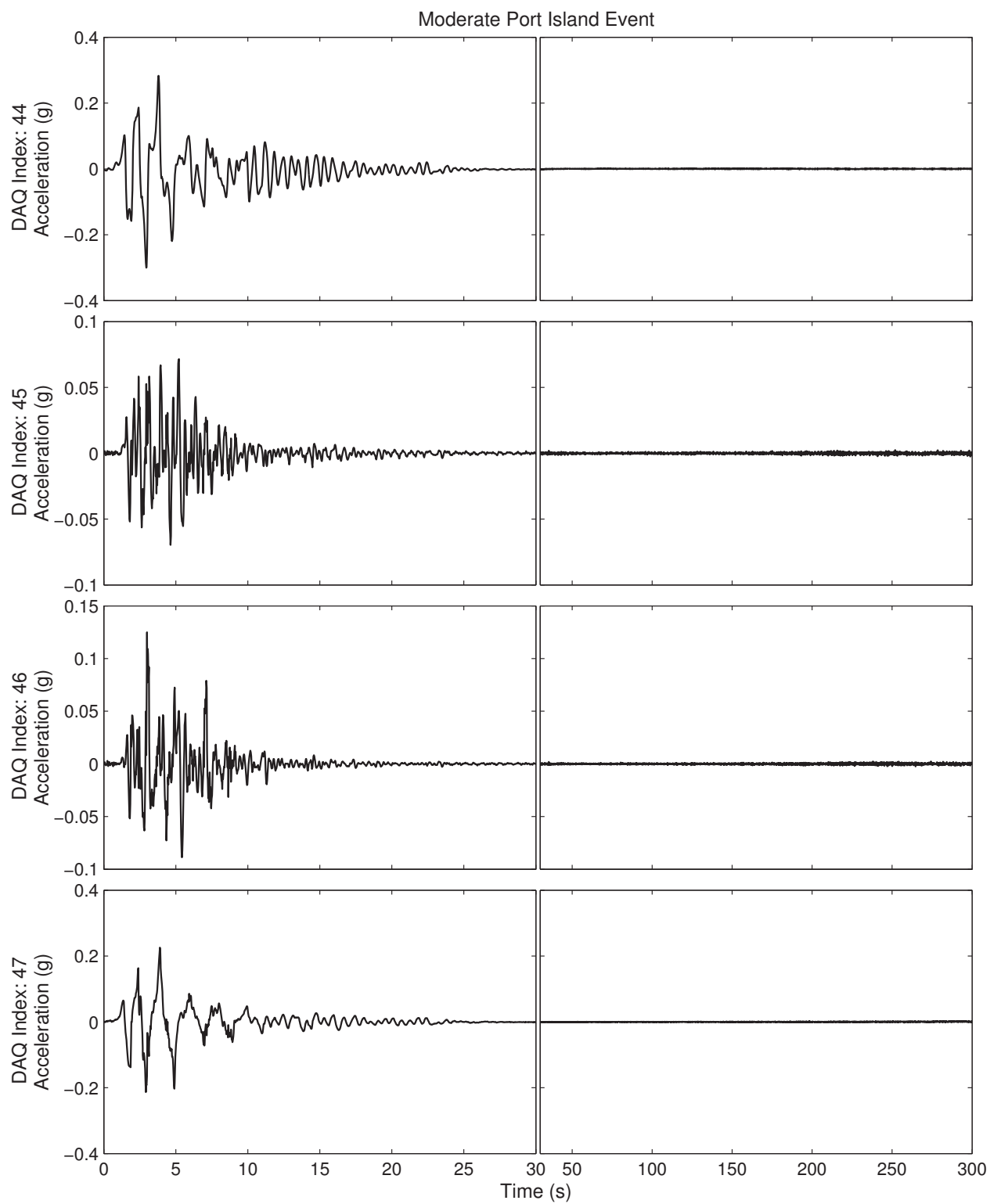


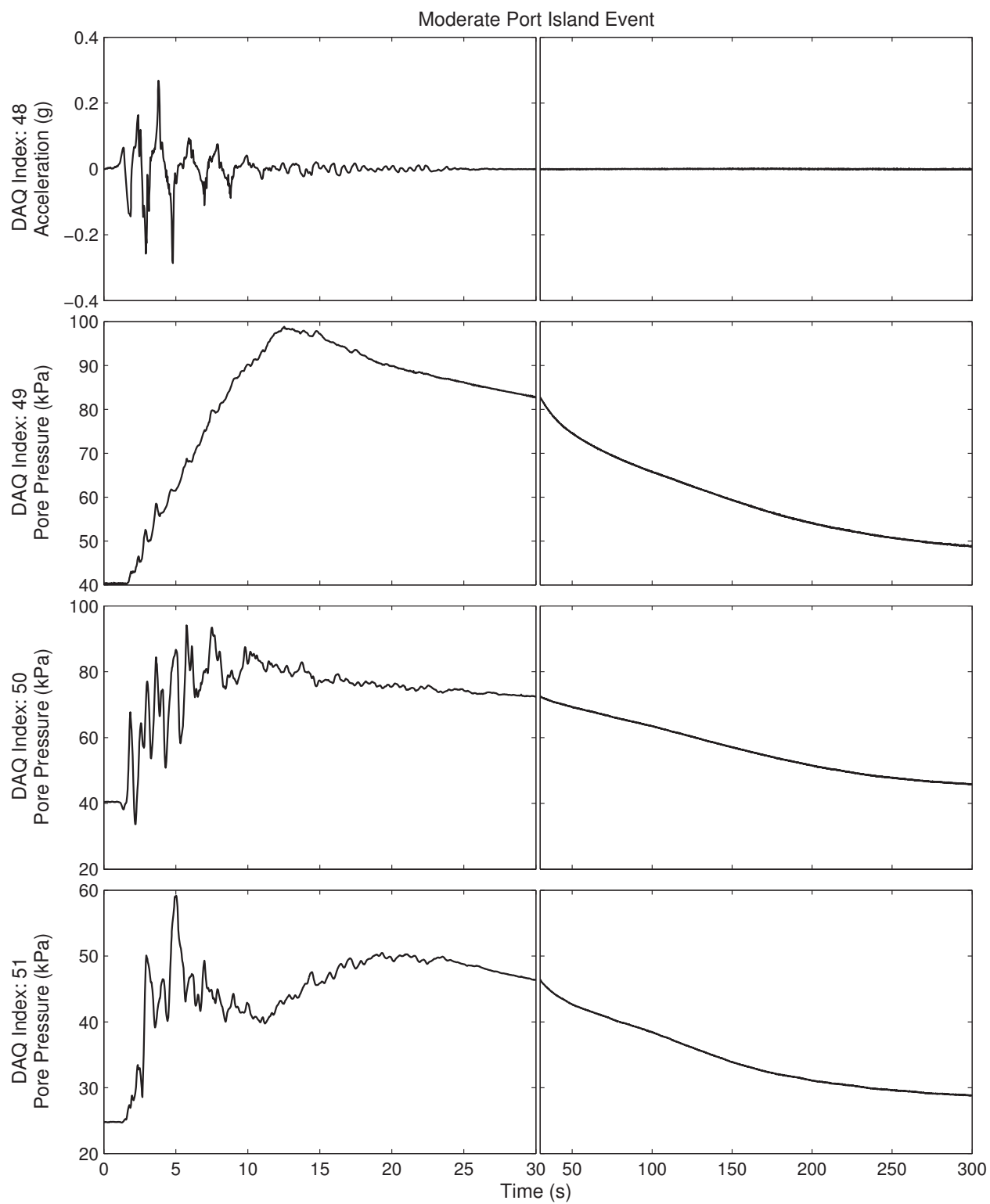


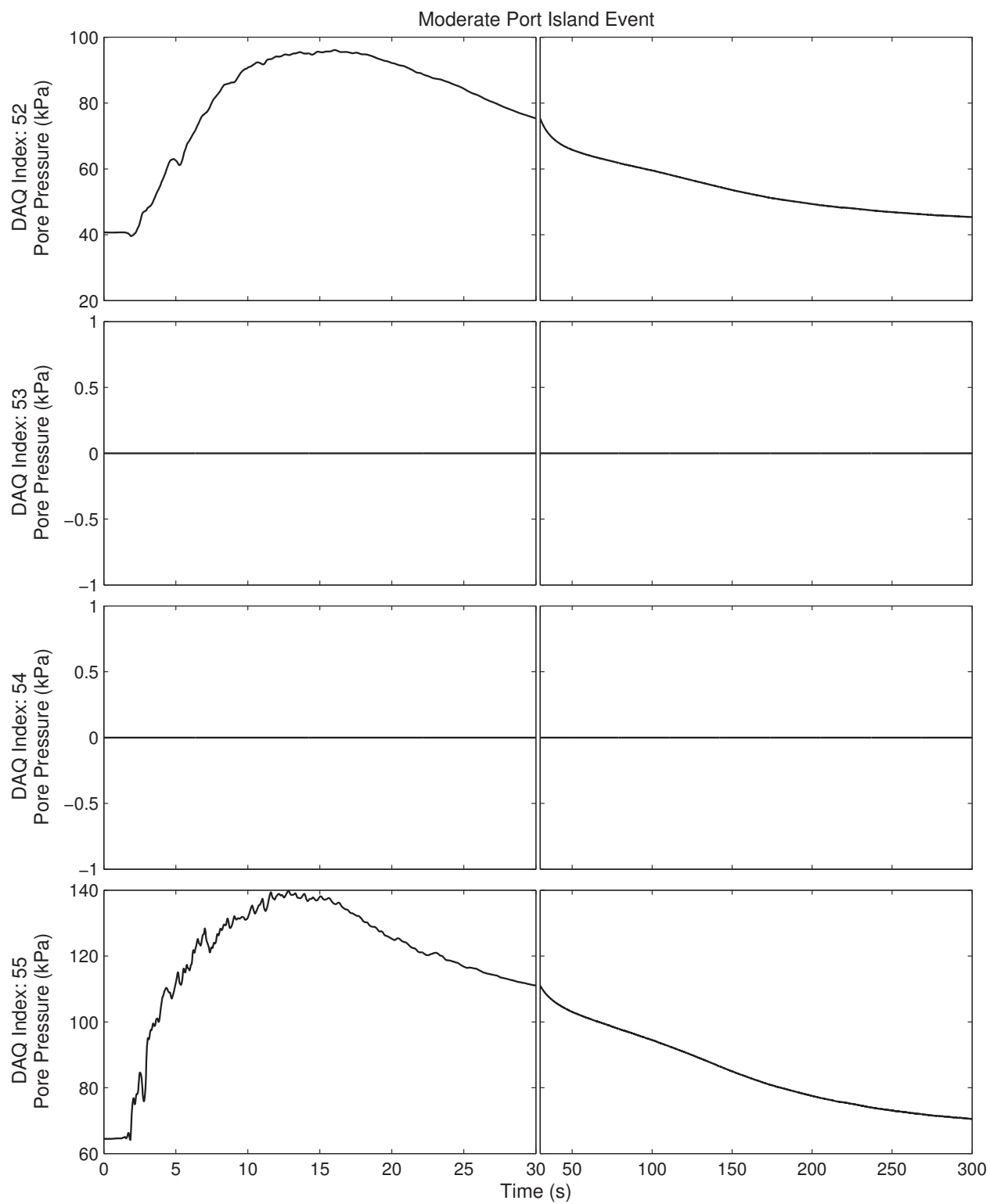


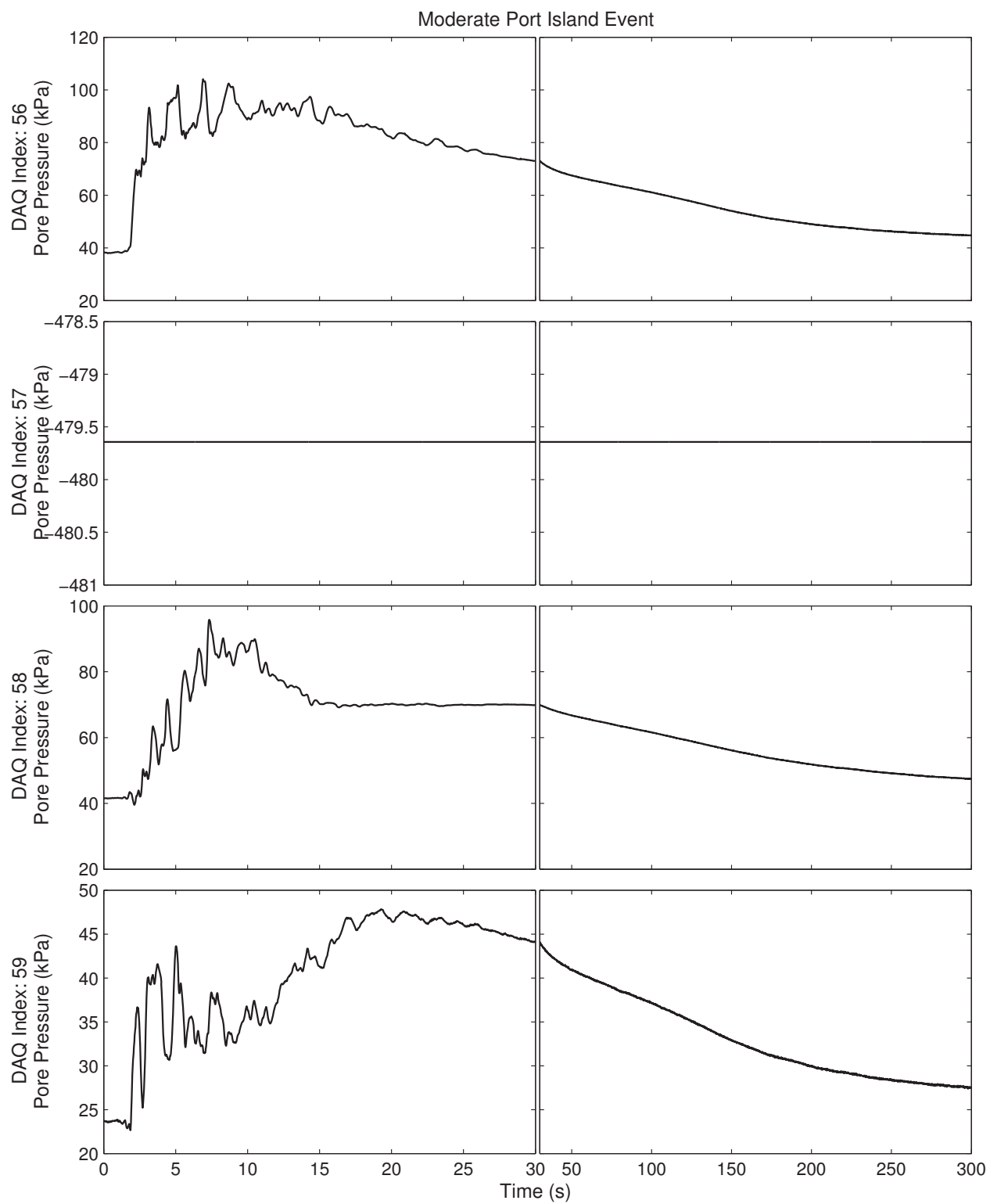


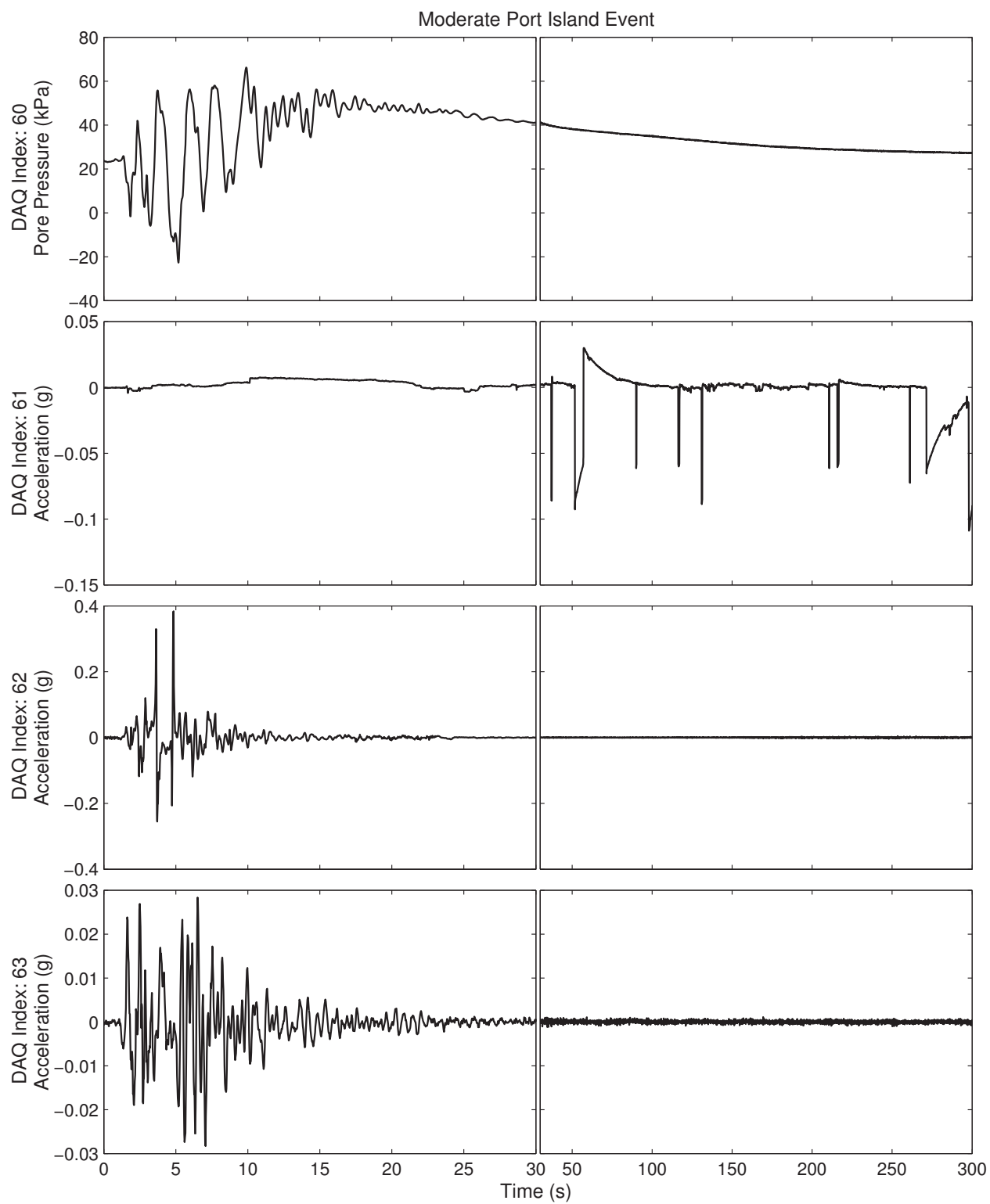


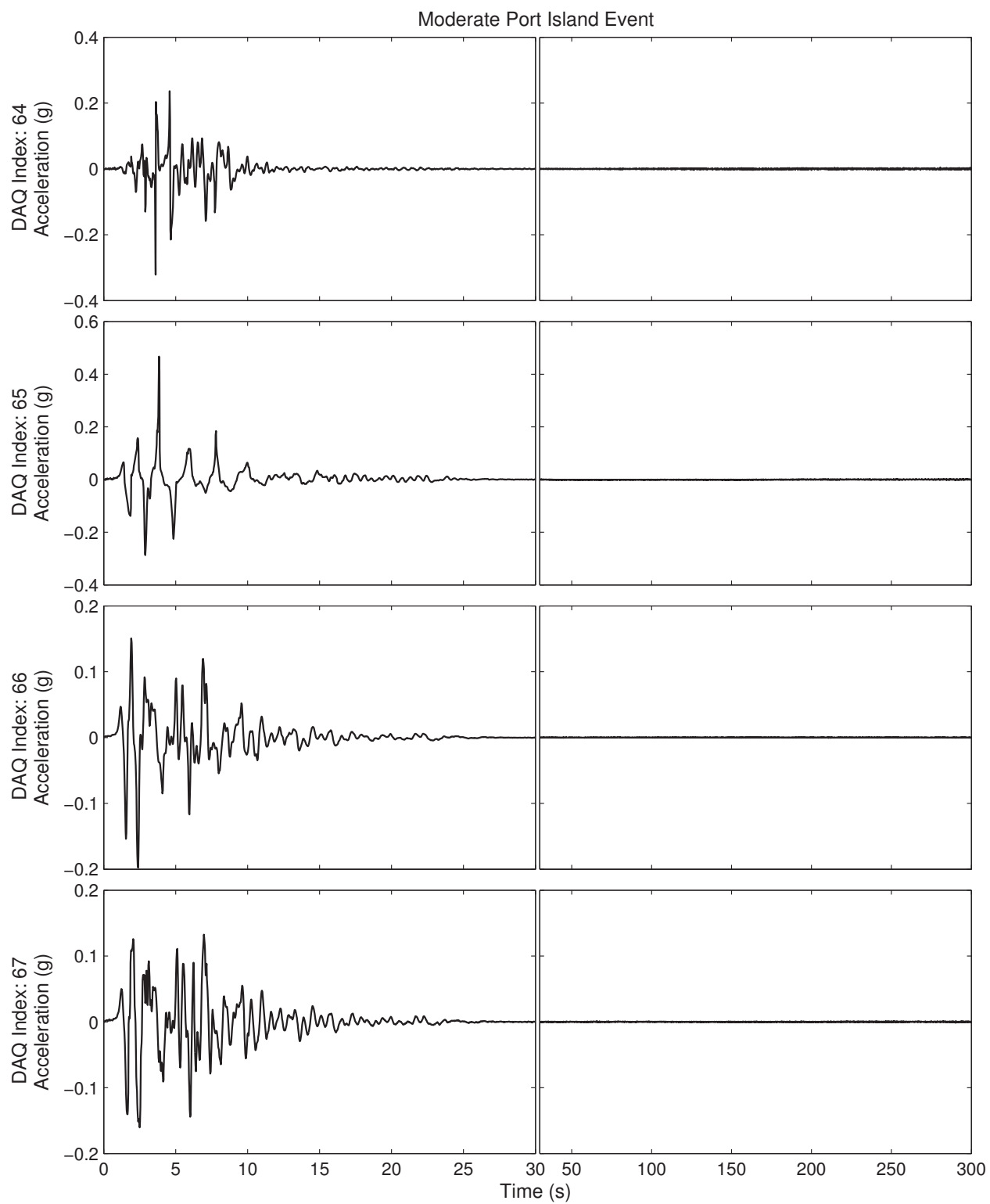


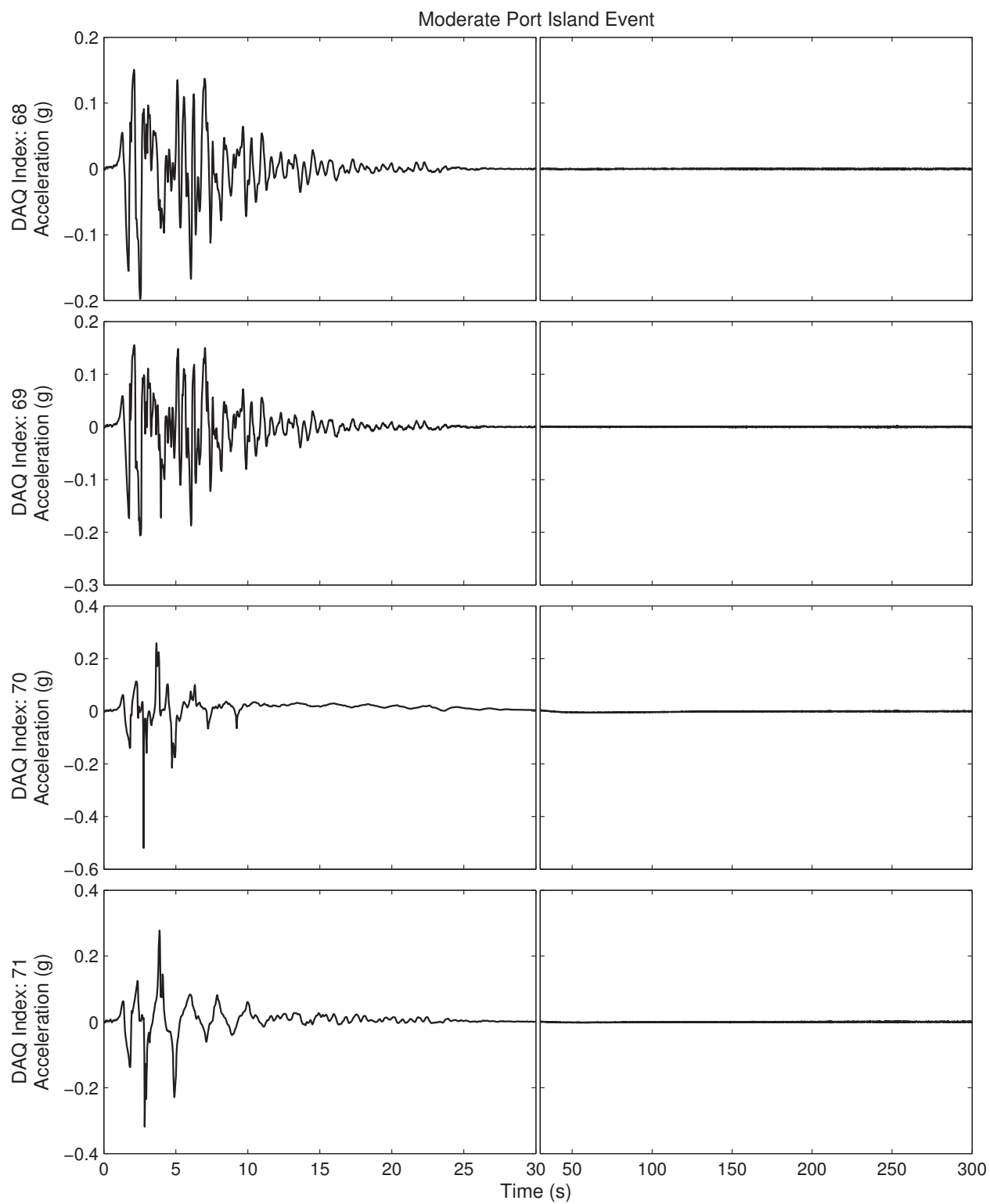


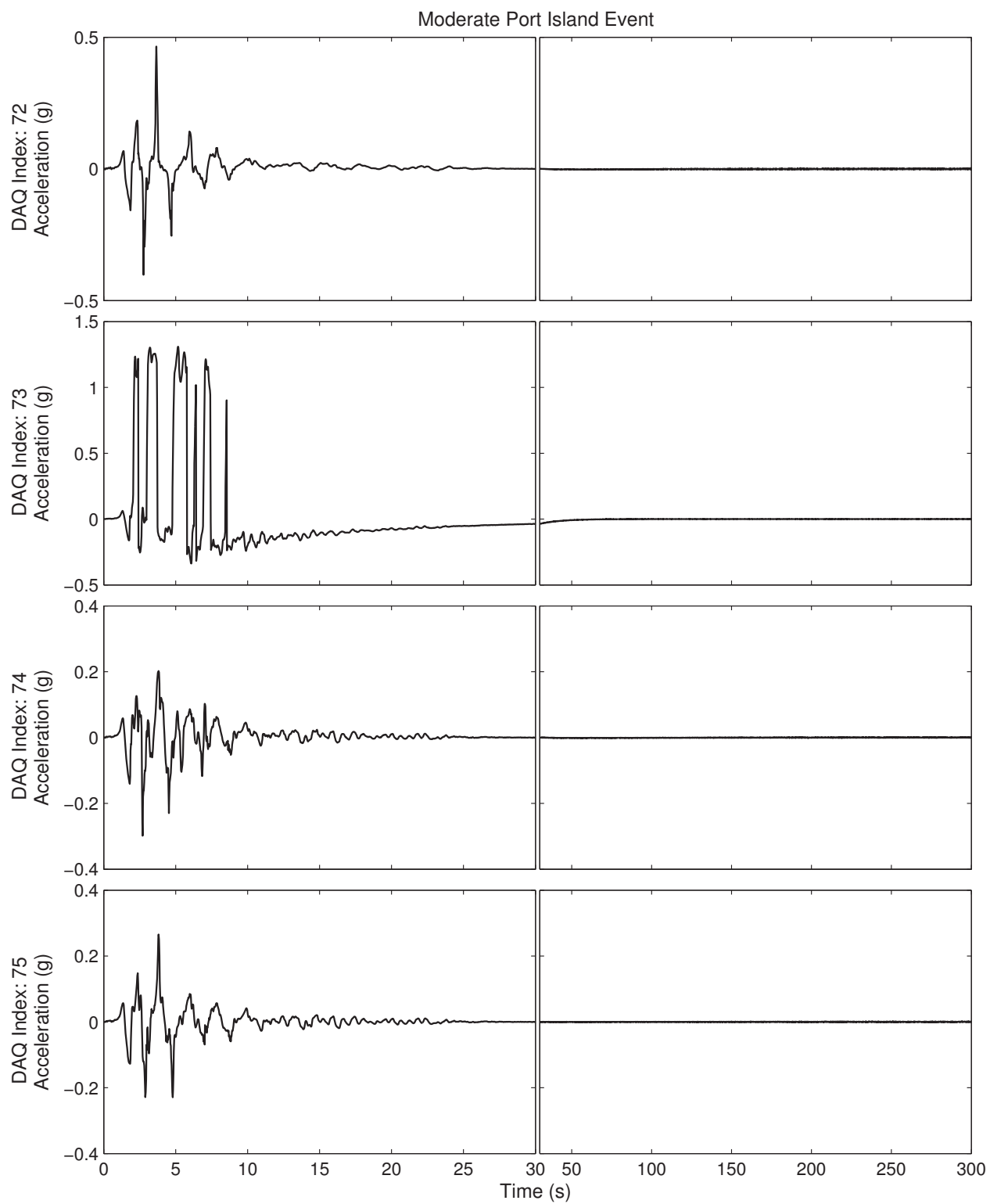


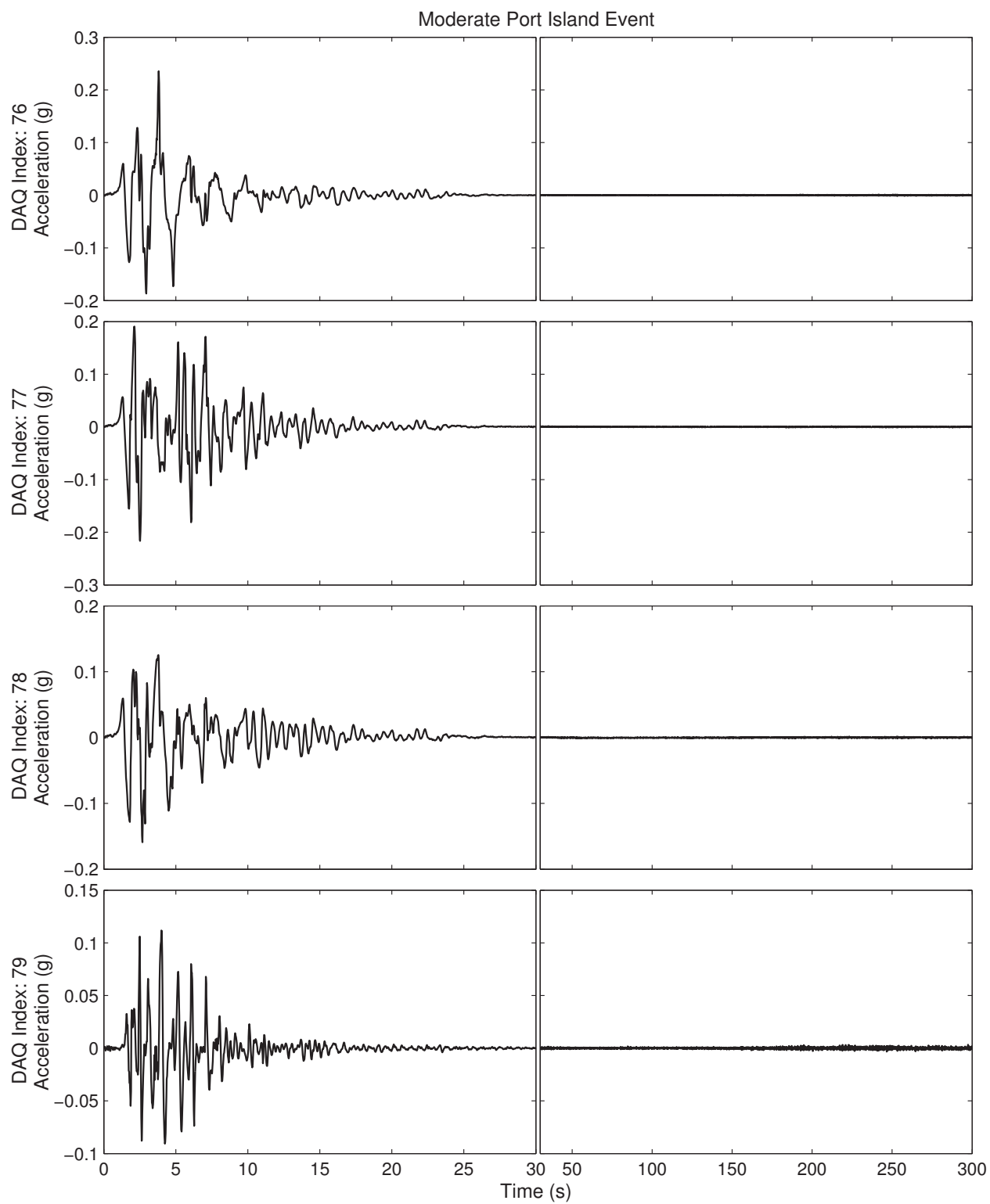


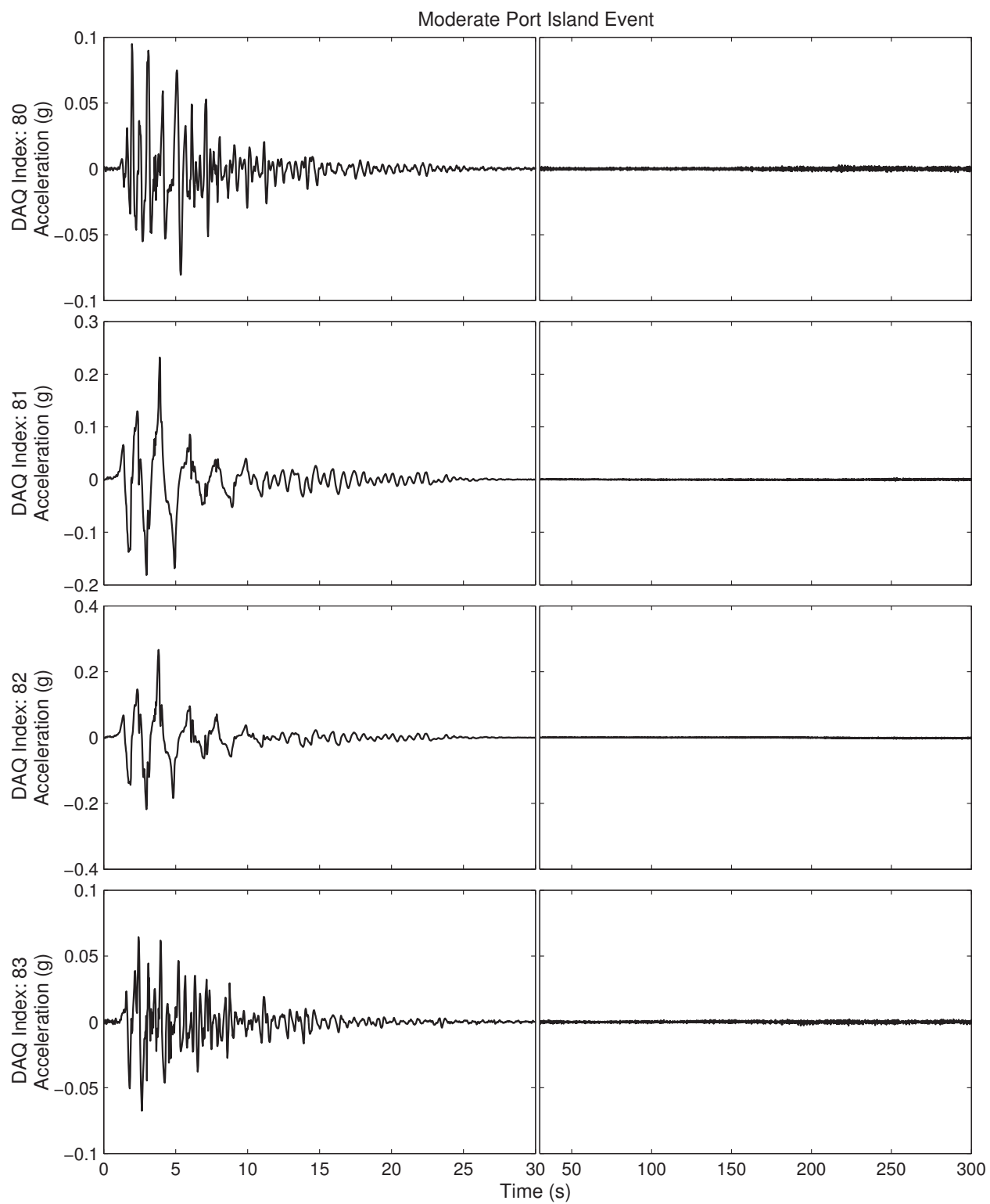


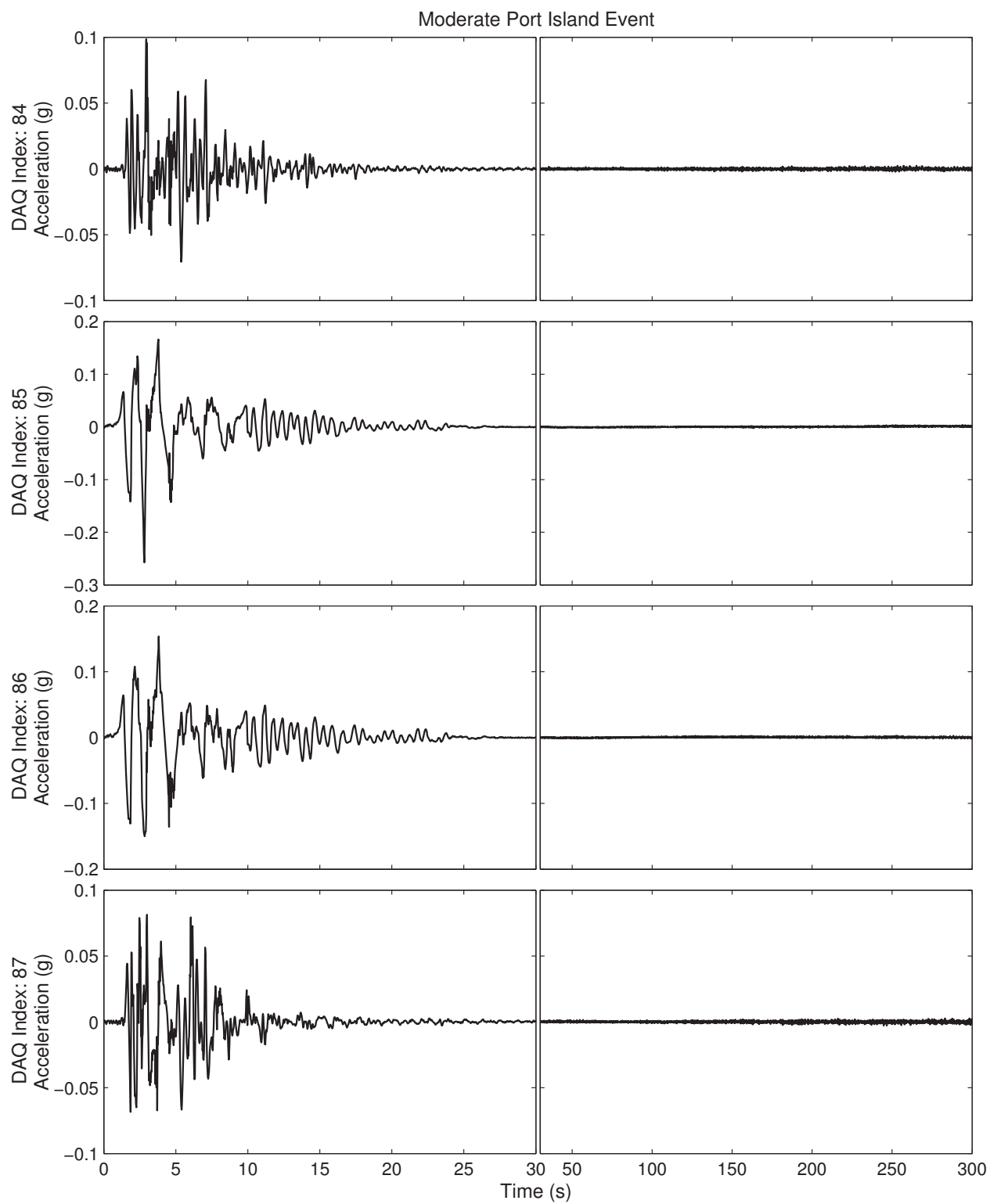


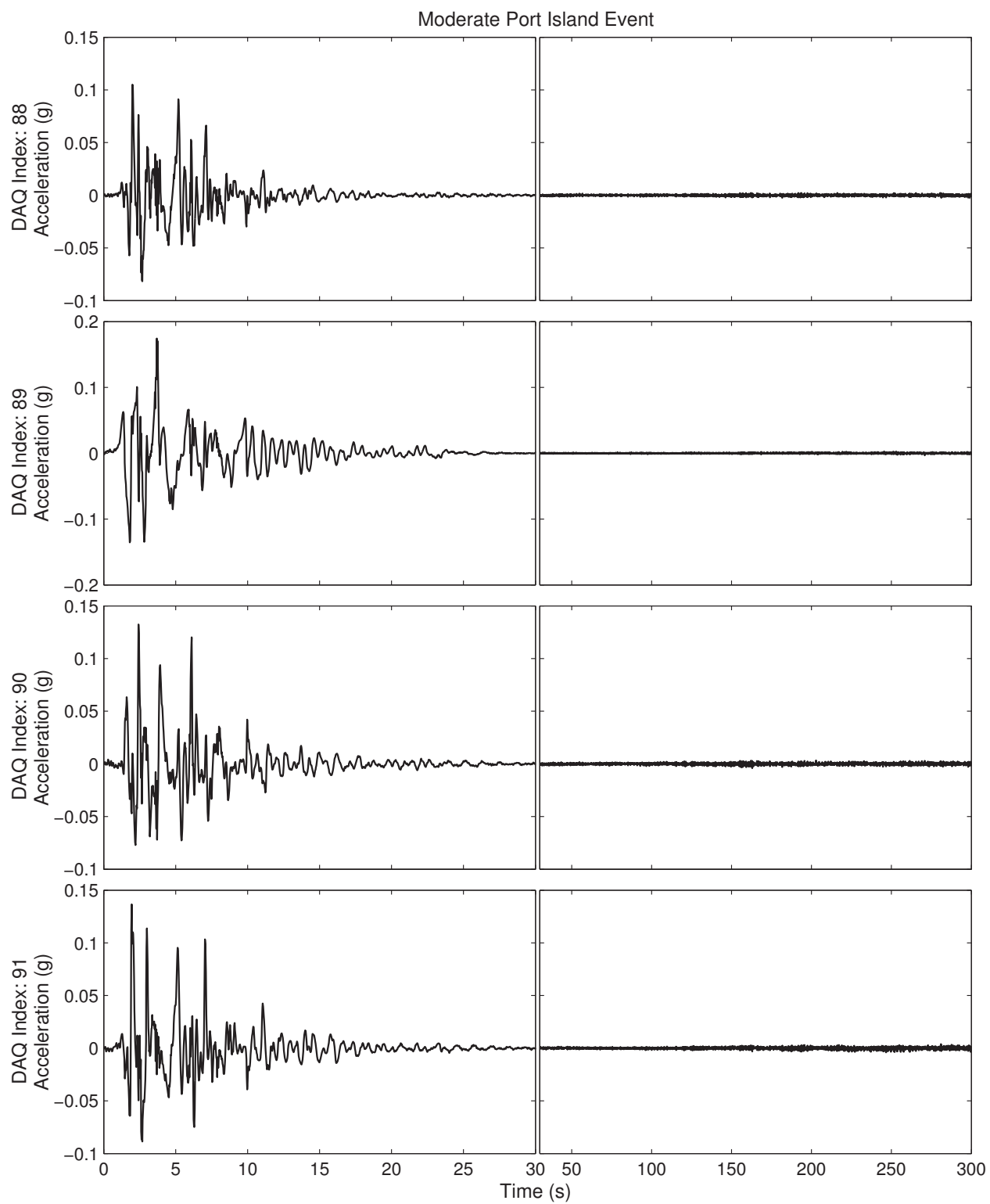


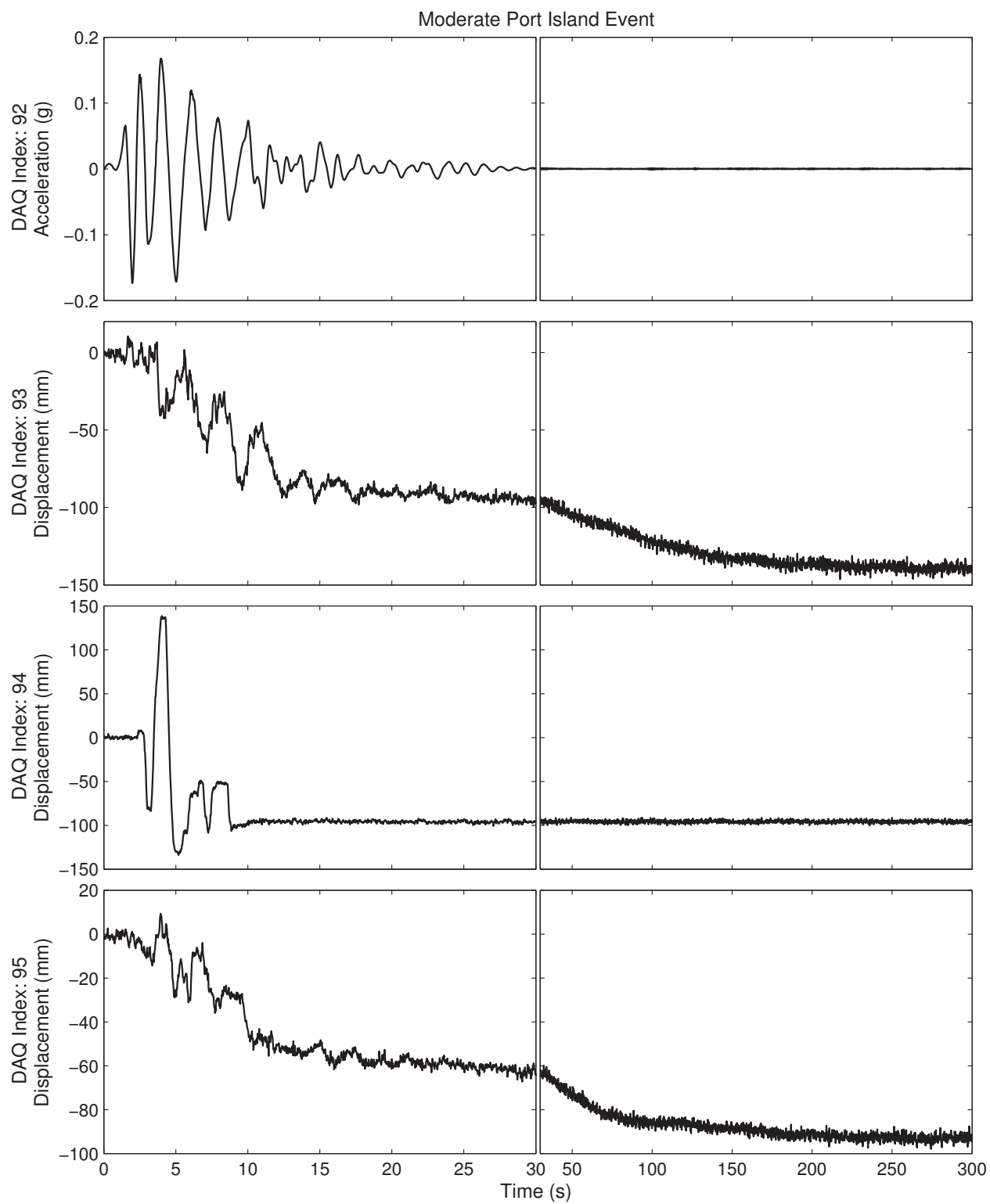


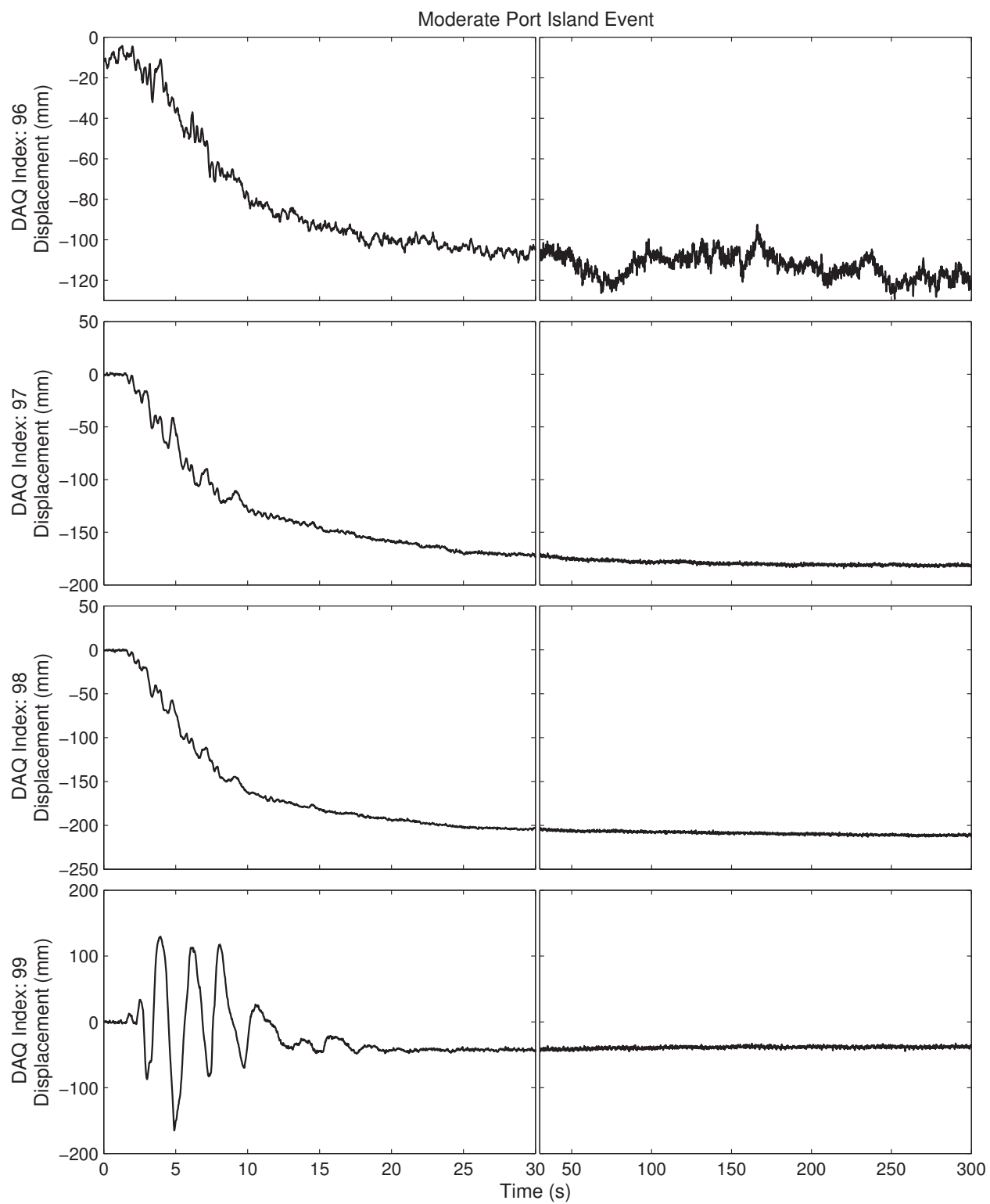


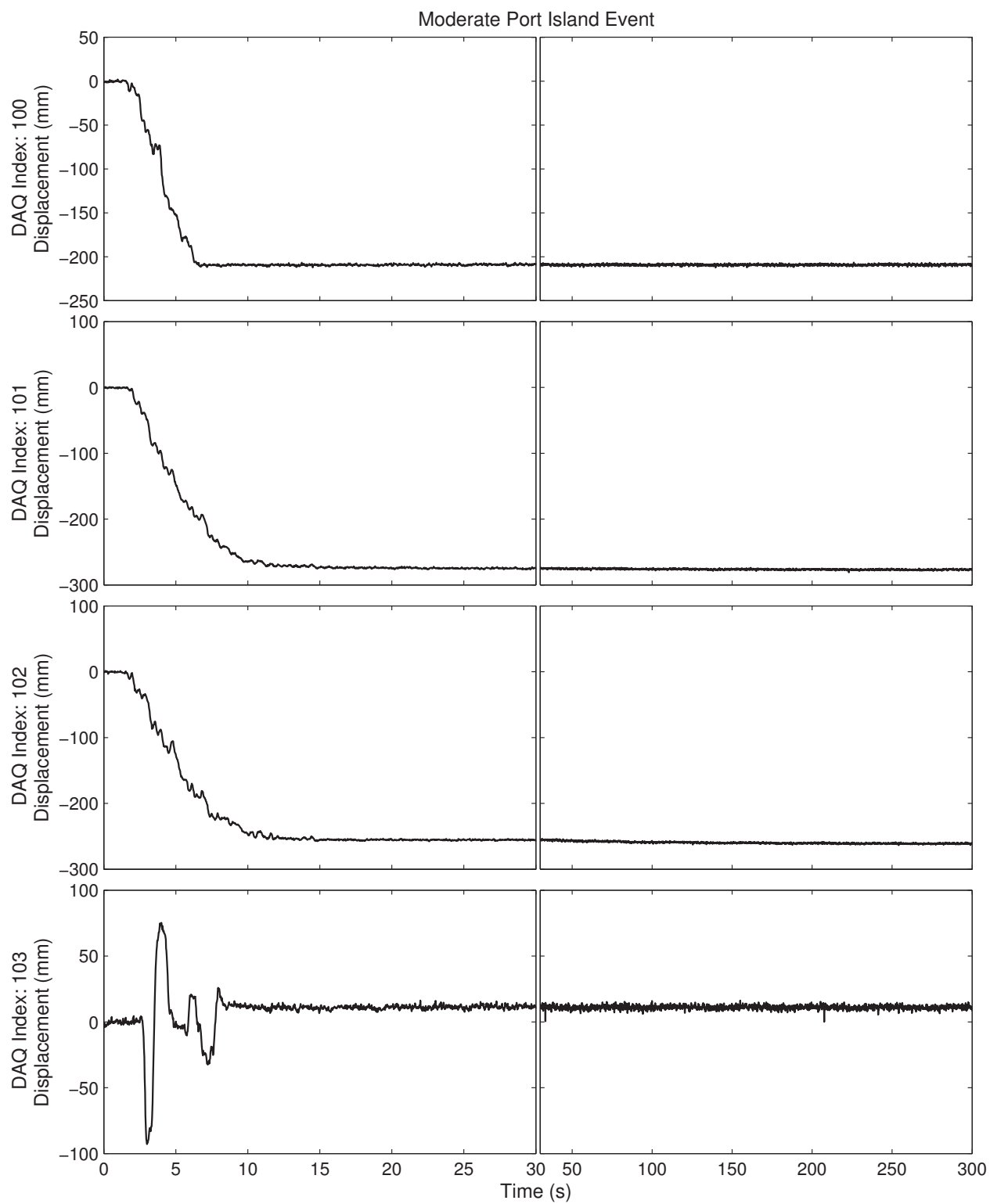


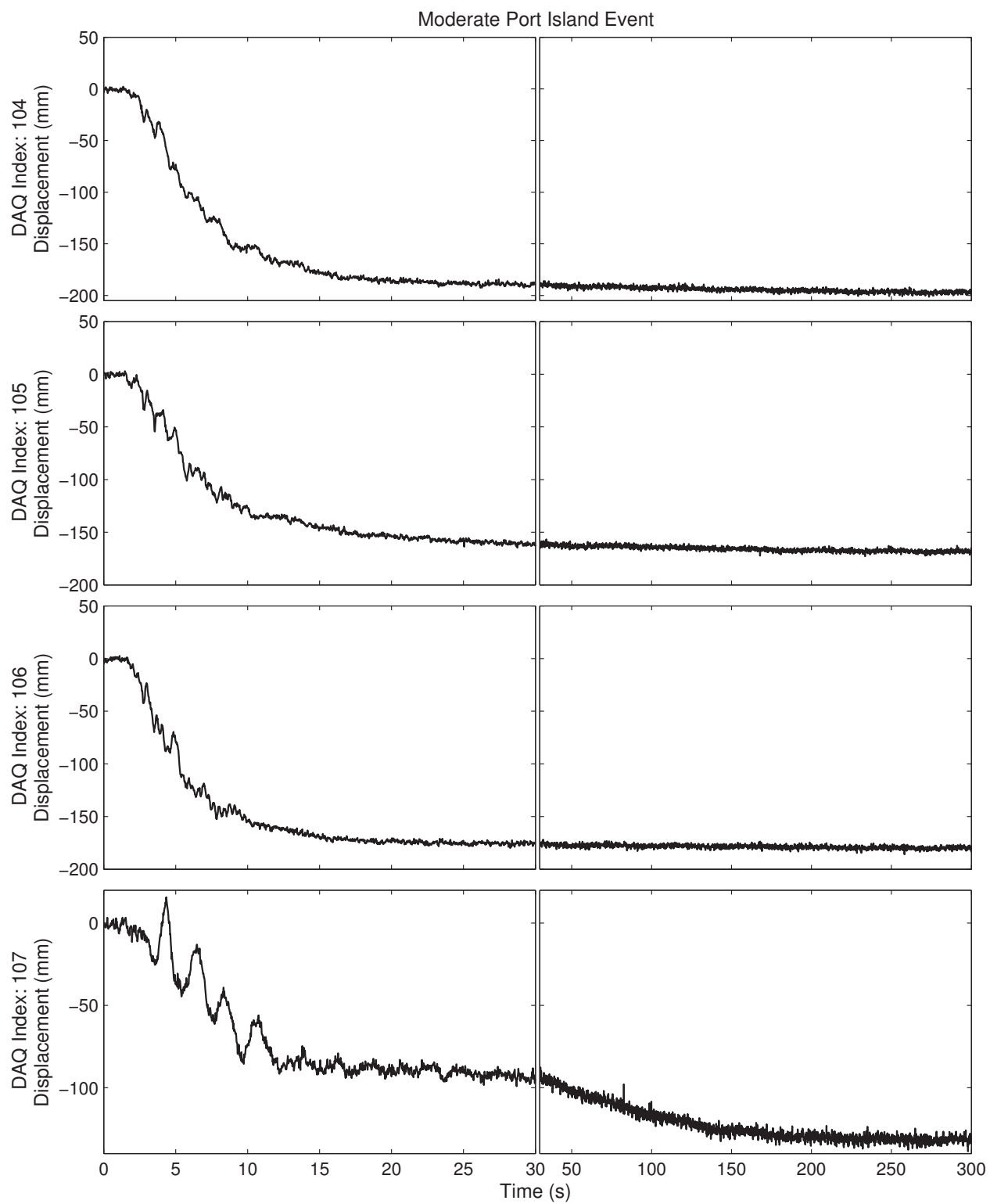


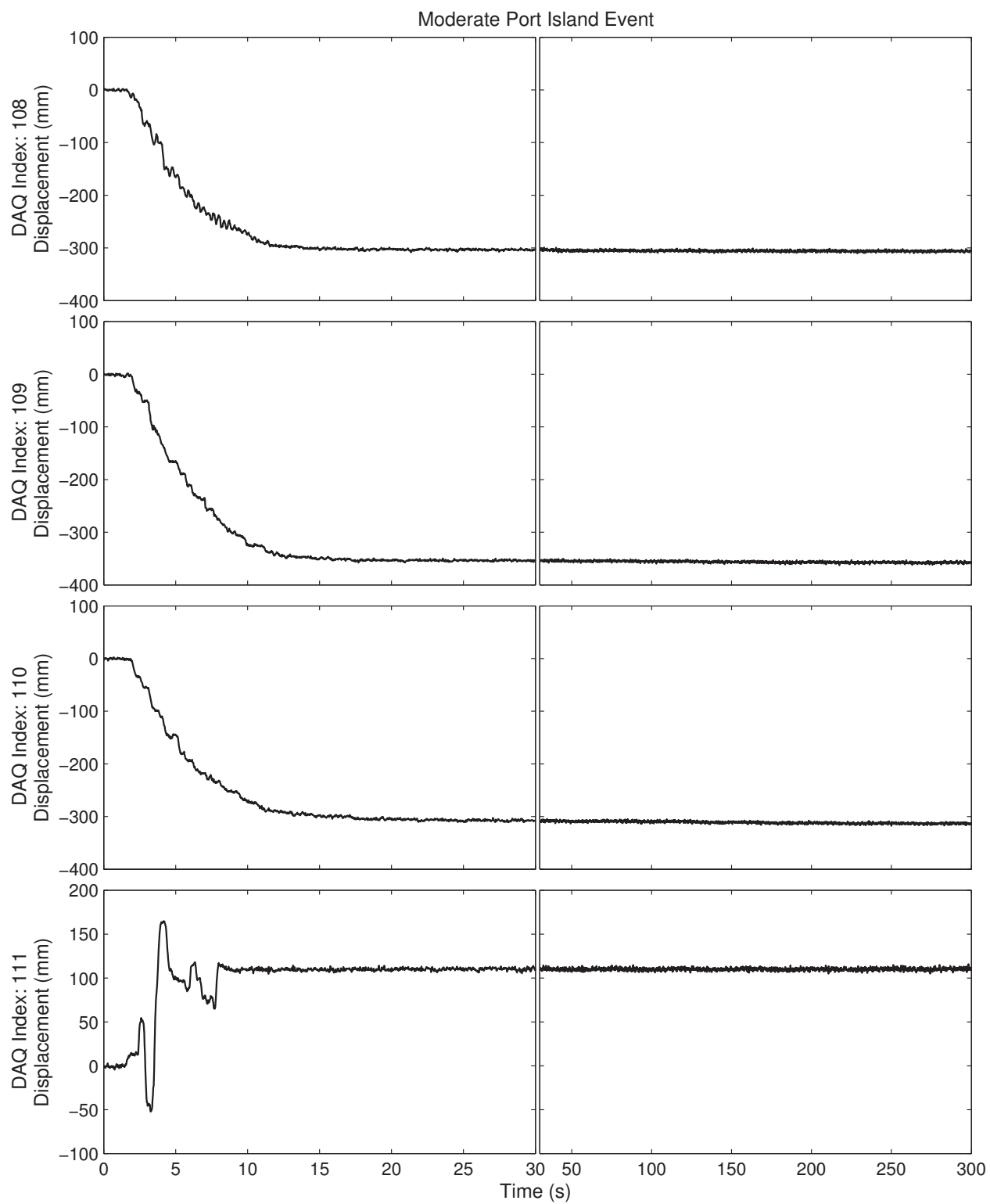


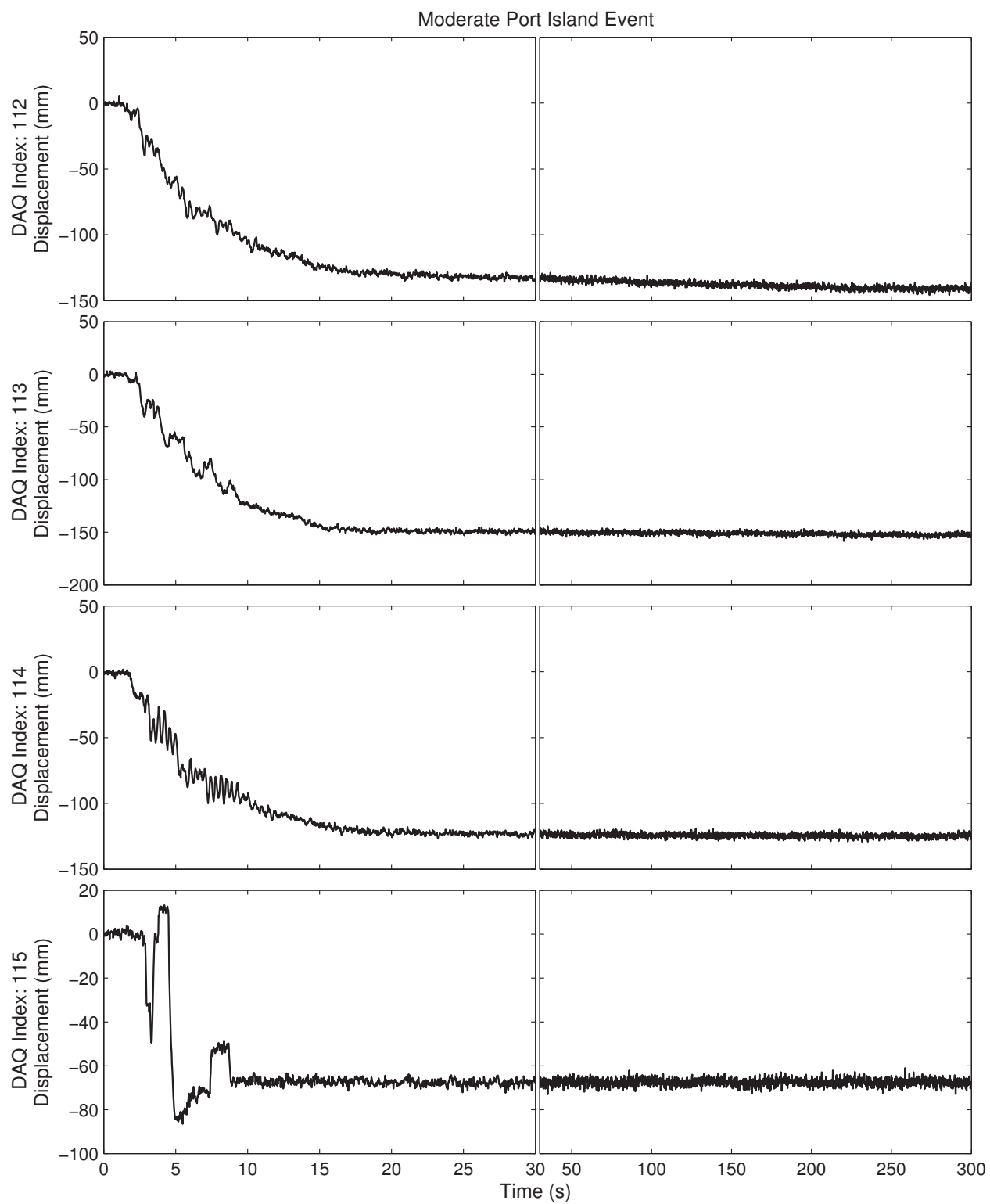


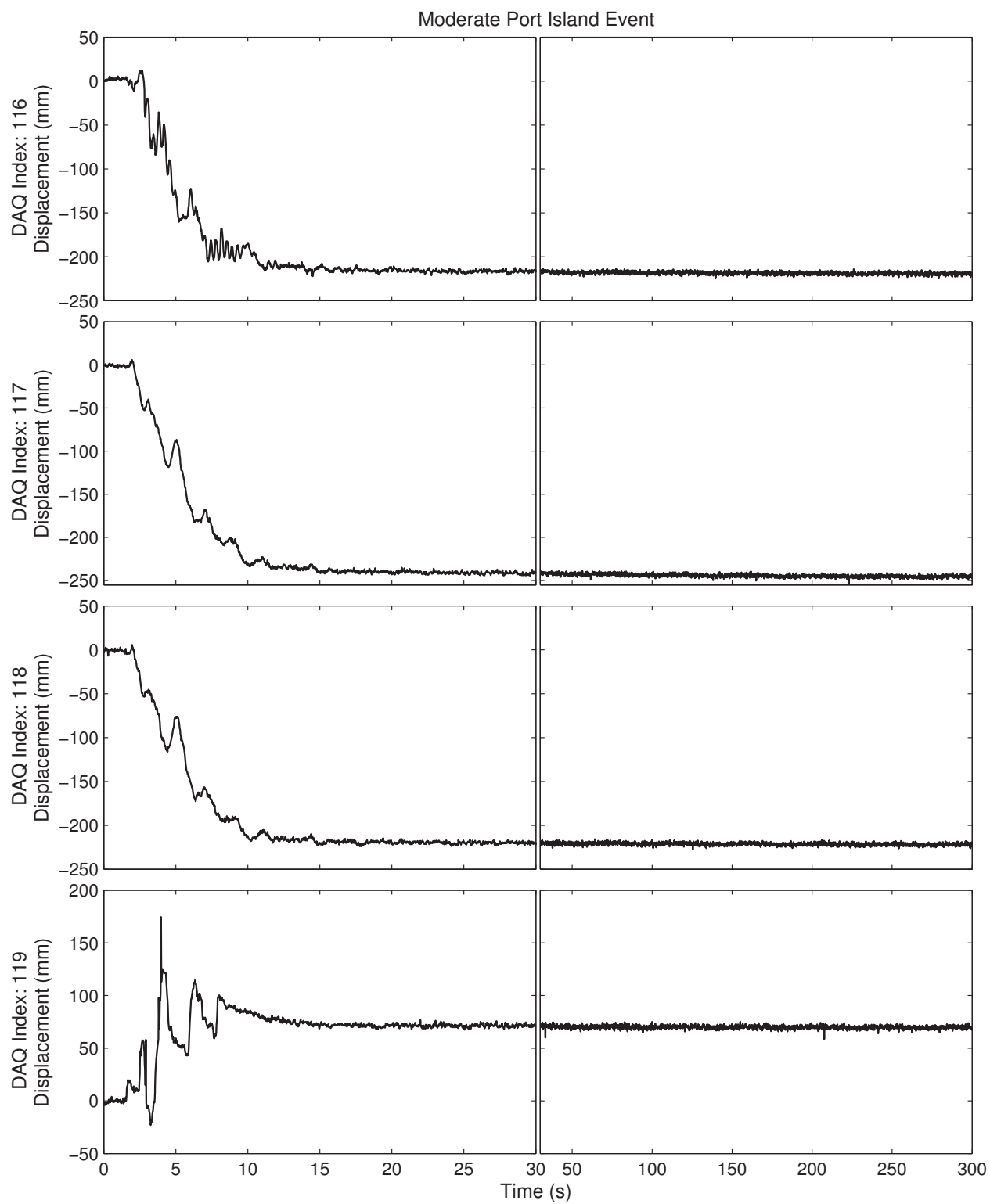


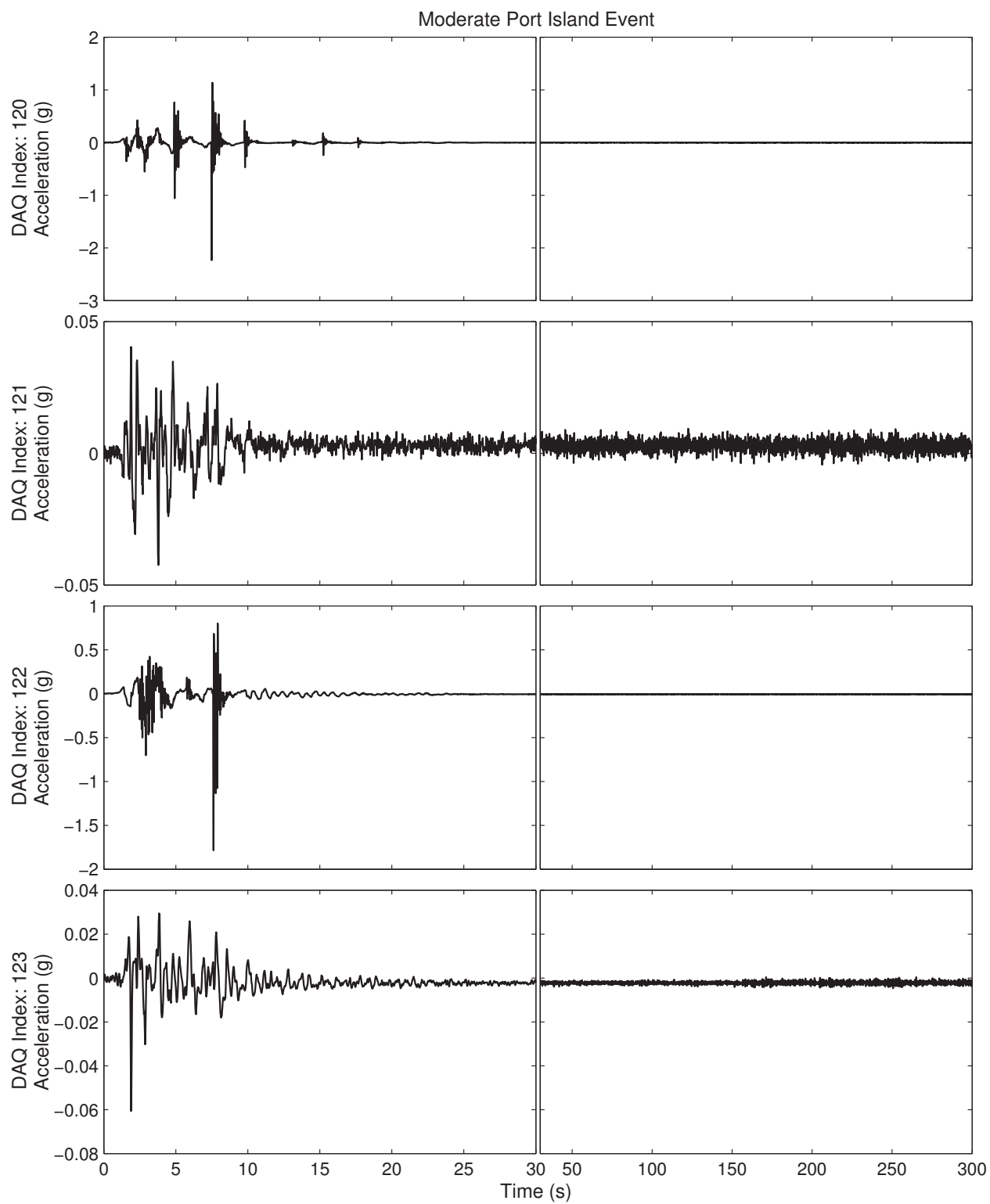


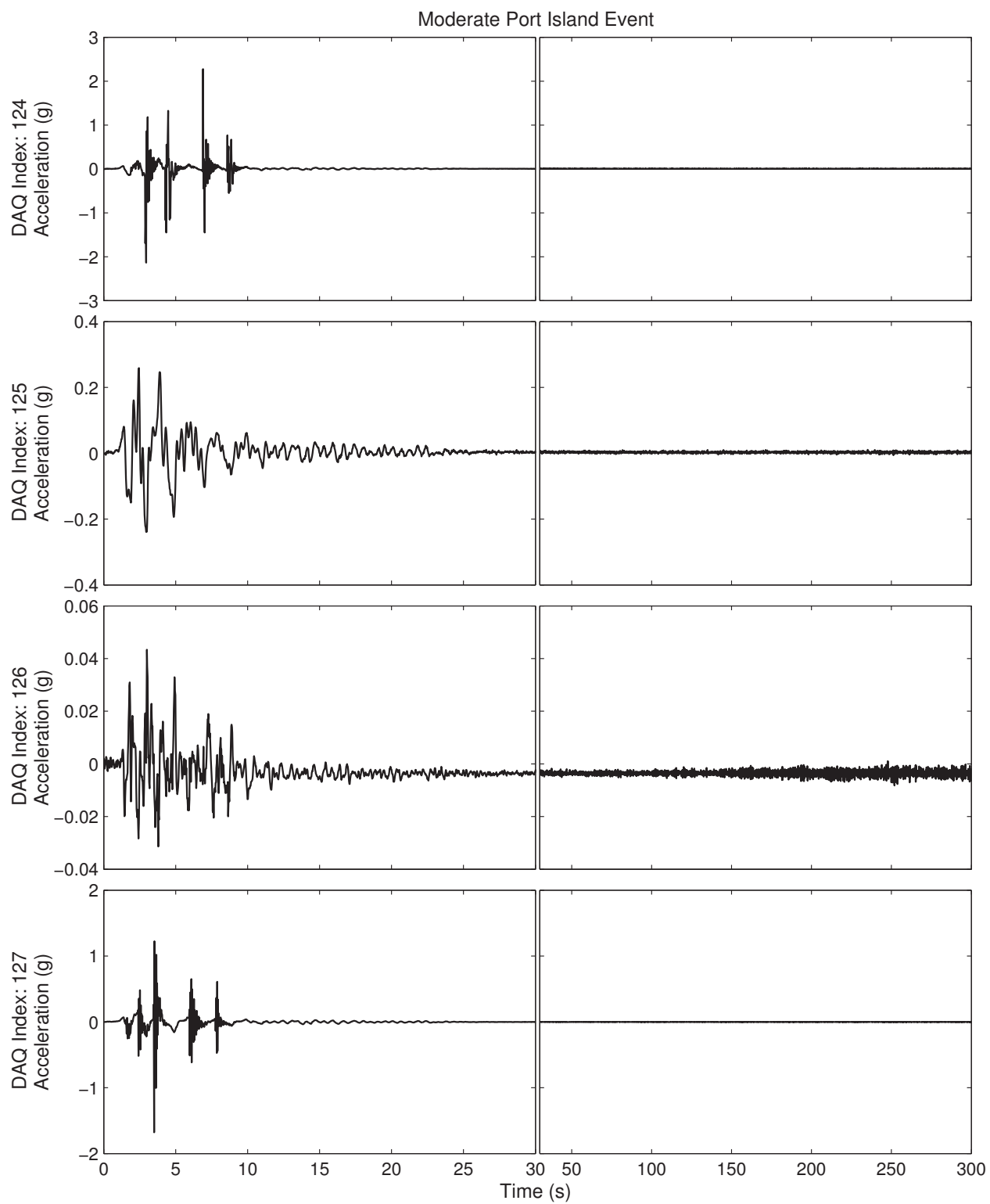


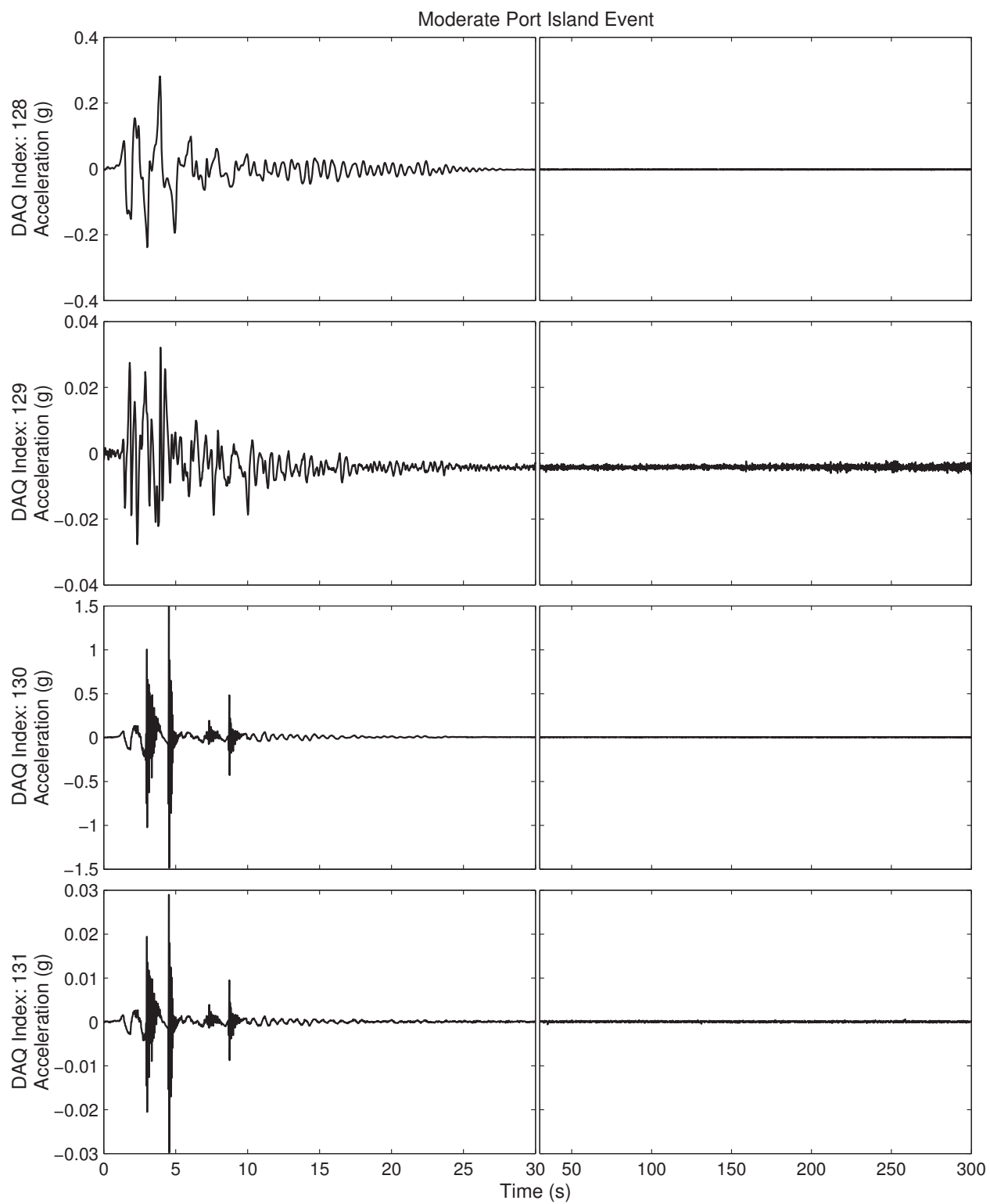


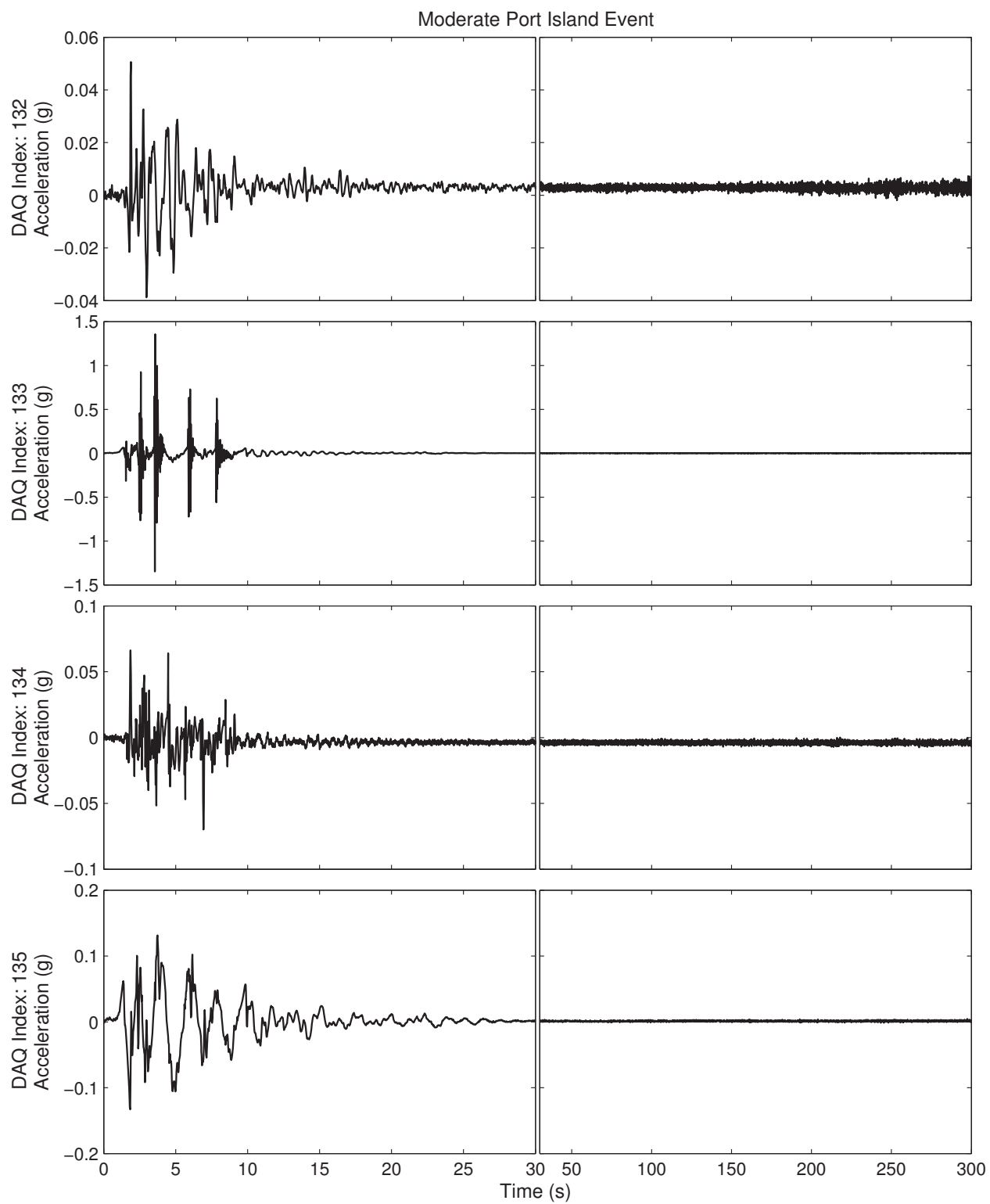


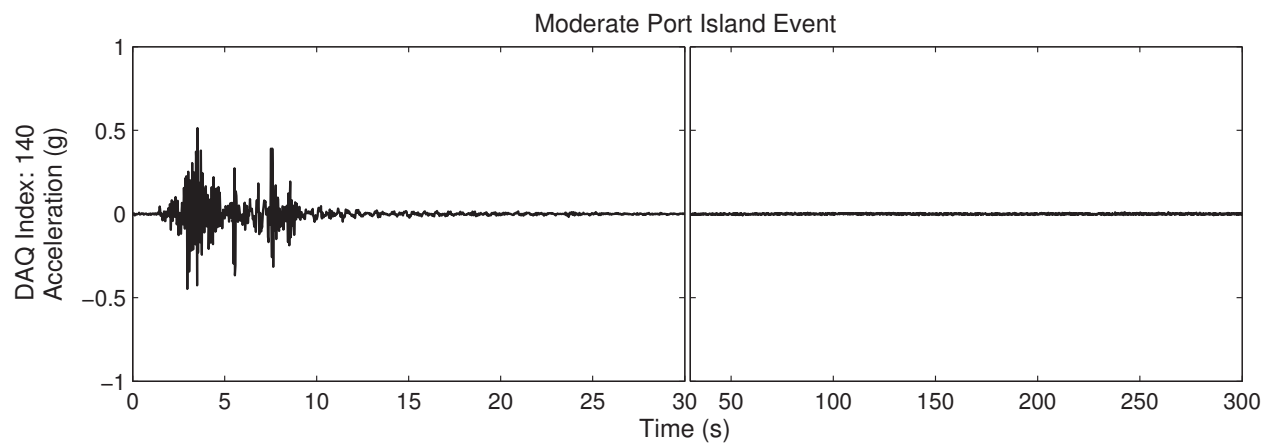


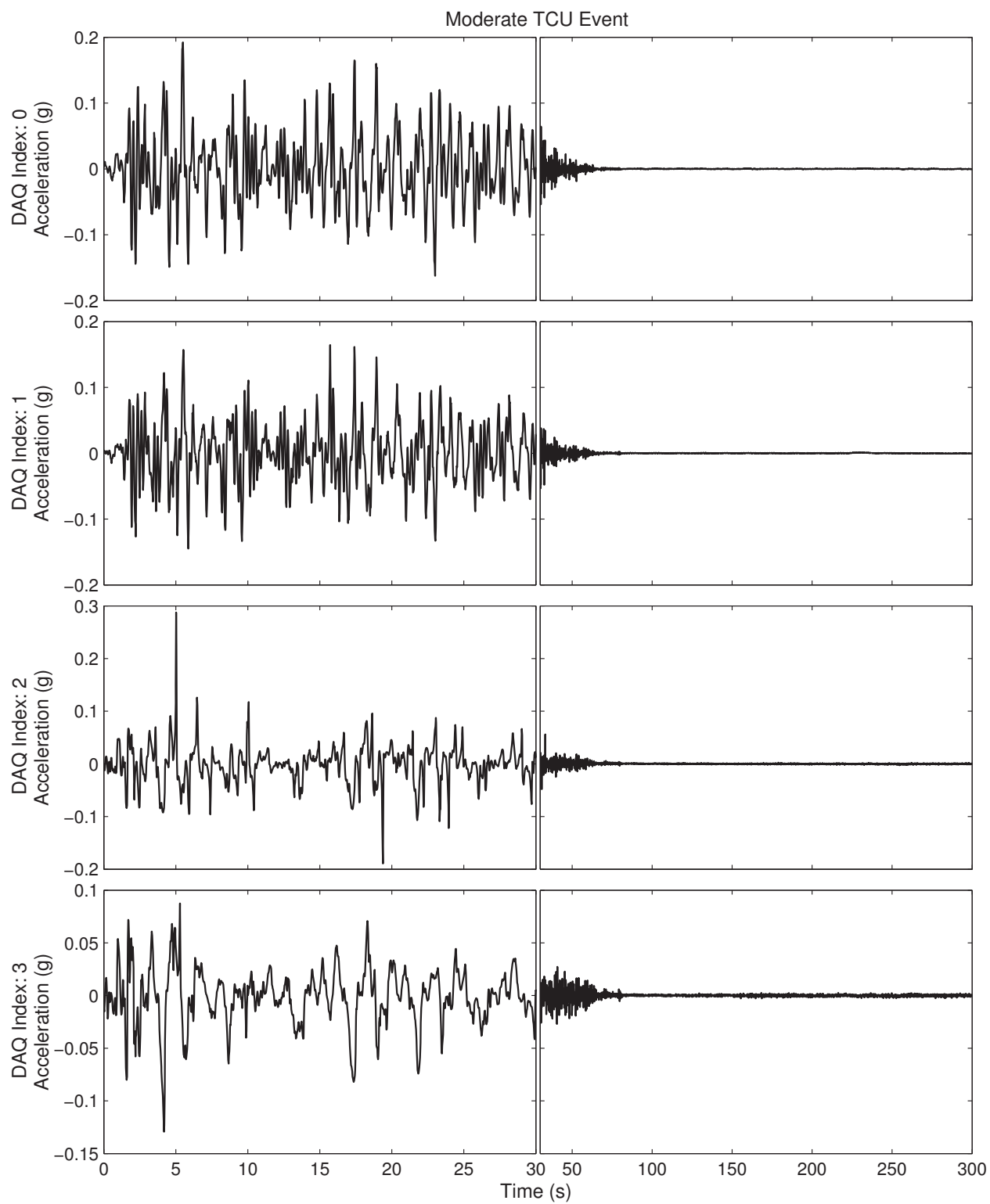


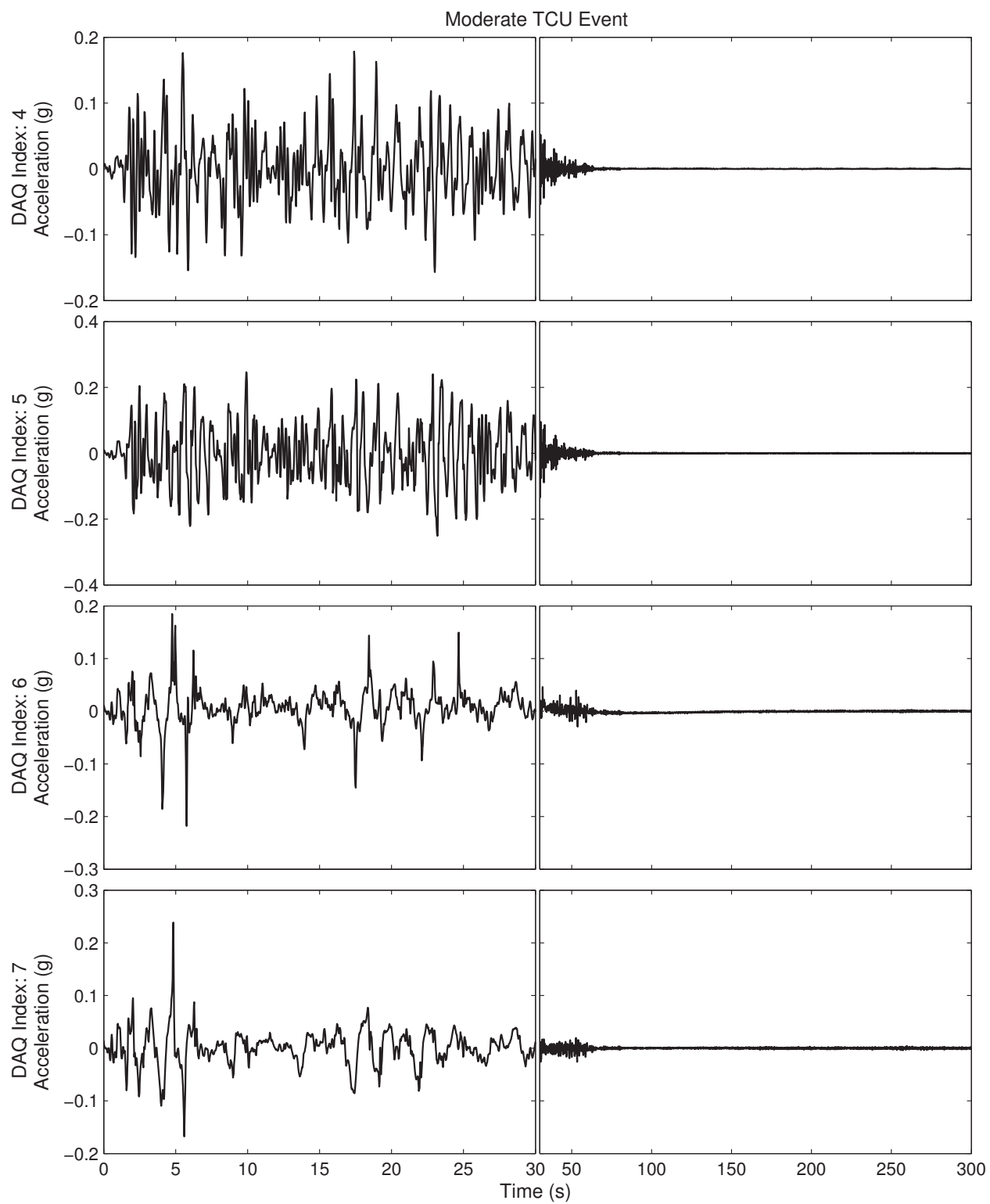


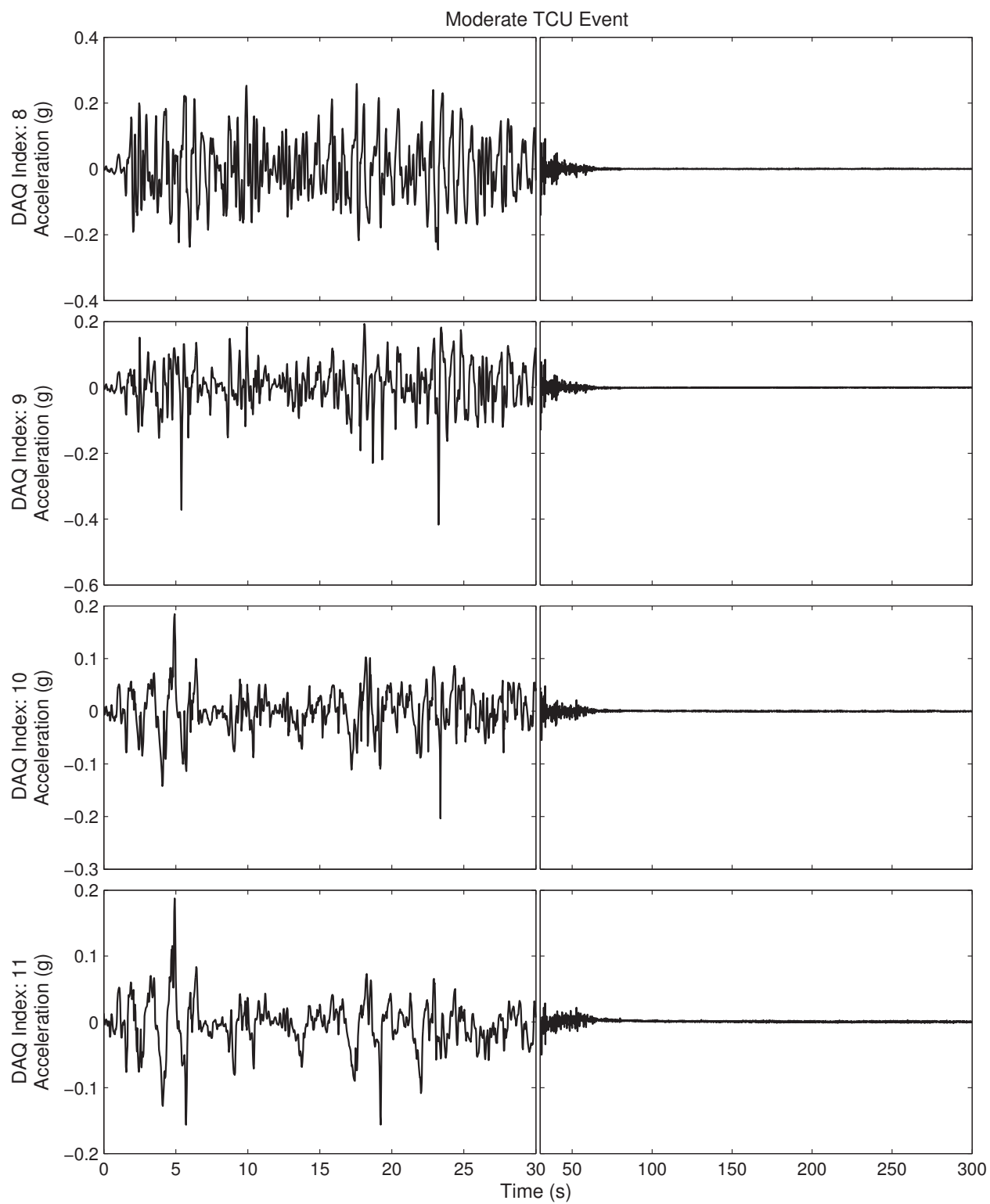


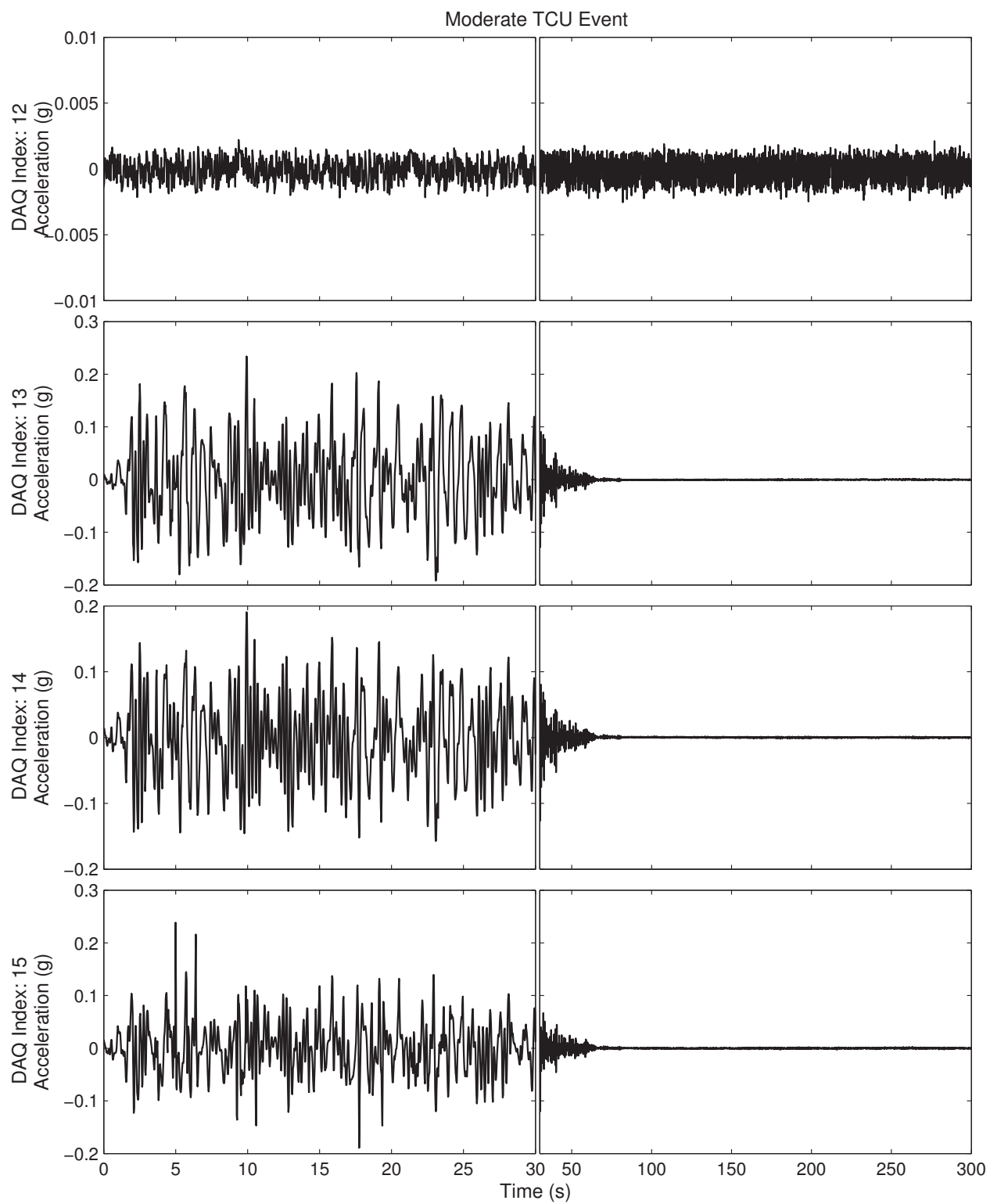


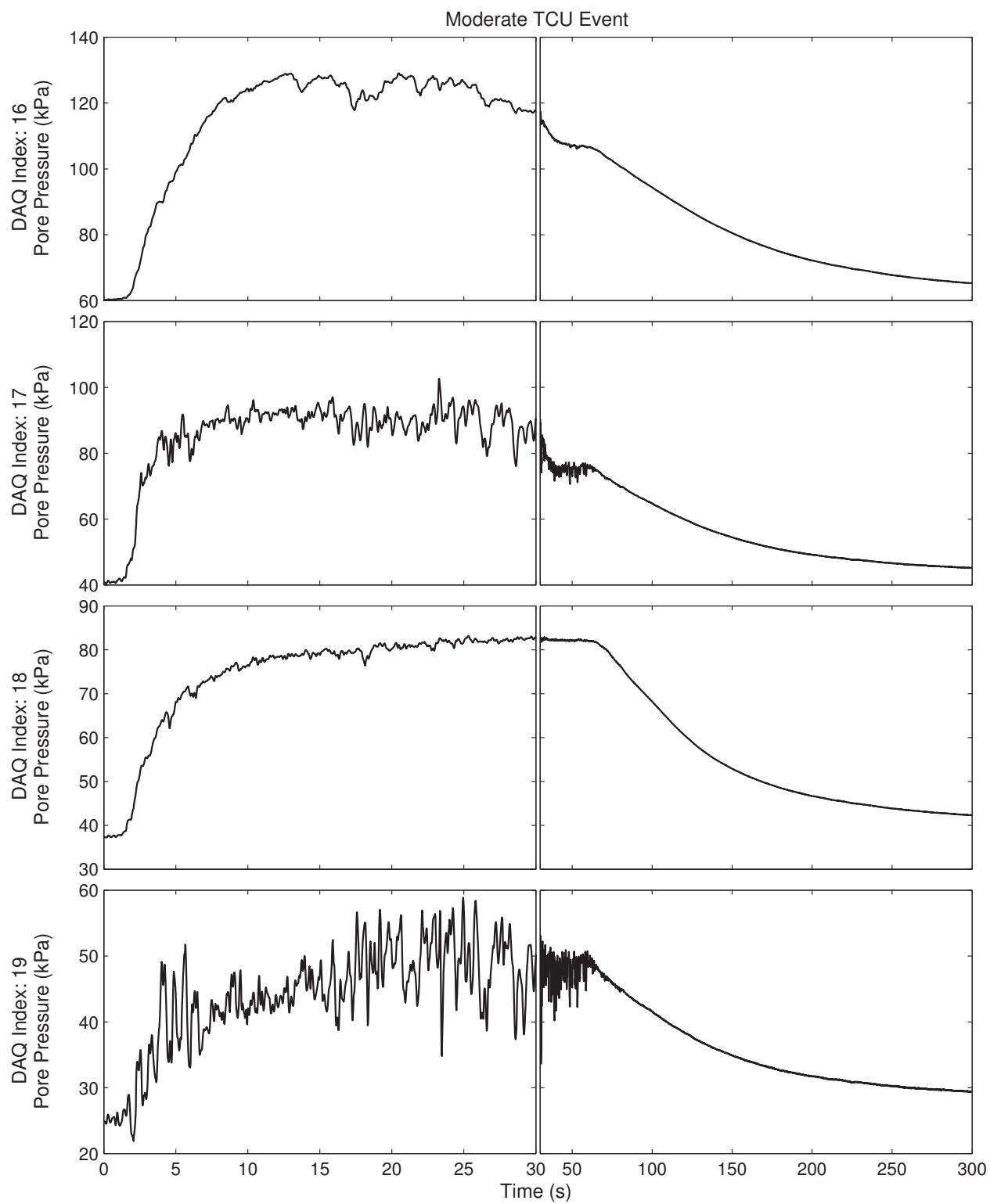


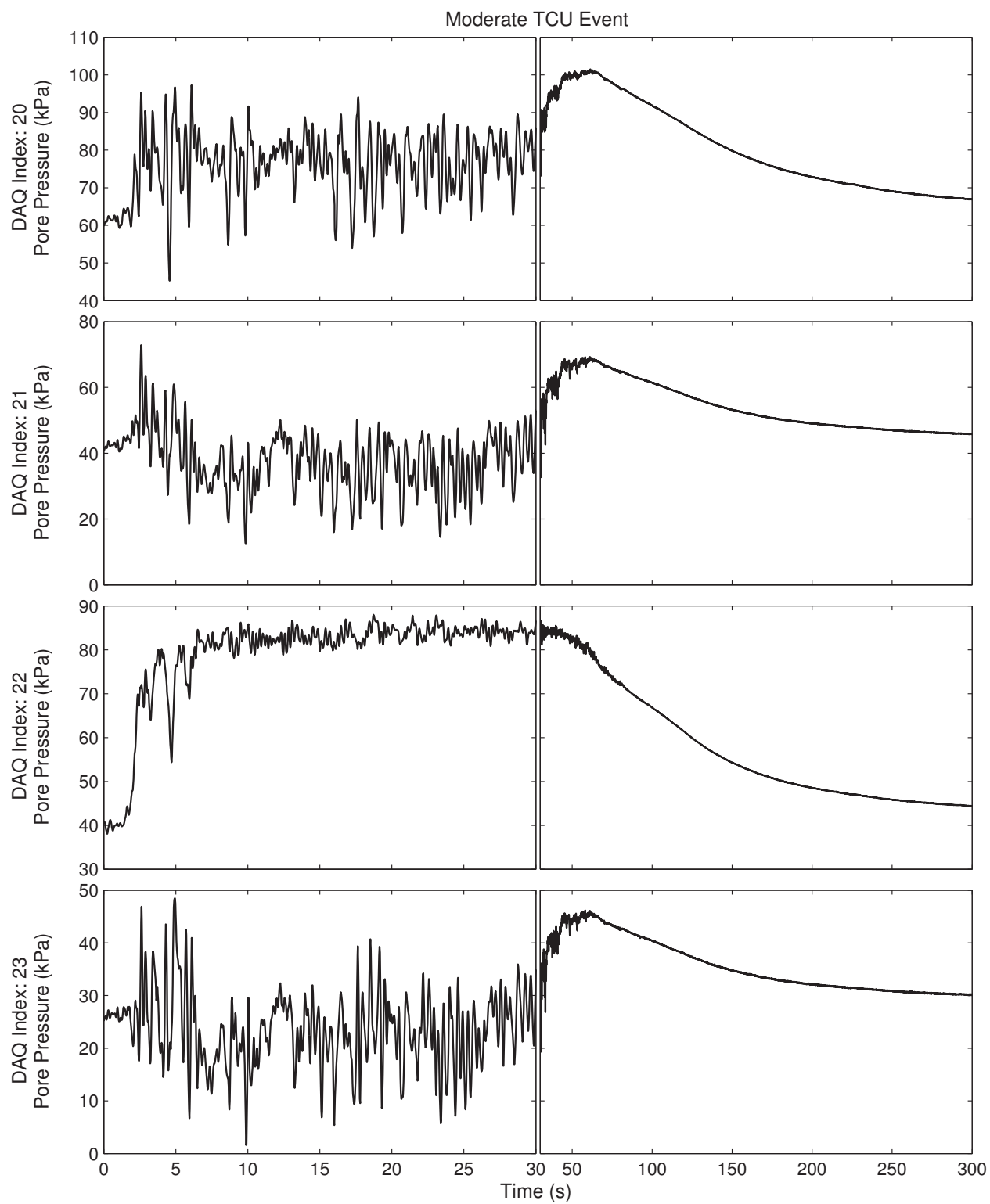


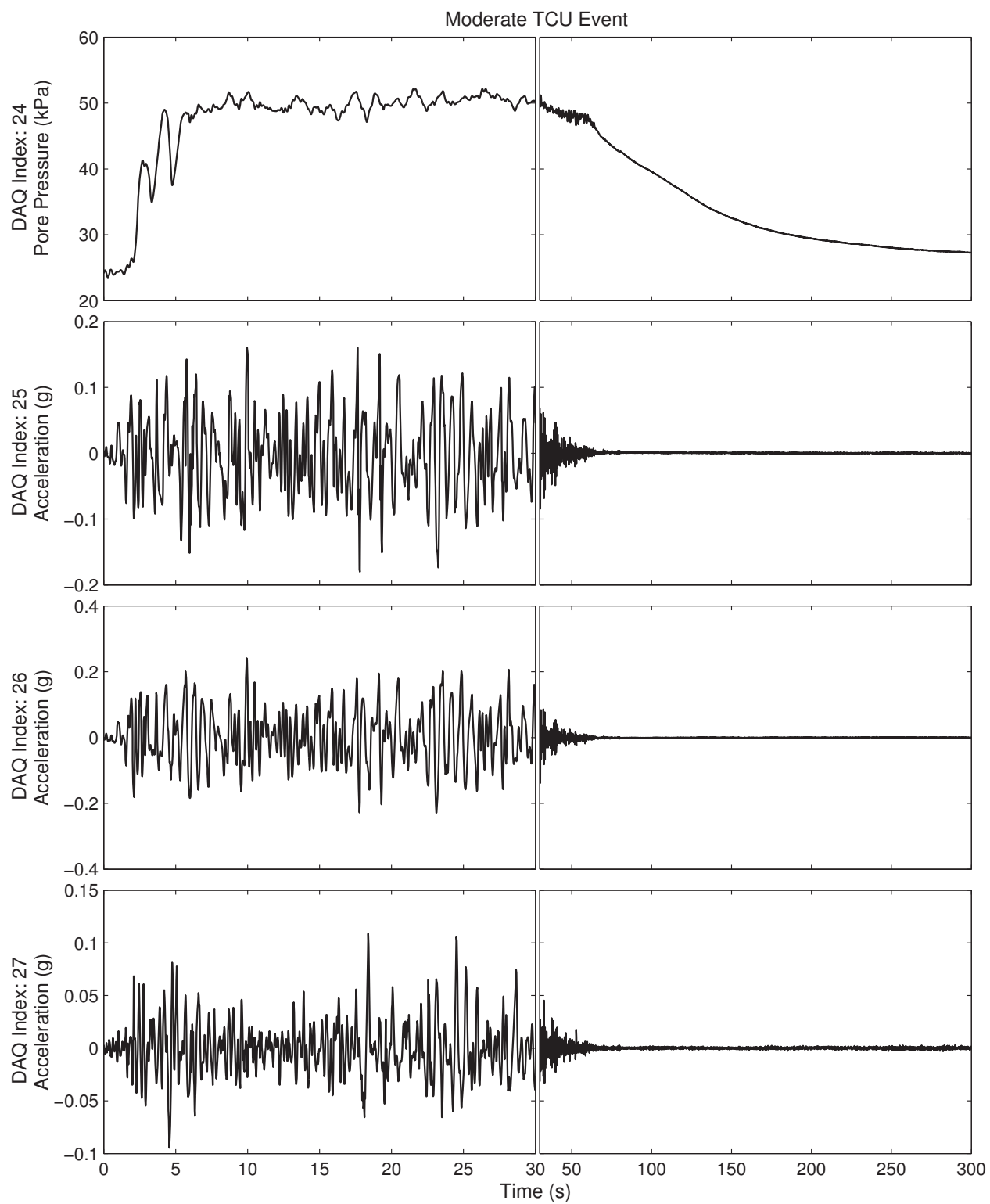


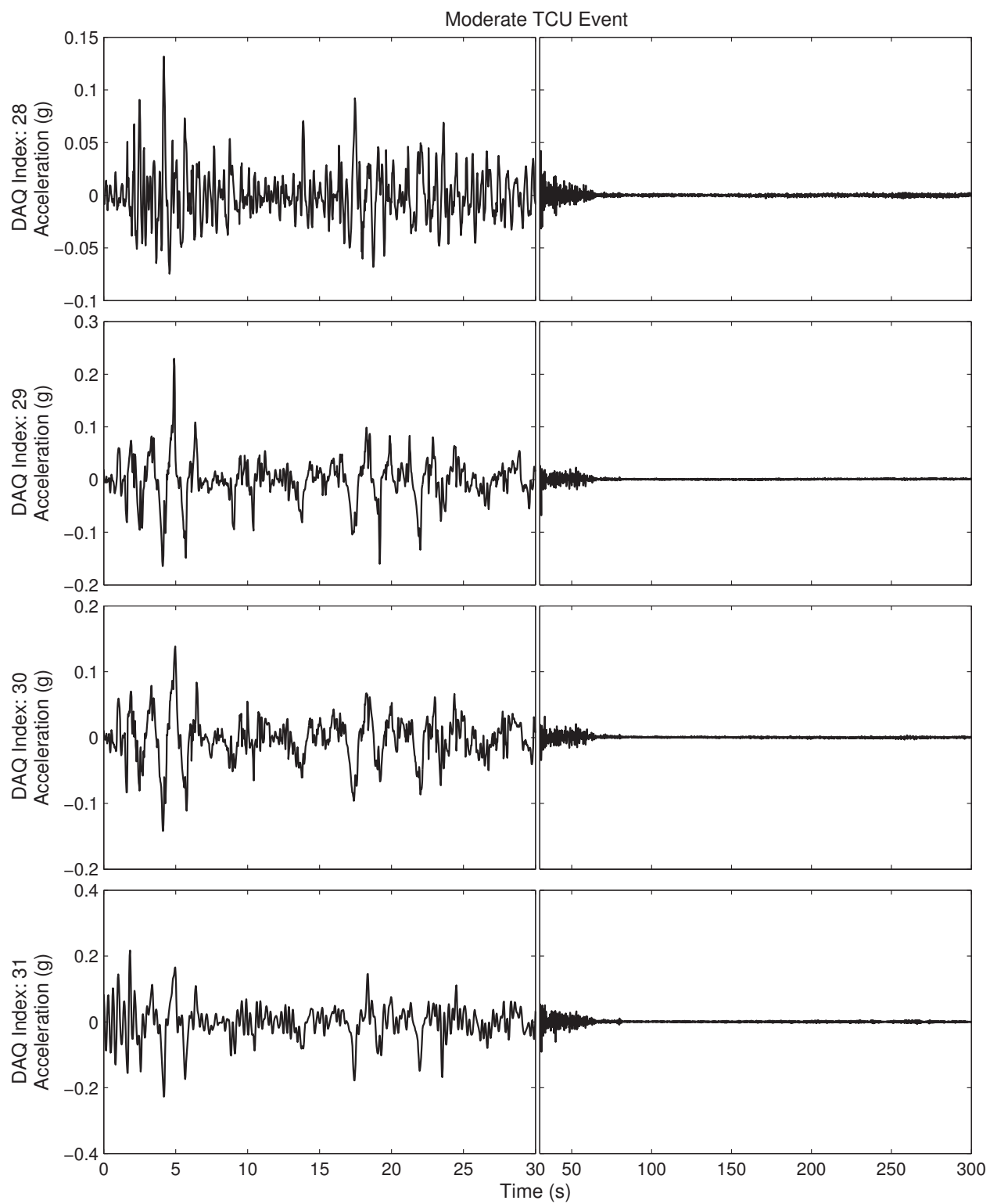


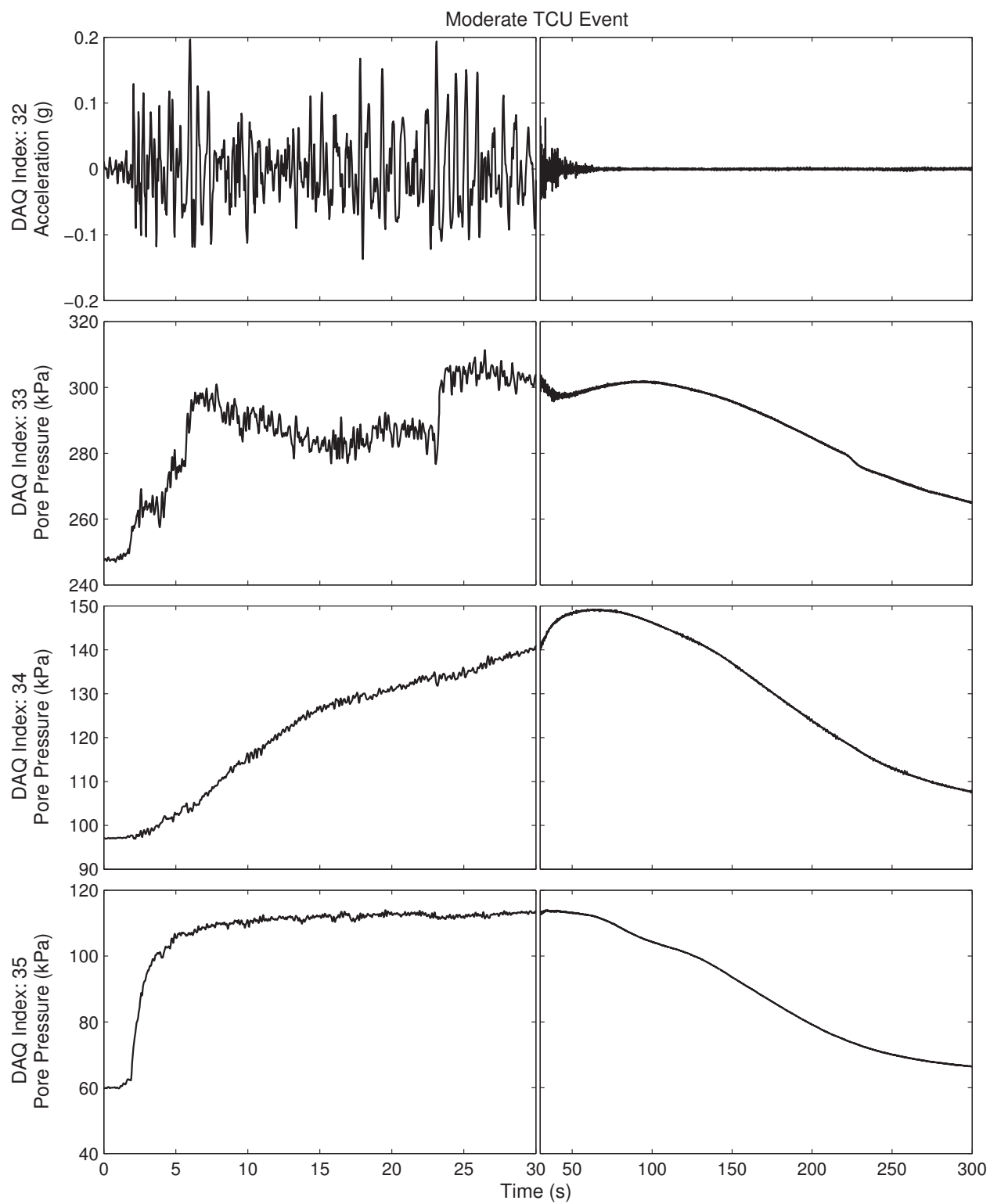


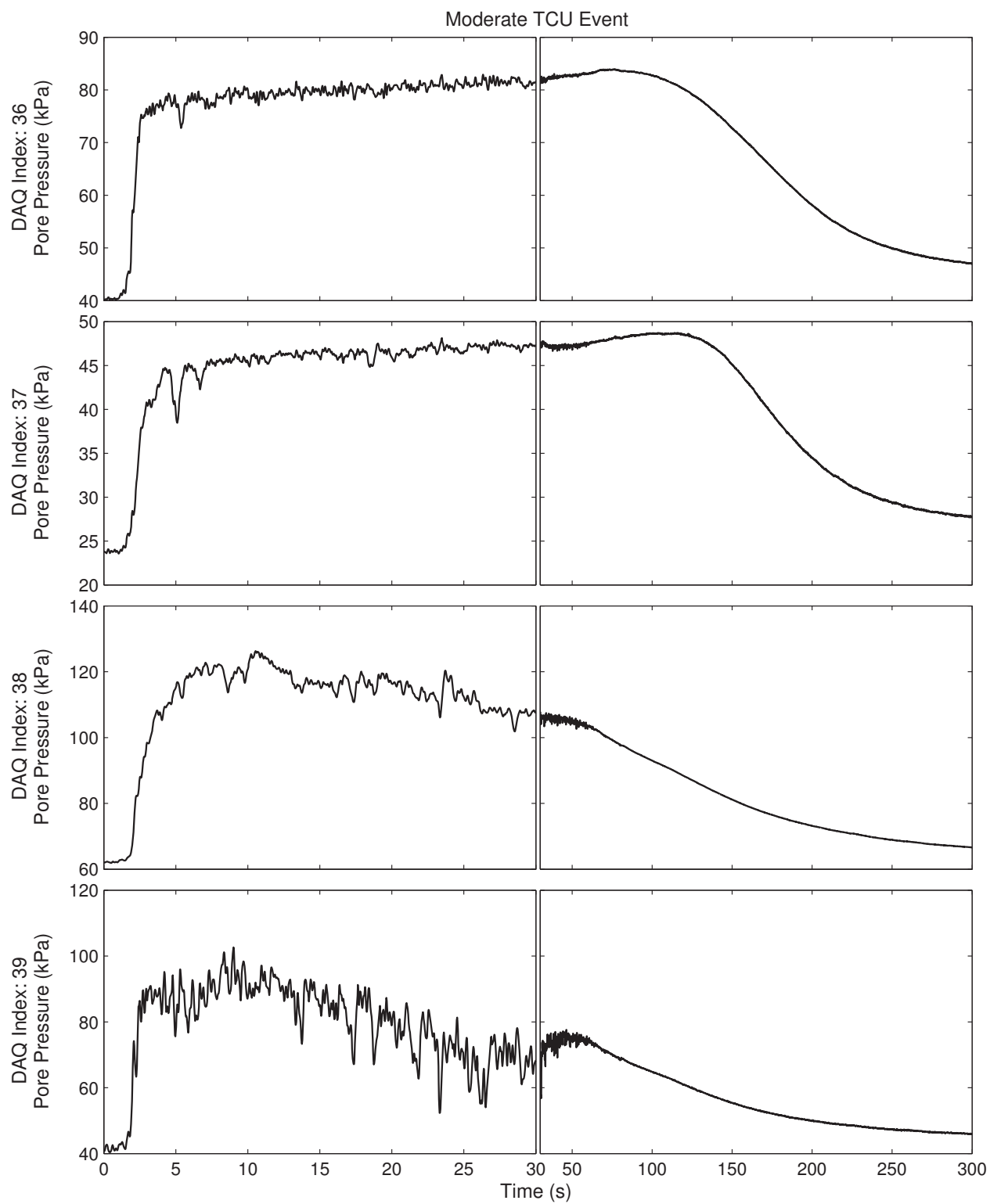


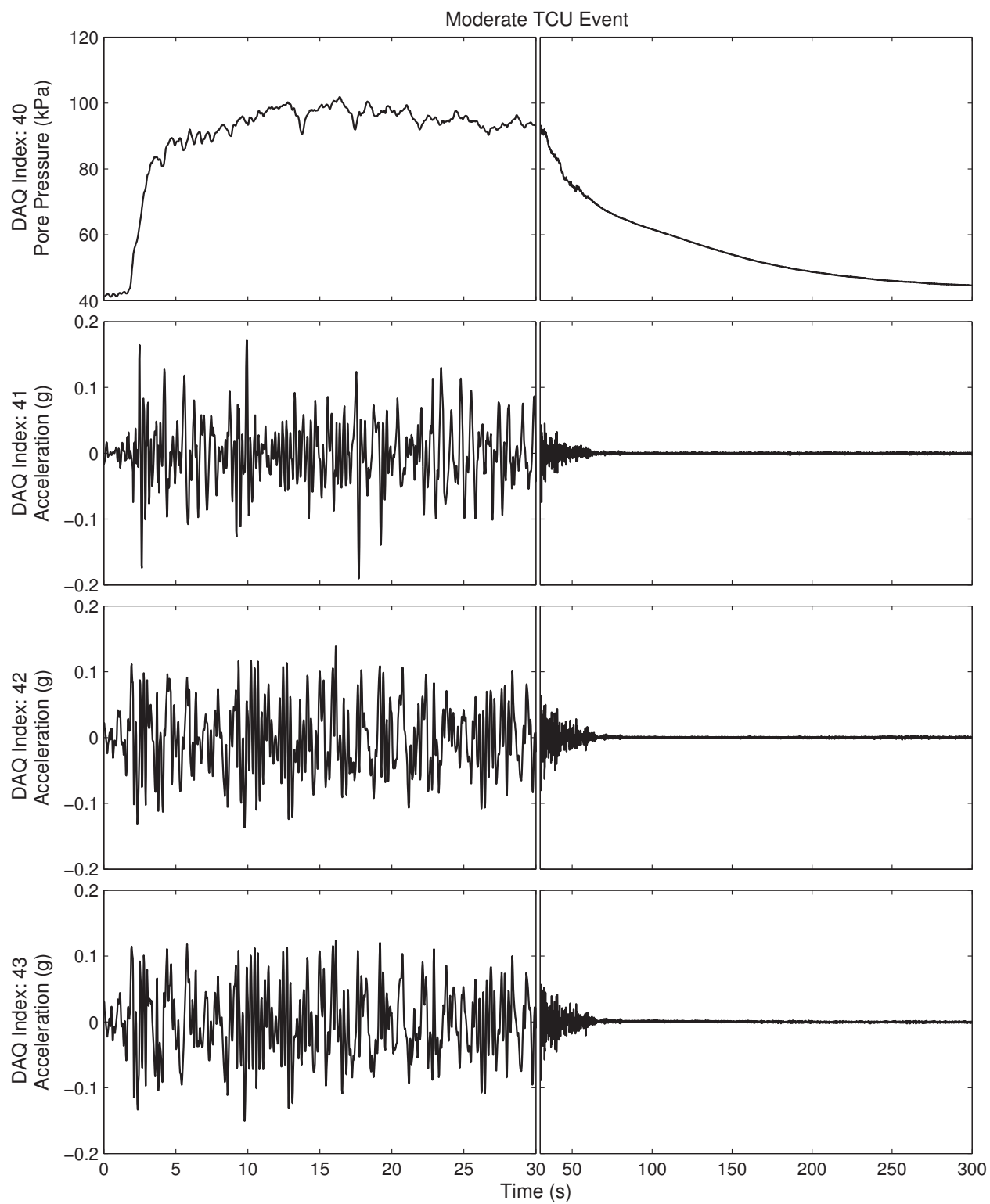


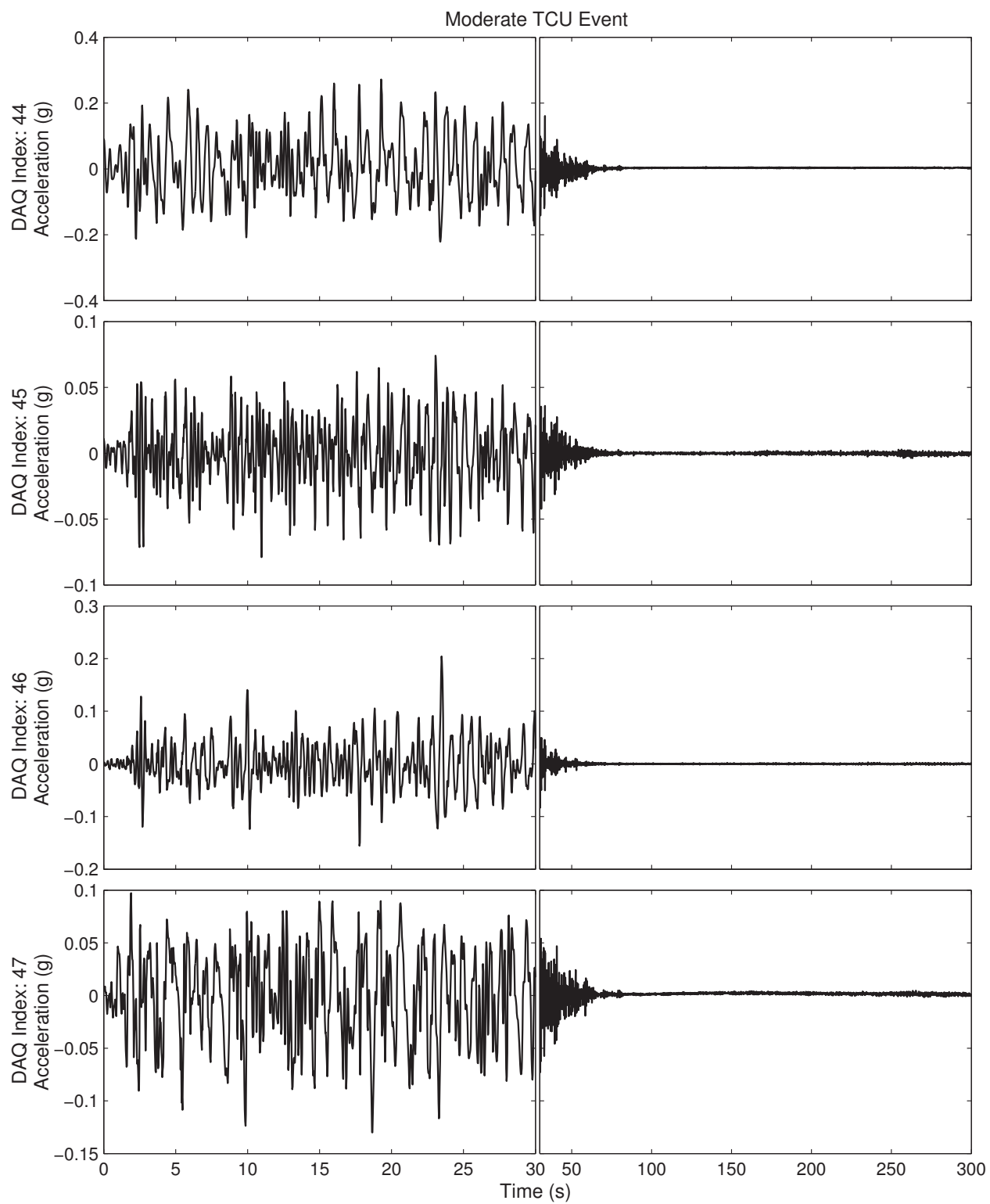


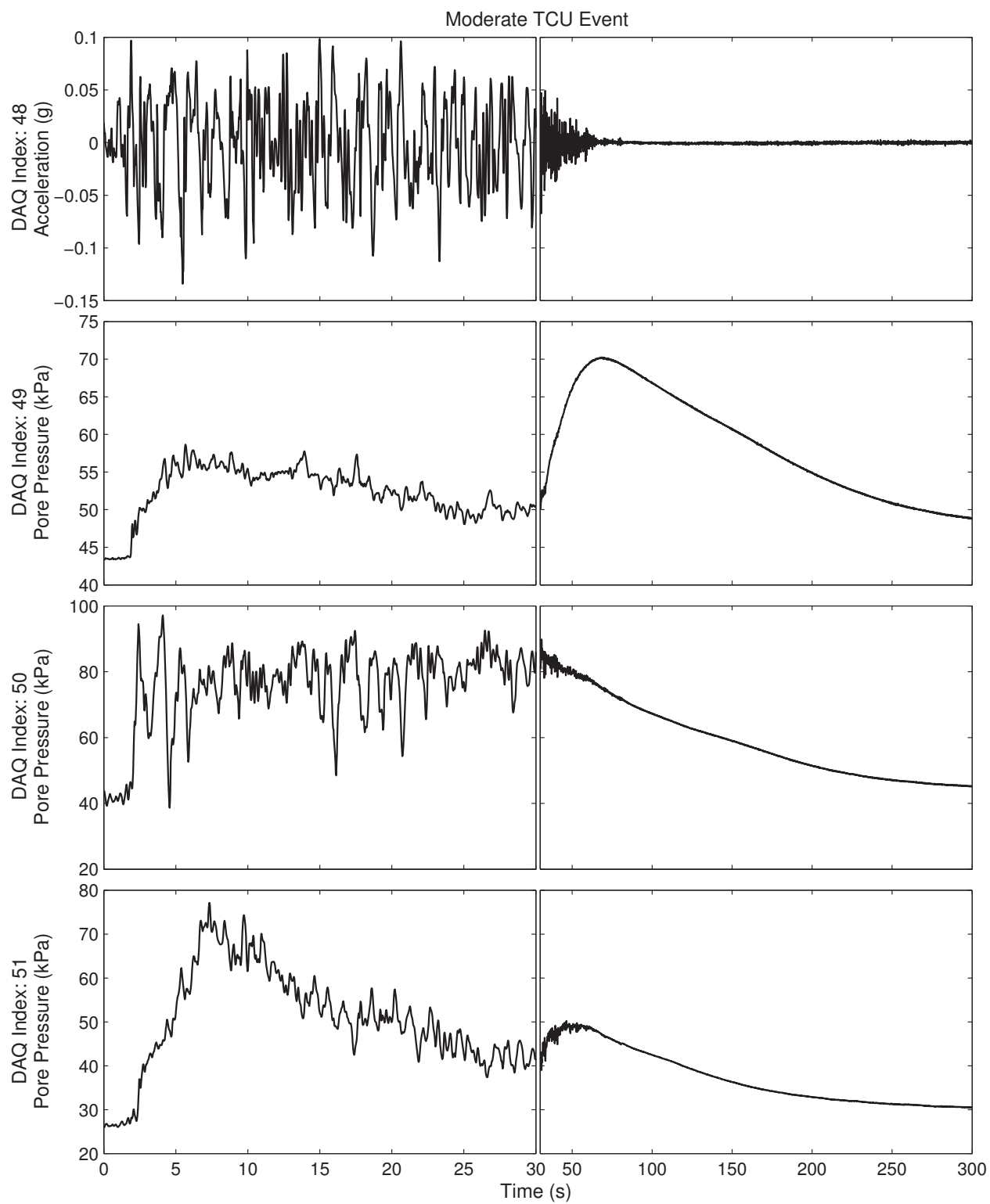


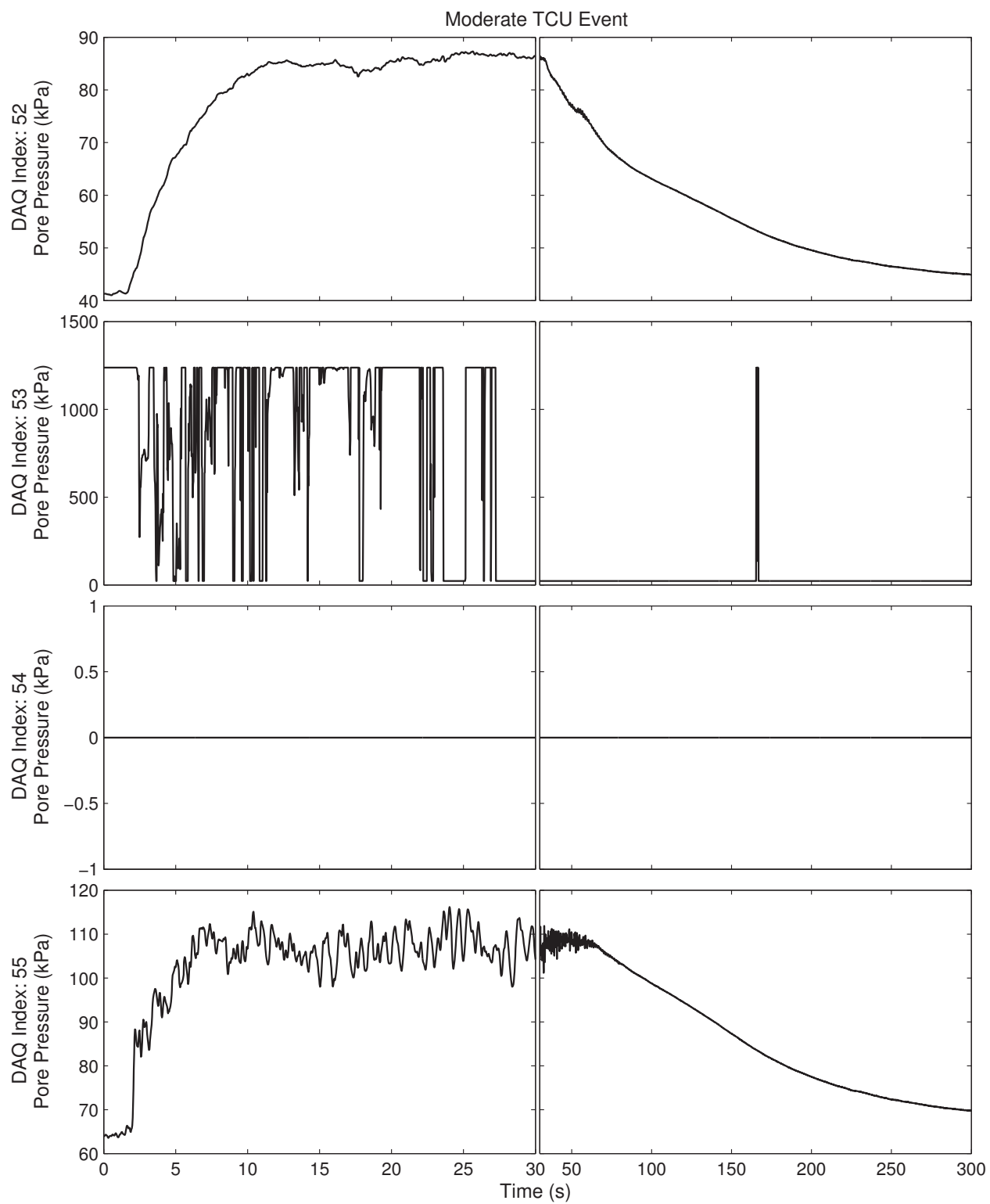


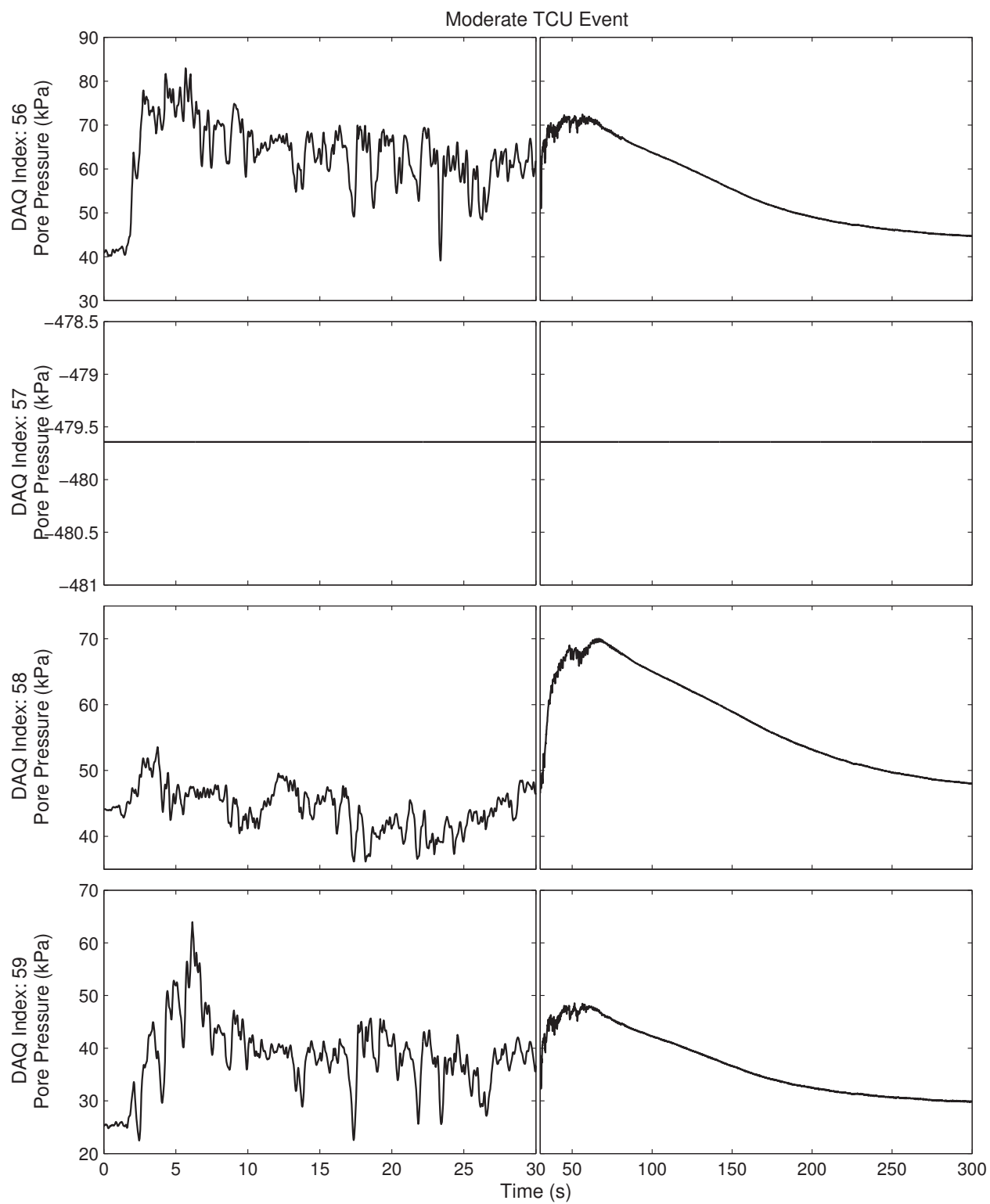


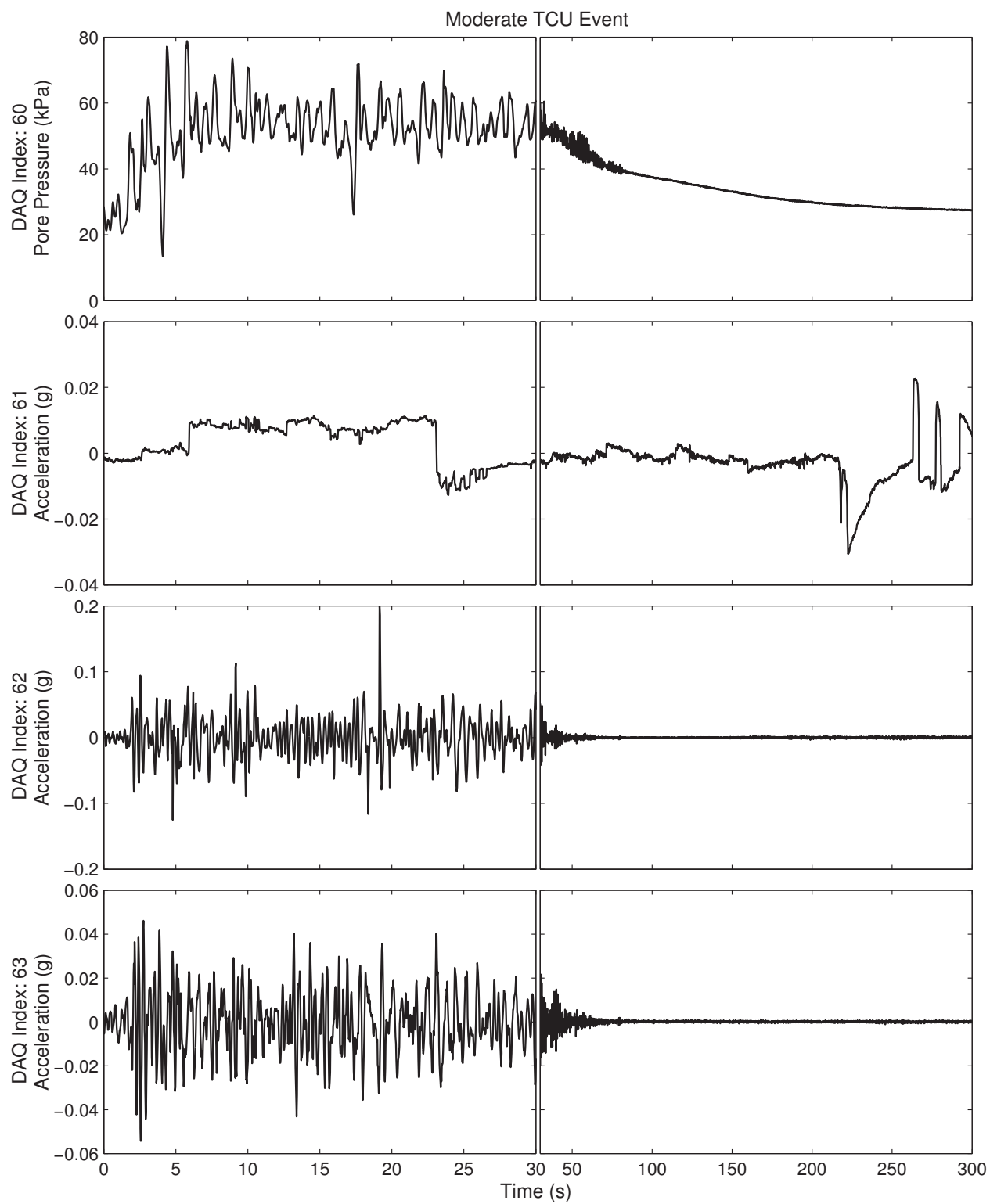


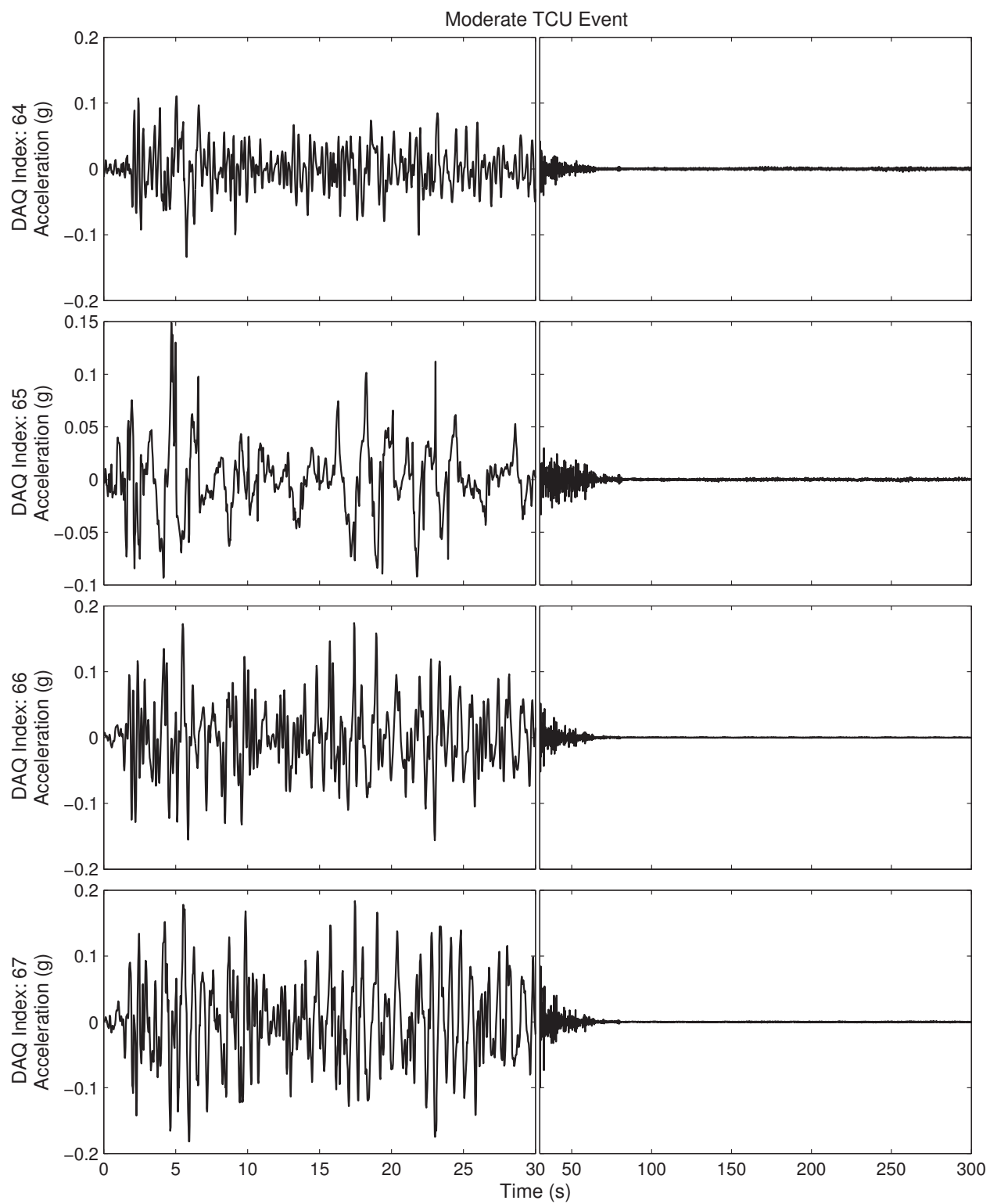


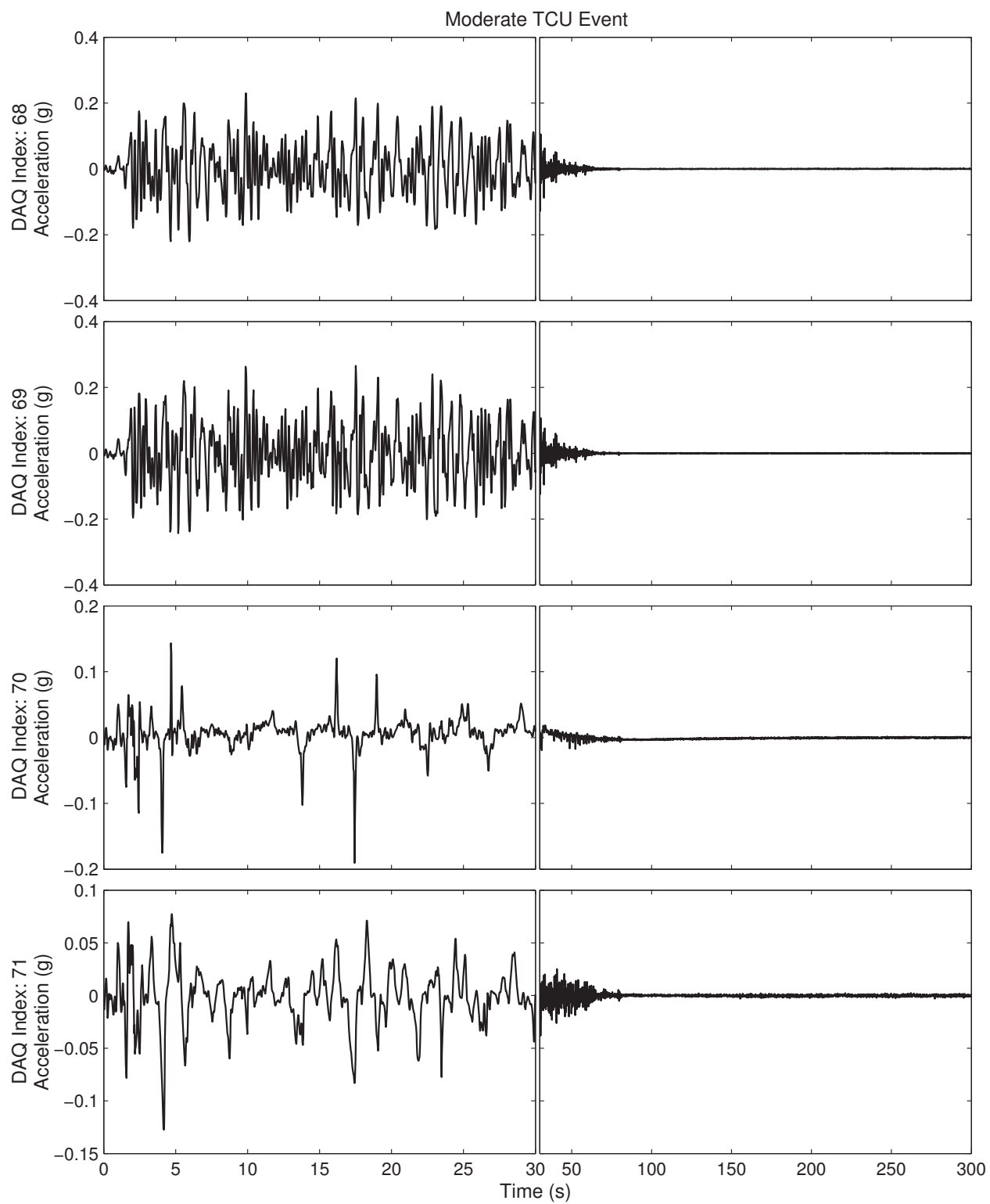


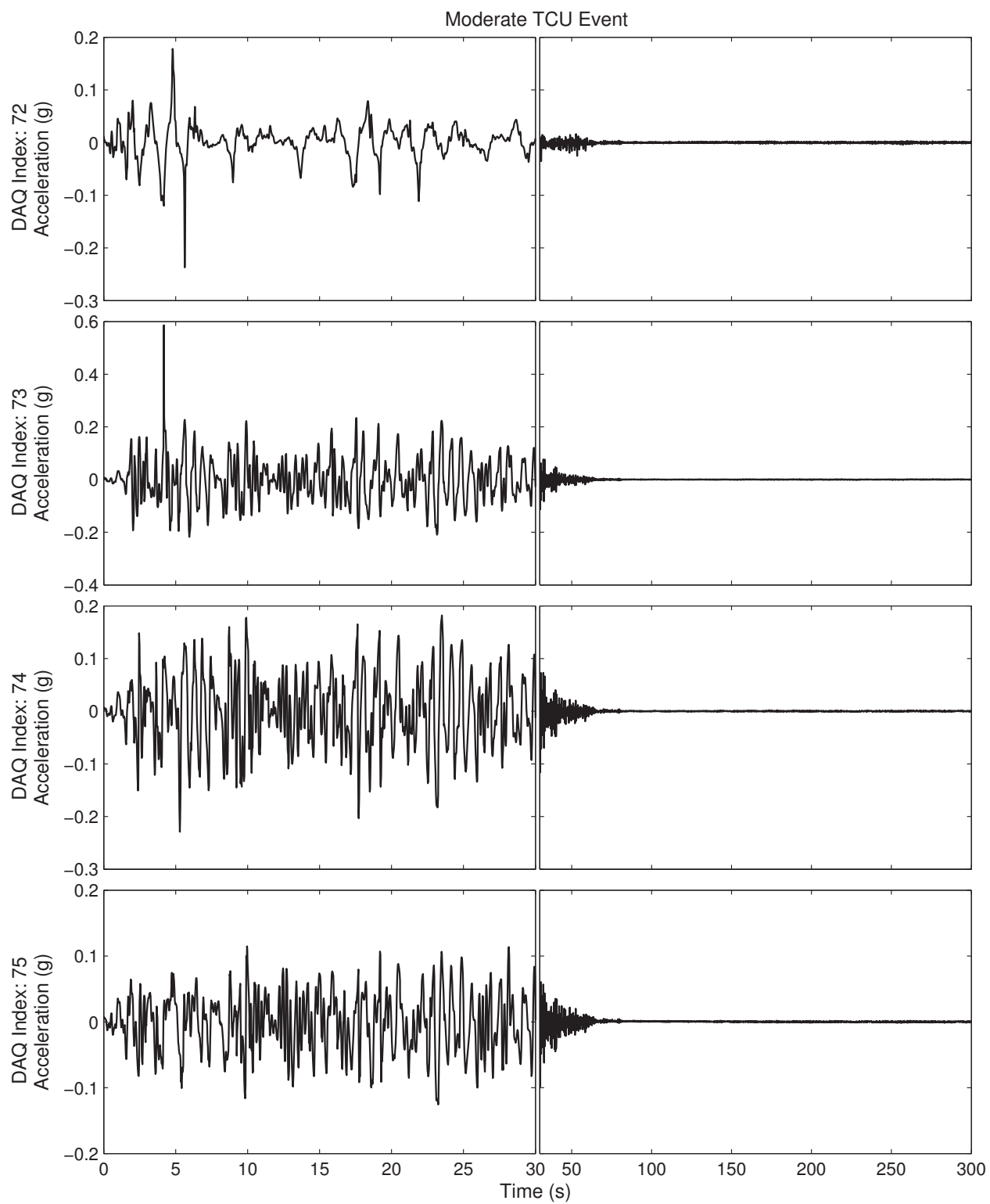


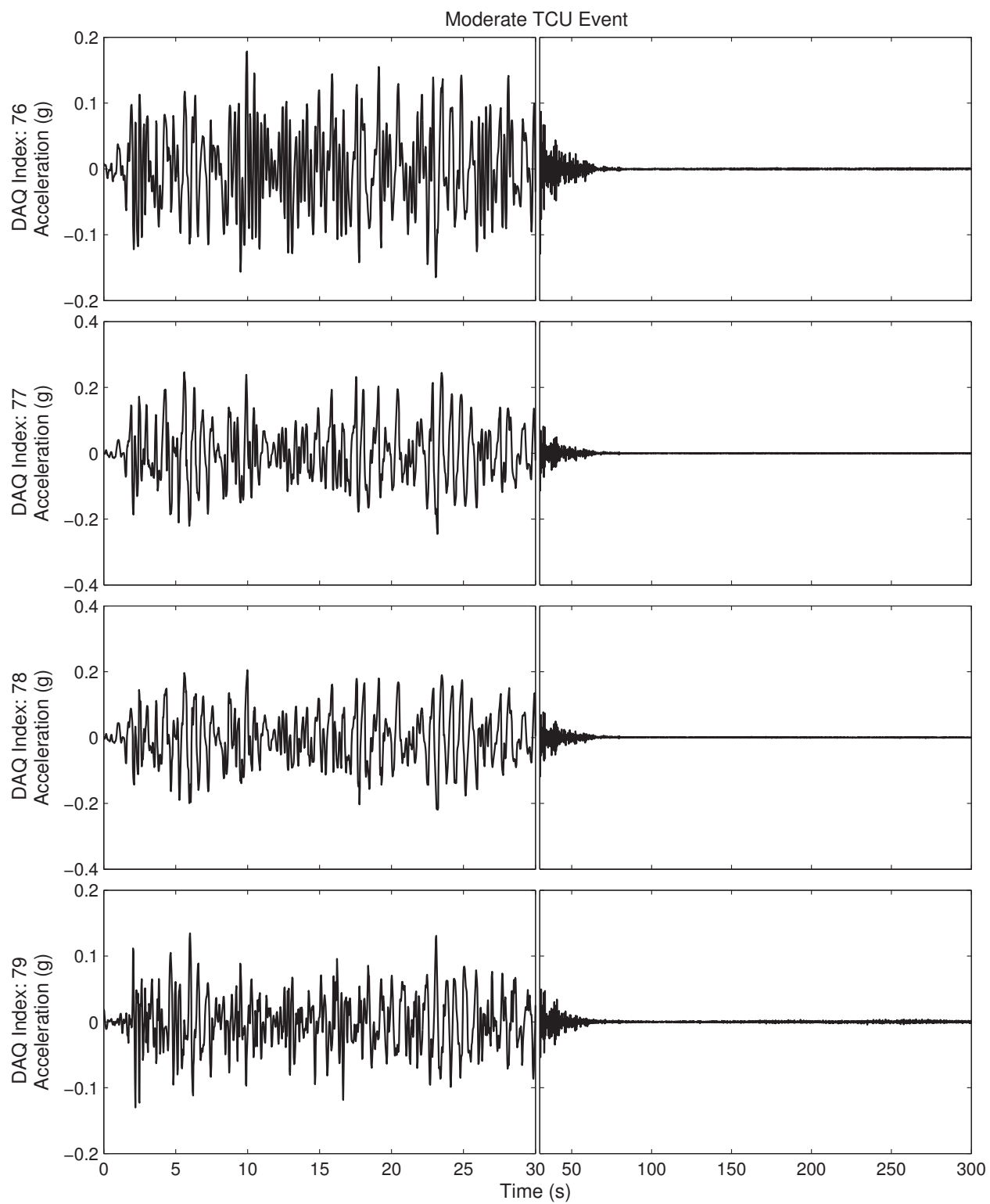


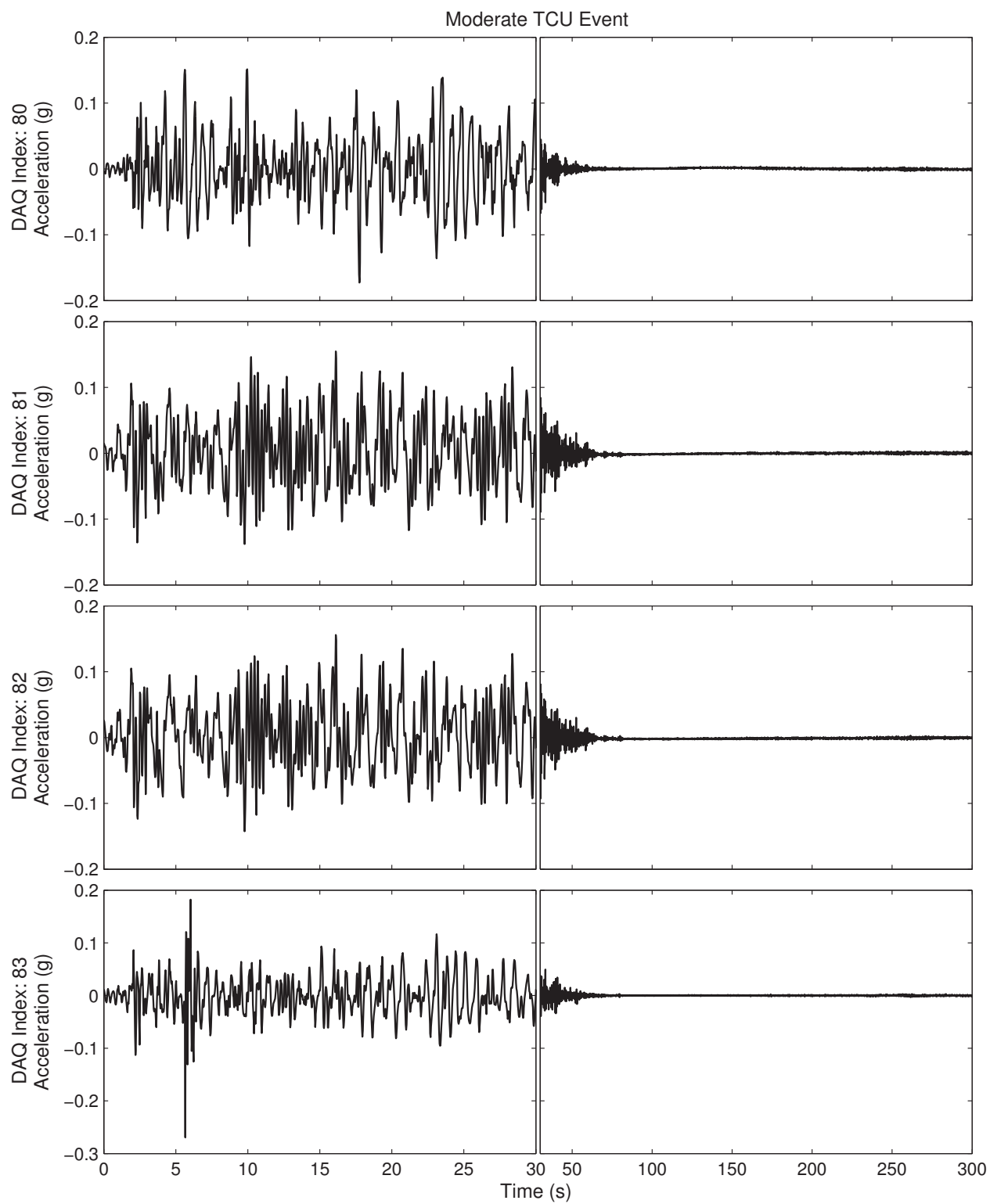


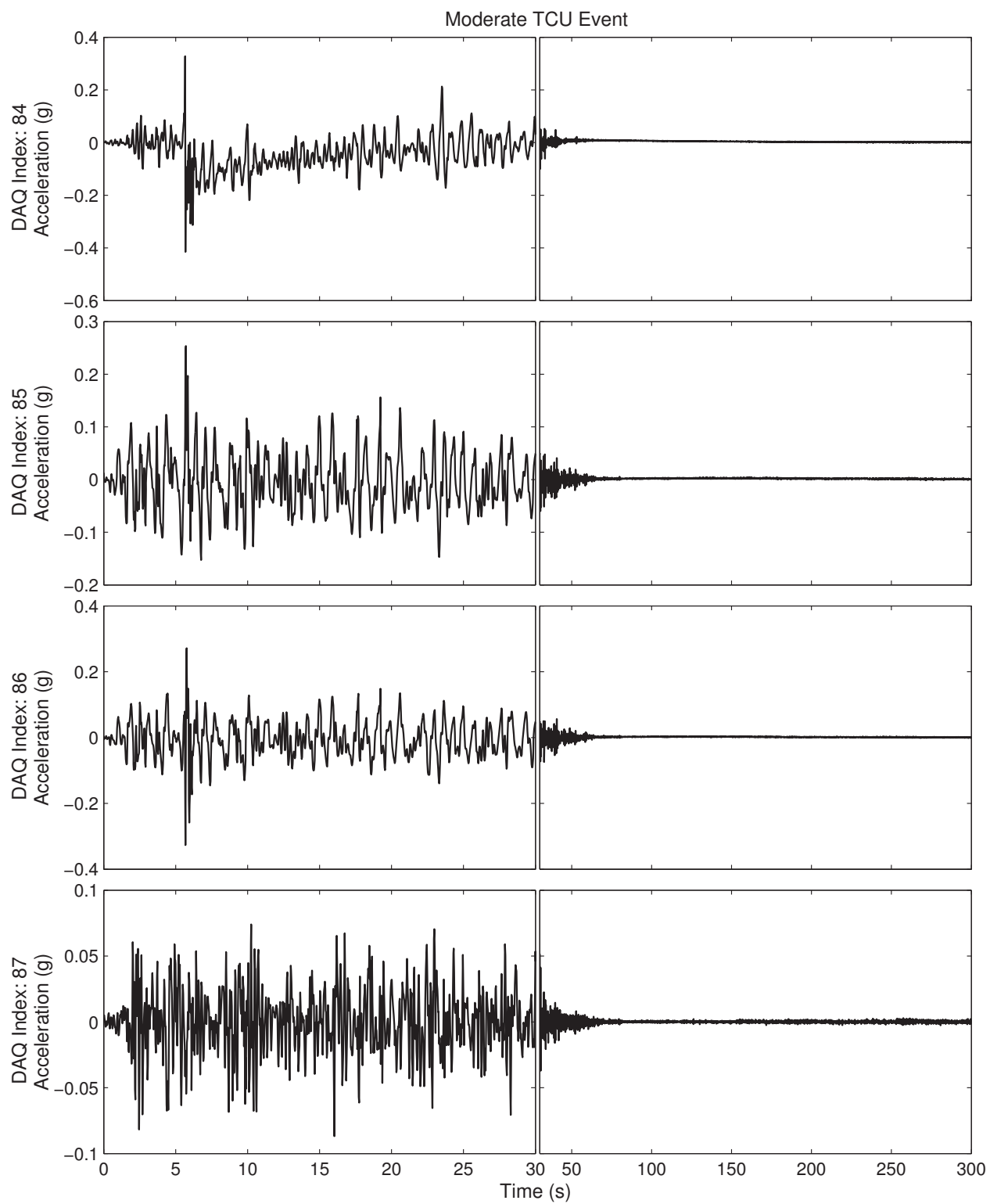


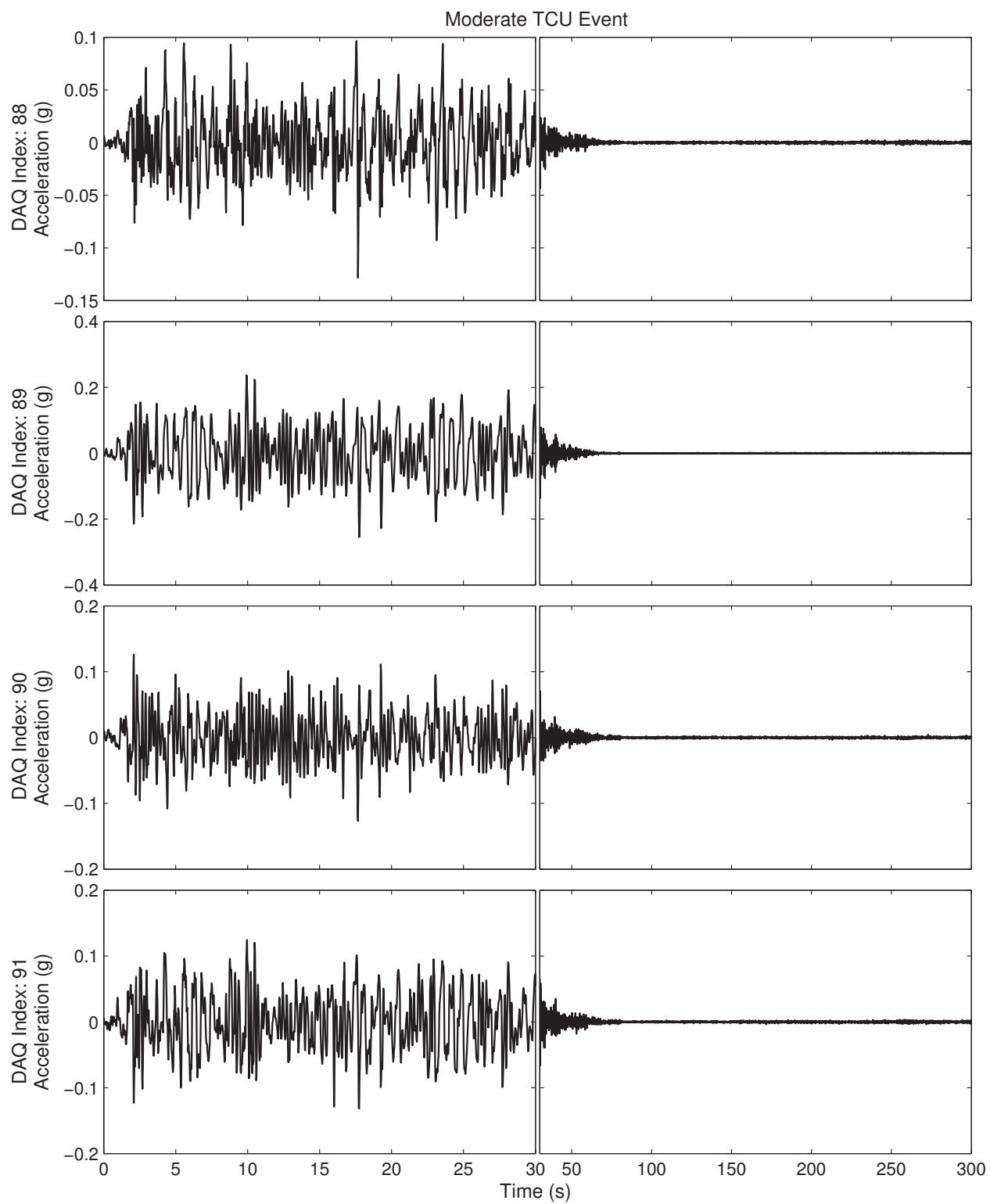


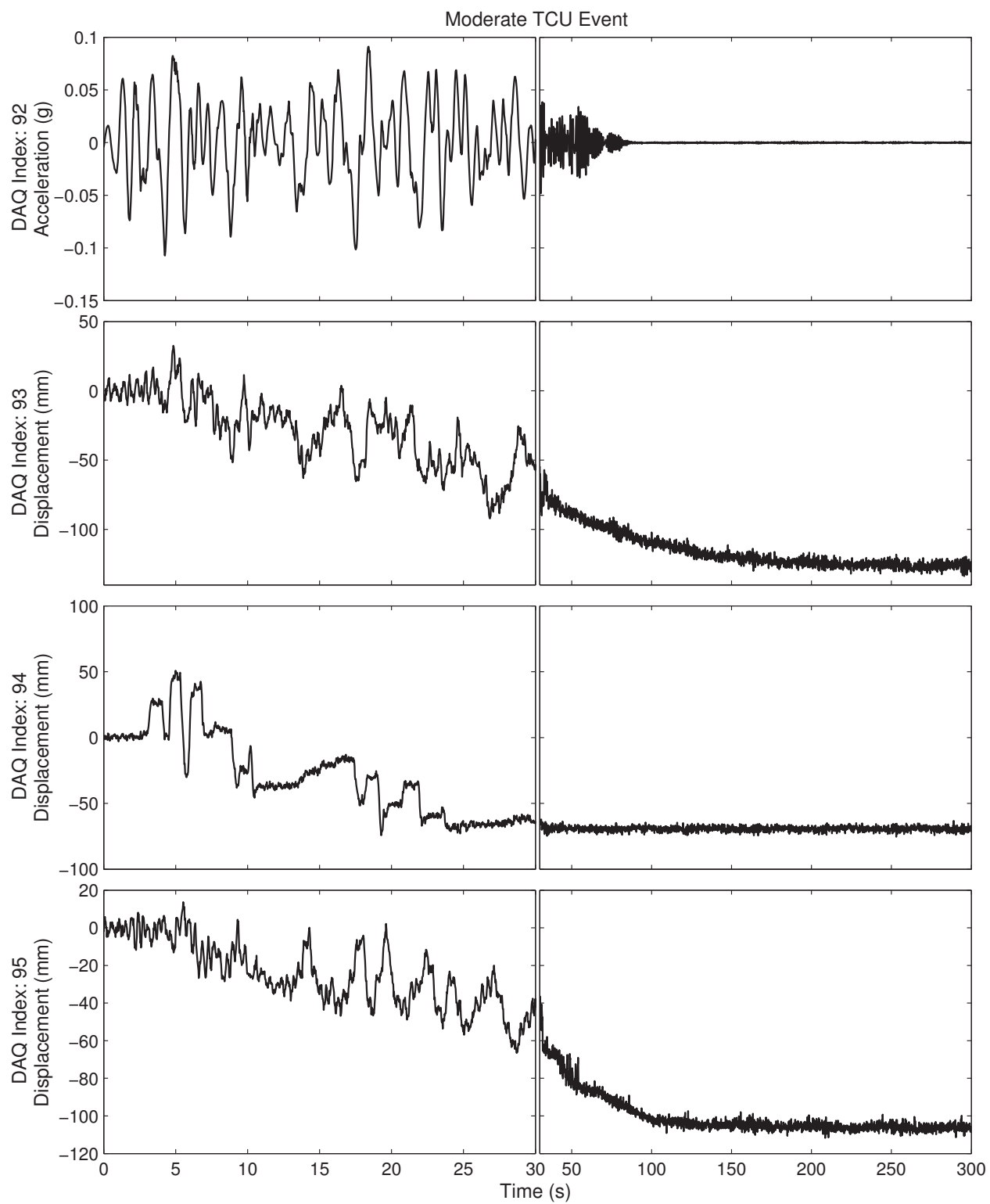


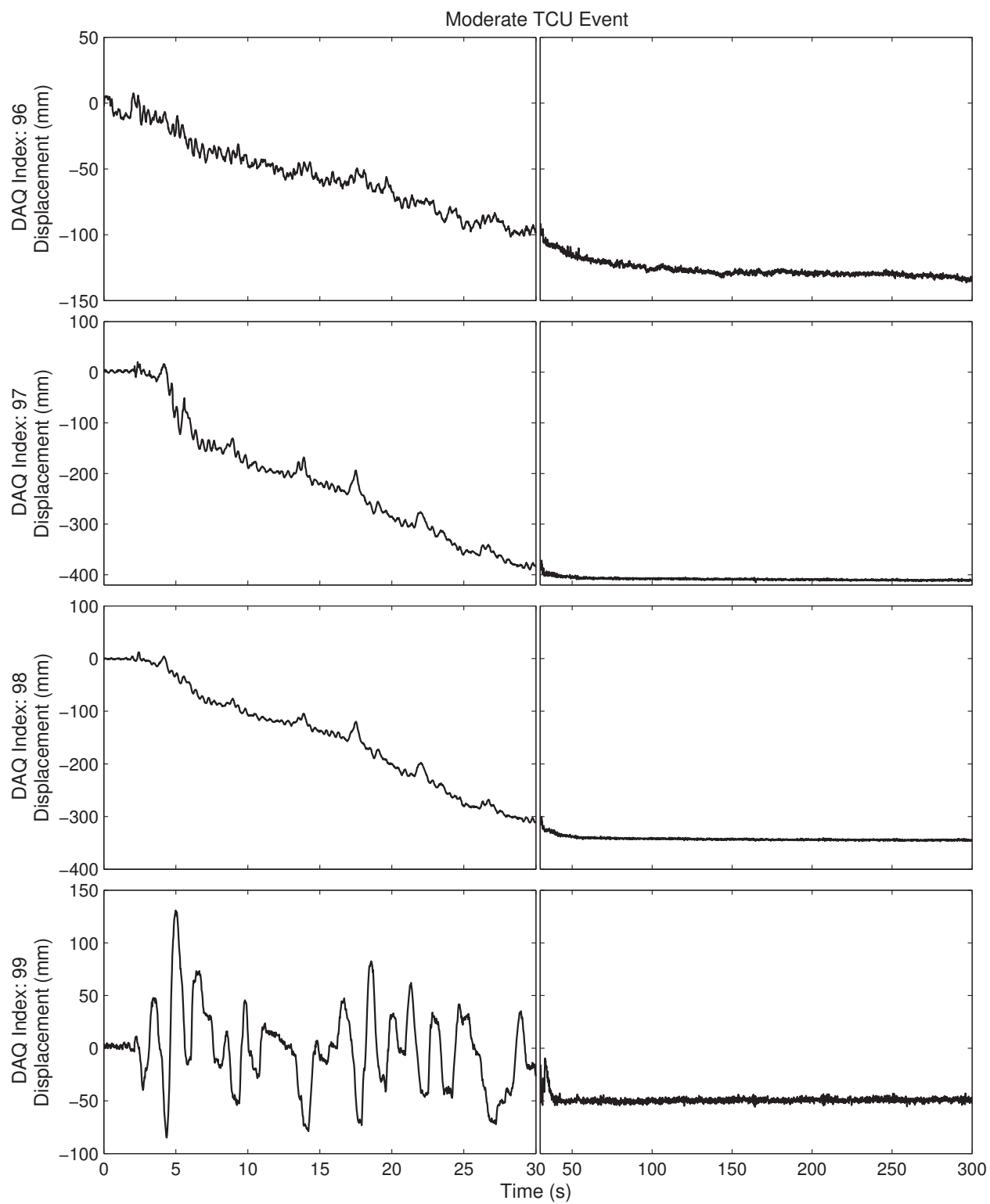


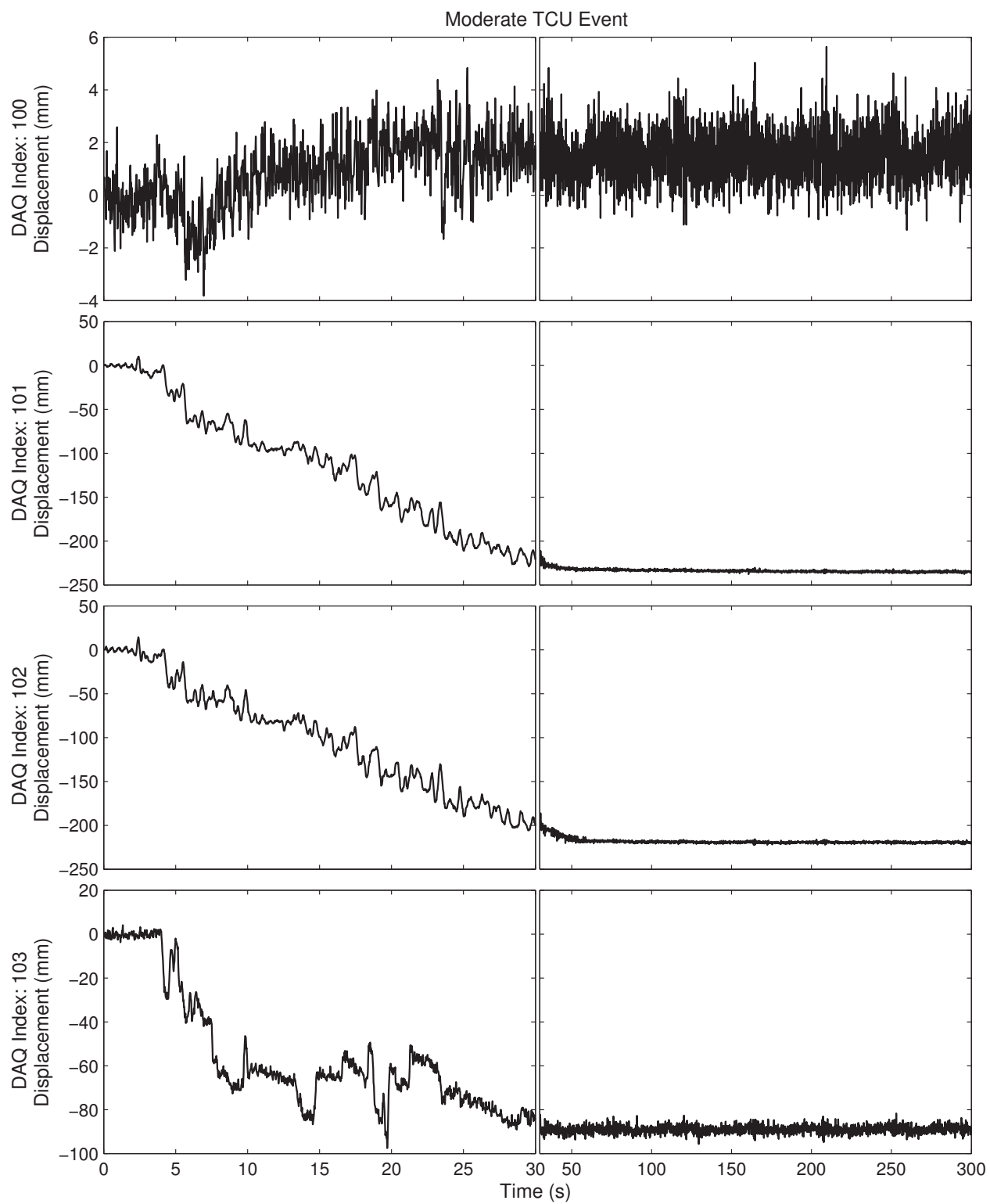


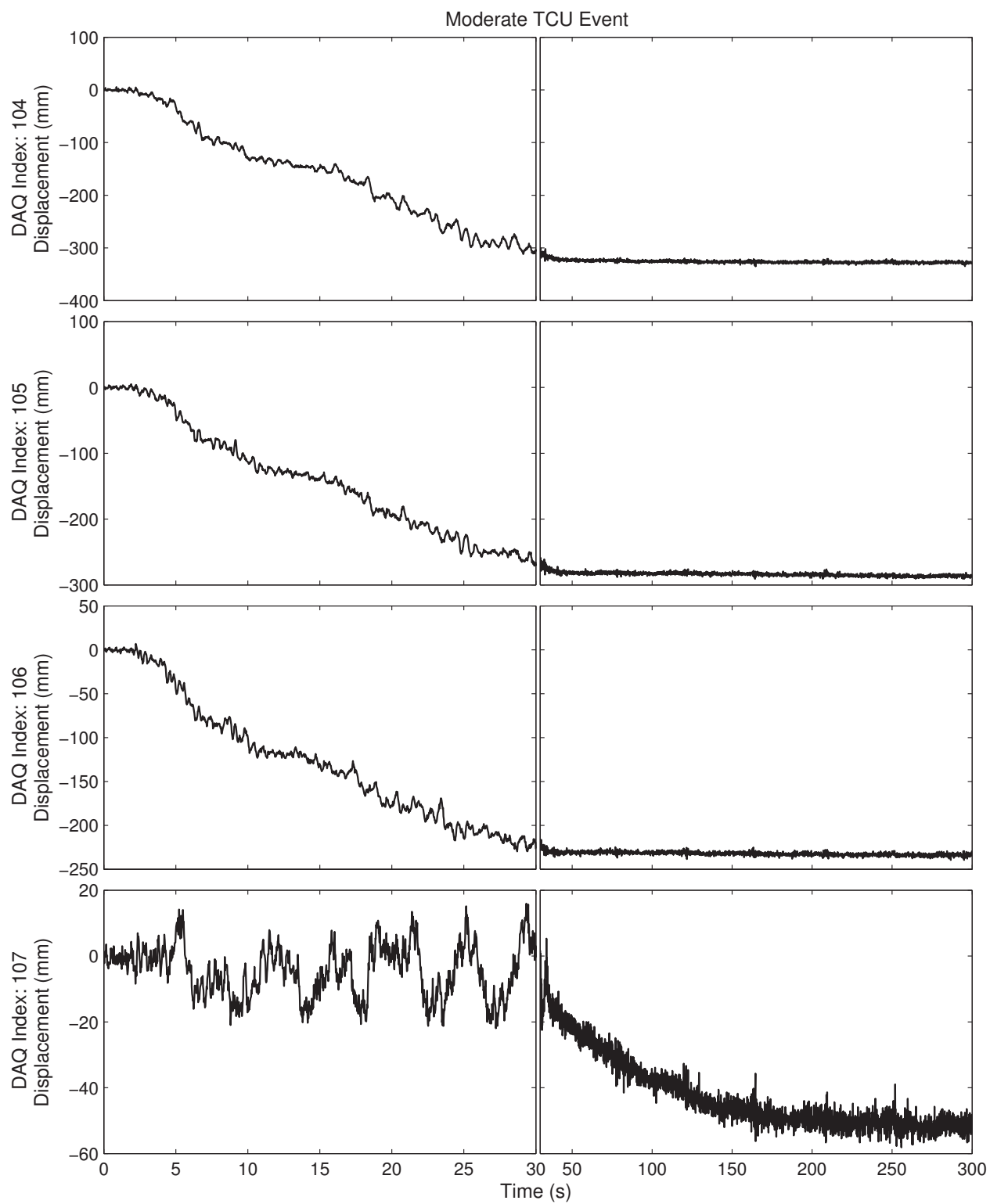


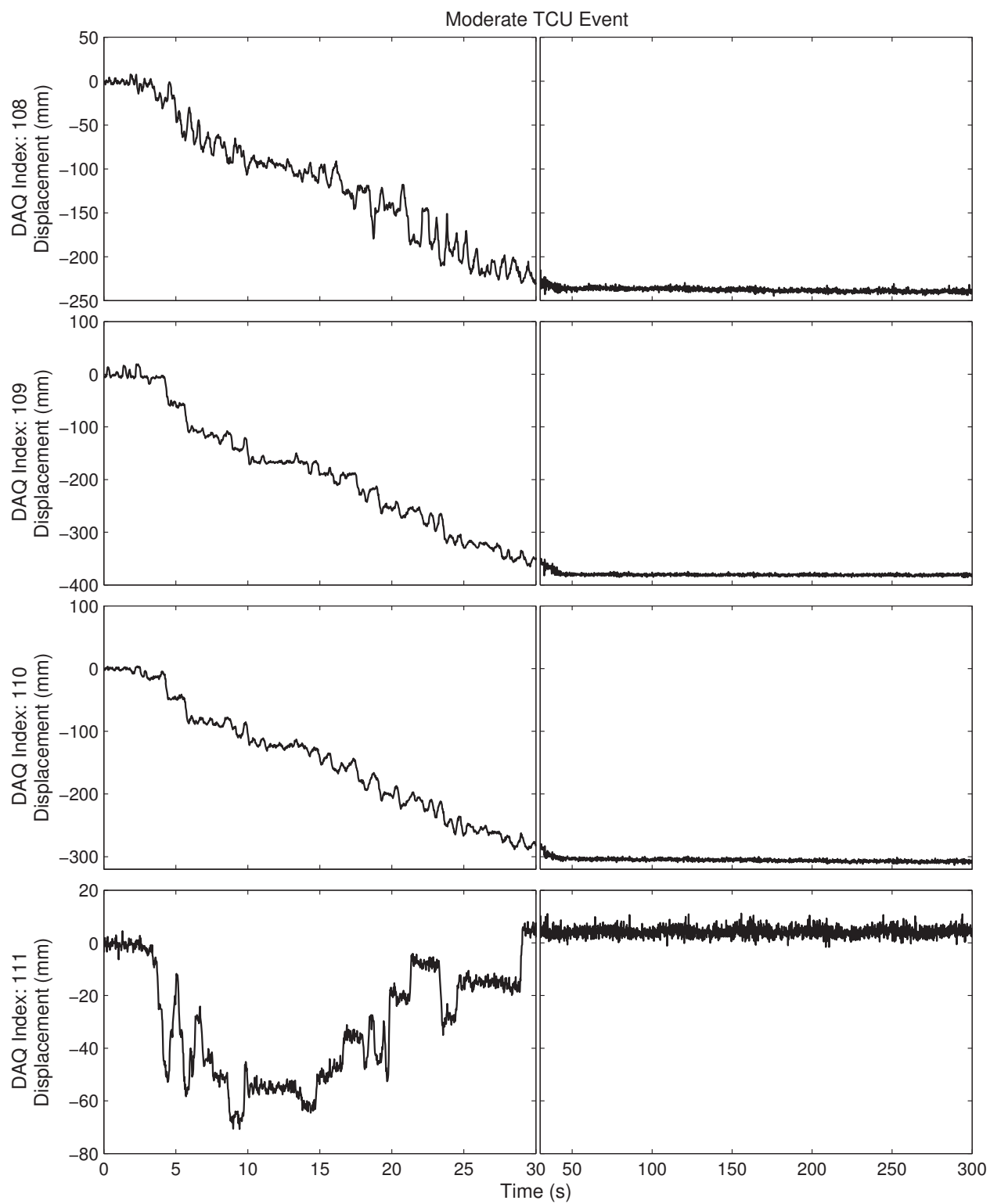


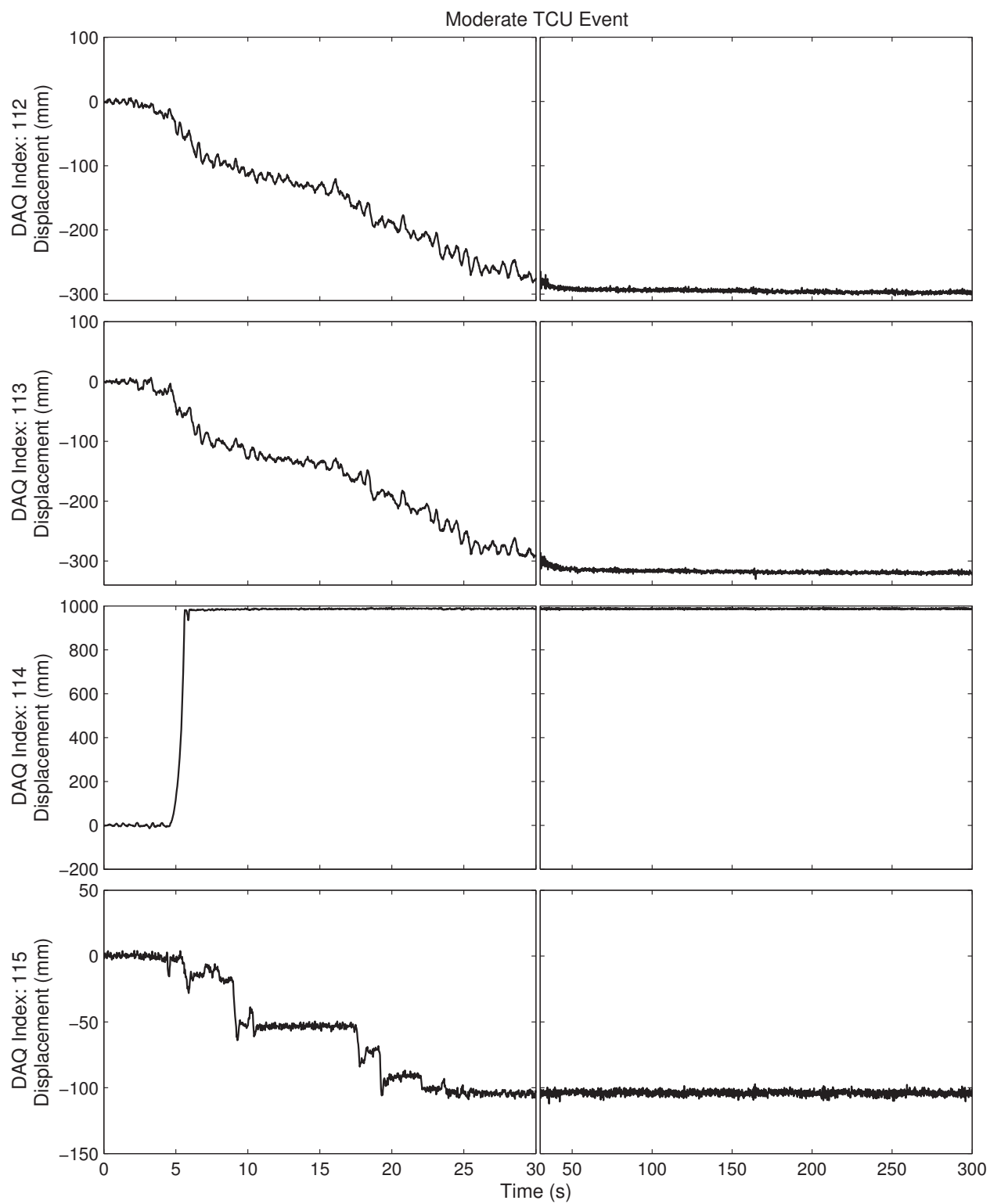


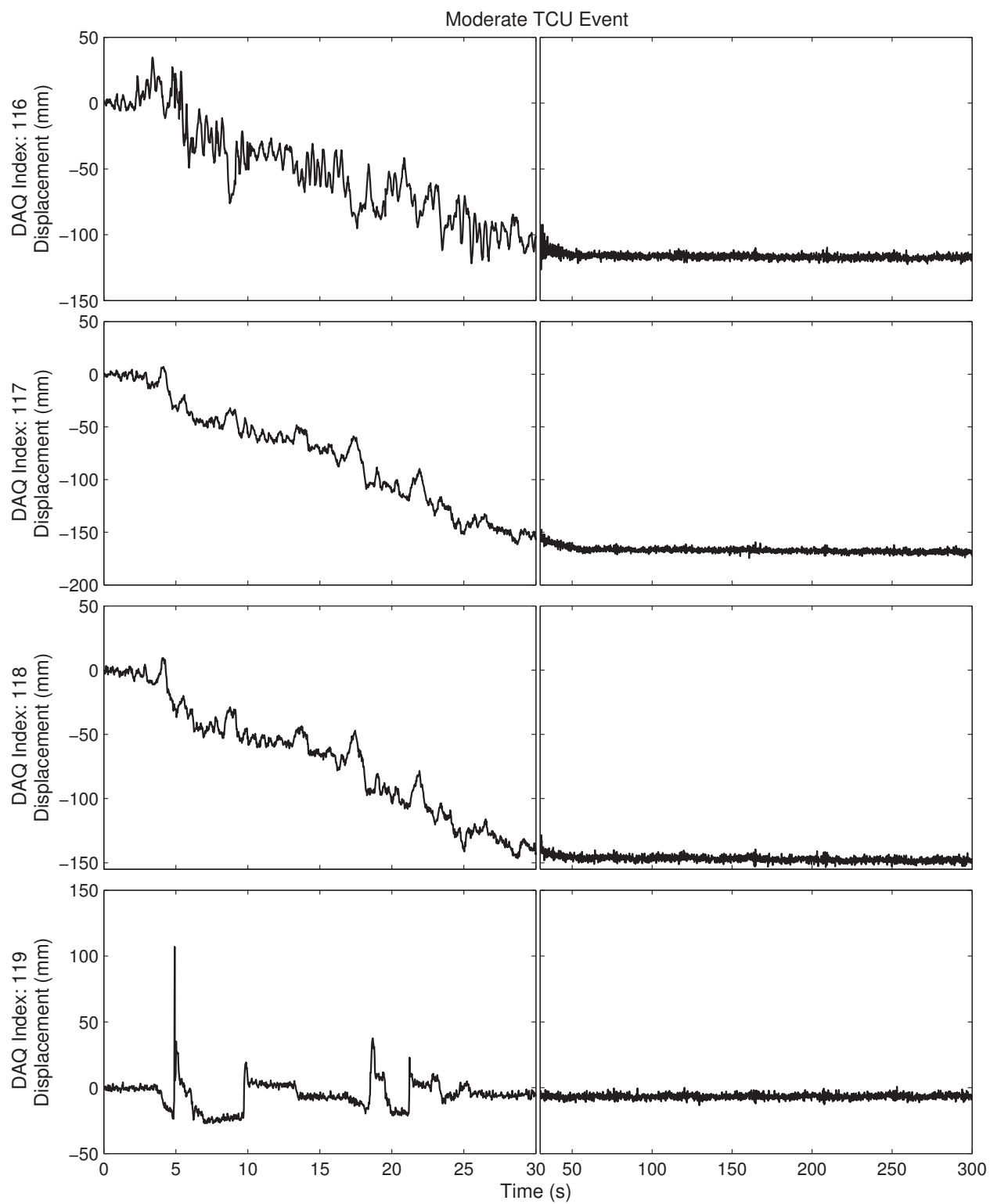


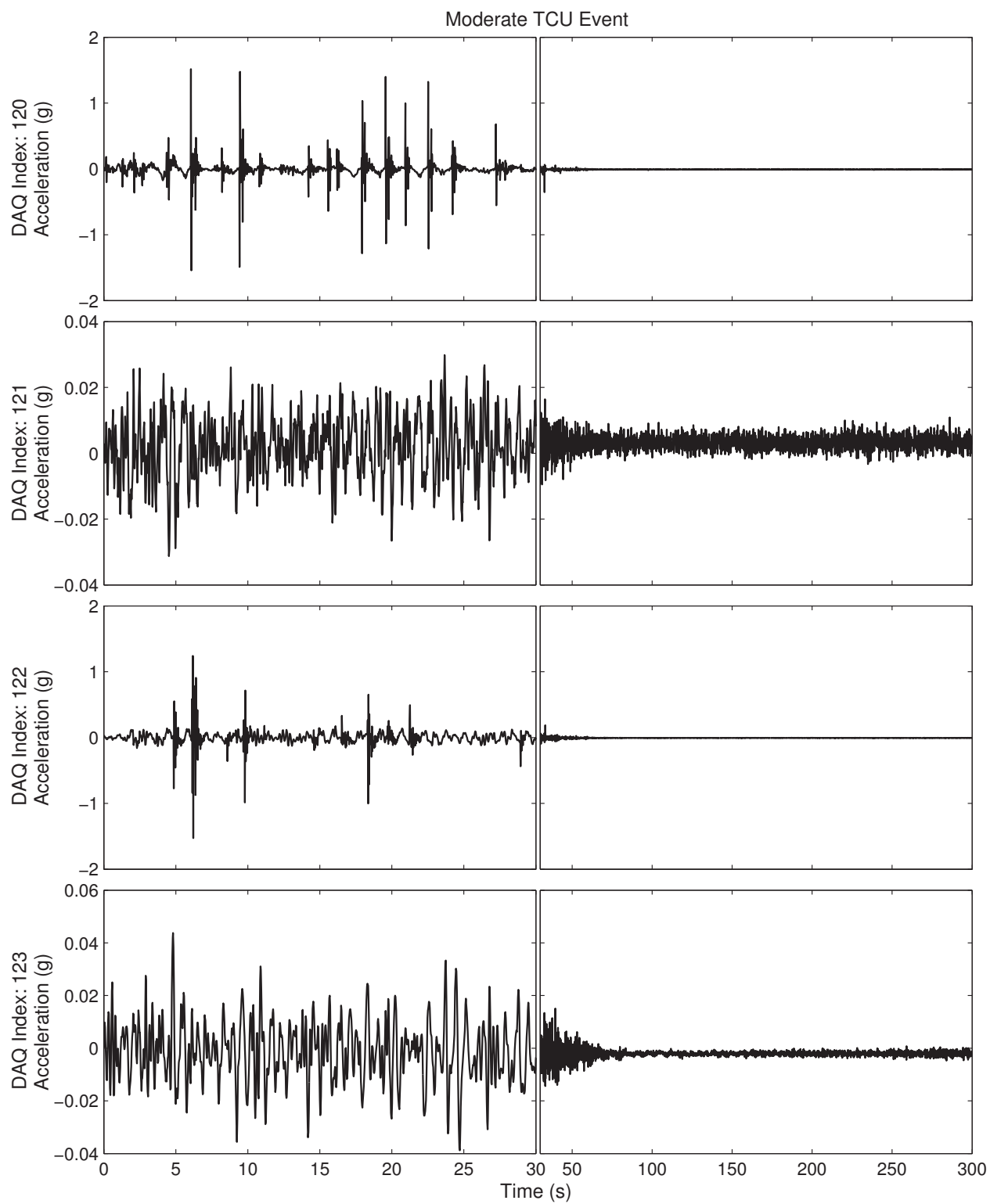


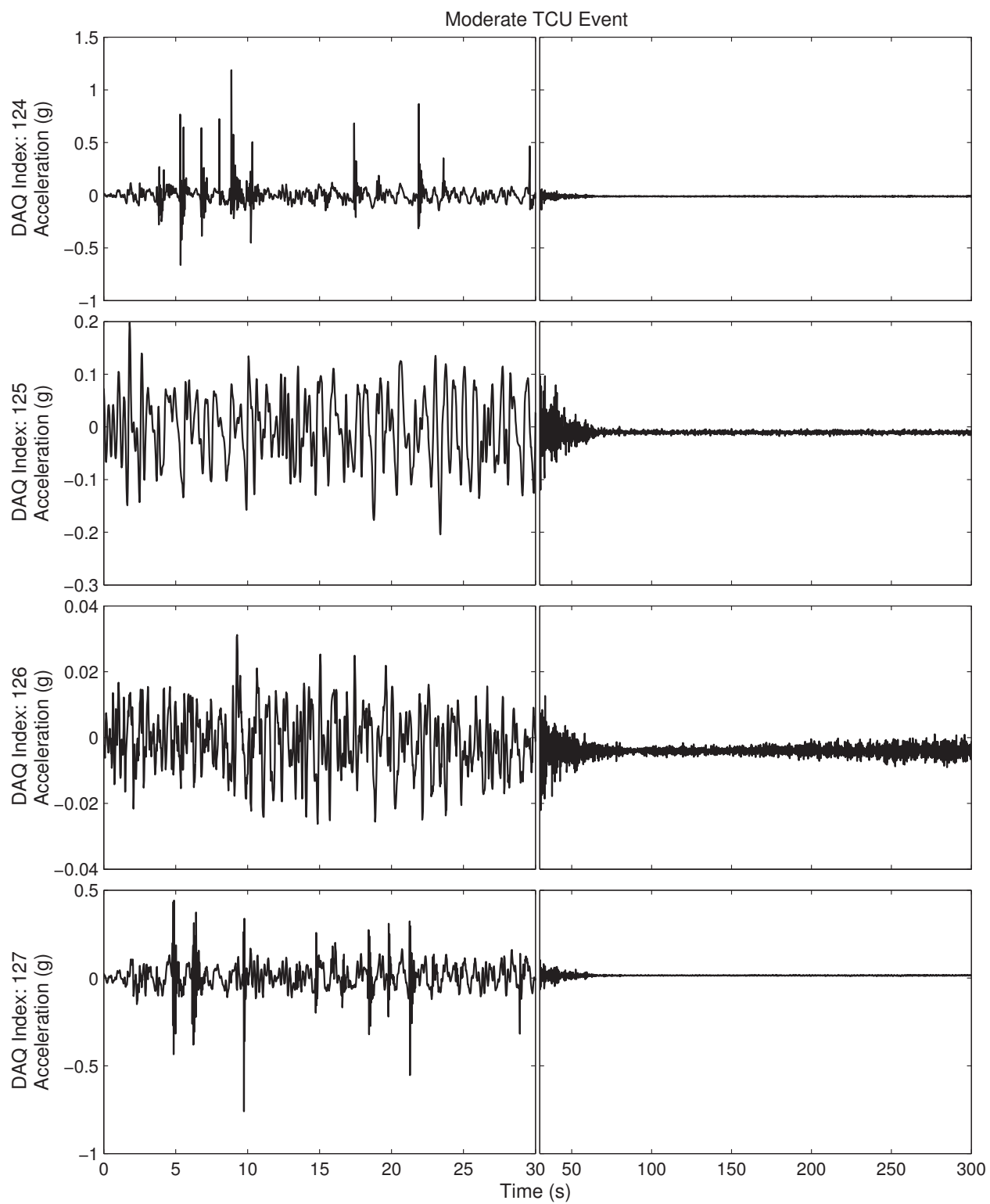


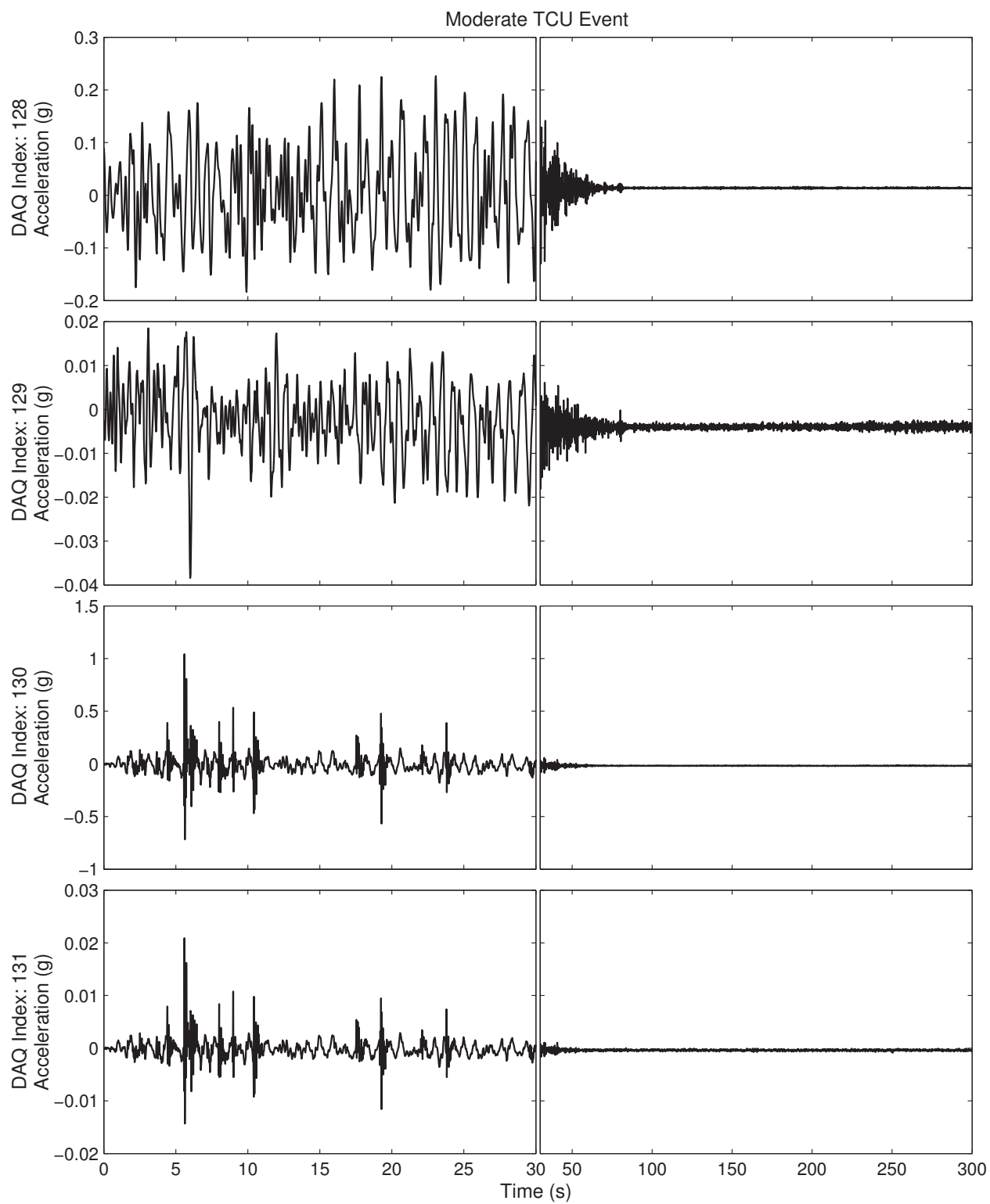


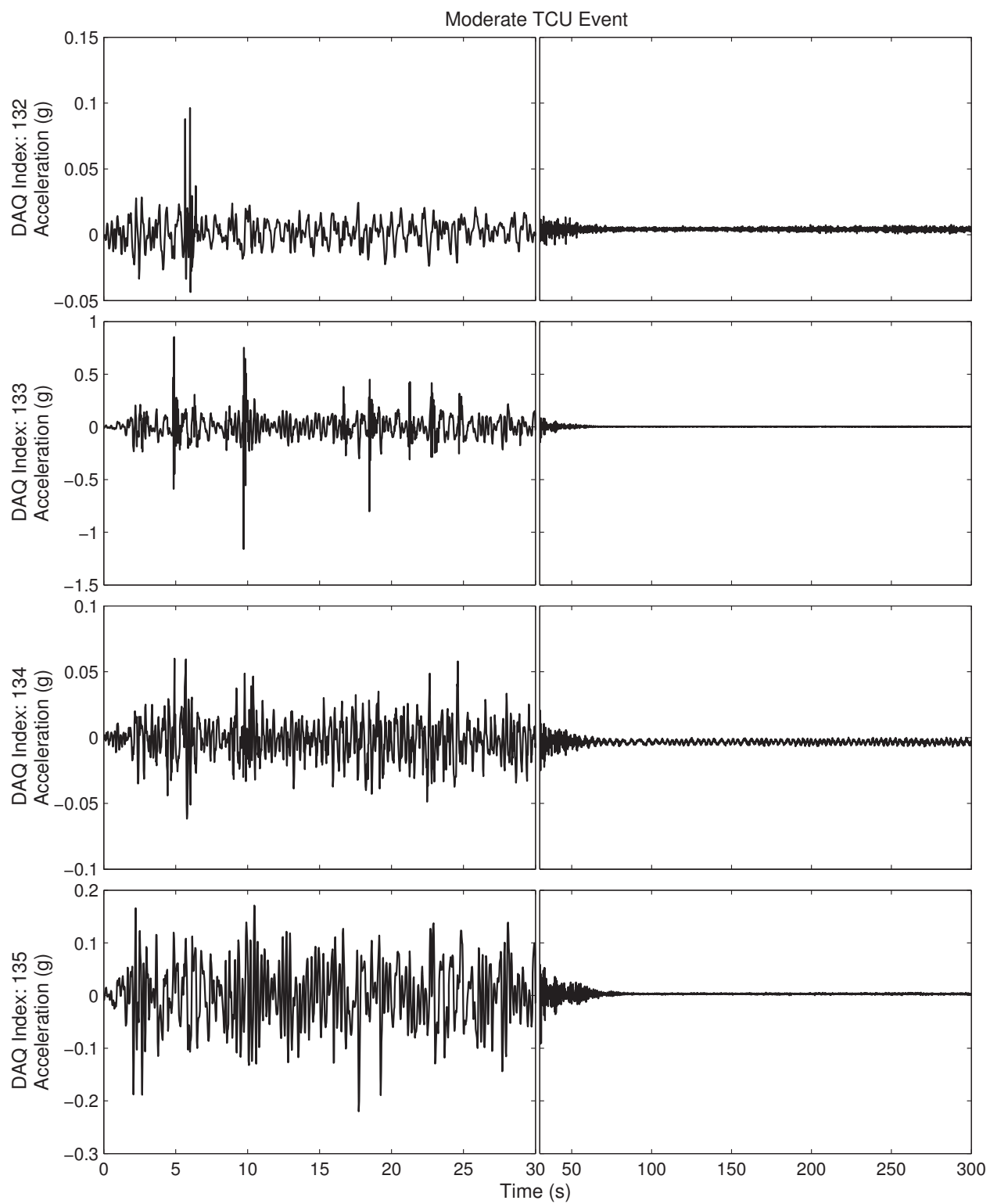


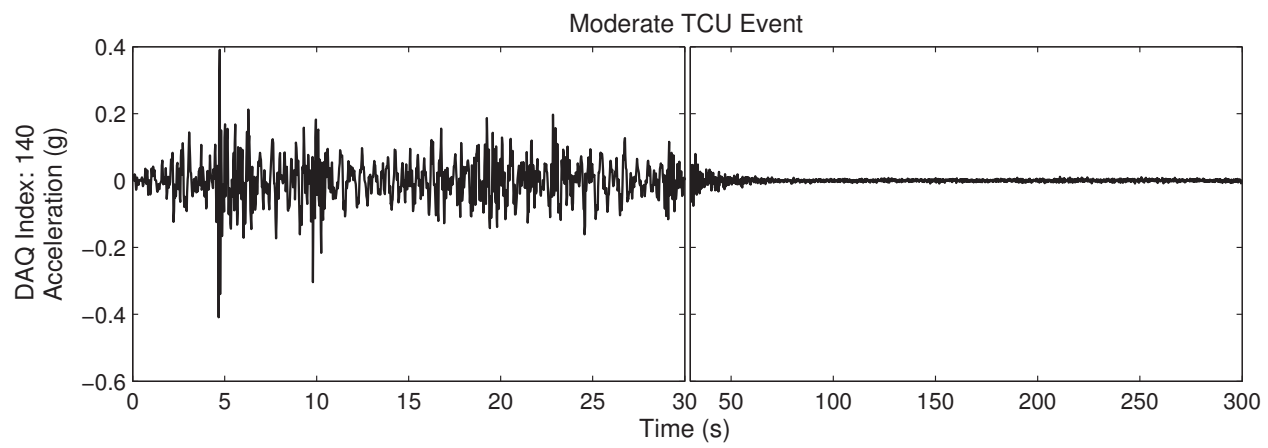


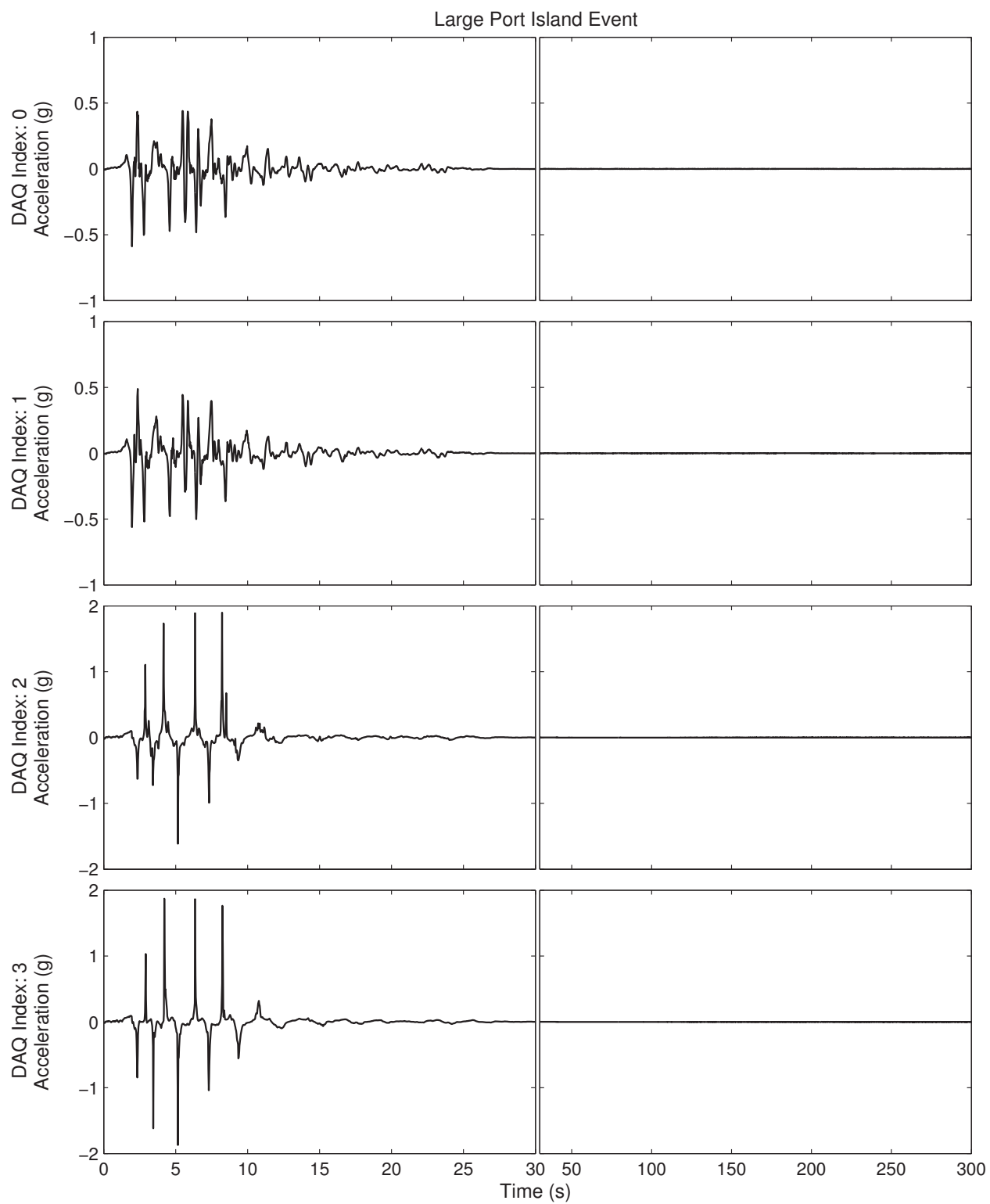


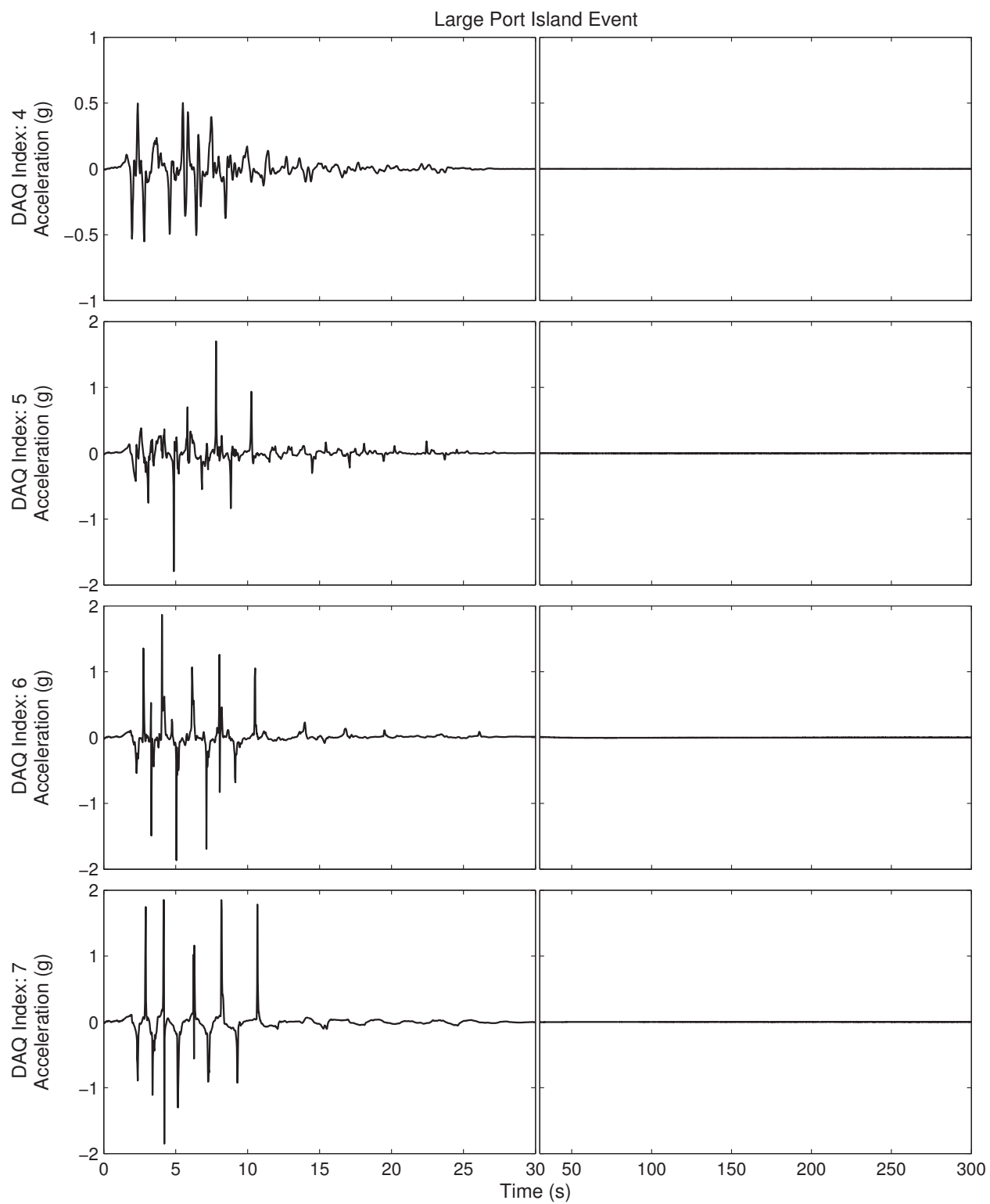


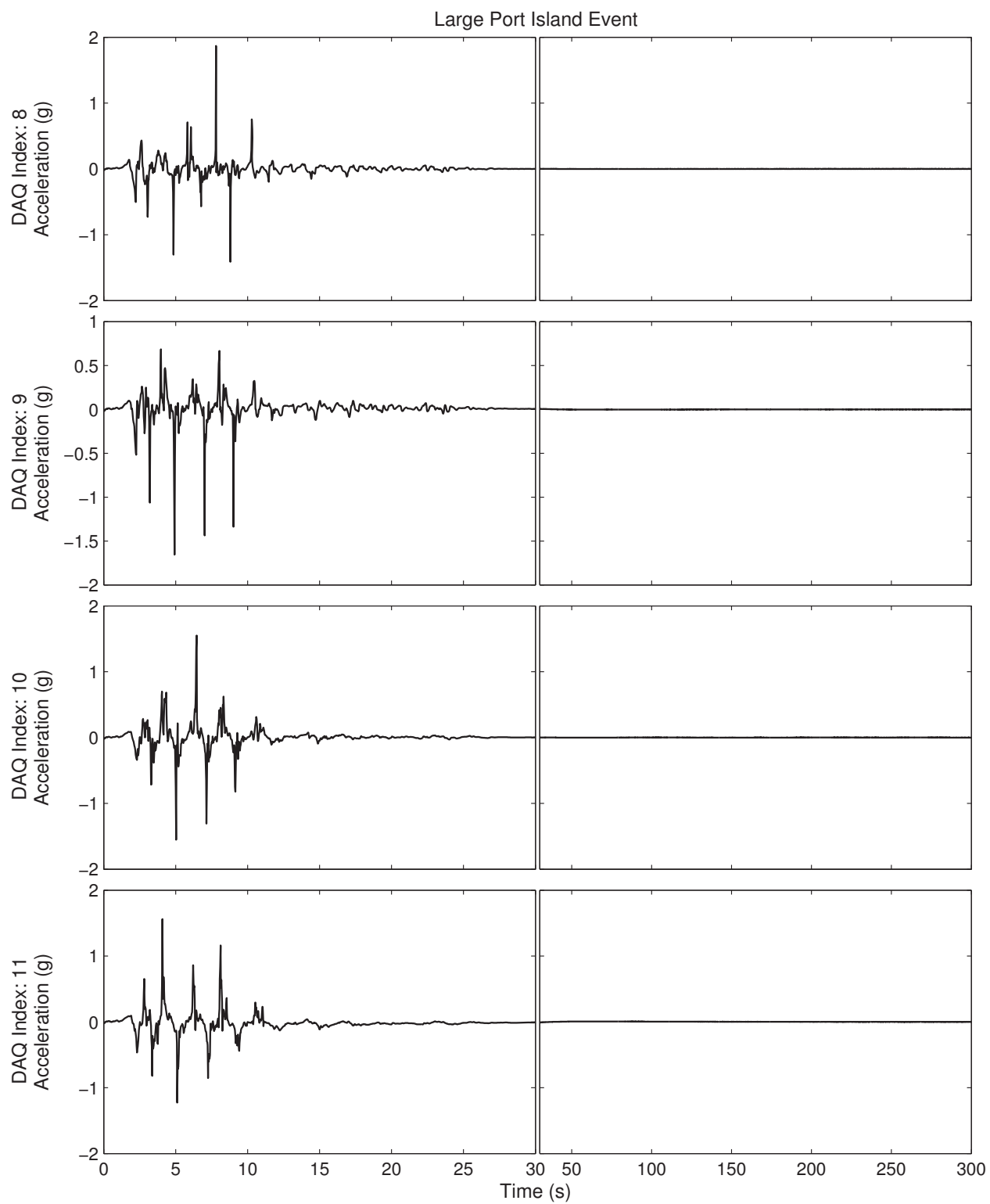


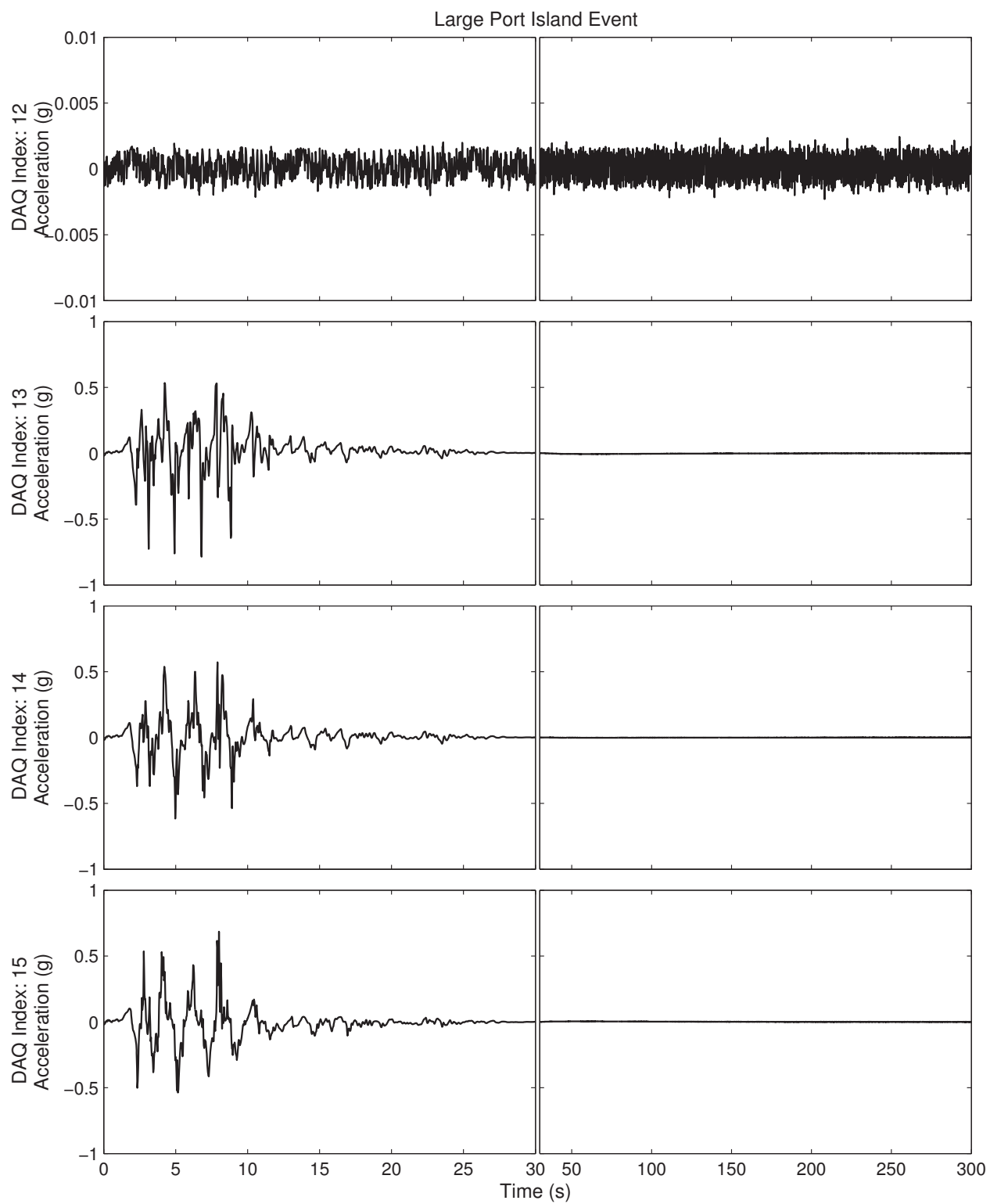


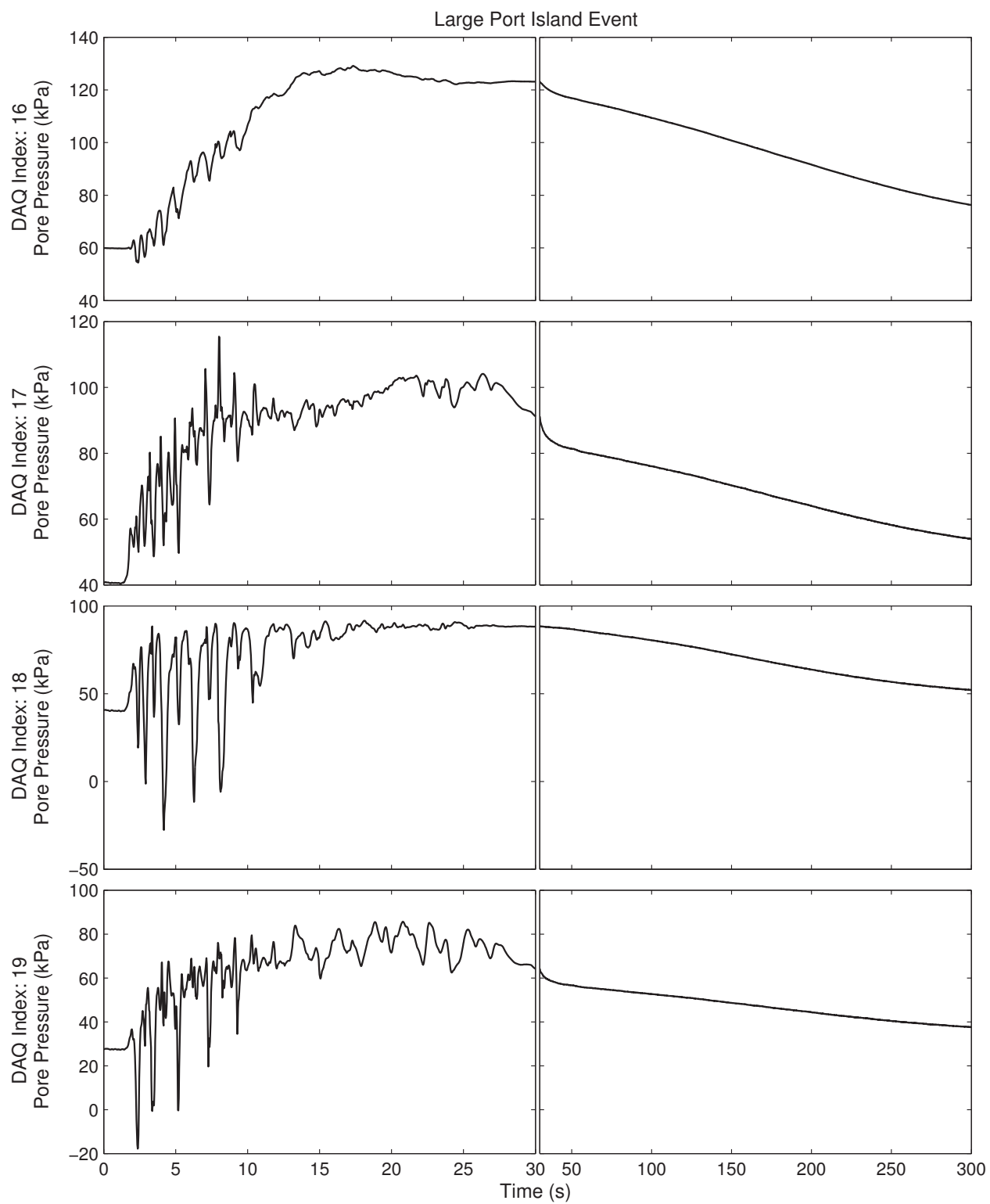


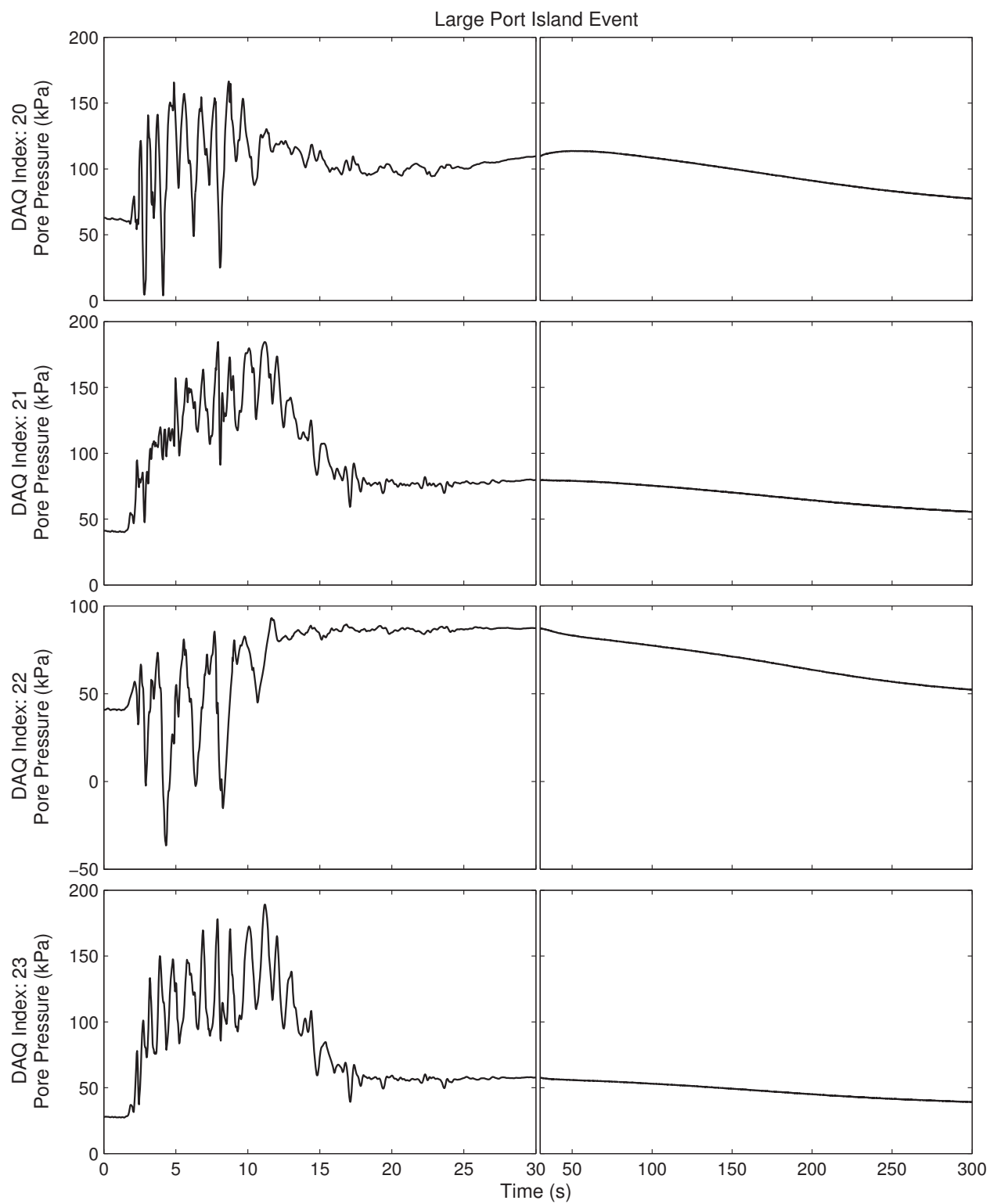


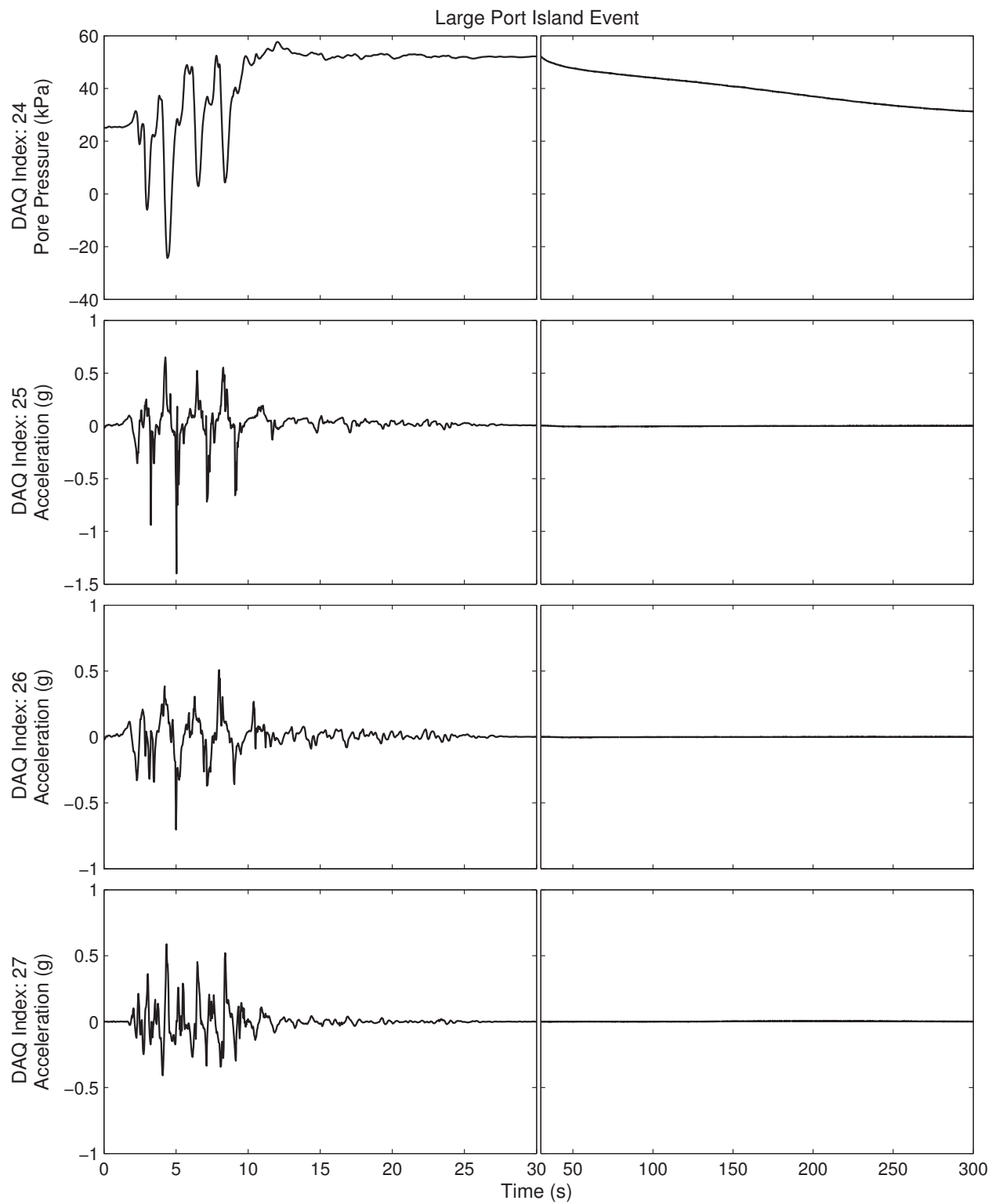


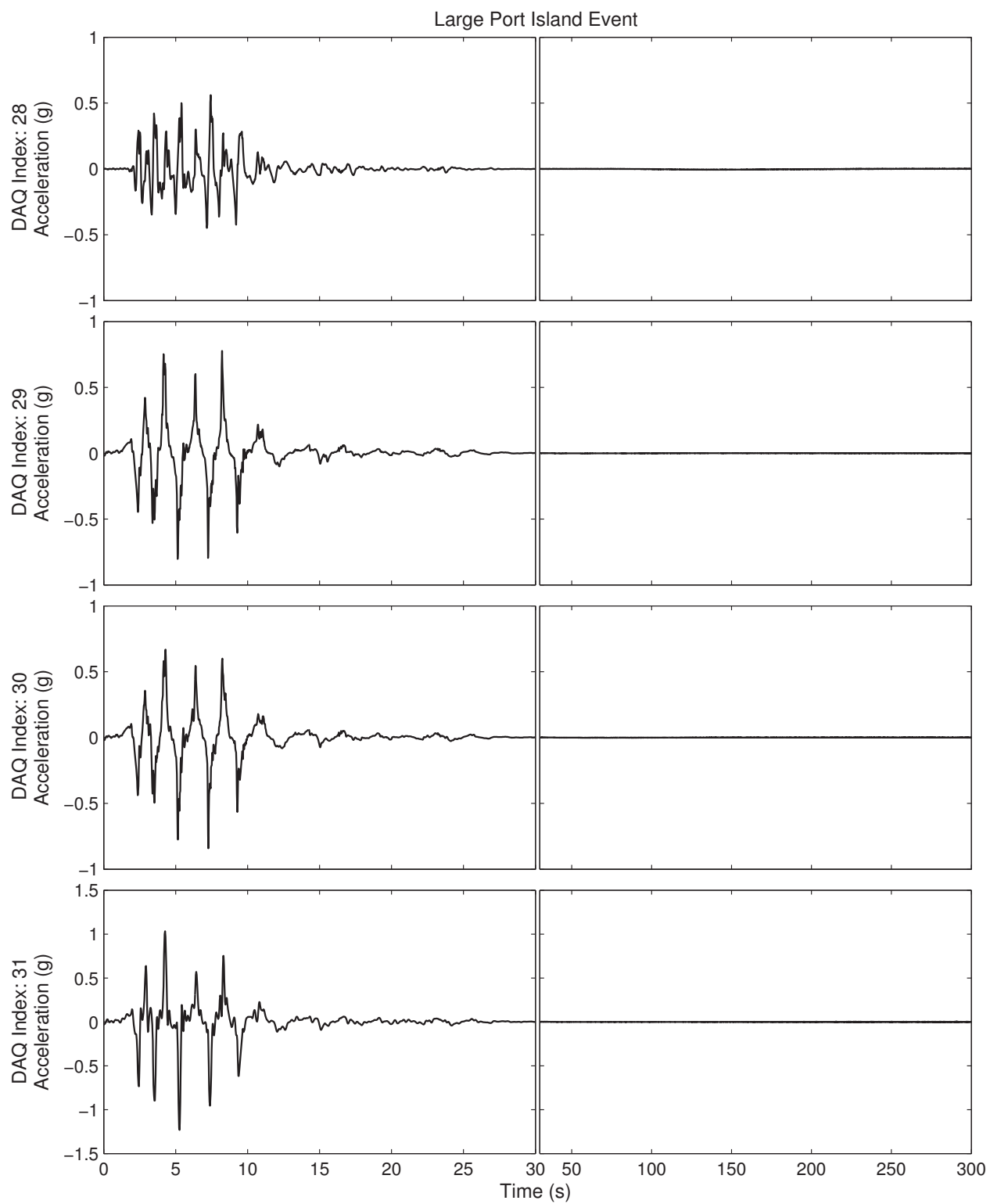


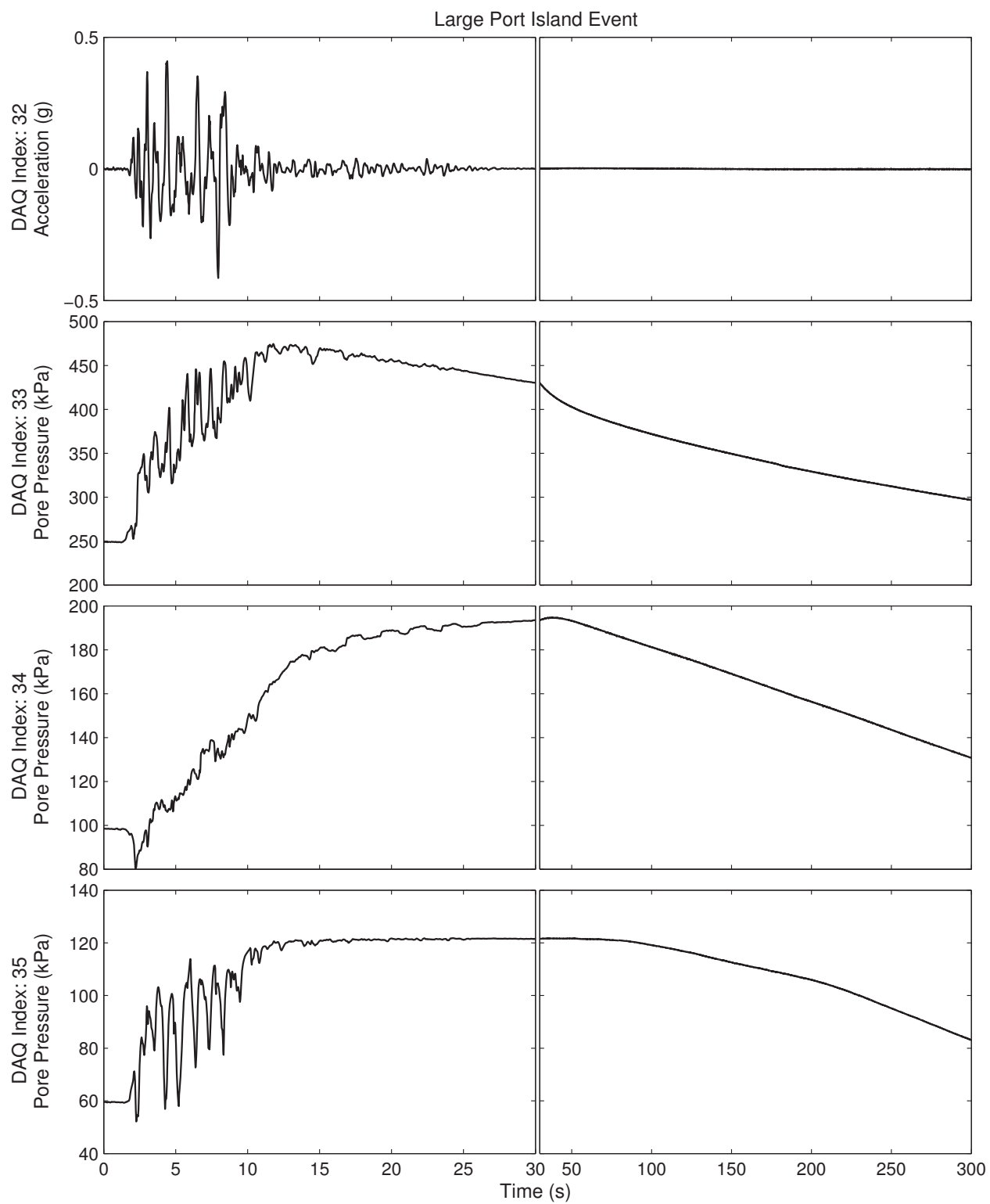


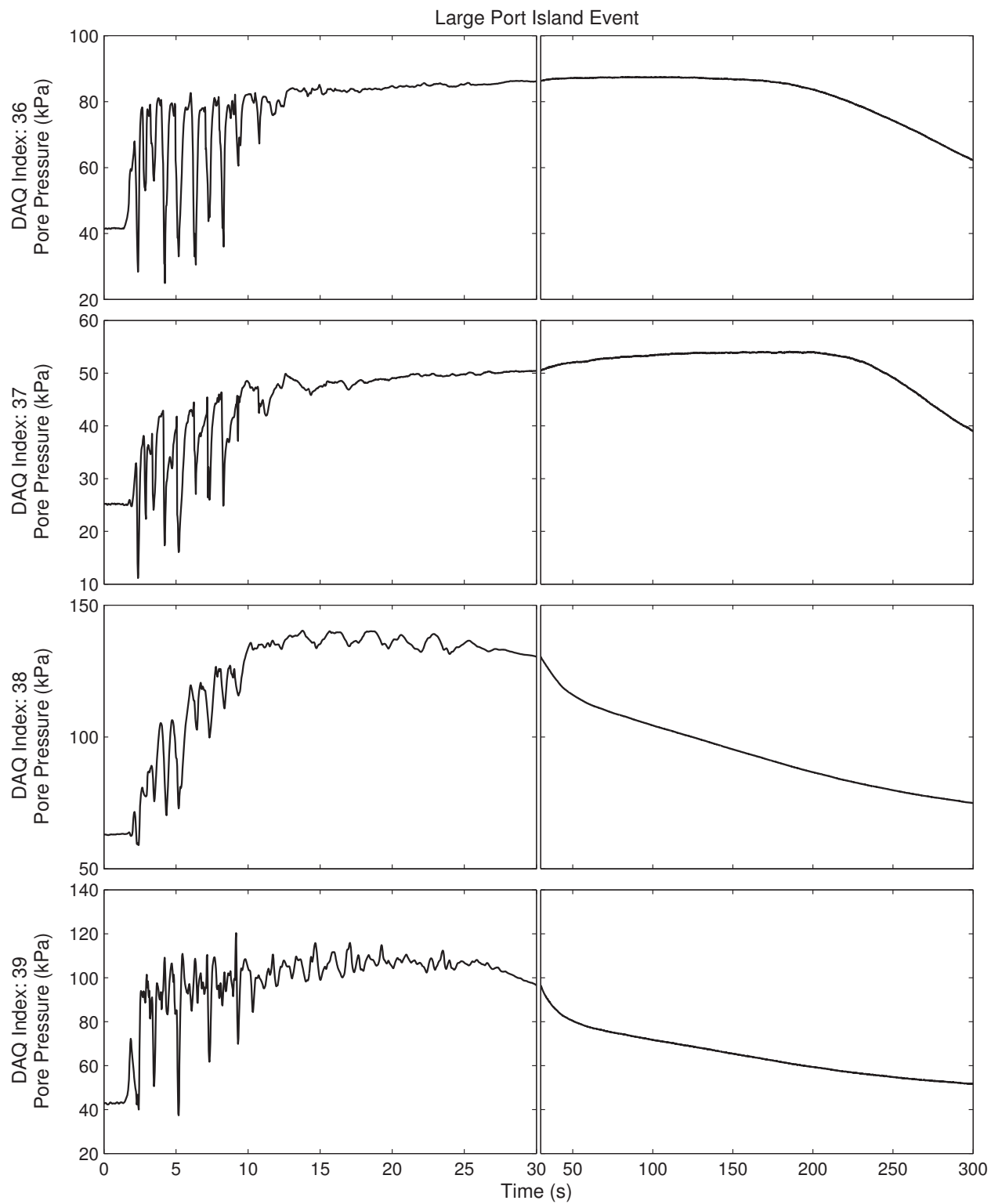


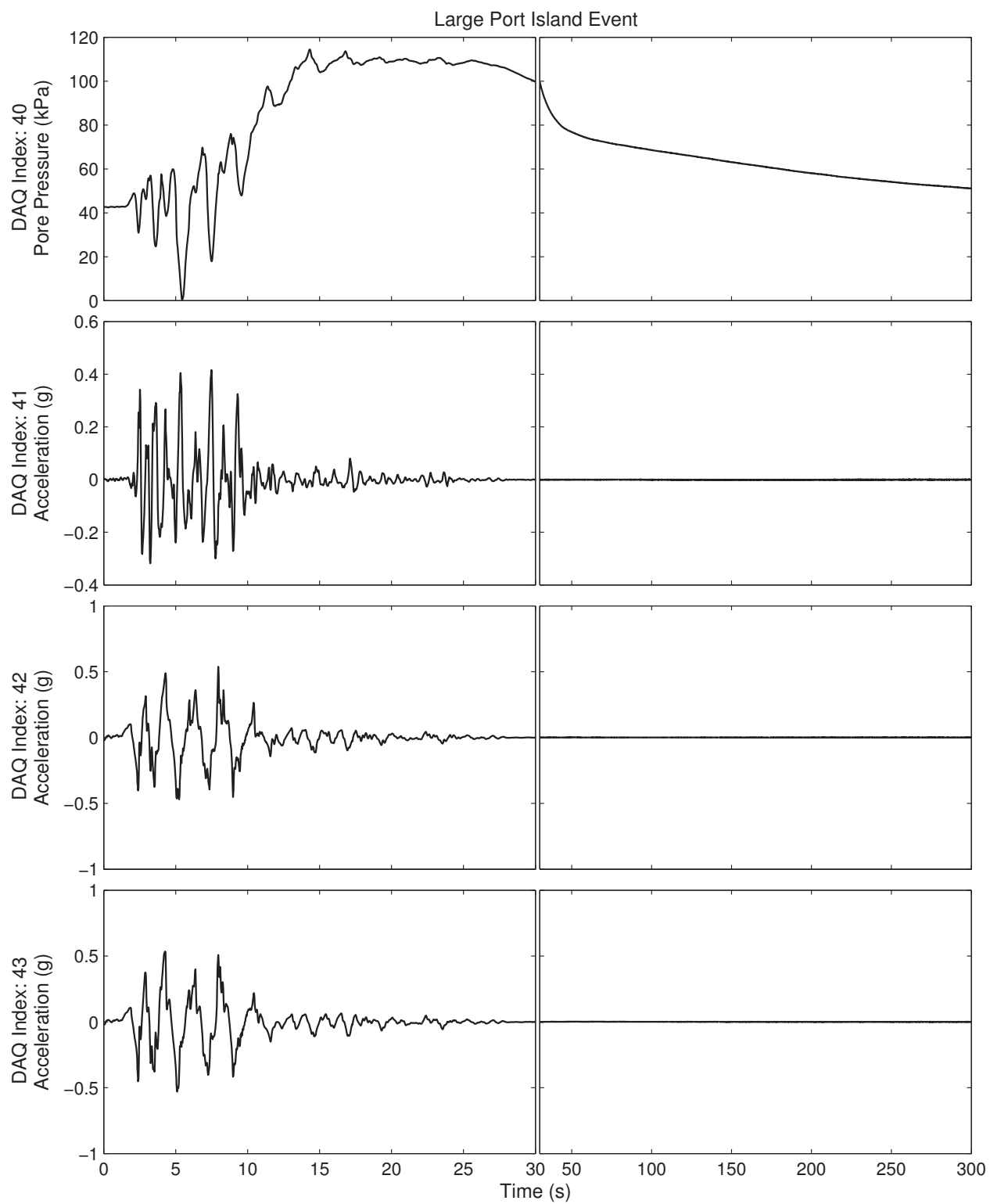


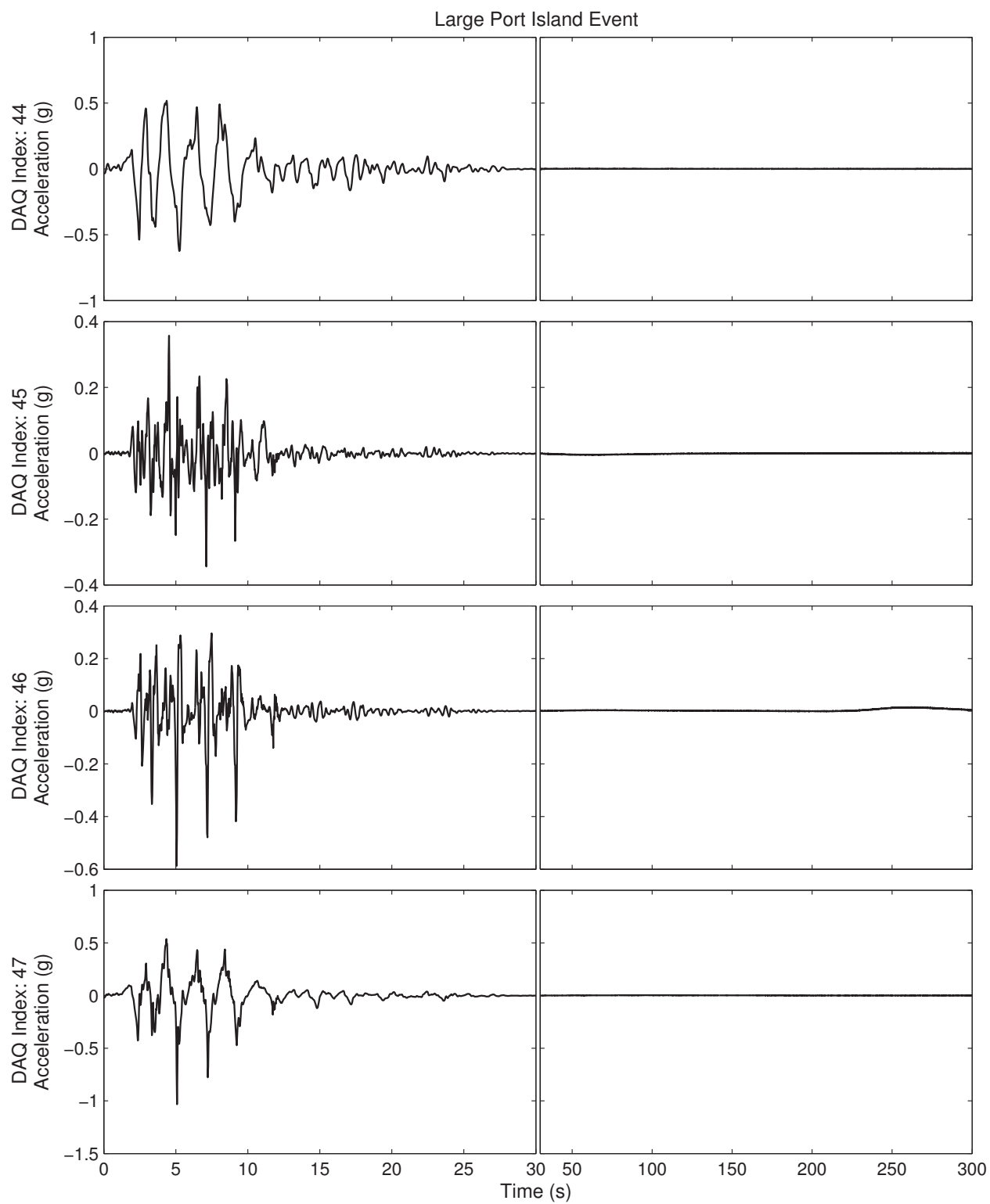


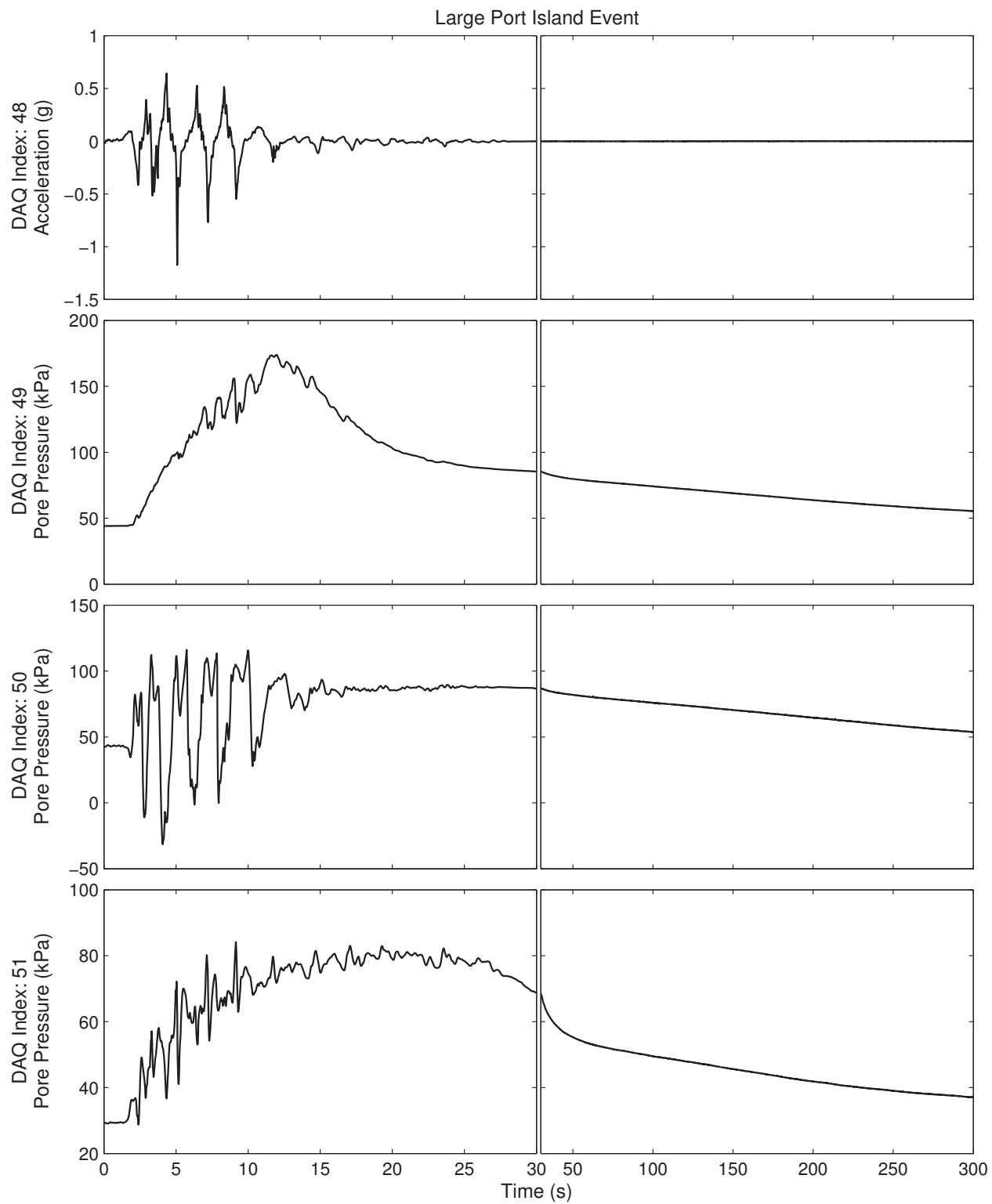


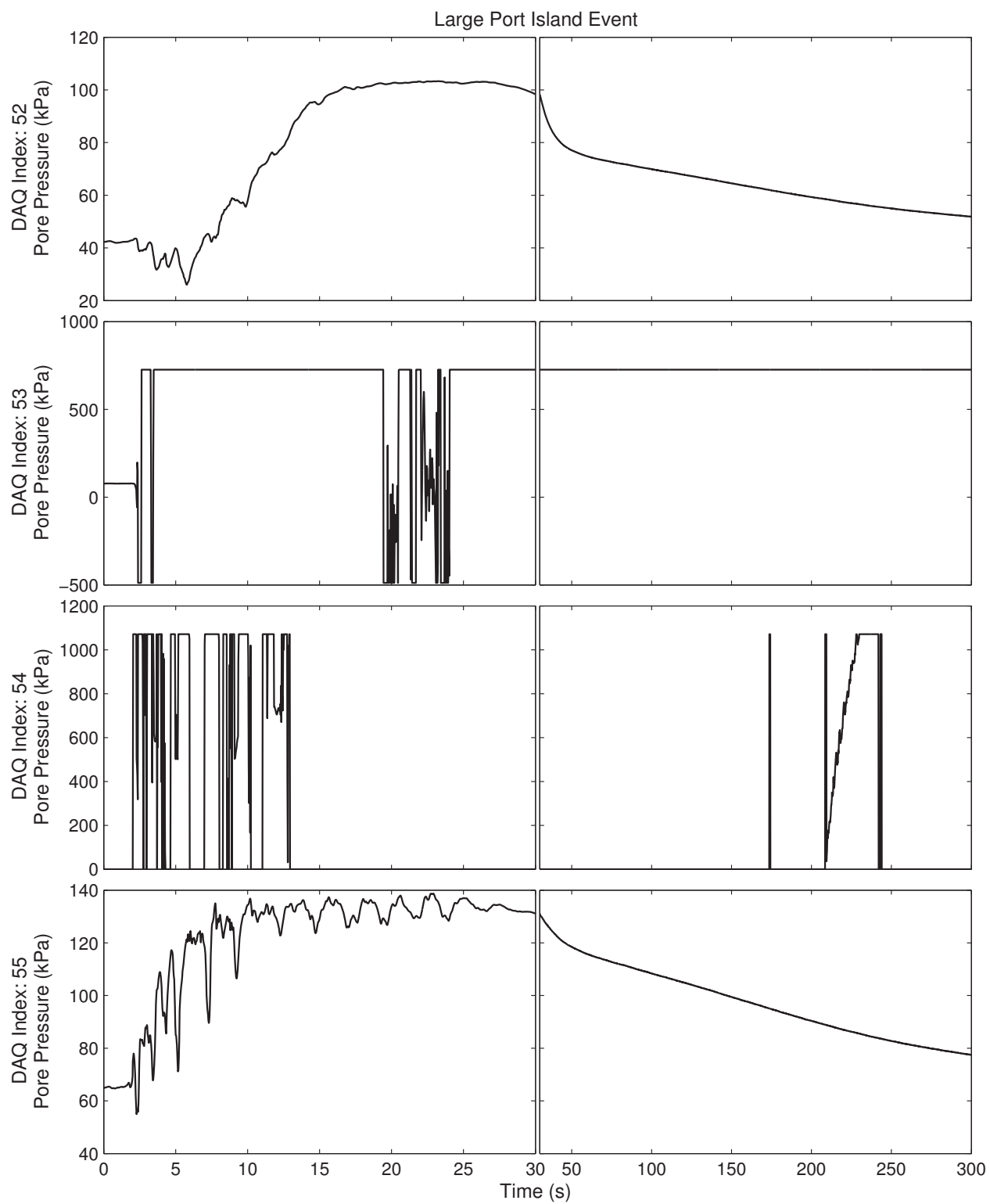


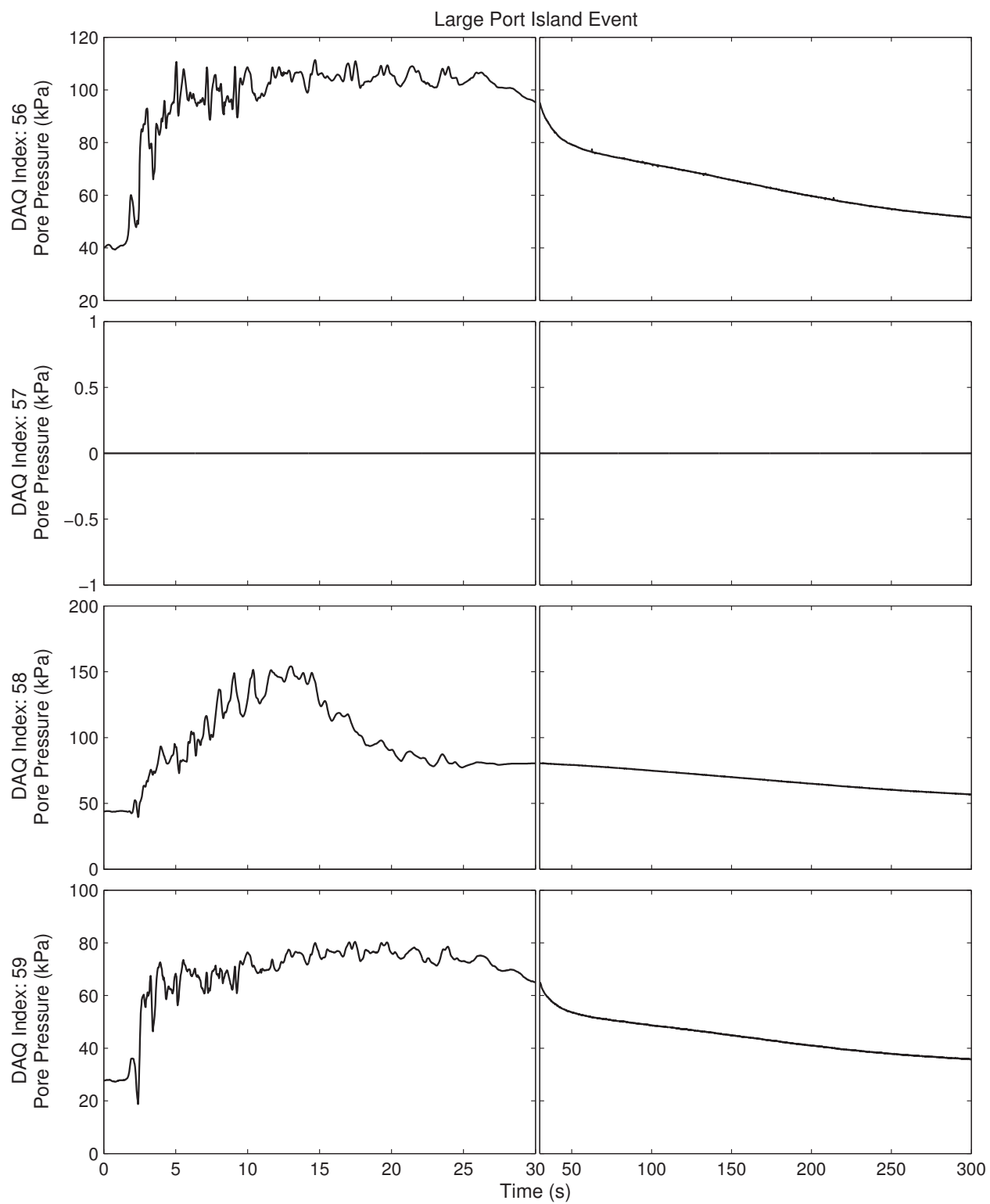


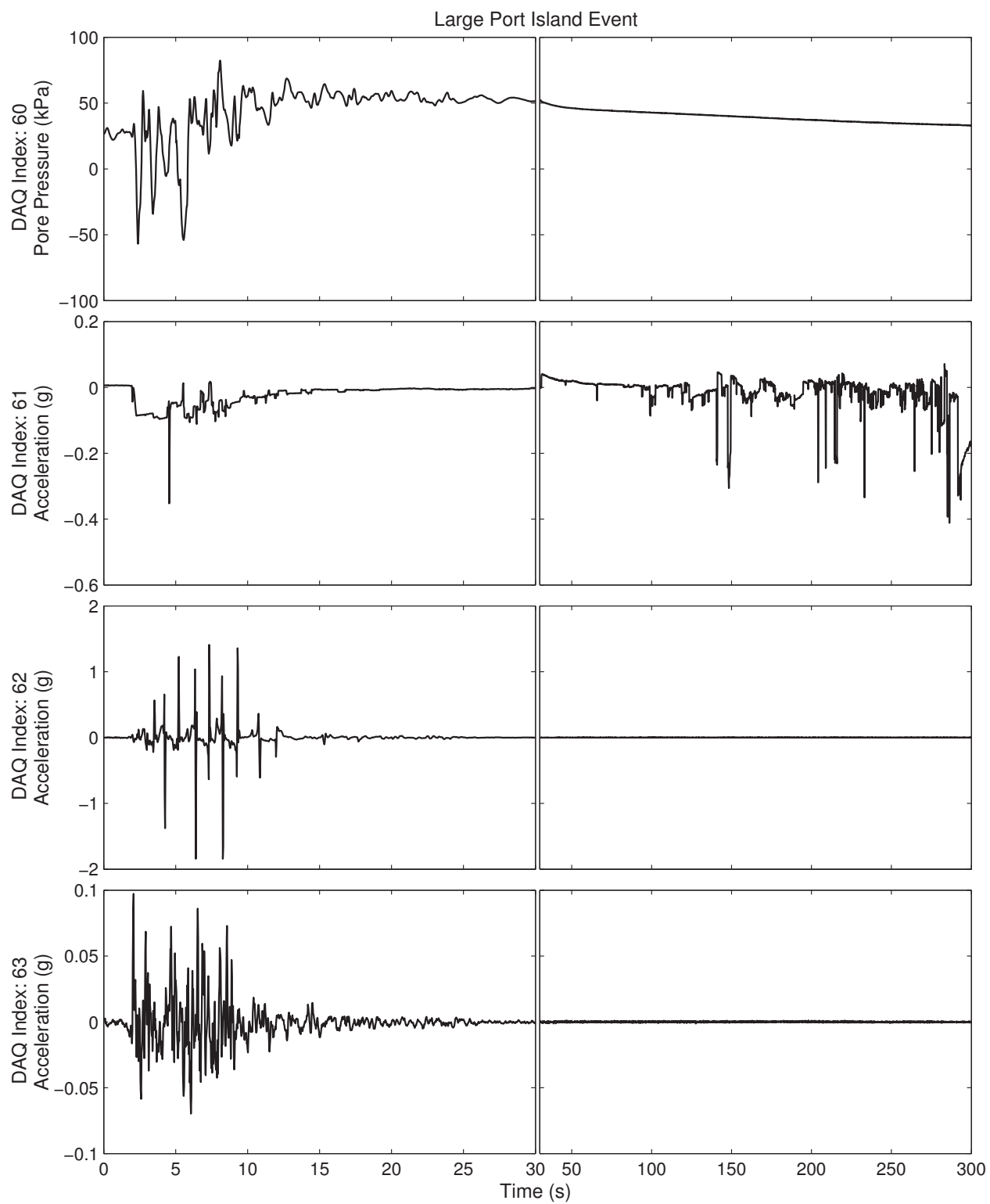


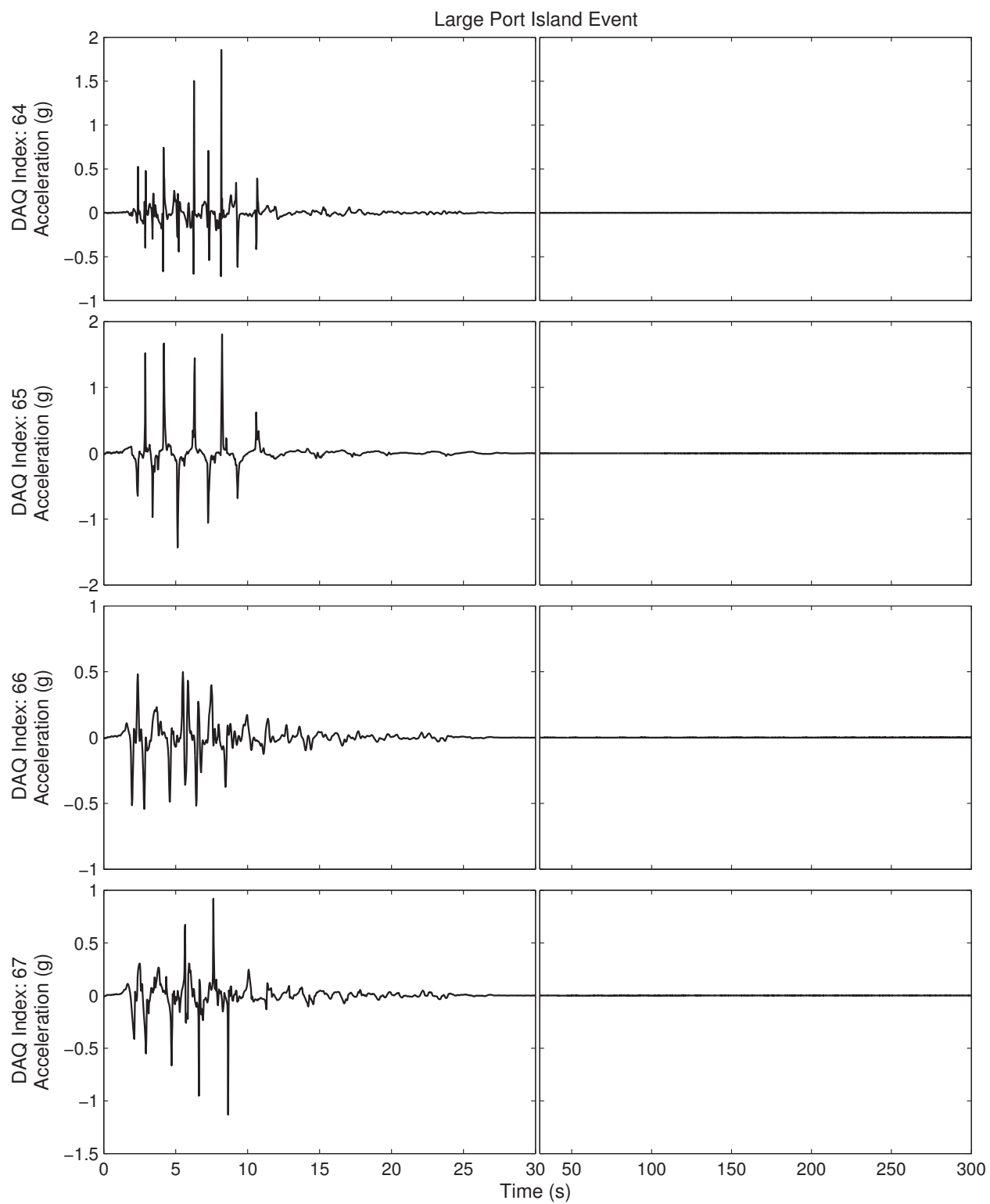


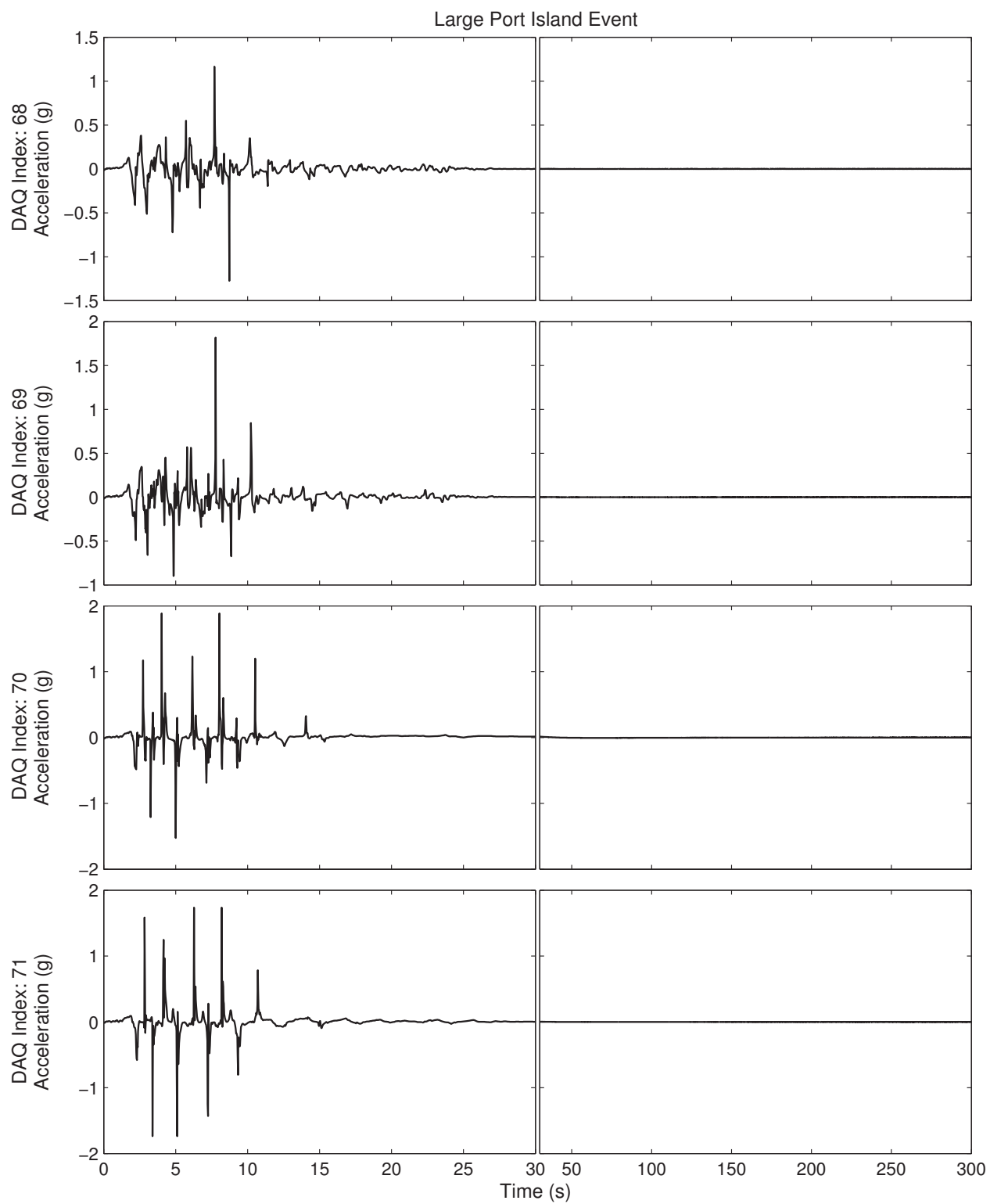


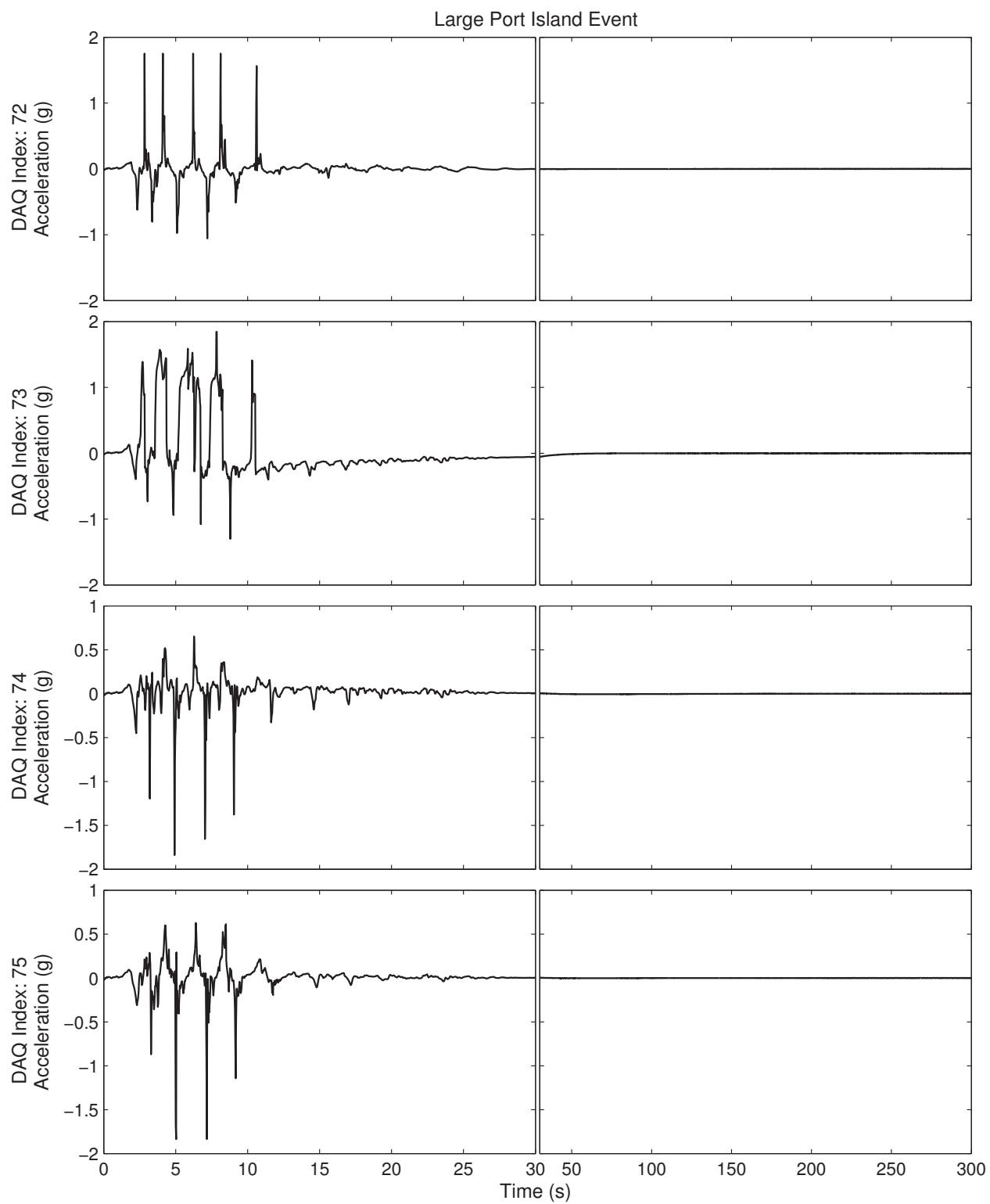


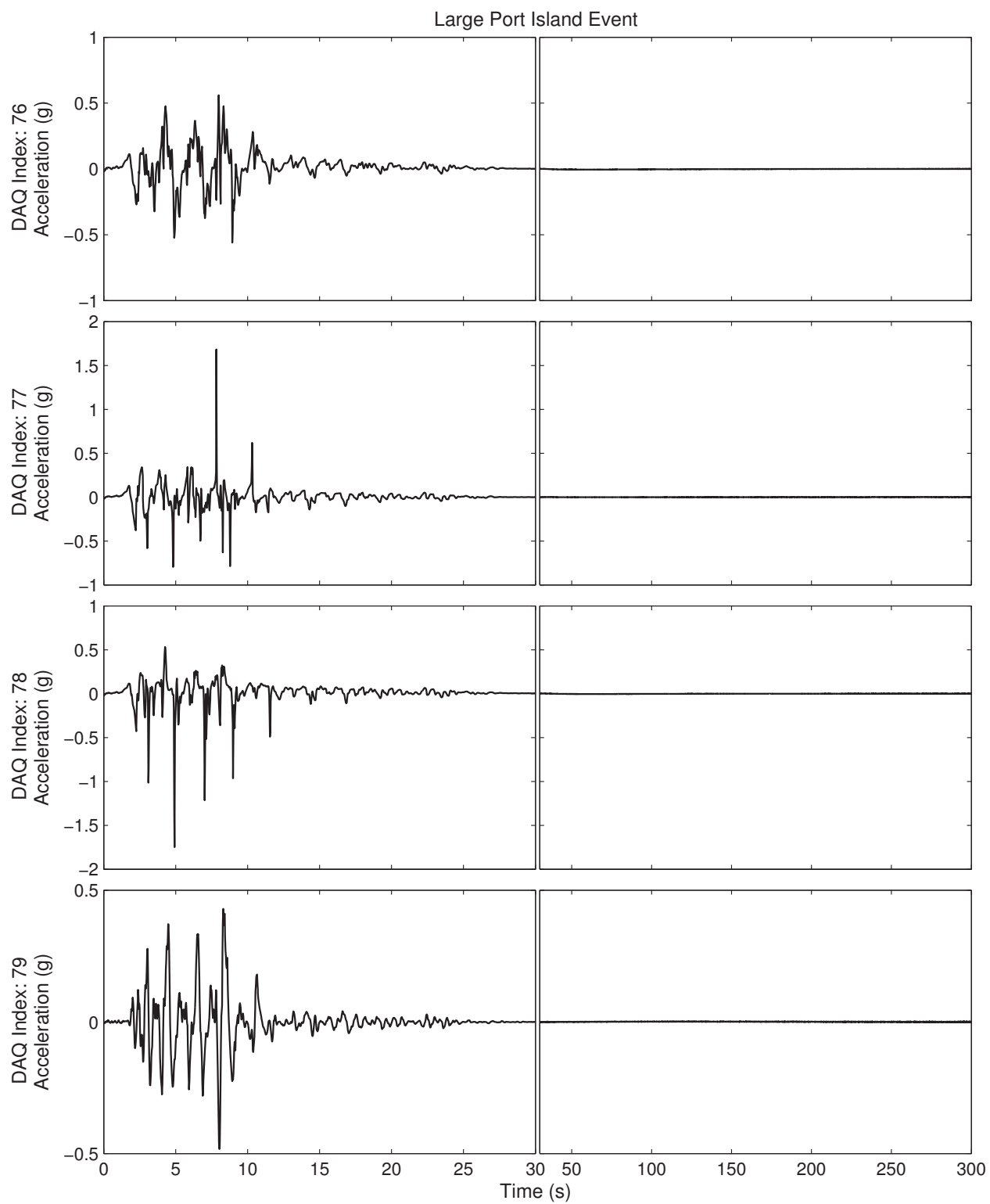


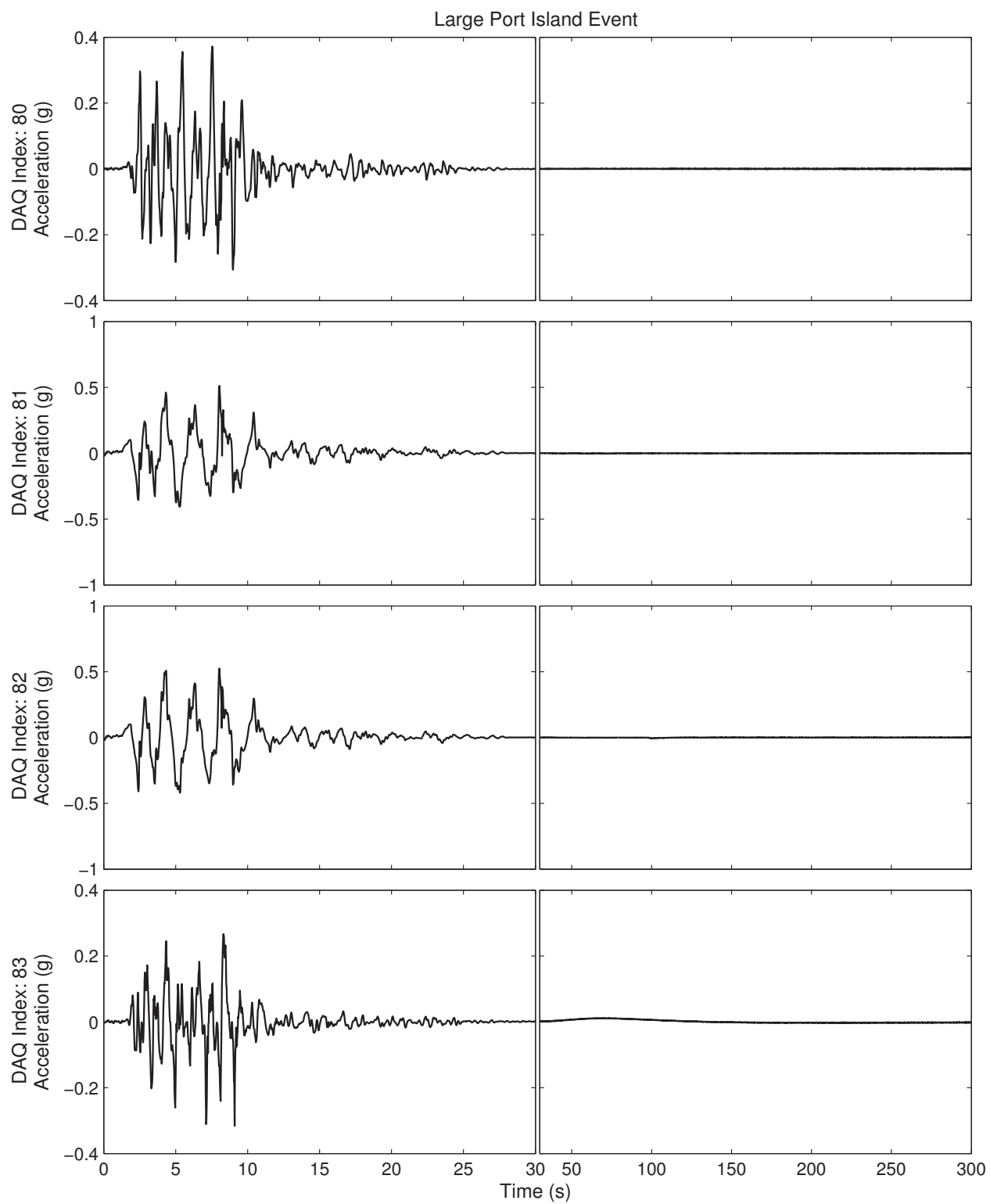


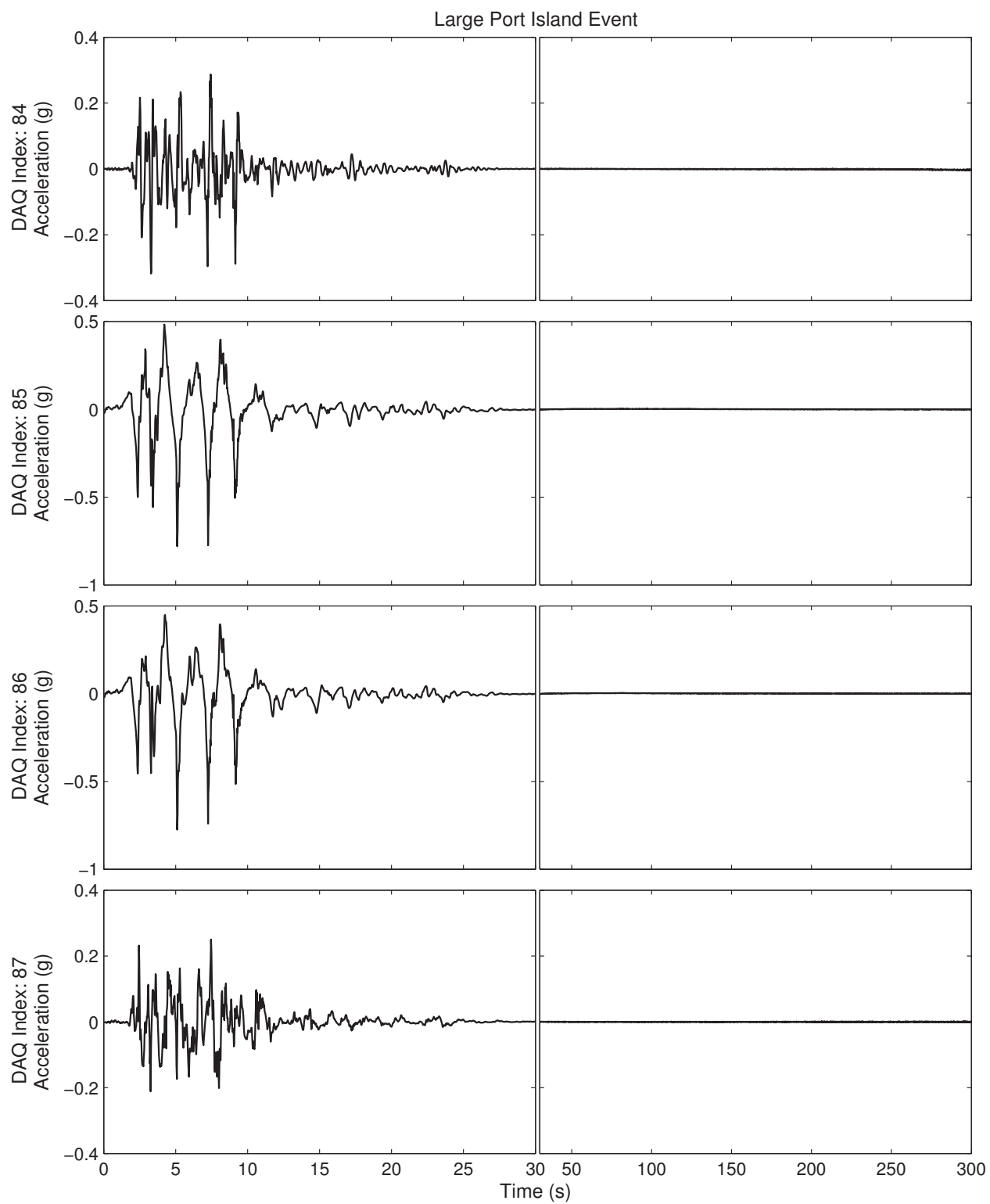


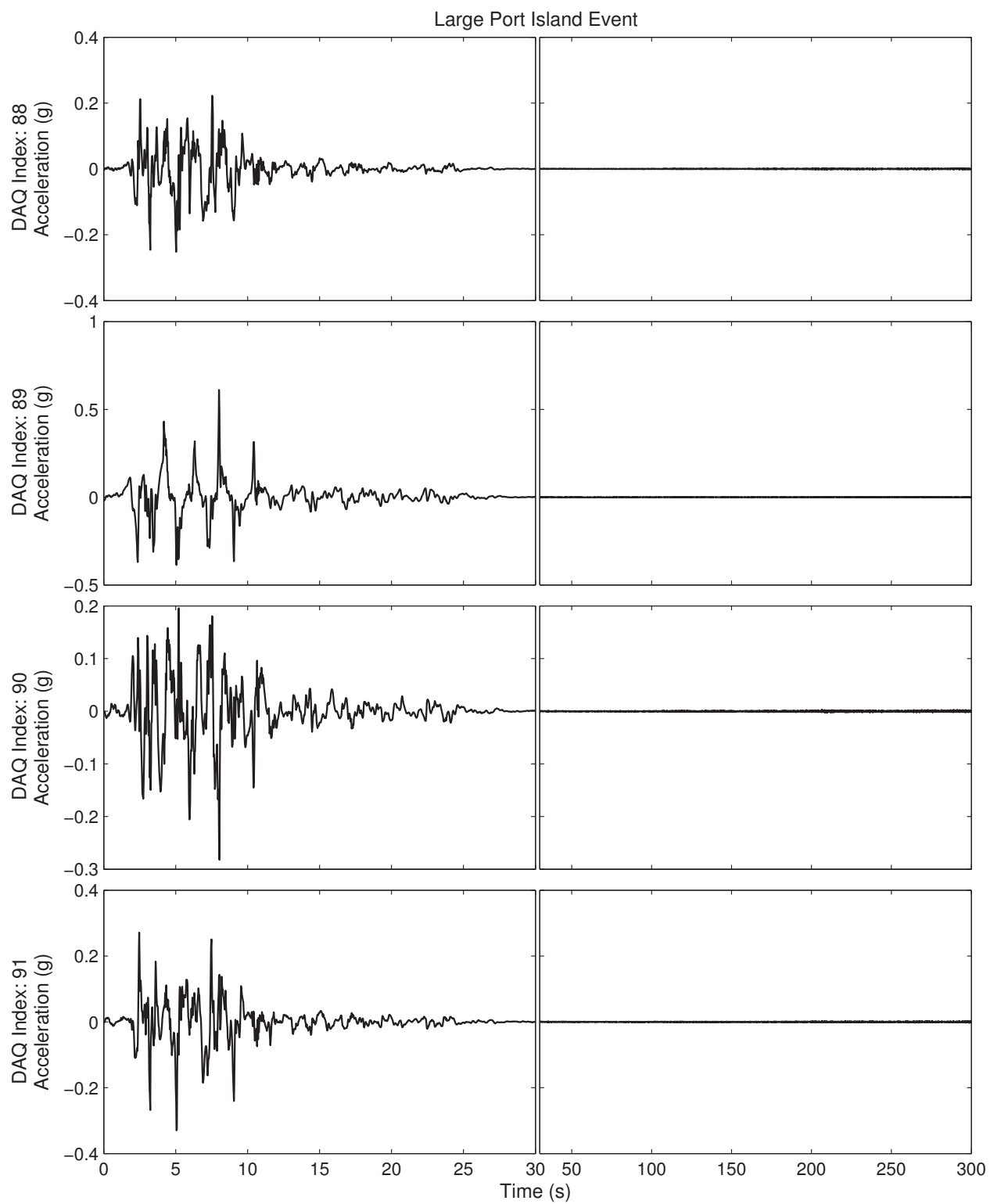


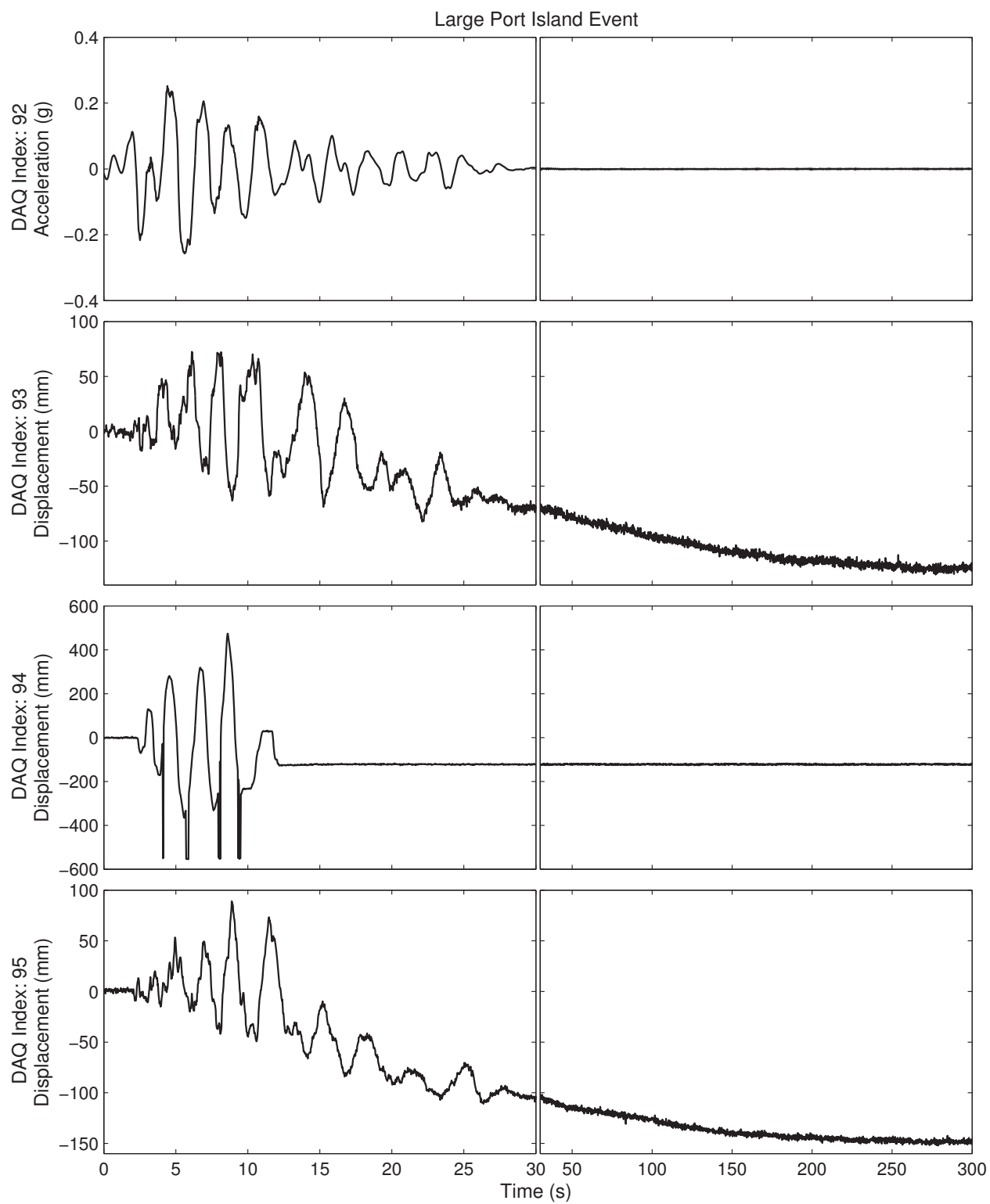


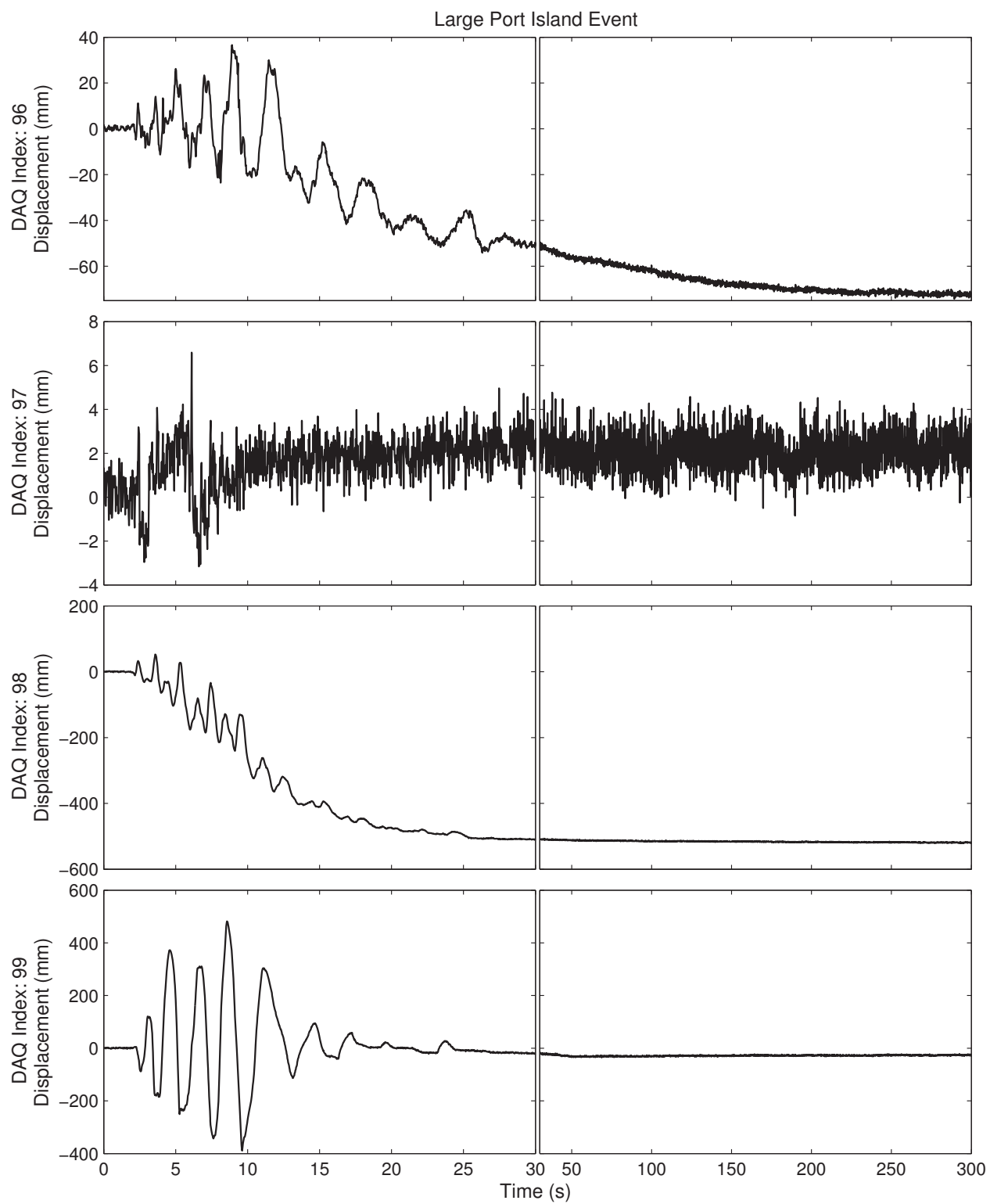


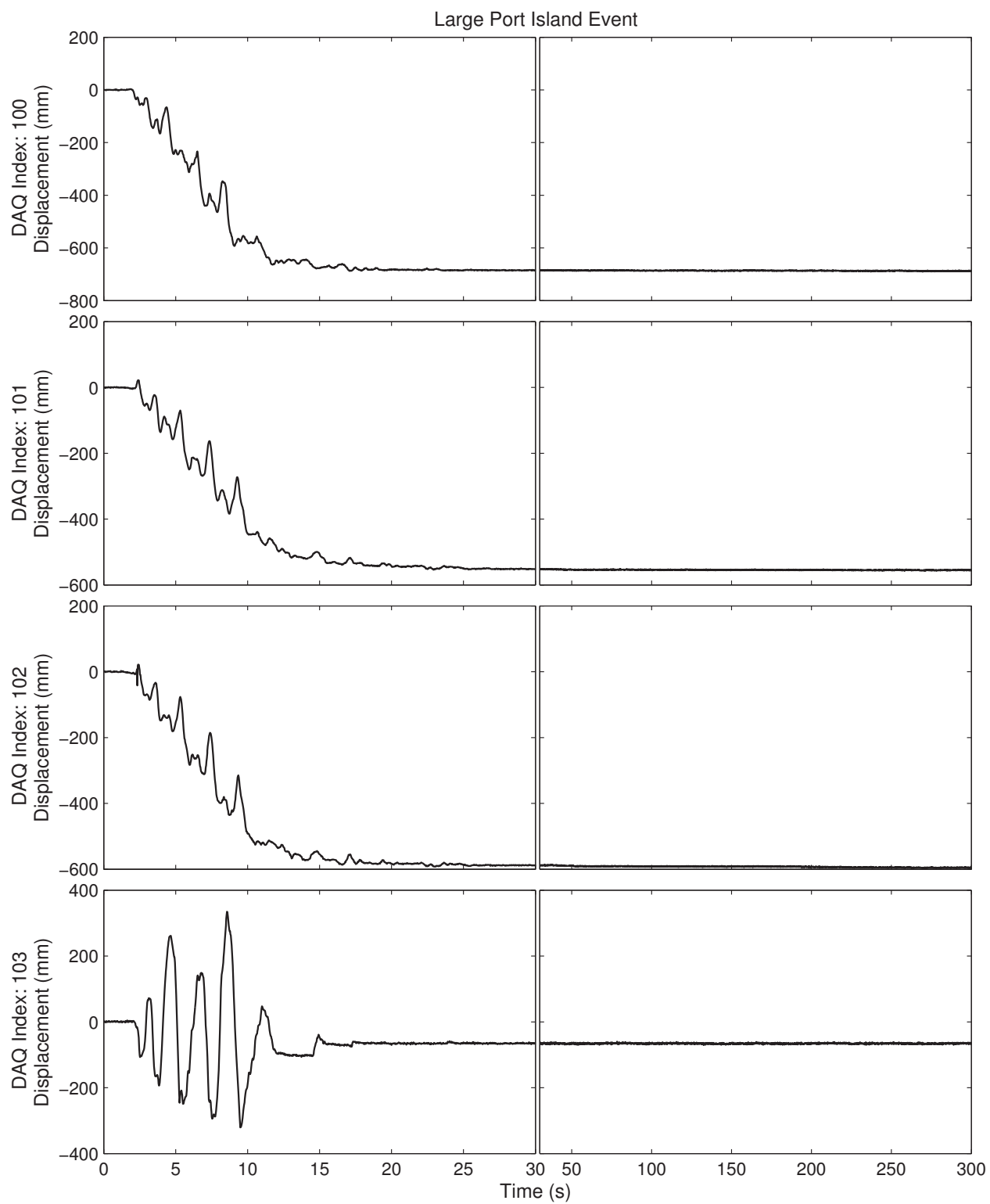


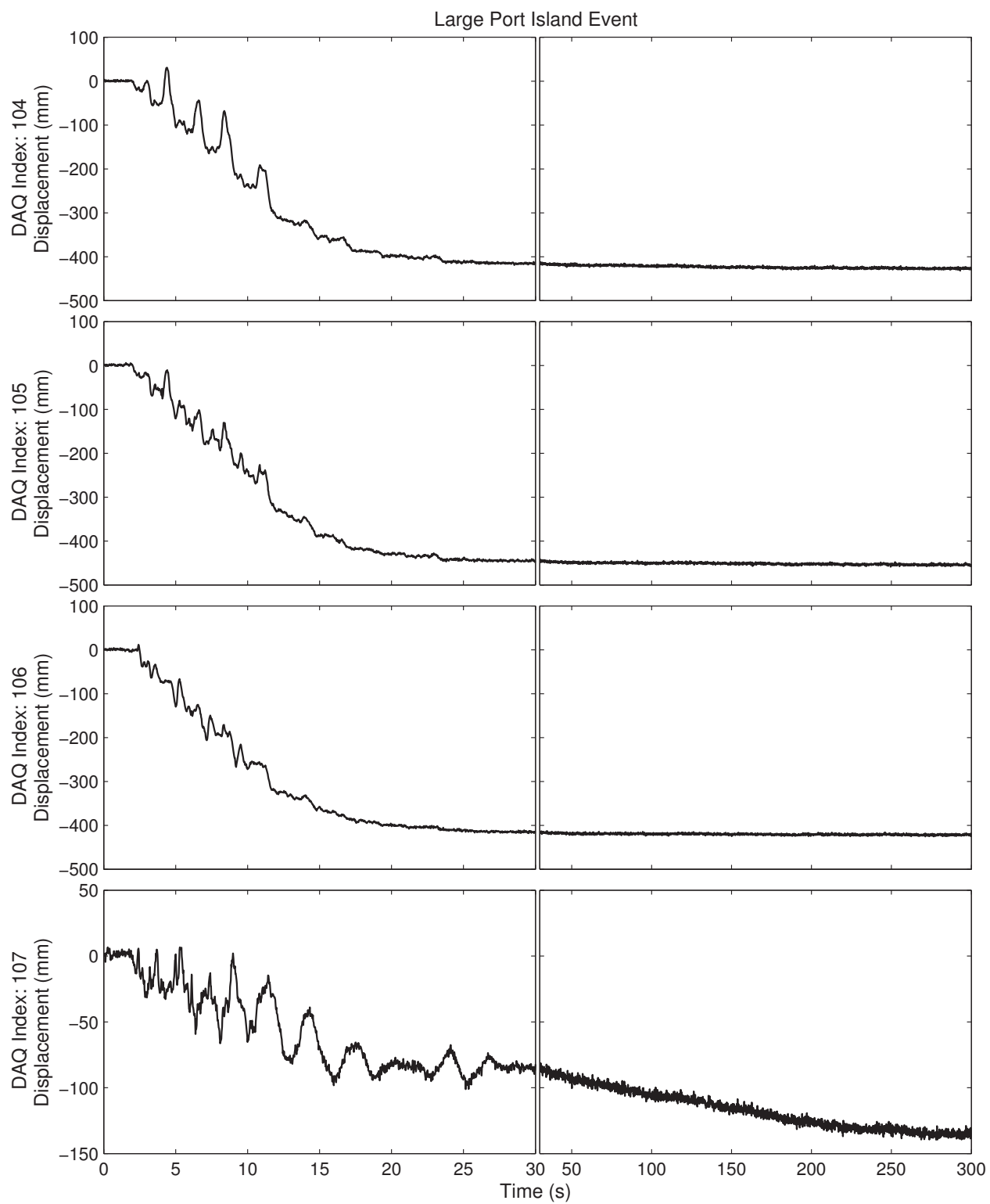


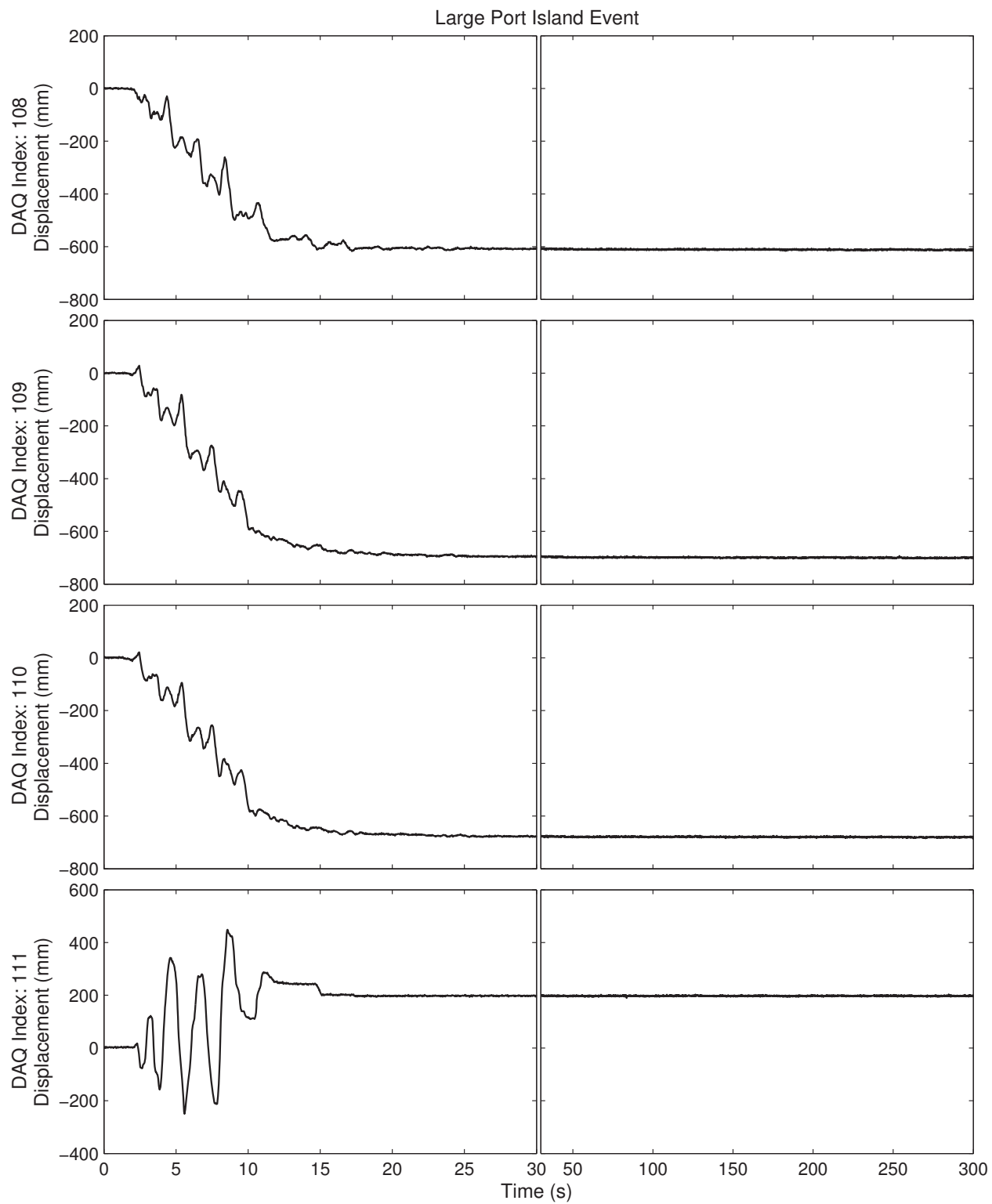


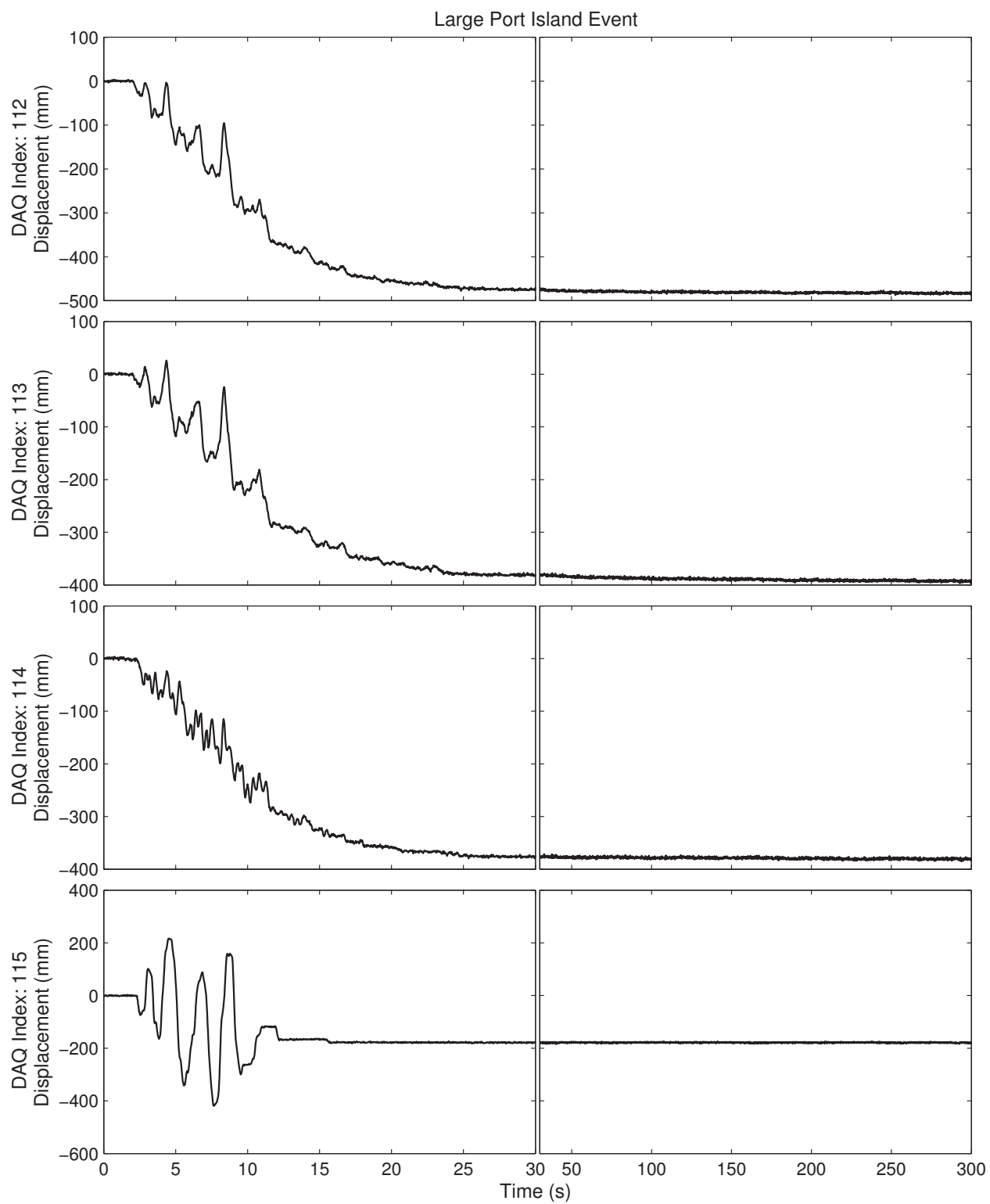


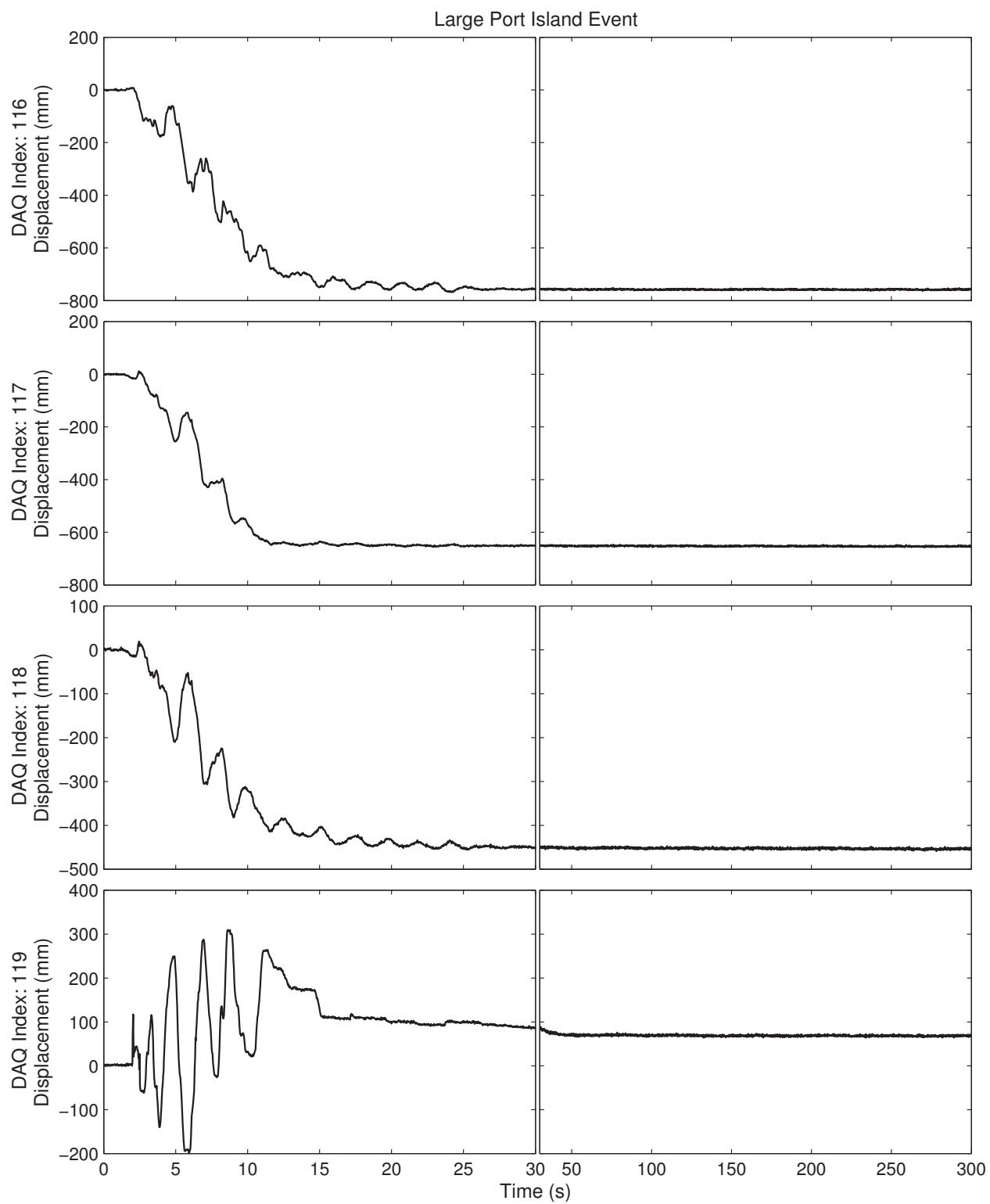


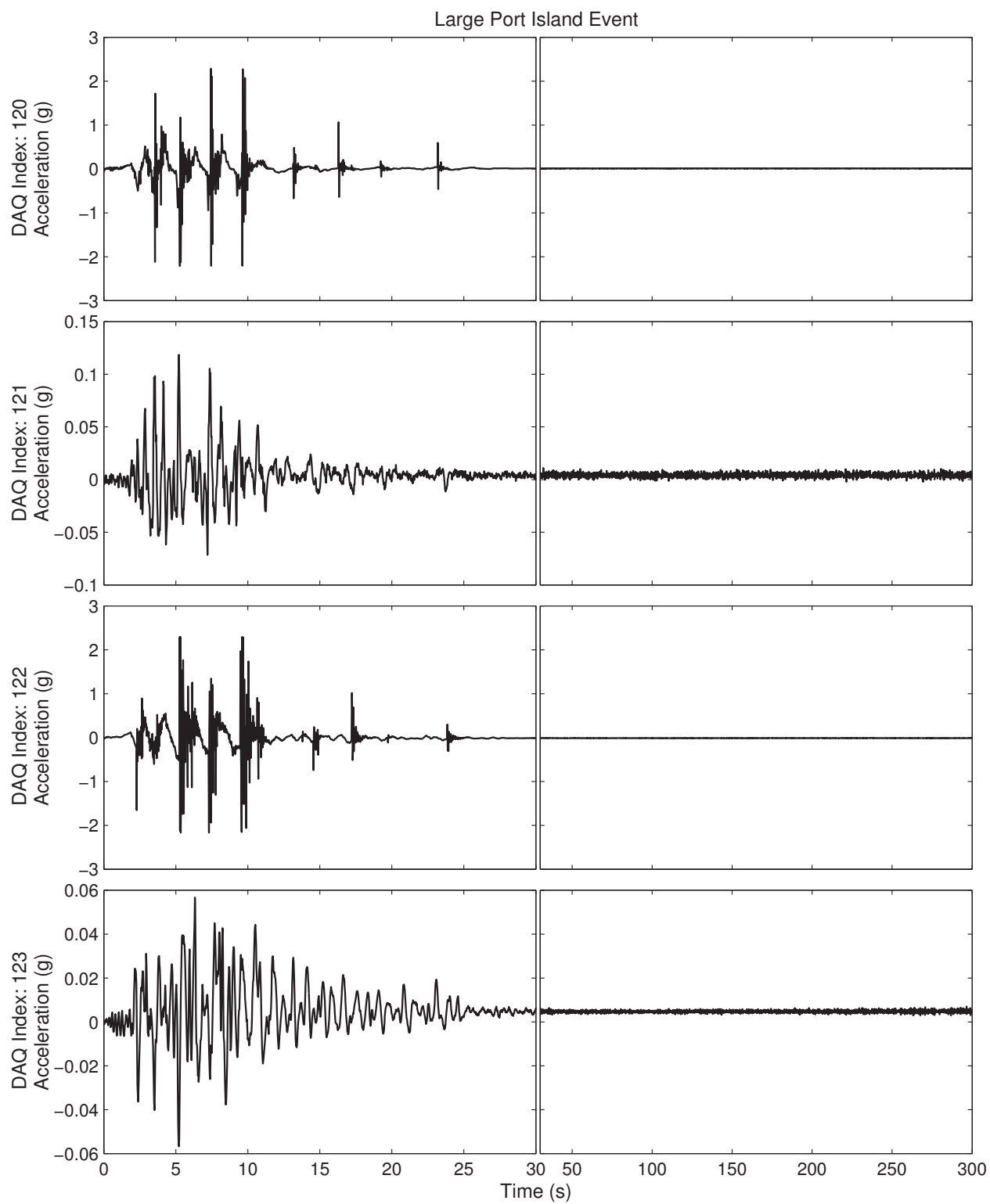


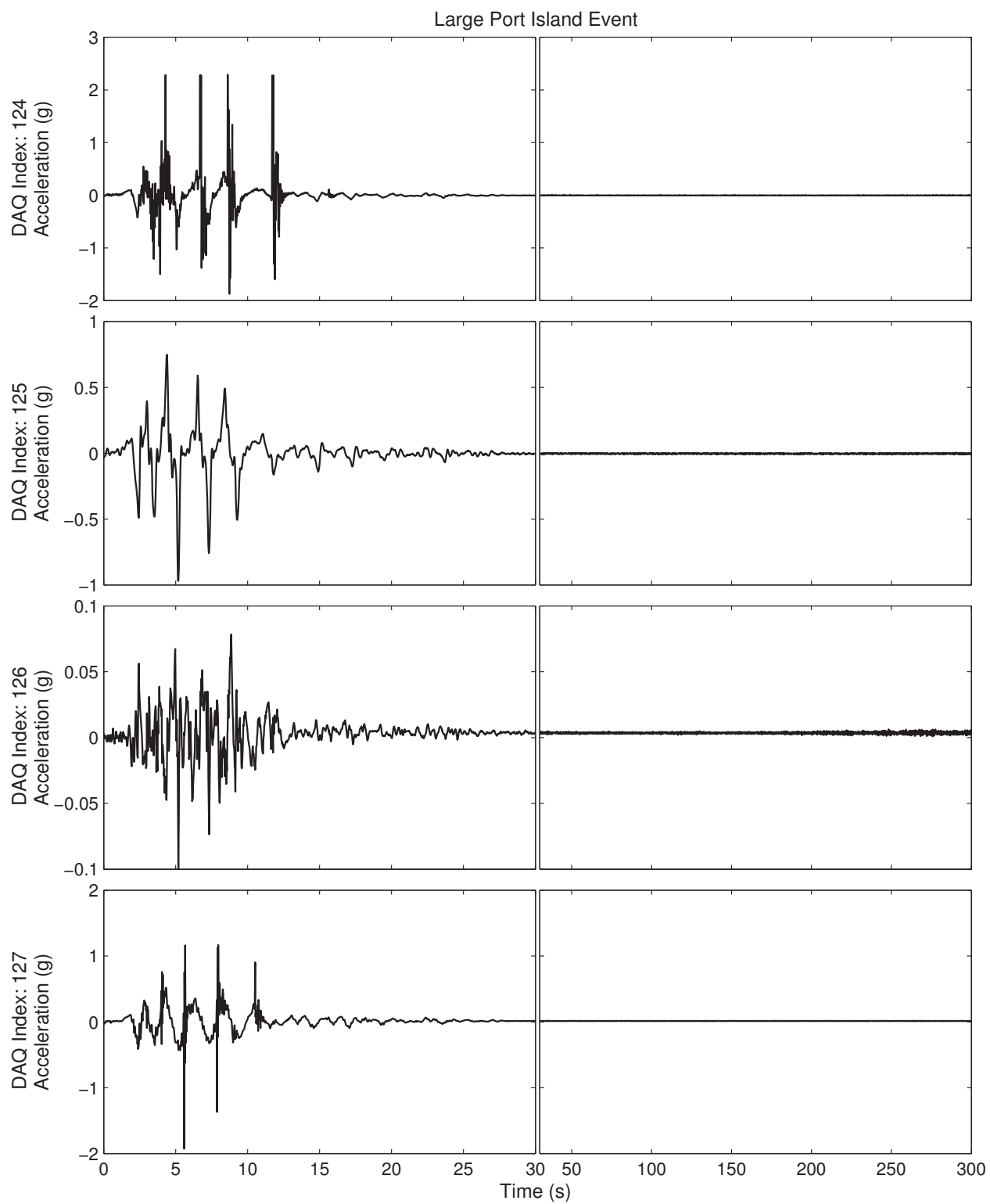


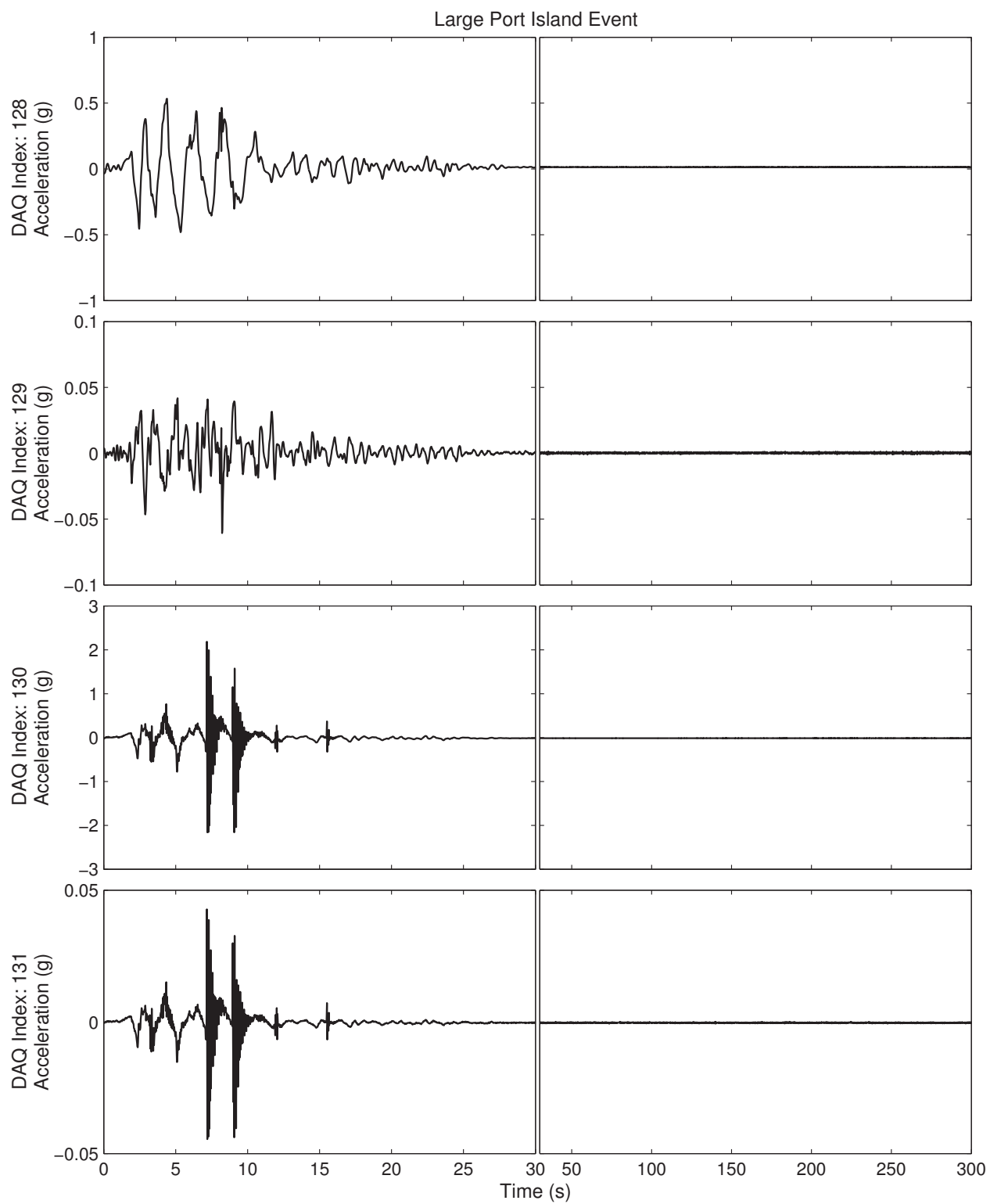


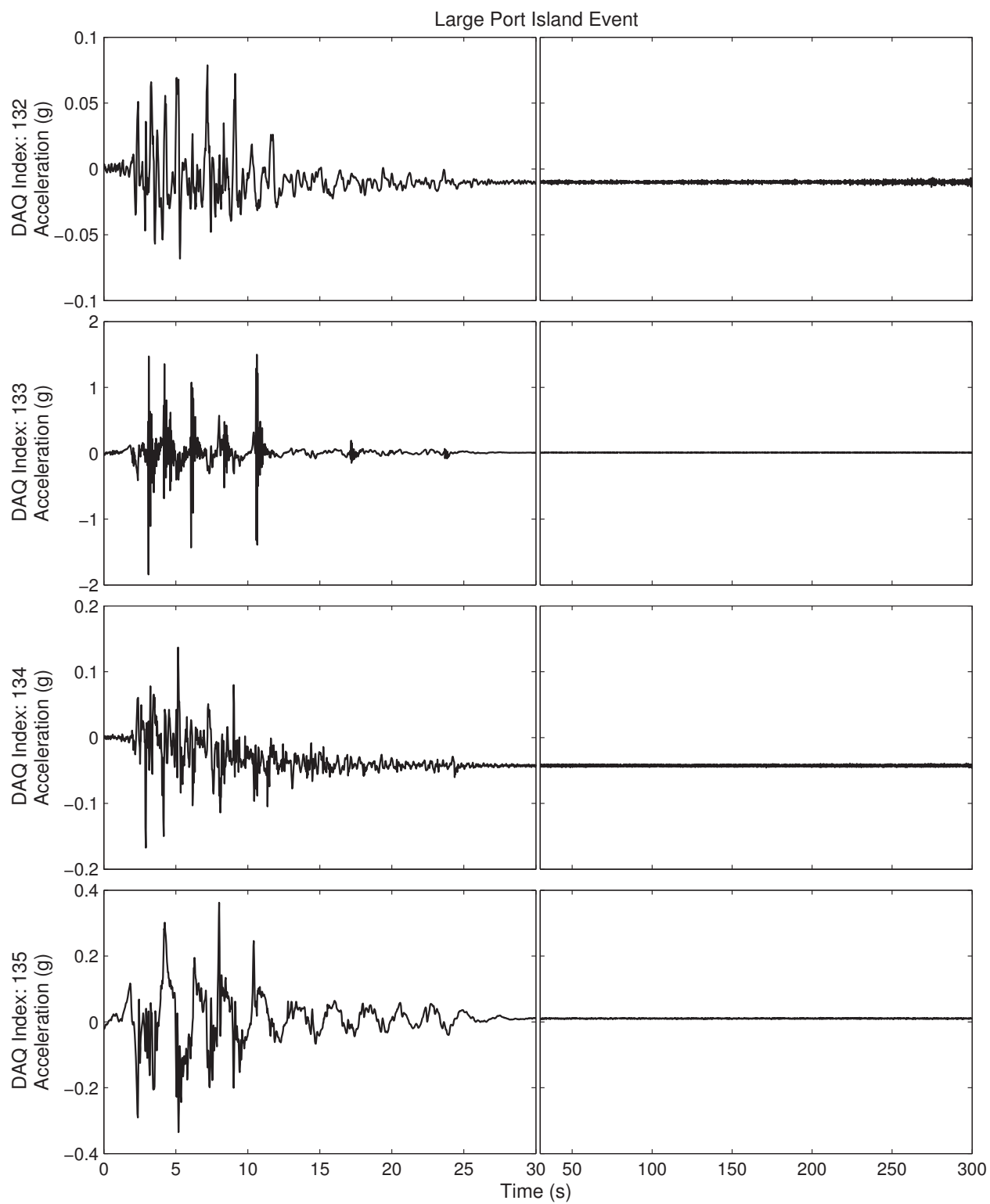


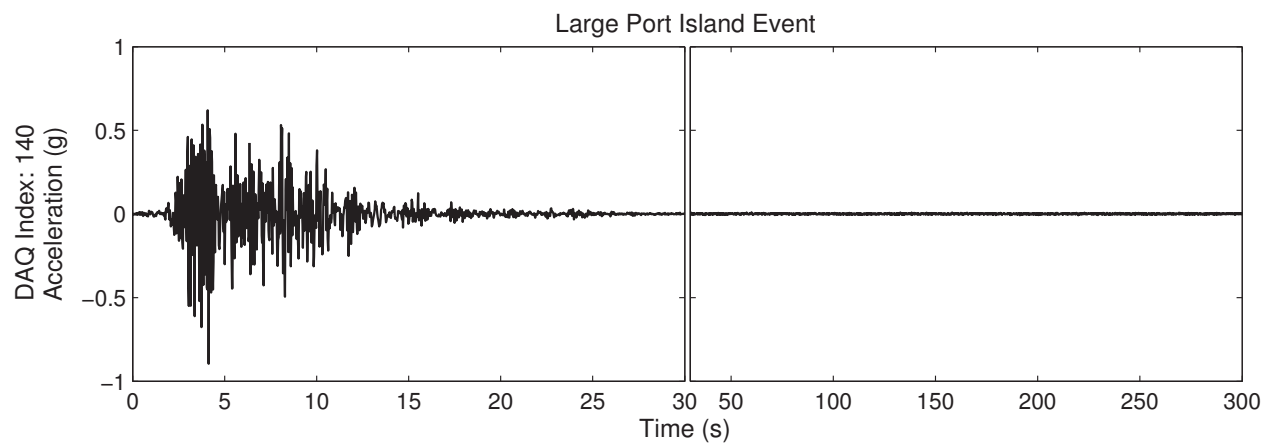










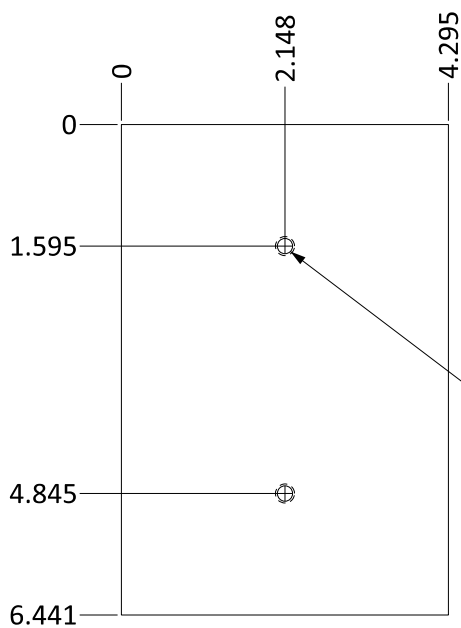


Appendix B1-B

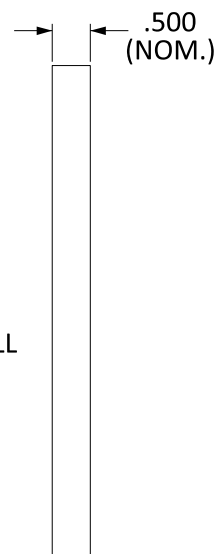
Test-6 Shop Drawings and Example Spreadsheet for K
Structure Modifications

FOUNDATION, STRUCTURE K
 MAT'L: STEEL, 1/2" THICK
 QUANTITY: 2
 DATE: 15 APRIL, 2013

CENTER FOR GEOTECHNICAL MODELING
 UNIVERSITY OF CALIFORNIA, DAVIS
 CONNOR HAYDEN
 510-926-1832



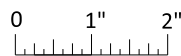
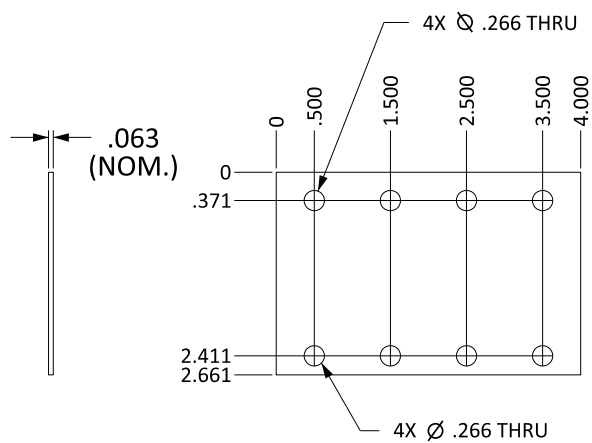
2X Ø .201 THRU ALL
 1 / 4 - 20 UNC THRU ALL



All units are inch unless otherwise noted.
 Tolerance: XX ± .01
 XXX ± .005

SIDE PLATE, STRUCTURE K
 MAT'L: PRECISION GROUND O1 TOOL STEEL, $\frac{1}{16}$ " THICK
 QUANTITY: 4
 DATE: 15 APRIL, 2013

CENTER FOR GEOTECHNICAL MODELING
 UNIVERSITY OF CALIFORNIA, DAVIS
 CONNOR HAYDEN
 510-926-1832



All units are inch unless otherwise noted.
 Tolerance: XX ± .01
 XXX ± .005

STRUCTURE K

	Height (in)	Length (in)	Width (in)	Volume (in ³)	Volume (cm ³)	ρ _{material} (g/cm ³)	Mass (kg)	TOTAL (kg)	Individual Center of Mass (mm)	Distance from Footing Base (mm)
DECK										
D1 - Deck (M. Steel)	0.743	4.500	1.906	6.373	104.430	7.875	0.822	0.822		
D2 - Left Clamp (M. Steel)	0.743	4.500	0.250	0.836	13.698	7.875	0.108	0.108		
D3 - Right Clamp (M. Steel)	0.743	4.500	0.250	0.836	13.698	7.875	0.108	0.108		
D4 - Added Top Mass	0.625	5.000	1.700	5.313	87.056	11.340	0.987	0.987		
D5 - Added Bottom Mass	0.625	5.000	1.700	5.313	87.056	11.340	0.987	0.987		
	Total Width=		5.806				3.308	3.013	9.4361	70.8533
COLUMN										
C1 - Left Column (M. Steel)	2.661	4.000	0.063	0.665	10.901	7.875	0.086	0.086		
C2 - Right Column (M. Steel)	2.661	4.000	0.063	0.665	10.901	7.875	0.086	0.086		
								0.172	33.7947	46.4947
ADDED FOOTING MASS										
F2 - Added Mass (Lead)	0.375	5.000	1.700	3.188	52.234	11.340	0.592	0.592		
								0.592	4.76	30.16
ADAPTER										
F2 - Adapter (Aluminum)	0.500	4.000	1.906	3.812	62.467	2.700	0.169	0.169		
F3 - Left Clamp (Aluminum)	0.500	4.000	0.375	0.750	12.290	2.700	0.033	0.033		
F4 - Right Clamp (Aluminum)	0.500	4.000	0.375	0.750	12.290	2.700	0.033	0.033		
	Total Width=		2.656					0.235	6.35	19.05
FOOTING										
F1 - Footing (STEEL)	0.500	6.441	4.295	13.832	226.667	7.875	1.785	1.785	6.35	6.35
	Mass Clearance		0.418 inches					1.785	6.35	6.35

Model Properties

Deck Mass (kg)	Footing Mass (kg)	Total Mass (kg)	Center of Mass (mm)	Footing Area (mm ²)	Structure Load (kN)	Bearing Pressure (kPa)	I of single Column (mm ⁴)			
3.01	2.61	5.80	44.0	17847.8	0.0569	3.186	33.9			
Prototype Properties										
Nscale = 55										
Deck Mass (kg)	Footing Mass (kg)	Total Mass (kg)	Center of Mass (m)	Footing Area (m ²)	Structure Load (kN)	Bearing Pressure (kPa)	I of single Column (m ⁴)	E of Steel (GPa)	Stiffness of both columns (N/m)	Fixed Base Period (sec)
501214.5	434631.5	964412.3	2.42	54	9460.9	175.2	0.000310	207	1.98E+08	0.32

1 psi = 0.000006895 Gpa
206.85

SUMMARY

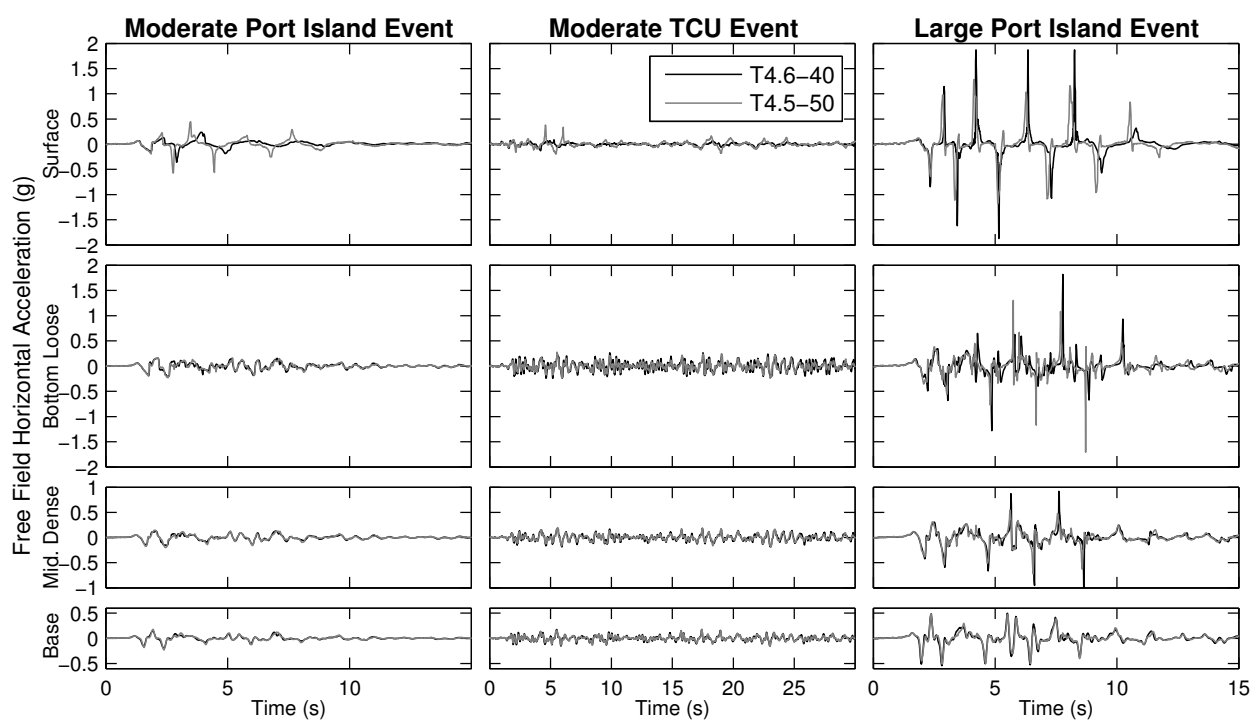
	Center of Mass (mm)	Bearing Pressure (kPa)	FB Period (sec)	Deck Mass/Hcg	Total Mass/CoM
Structure A	43.6	60.9	0.28	0.043	0.046
Structure J	245.3	186.3	0.89	0.019	0.034
Structure K	44.0	175.2	0.32	0.043	0.132

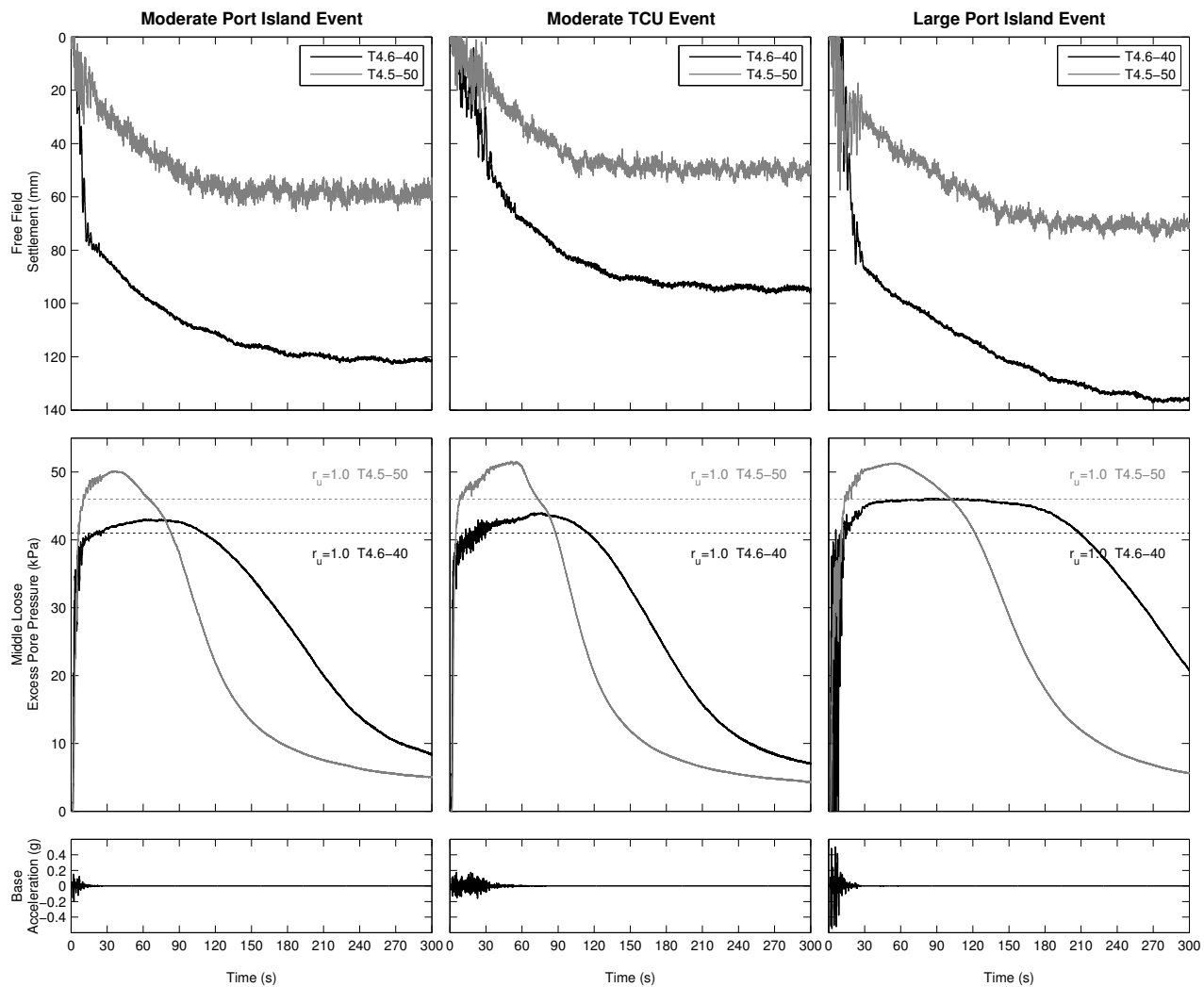
Minimum (kPa) 167.700684
Maximum (kPa) 204.9675027

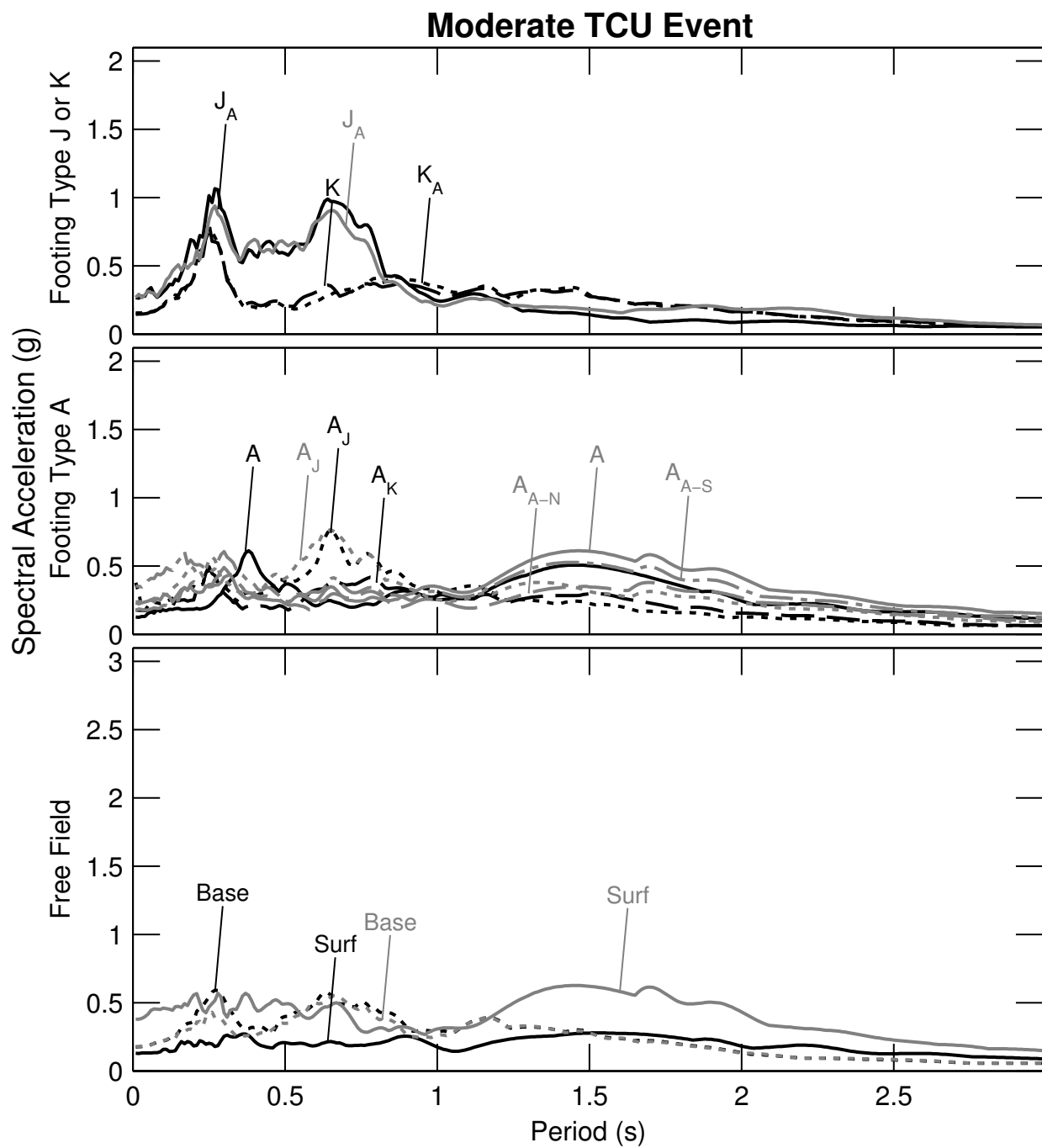
APPENDIX B-2

Supplemental Figures

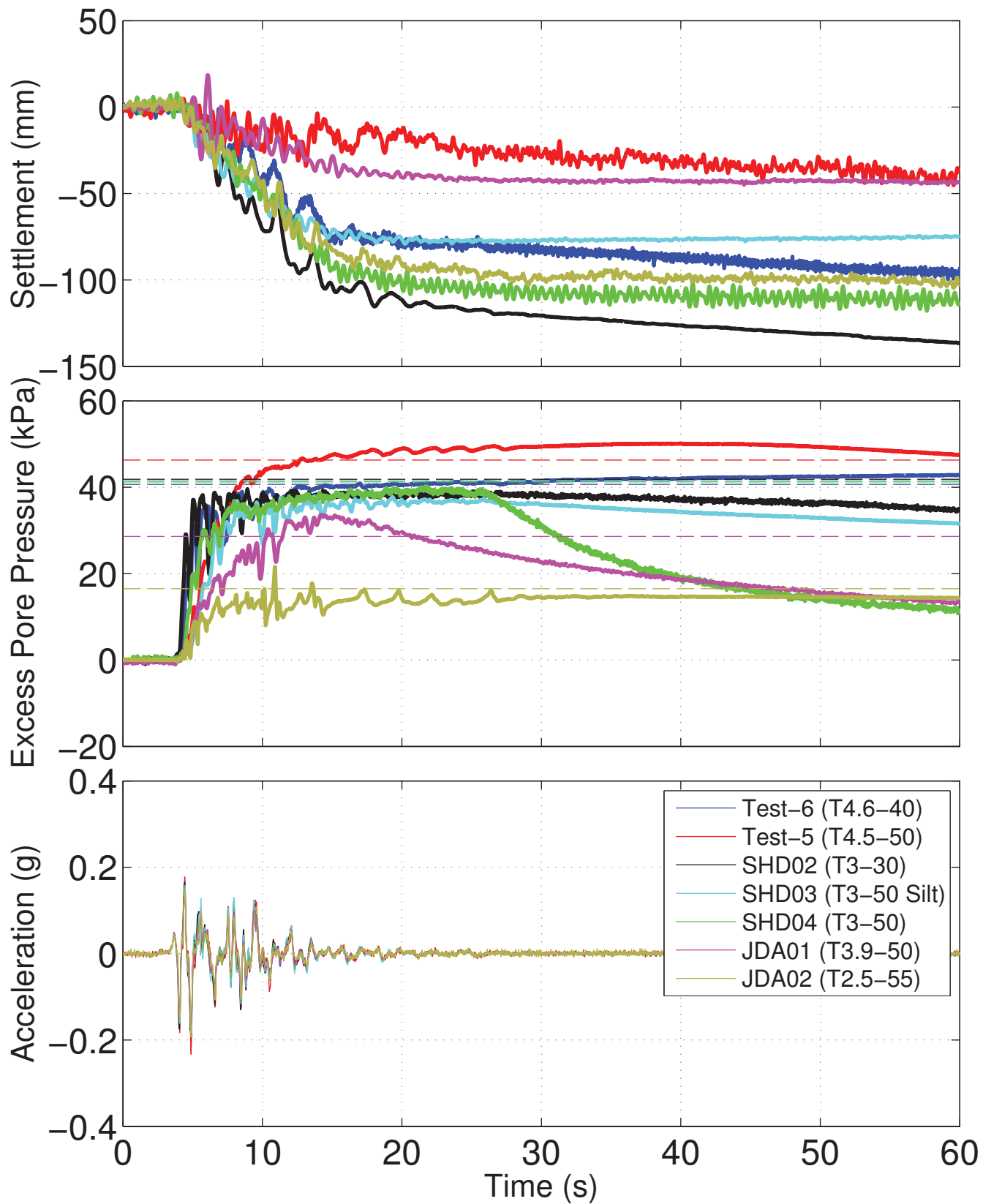
This appendix contains supplements to figures 3.4, 3.5, and 3.11. These supplemental figures show all three primary events. There are also additional figures showing a comparison between the T4.5-50, T4.6-40, SHD02-04 (Dashti et al. 2010a; Dashti et al. 2010b), and JDA01-02 (Allmond and Kutter 2012) test results.



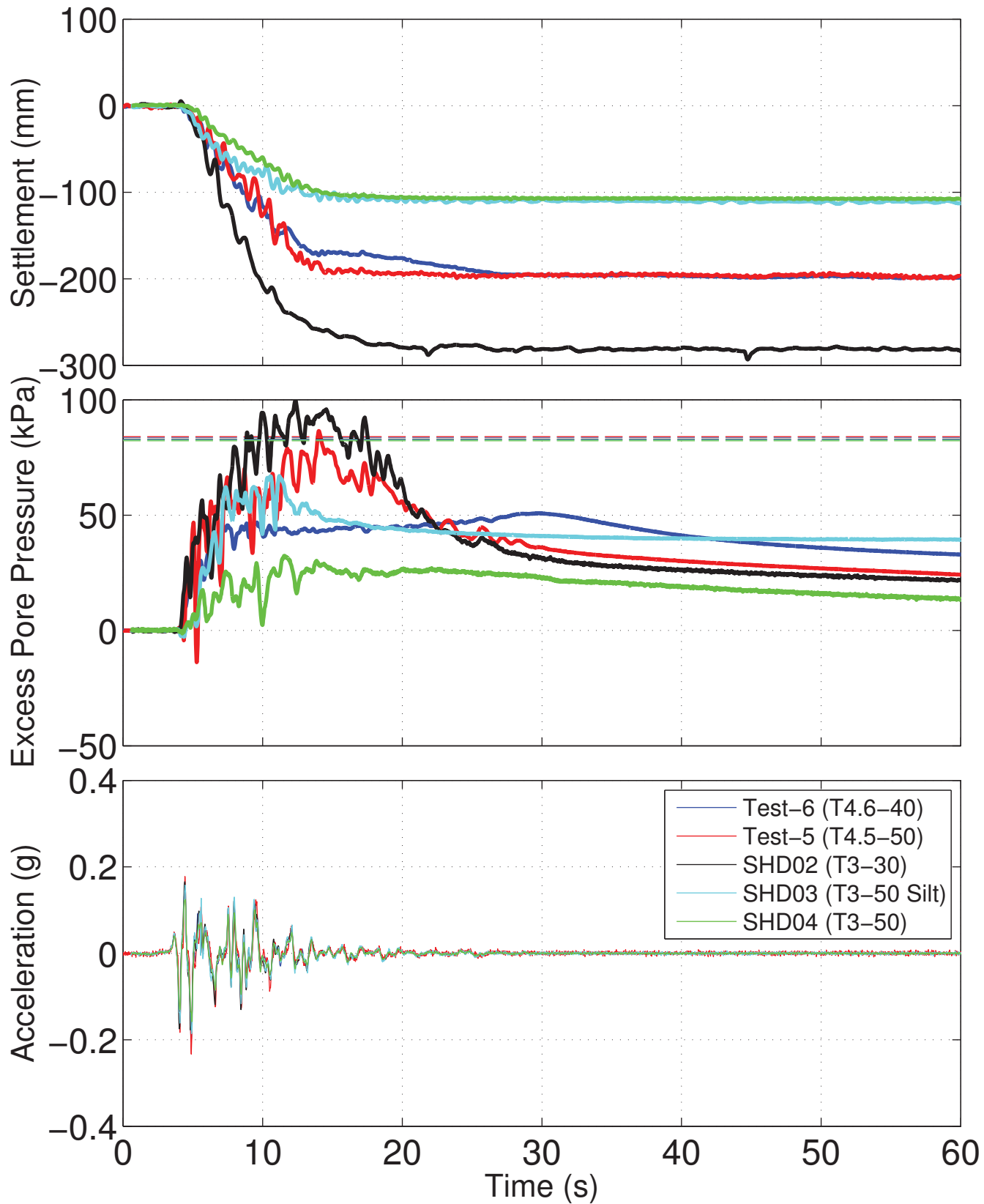




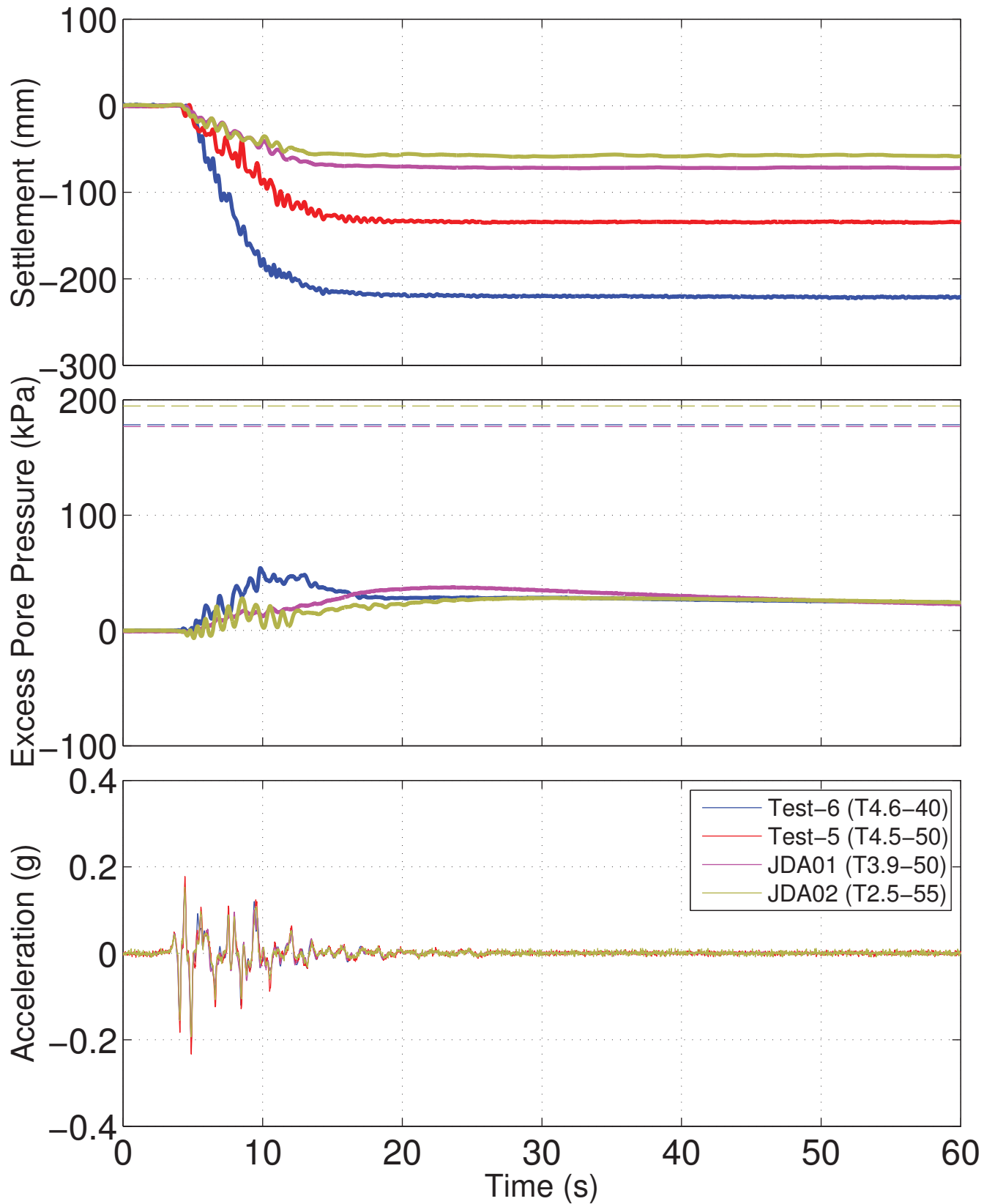
PRI Mod: Free Field



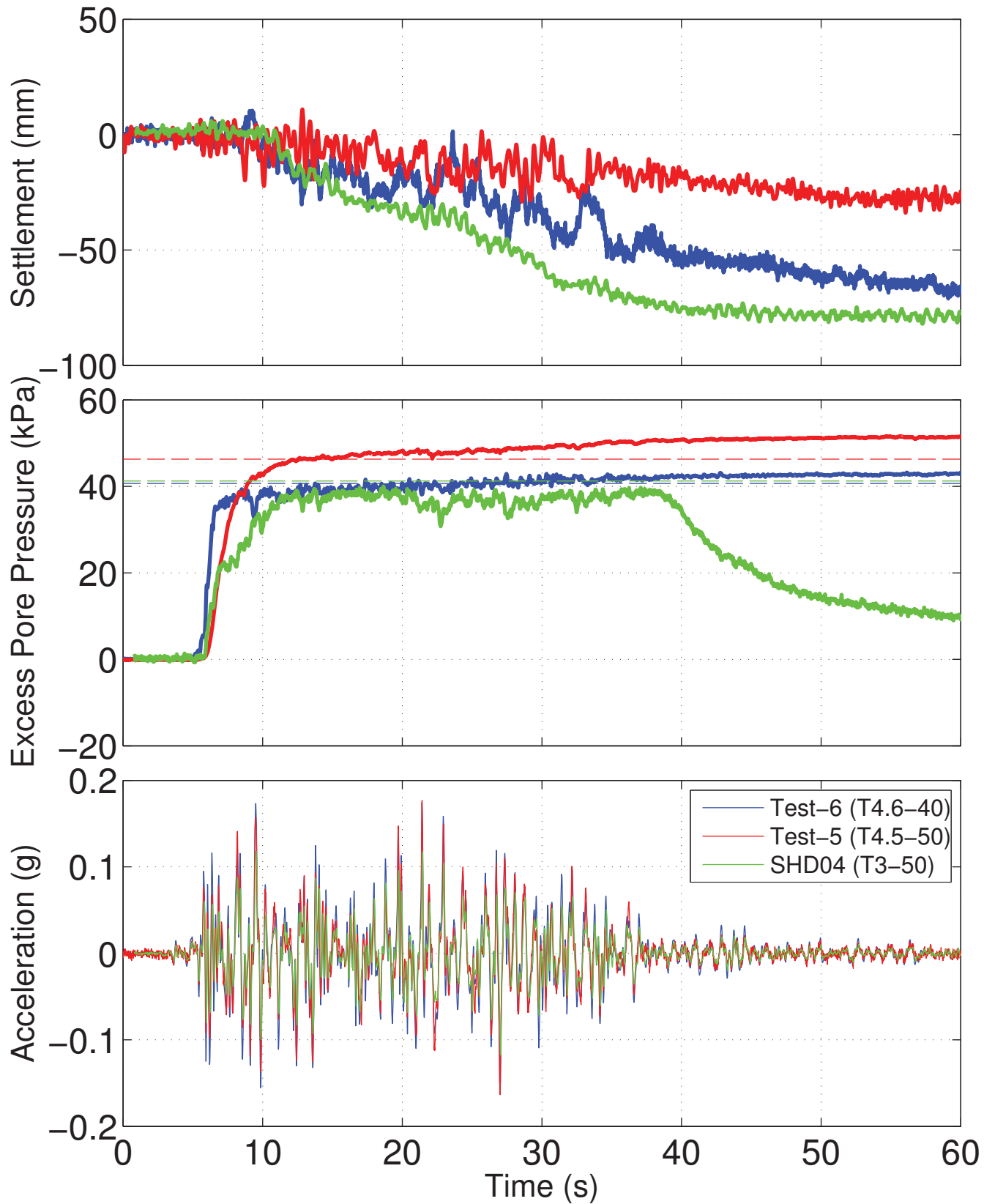
PRI Mod: Structure A



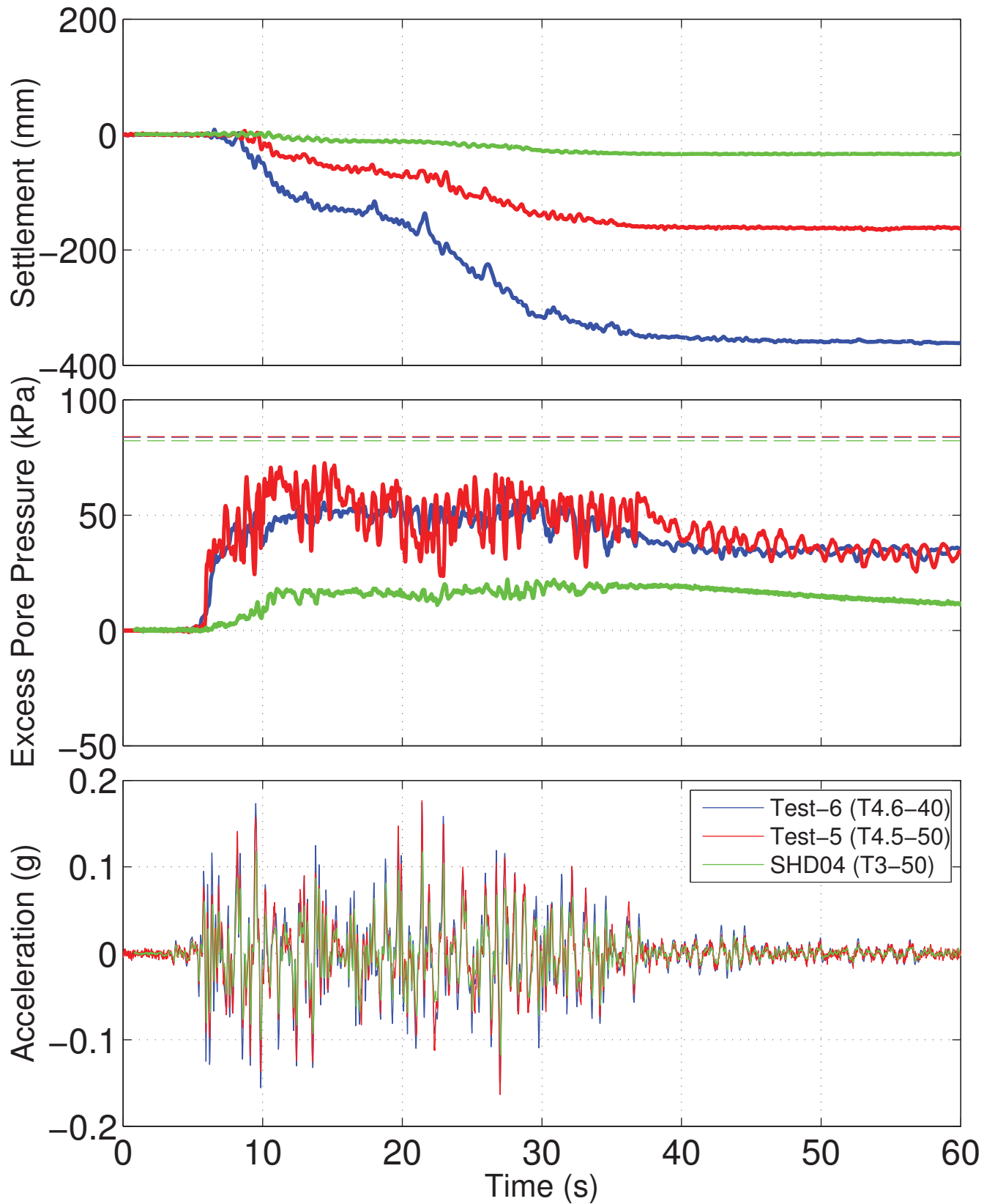
PRI Mod: Structure J



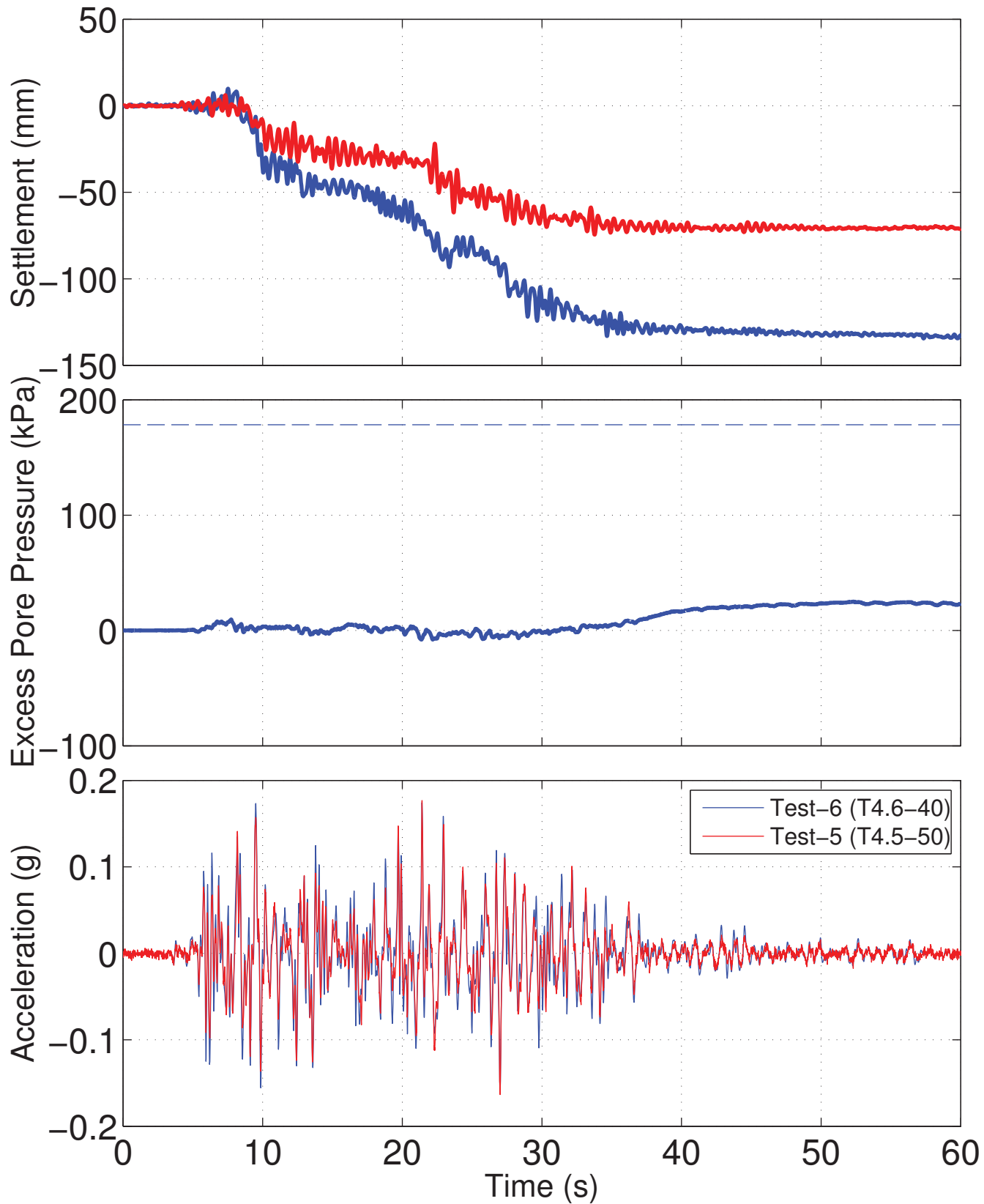
TCU Mod: Free Field



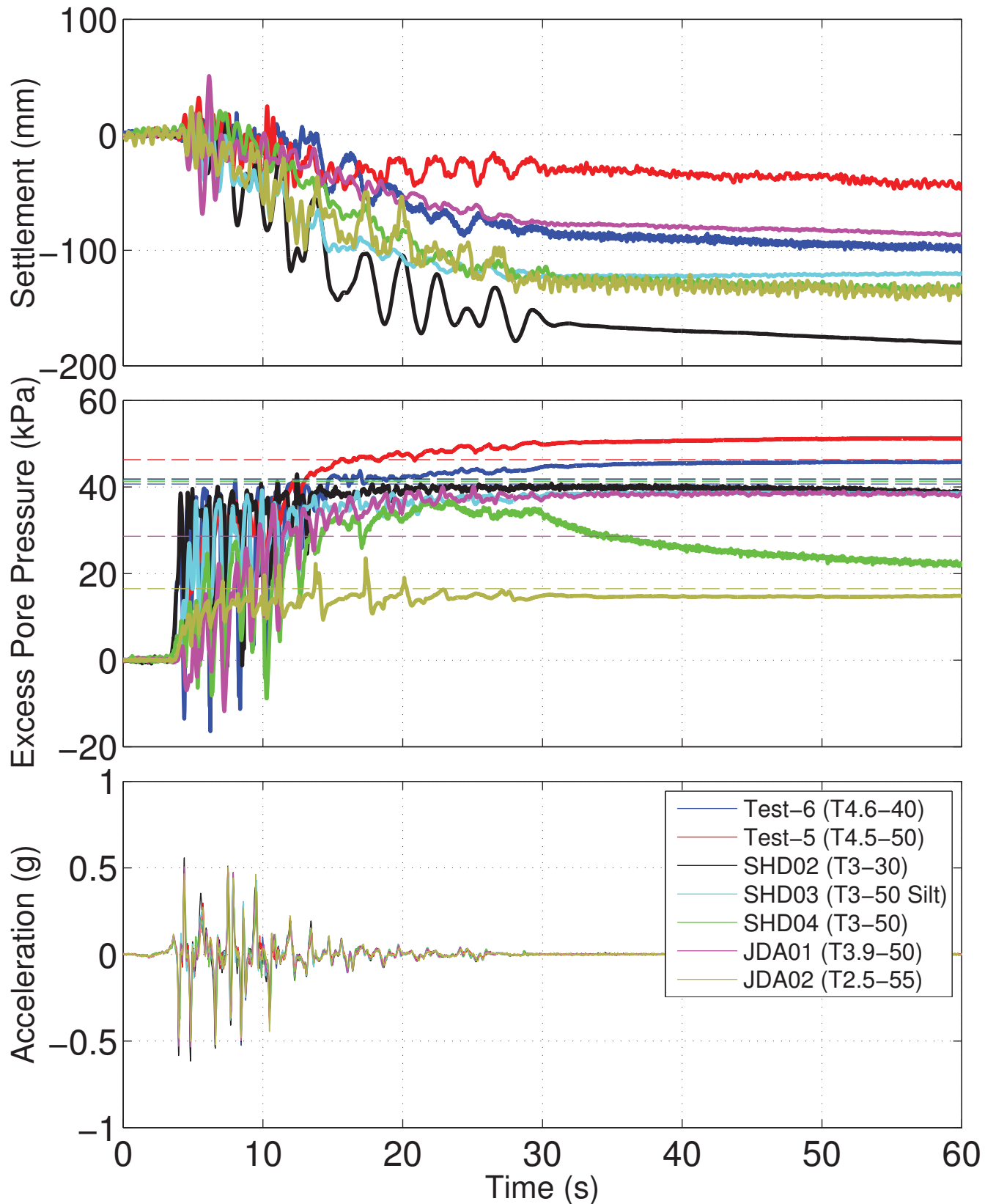
TCU Mod: Structure A



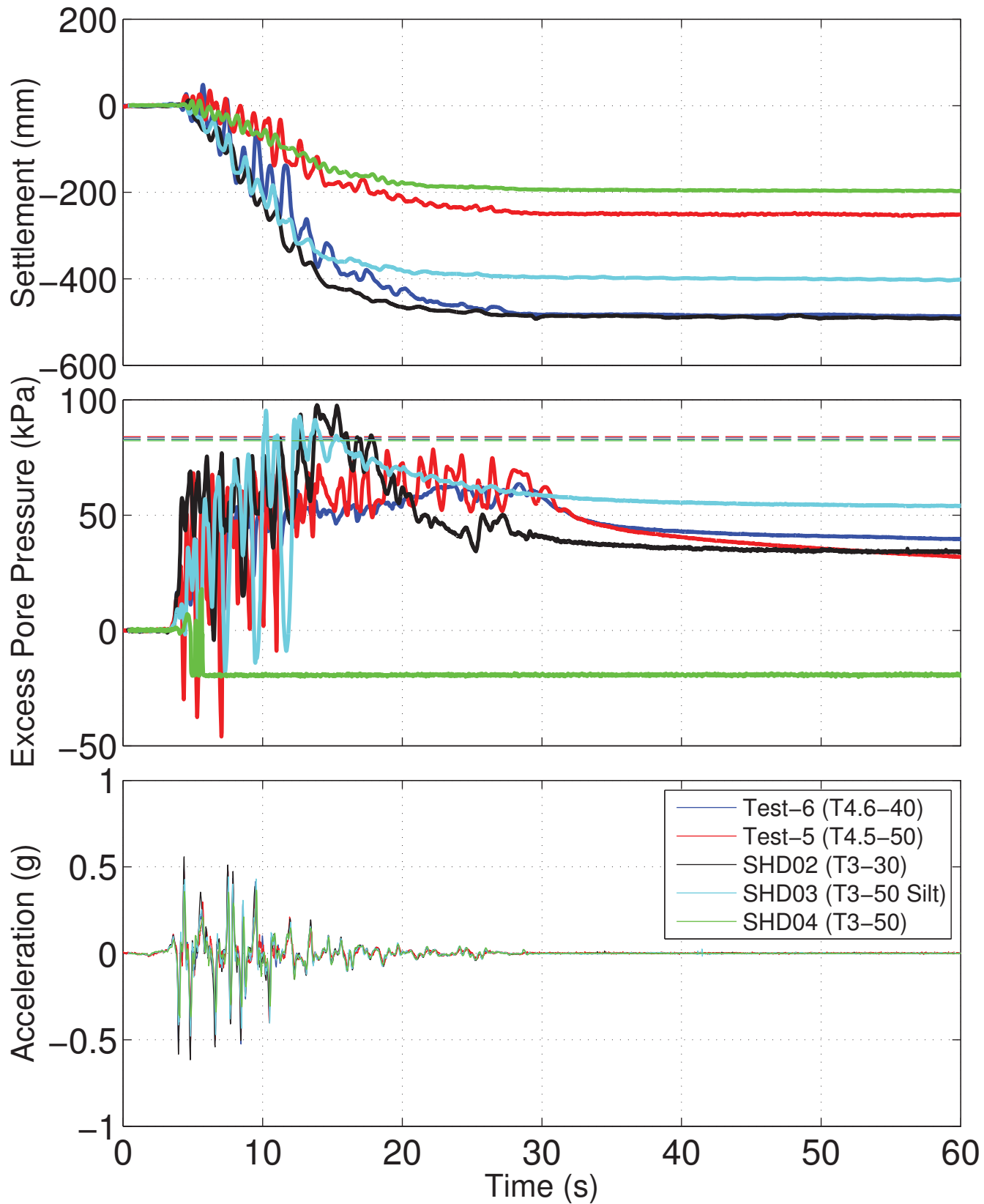
TCU Mod: Structure J



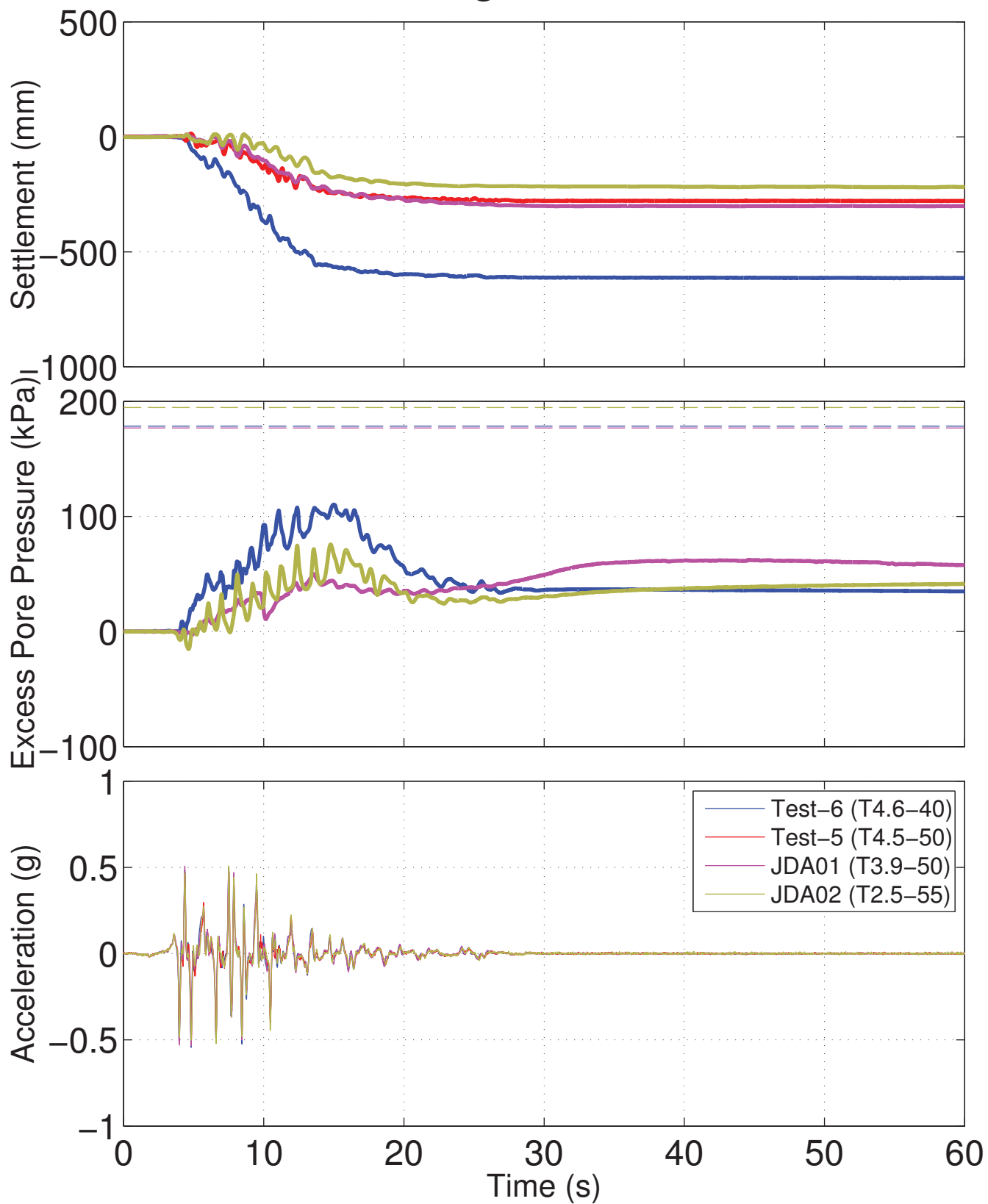
PRI Large: Free Field



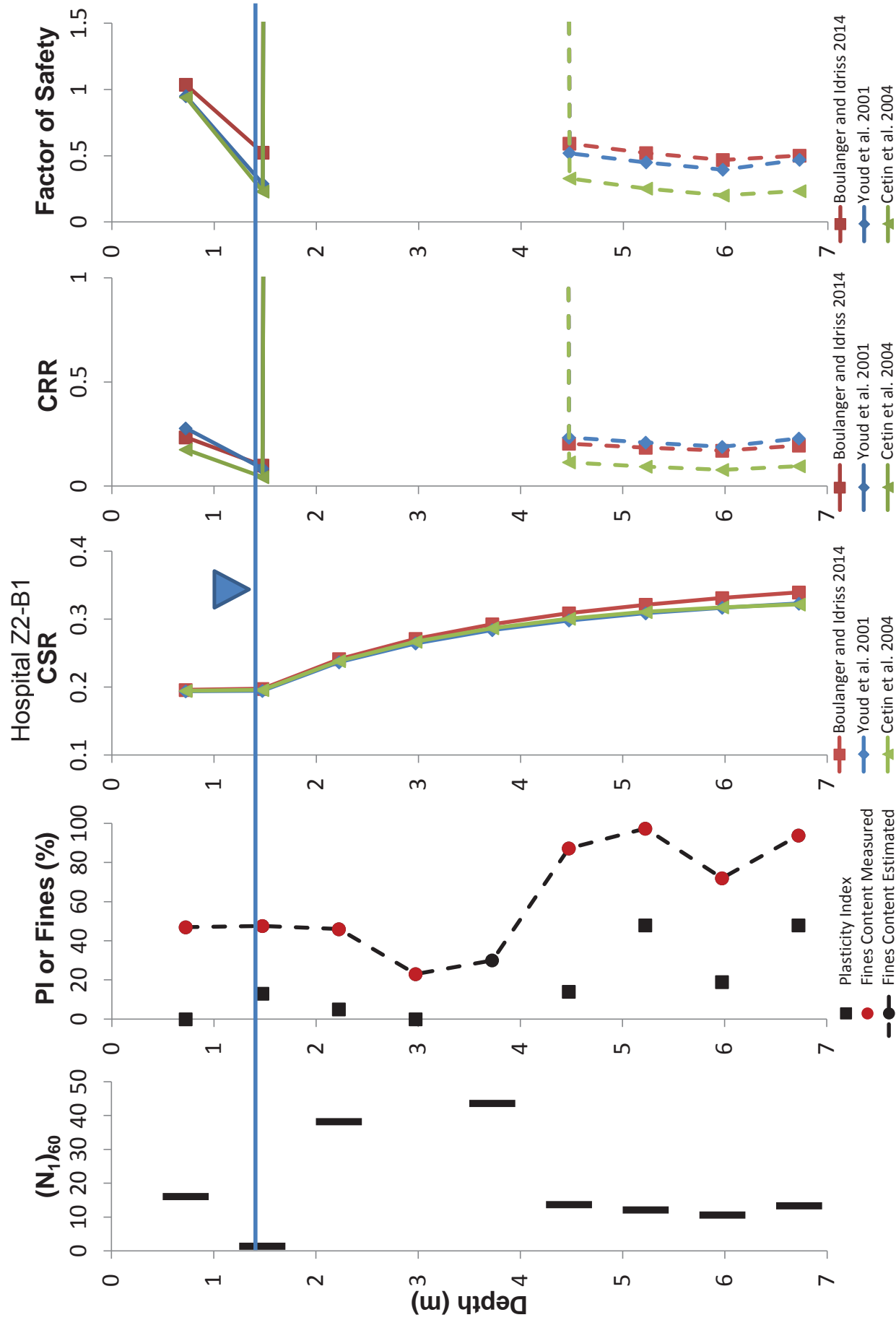
PRI Large: Structure A

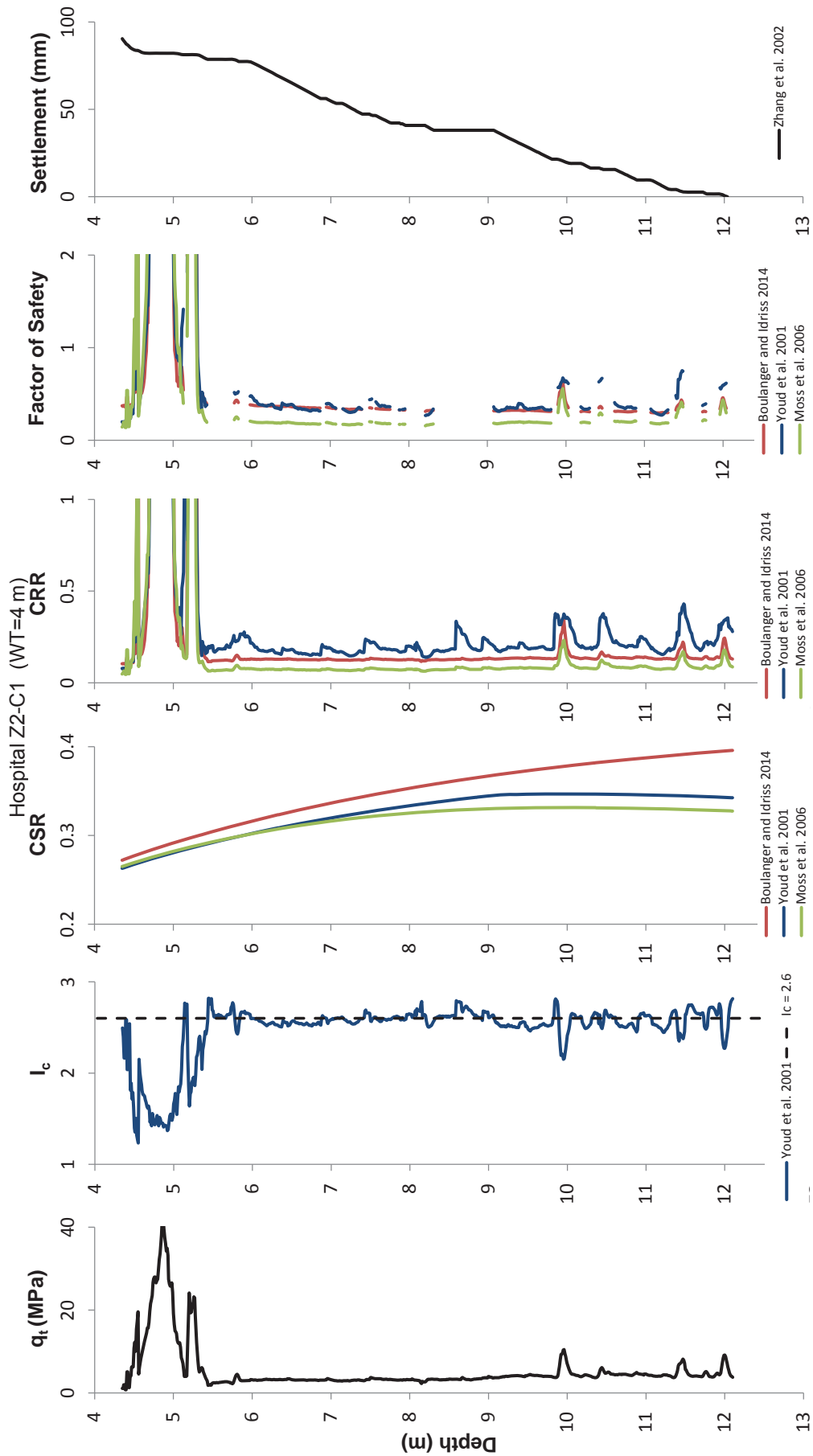


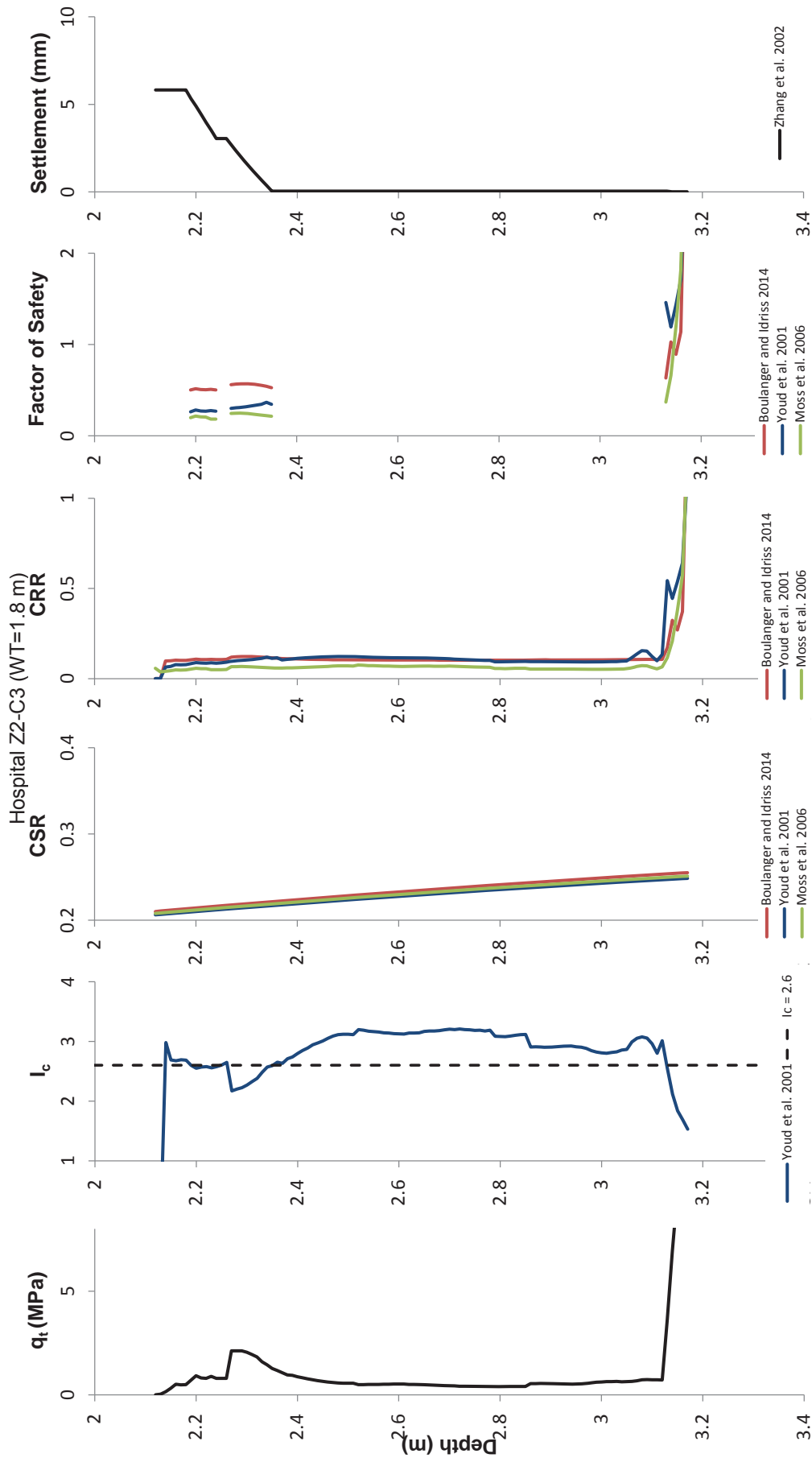
PRI Large: Structure J

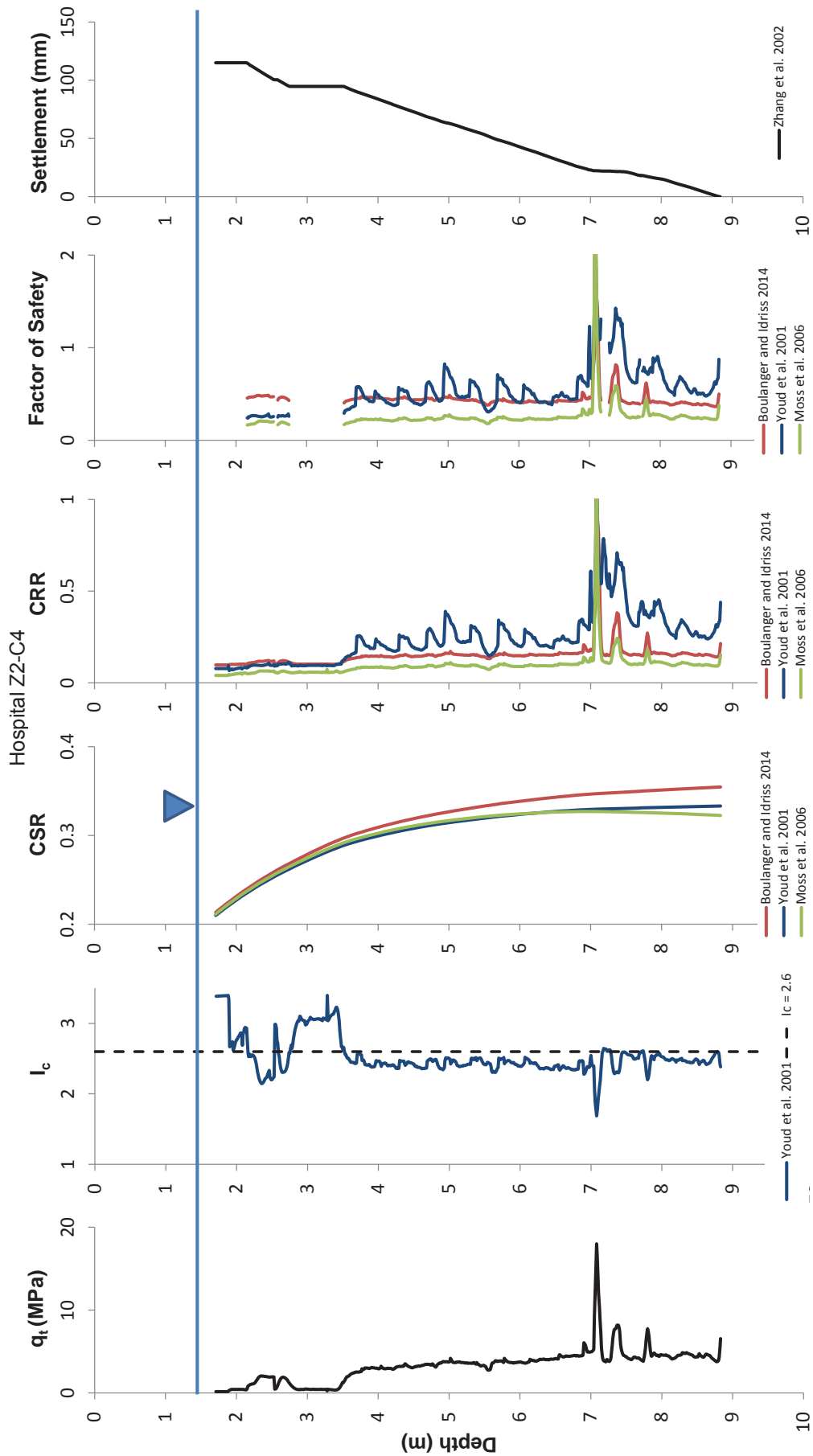


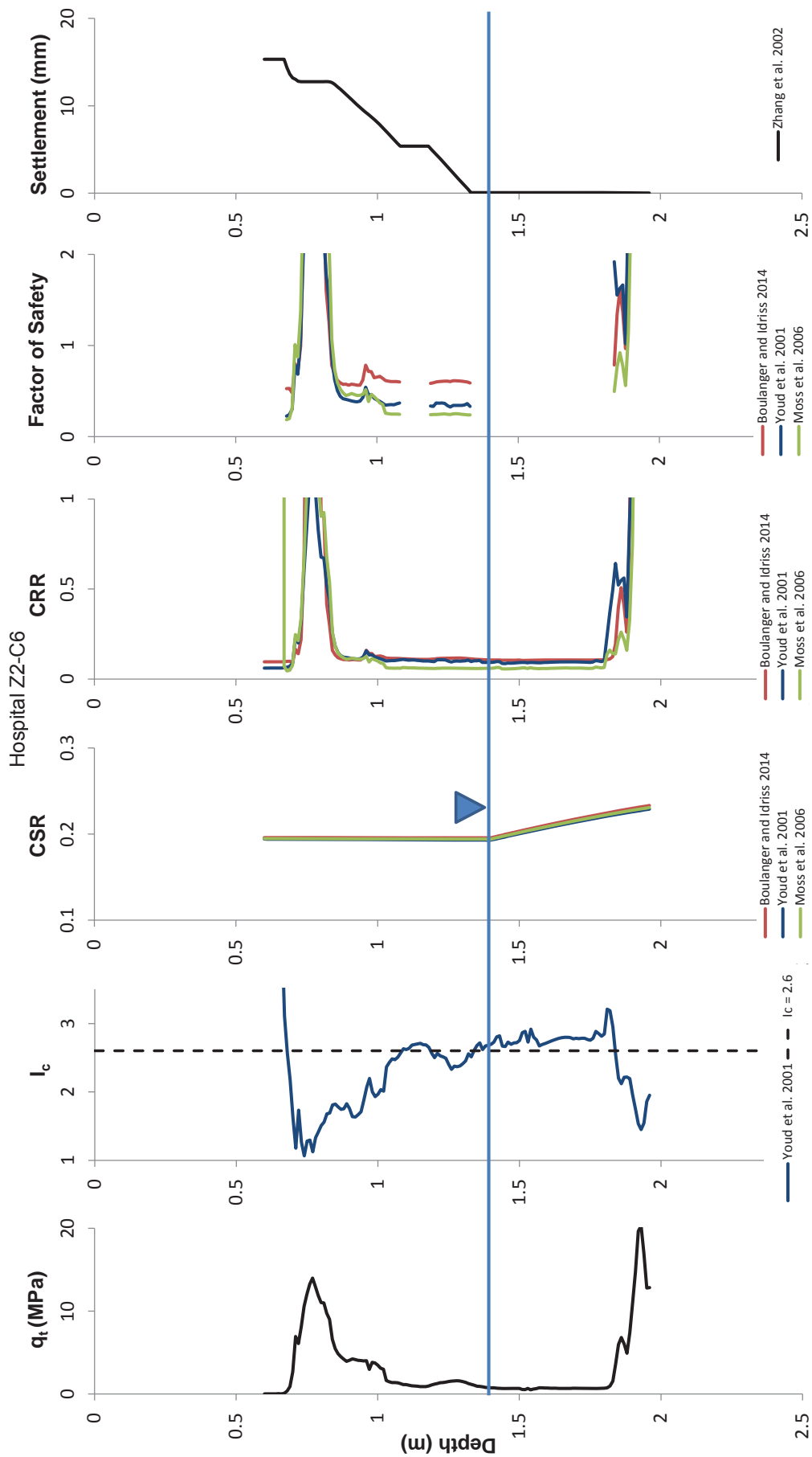
APPENDIX C-1
SPT and CPT Results

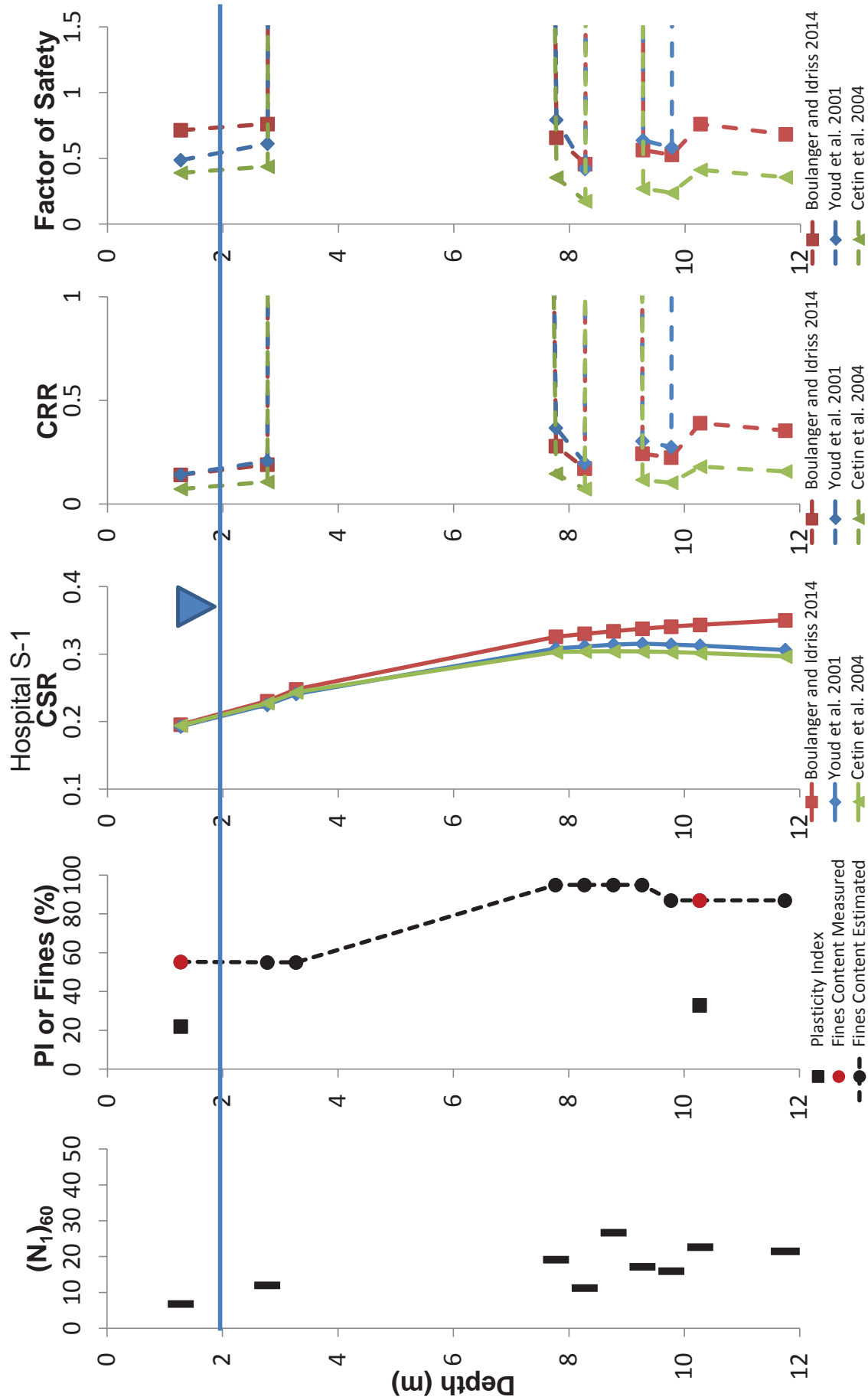


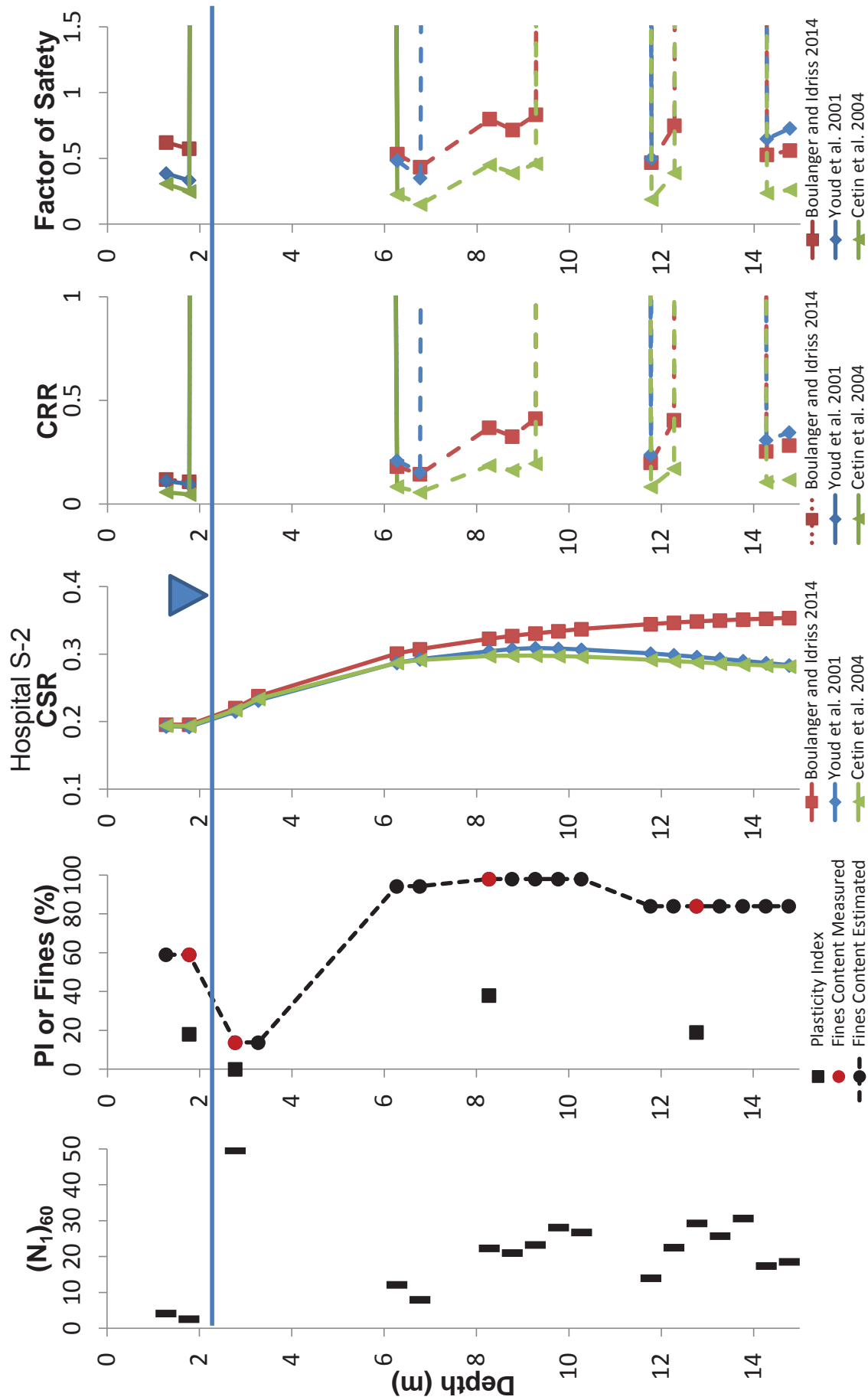


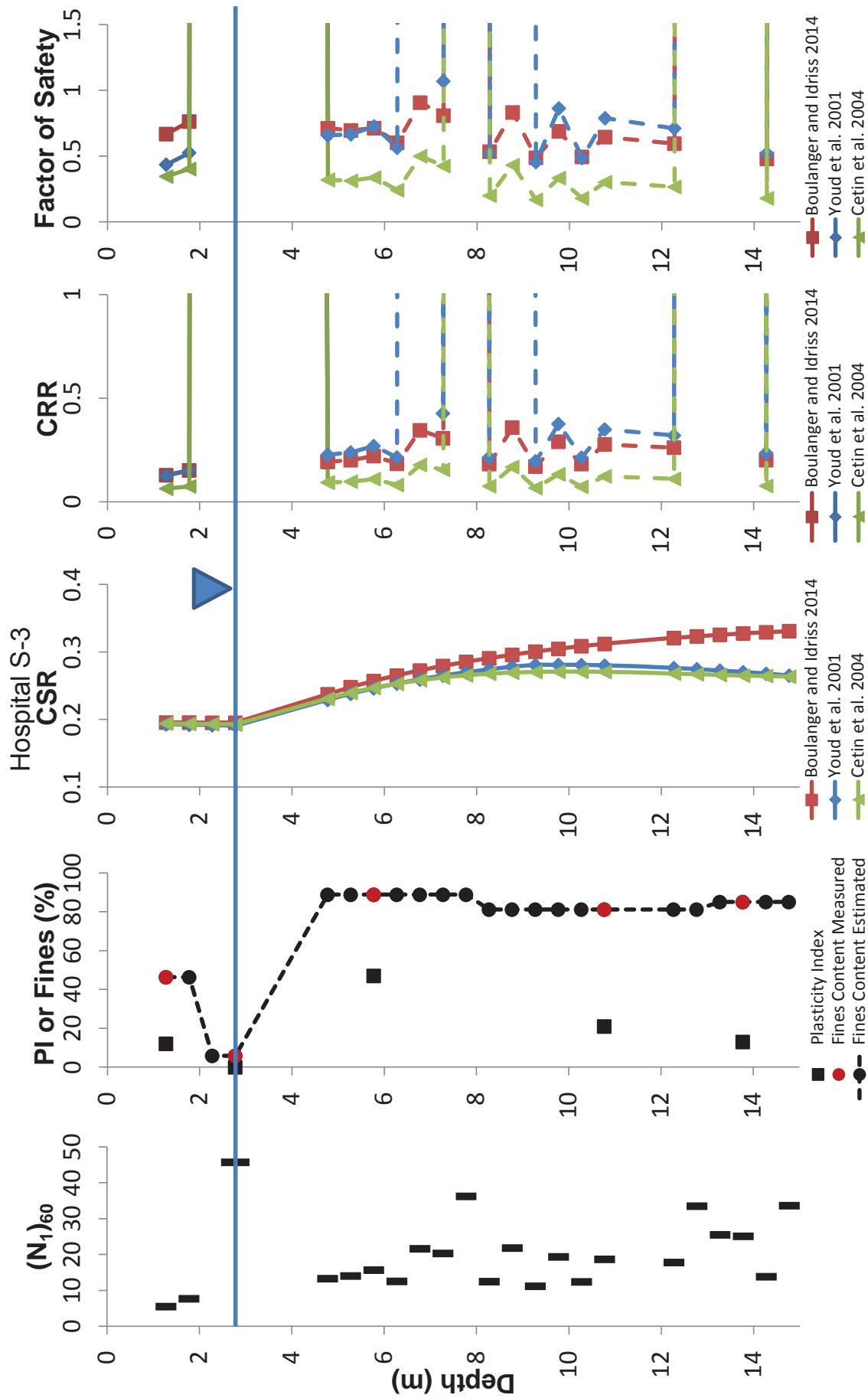




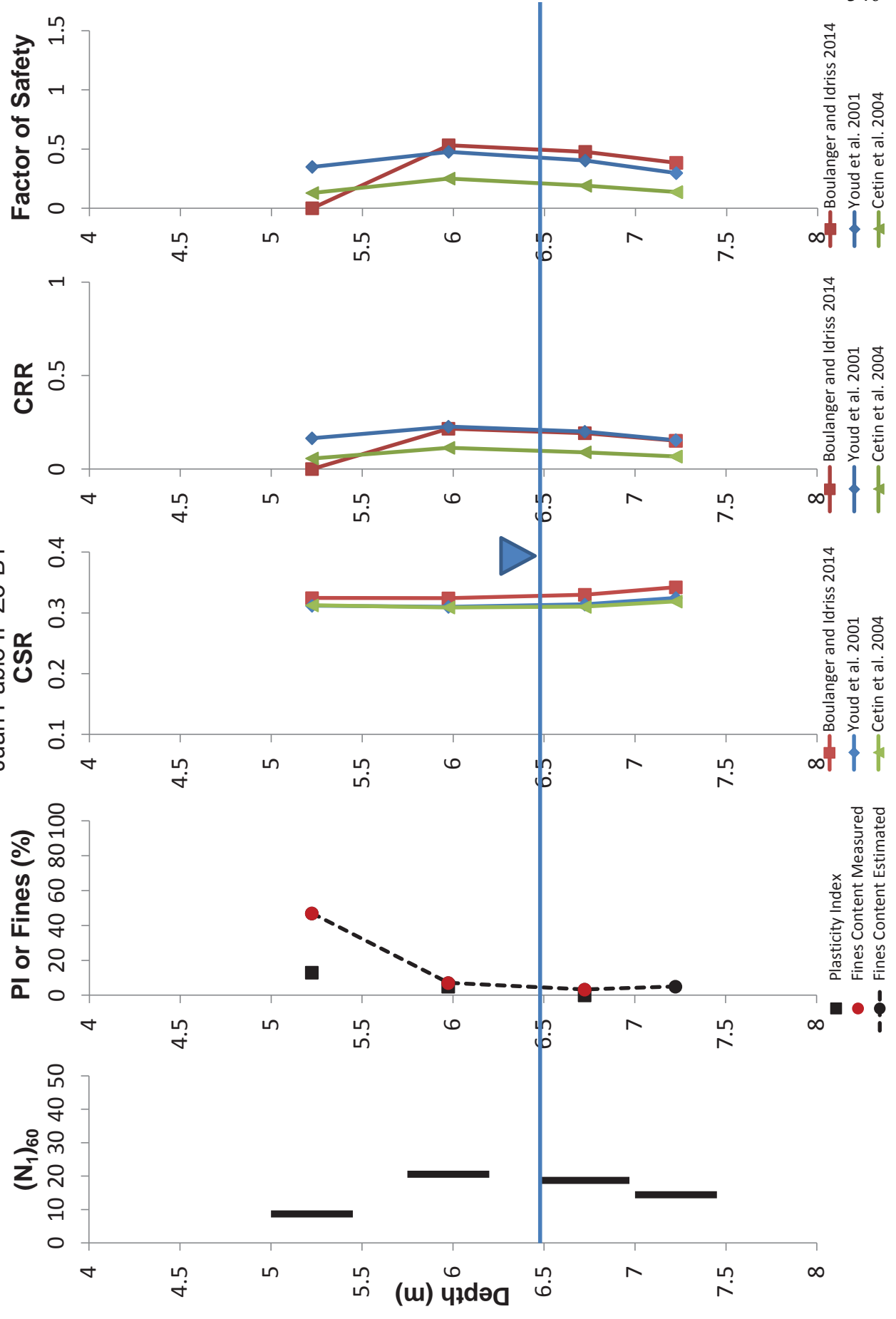


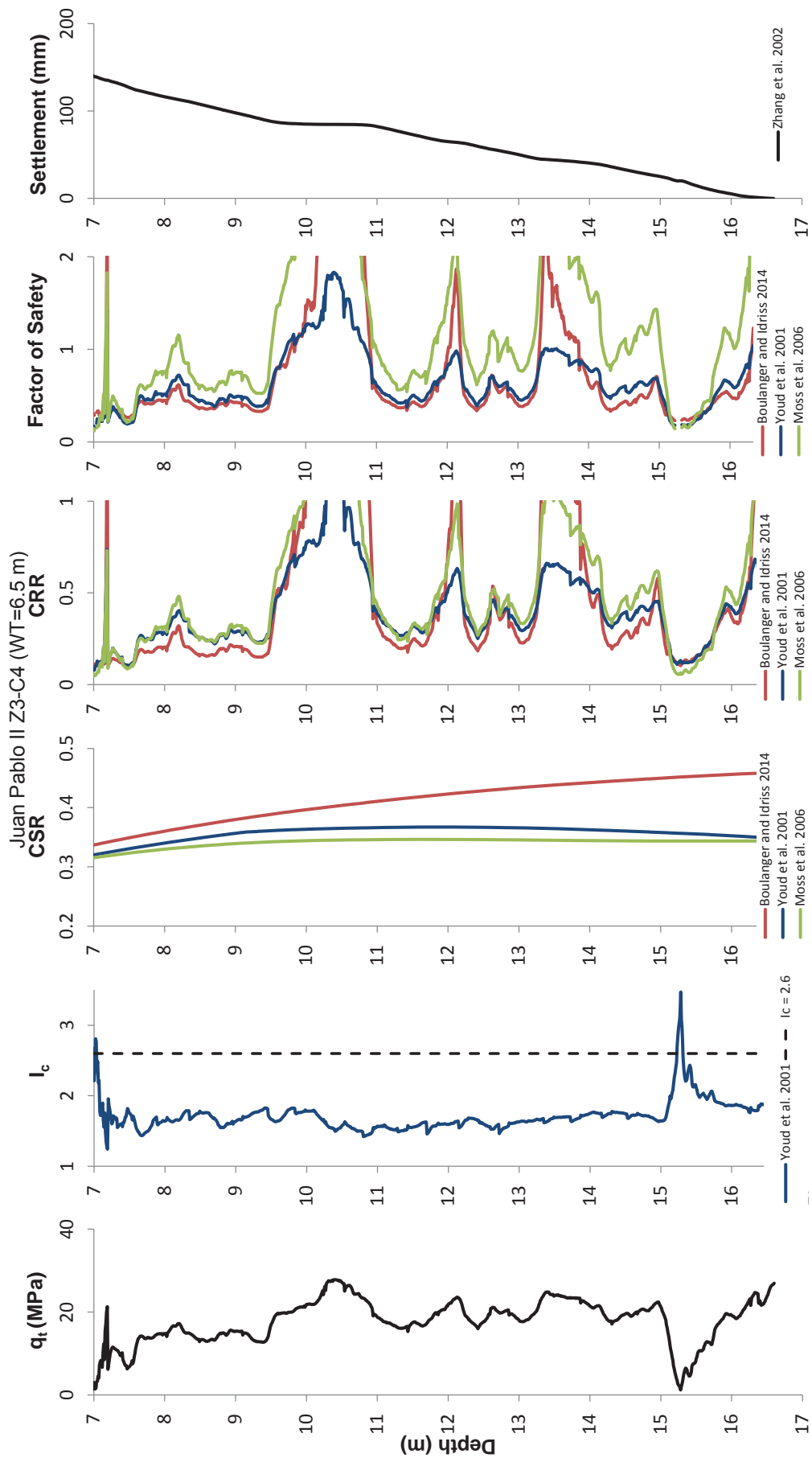


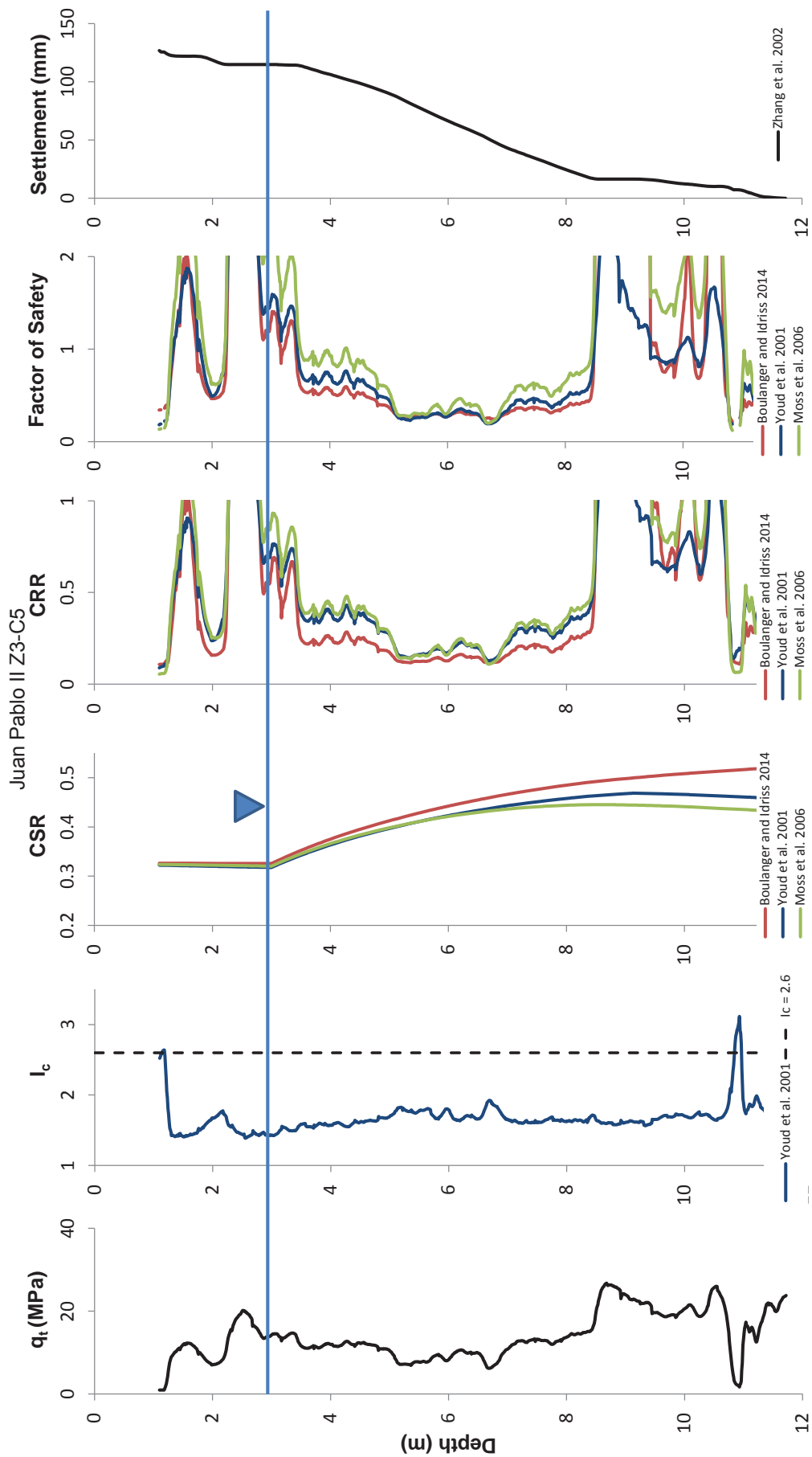


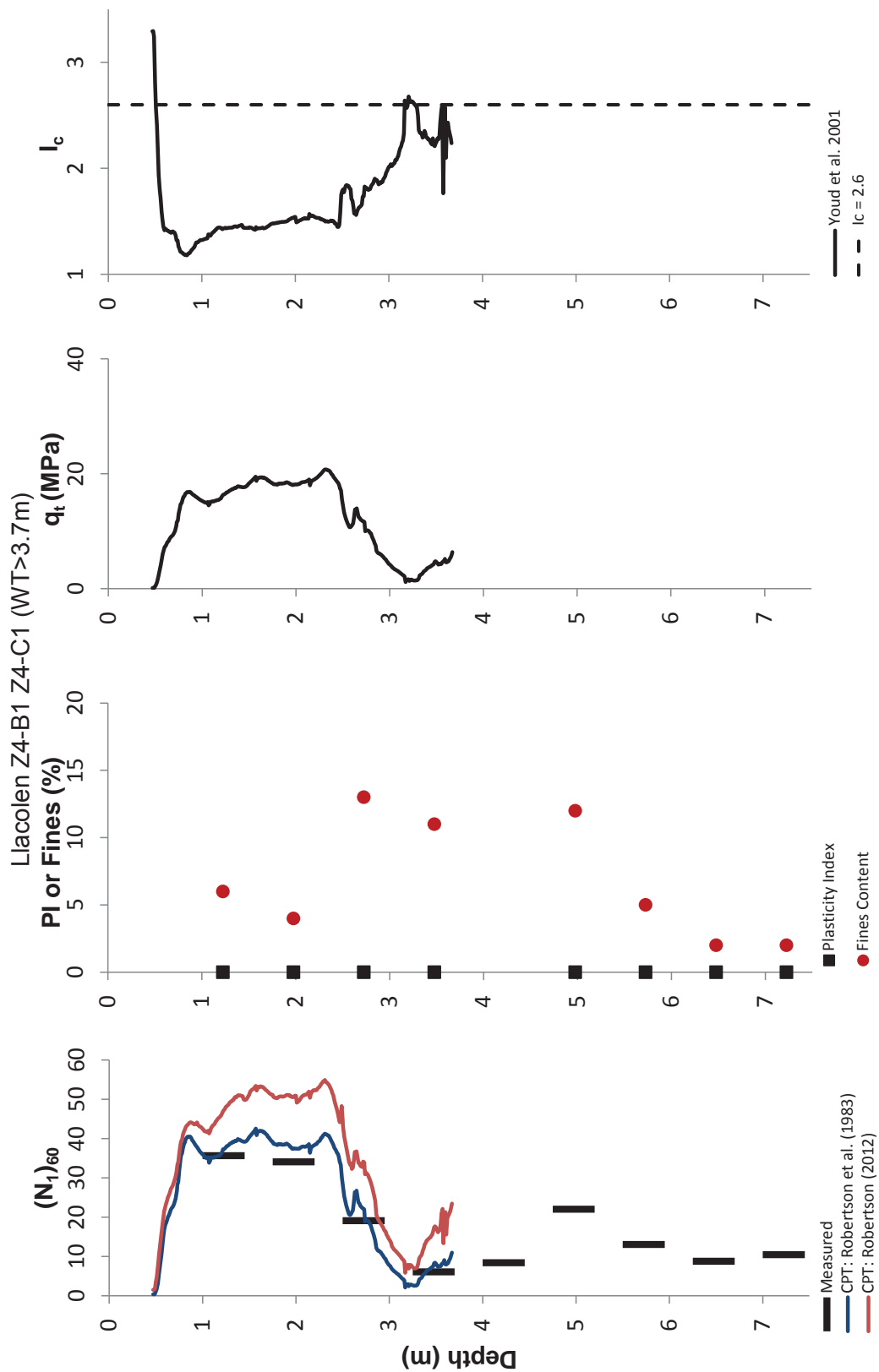


Juan Pablo II Z3-B1







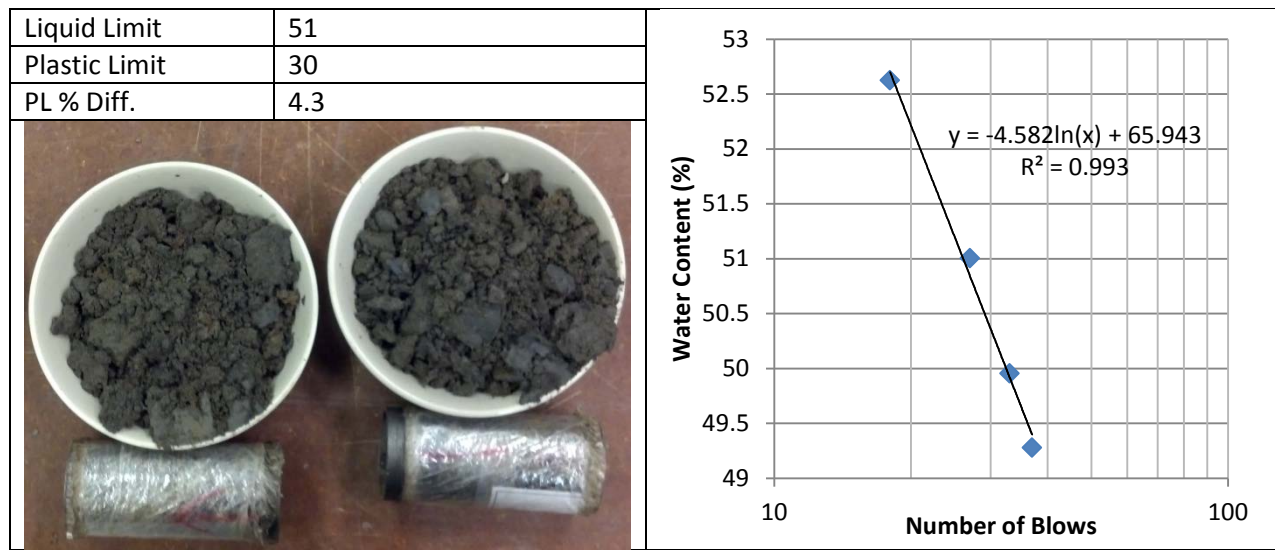
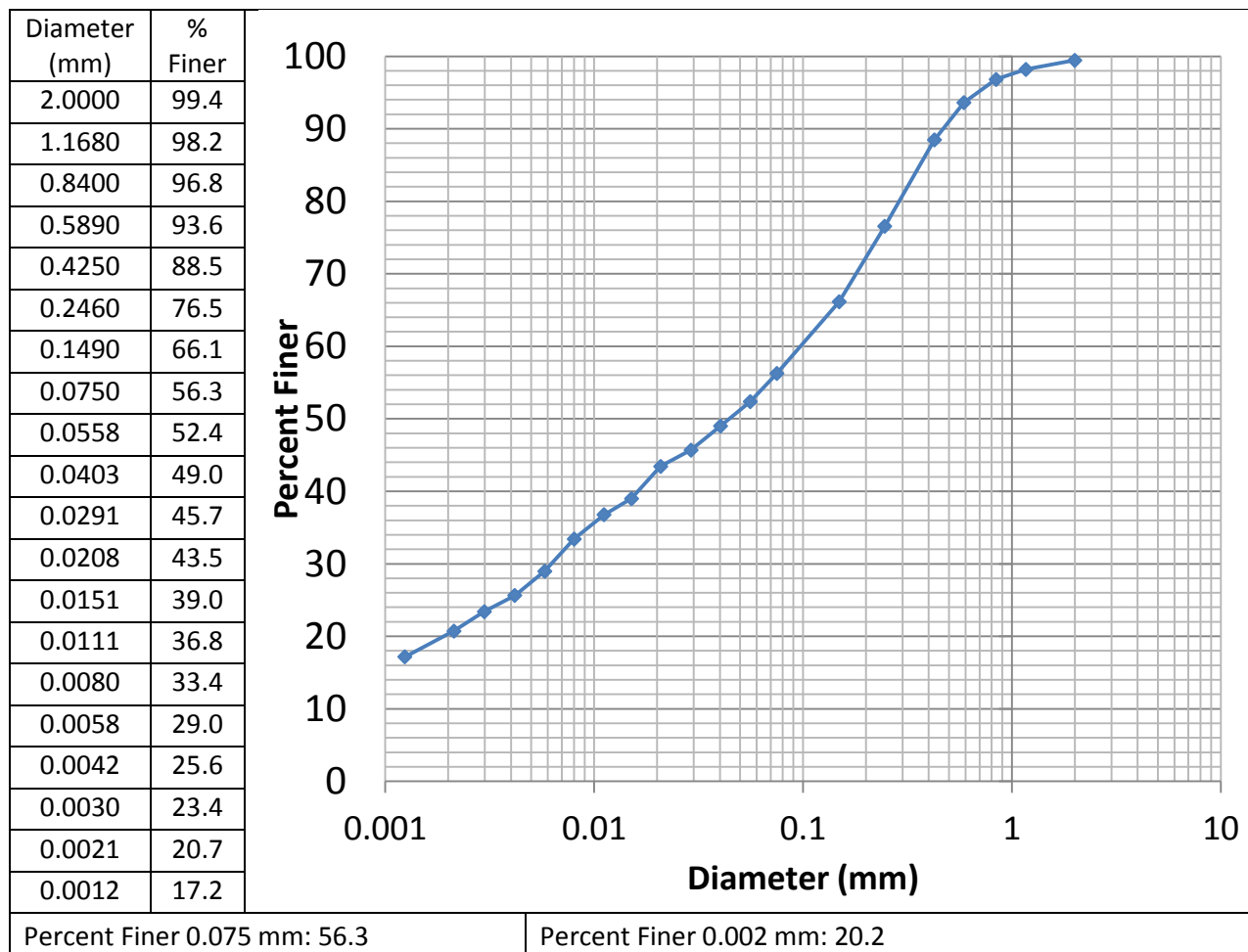


APPENDIX C-2

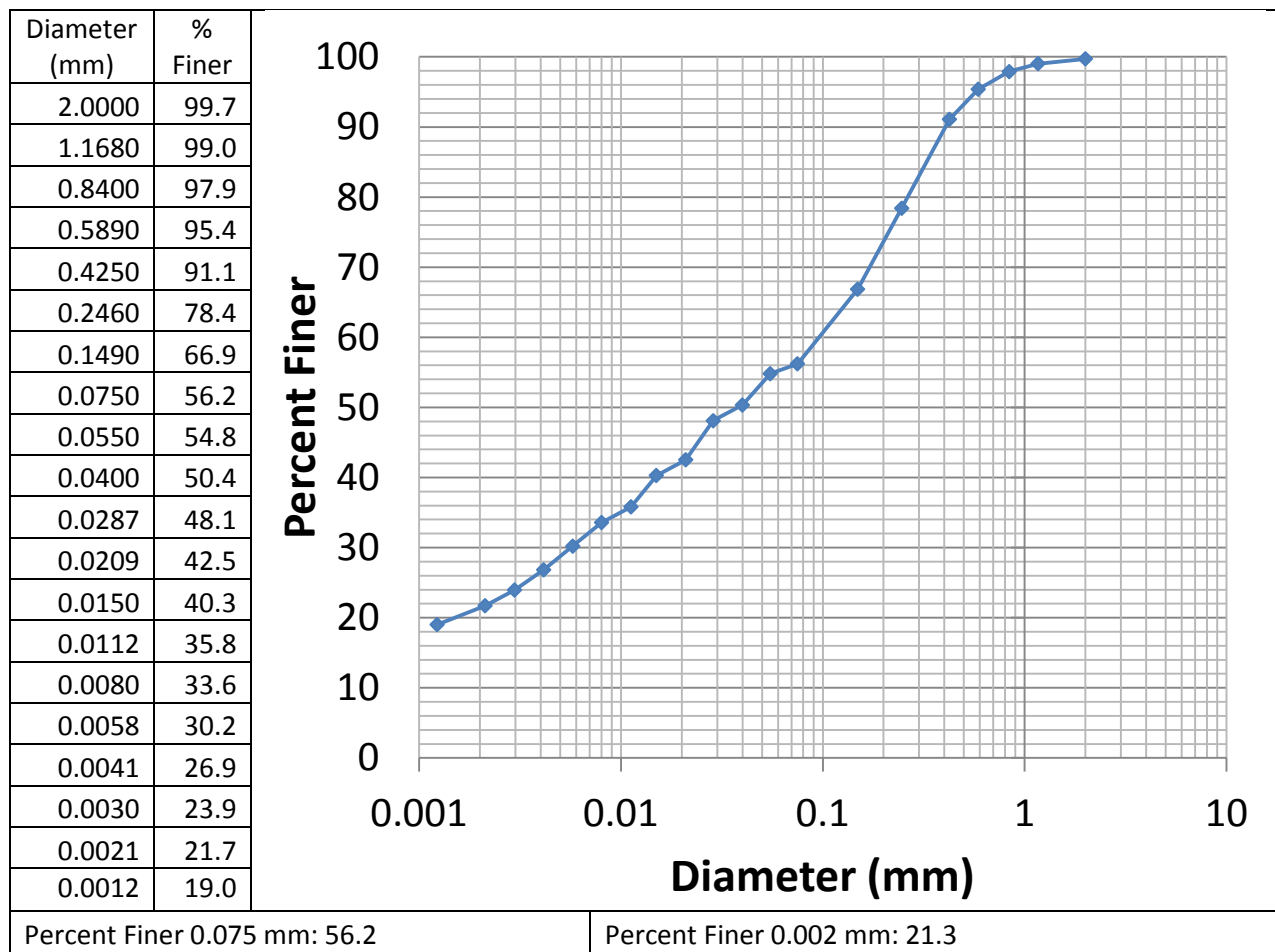
Index Test Results and Sample Photos

This appendix contains gradation curves, Atterberg limit results, and photographs of samples.

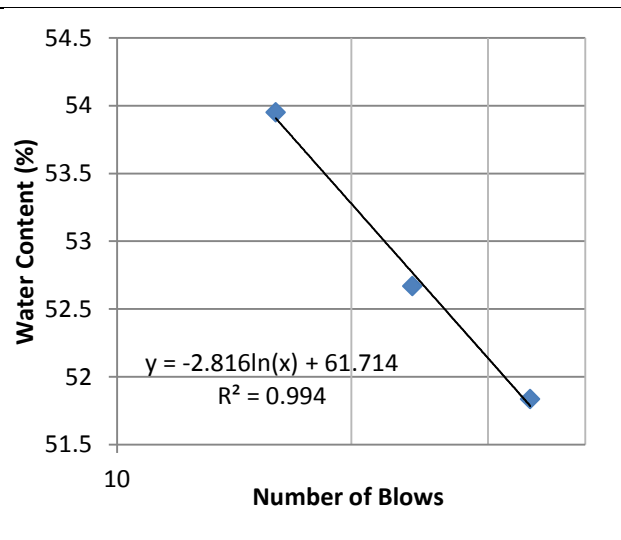
Boring: Z2-C4	Depth (m): 1.80-2.03	Sample Type: hand	Sample Label(s): Shelby A
Tested at: UCB	Notes: Pushed by hand what they called "Shelby" but smaller diameter		



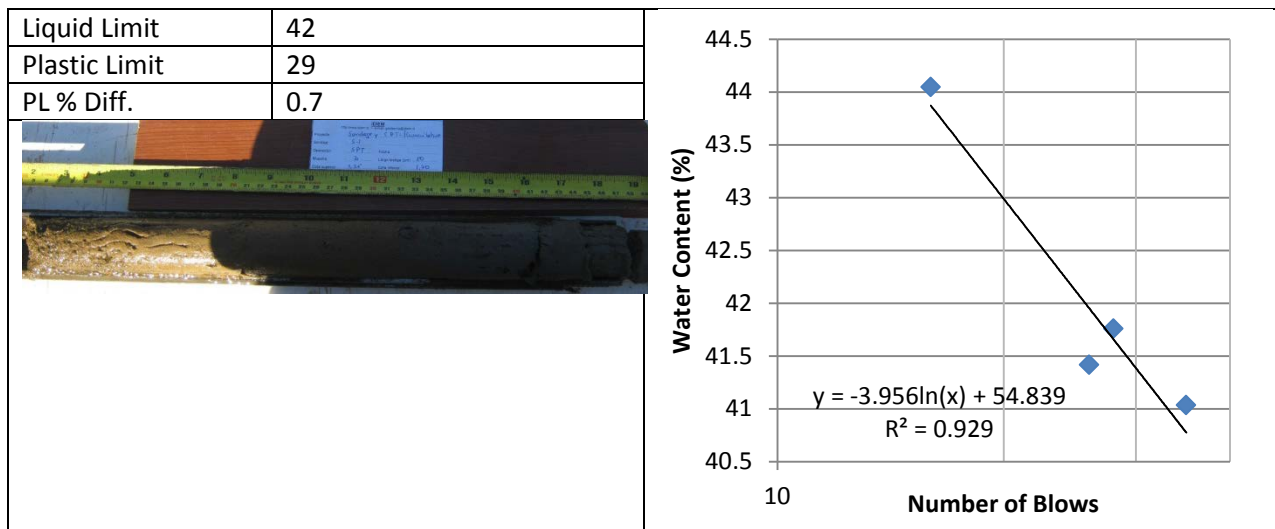
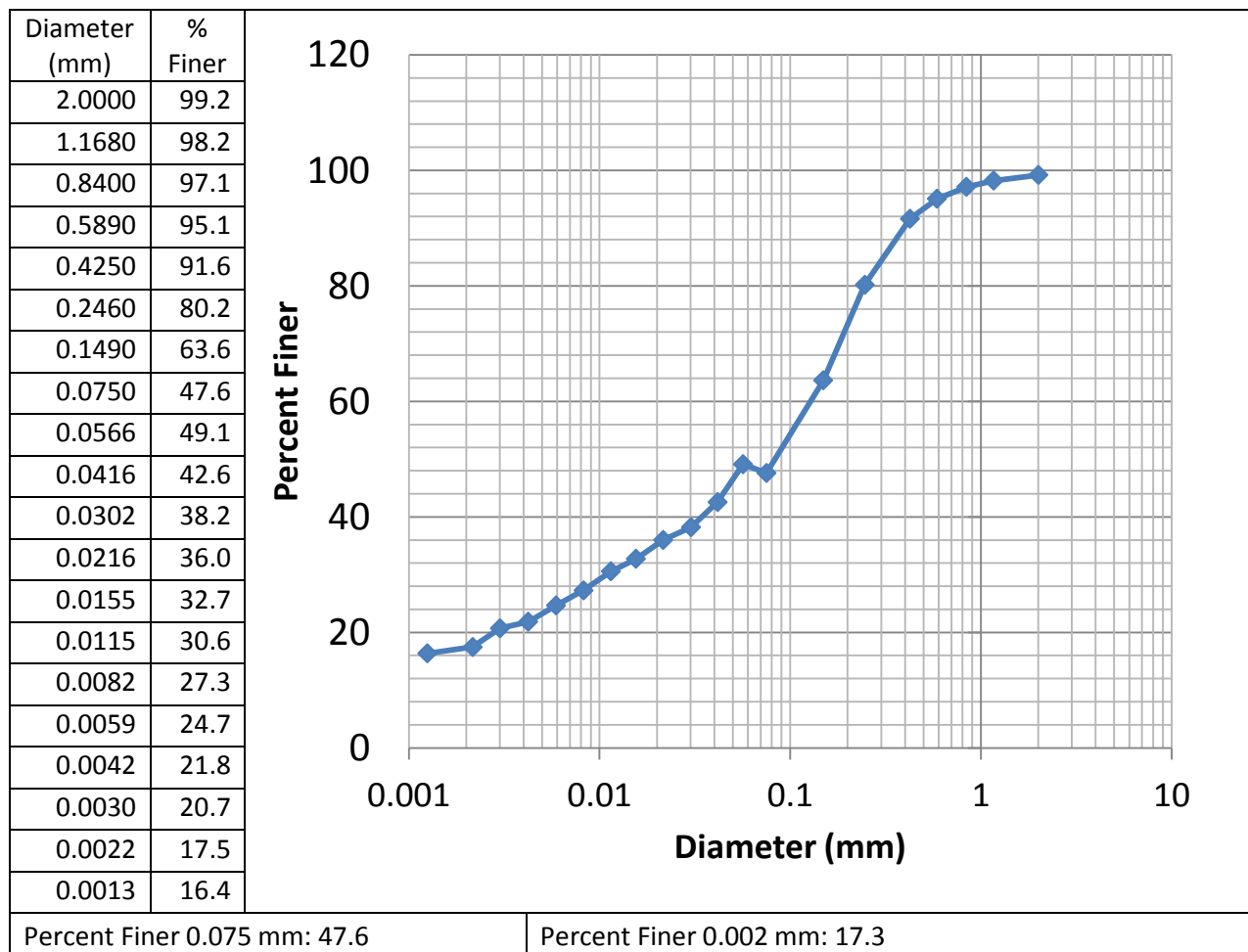
Boring: Z2-C4	Depth (m): 2.03-2.25	Sample Type: hand	Sample Label(s): Shelby B
Tested at: UCB	Notes: Pushed by hand what they called "Shelby" but smaller diameter		



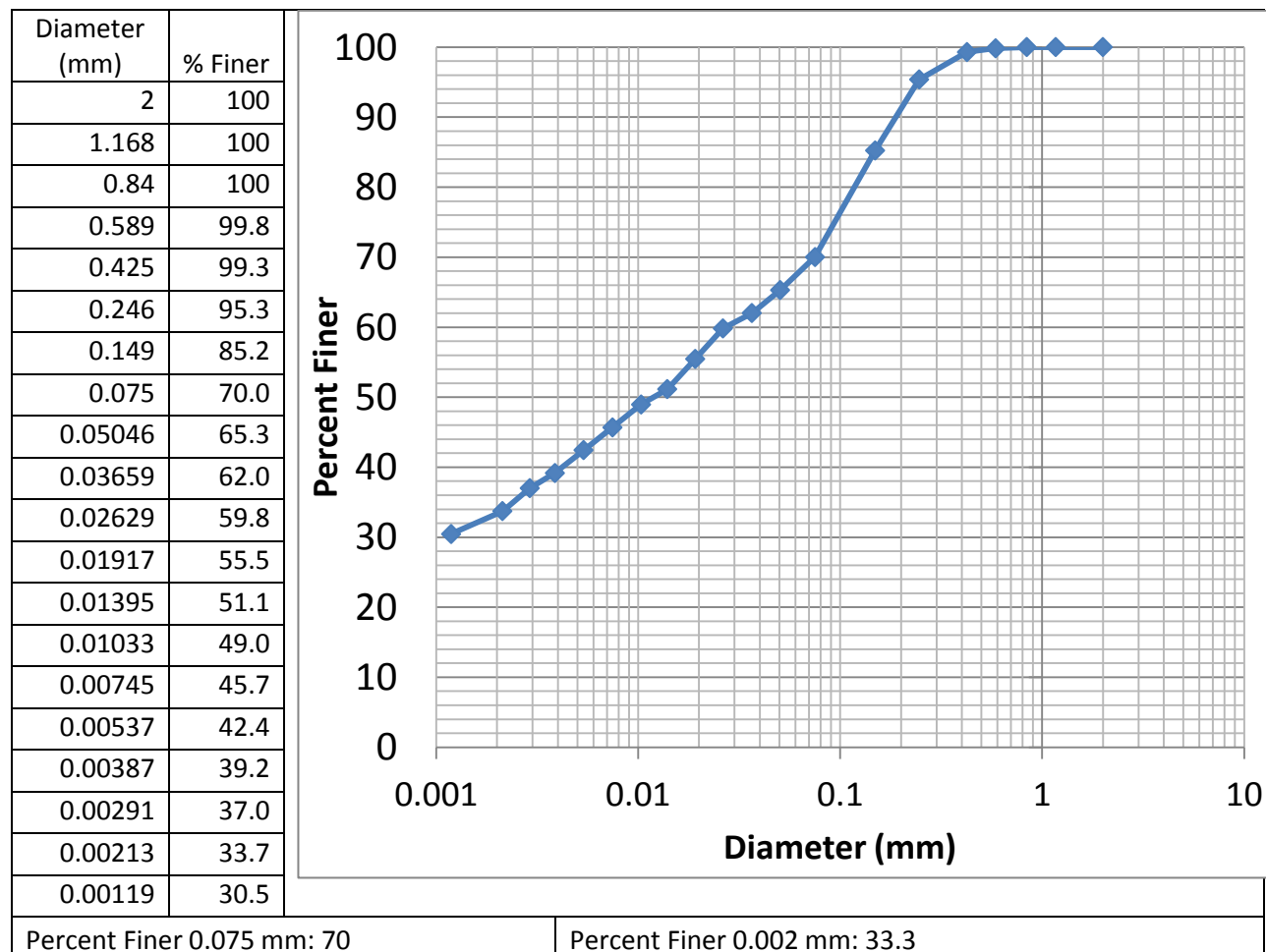
Liquid Limit	53
Plastic Limit	28
PL % Diff.	1.2



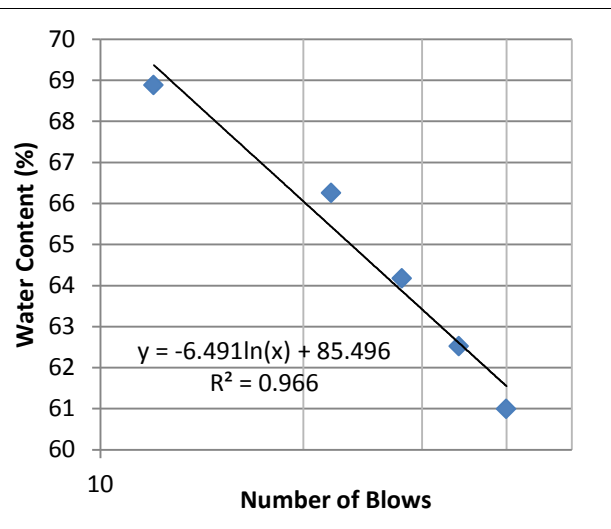
Boring: Z2-B1	Depth (m): 1.25-1.75	Sample Type: SPT	Sample Label(s): C1
Tested at: UCB	Notes:		



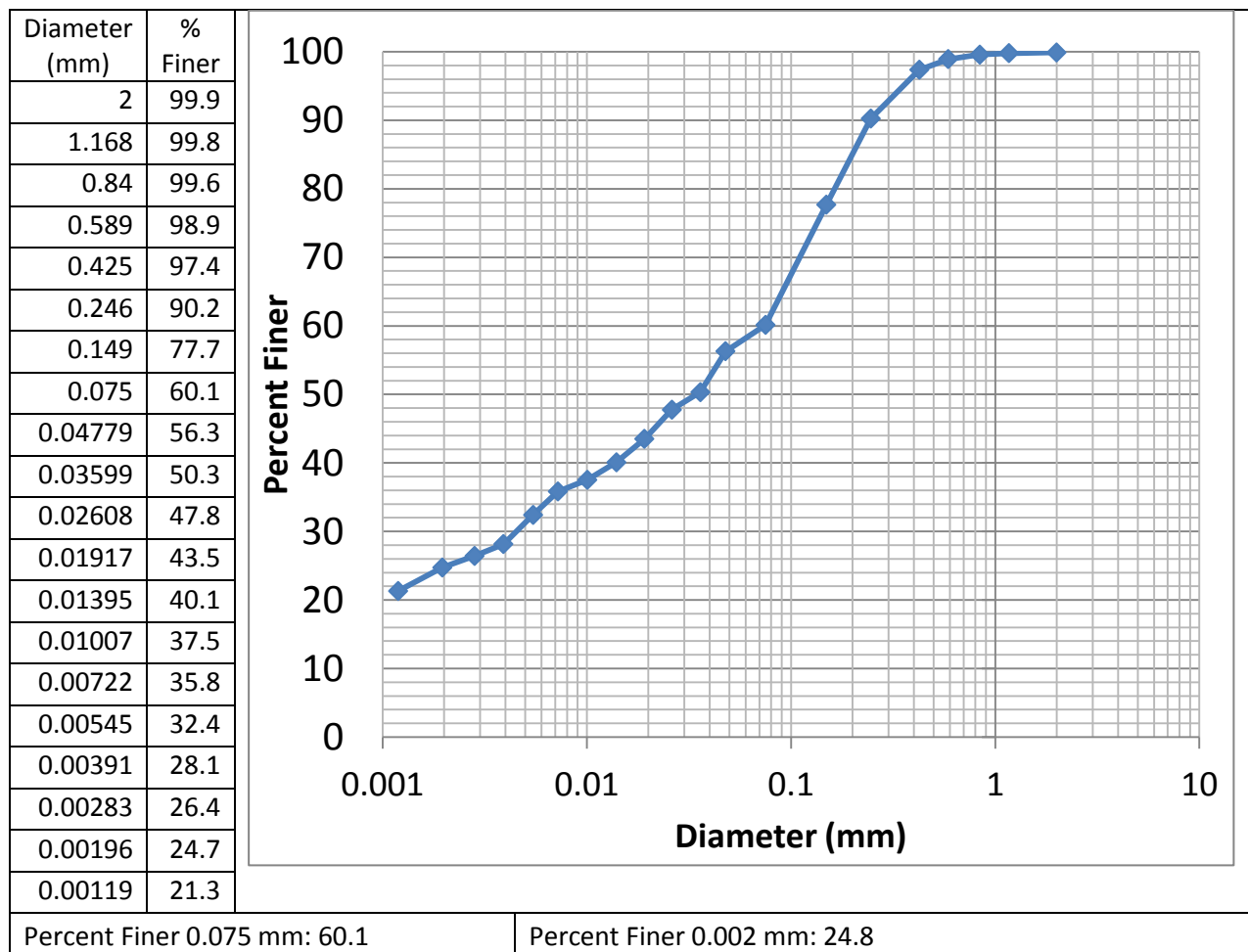
Boring: Z2-C1	Depth (m): 2.00-3.00	Sample Type: HQ3	Sample Label(s): C4
Tested at: UCB	Notes: From Predrilling		



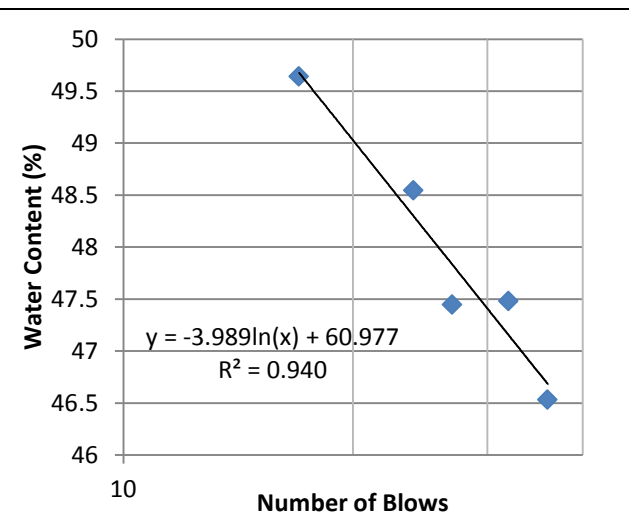
Liquid Limit	65
Plastic Limit	34
PL % Diff.	2.7



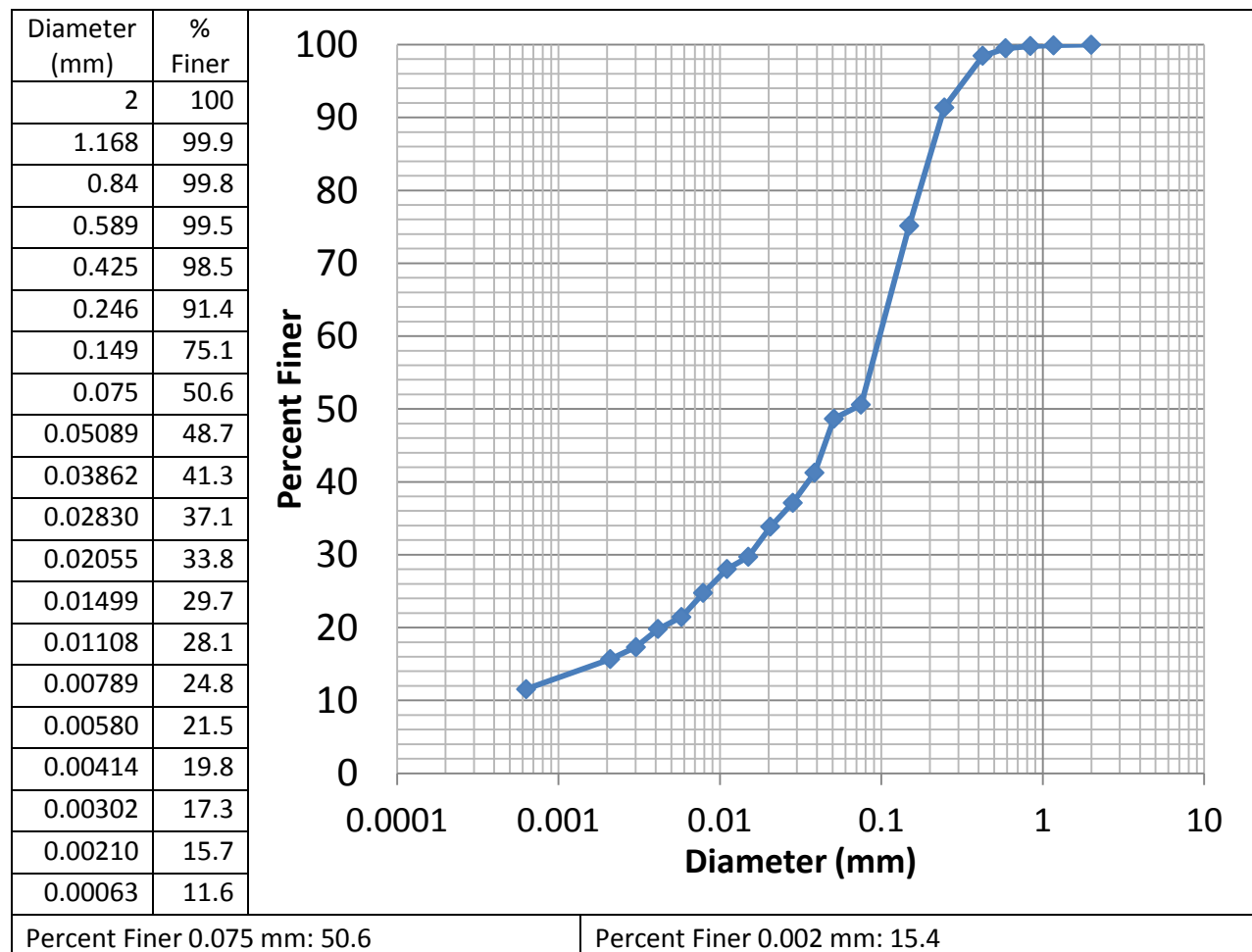
Boring: Z2-C1	Depth (m): 3.00-3.3	Sample Type: HQ3	Sample Label(s): C6b
Tested at: UCB	Notes: From predrilling		



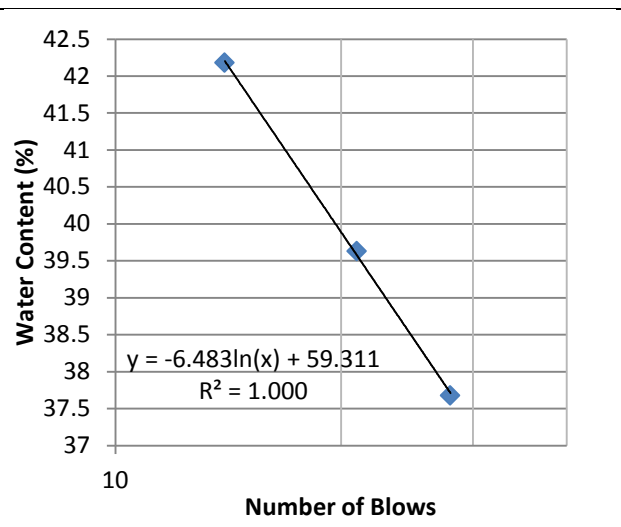
Liquid Limit	48
Plastic Limit	31
PL % Diff.	2.1



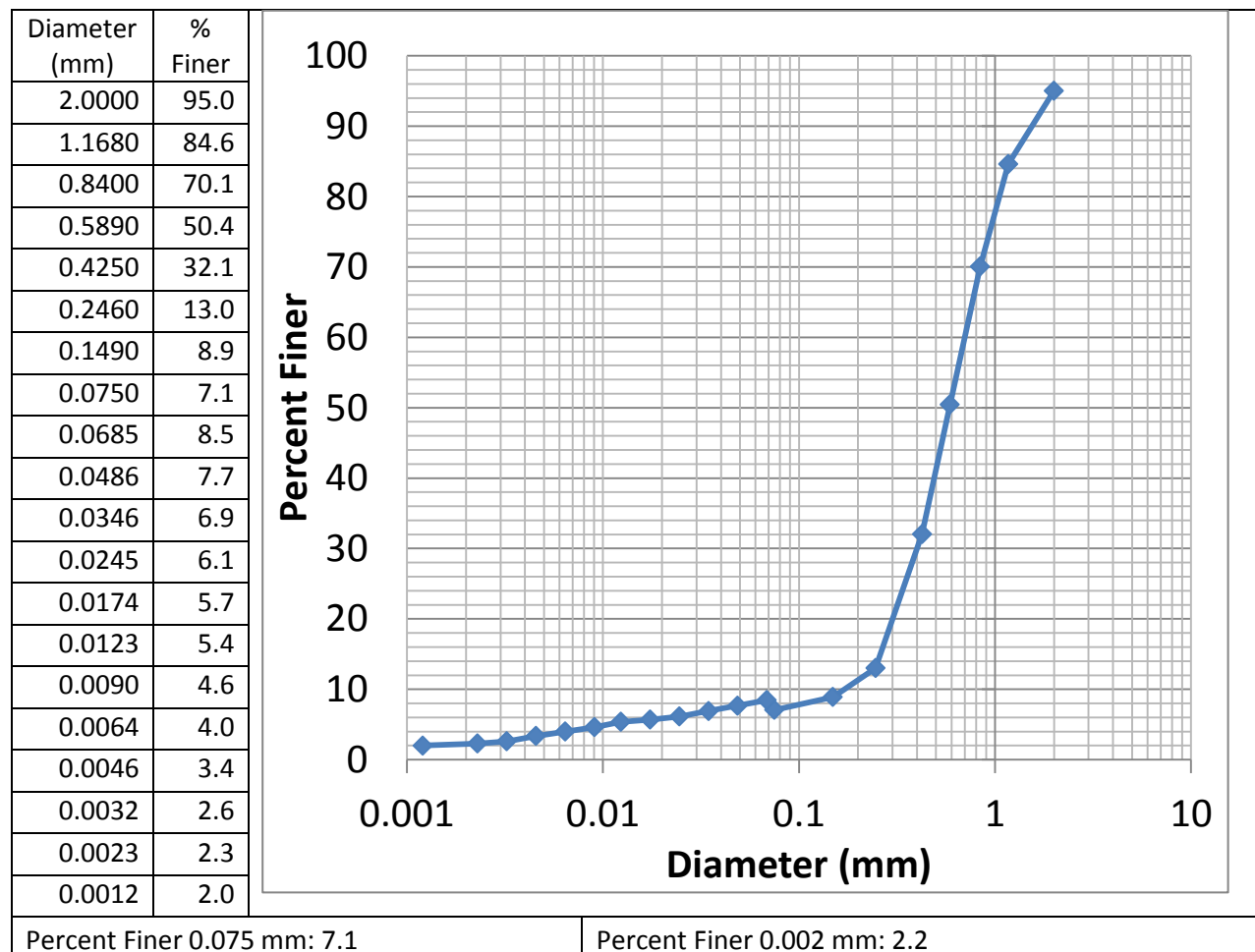
Boring: Z2-C1	Depth (m): 3.30-3.50	Sample Type: HQ3	Sample Label(s): C6a
Tested at: UCB	Notes: From Predrilling		



Liquid Limit	38
Plastic Limit	27
PL % Diff.	1.0

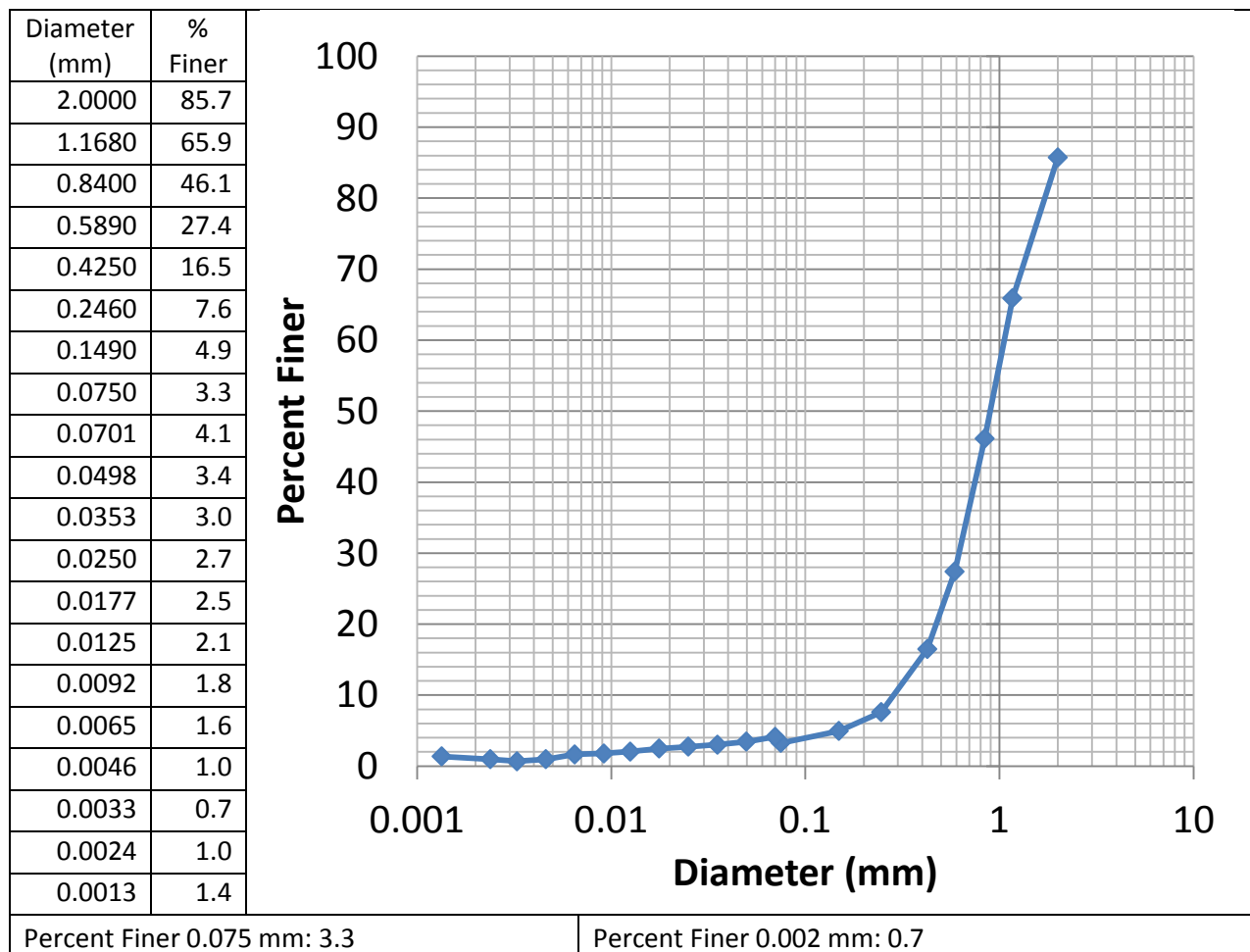


Boring: Z3-B1	Depth (m): 5.75-6.20	Sample Type: SPT	Sample Label(s): J1
Tested at: UCB	Notes:		



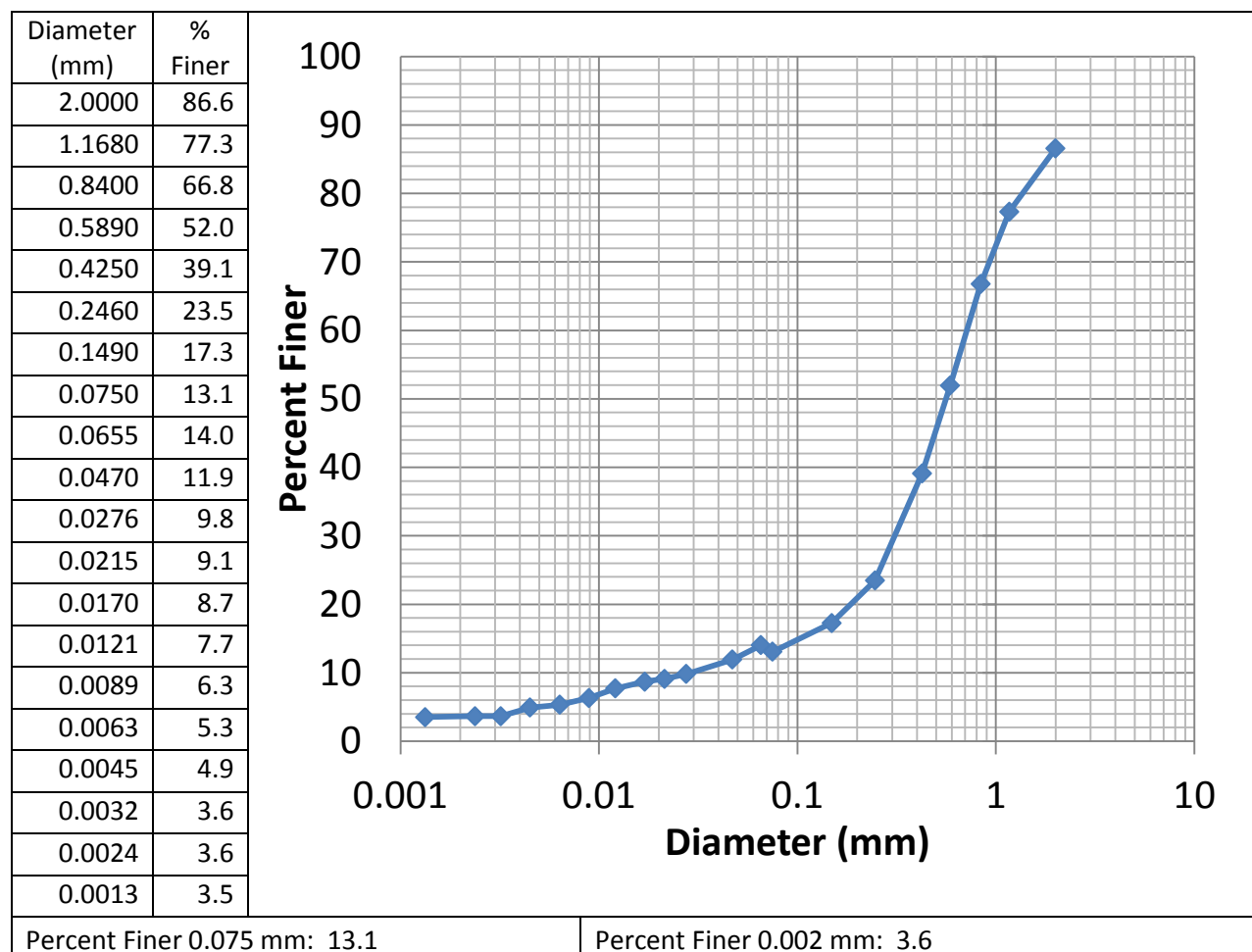
Liquid Limit	NP
Plastic Limit	NP
PL % Diff.	

Boring: Z3-B1	Depth (m): 6.50-6.95	Sample Type: SPT	Sample Label(s): J2
Tested at: UCB	Notes:		



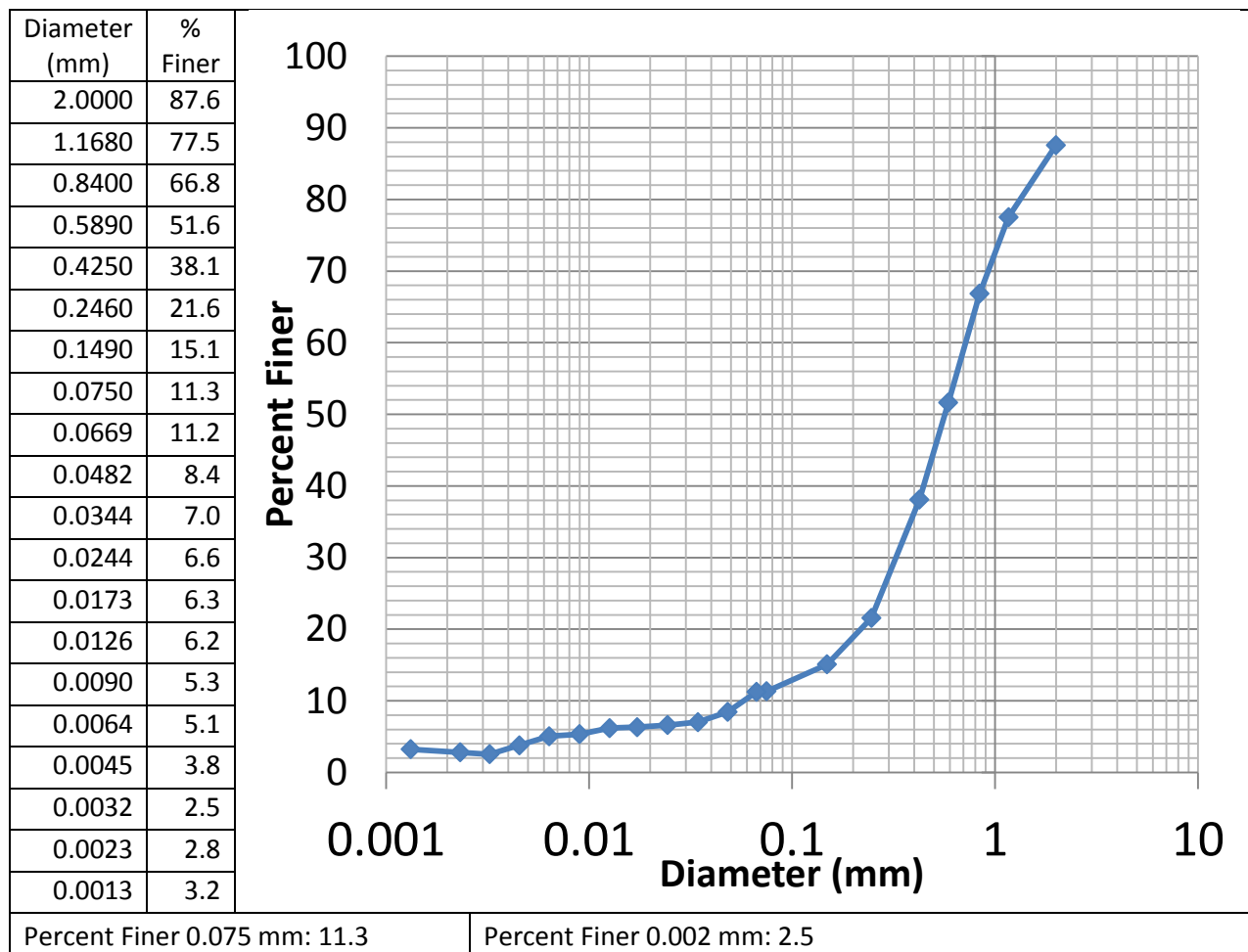
Liquid Limit	NP	
Plastic Limit	NP	
PL % Diff.		

Boring: Z4-B1	Depth (m): 2.50-2.95	Sample Type: SPT	Sample Label(s): L1
Tested at: UCB	Notes:		



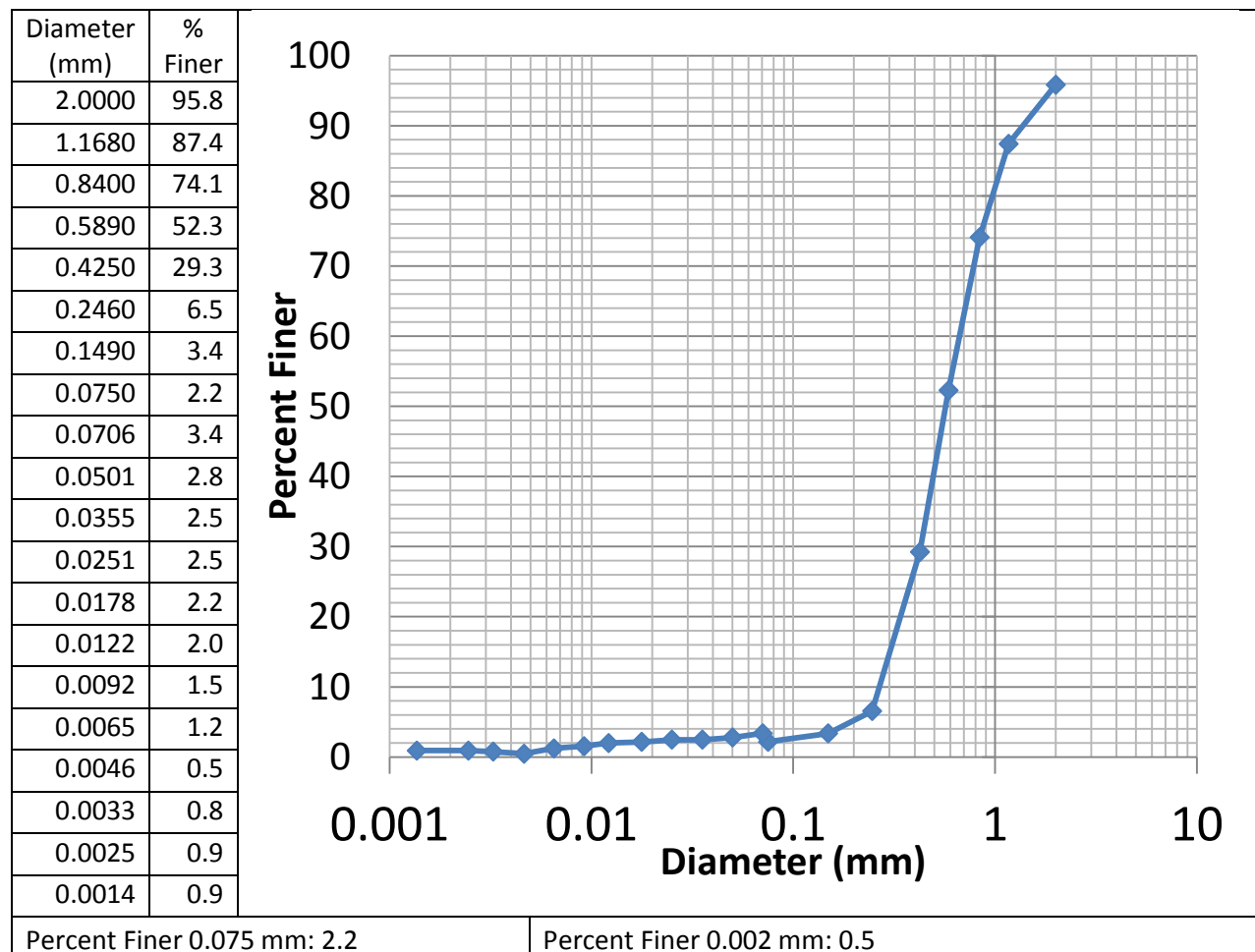
Liquid Limit	NP
Plastic Limit	NP
PL % Diff.	

Boring: Z4-B1	Depth (m): 3.25-3.70	Sample Type: SPT	Sample Label(s): L2
Tested at: UCB	Notes:		



Liquid Limit	NP
Plastic Limit	NP
PL % Diff.	

Boring: Z4-B1	Depth (m): 6.25-6.70	Sample Type: SPT	Sample Label(s): L3
Tested at: UCB	Notes:		



Liquid Limit	NP
Plastic Limit	NP
PL % Diff.	

